

LOW-CYCLE FATIGUE AND LIFE PREDICTION

Amzallag/Leis/Rabbe, editors

 **STP 770**

LOW-CYCLE FATIGUE AND LIFE PREDICTION

A symposium
sponsored by
French Metallurgical Society
and ASTM
Firminy, France, 23-25 Sept. 1980

ASTM SPECIAL TECHNICAL PUBLICATION 770
C. Amzallag, Creusot-Loire
B. N. Leis, Battelle Columbus Laboratories
P. Rabbe, Creusot-Loire
editors

ASTM Publication Code Number (PCN)
04-770000-30



1916 Race Street, Philadelphia, Pa. 19103

Copyright © by AMERICAN SOCIETY FOR TESTING AND MATERIALS 1982
Library of Congress Catalog Card Number: 81-70264

NOTE

**The Society is not responsible, as a body,
for the statements and opinions
advanced in this publication.**

**Printed in Baltimore, Md. (a)
August 1982**

Foreword

The International Symposium on Low Cycle Fatigue and Life Prediction, sponsored by the French Metallurgical Society and ASTM, was held in Firminy, France, on 23–25 September 1980. C. Amzallag and P. Rabbe, Creusot-Loire, served as chairmen. Messrs. Amzallag and Rabbe, and B. N. Leis, Battelle Columbus Laboratories, have edited this publication.

Related ASTM Publications

**Design of Fatigue and Fracture Resistant Structures, STP 761 (1982),
04-761000-30**

**Methods and Models for Predicting Fatigue Crack Growth under Random
Loading, STP 748 (1981), 04-748000-30**

Statistical Analysis of Fatigue Data, STP 744 (1981), 04-744000-30

**Fatigue Crack Growth Measurement and Data Analysis, STP 738 (1981),
04-738000-30**

Tables for Estimating Median Fatigue Limits, STP 731 (1981), 04-731000-30

Fatigue of Fibrous Composite Materials, STP 723 (1981), 04-723000-33

**Effect of Load Variables on Fatigue Crack Initiation and Propagation, STP
714 (1980), 04-714000-30**

Part-Through Crack Fatigue Life Prediction, STP 687 (1979), 04-687000-30

Fatigue Mechanisms, STP 675 (1979), 04-675000-30

**Service Fatigue Loads Monitoring, Simulation, and Analysis, STP 671 (1979),
04-671000-30**

**Cyclic Stress-Strain and Plastic Deformation Aspects of Fatigue Crack
Growth, STP 637 (1977), 04-637000-30**

A Note of Appreciation to Reviewers

This publication is made possible by the authors and, also, the unheralded efforts of the reviewers. This body of technical experts whose dedication, sacrifice of time and effort, and collective wisdom in reviewing the papers must be acknowledged. The quality level of ASTM publications is a direct function of their respected opinions. On behalf of ASTM we acknowledge with appreciation their contribution.

ASTM Committee on Publications

Editorial Staff

Jane B. Wheeler, *Managing Editor*
Helen M. Hoersch, *Senior Associate Editor*
Helen P. Mahy, *Senior Assistant Editor*
Allan S. Kleinberg, *Assistant Editor*
Virginia M. Barishek, *Assistant Editor*

Contents

Introduction	1
RESEARCH	
Influence of Microstructure on Elevated-Temperature Fatigue Resistance of a Titanium Alloy—C. HOFFMANN, D. EYLON, AND A. J. McEVILY	5
Low-Cycle Fatigue Damage Accumulation of Aluminum Alloys—C. BATHIAS, M. GABRA, AND D. ALIAGA	23
Creep and Cyclic Tension Behavior of a Type 316 Stainless Steel at Room Temperature—A. M. NOMINE, D. DUBOIS, D. MIANNAY, P. BALLADON, AND J. HERITIER	45
Evaluation of the Resistance of Type 316 Stainless Steel Against Progressive Deformation—A. PELLISSIER-TANON, J. L. BERNARD, C. AMZALLAG, AND P. RABBE	69
Lifetime Predictions and Cumulative Damage under High-Temperature Conditions—J. L. CHABOCHE	81
An Evaluation of Four Creep-Fatigue Models for a Nickel-Base Superalloy—H. L. BERNSTEIN	105
Damage Accumulation and Fracture Life in High-Temperature Low-Cycle Fatigue—V. M. RADHAKRISHNAN	135
Behavior in Fatigue-Relaxation of a High-Creep Resistant Type 316L Stainless Steel—M. MOTTOT, P. PÉTREQUIN, C. AMZALLAG, P. RABBE, J. GRATTIER, AND S. MASSON	152
Assessment of High-Temperature Low-Cycle Fatigue Life of Austenitic Stainless Steels by Using Intergranular Damage as a Correlating Parameter—C. LEVAILLANT AND A. PINEAU	169
Cumulation of High-Temperature Low-Cycle Fatigue Damage in Two-Temperature Tests—J. REUCHET, M. REGER, F. REZAI-ARIA, AND L. RÉMY	194

Low-Cycle Fatigue Damage Mechanisms in Body-Centered-Cubic Materials—T. MAGNIN AND J. H. DRIVER	212
Effect of Discontinuities on Low-Cycle Fatigue Behavior of NiMoV Rotor Forging Steel—G. A. MILLER, T-T. SHIH, H. S. REEMSNYDER, AND C. E. SWENSON	227
Application of Low-Cycle Fatigue Test Results to Crack Initiation from Notches—M. TRUCHON	254
Prediction Capability and Improvements of the Numerical Notch Analysis for Fatigue Loaded Aircraft and Automotive Components—H. NOWACK, D. HANSCHMANN, J. FOTH, G. LÜTJERING, AND G. JACOBY	269
Low-Cycle Fatigue Behavior of Thick High-Strength Steel Plates for Pressure Vessels—R. D'HAEYER AND P. SIMON	296
Low-Cycle Fatigue Behavior of Welded Joints in High-Strength Steels—H.-P. LIEURADE AND C. MAILLARD-SALIN	311
Growth of Short Cracks During High Strain Fatigue and Thermal Cycling—R. P. SKELTON	337
Prediction of Fatigue Life of Smooth Specimens of SG Iron by Using a Fracture Mechanics Approach—M. S. STARKEY AND P. E. IRVING	382
Growth of Physically Short Corner Cracks at Circular Notches—B. N. LEIS AND R. D. GALLIHER	399
Fatigue Crack Initiation of Cr-Mo-V Steel in High-Temperature Environment—KAORU WADA, YUTAKA IINO, AND MASAHICO SUZUKI	422
Fatigue Behavior of Carbon Steel Components in High-Temperature Water Environments—S. RANGANATH, J. N. KASS, AND J. D. HEALD	436
Effect of Light-Water Reactor Environments on Fatigue Crack Growth Rate in Reactor Pressure Vessel Steels—KARI TÖRRÖNEN AND W. H. CULLEN, JR.	460
Two Decades of Progress in the Assessment of Multiaxial Low-Cycle Fatigue Life—M. W. BROWN AND K. J. MILLER	482
Multiaxial Nonproportional Cyclic Deformation—D. L. McDOWELL, D. F. SOCIE, AND H. S. LAMBA	500

Low-Cycle Fatigue under Biaxial Strain—A. MOGUEROU, R. VASSAL, G. VESSIERE, AND J. BAHUAUD	519
---	------------

APPLICATIONS

The Concept of Uniform Scatter Bands for Analyzing <i>S-N</i> Curves of Unnotched and Notched Specimens in Structural Steel— E. HAIBACH AND C. MATSCHKE	549
--	------------

Fatigue Life Evaluation of the A-7E Arresting Gear Hook Shank— D. J. WHITE, J. R. ELLIS, C. E. DUMESNIL, AND T. D. GRAY	572
--	------------

Use of Low-Cycle Fatigue Data for Pressure Vessel Design—C. W. LAWTON	585
--	------------

Materials-Data Needs for Fatigue Design of Pressure Vessel Systems— C. E. JASKE	600
--	------------

Influence of Local Strain Distribution on Low-Cycle Fatigue Behavior of Thick-Walled Structures—VATROSLAV GRUBISIC AND C. M. SONSINO	612
---	------------

SUMMARY

Summary	633
Index	639

Introduction

Design against fatigue has been a concern of engineers since the identification of fatigue as a failure mode in the middle of the 19th century. Since that time, several key studies have given definition to the process and led to the development of rational design tools. One major development was the isolation of cyclic plastic strain as a measure of materials fatigue damage and as a basis for correlating materials cyclic deformation and fatigue life behavior. Another major development made use of fracture mechanics concepts to characterize the driving force for cracking and the materials resistance to that driving force.

This volume includes papers presented at the Conference on Low-Cycle Fatigue and Life Prediction, organized under the auspices of the French Metallurgical Society and ASTM by Messrs. P. Rabbe and C. Amzallag. This symposium truly had an international flavor. Forty-four papers were presented at Maison de la Culture—Le Corbusier, de Firminy, in September 1980, to an audience representing more than 14 countries from 4 continents.

Papers selected in response to the call for papers fell into three broad categories. The first category was basic research on the fatigue of metals. Three conference sessions were devoted to this, embracing aspects such as nonproportional plasticity, short cracks, and damage theories. The second category was phenomenology and modeling. Three sessions were also allocated to this category, which included subjects such as effects of service environment (temperature/atmosphere) and the evaluation and verification of popular modeling techniques. Lastly, the third category focused on applications and design aspects. The single session devoted to this topic included consideration of aspects such as multiaxial stressing and the integration of research data and phenomenology into design codes.

Because of the range of subjects covered, this volume should become a valuable source of information for all those involved in designing against fatigue. The assistance of the organizing committee, which was essential to the development and running of the conference, is gratefully acknowledged, as are the contributions of the session chairmen and the reviewers. We appreciated the advice and help of the ASTM staff. Lastly, the support of both Battelle Columbus Laboratories and Creusot-Loire is acknowledged, along

with the help of Ms. Cheryl Nance (BCL) who carried on the bulk of the correspondence during the editorial process.

C. Amzallag

Creusot-Loire, Firminy, France; symposium
co-chairman and co-editor

B. N. Leis

Battelle Columbus Laboratories, Columbus,
Ohio; co-editor

P. Rabbe

Creusot-Loire, Firminy, France; symposium
co-chairman and co-editor

Research

Influence of Microstructure on Elevated-Temperature Fatigue Resistance of a Titanium Alloy

REFERENCE: Hoffmann, C., Eylon, D., and McEvily, A. J., "Influence of Microstructure on Elevated-Temperature Fatigue Resistance of a Titanium Alloy," *Low-Cycle Fatigue and Life Prediction*, ASTM STP 770, C. Amzallag, B. N. Leis, and P. Rabbe, Eds., American Society for Testing and Materials, 1982, pp. 5-22.

ABSTRACT: The strain-controlled, elevated-temperature, low-cycle fatigue behavior of a near α titanium alloy, Ti-6Al-2Sn-4Zr-2Mo-0.1Si (Ti-6242S), has been studied in both air and vacuum (10^{-5} torr) at 525°C over a range of frequency and strain. Of particular interest in this investigation were the influence of microstructure and environment on fatigue behavior. Two different microstructures were obtained by combinations of mechanical processing and heat treatment above and below the β -transus temperature. Particular attention was given to these microstructural variations and to the effect of environment on the high-temperature low-cycle fatigue behavior of this alloy. The nature of fatigue crack initiation sites was examined by a precision sectioning method. The microstructure was found to have a pronounced effect on fatigue life as well as on the fatigue crack initiation process. Tests performed in vacuum revealed no influence of frequency on fatigue life, which indicated that environmental factors were responsible for the observed frequency effect on tests performed in air. It was also observed that testing in vacuum led to the formation of a number of subsurface crack nucleation sites and to a longer fatigue life. Crack origins in specimens tested in air were located at the surface, and the initiation sites were larger than those observed in vacuum. The features of a fatigue resistant microstructure in addition to environmental effects at elevated temperature are identified and discussed.

KEY WORDS: fatigue (materials), titanium alloys, elevated temperature, microstructure, crack initiation, subsurface cracking

A wide variety of microstructures can be produced in titanium alloys by altering mechanical-processing and heat-treatment parameters. Studies have shown that microstructure can play an important role in determining the mechanical properties, such as tensile properties, fracture toughness, and creep, as well as the fatigue behavior of the alloy [1-12].³ It has been deter-

¹ Graduate Assistant and Professor, respectively, Department of Metallurgy, University of Connecticut, Storrs, Ct. 06268.

² Metcut-Materials Research Group, Wright-Patterson Air Force Base, Ohio 45433.

³ The italic numbers in brackets refer to the list of references appended to this paper.

mined that certain microstructures which can produce optimum characteristics in terms of any one property may not provide adequate all-around performance with respect to other important material property requirements. Thus microstructures must be developed that have the necessary combination of properties for particular applications. The strong microstructure influence on mechanical properties of titanium alloys results in conflicts in terms of material property requirements when designing for resistance to fatigue crack initiation and resistance to fatigue crack growth that are used as criteria for "fail safe" design [5]. In general, it has been found that microstructures produced at temperatures above the β -transus temperature (β processed) yield better fatigue crack growth characteristics [1,5,6], while microstructures produced at temperatures below the β -transus ($\alpha+\beta$ processed) provide better resistance to fatigue crack initiation [7-10,12]. Conflicting microstructural requirements such as these have led to the suggestion [12] that in future applications it may be necessary to produce components of dual microstructure that will provide resistance to fatigue crack initiation at the surfaces while the material in the interior will have a microstructure that is resistant to fatigue crack growth.

The fatigue crack propagation process is generally believed to be more important than the crack initiation process in determining low-cycle fatigue behavior, since fatigue crack initiation usually occurs very early in the fatigue lifetime and thus the majority of low-cycle fatigue cycles are expended in propagating a fatigue crack to failure. For titanium alloys, however, it has been shown that the fatigue crack initiation process and the fracture toughness can assume dominant roles in determining low-cycle fatigue lifetimes [1,13,14]. All three of these parameters—crack initiation, crack growth, and fracture toughness—are dependent upon microstructure, therefore we can expect that low-cycle fatigue behavior will also be microstructurally dependent.

In addition to the effect of microstructure, high-temperature low-cycle fatigue (HTLCF) behavior is affected by the environment. There is only a limited amount of information available on high-temperature low-cycle fatigue of titanium alloys, and the effect of oxidation during elevated-temperature low-cycle fatigue has not been examined in any great detail. Oxidation of titanium is known to occur in a two-stage process [12,15-17]. Formation of an oxide scale and diffusion of oxygen into the metal may be enhanced at grain boundaries and interfaces between phases [10,11]. Formation of an oxygen-enriched diffusion layer leads to an increase in hardness and a decrease in ductility at the surface, which may lead to premature crack initiation. Strain cycling at elevated temperature can enhance diffusion rates due to the generation of large numbers of defects. The depth of oxidation contamination, particularly along α/β interfaces, may be increased, which would lead to even earlier low-cycle fatigue failure.

The object of this work was to establish the effects of both microstructure

TABLE 1—Processing and heat treatment of Ti-6242S ($T_{\beta} = 995^{\circ}\text{C}$).

Condition Designation	Extrusion Temperature, $^{\circ}\text{C}$	Swaging Temperature, $^{\circ}\text{C}$	Solution Temperature and Time	Stabilizing Temperature and Time
6.1	$T_{\beta}+42$	$T_{\beta}+42$	$T_{\beta}-28^{\circ}\text{C}/2\text{h}/\text{AC}$	$595^{\circ}\text{C}/8\text{h}/\text{AC}$
6.4	$T_{\beta}-83$	$T_{\beta}-42$	$T_{\beta}-11^{\circ}\text{C}/1\text{h}/\text{AC}$	$595^{\circ}\text{C}/8\text{h}/\text{AC}$

and oxidation on the high-temperature low-cycle fatigue behavior of a near α titanium alloy, Ti-6Al-2Sn-4Zr-2Mo-0.1Si (Ti-6242S), at 525°C . Two different microstructures were tested in air and vacuum, and comparisons are made between the test results for each condition.

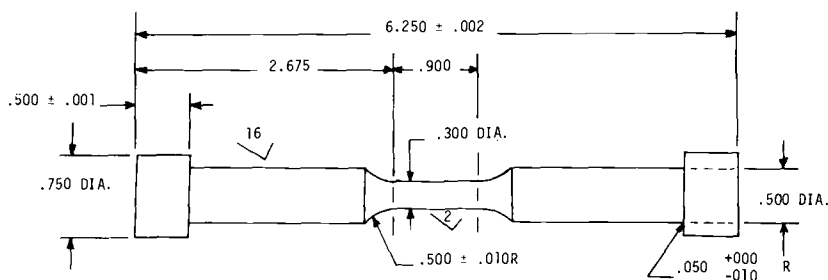
Experimental Procedures

Material

Two different microstructures were prepared from a Ti-6242S alloy produced by RMI (Reactive Metals Inc.) and supplied in the form of 75-mm-diameter round bars. The β -transus temperature of this alloy was determined to be $995 \pm 5^{\circ}\text{C}$. The material was hot-worked in a two-step process, a 6:1 ratio extrusion followed by a 3:1 ratio hot swage. Processing temperatures are summarized in Table 1.

Testing

High-temperature low-cycle fatigue tests were performed under total axial strain control at 525°C in a servohydraulic test machine. A uniform gage section specimen was used with buttonhead ends for gripping (Fig. 1). Both microstructures of the Ti-6242S alloy were tested in air and in vacuum (10^{-5} torr) at 0.25 and 0.04 Hz. A triangular waveform was used at 0.25 Hz. At the



ROUND BUTTONHEAD LCF SPECIMEN (ALL DIMENSIONS IN INCHES).

FIG. 1—Specimen design for high-temperature low-cycle fatigue testing under axial strain control.

lower frequency of 0.04 Hz, 10-s hold periods were introduced into the same triangle wave at peak tensile and compressive strains. In so doing, similar strain rates were achieved for both test frequencies. The number of cycles to failure, N_f , was taken as the point at which the peak tensile stress decreased by 5 percent from the saturated value. An x-y recorder was used to periodically record hysteresis loops while a strip chart recorder maintained continuous load versus time and strain versus time records. Some tests were continued to final separation. Others were terminated prior to fracture and the samples were pulled apart at room temperature to permit examination of the fracture surfaces.

Microscopy

The two microstructures obtained in the Ti-6242S alloy were characterized using optical microscopy. The nature of fatigue crack initiation sites was studied using a precision sectioning technique [18]. Specimens at higher total strain ranges were selected for this examination, since in previous work high strain range values led to more crack initiation sites, which made characterization easier [11].

Specimens were prepared for observation by precision sectioning on a plane parallel to the tensile axis through the initiation locations. This method has been successfully used to determine the nature of surface subsurface fatigue crack origins in titanium alloy forgings [2], castings [19,20], and powder compacts [16,21].

Scanning electron microscopy (SEM) was used to examine fracture surfaces of fatigue specimens and precision sectioned specimens.

Results

Microstructures

The Ti-6242S microstructures tested in this investigation are shown in Fig. 2. The microstructure of condition 6.1 (Fig. 2a) is a coarse α annealed structure that resulted from the combination of β -work and $\alpha+\beta$ heat treatment (Table 1). This microstructure consists of α platelets separated by thin layers of β phase. The microstructure of condition 6.4 (Fig. 2b) is an $\alpha+\beta$ structure with a relatively low percentage of equiaxed alpha particles present. The equiaxed α is surrounded by a transformed β matrix consisting of fine α platelets surrounded by a thin film of β phase.

High-Temperature Low-Cycle Fatigue

Results of high-temperature low-cycle fatigue tests performed in air are given in Fig. 3. It can be seen that the $\alpha+\beta$ microstructure of condition 6.4

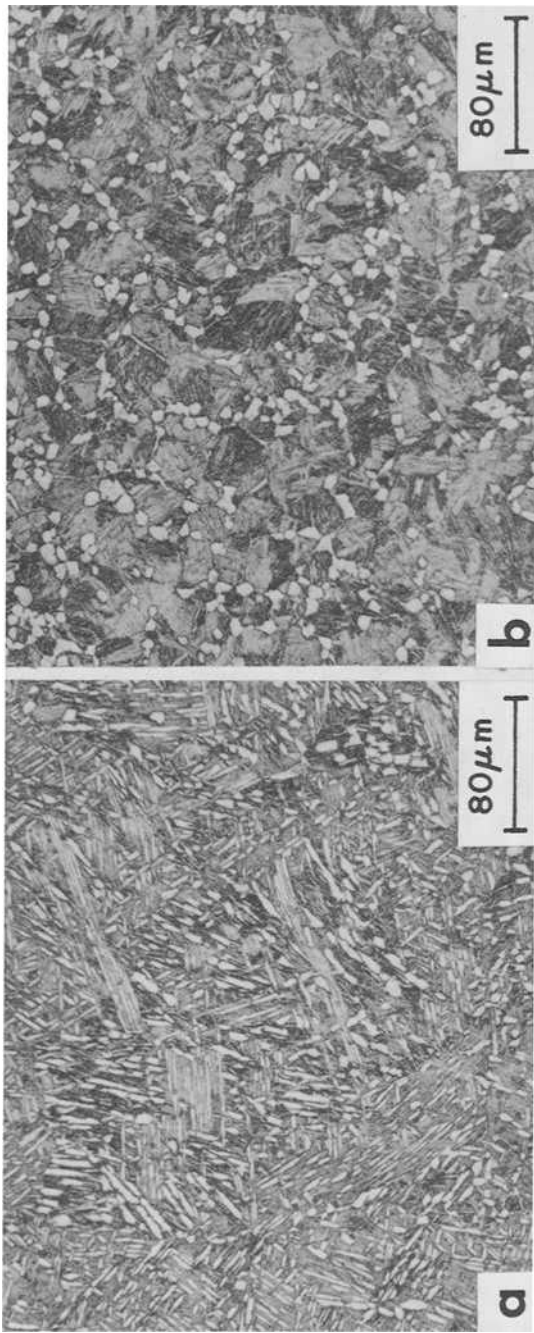


FIG. 2—Microstructures of Ti-6242S. (a) Condition 6.1, β -processed structure showing coarse elongated α platelets. (b) Condition 6.4, $\alpha + \beta$ structure consisting of equiaxed α surrounded by a transformed β matrix. (Etchant is 7 percent HNO_3 , 2 percent HF , and 91 percent H_2O .)

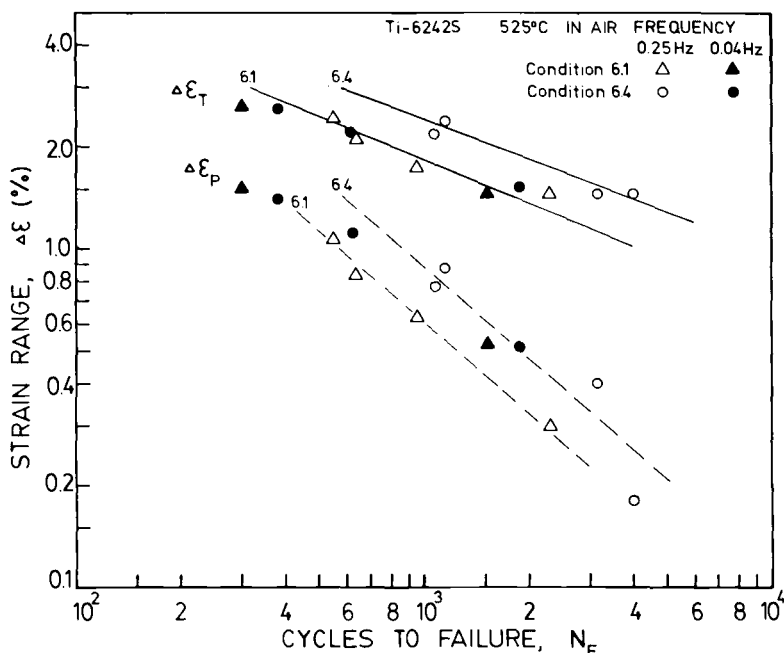


FIG. 3—Strain range versus cycles to failure for Ti-6424S. Conditions 6.1 and 6.4 tested at 0.25 and 0.04 Hz at 525°C in air.

has superior low-cycle fatigue resistance to the β processed microstructure of condition 6.1. This result is in agreement with previous findings, at both room and elevated temperature, that $\alpha+\beta$ microstructures have better low-cycle fatigue resistance than β processed structures [1,7-10,12-14].

Decreasing the cycle frequency has a tendency to reduce lifetimes when they are compared in terms of total strain range (Fig. 3). This result follows the general trend observed for most materials in low-cycle fatigue at elevated temperature. This behavior has been observed for other titanium alloys [7,10]. The frequency effect is not as easily recognized when tests results are compared on the basis of the plastic strain range. However, the frequency effect is present in the form of an increased plastic strain range that occurs due to the relaxation during hold periods.

Figure 4 compares high-temperature low-cycle fatigue results in air and vacuum. It is apparent that lifetimes are significantly improved in vacuum tests. Plastic strain ranges are also higher in vacuum for a given total strain range than they are in air. Tests at the lower frequency, 0.04 Hz, in vacuum did not reveal any frequency effect in terms of either total or plastic strain range in the absence of the air environment. No significant increase occurred in the plastic strain range for tests conducted at 0.04 Hz in vacuum. Additionally, it was observed that the saturated stress range was higher in air for a given plastic strain range than in vacuum tests (Fig. 5).

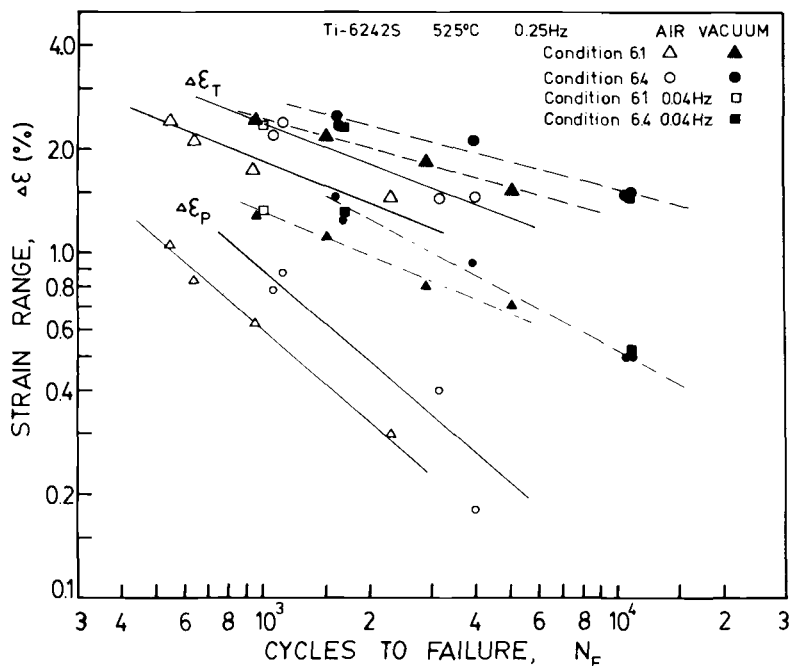


FIG. 4—Strain range versus cycles to failure for Ti-6242S. Conditions 6.1 and 6.4 tested at 525°C in air and vacuum (10^{-5} torr).

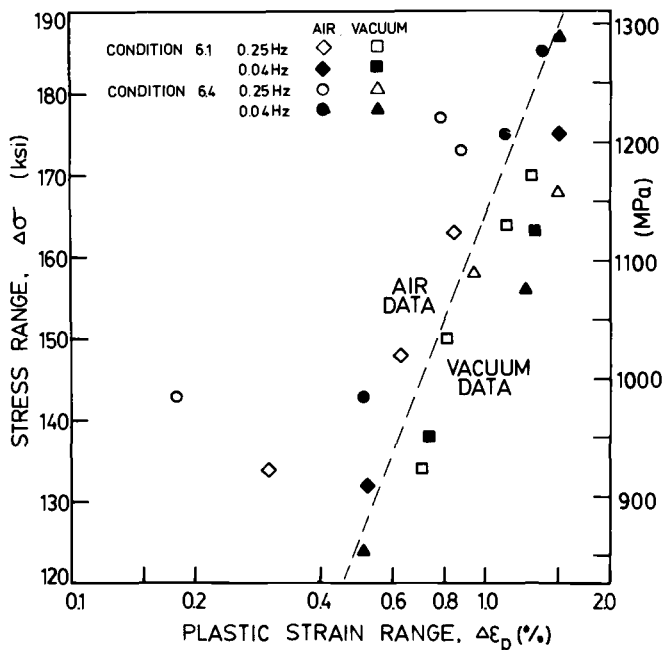


FIG. 5—Saturated stress range versus plastic strain range for air and vacuum (10^{-5} torr). Higher stress ranges are observed in air tests for a given plastic strain range.

Microscopy

Fracture surfaces of air and fatigue specimens were examined by SEM. In general it was observed that the fracture surface of the vacuum tested specimens was more faceted and tortuous than air-tested specimens as a result of multiple subsurface initiation sites occurring during HTLCF in vacuum. It was previously demonstrated in other titanium alloys both at room [1,13] and elevated temperatures [14] that the fatigue lives are predominantly controlled by crack initiation. Therefore the crack initiation characteristics of the vacuum and air-tested specimens were examined by the precision sectioning technique in order to understand the differences in their fatigue strength and fracture morphology. All observed air test initiation sites were at the specimen surface (Figs. 6a to 6d). Most cracks initiated along α/β interfaces (Figs. 6a to 6c), with a few cracks initiating across colonies of α plates (Fig. 6d). Cracks were more numerous and greater in length in the condition 6.1 microstructure than in the condition 6.4 microstructure.

On the other hand, most of the vacuum test cracks initiated from subsurface locations (Figs. 7a, 7b, and 7d), although a few small surface cracks were also observed (Fig. 7c). Some internal cracks partially follow α plate boundaries (Fig. 7b at A and B), and some are parallel to intense shear bands (Fig. 7d at C and D); the latter can be observed in the microstructure (Fig. 8).

SEM examination of fracture surfaces revealed numerous subsurface initiation sites in specimens tested in vacuum (Fig. 9). Fracture facets were located at the origins of some of these subsurface cracking sites (Fig. 10). Microstructural features are often revealed on the facet surface that correspond to interfaces between α platelets. Another interesting feature of the fracture facet was that in many cases a small pore seemed to be located at the base or point of origin of the facet (Fig. 10 at A).

Discussion

The results of the high-temperature low-cycle fatigue tests in this program have shown that the $\alpha+\beta$ microstructure (condition 6.4) has better low-cycle fatigue resistance than the β processed microstructure (condition 6.1). Previous investigations have found this to be true for other titanium alloys both at room temperature [1,13] and elevated temperature [7-12]. It is generally believed that the cause for the difference in fatigue lifetime is due to the effects of the different microstructures on the fatigue crack initiation process [7-12]. The β processed structures have long α/β interfaces at which crack initiation can occur with relative ease.

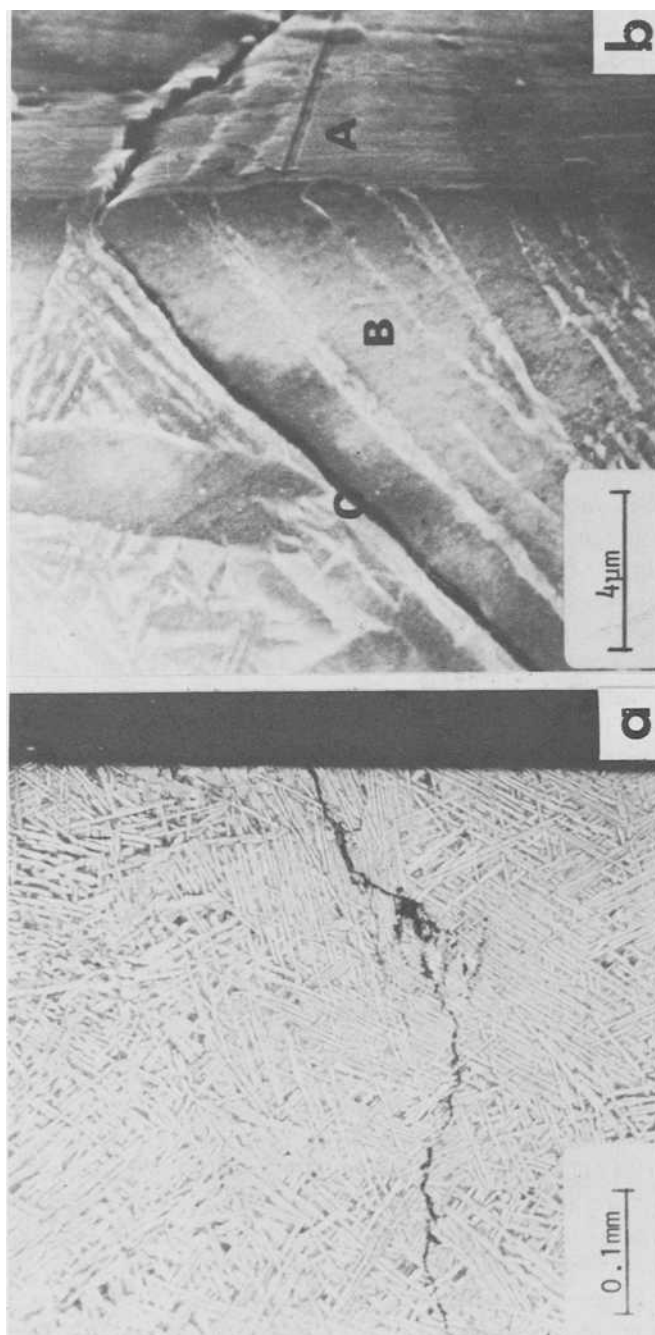
The environment is also an important factor in determining the low-cycle fatigue behavior of titanium alloys, as evidenced by the comparison of air and vacuum tests in Fig. 4. Oxidation at elevated temperature can accelerate crack initiation by enhanced diffusion of oxygen along α/β interfaces. Eylon and co-workers [10,11] have also accounted for the effects of frequency and

temperature in terms of increased oxidation. For tests in air, a distinct decrease in cycles-to-failure versus total strain range is observed when the frequency is reduced from 0.25 to 0.04 Hz. The frequency effect is not as obvious when comparing plastic strain range versus cycles-to-failure at the two cyclic frequencies. This is because of stress relaxation that occurs at the lower cyclic frequency with hold times. The relaxation results in an increase in the amount of plastic strain for a given total strain range. The apparent absence of any frequency effect in vacuum tests in terms of either total or plastic strain range is further evidence that the major time-dependent influence is that of the environment.

Plastic strain ranges for tests in vacuum at both frequencies are generally found to be larger than those in air for a given total strain range. During tests in air, oxidation of the surface of the specimen results in an increase in strength level and a decrease in ductility. These changes reduce the amount of plastic strain at a particular total strain range, and also explain the result that saturated stress range levels are generally observed to be higher for tests in air than in vacuum for equal amounts of plastic strain (Fig. 5). These observations are an indication that oxygen penetration into the material could be occurring to fairly substantial depths. If oxidation is going to affect the bulk properties of the alloy, such as yield strength, then oxygen must be penetrating relatively deep into the material. However, for the times and temperatures involved in the present test program, bulk diffusion of oxygen could not possibly occur to a great enough depth to alter the bulk material properties. The observed changes, therefore, lend further credence to the possibility that interface diffusion plays an important role. It is known that oxygen diffusion rates are higher in β -titanium and that oxidation rates are also higher for β -titanium alloys. Pipe diffusion of oxygen along α/β interfaces, which will induce β to α transformation and will generate new dislocations, appears to be the only available mechanism which can allow sufficient oxygen penetration to occur such that bulk material properties might be affected.

Most air test cracks were initiated along α/β interfaces. Because of the lamellar morphology of the α phase, the interfaces are planar and, consequently, the initial cracks are also planar (Fig. 6b). In most cases, the cracked interfaces are at 30 to 60 deg to the tensile direction. This surface-connected interface cracking is an indication of environmental effects on fatigue crack initiation. A very similar initiation mode was observed in previous work [11] on Ti-5Al-5Sn-2Zr-2Mo-0.1Si (Ti-5522S) with a similar microstructure and under similar test conditions. Environmental-assisted crack initiation and growth can explain the decrease in fatigue life when temperature is increased and test frequency is decreased. It can also explain the lower fatigue life associated with testing in air.

The planar surface cracking across an α plate colony (Fig. 6d) was identified in previous works as the major mode of fatigue crack initiation in room-



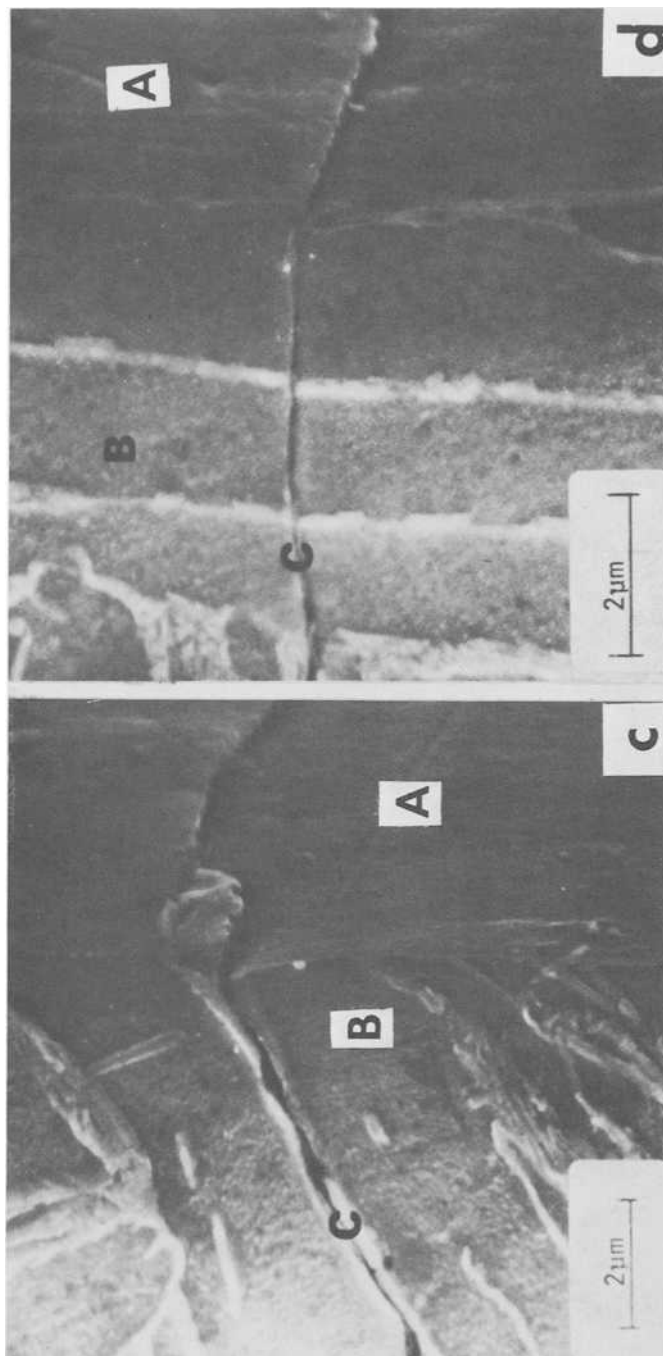
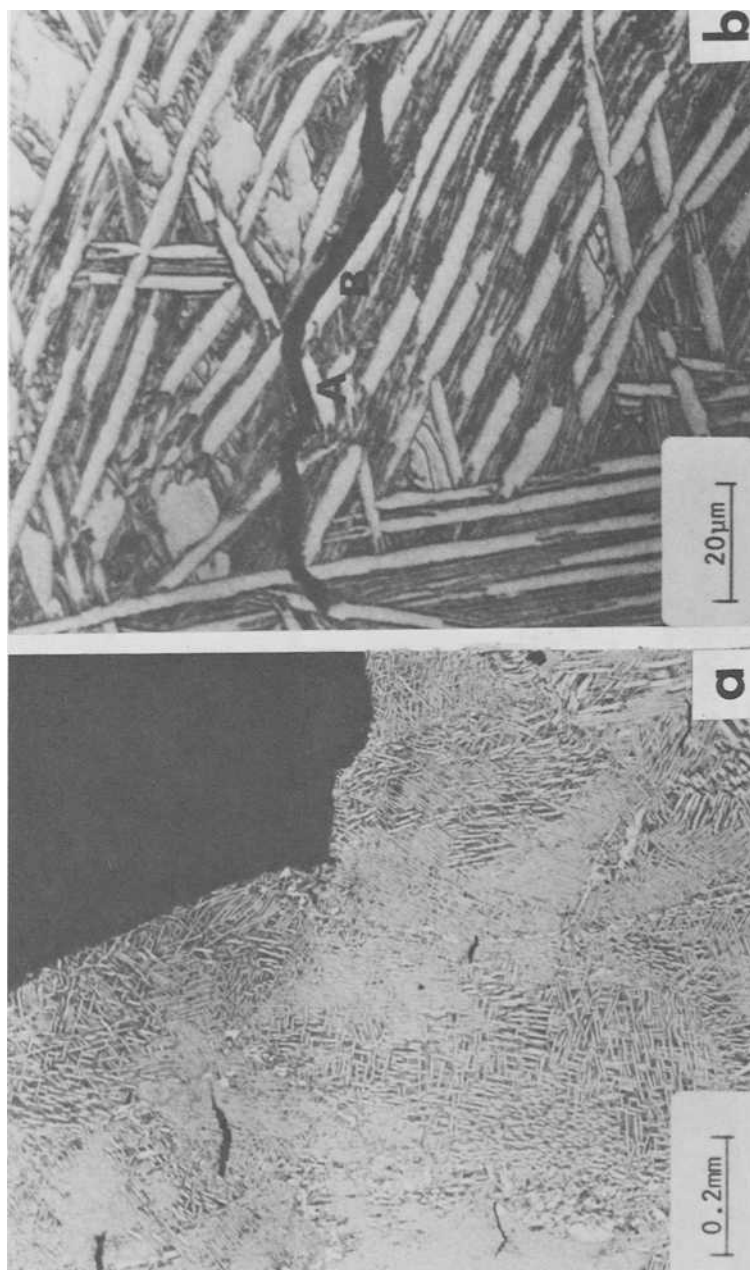


FIG. 6—Air test initiation sites in specimen sectioned parallel to the tensile axis. Plane A represents the specimen surface, Plane B represents the etched sectioned plane, and C is the initial crack.



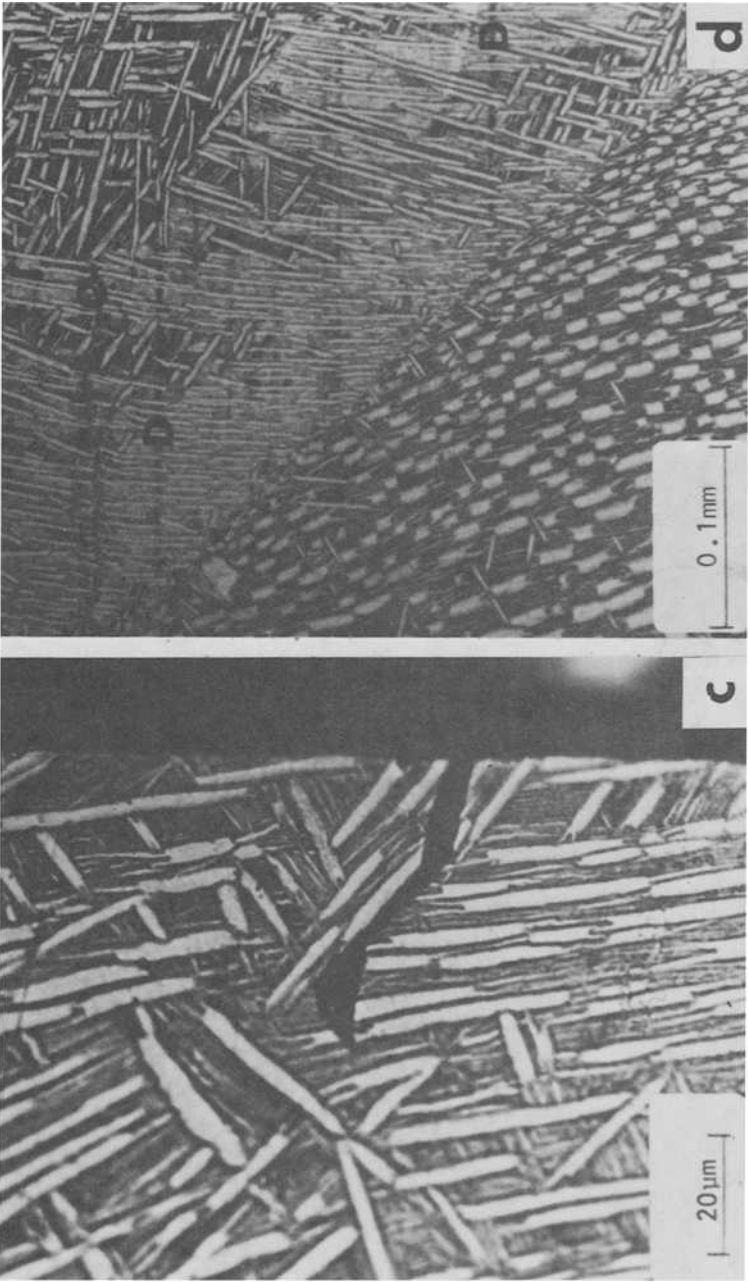


FIG. 7—Vacuum test crack initiation sites. (a) Multiple subsurface cracking sites. (b) Cracking along a platelets at A and B. (c) Surface initiation site observed in vacuum tested specimen. (d) Subsurface cracking parallel to intense shear bands.

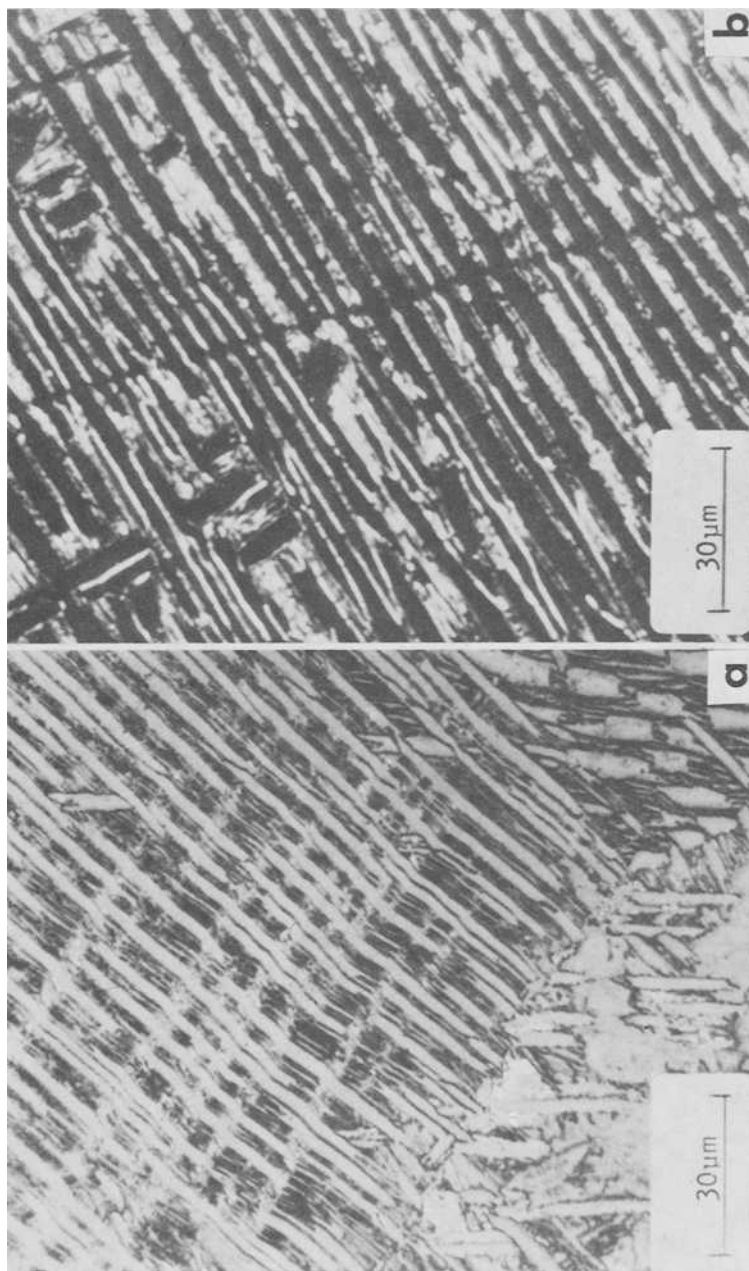


FIG. 8—Intense shear bands observed through the microstructure.

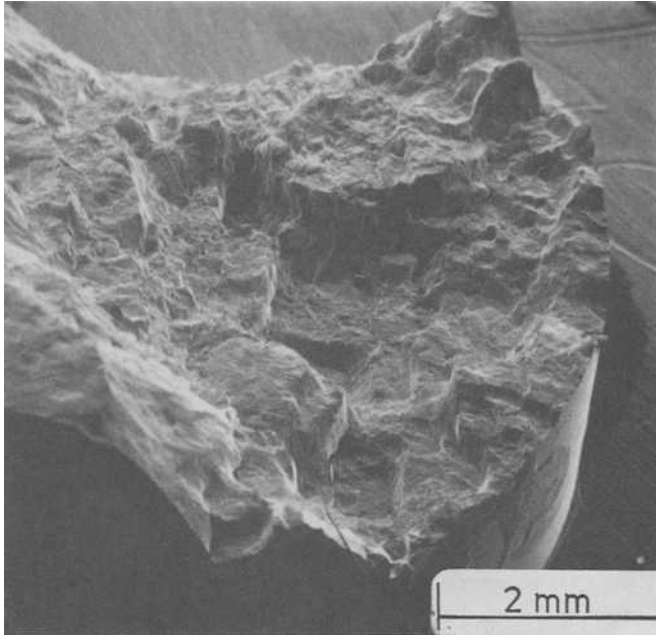


FIG. 9—Fracture surface of vacuum tested specimen revealing multiple subsurface crack initiation sites.

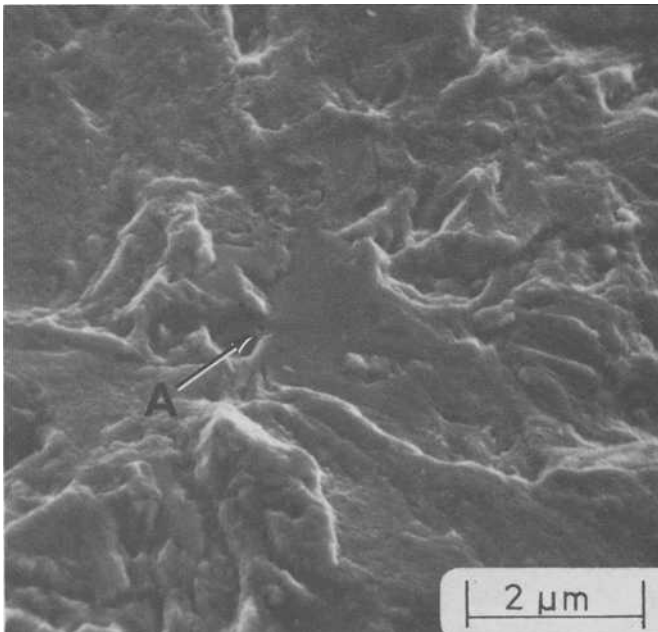


FIG. 10—Origin of subsurface crack initiation site. A small pore is observed associated with the cleavage facet at the point of crack initiation.

temperature tests of alloys with similar microstructures [2,16,22]. This cracking was related to the presence of intense shear bands across the α plate colonies on basal and prismatic planes [23]. An evidence of intense shear activity is shown in Figs. 8a and 8b, and was found in this study only in vacuum-tested material. This mode of cracking represents only a small portion of the initial cracks.

The surface-connected cracks in the vacuum tests (Fig. 7c) are very limited in size. The major fatigue failure was initiated by the linkage of many subsurface cracks throughout the gage section (Fig. 7a) that are responsible for the tortuous appearance of those fracture surfaces. Some segments of the subsurface initial cracks follow α plate boundaries (A and B in Fig. 7b) and some are parallel to intense shear bands (C and D in Fig. 7d). It seems that in the absence of environmental assistance surface cracks did not propagate as rapidly into the specimen as they did in the air tests. This increased the number of cycles that the material was subjected to, and at the same time, allowed enough internal damage, such as shear band formation, to accumulate and generate subsurface cracks. Fractographic examinations showed that most fatigue fracture areas initiated from the subsurface locations and that the role of the small surface cracks in the total failure is minimal. It seems that in vacuum conditions, the main factor responsible for the increased fatigue strength and change of the failure morphology is the lack of dominant surface cracks.

The fracture facets observed at the subsurface cracking sites are similar to the "cleavage rosettes" described in earlier work [2]. Subsurface origins containing small pores were found in titanium alloy IMI 685 after low-cycle fatigue testing at room temperature. The source of the porosity, which was associated with subsurface fatigue crack initiation, was believed to be from incompletely healed casting porosity.

Conclusions

The near α titanium alloy Ti-6Al-2Sn-4Zr-2Mo-0.1Si (Ti-6242S) was tested under elevated-temperature low-cycle fatigue conditions at 525°C. Two different microstructures were tested in both air and vacuum environments. The purpose of this investigation was to determine the effects of microstructure and environment on the high-temperature low-cycle fatigue behavior of this alloy. The following conclusions have been drawn:

1. The $\alpha+\beta$ processed microstructure has the superior HTLCF resistance of the two microstructures tested.
2. The fatigue resistance of the β processed microstructure is decreased because it has less resistance to fatigue crack initiation.
3. Crack initiation in air tests occurs at the specimen surface predominantly along α/β interfaces as a result of preferential oxidation at these locations.

4. Subsurface crack initiation sites in vacuum tests were the origins for fatigue fracture. The role of surface cracking in vacuum was minimal.

5. Air environment plays an important role in determining the fatigue life-time and fatigue crack initiation process during HTLCF of titanium alloys.

6. The observed frequency effect on tests in air is due to environmental effects, namely oxidation. This conclusion is based on the apparent absence of any frequency effect for tests performed in vacuum.

7. The observation that the saturated plastic strain range is higher in vacuum tests than in samples tested in air is an indication that oxidation has affected the bulk material properties by an increase in strength level. It is believed that pipe diffusion of oxygen along α/β interfaces, to depths much greater than would be expected from bulk diffusion of oxygen, is responsible for the observed changes in material properties.

Acknowledgments

The authors express their appreciation to Dr. F. H. Froes of the Air Force Wright Aeronautical Laboratories Materials Laboratory for his encouragement and support during this program. The financial support for this research provided by the Air Force Office of Scientific Research, Contracts F49620-79-C-004 and F33615-79-C-5152, is also gratefully acknowledged.

References

- [1] Eylon, D., Hall, J. A., Pierce, C. M., and Ruckle, D. L., *Metallurgical Transactions*, Vol. 7A, 1976, pp. 1817-1826.
- [2] Eylon, D. and Hall, J. A., *Metallurgical Transactions*, Vol. 8A, 1977, pp. 981-990.
- [3] Bania, P. J. and Eylon, D., *Metallurgical Transactions*, Vol. 9A, 1978, pp. 847-855.
- [4] Richards, N. L. and Barnby, J. T., *Materials Science and Engineering*, Vol. 26, 1977, pp. 221-229.
- [5] Stubbington, C. A. in *Alloy Design for Fatigue and Fracture Resistance*, AGARD Conference Proceedings No. 185, Brussels, 1975.
- [6] Paton, N. E., Williams, J. C., Chesnutt, J. C., and Thompson, A. W. in *Alloy Design for Fatigue and Fracture Resistance*, AGARD Conference Proceedings No. 185, Brussels, 1975.
- [7] Bania, P. J., "The High Temperature Low Cycle Fatigue Behavior of a Near-Alpha Titanium Alloy," Ph.D. dissertation, Department of Materials Science and Metallurgical Engineering, University of Cincinnati, 1977.
- [8] Funkenbusch, A. W. and Coffin, L. F., *Metallurgical Transactions*, Vol. 9A, 1978, pp. 1159-1167.
- [9] Sprague, R. A., Ruckle, D. L., and Smith, M. P. in *Titanium Science and Technology*, Vol. 3, R. I. Jaffee and H. M. Burte, Eds., Plenum Press, New York, 1973, pp. 2069-2079.
- [10] Eylon, D., Rosenblum, M. E., and Fujishiro, S. in *Proceedings, Fourth International Conference on Titanium*, H. Kumura and O. Izumi, Eds., American Institute of Mechanical Engineers, 1980, pp. 1845-1854.
- [11] Eylon, D., Bartel, T. L., and Rosenblum, M. E., *Metallurgical Transactions*, Vol. 11A, 1980, pp. 1361-1367.
- [12] Ruppen, J. A., Hoffmann, C. L., Radhakrishnan, V. M., and McEvily, A. J., *Twenty-Seventh Sagamore Army Materials Research Conference on Fatigue-Environment and Temperature Effect*, Bolton Landing, N. Y., July 1980, to be published.
- [13] Eylon, D. and Pierce, C. M., *Metallurgical Transactions*, Vol. 7A, 1976, pp. 111-120.

- [14] Eylon, D. and Kerr, W. R. in *Fractography in Failure Analysis*, ASTM STP 645, American Society for Testing and Materials, 1978, pp. 235-248.
- [15] Antony, K. C., *Journal of Materials*, Vol. 1, 1966, pp. 456-476.
- [16] Rudinger, K. and Weigand, H. H. in *Titanium Science and Technology*, Vol. 4, R. I. Jaffee and H. M. Burte, Eds., Plenum Press, New York, 1973, pp. 2555-2571.
- [17] Shamblen, C. E. and Redden, T. K. in *Science, Technology and Application of Titanium*, R. I. Jaffee and N. E. Promisel, Eds., Pergamon Press, Elmsford, N.Y., 1970, pp. 199-208.
- [18] Kerr, W. R., Eylon, D., and Hall, J. A., *Metallurgical Transactions*, Vol. 7A, 1976, pp. 1477-1480.
- [19] Eylon, D. and Strobe, B., *Journal of Materials Science*, Vol. 14, 1979, pp. 345-353.
- [20] Eylon, D., *Journal of Materials Science*, Vol. 14, 1979, pp. 1917-1922.
- [21] Eylon, D. and Birla, N., *Metallurgical Transactions*, Vol. 8A, 1977, pp. 367-369.
- [22] Eylon, D. and Bania, P. J., *Metallurgical Transactions*, Vol. 9A, 1978, pp. 1273-1279.
- [23] Shechtman, D. and Eylon, D., *Metallurgical Transactions*, Vol. 9A, 1978, pp. 1018-1020.

Low-Cycle Fatigue Damage Accumulation of Aluminum Alloys

REFERENCE: Bathias, C., Gabra, M., and Aliaga, D., "Low-Cycle Fatigue Damage Accumulation of Aluminum Alloys," *Low-Cycle Fatigue and Life Prediction, ASTM STP 770*, C. Amzallag, B. N. Leis, and P. Rabbe, Eds., American Society for Testing and Materials, 1982, pp. 23-44.

ABSTRACT: Tests of fatigue crack initiation are carried out on two different aluminum alloys by using low-cycle fatigue (LCF) data to predict initiation at notch tips with a radius between 0.1 and 10 mm. A comparison of the LCF properties of these alloys in terms of stress strain and cyclic plastic energy is made. Damage accumulation laws in the range of plastic strain and elastic stress are studied. Variable-amplitude loading represented by programmed blocks characterizing the standard TWIST flight loading are investigated. Fatigue crack initiation at notches is determined; initiation is detected by the electric potential method. It is found that the energy approach is an accurate method of determining a realistic cyclic mechanical behavior of aluminum alloys. Constant-amplitude loading of low ΔK (stress intensity factor range) that causes no crack initiation decreases the number of cycles to crack initiation, when the loading program is composed of a higher ΔK and this low ΔK to form block loading.

KEY WORDS: low-cycle fatigue, crack initiation, plastic strain energy, function of damage, fatigue notch factor, programmed block loading, damage accumulation

Even in the case of nominal elastic loading, some zones have stress concentrations leading to plastic fatigue. Results obtained from classical fatigue tests must be used when dimensioning the structures. If the three phases of endurance (initiation + propagation + rupture) are considered, the results obtained are more accurate than those given by the Wöhler approach.

Fatigue crack initiation at the notch root is considered to be due to localized low-cycle fatigue (LCF). The cyclic behavior of the aluminum alloys was investigated in terms of stress, strain, and plastic strain energy. Results of LCF and cyclic stress-strain response were correlated to evaluate the crack initiation in notched specimens for uniform loading.

In reality, variable-amplitude loading is frequently met in aeronautical structures. The present paper is restricted to a study of the cumulative fatigue damage in two simple cases: (1) for the whole life duration, under cyclic strain control with zero mean strain; and (2) for the initiation under cyclic

¹ University of Technology, Compiègne, France.

² Societe Nationale Industrielle Aerospatiale, Suresnes, France.

TABLE 1—Chemical composition (weight percent).

Aluminum Alloy	Si	Fe	Cu	Mn	Mg	Cr	Ni	Zn	Ti	Ti+Zr
2124 T 351	0.11	0.23	4.35	0.60	1.45	0.01	...	0.04	0.02	...
2618 AT 6 (aged 10 h at 190°C)										
2618 AT 6 (aged 22 h at 203°C)	0.21	1.07	2.62	0.03	1.48	0.01	1.22	0.04	0.10	...

TABLE 2—*Tensile properties.*

Aluminum Alloy	Sense	0.2 MPa	<i>m</i> , MPa	<i>A</i> , %
2124 T 351	. . .	274	439	18.1
2618 AT 6 (aged 10 h at 190°C)	TL	329	444	9.1
2618 AT 6 (aged 10 h at 203°C)	. . .	371	427	7.3

load control where plastic cycles are combined with elastic ones but with a different mean load level. Only in the first case is a linear damage accumulation found.

Our investigations are not directed to the study of the case of different mean stresses and their effect on damage accumulation, but rather to the response of aluminum alloys used in aircraft industry to these two particular loading types.

Cyclic Stress-Strain Curves

Experimental Procedure

The materials used are aluminum alloys 2124 T 351, 2618 AT 6 (aged 10 h at 190°C), and 2618 AT 6 (aged 22 h at 203°C). Chemical compositions, tensile properties, and heat treatments are shown in Tables 1, 2, and 3, respectively.

Experiments were carried out on a servo-valve Instron machine (force of 10 tons, with diametral strain imposed upon cylindrical specimens, by applying sinusoidal signals with a frequency of 0.05 Hz. Cyclic stress-strain curves are determined by several methods—namely, one specimen for one strain level, one specimen for one stress level, increments, and a cumulation of strain levels with a constant number of cycles per strain level.

Experimental Results

Cyclic stress-strain curves determined experimentally are shown in Fig. 1,

TABLE 3—*Heat treatment.*

Aluminum Alloy	Heat Treatment
2124 T 351	normal air
2618 AT 6 (aged 10 h at 190°C)	water tempered at 55°C + 10 h at 190°C
2618 AT 6 (aged 22 h at 203°C)	boiled water tempered + 22 h at 203°C

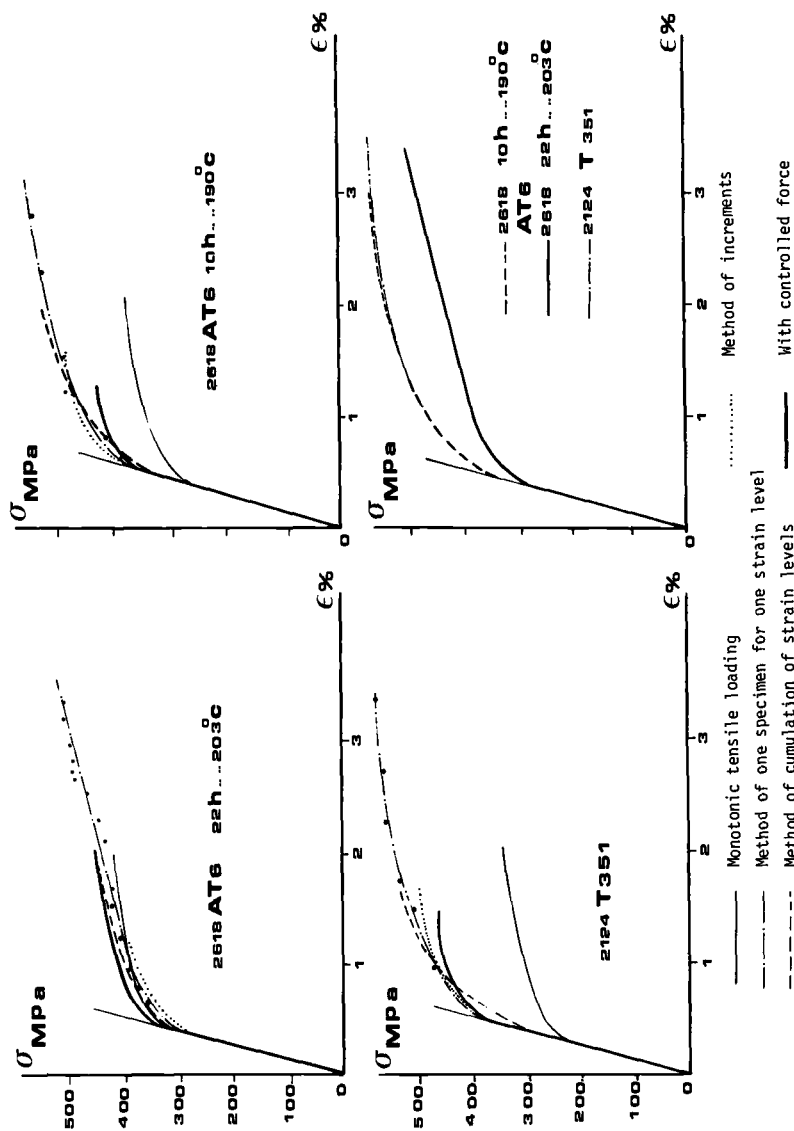


FIG. 1—Cyclic stress-strain curves.

where σ is the real or rational stress and ϵ_t is the real longitudinal strain.

$$\epsilon_t = \frac{\sigma}{E} \left(1 - \frac{\nu_e}{\nu_p} \right) + \frac{\epsilon_d}{\nu_p}$$

where

- $\epsilon_d = \text{Ln}(1 + e)$, real diametral strain,
- $e = (d_o - d)/d_o$, apparent diametral strain,
- ν_e, ν_p = Poisson's elastic and plastic ratio, respectively, and
- E = Young's modulus.

When examining these curves it is found:

1. For aluminum alloy 2124 T 351, under cyclic loading with imposed strain or stress, hardening occurs and σ_y is increased by about 60 percent for the strain case and by a lesser percentage for the stress case.
2. 2618 AT 6 (aged 10 h at 190°C) also shows some hardening but less than 2124 T 351; only a 30 percent increase in σ_y is observed. Greater hardening is achieved in the case of imposed strain.
3. For 2618 AT 6 (aged 22 h at 203°C), both monotonic and cyclic loading curves are very near to each other, but one can notice some softening followed by some hardening, depending on the loading. For the controlled load case it is slightly hardened, while for the strain case it softens and then hardens with an increase in strain values. Thus 2124 T 351 and 2618 AT 6 (aged 10 h at 190°C) are hardened with controlled strain, while 2618 AT 6 (aged 22 h at 203°C) remains relatively stable.

From these results monotonic tensile and cyclic curves can be approximated by $\sigma = K(\epsilon_p)^n$ and $\sigma_a = K'(\epsilon_{pa})^{n'}$ respectively where $K(K')$ are monotonic (cyclic) strength coefficients and $n(n')$ are monotonic (cyclic) strain-hardening exponents. K, K', n , and n' are calculated by linear regression (Table 4). Examining these results it is found:

1. For 2124 T 351 and 2618 AT 6 (aged 10 h at 190°C), values of n', K' , obtained by the method of strain cumulation are the highest, while those obtained by increments are the lowest.
2. For all methods, values of K' are greater than K , while values of n' close to n are obtained by the method of one specimen for one strain level.
3. For 2618 AT 6 (aged 22 h at 203°C), n', K' , depend greatly on the method applied; generally they are greater than n, K .

Low-Cycle Fatigue (LCF)

The life duration as a function of elastic and plastic strain is [1,2]³

$$\epsilon_t = \epsilon'_f (2N_f)^c + \frac{\sigma'_f}{E} (2N_f)^b$$

³ The italic numbers in brackets refer to the list of references appended to this paper.

TABLE 4—Principal monotonic and cyclic characteristics.

Material	R , 0.2 MPa	R' , 0.2 MPa	n	n'	K	K'
2124 T 351	276	420 ^a	0.111	0.155 ^a	545	1100 ^a
		442 ^b		0.113 ^b		890 ^b
		445 ^c		0.071 ^c		695 ^c
2618 AT 6 (aged 10 h at 190°C)	330	420 ^a	0.100	0.143 ^a	615	1030 ^a
		440 ^b		0.127 ^b		955 ^b
		455 ^c		0.066 ^c		690 ^c
2618 AT 6 (aged 22 h at 203°C)	375	366 ^a	0.055	0.095 ^a	530	670 ^a
		358 ^b		0.090 ^b		635 ^b
		342 ^c		0.101 ^c		650 ^c

^a Method of strain level cumulation.^b Method of one specimen for one strain level.^c Method of increments.

where

c = fatigue ductility exponent,

ϵ'_f = fatigue ductility coefficient,

b = fatigue strength exponent,

σ'_f = fatigue strength coefficient, and

E = Young's modulus.

Ductile materials having higher ϵ'_f give a higher resistance to fatigue in the case of imposed strain than in the case of imposed stress. For $N_f > 10^5$ cycle, ϵ_p is negligible relative to ϵ_a ; $\epsilon_t \approx \sigma'_f/E (2N_f)^b$; for $N_f < 10^5$ cycle, ϵ_a is negligible relative to ϵ_p ; $\epsilon_t \approx \epsilon'_f (2N_f)^c$.

Experimental Procedure

Experiments are done in symmetrical tension compression by using a frequency of 0.1 Hz and a sinusoidal form; the strain is recorded by a diametral extensometer. For life duration with controlled strain we apply the method of one specimen for one strain level, while for that with imposed force we apply the Wöhler method by changing the nominal stress to obtain a life duration between 1 and 10^5 cycles.

Experimental Results

Low-Cycle Fatigue with Controlled Strain—From the experimental results, we obtain the following relations for the three aluminum alloys:

$$\begin{aligned}
 2124 \text{ T } 351 & \quad \epsilon_t = 0.0087 (2N_f)^{-0.052} + 0.0845 (2N_f)^{-0.527} \\
 2618 \text{ AT } 6 \text{ (aged 10 h at } 190^\circ\text{C)} & \quad \epsilon_t = 0.0093 (2N_f)^{-0.0688} + 0.0835 (2N_f)^{-0.578} \\
 2618 \text{ AT } 6 \text{ (aged 22 h at } 203^\circ\text{C)} & \quad \epsilon_t = 0.0082 (2N_f)^{-0.0652} + 0.0974 (2N_f)^{-0.461}
 \end{aligned}$$

where $(2N_f)$ is reversals to failure.

Examining these results, one can see that in the range of short life duration ($<10^3$ cycles) 2618 AT 6 (aged 22 h at 203°C) has the best resistance to fatigue with strain controlled, whereas in the range of life duration $>10^3$ cycles 2124 T 351 has the best resistance; however, the difference is not that significant.

Low-Cycle Fatigue with Force Controlled—Curves of life duration are shown in Fig. 2. We observe that in the range of short life duration ($<10^2$ cycles) the three alloys have approximately the same resistance to fatigue, whereas, in the range of life duration between 10^2 and 10^5 cycles, both 2124 T 351 and 2618 AT 6 (aged 10 h at 190°C) have similar resistance; 2618 AT 6 (aged 22 h at 203°C) has the worst resistance to fatigue as it has not been hardened.

When calculating σ'_f and ϵ'_f it was noticed that for alloys that harden [2124 T 351, 2618 AT 6 (aged 10 h at 190°C)] $\sigma'_f > \sigma_f$ and $\epsilon'_f < \epsilon_f$ whereas $\epsilon'_f > \epsilon_f$ for 2618 AT 6 (aged 22 h at 203°C).

Low-Cycle Fatigue and Energy Dissipation

It is unclear whether the stress or the strain controls the fatigue process in aeronautical structures. Let us consider each by studying its energy criterion. According to Halford [3], life duration as a function of energy dissipated by plastic strain is

$$W_f = N_f \cdot \Delta W$$

where ΔW is the plastic strain energy dissipated by one cycle and is to be calculated as the area of the hysteresis loop by

$$\Delta W = 2 \sigma_a \cdot \Delta \epsilon_p \left(\frac{1 - n'}{1 + n'} \right)$$

where n' is the strain-hardening exponent. This plastic strain energy is accumulated until rupture; experimental results give an exponential relation for W_f as a function of $(2N_f)$; thus $W_f = (W'_f/2) (2N_f)^a$.

2124 T 351	$W_f = 0.0850 (2N_f)^{0.442}$
2618 AT 6 (aged 10 h at 190°C)	$W_f = 0.0865 (2N_f)^{0.355}$
2618 AT 6 (aged 22 h at 203°C)	$W_f = 0.0807 (2N_f)^{0.522}$

$W'_f/2$ represents the mean energy dissipated by one reversal. Examining these relations, we can say that for the life duration range of 1 to 10^3 cycles, 2618 AT 6 (aged 10 h at 190°C) has the best resistance to fatigue, 2618 AT 6 (aged 22 h at 203°C) the worst, and 2124 T 351 in between.

Crack Initiation at Notch Root

Previous studies provide us with the necessary parameters for determining the crack initiation at a notch root. Two questions remain to be answered:

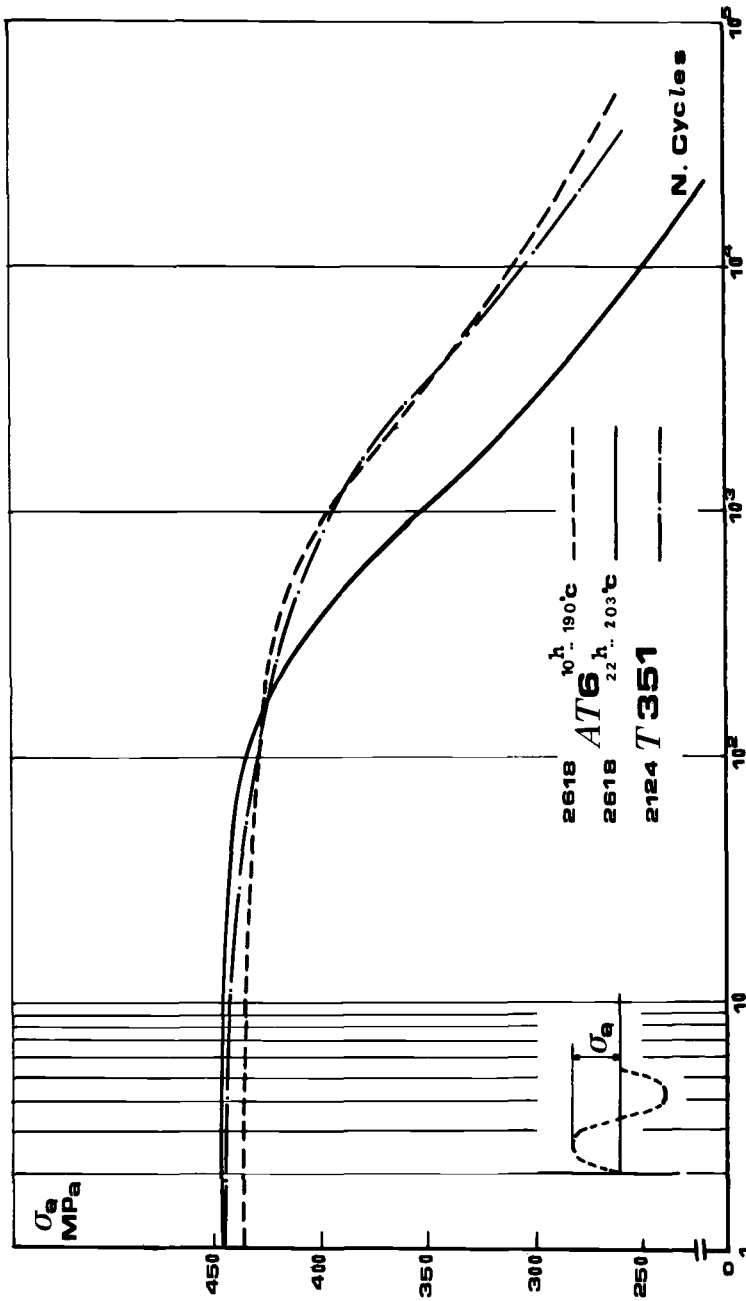


FIG. 2—Life duration with controlled stress.

(1) How can crack initiation be detected? and (2) What is the initiation criterion and the effect of material and geometrical defects?

Experimental Conditions

Compact specimens are chosen with a width W of 75 mm and a thickness B of 12 mm; five radii at notch root are chosen, giving different values of stress concentration, while the length of notch is constant in all cases, $(a/W) = 0.5$.

To determine the stress concentration factor K_t we consider the perfect elastic behavior

$$K_t = \Delta\sigma_{\max}/\Delta\sigma_{\text{nom}}$$

According to Clark [4], $\Delta\sigma_{\text{nom}} = [\Delta P/B (W - a)] [1 + 3 (W + a)/(W - a)]$ and $\Delta\sigma_{\max} = 2\Delta K/\sqrt{\pi\rho}$ where ΔK is the stress intensity factor calculated as $\Delta K = \Delta P/B\sqrt{W} \cdot [f(a/W)]$. Both the effect of crack length and the depth of mechanical notch are considered in the polynomial expression

$$f(a/W) = 29.6 (a/W)^{0.5} - 185.5 (a/W)^{1.5} \\ + 655.7 (a/W)^{2.5} - 1017 (a/W)^{3.5} + 638.9 (a/W)^{4.5}$$

See Table 5.

Specimens are loaded in tension by a servo-valve MTS machine of ± 15 kN; sinusoidal signals of 10-Hz frequency loading was chosen so as to study different domains of initiation for total life duration ranging from 10^3 to 10^5 cycles. To detect the crack initiation we applied the electrical potential method, which is simply measuring the change of specimen electrical resistance during the experiment. Specimens were supplied by either an alternating or direct current of about 10 A/mm² to avoid heating. As an initiation criterion, one can accept the number of cycles corresponding to a measurable deviation of electric energy during the experiment to be an initiation (N_i) corresponding to the beginning of the microcrack to open in Mode I ($V_0 = 82$ mV; $V = 0.2$ mV; $\Delta V/V_0 = 0.0024$).

Analysis of Experimental Results

Function of Nominal Stress—By Clark's formula [4] we calculate $\Delta\sigma_{\text{nom}}$ as the stress amplitude in the place of notch and plot it versus N_i (Fig. 3). We find that (1) for the same notch radius the relation is linear; (2) for the same N_i , a higher load amplitude must be applied as the notch radius increases;

TABLE 5—Elastic stress concentration factor.

mm	0.1	0.5	1	5	10
K_t	14.9	6.9	4.7	2.1	1.5

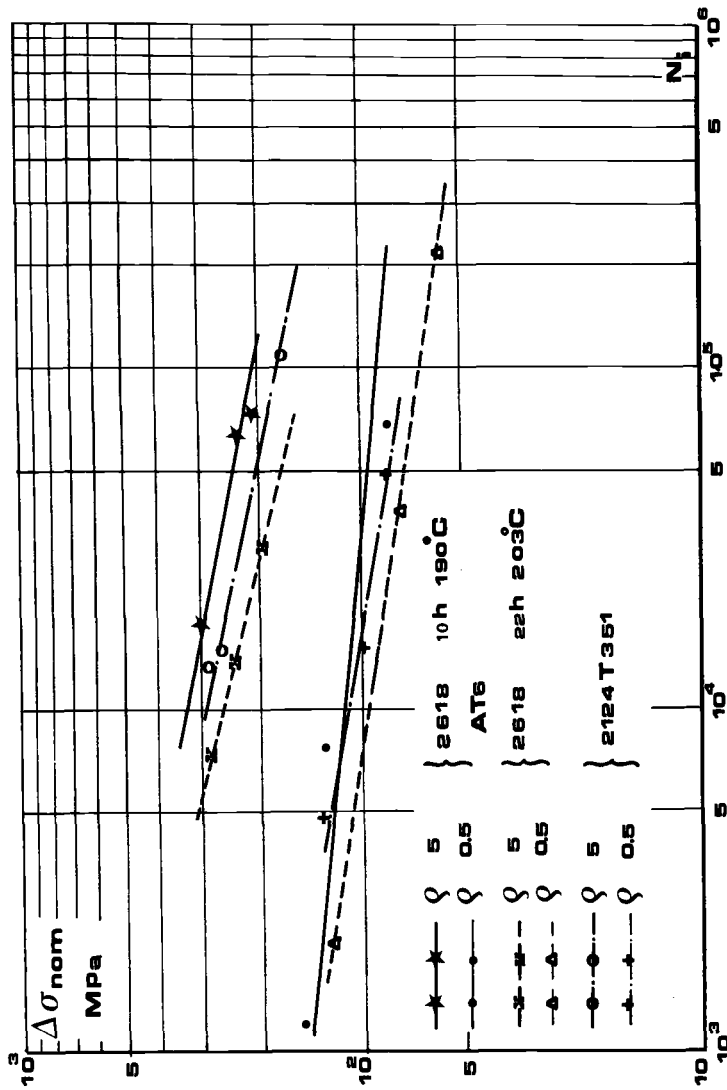


FIG. 3—Analysis of crack initiation in terms of $\Delta\sigma_{nom}$.

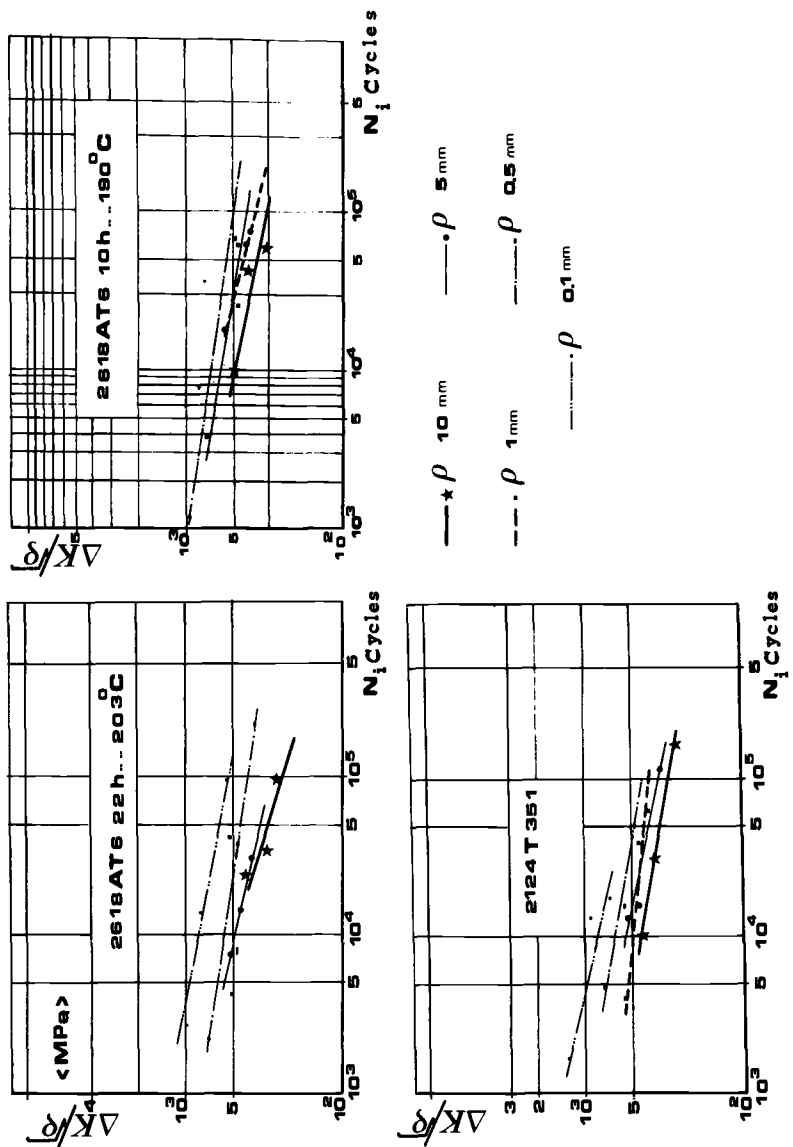


FIG. 4—Analysis of crack initiation in terms of $\Delta K/\sqrt{\rho}$.

and (3) the values for notched 2618 AT 6 (aged 10 h at 190°C) are greatest, followed by 2124 T 351 and then 2618 AT 6 (aged 22 h at 203°C).

Utilization of Fracture Mechanics—Barsom et al proposed that there is some relation between $K/\sqrt{\rho}$ and N_i , where ΔK is the stress intensity factor range and ρ is the notch radius [5,6]. This is linear in bilogarithmic coordinates (Fig. 4), as it is possible to write

$$K_t = \frac{1}{\Delta\sigma_{\text{nom}}} \times \frac{2\Delta K}{\sqrt{\pi\rho}}$$

thus the parameter K_t and the value $K/\sqrt{\rho}$ issue from the same elastic analysis. Neglecting the plastic strain developed at the notch root, one can easily see that the dispersal of results are reduced relative to the previous analysis.

Use of Fatigue Notch Factor K_f —If we were to use K_t by itself, we would always err in our investigations of the crack initiation at notches; therefore we must use the other experimental factor K_f which considers the notch effect, notch characteristics, and materials [7]. K_f is defined as the ratio of two endurance limits of the same testing type:

$$K_f = \frac{\text{endurance limit of smooth specimen}}{\text{endurance limit of notched specimen}}$$

K_f is calculated according to the Heywood empirical formula [8]

$$K_f = \frac{K_t}{1 + 2 \left(\frac{K_t - 1}{K_t} \right) (A/\rho)^{1/2}}$$

where A is a material constant

$$(A)^{1/2} = \left(\frac{282}{\sigma_m} \right)^3 \text{ mm}^{1/2}$$

and σ_m is ultimate stress in tension. See Table 6.

TABLE 6—Fatigue notch factor.

mm	K_f		
	2618 AT 6 (aged 10 h at 190°C)	2618 AT 6 (aged 22 h at 203°C)	2124 T 351
0.1	5.94	5.58	5.81
0.5	4.15	3.98	4.09
1	3.35	3.25	3.31
5	1.87	1.85	1.86
10	1.42	1.41	1.42

Knowing K_t , we calculate $\Delta\sigma_{\max} = K_t \times \Delta\sigma_{\text{nom}}$ to be the maximum stress range at the notch root. Figure 5 represents relations between $\Delta\sigma_{\max}$ and N_i , which depend slightly on notch radius.

Analysis Based on Function of Damage $\sqrt{E \Delta\sigma \Delta\epsilon}$ —Based on the Neuber rule [9,10], $K_t^2 = K_\sigma \times K_\epsilon$ where $K_\sigma = \Delta\sigma / \Delta\sigma_{\text{nom}}$ is the stress concentration factor in the elastoplastic domain and $K_\epsilon = \Delta\epsilon / \Delta\epsilon_{\text{nom}}$ is the strain concentration factor. According to the Morrow et al modification that replaces K_t with K_f , $K_f^2 = (\Delta\sigma / \Delta\sigma_{\text{nom}}) \times (\Delta\epsilon / \Delta\epsilon_{\text{nom}})$ for specimens tested with $\Delta\sigma_{\text{nom}}$ less than the elastic limit. This yields $\sqrt{E \Delta\sigma \Delta\epsilon} = K_f \times \Delta\sigma_{\text{nom}}$ which is adapted as the function of damage to be computed according to Sanz et al [11]. Figure 6 represents the linear relation between this function and N_i which shows a small scatter behavior for all radii.

Damage Accumulation

Previous studies were concerned with the constant amplitude loading with strain or stress controlled. In reality, loading is of a variable amplitude nature, so low-cycle fatigue laws must be modified to suit this amplitude variation when predicting the life duration. We can define damage generally at any time of a component history as the ratio of the number of cycles through which the piece is loaded (by stress or strain imposed) to the number of cycles to rupture exhibited at the same level of stress or strain.

The principal laws of damage accumulation consider the linear accumulation as Miner's law: $D_i = n_i / N_i$, where n_i is the number of cycles applied at stress level σ_i and N_i is the number of cycles to rupture at the same stress level σ_i . Rupture is attained when $\sum D_i = 1$. Depending on the sequence of stress level changes, $\sum D_i$ is between 0.61 and 1.45. Stress changes in an ascending order, $\sum (n_i / N_i) > 1$, are termed understressing, and stress changes in a descending order, $\sum (n_i / N_i) < 1$, are termed overstressing, where in both cases the stress levels are greater than the σ_a endurance limit [12,13].

Experimental results show that this law leads to some error in the case of overloading (whether positive or negative overloading). Landgraf, considering the cycle properties of materials, proposed a law to evaluate the damage per cycle; this law helped to deal with complex and variable strain. He used the value of $2N_f$ (transition life duration where $\Delta\epsilon_e = \Delta\epsilon_p$) to express damage per cycle

$$d_i = \frac{1}{2N_f} \left(\frac{\Delta\epsilon_p}{\Delta\epsilon_e} \right)^{1/b-c}$$

considered as linearly accumulated; thus rupture was attained, $\sum d_i = 1$ [14].

Damage Accumulation for Smooth Specimens

Experiments were conducted on 2124 T 351 and 2618 AT 6 (aged 22 h at 203°C) by controlling the diametral plastic strain (using calculator PDP 11)

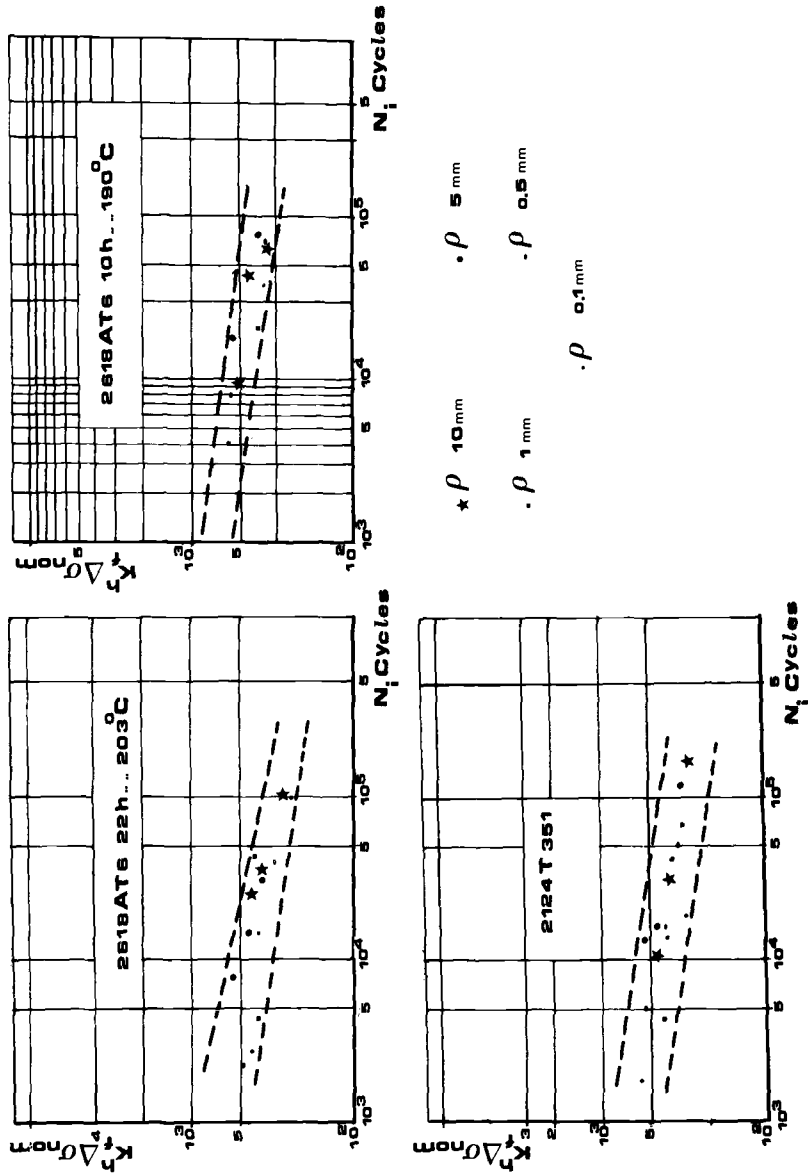


FIG. 5—Analysis of crack initiation in terms of fatigue notch factor K_t and $\Delta\sigma_{nom}$.

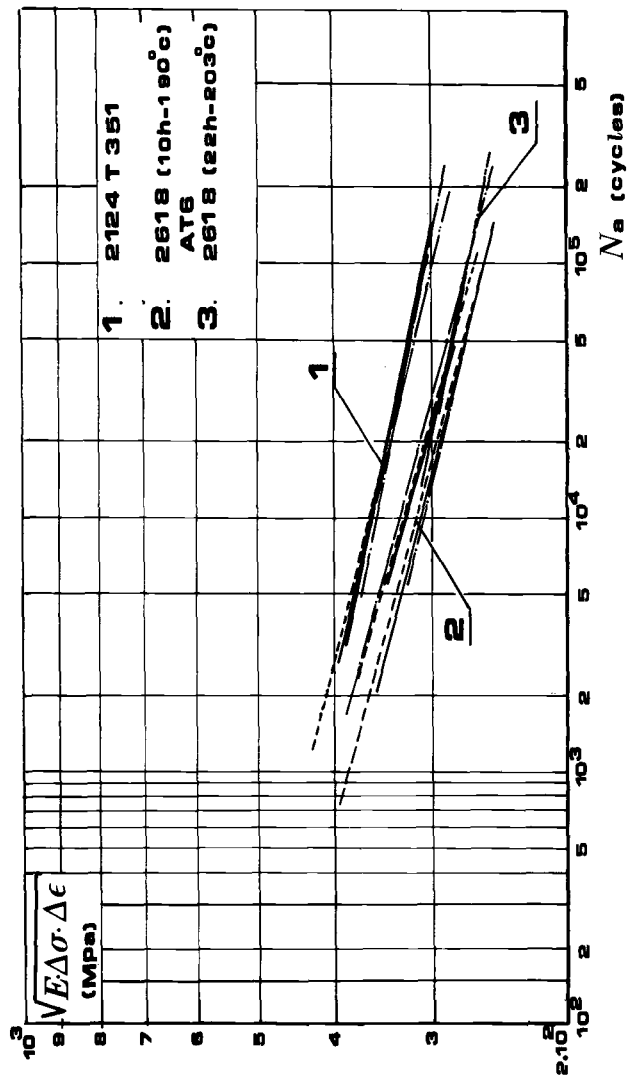


FIG. 6—Analysis of crack initiation in terms of function of damage $\sqrt{E\Delta\sigma\Delta\epsilon}$.

and using loading signals of a triangular form with a frequency of 0.05 Hz. Applying the shown pattern of loading where $\epsilon_0 = 1$ percent and $\epsilon_{pic} = 1.5$ percent, n_0 , n' , and n'' were programmed as shown in Cases A and B in Fig. 7. For 2124 T 351 we have additionally studied Cases C, D, and E, where $\epsilon_0 = 0.5$ percent and $\epsilon_{pic} = 1$ percent.

Experimental Results—Test results with the application of both cumulation laws are shown in Table 7. Besides applying Miner's law for the stress-imposed case, we have applied it to the case of strain imposition. Here $D_i = n_i/N_i$, where both n_i and N_i have the previous definition but are at strain level ϵ_i and rupture is attained when $\Sigma (n_i/N_i) = 1$. In addition, we modified Miner's law so as to evaluate rupture by damage accumulation given by plastic strain energy dissipated per cycle. Total plastic strain energy dissipated in the case of constant strain amplitude, $W_t = N_t \Delta W$; therefore we calculate W_n as energy dissipated by plastic strain for n_i cycles to be $W_n = n_i \Delta W_i$. Knowing W_n one can calculate N_n to rupture from the relation

$$W_n = \frac{W'_t}{2} (2N_n)^a$$

where both W'_t and a were calculated as before and rupture is attained when $\Sigma n_i/N_i = 1$.

Discussion of Results—Reviewing the results given in Table 7 we conclude:

1. The modified Miner law (energy criterion) is generally verified in all cases with remarkable precision, because of the fact that it considers both stress and strain simultaneously. This conclusion is limited to LCF with zero mean strain.

2. Miner's law with strain is verified with less precision.

3. Landgraf's law is less precise than Miner's with strain, because of its difficulty in application.

4. Miner's law with stress is difficult to apply in LCF and gives errors if mean stress is not considered.

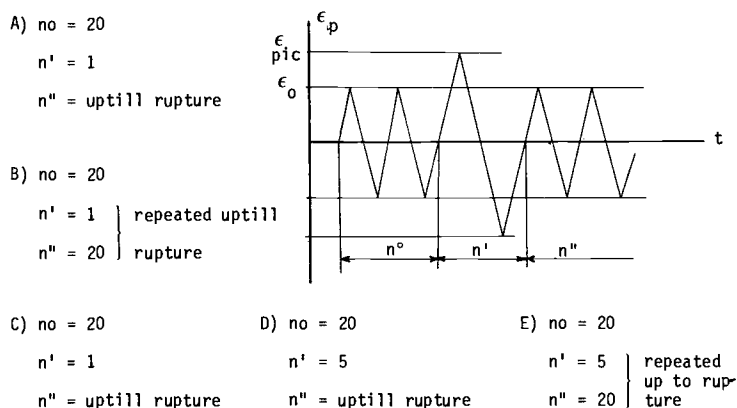


FIG. 7—Damage accumulation for smooth specimens.

TABLE 7—Results of damage accumulation.

2124 T 351		Number of cycles			MINER		LANDGRAF 2 Nt = 136
		$\epsilon_p = 1.5\%$	$\epsilon_p = 1\%$	$\epsilon_p = 0.5\%$	Strain	Energy	
n° 20 n' 1 n" uptill rupture	A	1	24		0.99	1.14	0.75
		1	26		1.07	1.17	0.83
		1	33		1.36	1.29	1.07
n° = 20 n' = 1) * n" = 20)	B	-	-		-	-	-
		-	-		-	-	-
		-	-		-	-	-
n° = 20 n' = 1 n" uptill rupture	C		1	82	0.87	0.96	0.74
			1	92	0.93	1.00	0.82
			1	97	1.01	1.04	0.93
n° = 20 n' = 5 n" uptill rupture	D		5	50	0.69	0.98	0.60
			5	58	0.74	0.97	0.66
			5	75	0.93	1.13	0.80
n° = 20 n' = 5) * n" = 20)	E		6	40	0.68	0.95	0.58
			6	40	0.63	0.99	0.54
			8	40	0.72	1.04	0.58

2618 AT 6 (22 h at 203°C)		Number of cycles		MINER		LANDGRAF 2 NT = 480
		$\epsilon_p = 1.5\%$	$\epsilon_p = 1\%$	Strain	Energy	
n° = 20 n' = 1 n" uptill rupture	A	1	55	0.79	1.01	0.80
		1	59	0.86	1.05	0.92
		1	77	1.08	1.14	1.20
n° = 20 n' = 1) * n" = 20)	B	2	45	0.69	1.01	0.71
		2	53	0.81	1.08	0.81
		2	55	0.79	1.03	1.11

* n' & n" are repeated uptill rupture

Crack Initiation at Notch Root under Spectrum Loading

In reality, most of the components used specially in aeronautical structures are exposed to variable amplitude loading that forms some spectrum. Two aluminum alloys [2618 AT 6 (aged 19 h at 190°C) and 2124 T 351] were tested under programmed loading blocks characterizing the standard TWIST flight loading.

Experimental Procedure—Compact specimens are chosen with width $W = 75$ and thickness $B = 12$ mm; for each material 2 radii at notch root are chosen, 5 mm and 0.5 mm (Tables 5 and 6).

Two constant amplitudes of different values of ΔP were used, from which programmed loading blocks were formed with different combinations so as to resemble the standard TWIST loading (Fig. 8). Specimens are loaded in

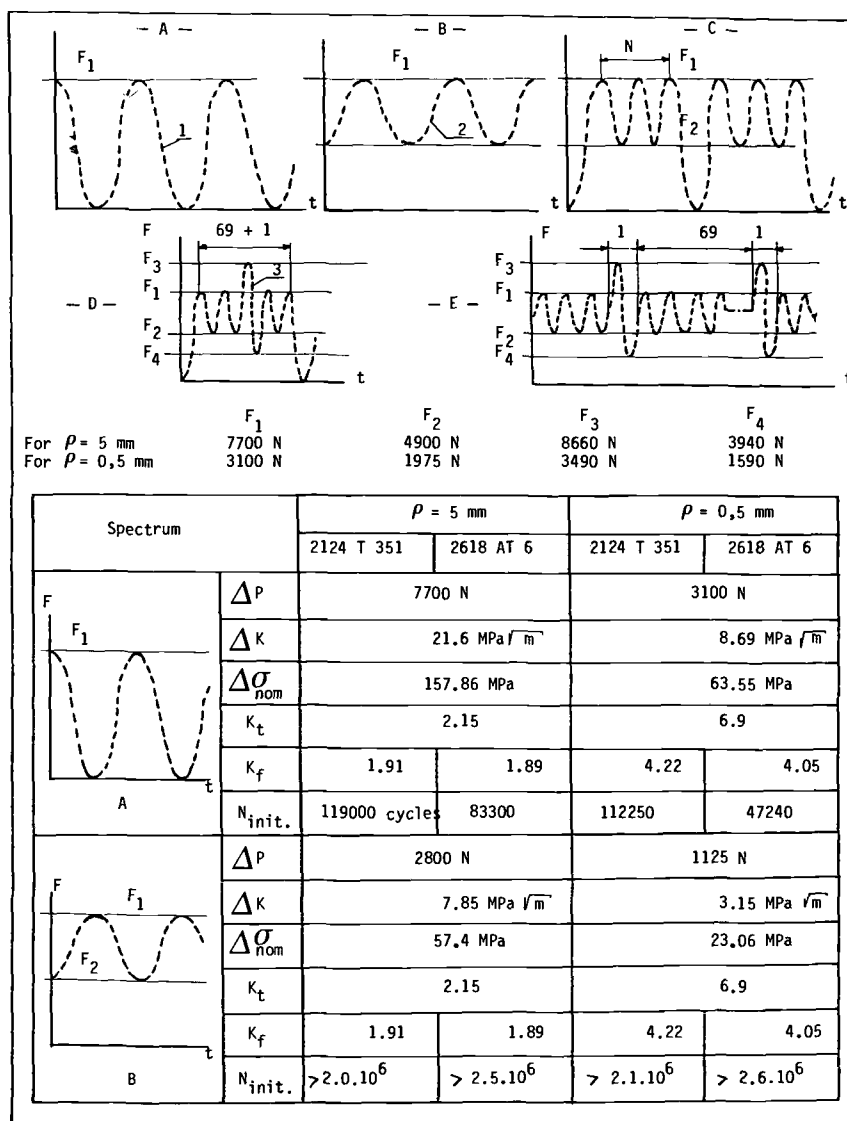
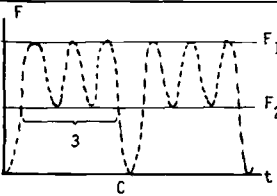
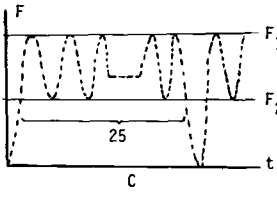
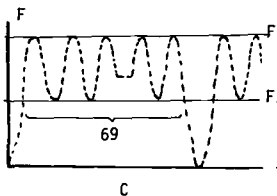
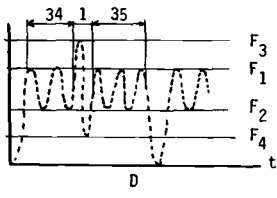
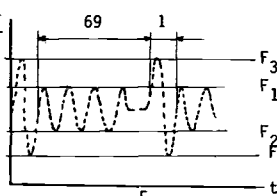


FIG. 8—Loading pattern and principal values.

tension by a servo-valve Mayes machine of ± 50 kN with a sinusoidal form of signal with frequency 10 Hz; crack initiation was detected by the electrical potential method.

Analysis of Experimental Results—Results of fatigue crack initiation and damage accumulation are shown in Fig. 8 and Table 8. From these results it is found that:

TABLE 8—Results of damage accumulation under spectrum loading.

Spectrum		$\rho = 5 \text{ mm}$		$\rho = 0.5 \text{ mm}$	
		2124T351	2618AT6	2124T351	2618AT6
	N° of BL. to initiation	73 625	69 230	69 606	23 200
	$\sum \frac{n_i}{N_i}$	0.64	0.85	0.653	0.497
	N° of blocks	37 800	42 300	17 200	6 700
	$\sum \frac{n_i}{N_i}$	0.411	0.612	0.19	0.157
	N° of blocks	24 232	33 266	6 400	3 169
	$\sum \frac{n_i}{N_i}$	0.372	0.628	0.101	0.089
	N° of blocks	7 954	21 522	3 421	2 174
	$\sum \frac{n_i}{N_i}$	0,122	0,409	0,054	0,061
	N° of blocks	>125 600	>120 925	20 900	29 190
	$\sum \frac{n_i}{N_i}$	no crack initiation		0,236	0,41

1. For constant amplitude loading, aluminum alloy 2124 T 351 has a better resistance to fatigue than 2618 AT 6 (aged 19 h at 190°C).
2. For programmed loading blocks characterizing the standard TWIST during flight, the resistance of both materials to fatigue decreases.
3. Although constant amplitude loading of a small value of ΔK (load type B) causes no crack initiation, when introduced combined with those of great ΔK value (load type A) to form the programmed loading blocks, they cause certain pronounced damage that decreases the number of blocks to crack initiation and consequently the whole life duration. Table 8 shows that a linear accumulation is inapplicable in this case, simply because the damage due to cycles of low ΔK are accumulated with the microcracks created by the cycles of high ΔK .
4. Increasing the number of cycles of small ΔK value per block reflects a great deterioration of the fatigue crack initiation stage (that is, accelerating crack initiation) (Fig. 9; Table 8).
5. We have increased the number of cycles per block to 1000 cycles for 2124 T 351 with a notch root radius of 5 mm to discover whether or not there will be an asymptote. We noticed a great deterioration of the initiation stage, which shows that the crack is initiated on the notch surface as a small microcrack and then propagates due to these cycles of small ΔK into a macrocrack. This is why there is great damage accumulated due to these cycles during initiation and consequently during propagation.

Discussion and Conclusions

We have attempted to survey how, by using low-cycle fatigue data, crack initiation at a notch root or around a hole in aluminum alloys can be evaluated. When examining these parameters, namely $\Delta\sigma_{\text{nom}}$, $\Delta K/\sqrt{\rho}$, $K_t^N \times \Delta\sigma_{\text{nom}}$ and $\sqrt{E\Delta\sigma\Delta\epsilon}$, we find that they do not give the same precision for calculating the number of cycles to crack initiation; however, we can say that the analysis based on the function of damage $\sqrt{E\Delta\sigma\Delta\epsilon}$ is very helpful and shows a small scatter behavior for all notch radii.

Concerning the damage accumulation in the case of smooth specimens with controlled programmed strain, although Miner's law is applicable for variable strain amplitude loading with the same value of mean strain and in the plastic domain, it is completely inapplicable for variable amplitude loading with different mean stress levels [15]; this is also noticed in the case of variable amplitude stress loading [16]. When mean strain is kept zero for both cycles, we found that Miner's law modified by the energy criterion was generally verified with a remarkable precision, because it considers both the stress and strain simultaneously. Miner's law with strain and Landgraf's law were verified with less precision.

In the case of notched specimens with controlled programmed load characterizing the standard TWIST, which involves different mean stress levels,

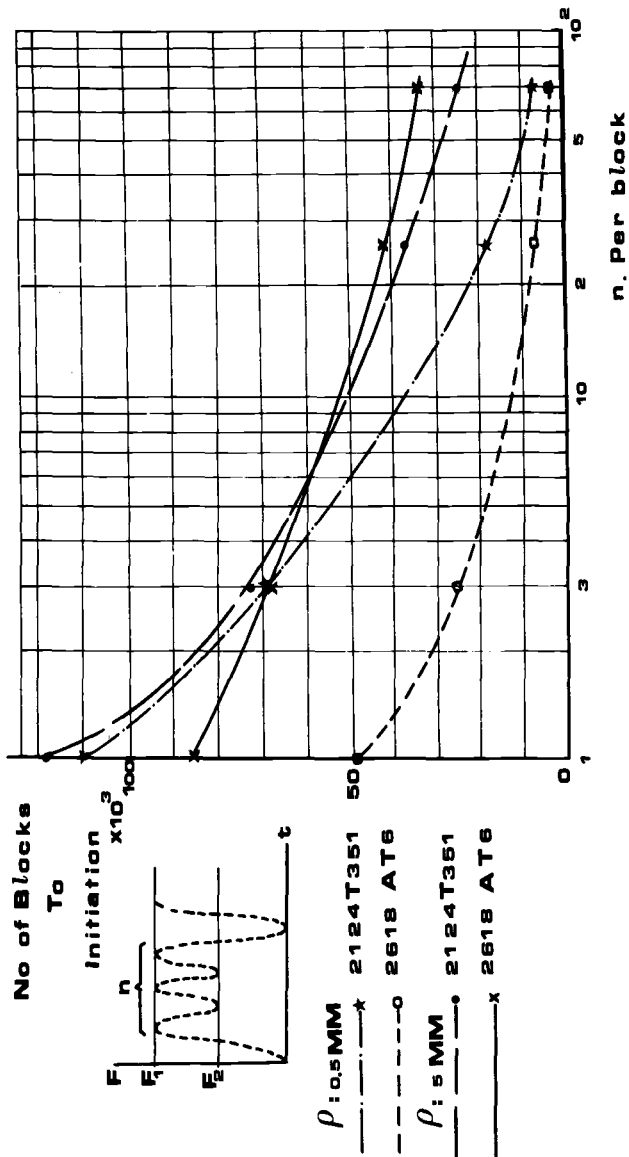


FIG. 9—Influence of number of cycles (of small ΔK) on initiation stage.

the cycles of higher mean stress cause no crack initiation if applied as a uniform load. Cycles with a greater value of ΔK contribute mostly to the initiation of the small fatigue microcracks on the notch surface, while cycles of small ΔK but with high mean stress contribute to their propagation into macrocracks. Miner's law is completely inapplicable here because it ignores the difference in the nature of damage caused by initiation and propagation, which exist simultaneously during this type of loading.

References

- [1] Basquin, O. H. in *Proceedings*, American Society for Testing and Materials, Vol. 10, Part II, 1910, p. 625.
- [2] Endo, T. and Dean Morrow, J. O., *Journal of Materials*, Vol. 4, No. 1, March 1969, pp. 159-175.
- [3] Halford, G. R., *Journal of Materials*, Vol. 1, No. 1, March 1966, pp. 3-17.
- [4] Clark, W. G. in *Fracture Toughness and Slow-Stable Cracking*, ASTM STP 559, American Society for Testing and Materials, 1974, pp. 205-244.
- [5] Barsom, J. M. and McNicol, R. C. in *Fracture Toughness and Slow-Stable Cracking*, ASTM STP 559, American Society for Testing and Materials, 1974, pp. 183-204.
- [6] Rabbe, P. and Amzallag, C., "Etude de l'amorçage des fissures et de la vitesse de fissuration par fatigue de quelques aciers inoxydables austénitiques," *Revue Metallurgie*, Dec. 1974.
- [7] Rabbe, P., *Mecanique*, Nov. 1963, p. 38.
- [8] Heywood, R. B., *Designing Against Fatigue*, Chapman and Hall, London, 1962.
- [9] Neuber, H., *Journal of Applied Mechanics*, Vol. 28, No. 4, Dec. 1961, pp. 544-560.
- [10] Wundt, B. M., *Effect of Notches on Low-Cycle Fatigue*, ASTM STP 490, American Society for Testing and Materials, 1972, pp. 11-12.
- [11] Baus, A., Lieurade, H. P., and Sanz, G. in *Flaw Growth and Fracture*, ASTM STP 631, American Society for Testing and Materials, 1977, pp. 96-111.
- [12] Miner, M. A., *Journal of Applied Mechanics*, Vol. 12, Sept. 1945, pp. 159-164.
- [13] Hardrath, H. F. and Naumann, E. C. in *Symposium on Fatigue of Aircraft Structures*, ASTM STP 274, American Society for Testing and Materials, 1960, pp. 125-137.
- [14] Landgraf, R. W. in *Cyclic Stress-Strain Behavior—Analysis, Experimentation, and Failure Prediction*, ASTM STP 519, American Society for Testing and Materials, 1973, pp. 213-228.
- [15] Taupin, P., "Etude du cumul de l'endommagement en fatigue oligocyclique sur un acier austénitique Z3 CND 17-12," Diplôme de Docteur-Ingénieur, Université de Compiègne, 1978.
- [16] Aliaga, D., Societe Nationale Industrielle Aerospatiale, Aurol. 1980, P.V. No. 39.317/F.

A. M. Nomine,¹ D. Dubois,¹ D. Miannay,¹
P. Balladon,² and J. Heritier²

Creep and Cyclic Tension Behavior of a Type 316 Stainless Steel at Room Temperature

REFERENCE: Nomine, A. M., Dubois, D., Miannay, D., Balladon, P., and Heritier, J., "Creep and Cyclic Tension Behavior of a Type 316 Stainless Steel at Room Temperature," *Low-Cycle Fatigue and Life Prediction, ASTM STP 770*, C. Amzallag, B. N. Leis, and P. Rabbe, Eds., American Society for Testing and Materials, 1982, pp. 45-68.

ABSTRACT: The behavior of a Type 316 L austenitic stainless steel subject to creep and cyclic tension under imposed load is examined at room temperature. Tests are carried out on the material in both the annealed and work-hardened state; in the latter case the influence of an initial hardening by cyclic tension on the subsequent creep behavior, together with the influence of creep hardening on the subsequent cyclic tension behavior, are determined. All tests are conducted with stresses from half the 0.2 percent yield stress up to a stress leading to an initial plastic strain of about 10 percent.

We demonstrate the existence of a (critical) stress limit for creep and a stress limit for (cyclic) accommodation. The creep strain, for a given time interval, increases with the applied stress and, in general, the material continues to creep after 10 000 h. The plastic elongation, between the 1st and the 1000th cycle, that occurs during cyclic tension tests on the annealed materials goes through a maximum when plotted as a function of the maximum applied stress. The creep strain obtained after prior cyclic tension (1000 cycles at the same maximum stress level) has the same stress dependence as the plastic strain that occurs between the 1st and the 1000th cycle, and exhibits a maximum. A creep pre-strain before the cyclic tension tests considerably decreases the elongation measured during cycling.

KEY WORDS: creep, cyclic tension, stainless steel, room temperature, accommodation, creep strain, cyclic strain

The use of austenitic stainless steels in engineering applications, particularly for the construction of pressure vessels, makes it necessary to know the mechanical behavior of these materials in service conditions. The application of static or cyclic loads can in fact lead to certain dimensional changes of the structures under load; the prediction of the amount of these deformations is indispensable.

¹ Research Engineer, Research Engineer, and Head of Fracture Mechanics Group, respectively, Commissariat à l'Energie Atomique, Service Métallurgie, Paris, France.

² Research Engineer, Department of Mechanics, Creusot-Loire, Centre de Recherches d'Unieux, Firminy, France.

A number of studies [1-3] have demonstrated that austenitic stainless steels creep at room temperature under very low stress levels—that is, lower than the 0.2 percent yield stress—and that, in general, creep is not exhausted even after tests of 1000 h.³ Furthermore, (cyclic) room-temperature plastic accommodation has been the subject of several publications [4-6]. In particular, Lieurade et al [6] have shown that the determination of the accommodation limit—that is, the maximum stress level which, when applied periodically, can eventually give rise to a purely elastic behavior—depends upon the shape of the applied loading cycles and the test frequency. More recently, Pellissier-Tanon et al have shown that when a Type 316 L steel is cyclically loaded progressive deformation appears when the maximum stress exceeds a certain value.⁴

Relatively few studies have examined the behavior of austenitic stainless steel at room temperature under loads that are alternately static and cyclic. Krempl [7] and Kujawski et al [8] have recently studied the monotonic and cyclic creep of a Type 304 steel at room temperature, albeit for relatively short periods of time and essentially concentrating on the influence of the deformation and loading rates.

In general, systematic comparisons of the room-temperature behavior of an austenitic stainless steel under static and cyclic loading, together with the combined influence of these two loading modes, have not been studied in detail. This paper presents the results obtained on a Type 316 L steel during the course of such an investigation.

Experimental Program

Materials and Specimens

The steel examined is AISI Type 316 L, produced by vacuum remelting and forged to a bar of diameter of 135 mm. The chemical composition and mechanical properties of the material are given in Tables 1 and 2, respectively.

Figure 1 shows the form of the specimen. Specimens were machined from samples taken in the longitudinal direction of the bar at 46.5 mm from the bar axis. The samples were water quenched after a heat treatment of 1 h at 1080°C before final machining. This treatment gives a grain size of index ASTM 3 to 4.

TABLE 1—*Chemical composition of the steel (weight percent).*

C	Si	Mn	S	P	Ni	Cr	Mo	Cu	N
0.0145	0.39	1.52	0.0035	0.0105	13.64	17.17	2.55	0.02	0.0101

³The italic numbers in brackets refer to the list of references appended to this paper.

⁴This publication, pp. 69-80.

constant loading rate equal to that obtained during the test where the minimum load is $0.1 \sigma_{\max}$ and the frequency is 0.06 Hz.

For each test the experimental values of the maximum stress (σ_{\max}) and the plastic deformation at the 1st (ϵ_{p1}) and between the 1st and N th cycle (ϵ_p^{1-N}) were determined.

After testing, a transmission electron microscope (TEM) study was performed on thin foils from a number of specimens. The foils were taken parallel to the specimen axis at a distance from the surface of about 0.5 mm.

Test Program

The stresses chosen for the creep tests (which were also the maximum stress levels used for the cyclic tests) were determined from the room-temperature monotonic tension test curve of the material and corresponded to $(1/2)R_{0.002}$, $(3/4)R_{0.002}$, $R_{0.002}$, $R_{0.005}$, $R_{0.01}$, $R_{0.025}$, $R_{0.05}$, $R_{0.1}$ (R_x being the nominal stress to produce a plastic strain x). The creep tests were carried out on both the annealed material and on material that had previously been cycled in repeated tension for 1000 cycles with a maximum stress level corresponding to the creep stress. Most creep tests were conducted for 1000 h, but some tests lasted between 2000 and 10 000 h.

The cyclic tension tests were performed on material in both the annealed state and after 1000-h creep at a stress equal to the maximum stress of the cyclic tension tests. Most tests were carried out for 1000 cycles, although some tests were continued for much longer. The different types of tests are shown in Tables 3 to 5.

TABLE 3—Creep test results of the annealed material.

Specimen No.	Stress, MPa	a_i , %	a_{pt} (1000 h), %	a_{pt} (10 000 h), %
25	$R_{0.002}/2 = 105$	0.12	0.017	...
35	$R_{0.002}/2 = 105$	0.20	0.03	0.055
19	$3R_{0.002}/4 = 157$	0.32	0.08	...
				(2000 h)
38	$3R_{0.002}/4 = 157$	0.32	0.143	0.151
17	$R_{0.002} = 209$	0.73	0.33	...
34	$R_{0.002} = 209$	0.67	1.20	1.616
24	$R_{0.005} = 235$	1.17	0.80	...
18	$R_{0.01} = 256$	1.75	1.38	...
				(2000 h)
40	$R_{0.01} = 256$	1.05	0.67	0.73
26	$R_{0.025} = 283$	3.98	1.83	...
				(6000 h)
12*	$R_{0.025} = 283$	3.70	2.38	2.69
27	$R_{0.05} = 323$	5.37	2.97	...
33	$R_{0.05} = 323$	6.87	2.78	3.211
A5	$R_{0.1} = 391$	12.92	4.83	...
				(5000 h)
10*	$R_{0.1} = 391$	12.63	4.15	4.46

Results

Applied Stress Levels

Figure 2 shows the tensile stress-strain curve of the material and the stress values chosen for the creep and cyclic tension tests. In the upper half of this figure, the points (σ_{\max} , ϵ_{pl}) of the cyclic tension tests and (σ , a_i) of the creep tests on the annealed material are shown for comparison. The slight scatter of these points about the tensile stress-strain curves can be partly explained by the fact that ϵ_{pl} does not include the elastic part of the elongation, and also by the fact that the loading rates are different from those of the tension test.

Creep of the Annealed Material

Table 3 summarizes the creep test results of the annealed material. The material creeps when the applied stress is higher than or equal to $(\frac{3}{4})R_{0.002}$. Figure 3 shows a semi-logarithmic plot of the variation of a_{pf} with time for times of 1 to 1000 h. With the exception of the highest stress levels ($R_{0.05}$ and $R_{0.1}$) the creep elongation between 1 and 1000 h can be written in the form

$$a_{pf} = \alpha \log t + k \quad (a_{pf} \text{ in } \%, t \text{ in hours})$$

where k corresponds to the value of a_{pf} after 1 h. α and k depend upon the applied stress and can be expressed as a linear function of the stress according to the equations

$$\begin{aligned}\alpha &= -4.679 \times 10^{-3} + 2.918 \times 10^{-5} \sigma \\ k &= -2.81 \times 10^{-2} + 1.38 \times 10^{-4} \sigma\end{aligned}$$

where σ is in megapascals. The correlation coefficients obtained with these expressions are good (0.96 and 0.95). The equations are valid for the higher stress levels $R_{0.05}$ and $R_{0.1}$ except for α when t is between 1 and 100 h. When t is greater than 100 h the α -values decrease.

For tests longer than 1000 h, and irrespective of the stress level, this type of representation is no longer valid. An expression of the form $a_{pf} = \beta t^\alpha$ appears to be more representative. Figure 4 shows the variation of a_{pf} with time for tests lasting up to 10 000 h. In general, at stresses higher than or equal to $(\frac{3}{4})R_{0.002}$, stabilization is not observed, although the creep rate decreases continuously throughout the test whatever the test duration. However, the appearance of secondary creep leading to rupture cannot be excluded for longer times.

Cyclic Tension Tests on the Annealed Material

Table 4 summarizes the cyclic tension test results. Accommodation is not observed at less than 1000 cycles for stresses higher than or equal to

TABLE 4—Cyclic tension test results on the annealed material.

Specimen No.	Conditions ^a	σ_{max} , MPa	σ_{min} , MPa	ϵ_p (1st cycle), %	ϵ_p (1 to 1000), %	ϵ_p (1 to N), %
14	EA	$R_{0.002}/2 = 105$	10.5	0.006	0.006	...
32	ES	$R_{0.002}/2 = 105$	10.5	...	0.01	...
12	EA	$3R_{0.002}/4 = 157$	15.7	0.096	0.046	...
10	EA	$R_{0.002} = 209$	20.9	0.248	0.248	...
1*	ES	$R_{0.002} = 209$	20.9	0.169	0.625	...
6*	ES	$R_{0.002} = 209$	20.9	0.173	0.515	...
31	ES	$R_{0.002} = 209$	20.9	0.288	0.913	1.344 ($N = 79\,800$)
8	EA	$R_{0.005} = 235$	23.5	0.478	0.362	...
2*	HS	$R_{0.005} = 235$	23.5	0.63	0.657	0.692 ($N = 5000$)
6	EA	$R_{0.01} = 256$	25.6	1.538	0.500	...
3*	HS	$R_{0.01} = 256$	25.6	1.29	0.83	1.27 ($N = 2200$)
7*	ES	$R_{0.02} = 277$	27.7	3.519	0.308	0.317 ($N = 5000$) 1.034

9*	ES	$R_{0.02}$	= 277	27.7	2.037	0.985	(N = 1500)
21	EA	$R_{0.025}$	= 283	28.3	2.981	0.482	...
							1.11
4*	HS	$R_{0.025}$	= 283	28.3	2.80	1.08	(N = 1240)
							0.376
11*	ES	$R_{0.025}$	= 283	28.3	4.211	0.356	(N = 5000)
22	EA	$R_{0.05}$	= 323	32.3	5.346	0.212	...
37	ES	$R_{0.05}$	= 323	32.3	8.97	0.18	...
5*	HS	$R_{0.05}$	= 323	32.3	4.48	0.73	...
A3	HS	$R_{0.1}$	= 391	39.1	7.98	0.54	...
							0.23
8*	ES	$R_{0.1}$	= 391	39.1	13.9	0.16	(N = 31 900)
99	ES	$R_{0.01}$	= 256	25.6	0.708	0.878	...
11	ES	$R_{0.01}$	= 256	71.7	1.119	1.181	...
13	ES	$R_{0.01}$	= 256	117.8	0.792	1.057	...
23	ES	$R_{0.01}$	= 256	163.8	0.85	1.227	...
41	ES	$R_{0.01}$	= 256	209.9	0.608	1.342	...

* EA = Electro-mechanical equipment, variations in frequency.

ES = Electro-mechanical equipment, constant frequency.

HS = Hydraulic equipment, constant frequency.

TABLE 5—Creep + cyclic tension test and cyclic tension + creep test results.

Specimen No.	σ , MPa	Creep			Cyclic Tension		
		a_i , %	a_{pf} (1 to 1000 h), %	ϵ_p (1st cycle), %	ϵ_p (1 to 1000 h), %	$a_{tot} + \epsilon_{tot}$, %	
25	$R_{0.002}/2 = 105$	0.12	0.017	0.023	0.013	0.173	
19	$3R_{0.002}/4 = 157$	0.32	0.08	. . .	0.012	0.412	
17	$R_{0.002} = 209$	0.73	0.33	0.037	0.017	1.114	
24	$R_{0.005} = 235$	1.17	0.80	0.041	0.021	2.032	
18	$R_{0.01} = 256$	1.75	1.38	0.048	0.017	3.195	
26	$R_{0.025} = 283$	3.98	1.83	0.032	0.008	5.850	
27	$R_{0.05} = 323$	5.37	2.97	0.050	0.027	8.417	
A5	$R_{0.1} = 391$	12.92	4.83	0.24	0.016	18.006	

Specimen No.	σ , MPa	Cyclic Tension			Creep		
		ϵ_p (1st cycle), %	ϵ_p (1 to 1000 h), %	a_i , %	a_{pf} (1 to 1000 h), %	$\epsilon_{tot} + a_{tot}$, %	
14	$R_{0.002}/2 = 105$	0.006	0.006	0.22	0	0.232	
12	$3R_{0.002}/4 = 157$	0.096	0.046	0.27	0.14	0.552	
10	$R_{0.002} = 209$	0.248	0.248	0.27	0.40	1.166	
8	$R_{0.005} = 235$	0.478	0.362	0.22	0.62	1.68	
6	$R_{0.01} = 256$	1.538	0.500	0.30	0.93	3.268	
21	$R_{0.025} = 283$	2.981	0.482	0.35	0.85	4.663	
22	$R_{0.05} = 323$	5.346	0.212	0.63	0.22	6.408	

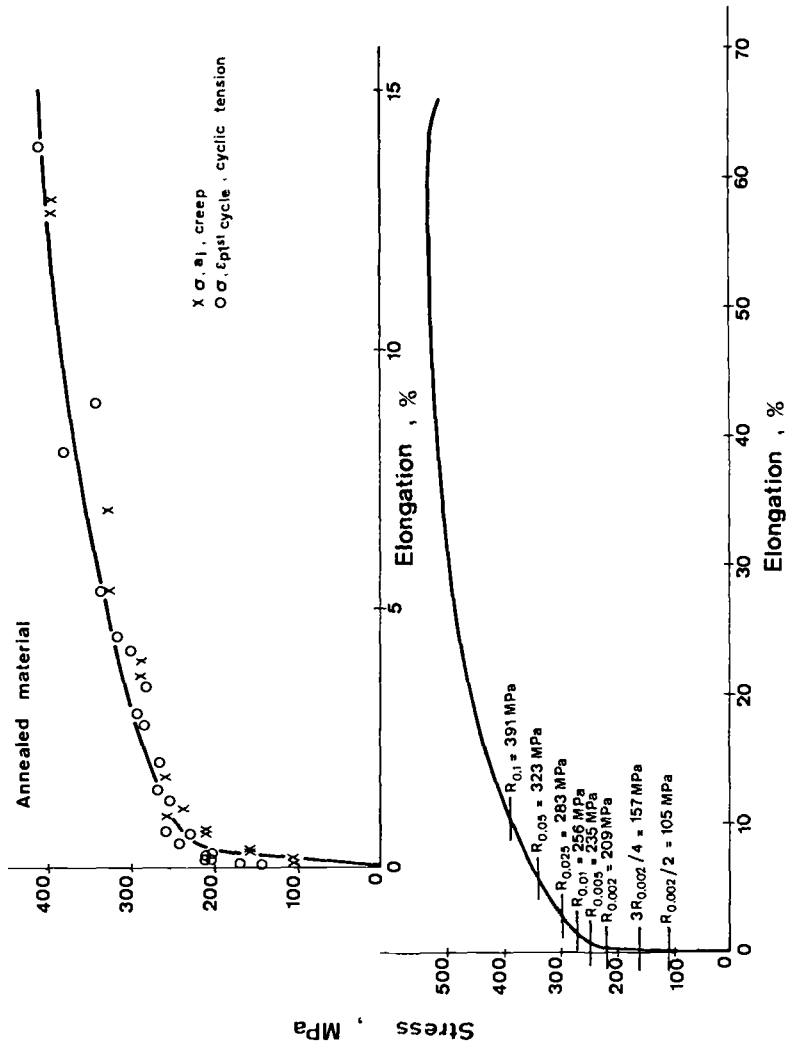


FIG. 2—Comparison between the stress-strain levels determined from the monotonic tensile curve and the experimental level.

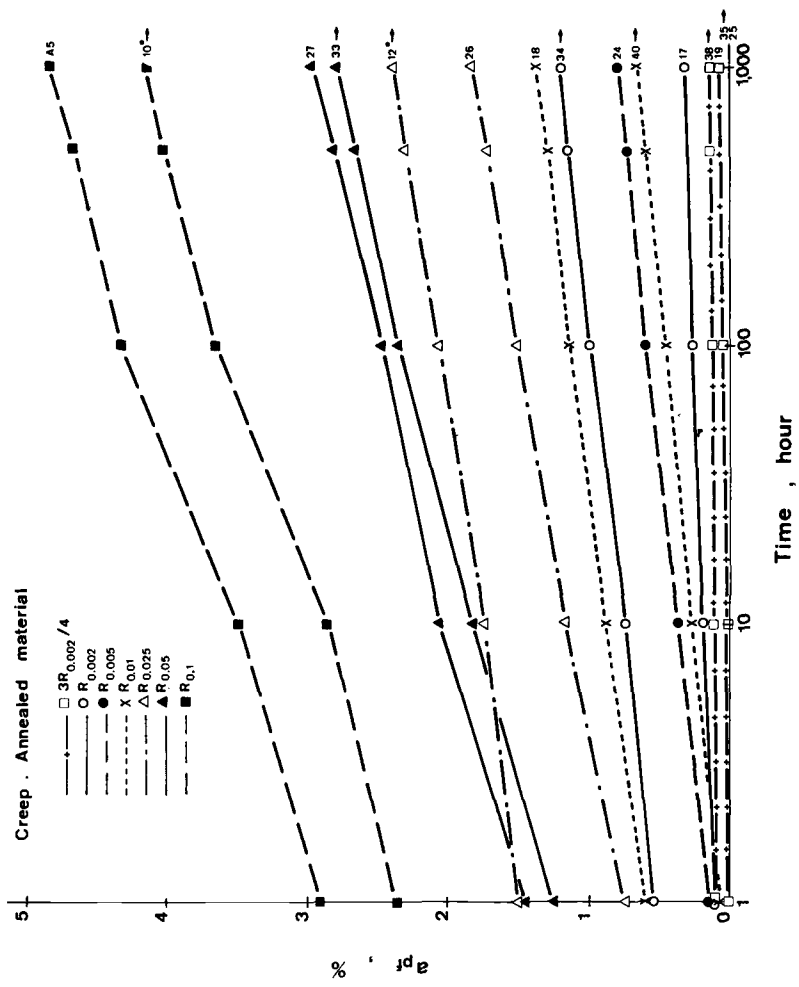


FIG. 3—Creep elongation as a function of time up to 1000 h.

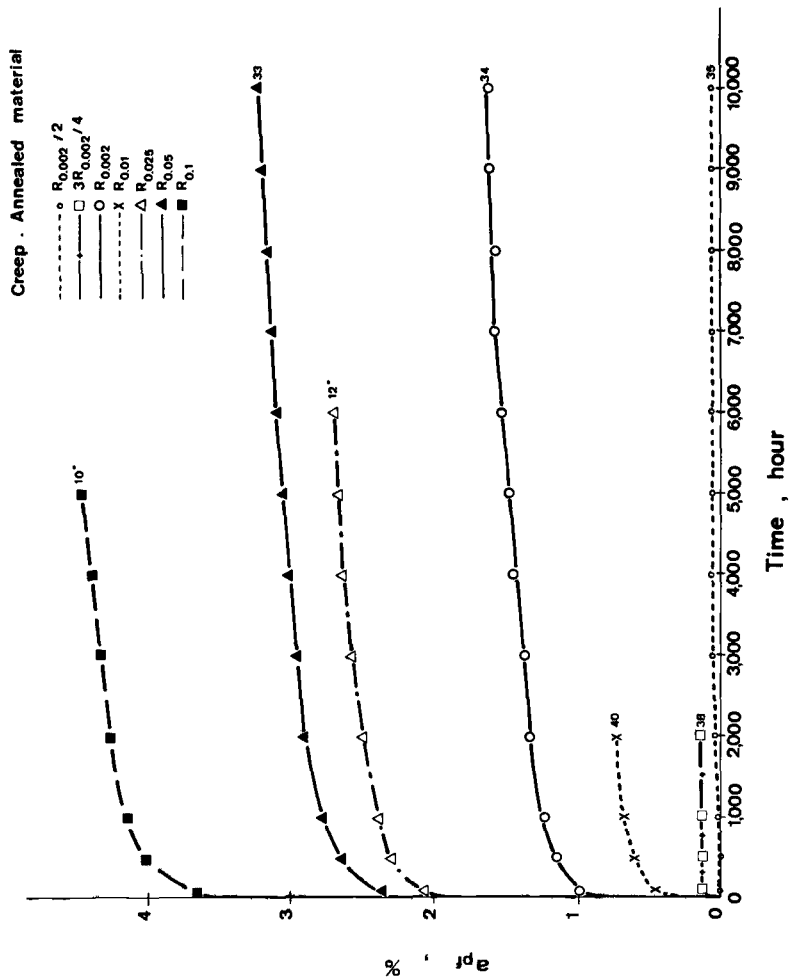


FIG. 4—Creep elongation as a function of time up to 10 000 h.

$(\frac{3}{4})R_{0.002}$. The accommodation limit occurs between 147 and 167 MPa—that is, around $0.7 R_{0.002}$ —which is in good agreement with the results obtained by other authors on Type 304 steels [6]. If one considers that the plastic deformation of the 1st cycle corresponds to the initial loading during a creep test, then it is reasonable to pay particular attention to the elongation that occurs after the 1st cycle. Figures 5 and 6 depict the elongation measured between the 1st and N th cycles as a function of the number of cycles.

We have been unable to find a simple equation that describes this elongation as a number of cycles. In order to evaluate the influence of the maximum cyclic stress on the dimensional changes of the material, the plastic elongation measured between the 1st and 1000th cycles has been plotted (Fig. 7) as a function of the plastic elongation during the 1st cycle (which depends in fact on the maximum stress level). These results concern the tests with $\sigma_{\min} = 0.1 \sigma_{\max}$. In general, the plastic elongation between the 1st and the 1000th cycle increases rapidly with the deformation of the 1st cycle, ϵ_{p1} , goes through a maximum for ϵ_{p1} between 1 and 3 percent, then decreases rapidly to relatively low levels at the higher values of ϵ_{p1} (owing to the high stress levels). The maximum value depends upon the test frequency. Tests conducted with a higher frequency after the first 20 cycles exhibit a less pronounced maximum; separating the elongation between the 1st and 20th cycles and the 20th and 1000th cycles shows that the increase in frequency is responsible for the lower value of the elongation (Fig. 8). One also observes that the test machine appears to exert some influence. Finally, the results show that, for a given maximum stress, a change in the minimum stress does not have a strong influence on the deformation behavior.

Creep of Material Deformed in Cyclic Tension

The initial elongation does not depend very much on the applied stress and remains very small, as does the creep elongation after 1 h. The logarithmic representation used for the creep behavior of the annealed material can not be applied in this case. The creep elongation after 1000 h varies with the applied stress in the same manner as the elongation between the 1st and 1000th cycle during the previous cyclic tension testing (Fig. 9).

Cyclic Tension on Material Deformed in Creep

The plastic elongations between the 1st and the 1000th cycle are very small at all the applied stress levels, and one can consider that the material has been accommodated whatever the maximum stress. The elongation during the 1st cycle remains small—that is, less than 0.05 percent for stresses less than or equal to $R_{0.05}$ —and is equal to 0.24 percent for a stress equal to $R_{0.1}$. Figure 10 shows the creep elongation after 1000 h as a function of the applied stress for the annealed material, and the elongation between the 1st and 1000th cycles during cyclic tension of the material after creep.

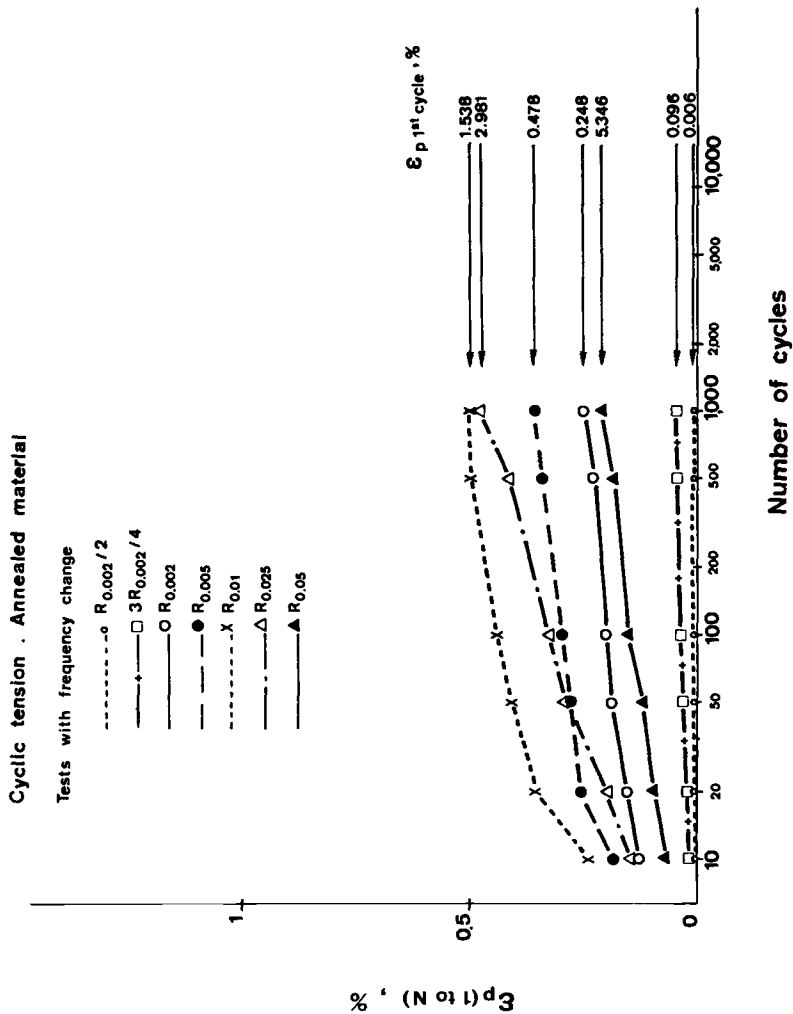


FIG. 5—Elongation during cyclic tension as a function of the number of cycles.

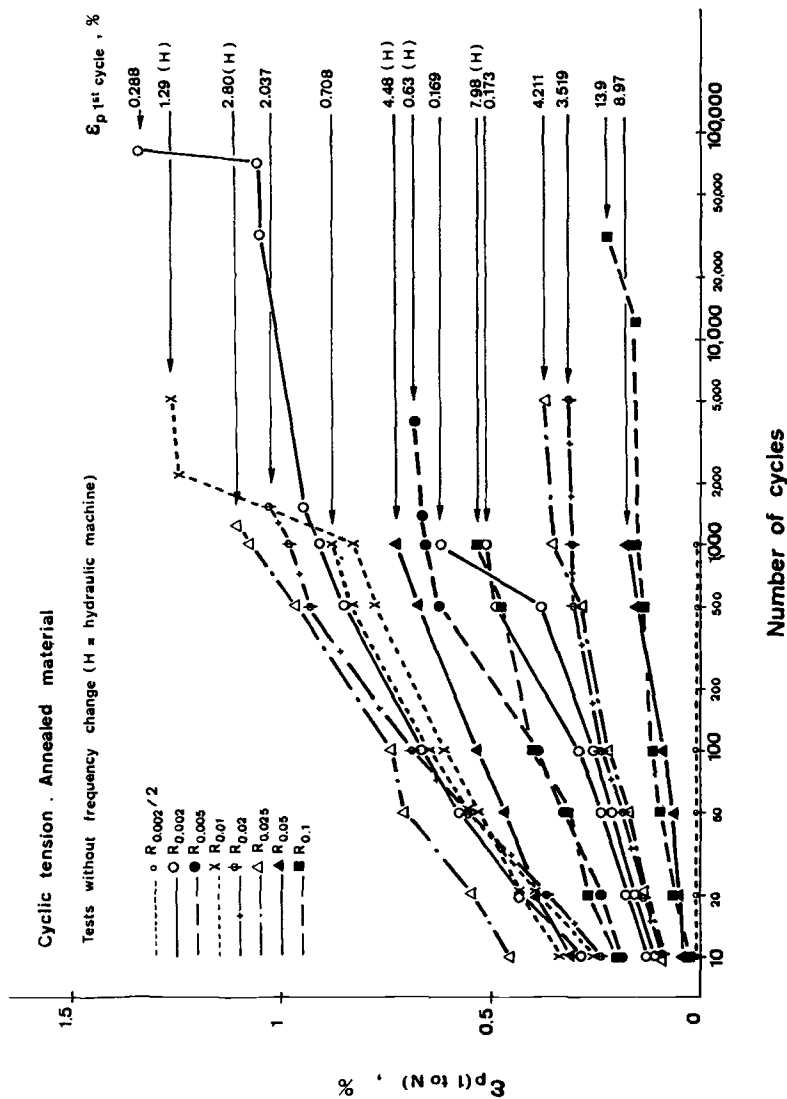


FIG. 6—Elongation during cyclic tension as a function of the number of cycles.

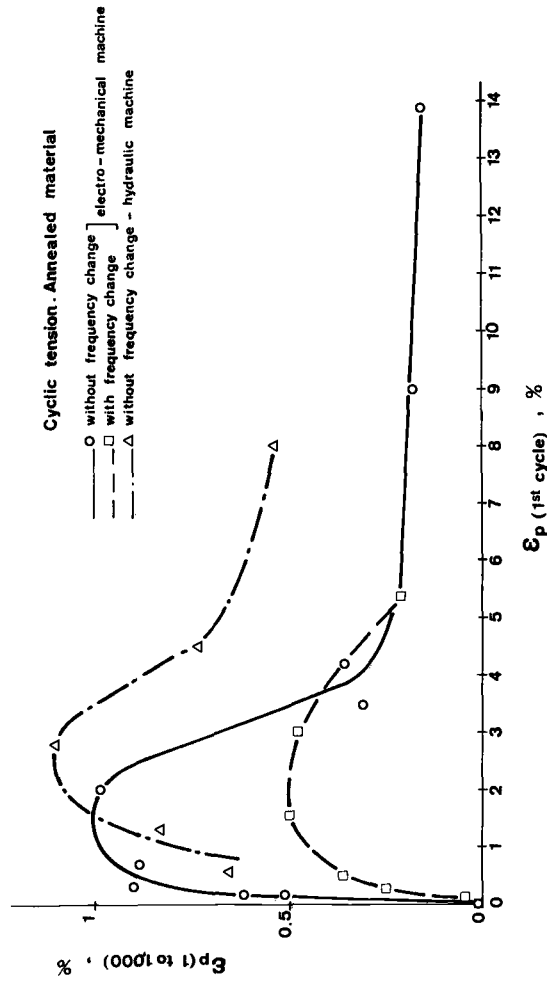


FIG. 7—Elongation during cyclic tension between the 1st and the 1000th cycle (annealed state).

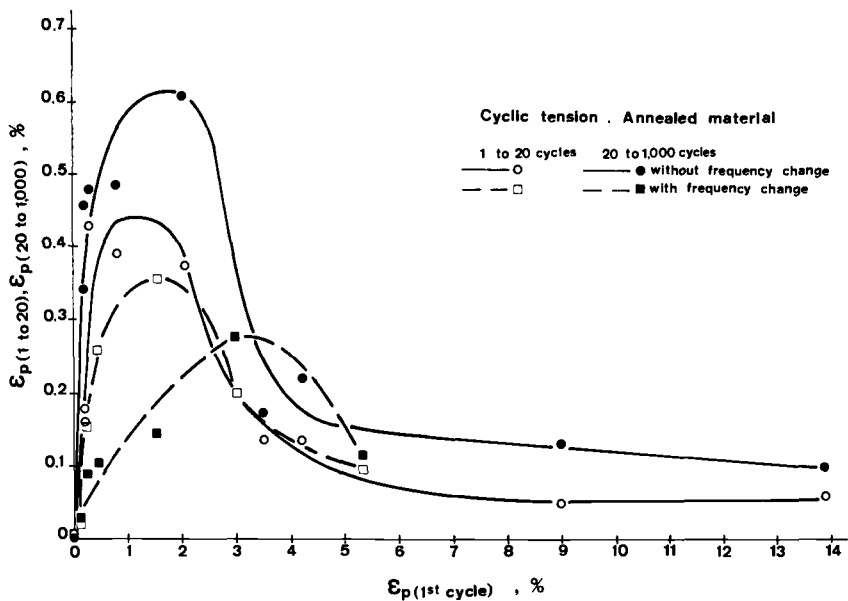


FIG. 8—Elongation during cyclic tension between the 1st and the 1000th cycle (annealed state).

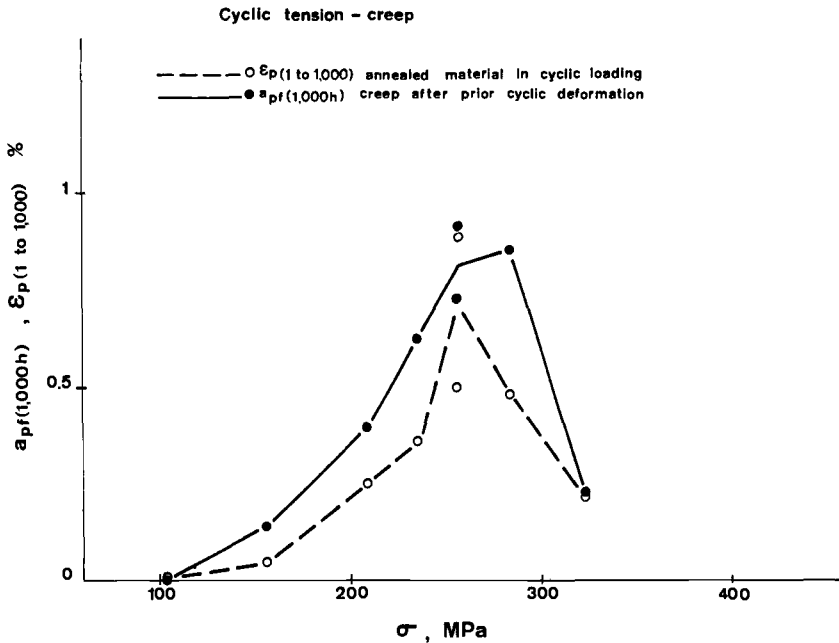


FIG. 9—Creep elongation after 1000 h (on pre-cycled specimens).

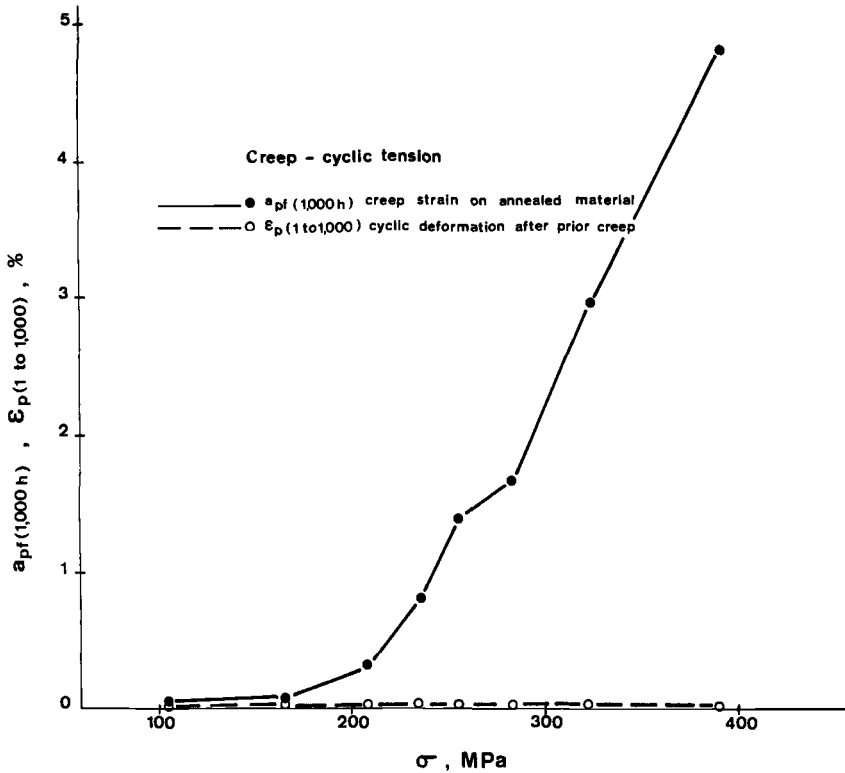


FIG. 10—Elongation during cyclic tension between the 1st and the 1000th cycle (on pre-crept specimens).

Comparison Creep + Cyclic Tension and Cyclic Tension + Creep

Figure 11 shows the total elongation of specimens after 1000-h creep plus 1000 cycles of repeated tension and also 1000 cycles of repeated tension plus 1000-h creep, as a function of the maximum stress. It is to be noted that the order in which the different tests are carried out has practically no influence on the total elongation up to a stress level on the order of $R_{0.01}$ (256 MPa). For higher stresses the sequence creep + cyclic tension produces a total elongation greater than that of the sequence cyclic tension + creep. This point remains to be confirmed for the stress level $R_{0.1}$ (391 MPa). Table 5 shows all test results.

Micrographic Study

A thin-foil TEM study was carried out to determine the changes in the dislocation substructure between the 1st and the N th cycle during cyclic tension. The stress levels were chosen so that the deformation between the 1st and the 1000th cycles corresponded to the highest and lowest of the observed

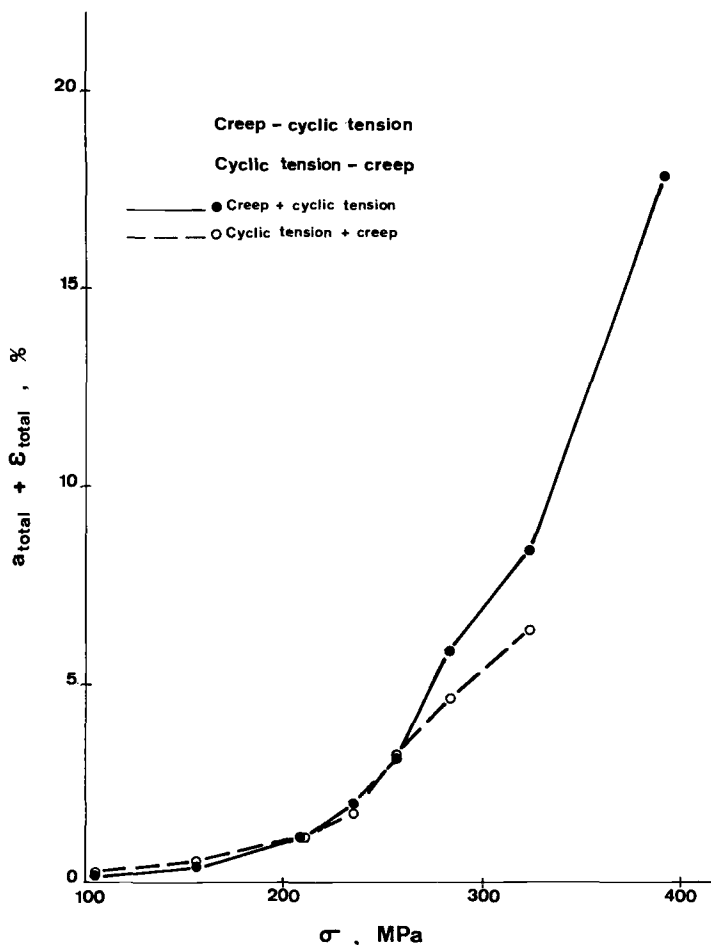


FIG. 11—Total elongation of creep + cyclic tension and cyclic tension + creep.

values. Figure 12 shows the structures observed in a specimen after 1 cycle with a deformation of 2 percent, and in a specimen after 45 700 cycles with a deformation of 2 percent during the 1st cycle and 1.13 percent during the following cycles. After the 1st cycle a relatively low dislocation density is observed; some regions contain free dislocations while other regions show the beginning of dislocation rearrangements.

After 45 700 cycles the dislocation substructure is rather heterogeneous, and regions of both high (cellular arrangements) and low dislocation density can be observed.

Figure 13 shows the substructures observed in a specimen after 1 cycle at 14 percent deformation, and another specimen after 31 900 cycles with a deformation of 14 percent in the 1st cycle and 0.23 percent for the following cy-

cles. After the 1st cycle one observes a high density of dislocations arranged either into cellular configurations or along slip planes or slip bands. After 31 900 cycles the structure is cellular and the density of free dislocations in the interior of the cells is relatively low.

One cannot see any difference between the structures produced by a deformation of 14 percent obtained in a monotonic or a cyclic way.

Discussion

These tests confirm that creep occurs in austenitic stainless steels at room temperature. The 1000-h creep law of the annealed material is, however, only valid for this particular steel grade, and a study of the influence of the composition on the coefficients of the creep equations would be useful.

The material continues to creep with a continuously decreasing creep rate for periods of time up to 10 000 h. A constant creep rate region is not observed. The creep elongation, at a given instant, increases with the applied stress.

The behavior in cyclic tension is completely different. Thus the elongation between the 1st and the 1000th test cycle initially increases with the maximum stress, then decreases and becomes very small at high stresses. The creep elongation cannot therefore be related (directly) to the cyclic elongation. Moreover, the commutated tests (creep + cyclic tension and cyclic tension + creep) show that the test order affects the results. The total elongation is smaller in cyclic tension + creep at the highest stress levels because of the accommodation that occurs during cyclic testing.

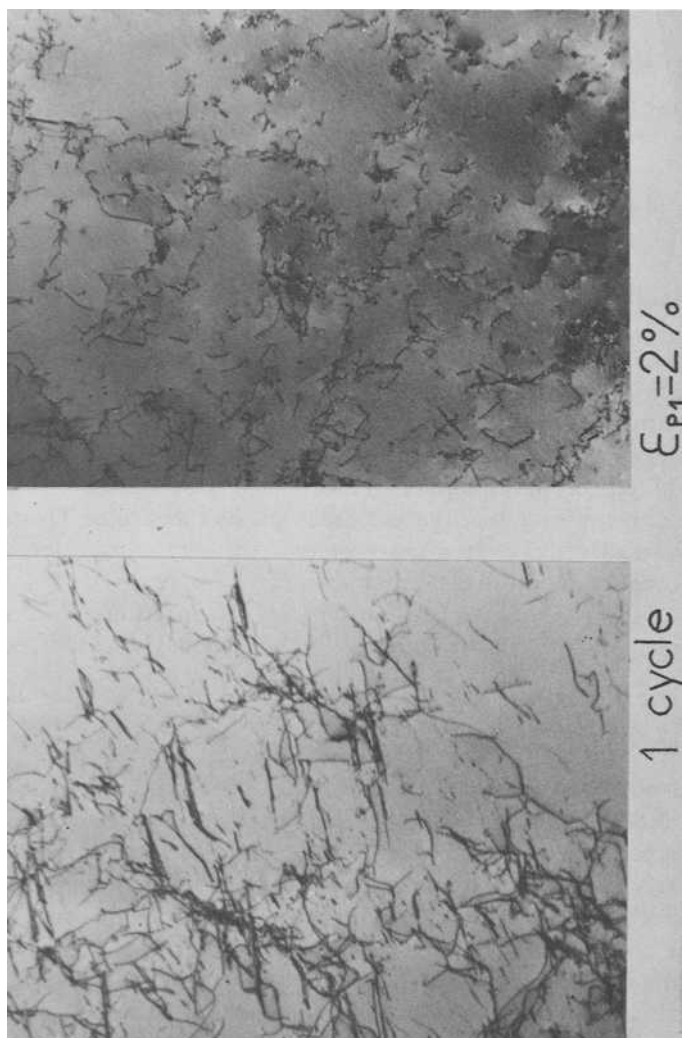
The TEM study of the dislocation substructures is not developed enough to explain in a quantitative way the different behaviors observed during the tests.

Conclusions

The phenomenon of room-temperature creep of annealed austenitic stainless steels has been confirmed by tests on a Type 316 L steel. The creep stress limit is between $0.5 R_{0.002}$ and $0.75 R_{0.002}$. The creep elongation increases with the stress level, and no stabilization is observed for creep times up to 10 000 h. The creep rate always decreases with time for all applied stresses.

The accommodation limit obtained by cyclic tension on the annealed material is about $0.7 R_{0.002}$. The deformation between the 1st and the 1000th cycle does not increase (monotonically) with the maximum stress, but goes through a maximum for a stress of about $R_{0.01}$.

For a material deformed by cyclic tension, the subsequent application of a static stress equal to the maximum cyclic stress produces a creep strain that does not increase with the applied stress, as is the case for the annealed material. This deformation obeys the same law as that obtained by cycling, and is on the same order of magnitude.



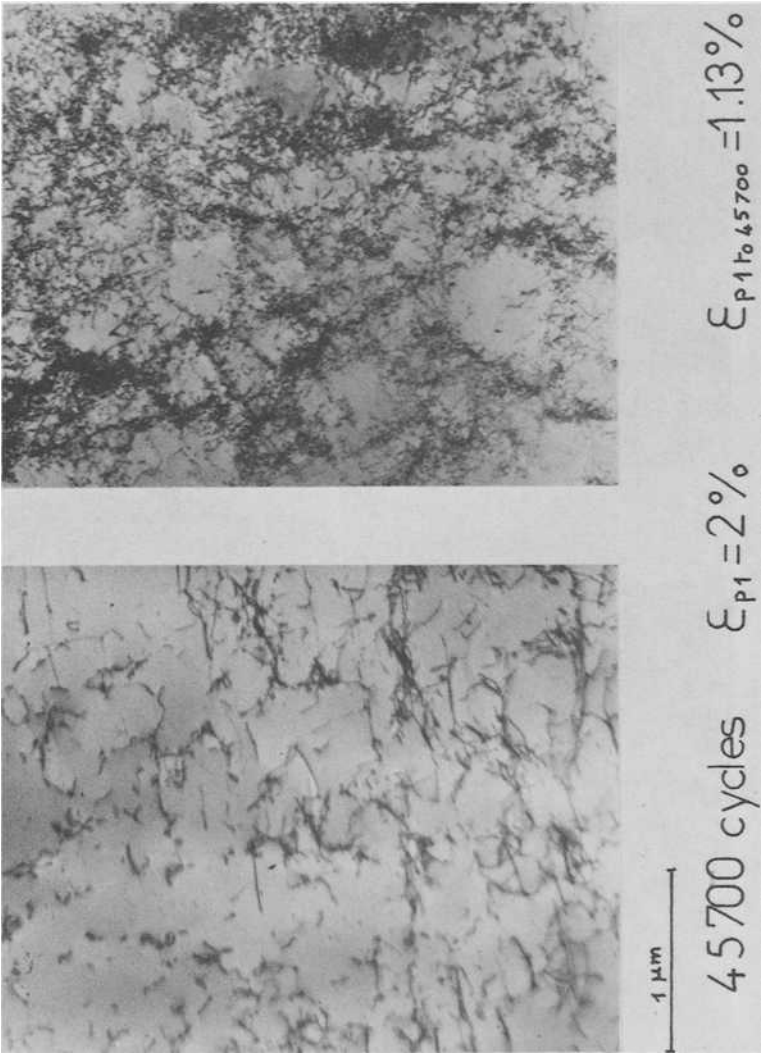
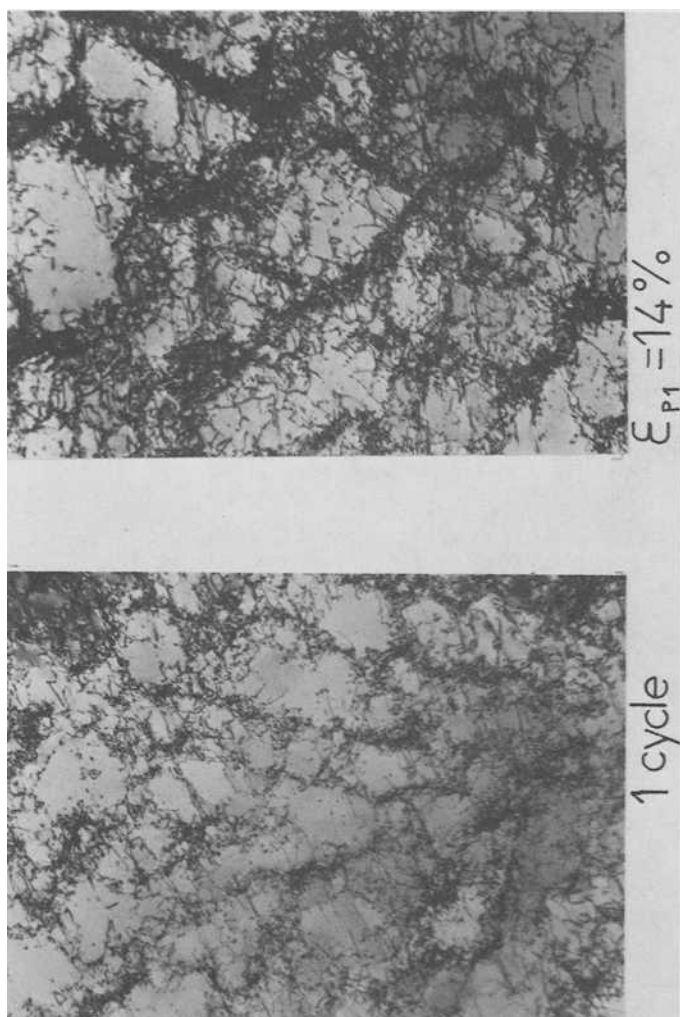


FIG. 12—TEM micrographs; $\epsilon_{p1} = 2$ percent.



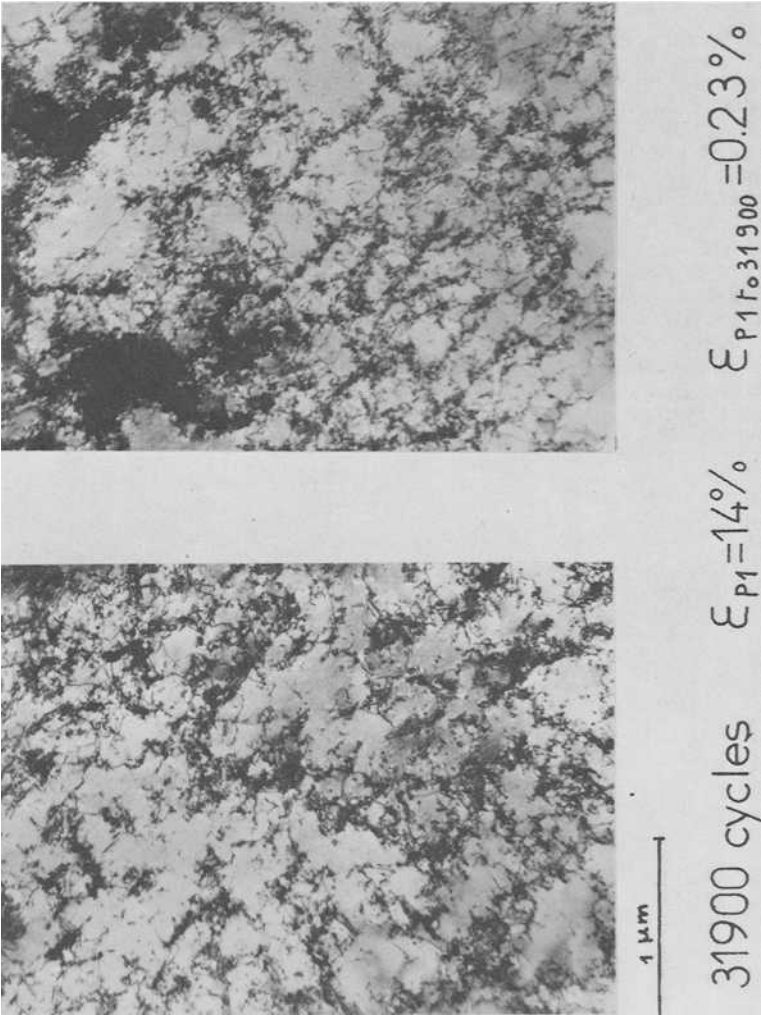


FIG. 13—TEM micrographs; $\epsilon_{P1} = 14$ percent.

For creep-deformed material the subsequent application of tensile stress cycles (of maximum stress equal to the creep stress) produces a very small deformation. Accommodation takes place rapidly after a few cycles at all stress levels.

The order in which the combinations of static and cyclic stresses are carried out has practically no influence on the deformations at stress levels below $R_{0.01}$. At higher stress levels, the creep—cyclic—tension sequence leads to higher strains than the cyclic—tension—creep sequence.

References

- [1] Castro, R. and De Cadenet, J. J., *Revue de Metallurgie*, Vol. 63, 1966, p. 903.
- [2] Dubois, D., Poirier, J., Leroy, F., and Rabbe, P., paper presented at the Special Steels Colloquium, St. Etienne, May 1976.
- [3] Ellis, J. R., Robinson, D. N., and Pugh, C. E., *Nuclear Engineering and Design*, 1978, Vol. 47, p. 115.
- [4] Plenard, E., *Revue de Metallurgie*, Vol. 65, 1968, p. 845.
- [5] Nishijima, S., *Transactions of the National Research Institute of Metals*, Vol. 11, No. 6, 1969.
- [6] Lieurade, H. P., Rabbe, P., and Roesch, L., *Memoires Scientifiques de la Revue de Metallurgie*, Vol. 69, No. 11, 1972, p. 816.
- [7] Krempl, E., *Journal of the Mechanics and Physics of Solids*, Vol. 27, 1979, pp. 363–375.
- [8] Kujawski, D., Kallianpur, V., and Krempl, E., *Journal of the Mechanics and Physics of Solids*, Vol. 28, 1980, pp. 129–148.

Evaluation of the Resistance of Type 316 Stainless Steel Against Progressive Deformation

REFERENCE: Pellissier-Tanon, A., Bernard, J. L., Amzallag, C., and Rabbe, P., "Evaluation of the Resistance of Type 316 Stainless Steel Against Progressive Deformation," *Low-Cycle Fatigue and Life Prediction, ASTM STP 770*, C. Amzallag, B. N. Leis, and P. Rabbe, Eds., American Society for Testing and Materials, 1982, pp. 69-80.

ABSTRACT: An experimental program has been conducted on Type 316 stainless steel uniaxial specimens to determine the main characteristics of their behavior under repeated loading. The cyclic stress-strain curve measured under constant repeated load, without high preloads, is independent of the level of the mean stress. Two different behaviors with respect to the occurrence of progressive deformation have been observed: (1) at room temperature, progressive deformation occurs when the *maximum* value of the tensile stress exceeds a critical value, and (2) at 320°C and for loading with temperature cycling between ambient temperature and 320°C, progressive deformation occurs when the *amplitude of stress* exceeds a critical value.

These results show that Section III of the ASME Code, which limits the range of variation of the primary plus secondary stress intensity to the value of $3 S_m$, gives an effective guarantee against progressive deformation for operating conditions in the range of 20 to 320°C. It is recalled that the absence of progressive deformation is a necessary condition for the validity of conventional low-cycle fatigue analysis.

KEY WORDS: stainless steels, cyclic behavior, shakedown analysis, progressive deformation, plastic accommodation, low-cycle fatigue creep, strain, aging

Large industrial pressure vessels and boilers are designed so that, for all in-service repeated loadings, progressive deformation of the structure cannot occur and the zones of localized plastic strain remain contained within a globally elastic field. The analysis rules proposed in the ASME Code for this purpose [1] are presented with reference to limit load or plastic shakedown criteria; this implies that the material behavior is described by a perfectly plastic stress-strain law in which the yield stress is equated with a plastic flow limit [2].³ In practice, the Code limits are established by reference to the con-

¹ Engineer, Framatome, Tour Fiat, Paris la Defense, France.

² Materials Engineer, Department of Mechanics, Creusot-Loire, Centre de Recherches d'Unieux, Firminy, France.

³ The italic numbers in brackets refer to the list of references appended to this paper.

ventional yield stress of the tension test, thus ignoring the actual behavior of the steels under cyclic loads. To check the adequacy of these rules, it is necessary to know the limiting conditions below which progressive plastic flow of the material does not occur under repeated loading. These limiting conditions are those which characterize the transition between progressive deformation and plastic shakedown.

A material element in a structure is said to have reached a state of "plastic accommodation" under repeated loading [3,4], if it ultimately presents steady cycle elastoplastic reversible behavior (with the possible exception of the first few cycles). The difference between progressive deformation and plastic accommodation of a uniformly strained material element, here a test specimen, is illustrated in Fig. 1.

The accommodation limit under repeated tension ($\sigma_{\min} = 0$) has been defined by Plenard [3] to characterize the yield limit of cast iron. Lieurade et al [5] have investigated the relation between this "accommodation limit" and the conventional yield and flow properties for stainless steels at room temperature. However, the stress state applied to any material element in a structure is seldom that of repeated tension.

For this reason, we have looked for a wider description of the material "plastic accommodation" region under imposed uniaxial stress as a function of the alternating stress amplitude σ_a and the value of the mean stress σ_m (Fig. 2).

In a similar test program performed on a 2¼Cr-1Mo quenched and tempered steel [6] at room temperature, the limit for plastic accommodation was shown to be associated with a limiting value σ_a' of the alternating stress amplitude. In addition to the determination of the limiting loading conditions between "plastic accommodation" and progressive deformation, it is necessary to characterize the cyclic stress-strain curve under alternate loading in order to better understand the behavior of the steel.

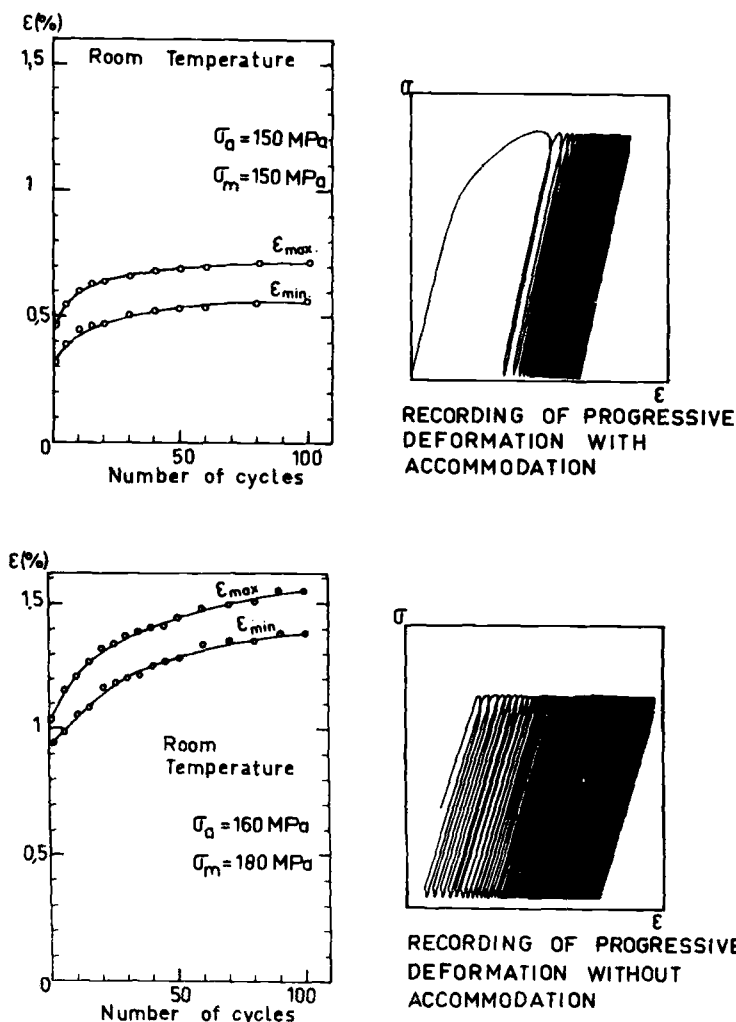
Experimental Procedure

Material

The material investigated is an annealed Type 316 stainless steel, with low carbon content and controlled nitrogen, used in the primary loop of Pressurized Water Reactors (PWR). Test specimens were taken from a 30-mm-thick plate, in the rolling direction. Chemical analysis and mechanical characteristics are given in Tables 1 and 2, respectively.

Description of Tests

The tests were conducted at 20 and 320°C, which are close to the limits of the operating temperature range of the PWR. These tests are shown schematically on Fig. 2 together with a key to the symbols used. Tests were per-



formed on a servohydraulic test machine under strain (Fig. 2a) or load (Figs. 2b to 2d) control. The specimen used is a smooth specimen with a cylindrical gage length (Fig. 3).

Cyclic stress-strain curves have been determined at room temperature and at 320°C, under strain control, using the multiple-step test method. These curves are drawn on solid lines in Figs. 4 and 5.

The conditions of "plastic accommodation" and the occurrence of progressive deformation were determined by tests under load control between $\sigma_{\max} = \sigma_m + \sigma_a$ and $\sigma_{\min} = \sigma_m - \sigma_a$, until the tendency to stabilization or

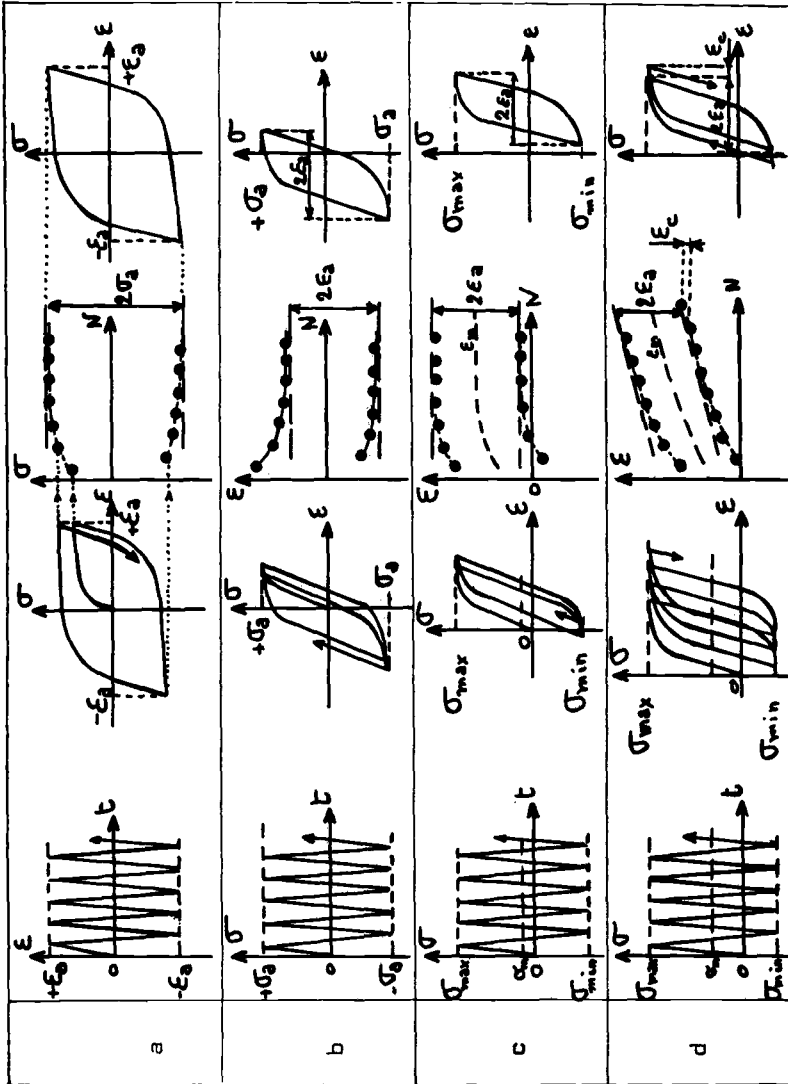


FIG. 2—Representation of tests.

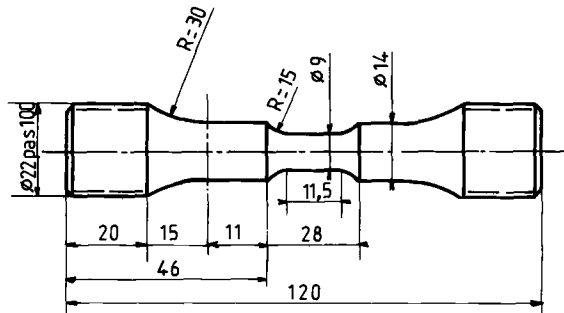
TABLE 1—*Chemical analysis.*

C	Mn	Si	S	P	Ni	Cr	Mo	N	Cu	Co
0.029	1.80	0.50	0.012	0.032	12.60	17.54	2.38	0.077	0.26	0.18

TABLE 2—*Mechanical characteristics.*

Temperature	2 % Yield Strength, MPa	Ultimate Tensile Strength, MPa	Percent Elongation (5d)	Percent Reduction of Area
Room temperature	284	539	52	81
	283	590	52	80
320°C	149	471	40	67
	155	472	39	64

progressive deformation occurred. Two types of tests were performed: (1) σ_a constant, σ_m increasing, by steps, and (2) σ_m constant, σ_a increasing, by steps. In these tests the number of cycles at each step has to be sufficient to reveal a tendency to stabilization or to progressive deformation, but is limited to avoid extensive low-cycle fatigue damage. In a previous study [6] on a 2¼Cr-1Mo steel, these tendencies appeared clearly after 10 to 20 cycles. For the stainless steel, this number of cycles is insufficient. Moreover, we have noted that, even for small loading amplitudes, there is often a slight increment of deformation at each cycle. Therefore it is necessary to define a criterion to characterize the tendency to "plastic accommodation" or to progressive deformation. The criterion retained is as follows: if the increment of mean deformation is below 0.1 percent between 50 and 100 cycles [$(\Delta\epsilon_m/\Delta N) < (2 \cdot 10^{-5}/\text{cycle})$], the material is taken to be stabilized. Figure 1 gives an example of the behavior of two specimens located just below and above the accommodation limit according to this criterion.

FIG. 3—*Specimen dimensions.*

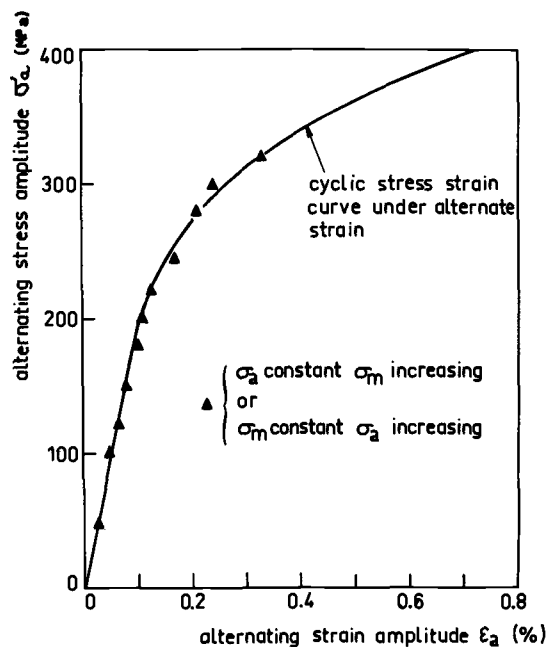


FIG. 4—Cyclic stress-strain relation at room temperature.

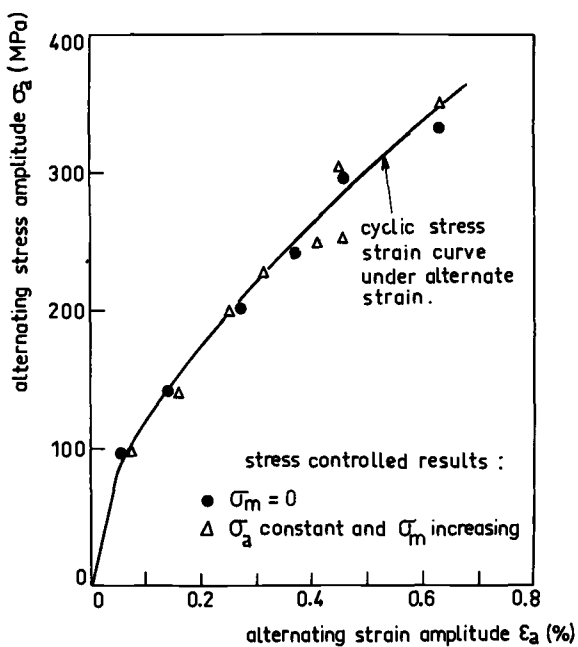


FIG. 5—Cyclic stress-strain relation at 320°C.

Results of Tests on Determination of Progressive Deformation

Tests at Room Temperature

The reference tests were carried out with a constant alternating stress amplitude and increasing mean stresses. The results obtained are plotted on a diagram ($\sigma_a - \sigma_m$) (Fig. 6). These results show that the points corresponding to progressive deformation are practically above the line

$$\sigma_a + \sigma_m = \sigma_{\max} = 350 \text{ N/mm}^2$$

The limiting condition for "plastic accommodation" depends only on the maximum stress, whatever the level of the alternating component. We have examined the influence of the test method on the determination of progressive deformation by performing tests with a constant mean stress and increasing alternating stresses. These tests led to equivalent results.

Tests at 320°C

The reference tests were performed with a constant alternating stress amplitude and increasing mean stresses. Figure 7 shows the variation of the mean stress as a function of the alternating stress; in contrast to the room-temperature behavior, an abrupt transition is observed between stress states for which the material undergoes "plastic accommodation" and states for

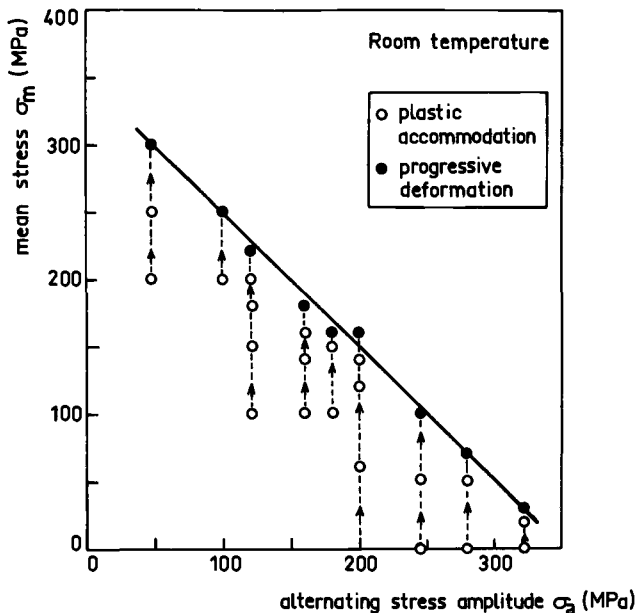


FIG. 6—Progressive deformation threshold at room temperature.

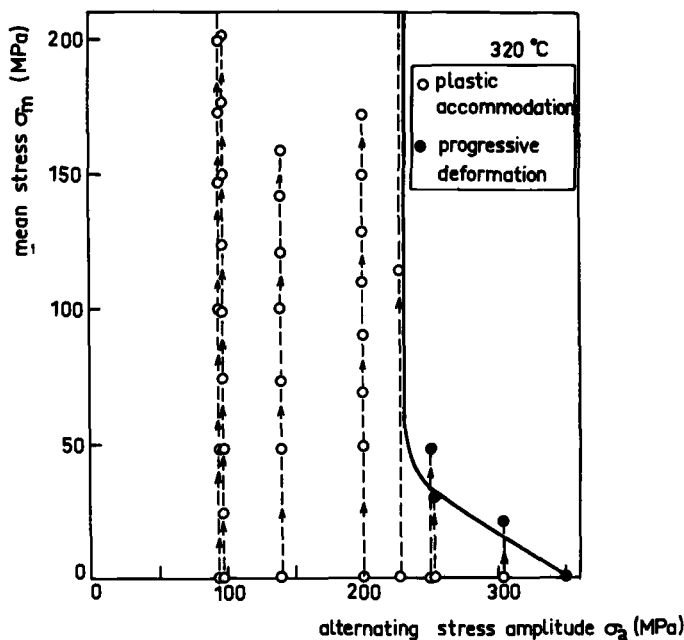


FIG. 7—Progressive deformation threshold at 320°C.

which progressive deformation occurs. The values of the mean stresses applied had to be limited owing to the value of σ_a chosen, in order to avoid an excessive elongation of the specimen. The lower value of the monotonic flow stress at 320°C explains why the maximum values of the mean stresses are lower at 320°C than at 20°C. We can therefore define for this temperature a limiting value of the alternating stress amplitude below which plastic accommodation occurs for levels of mean stresses lower than 150 to 200 MPa; this value, σ_a^l , is between 230 and 250 MPa.

Relation to the Creep Behavior of the Material

The very different behaviors observed at room temperature and at 320°C can be related to the creep behavior of the material at these temperatures. Creep tests performed between room temperature and 350°C, at equivalent stress levels, on a similar steel [7,8], have shown that (1) the steel creeps under load at room temperature, (2) when the temperature increases, the creep elongation decreases, and (3) at 350°C there is practically no creep.

The difference in creep behavior between 20 and 350°C may be interpreted by the phenomenon of strain aging at higher temperatures. Thus at room temperature, because of the creep phenomenon, a time-dependent deformation appears as soon as the stress reaches a sufficient value.

At 320°C, as there is no creep, only the alternating amplitude of the stress

cycle governs the “accommodation” phenomenon. The value of the amplitude of the stress cycle determines the value of the amplitude of the strain cycle according to the cyclic stress strain curve (see below). The strain amplitude has to be sufficient for the occurrence of progressive deformation.

Tests at Room Temperature Preceded by Tests at 320°C

As the tests had shown a very different behavior at room temperature and at 320°C, it was of interest to verify if preliminary loadings at 320°C would have an effect on the behavior of the material at lower temperatures. The results of the tests (Fig. 8) show that, for a given loading ($\sigma_a - \sigma_m$), if “accommodation” occurs at 320°C, it also occurs at room temperature. Furthermore, “accommodation” takes place at significantly higher stresses. This shows a memory effect of the material; it retains at room temperature the “accommodation” capacity acquired at 320°C.

Cyclic Stress-Strain Curves

Figure 2 shows how it is possible to determine the cyclic stress-strain relation even in the presence of progressive deformation. Figures 4 and 5 present the cyclic stress-strain curves obtained under alternate strain (solid line)

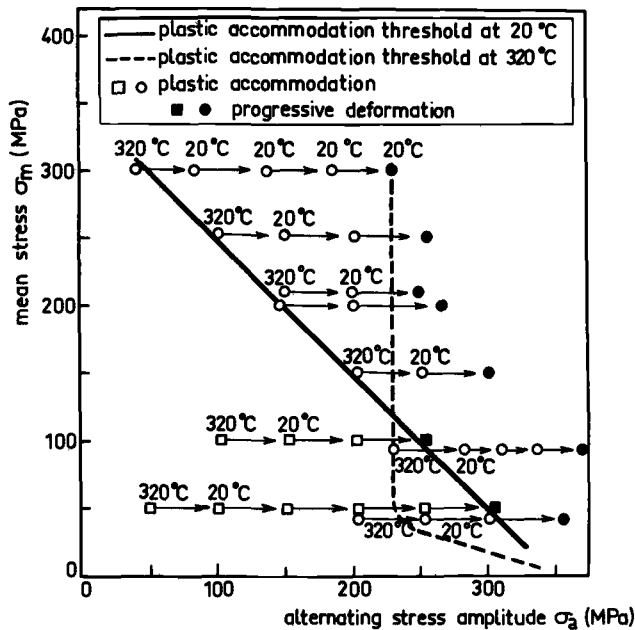


FIG. 8—Influence of preliminary solicitations at 320°C on the progressive deformation threshold at ambient temperature.

with the measurements made with stabilized values of σ_a and ϵ_a under stress control with or without mean stress. Figures 4 and 5 show that the cyclic stress-strain curve is independent of the nature of the loading sequence. This observation is of interest for the modeling of the material stress-strain relation for numerical elastoplastic structure analysis. Indeed, it confirms models, for example as proposed by Eisenberg [9], which assume that the material tends to reach asymptotically stable loops depending only on the amplitude of the stress or strain cycle.

Application of the Material "Plastic Accommodation" Limit to Structural Analysis

Tests performed on Type 316 stainless steel have shown different results at room temperature and at 320°C. At room temperature, the capacity for "plastic accommodation" is related to the existence of a creep flow stress under cyclic load. Repeated loading cycles above the cyclic flow limit have the same effect as constant load in a conventional creep test. Thus the resistance to progressive deformation under repeated loading can be calculated by using a model similar to the one used to analyze the resistance to excessive deformation under constant load for a creeping material or, even more schematically, for an elastic perfectly plastic material. A practical simplified method to solve this type of problem may be the use of limit load analysis in the same manner as for the application of the reference stress concept to creep analysis.

At about 320°C and for cycles between room temperature and 320°C, the capacity for "plastic accommodation" is directly related to the alternating stress amplitude during the repeated cycles. For any components and any loadings, if the alternating stress amplitude computed elastically for the most highly loaded material fiber remains lower than the material "plastic accommodation limit," the whole component must reach plastic shakedown. Indeed, this material fiber is subject to a stress amplitude that cannot be physically higher than the elastically computed one owing to the process of plastic stress redistribution within the structure. This material element must then necessarily attain "plastic accommodation," so must the remaining parts of the structure which sustain lower stress amplitudes. Thus the plastic shakedown of the structure is assured.

However, when loading a structure to the level allowed by the aforementioned considerations, there remains a risk that the amount of accumulated plastic deformation preceding plastic shakedown will be too high with respect to the design requirements. To avoid such a risk, one may consider a more stringent practical definition of the material "plastic accommodation" than the one given in this study (accumulated strain lower than 10^{-3} between the 50th and the 100th cycle). One may also apply a safety factor.

In addition, a transposition of the results obtained on the steel under uniaxial loading to the analysis of the behavior of a structure requires that a

multiaxial stress state should be considered. One can reasonably then employ the usual plastic flow criteria (Von Mises or Tresca), since the material "plastic accommodation" process takes place physically at the level of polycrystalline structure in the same manner as for the monotonic strain-hardening process.

For both conventional and nuclear boilers, which have operating cycles combining start-ups, shut-downs, and power fluctuations, all cycles are at elevated temperatures or between room and high temperatures. Therefore plastic shakedown in Type 316 stainless steel components would be governed by the alternating stress amplitude. This situation perfectly fits the ASME Code, Section III or Section VIII, Division 2 criterion for the primary and secondary stresses:

$$Pl + Pb + Q \leq 3 Sm$$

in which the left-hand term represents the range of variation of the Tresca equivalent stress resulting from the superposition of primary and secondary, and membrane and bending parts of the applied cyclic loading.

It is of interest to compare the "plastic accommodation" limit measured at 320°C in this study to the $3 Sm$ value given in ASME Code Section III for the Type 316 stainless steel [1]. At 320°C, $2 \sigma_a' = 460$ MPa, while $3 Sm = 390$ MPa. Actually, the loading cycles in operating plants have a larger duration than the tests presented here. We did not perform low-frequency tests or tests with hold time. However, it may be reasonably expected that the dislocation interstitial pinning that forms the basis of the dynamic-hardening effects revealed in the 320°C or 20 to 320°C tests should confer on the Type 316 stainless steel a large resistance to these time-dependent effects. Therefore the foregoing comparison between $2 \sigma_a'$ and $3 Sm$ shows that the present $3 Sm$ stress limitation of the ASME Code should provide a safe guarantee of plastic shakedown for austenitic Type 316 stainless steel structures.

To understand the mechanical meaning of such an approach compared to the thermal ratchet type criteria, one must consider that the $2 \sigma_a'$ "plastic accommodation" criterion is a sufficient but not necessary condition for the occurrence of plastic shakedown of the structure. In fact, in the case of combined mechanical and thermal loadings, it is the rate of progressive deformation beyond the $2 \sigma_a'$ loading limit which depends on the severity of the loading situation, as described by thermal ratchet criteria. And the same would hold, to a lesser extent, for the value of the strain accumulation preceding plastic shakedown just below the $2 \sigma_a'$ limit.

Conclusion

The salient result of this study is the demonstration that the possibility of a steady-state flow behavior of Type 316 stainless steel under repeated cyclic loading at 320°C or for cycles between 20 and 320°C depends only on the al-

ternating stress amplitude for levels of mean stresses lower than 150 to 200 MPa. The capacity for "plastic accommodation" of the steel for tensile cyclic loading is then related to a limiting value of the cyclic stress amplitude σ_a . For all Type 316 stainless steel structures for which the level of mean stress under cyclic loading is lower than 150 to 200 MPa, which is expected to be the most general case, this limiting value can be used within an elastic analysis as a sufficient condition to guarantee the plastic shakedown of the structure.

References

- [1] American Society of Mechanical Engineers, *ASME Boiler and Pressure Vessel Code*, Section III, NB 3200.
- [2] *ASME Boiler and Pressure Vessel Code*, Section III, 1963.
- [3] Plenard, E., *Revue de Métallurgie*, Vol. LXV, 1968, p. 845.
- [4] Halphen, B., "Accommodation et adaptation des structures élastoplastiques et plastiques," Colloque Matériaux et Structures sous Sollicitations cycliques, Ecole des Ponts et Chaussées, Paris, 1978, pp. 203-229.
- [5] Lieurade, H. P., Rabbe, P., and Roesch, L., "Comportement des aciers inoxydables austénitiques sous contrainte maintenue ou répétée," *Mémoires Scientifiques de la revue de Métallurgie*, Vol. LXIX, No. 11, 1972, pp. 815-828.
- [6] Pellissier-Tanon, A., Rabbe, P., and Amzallag, C., "Defining a Proper Material Characteristic for the Shakedown Analysis," *Third International Conference on Pressure Vessel Technology*, Part 1, ASME, 1977, pp. 223-232.
- [7] Rabbe, P. and Leroy, F., "Etude du fluage des aciers inoxydables austénitiques entre 20 et 350°C. Etude des corrélations possibles avec la tenue en corrosion sous tension," Rapport Creusot-Loire No. 1249, Sept. 1976.
- [8] Dubois, D., Poirier, J., Leroy, F., and Rabbe, P., *Revue de Métallurgie*, Dec. 1976, pp. 807-815.
- [9] Eisenberg, M. A., *Journal of Engineering and Materials Technology*, July 1976, pp. 226-228.

Lifetime Predictions and Cumulative Damage under High-Temperature Conditions

REFERENCE: Chaboche, J. L., "Lifetime Predictions and Cumulative Damage under High-Temperature Conditions," *Low-Cycle Fatigue and Life Prediction, ASTM STP 770*, C. Amzallag, B. N. Leis, and P. Rabbe, Eds., American Society for Testing and Materials, 1982, pp. 81-104.

ABSTRACT: Lifetime of a structure is considered as the time needed to initiate some macroscopic crack, propagation of which is then calculated with the help of Fracture Mechanics concepts. The paper gives a brief discussion of the possibilities of lifetime parametric relations, based on strain variables, in the high-temperature range. Alternative approaches based on Continuous Damage Mechanics are then developed and discussed; they introduce internal damage variables, describing the progressive deterioration of the material before macroscopic crack initiation. A particular definition of damage, based on the effective stress concept, gives a macroscopic measure, which constitutes a guideline to the development of differential damage equations. Some examples show the possibilities of these approaches and deal with nonlinear cumulative effects (or sequence effects) and creep-fatigue interaction.

KEY WORDS: fatigue life, crack initiation, cumulative damage, refractory alloys, creep properties, fatigue materials

In the field of jet engines, gas turbines, and nuclear and chemical plants, structural components working at high temperature under cyclic conditions are the location of many complex phenomena. The very severe requirements in design procedures (safety, reliability, efficiency, economy, etc.) require the development of sophisticated lifetime prediction techniques, which take into account viscoplastic behavior as well as crack initiation under creep and fatigue conditions.

The prediction of macroscopic crack initiation is generally made through more or less simple parametric equations, relating lifetime to some stabilized cyclic quantities such as elastic or inelastic strain ranges. A complementary approach, initially introduced for creep but recently developed for creep-fatigue interaction, leads to a macroscopic description of the successive physi-

¹ Office National d'Etudes et de Recherches Aéronautiques (ONERA), Châtillon-sous Bagneux, France.

cal phenomena giving rise to the crack initiation. The two main tools of this Continuous Damage Mechanics are the introduction of damage as an internal state variable and the treatment of the damaged material as a macroscopically homogeneous volume element. The main purpose here is to introduce these concepts in relation to classical approaches and to evaluate their utility.

General Background

Lifetime and Macroscopic Crack Initiation

The physical processes occurring in metals at high temperature before crack initiation can be schematically separated into:

1. *A first phase*, where slip and dislocation motion generate plastic and creep strains and where the preponderant macroscopic effect is cyclic hardening or cyclic softening.
2. *The micro-damage stage*, where dislocations pile-up and nucleate irreversible decohesions such as surface microcracks and grain boundary cavities.
3. *A micro-propagation period*, during which microdefects grow and coalesce into a single main crack.

This final state corresponds generally to the macroscopic crack initiation—that is, the presence of a material discontinuity—sufficiently large as regards the microscopic heterogeneities (grains, subgrains, etc.); in such a case, the main macroscopic crack is assumed to be developed through several grains, in order to show a sufficient macroscopic homogeneity in size, geometry, and direction, leading to a possible treatment through the Fracture Mechanics concept (Fig. 1). Let us remark that, contrary to other definitions, the present one corresponds approximately to the breaking up of the tension-compression specimen.

Classical Parametric Correlation of Crack Initiation

Continuation of the initial works of Coffin [1] and Manson [2] leads to the development of equations relating the number of cycles to failure N_R (or macroscopic crack-initiation) to several parameters, defined with respect to cyclic stabilized conditions, such as elastic, inelastic, and total strain ranges, dissipated strain energy [3,4], temperature, frequency, strain rate, and hold times.²

Under high-temperature loading, several relations have been proposed, introducing directly the frequency or the strain rate to describe the time or creep effects. One has, for example, the Frequency-Modified Life Relations developed by Coffin [5,6]:

² The italic numbers in brackets refer to the list of references appended to this paper.

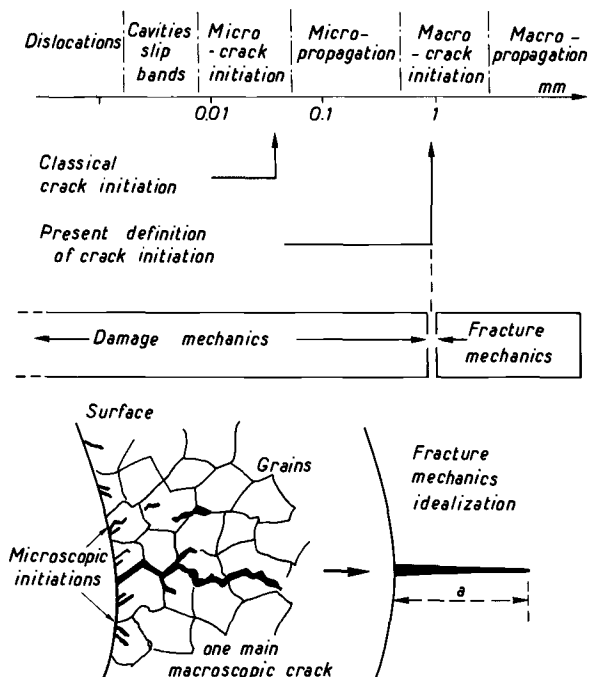


FIG. 1—Schematic of a macroscopic crack initiation concept.

$$\Delta\epsilon = C(N_f \nu^{k-1})^{-\beta} + \frac{A}{E} (C N_f^{-\beta})^{n'} \nu^{k_1 - \beta n'(k-1)} \quad (1)$$

where $\Delta\epsilon$ is the total strain range, N_f is the number of cycles to failure, and the modified frequency takes into account the cycle shape. A , C , k , k_1 , β , and n' are coefficients, depending on the material and temperature. Another modification, proposed by Berling and Conway [7], is

$$\Delta\epsilon = \frac{\epsilon_f^2}{\dot{\epsilon}} \left(\frac{N_f}{\nu} \right)^{-1} + 2 \frac{\sigma_f}{E} \left(\frac{N_f}{10} \right)^{-m/2} \quad (2)$$

where ϵ_f and σ_f are the true strain and the true stress for tensile failure (E is the Young's modulus). The Strain Range Partitioning (SRP) method [8,9] more directly recognizes the separation and the combination of creep damage and fatigue damage processes in terms of the corresponding creep and plastic strains occurring in the stabilized cycle. The difference between creep effects under tension or compression is accounted for by introducing four basic cyclic conditions: tensile plastic flow reversed by compressive plastic flow ($\Delta\epsilon_{pp}$ type inelastic strain range), tensile creep reversed by compressive creep ($\Delta\epsilon_{cc}$ type), and two mixed conditions ($\Delta\epsilon_{cp}$ and $\Delta\epsilon_{pc}$).

Four basic failure equations are associated with these four loading condi-

tions and determined by the corresponding tests, where plastic strain is defined as the inelastic strain under rapid loading and creep strain corresponds to hold times. These equations can be written as

$$N_{ij} = C_{ij} \Delta \epsilon_{in}^{-\gamma_{ij}} \quad i, j = p \text{ or } c \quad (3)$$

In the case of complex cycling, where three kinds of inelastic strain-range components can be present, several experimental [10] or numerical techniques [11] have been studied for the partitioning of the cycle. The prediction of cycles to failure N_f in the complex situation is then made by means of an additive rule such as

$$\frac{1}{N_f} = \frac{1}{\Delta \epsilon_{in}} \left[\frac{\Delta \epsilon_{pp}}{N_{pp}(\Delta \epsilon_{in})} + \frac{\Delta \epsilon_{cc}}{N_{cc}(\Delta \epsilon_{in})} + \frac{\Delta \epsilon_{cp}}{N_{cp}(\Delta \epsilon_{in})} + \frac{\Delta \epsilon_{pc}}{N_{pc}(\Delta \epsilon_{in})} \right] \quad (4)$$

Extension of the strain-range partitioning method to energetic concepts has been studied [12], but does not change the general utility of this approach.

The main advantage of parametric correlations such as Frequency Modified equations or Strain Range Partitioning holds from their simplicity; in fact, they apply easily in their range of determination. However, they appear as interpolation rules more than general constitutive equations and present several deficiencies:

1. Under temperature cycling (thermal fatigue), their application needs additional hypotheses and some specific techniques for creep and fatigue damage identification (strain partitioning is not so easy).
2. The three-dimensional generalizations are difficult to understand and apply when complex loadings are considered.
3. These formulations relate some stabilized cyclic conditions to the ultimate state of the damage process and ignore the progressive growth of the physical damage between the undamaged state and macroscopic crack initiation. This implies that under nonperiodic loading the sequence effects cannot be predicted; only the linear Miner's rule is applicable.
4. Extrapolation to long lifetimes, when the inelastic strain range is very small but hold times are very large, seems doubtful. The creep influence, for example, is minimized in the SRP method for strain cycling with large hold times (the ϵ_{cp} component becomes asymptotically constant as the hold time increases).

As can be seen by these remarks, the strain-range-based parametric correlations are already usable for design purposes, but many specific experimental determinations have to be carried out in order to extend and improve their utility. The Continuous Damage concepts, reviewed in the next sections, constitute an attempt to develop some complementary approaches.

Definitions and Measures of Damage

The usual engineering definition of damage, which ignores the details of the damage process, corresponds to the life ratios and leads to the use of the linear summation $t/t_c + N/N_F = 1$, where t_c is the nominal creep life and N_F is the number of cycles to failure under pure fatigue conditions. This definition, sufficient to introduce the linear cumulative Miner's rule, becomes inconsistent when physical aspects of damage are considered or when sequence effects have to be reproduced.

On the other hand, the physical studies of damage, limited to the microscopic scale, are important in increasing the understanding of phenomena, but are difficult to apply to engineering situations, because of their poor quantifiability. Let us note, however, progress in this domain [13-15]. Some macroscopic definitions of damage can be introduced through the measured changes in physical parameters such as density [16,17] and resistivity [18], but additional models are necessary to use these measurements for engineering purposes.

Damage Definition by the Residual Life

When lifetime predictions are considered, the natural way to introduce damage corresponds to the definition in terms of the remaining life; at each time of a given process the actual state of damage will influence the future life (or remaining life) under a particular nominal loading. This concept [19,20] is schematically illustrated in Fig. 2 and generally leads to the defini-

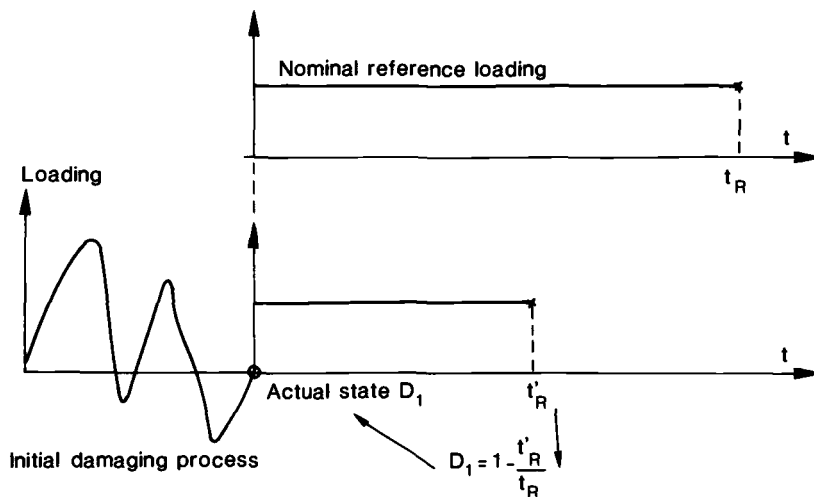


FIG. 2—Schematic of the damage measured by remaining life.

tion of the actual damage by $D_1 = 1 - (t'_R/t_R)$, where t'_R is the residual life for the same loading giving rise to life t_R for the undamaged material.

Such a definition of damage has been used in the past for creep [19] as well as for fatigue processes [21,22], but needs a considerable number of tests for implementation; at each time of the process being studied at least one specimen is necessary to measure damage in terms of the remaining life. Moreover, results of the measuring sequence can depend on the chosen reference loading (stress or strain level, temperature, creep loading, fatigue loading, etc.). In other words, these measurements are destructive and could lead to nonunique values of damage.

This concept can be used, however, as a theoretical definition of damage that permits the generally observed nonlinear cumulative effects (or sequence effects) to be described, as, for example, in stress-controlled fatigue tests under two-level sequence loadings. Figure 3a schematically illustrates that nonlinear cumulative damage can be associated with the stress dependence (or loading dependence) of the damage evolution curves as function of the life ratio N/N_F (where N_F is the nominal life under periodic loading). If damage D is considered as a unique internal state variable, it is easy to see that the summation of initial life ratio and the remaining-life ratio is different from unity. Such behavior agrees well with many experimental fatigue results [23-26].

Let us remark now that the remaining-life definition of damage is insufficient to completely quantify the damage state. Figure 3b shows schematically that the same remaining life after the same initial damaging process can be obtained for two very different kinds of damage evolution curves; for example, a biunivocal mapping between the two damage definitions,

$$D \leftrightarrow D' = D^{0.2}$$

does not change anything about the residual life and the sequence effects. This nonuniquity of damage gives no problem when only one damage process has to be considered, but leads to arbitrariness in the case where two damage processes, determined independently, are present simultaneously or sequentially. Such a situation arises under creep and fatigue interaction. The purpose of the next section is to develop a complementary measure of damage giving rise to a unique quantification.

Damage Definition by the Effective Stress Concept

The theory is supported by the physical idea that crack initiation is preceded by a progressive internal deterioration of the material, which induces a loss of strength in terms of strain as well as in terms of remaining life. Rabotnov first proposed to relate these two aspects through a macroscopic damage variable, introduced with the effective stress concept.

The effective stress concept is used to describe the effect of damage on the

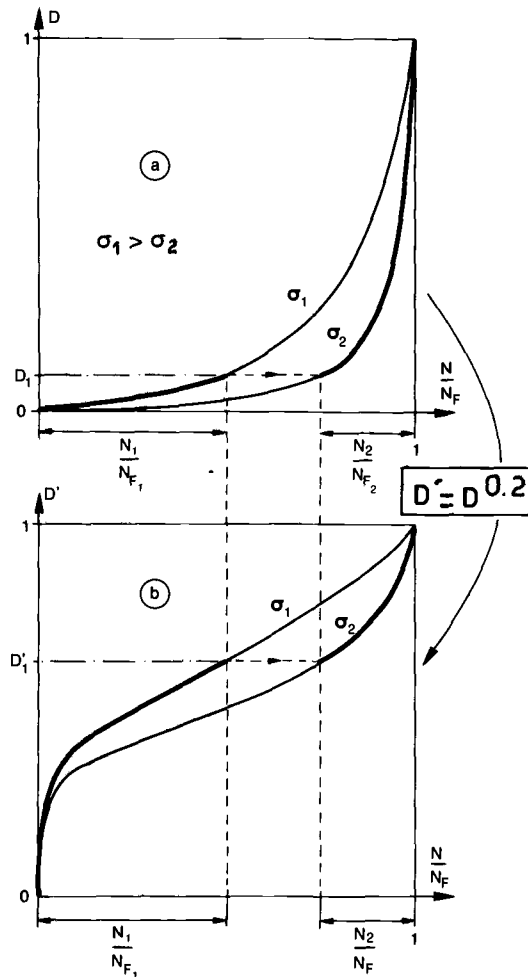


FIG. 3—(a) Nonlinear cumulative effect associated with nonunicity of damage evolution. (b) Nonuniqueness of damage measures by the remaining-life concept.

strain behavior. In this concept a damaged volume of material under the applied stress σ shows the same strain response as the undamaged one subjected to the effective stress (Fig. 4a); that is,

$$\tilde{\sigma} = \sigma / (1 - D) \quad (5)$$

Using this definition, D represents a loss effective area taking into account decohesions and local stress concentrations through homogenization concepts [27].

Under completely reversed stress-controlled tests, for example, measures of maximum plastic strain evolution (ϵ_{PM}) lead to damage measurements

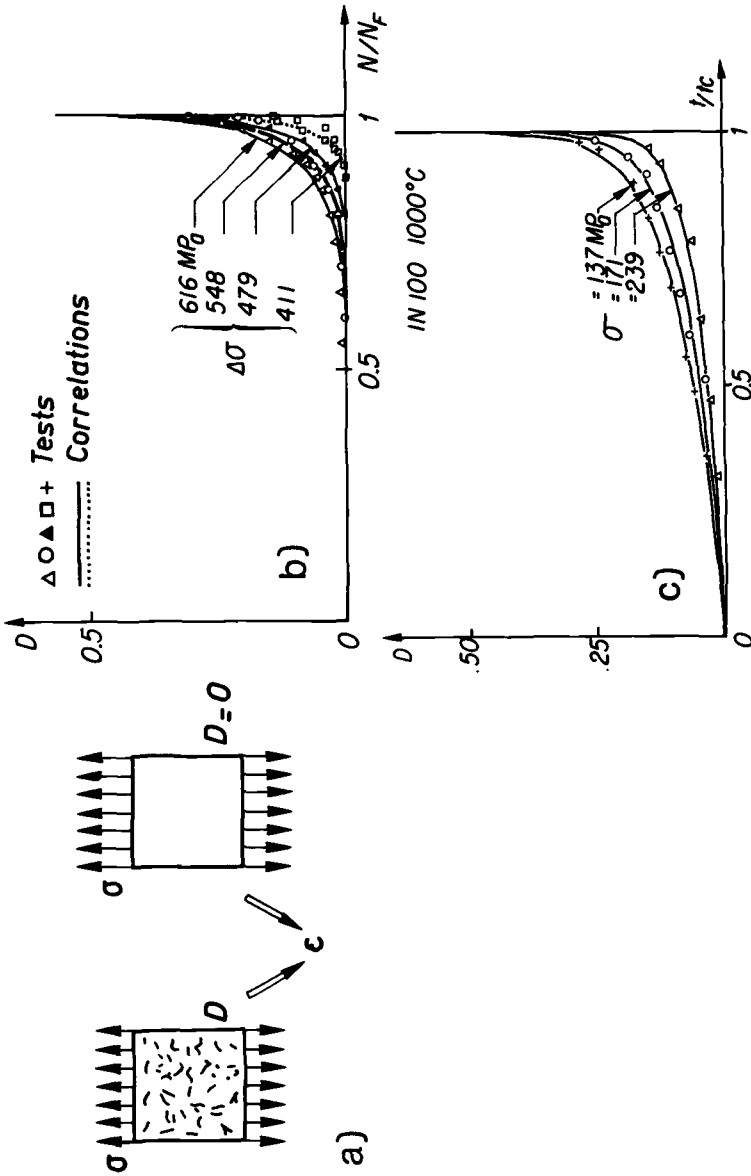


FIG. 4—Effective stress concept and its application to IN 100 alloy at 1000°C. (a) Schematic of the concept. (b) 5-Hz load controlled fatigue. (c) Creep tests.

through the power relation for the undamaged stabilized stress-strain behavior

$$\sigma_M = K \epsilon_{PM}^{*n'}$$

and the effective stress concept for the last part of the test

$$\frac{\sigma_M}{1-D} = K \epsilon_{PM}^{*n'} \quad (6)$$

where ϵ_{PM}^* is the maximum plastic strain under stabilized conditions, and the cyclic strain hardening exponent n' is determined from a set of cyclic tests. The damage follows by [28,29]

$$D = 1 - (\epsilon_{PM}^*/\epsilon_{PM})^{n'} \quad (7)$$

Figure 4b shows examples of such measurements made on the IN 100 nickel-base superalloy at 1000°C (5 Hz reversed stress control). One observes highly nonlinear damage evolution, owing to the more pronounced influence of damage processes in the micropropagation phase, and a stress dependency of these curves in the same order as in Fig. 3a, which correlates well with the generally observed cumulative effects [24,25,30]. Application of the method was also satisfactory with INCO 718 at 500°C [31] and 316L stainless steel at room temperature [32].

The method also applies in creep situations [33] by using Norton's equation as the reference undamaged behavior. As observed from remaining-life studies under creep [19,34], the different damage evolution curves are inversely ordered as regards the fatigue case (compare Figs. 4b and 4c).

As mentioned before, these damage measurements complete the remaining-life definition; they provide quantitative values of a macroscopic damage variable associated with actual physical processes. Although these measured values correspond more to the microcrack propagation, they give a sufficient indication and lead to a possible description of nonlinear creep-fatigue interaction. The quantitative difference in the damage rates under creep and under fatigue, evident from comparison of Figs. 4b and 4c, is sufficient to explain this nonlinearity for the IN 100 alloy. Let us note also the success of the approach for high-temperature creep and fatigue of 2¼Cr-1Mo steel at 550°C [35].

Damage Constitutive Equations

It is essential that these equations be developed in a differential form; an expression of D as a function of time, for example, constitutes only a response of the material to a particular forcing parameter [36]. All equations using the consumed potential (life ratio) as a damage parameter are so eliminated.

If nonlinear cumulative effects are needed, these equations must have inseparable variables in terms of damage and the chosen forcing parameter

[28,37]. In other words, the damage response functions have to be different under different loading conditions [30,38], as observed also by measuring damage through the effective stress concept.

Three types of damage increase can be investigated: (1) in terms of stress increment $d\sigma$ (or strain) in the static plastic failure, (2) as a function of the time increment dt for the creep processes (or for corrosion or irradiation processes), and (3) as a function of the cycle increment dN for the fatigue processes. Each has to be identified by some specific tests, independent of the others, leading to the determination of the corresponding differential damage equations. Considering only creep and fatigue processes, their one-dimensional isothermal form is [29,39]

$$\begin{aligned} dD_c &= f_c(\varphi, \alpha, D_c, \dots) dt \\ dD_F &= f_F(\varphi, \alpha, D_F, \dots) dN \end{aligned} \quad (8)$$

Here φ denotes the chosen forcing variables (stress or strain or plastic strain), and α represents the internal variables, describing, for example, the hardening state of the material.

Particular creep damage and fatigue damage constitutive equations are discussed in the next three sections, neglecting the influence of the hardening variable α .

Creep Damage

Creep damage develops at high temperature under constant or slowly varying loads. This time-controlled deterioration process corresponds on the microscale to the nucleation of grain boundary decohesions and their increase until formation of intergranular microcracks. The most popular creep-damage equation was first proposed by Kachanov [40] and relates damage rate to the applied stress and the actual creep damage. For the one-dimensional case its extended form writes as [29,33]

$$dD = \left(\frac{|\sigma|}{A} \right)^r (1 - D)^{-k(\sigma)} dt \quad (9)$$

Damage is 0 for the initial state and equals 1 to failure. The stress-dependent exponent $k(\sigma)$ is introduced in order to take account of the stress-dependent damage evolution curves. Under constant stress, integration of Eq 9 gives

$$D = 1 - \left(1 - \frac{t}{t_c} \right)^{\frac{1}{k(\sigma)+1}} \quad (10)$$

where t_c is the creep rupture time

$$t_c = \left(\frac{\sigma}{A} \right)^{-r} / [k(\sigma) + 1] \quad (11)$$

This creep damage equation gives a correct fit not only to the creep rupture curves [29,31] but also to the measured damage evolutions such as in Fig. 4b. Moreover, using the effective stress concept in addition to viscoplastic flow equations for the undamaged material can lead to a very accurate description of the whole creep curves [31] (Fig. 5). Primary creep is obtained from the strain-hardening equation; secondary and tertiary creep comes from coupling with the damage equation. Predictions of the creep strain at failure are also satisfactory, which supposes a correct creep ductibility description.

Let us mention other works on creep damage and its cumulative aspects, with similar approaches as Kachanov's [37,41-43], or by various concepts such as the exhaustion of ductility [44], the microcrack propagation approach [45], and the creep endurance limit [34]. These formulations are not really in opposition with the ones based on the effective stress concept; in the last theory [34], the nonlinearity of creep damage evolution is completely reversed, but the curves show the same kind of stress dependency which, as discussed before, allows a possible mapping between the two definitions of damage.

Fatigue Damage

The fatigue process generally involves surface defect nucleation and transgranular microcracking. Although some difficulties could be encountered under complex loading [31,46,47], the fatigue damage equations are generally written in terms of cycles; this hypothesis is supported by the usual observation of little dependence between fatigue life and frequency in the low temperature range. The problem of relating a formulation in terms of stress and stress rate (or strain and strain rate) to a formulation in terms of cycles has been studied by several researchers [37,47]. Three particular forms of damage growth equations are considered here:

1. *The bilinear cumulative damage rule*, introduced by Manson and his associates [24,25], uses the separation into a micronucleation stage and a micropropagation period with two independent linear damage evolutions. Stress-range dependency of the damage evolution, mentioned by the authors, is introduced in order to lead to nonlinear cumulative damage predictions when two-level fatigue tests are considered. However, the discontinuity in damage evolution, induced by the bilinear approximation, is physically unacceptable. A recently proposed cumulative approach [48], based on dissipated energy considerations, leads to the same kind of discontinuities and to some inconsistent results when considering limiting cases (N_2/N_{F2} does not equal 0 when $N_1/N_{F1} = 1$).

2. *The unified theory of Bui Quoc* [26,30] derives from a damage definition through the present fatigue limit of the material (after each damaging proc-

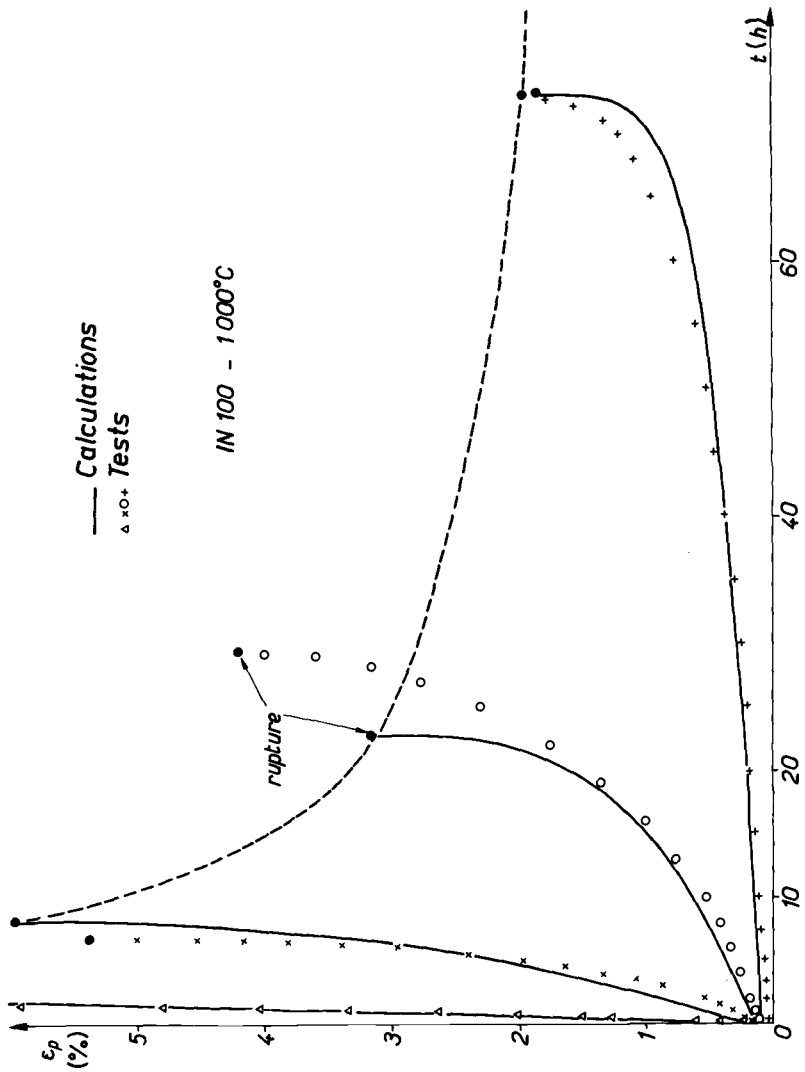


FIG. 5—Prediction of creep curves and creep failure through coupled viscoplastic and damage equations (IN 100 at 1000°C).

ess) and synthetizes together several damage equations [49–51]. The damage is measured through the relative variation of fatigue limit:

$$D = \frac{1}{A} \left(1 - \frac{\sigma'_t}{\sigma_t} \right)$$

where σ_t and σ'_t are the initial and present fatigue limits. D varies between 0 (virgin condition) and 1 (failure condition). The damage evolution is described by [30]

$$dD = \frac{1-R}{K} \sigma_M^b [\sigma_M - \sigma_t(1-AD)]^2 dN \quad (12)$$

$R = \sigma_m/\sigma_M$ is the stress ratio between minimum and maximum stress, b and K being material-dependent coefficients. An additional condition relates the residual static strength and fatigue limit as

$$\frac{\sigma'_t}{\sigma_t} = \left(\frac{\sigma'_u}{\sigma_u} \right)^m = 1 - AD \quad (13)$$

where σ_u and σ'_u are the initial and present values of ultimate tensile strength. Then, the failure condition leads to the expression for A of

$$A = 1 - \left(\frac{\sigma_M}{\sigma_u} \right)^m \quad (14)$$

Integration of these equations leads to stress-dependent damage evolution (as function of the life ratio) and to a correct description of S - N curves with the number of cycles to failure:

$$N_F = \frac{K}{(1-R)(\sigma_M - \sigma_t) \left[\sigma_M - \sigma_t \left(\frac{\sigma_M}{\sigma_u} \right)^m \right] \sigma_M^b} \quad (15)$$

The nonlinear cumulative effects are qualitatively described, with some limitations, however, owing to the form of Eqs 12 and 13, when increasing the difference between the two stress levels.

3. *A damage equation* based on the measures made through the effective stress concept incorporates very high nonlinearity for the damage evolution curves as well as for the cumulative effects (as mentioned previously, the two kinds of nonlinearities are not of the same nature). The first kind of nonlinearity is obtained by combining two simple differential equations into [28]

$$dD = [1 - (1-D)^{\beta+1}]^{\alpha(\sigma_M, \bar{\sigma})} \left[\frac{\sigma_M - \bar{\sigma}}{M(\bar{\sigma})(1-D)} \right]^\beta dN \quad (16)$$

Damage rate is zero in the initial state ($D = 0$) and infinite at failure ($D = 1$), which corresponds to the measured evolutions. For periodic loading (σ_M and $\bar{\sigma}$ constants), integration of (Eq 16) gives

$$D = 1 - \left[1 - \left(\frac{N}{N_F} \right)^{\frac{1}{1-\alpha}} \right]^{\frac{1}{\beta+1}} \quad (17)$$

where the number of cycles to failure N_F can be written as

$$N_F = \frac{1}{(\beta + 1) [1 - \alpha(\sigma_M, \bar{\sigma})]} \left[\frac{\sigma_M - \bar{\sigma}}{M(\bar{\sigma})} \right]^{-\beta} \quad (18)$$

The nonlinear cumulative effects are obtained through the stress dependence of the exponent α , which leads to inseparability and nonunicity of damage evolution curves.

For a large number of materials the following choice of functions is satisfactory [29]:

$$\begin{aligned} \alpha &= 1 - a \left\langle \frac{\sigma_M - \sigma_t(\bar{\sigma})}{\sigma_u - \sigma_M} \right\rangle \\ \sigma_t(\bar{\sigma}) &= \sigma_t(0) + [1 - b\sigma_t(0)]\bar{\sigma} \\ M(\bar{\sigma}) &= M_0(1 - b\bar{\sigma}) \end{aligned} \quad (19)$$

This formulation uses six material-dependent coefficients. The coefficients β , M_0 , σ_u , $\sigma_t(0)$ give the description of the S - N curve under zero mean stress, b introduces the mean stress dependency, and a scales the damage evolution (see the correct modeling in Fig. 4b). Under two-level stress control the integration of damage Eq 16 gives

$$\frac{N_2}{N_{F2}} = 1 - \left(\frac{N_1}{N_{F1}} \right)^p \quad (20)$$

where N_{F1} and N_{F2} are the nominal lives and p depends upon the two loading conditions by

$$p = \frac{1 - \alpha_2}{1 - \alpha_1} = \frac{\sigma_{M2} - \sigma_t}{\sigma_{M1} - \sigma_t} \frac{\sigma_u - \sigma_{M1}}{\sigma_u - \sigma_{M2}} = \frac{N_{F1}}{N_{F2}} \left(\frac{\sigma_{M1}}{\sigma_{M2}} \right)^\beta \quad (21)$$

Let us remark that the nonlinearity of cumulation in Eq 20 does not depend on the coefficient a , which scales the nonlinearity of damage evolution. Figure 6 shows the correct predictions made by Eqs 20 and 21 for IN 100 alloy [29]. Other experimental validations at high or at room temperature for various materials have been published [28,31]. Cumulative predictions with this model are very similar to those obtained by a theory based on the knee point of the S - N curve [52], where the exponent p of Eq 20 is replaced by $(\sigma_{M2} - \sigma_t)/(\sigma_{M1} - \sigma_t)$. Let us note also the recent similar treatment by Manson et al [53], where exponent p is replaced by $(N_{F1}/N_{F2})^{0.4}$.

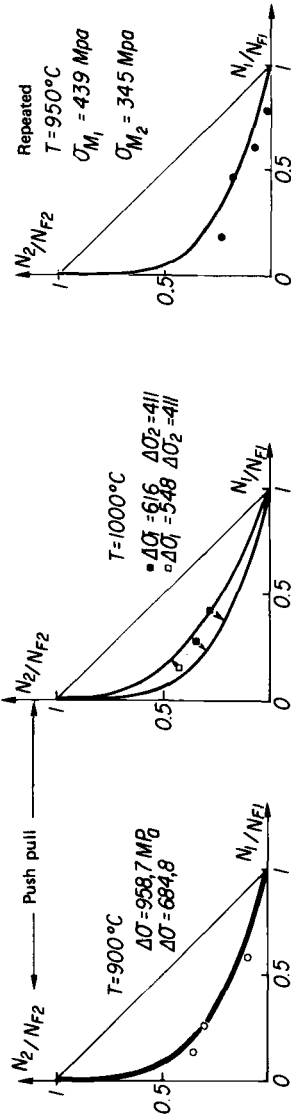


FIG. 6—Prediction of two-stress-level fatigue tests—IN 100 alloy.

Creep-Fatigue Interaction

When several processes act simultaneously, the interaction effect has to be determined through special tests. For example, the combination of creep and fatigue effect could be treated by introducing coupling terms in Eq 8:

$$\begin{aligned} dD_c &= f_c(\varphi, \alpha, D_c, D_F)dt \\ dD_F &= f_F(\varphi, \alpha, D_F, D_c)dN \end{aligned} \quad (22)$$

Although some microphysical studies [54] use such coupling parameters, most of the present day cumulative damage theories are based on the simplifying hypothesis that damage variables (here D_c and D_F) are of similar nature and interact in an additive manner, giving rise to

$$\begin{aligned} dD_c &= f_c(\varphi, \alpha, D_c + D_F)dt \\ dD_F &= f_F(\varphi, \alpha, D_c + D_F)dN \end{aligned} \quad (23)$$

As shown in several applications, the nonlinearities of interaction processes can effectively be described, because of different nonlinearities in functions f_c and f_F . Using this hypothesis only one damage variable has to be considered for the general case; combination of Eqs 23 leads to

$$dD = f_c(\varphi, \alpha, D)dt + f_F(\varphi, \alpha, D)dN \quad (24)$$

One more simplification arises if variables D and φ in Eq 24 are separable; that is, if

$$dD = h(D) f_1(\varphi, \alpha)dt + h(D) f_2(\varphi, \alpha)dN \quad (25)$$

The linear interaction rule of Robinson [55] and Taira [56] follows directly from this simplification.

Application of the nonlinear cumulative equation (24) to the high-temperature creep-fatigue behavior of IN 100 has been made [29,33,57] by using Eqs 9 and 16 to describe creep and fatigue damage, neglecting the influence of hardening. The two sets of coefficients were determined *independently* by pure creep and pure fatigue tests, including the damage measurements reported above. Creep-fatigue interaction results as a consequence; in the following examples the calculated lives are *predictions* and not correlations only.

Two situations have been considered. The first case is the two-level test where a portion of life is spent in fatigue, the remaining life being measured under creep. For IN 100, such testing leads to nonlinear effects with life summations greater than 1, because the measured fatigue damage rate (Fig. 4b) is much lesser than the creep damage rate (Fig. 4c) when they are normalized by the total life [31,58]. This has been experimentally checked and compared quite satisfactorily to integration of Eqs 9 and 16 (Fig. 7a).

The second case, more important for applications, appears when creep and fatigue act simultaneously during each cycle: low-frequency stress-

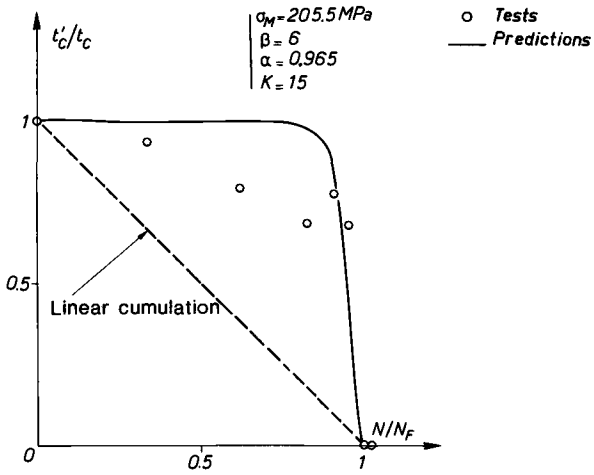


FIG. 7a—Creep fatigue interaction for IN 100 at 1000°C—creep after fatigue.

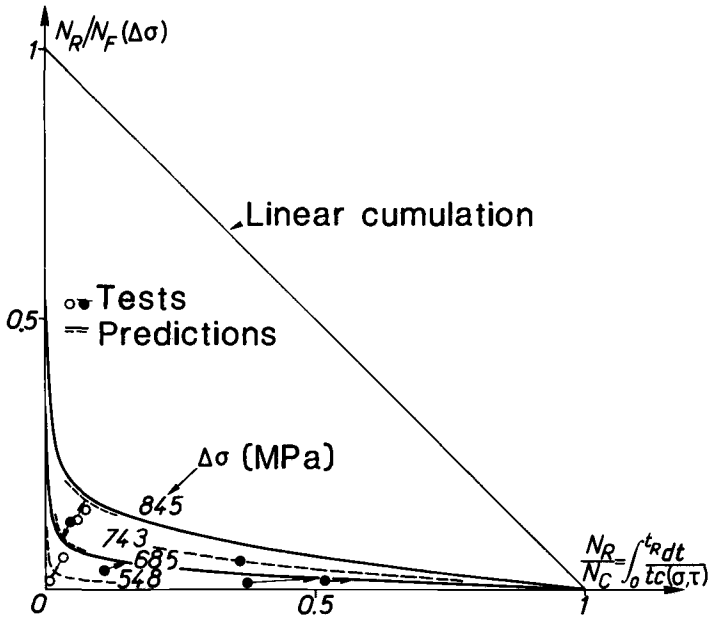


FIG. 7b—Creep-fatigue interaction for IN 100 at 1000°C—continuous cycling and cyclic creep.

controlled or strain-controlled cyclic tests, cyclic creep, and cyclic tests with hold times under strain control. In such cases, the developed damage equations are numerically integrated, after some rearrangement [29], as

$$dD = \left[\frac{(1-D)^{-k}}{(k+1)N_c} + \frac{[1-(1-D)^{\beta+1}]^\alpha}{(\beta+1)(1-\alpha)(1-D)^\beta N_f} \right] dN \quad (26)$$

where N_c is the number of cycles to failure that would be predicted for pure creep process. The nonlinear interaction is reproduced through the different damage rates under creep and under fatigue for a given damage value. This is supported by the physical idea that creep cavities nucleate early in the life and accelerate the nucleation and propagation of fatigue microcracks; moreover, the transgranular fatigue microcracks induce stress concentrations that accelerate the cavity growth.

Figure 7b shows that the theory predicts nonlinear creep-fatigue interaction with a stress-range dependency. The lower the stress, the greater the interaction; that is, the greater the life reduction by comparison with pure fatigue. Such predictions are consistent with experimental results reported in the literature [59-61] and agree fairly well with results of cyclic creep tests performed with IN 100. For this material, the low-cycle high-temperature fatigue under strain control, with or without hold times, is predictable from damage equations determined under pure creep and pure fatigue conditions, as shown in Fig. 8 (predictions are made from the measured stabilized stress-strain loops).

Critical Evaluation and Future Developments

Application to Stainless Steels

The linear creep-fatigue cumulative rule has been "caught out" on several occasions [60,62,63], particularly with cumulated creep damage much larger than 1 [62,64]. Such poor predictions could be improved by using the nonlinear creep-fatigue cumulation described above, with some modifications required to describe the particular behavior of stainless steels.

The first difficulty arises from the high ductility of stainless steels. In a large portion of the tensile creep test the stress applied to the specimen is no longer constant:

$$\sigma = (F/S)(1 + \epsilon)$$

where F is the applied constant load, S is the original cross-sectional area, and ϵ is the engineering strain. Under cyclic strain-controlled testing this ductility effect does not intervene; a correct prediction of creep damage from the measured stress evolution in the cycle then needs a correction for the associated creep rupture life. Taking account of this effect would decrease the creep ratio.

Unlike the IN 100 alloy, the stainless steels generally show a large cyclic

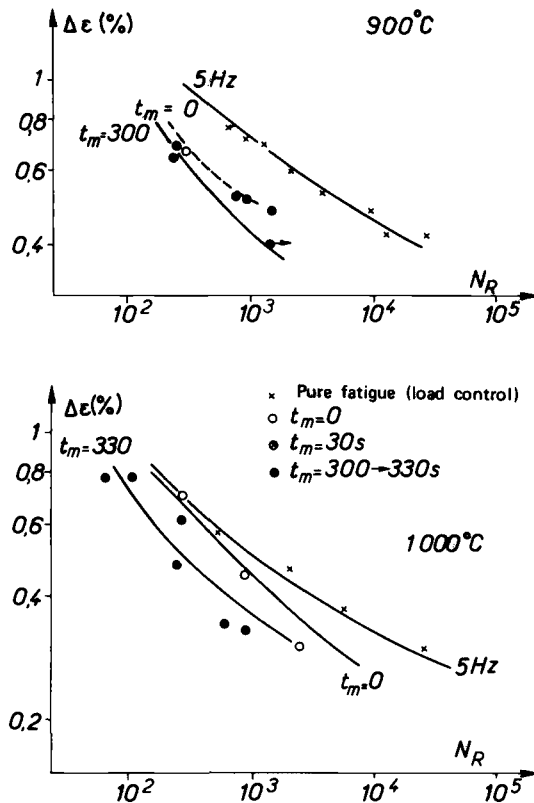


FIG. 8—Prediction of strain-controlled cyclic tests on IN 100, from the measured stabilized loops and the nonlinear creep-fatigue damage equations.

hardening effect that can be stored [65] and that can interact with damage processes [32]. The creep rupture reference has to take into account such a hardening effect by using hardening internal variables in damage equations [31] or by special creep tests (creep after cyclic hardening; special cyclic creep tests such as in Ref 66).

Complementariness to Other Approaches

In view of design situations, there is a specific advantage in using the presently developed damage concepts, generally based on stress, in parallel with classical relations, generally based on strain. Either the stress or the strain has to be calculated in the critical area of the structure; simplifying assumptions, inadequate constitutive equations or poor discretization of the structure can result in poor values of stress and strain. Owing to the stress redistribution effects (when plastic flow occurs), a stress overestimation corresponds generally to a strain underestimation; then, using damage equa-

tions in terms of stress and in terms of strain gives larger possibilities to bound the predicted lives or to detect a discrepancy.

This problem of extrapolation of fatigue data to large lifetimes is particularly relevant to nuclear applications. In this domain, the creep-fatigue damage cumulation approach presents some advantages because of its predictive character. Unlike the classical strain-based correlations, the predictions reported above were made from pure tensile creep and pure fatigue. Good agreement of this predictive approach in the domain where experimental results exist vouches for a better predictability in the extrapolation domain.

A special study of the IN 100 alloys shows the better applicability of the stress-based approach [67]. During the cyclic tests some specimens have been hardened by several temperature changes (leading to γ' precipitation). Under stress control this induces smaller inelastic strain ranges than usual [68] but the life does not increase appreciably; under strain control the stress is increased (inelastic strain decreases) and the measured life decreases. Unlike the present stress-based creep-fatigue cumulation, under such thermal cycling superposed to the mechanical cycling, the strain-based correlations have to be modified.

Possible Improvements

In addition to the particular studies needed to describe creep-fatigue interactions in several stainless steels (as previously mentioned), the present cumulative damage concepts could be developed in several directions.

The first point concerns the application of such theories to complex loading situations. Two aspects have to be treated. The first is the definition of equi-damage surfaces (or failure locus) in the stress space for a proportional triaxial loading. Several formulations have been proposed in this domain, for creep [69,70] as well as for fatigue conditions [31,46,71]. Such equi-damage surfaces contain as a particular situation the case of pure compressive creep [39], which can be important for creep-fatigue interaction studies. The second aspect is relevant to nonproportional loading and concerns the anisotropy of damage and of damage evolution; in this area, several tensorial formulations are being studied [72–75], but there is a need for more experimental data.

As mentioned before, the nonlinear cumulative effect comes from the inseparability of forcing and damage variables in damage rate equations, which leads to different damage evolutions associated with different forcings. However, if the hardening influence is neglected, the damage response curve is unique for a given loading; this induces a certain symmetry in the nonlinear cumulative rule, evident from Fig. 3, when the order of forcing levels is changed. When such a symmetry is in contradiction to the experimental evidence, two methods can be followed: (1) use the hardening variables to differentiate the internal state in the two situations (with the same damage

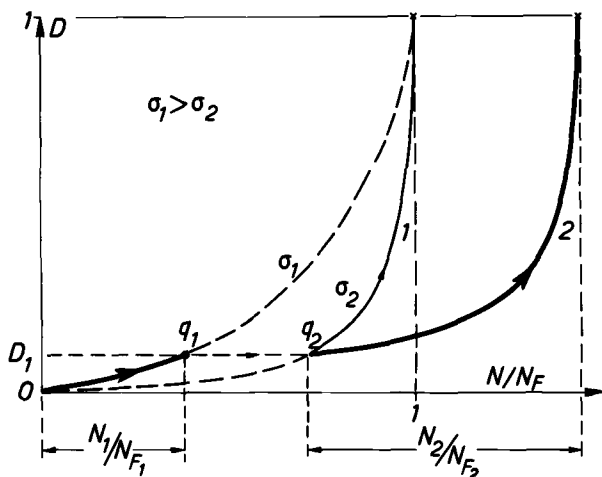


FIG. 9—Damage and interaction with another process.

state); this was recently done for the fatigue damage description of an austenitic stainless steel [32] and is schematically illustrated in Fig. 9, giving rise to the so-called interaction damage effect [76]; and (2) use the separation of microinitiation and micropropagation stages, introducing a new damage internal variable, which allows more degrees of freedom to the cumulative theory; this method is supported by some experimental observations [58].

A better modeling of fatigue damage could be obtained by developing damage rate equations in term of stress rate (or strain rate) [37,47,77], which is interesting under nonproportional loading, aperiodic loading, or under temperature cycling.

Another point concerns the separation, and the description by mechanical concepts, of environmental effects [78] and changes in the material properties induced by temperature changes [67,68] or by irradiation [79]. A study of the relations between this Continuous Damage approach and some microscopic theories [54] would lead to a better comprehension and modeling of physical processes. In the case of creep-fatigue interaction, cooperation between mechanicians and metallurgists is necessary in order to remove the simplifying hypothesis of additivity of creep and fatigue damages.

References

- [1] Coffin, L. F., *Transactions of ASME*, Vol. 76, 1954, p. 931.
- [2] Manson, S. S., *Thermal Stress and Low-Cycle Fatigue*, McGraw-Hill, New York, 1966.
- [3] Morrow, JoDean in *Internal Friction, Damping, and Cyclic Plasticity*, ASTM STP 378, American Society for Testing and Materials, 1965, pp. 45–87.
- [4] Halford, G. R., *Journal of Materials*, Vol. 1, 1966, pp. 3–17.
- [5] Coffin, L. F. in *Fatigue at Elevated Temperatures*, ASTM STP 520, American Society for Testing and Materials, 1973, pp. 5–34.

- [6] Coffin, L. F., "Fatigue at High Temperature—Prediction and Interpretation," James Clayton Lecture, University of Sheffield, 1974.
- [7] Berling, J. T. and Conway, J. B., *Transactions of the Metallurgical Society of AIME*, Vol. 25, 1969, pp. 1137–1140.
- [8] Manson, S. S., Halford, G. R., and Hirschberg, M. H., "Creep-Fatigue Analysis by Strain-Range Partitioning," NASA TMX 67838, Symposium on Design for Elevated Temperature Environment, ASME, 1971.
- [9] Hirschberg, M. H. and Halford, G. R., "Strain-Range Partitioning—A Tool for Characterizing High-Temperature Low-Cycle Fatigue," NASA TMX 71691, 1975.
- [10] Manson, S. S., Halford, G. R., and Nachtigall, A. J., "Separation of the Strain Components for Use in Strain-Range Partitioning," NASA TMX 71737, 1975.
- [11] Chaboche, J. L., Policella, H., and Kaczmarek, H., "Applicability of the SRP Method and Creep-Fatigue Approach to the LCHTF Life Prediction of IN 100 Alloy—Characterization of Low-Cycle High-Temperature Fatigue by Strain-Range Partitioning," AGARD CP-243, 1978.
- [12] Leis, B. N., *Journal of Pressure Vessels and Technology, Transactions of ASME*, 1977, pp. 524–533.
- [13] Dyson, B. F. and McLean, D., *Metal Science Journal*, Vol. 6, 1972, p. 220.
- [14] McLean, D. and Pineau, A., *Metal Science*, 1978, pp. 313–316.
- [15] Wilson, R. N., "Estimation of Remaining Creep Life of RR58 Aluminium Alloy Plate from Creep Crack Density Measurements," RAE Technical Report 76071, 1976.
- [16] Jonas, J. J. and Baudelet, B., *Acta Metallurgica*, Vol. 25, 1977, pp. 43–50.
- [17] Piatti, G., Bernasconi, G., and Cozzarelli, F. A., "Damage Equations for Creep Rupture in Steels," Paper L11/4, SMIRT-5 Conference, Berlin, 1979.
- [18] Cailletaud, G., Policella, H., and Baudin, G., "Mesure de déformation et d'endommagement par méthode électrique," *Recherche Aérospatiale*, No. 1980-1.
- [19] Woodford, D. A., "A Critical Assessment of the Life Fraction Rule for Creep Rupture under Nonsteady Stress or Temperature," International Conference on Creep Fatigue in Elevated Temperature Applications, Philadelphia (Sept. 1973), Sheffield (April 1974).
- [20] Goldhoff, R. M. and Woodford, D. A. in *Testing for Prediction of Material Performance in Structures and Components, ASTM STP 515*, American Society for Testing and Materials, 1972, pp. 89–106.
- [21] Kommers, J. B. in *Proceedings of ASTM*, American Society for Testing and Materials, Vol. 45, 1945, pp. 532–543.
- [22] Bennett, J. A. in *Proceedings of ASTM*, American Society for Testing and Materials, Vol. 46, 1946, pp. 693–711.
- [23] Erickson, W. H. and Work, C. E. in *Proceedings of ASTM*, American Society for Testing and Materials, Vol. 61, 1961, pp. 704–718.
- [24] Manson, S. S., Freche, J. C., and Ensign, C. R., "Application of a Double Linear Damage Rule to Cumulative Fatigue," NASA TN D-3839, 1967.
- [25] Manson, S. S., Nachtigall, A. J., Ensign, C. R., and Freche, J. C.,—"Further Investigation of a Relation for Cumulative Fatigue Damage in Bending," *Journal of Engineering for Industry, Transactions of ASME*, Feb. 1965.
- [26] Bui-Quoc, T., Dubuc, J., Bazergui, A., Biron, A., *Journal of Basic Engineering, Transactions of ASME*, 1971, pp. 691–698.
- [27] Duvaut, G., "Analyse fonctionnelle—Mécanique des milieux continus et Homogénéisation," in *Theoretical and Applied Mechanics*, North Holland, 1976.
- [28] Chaboche, J. L., "Une loi différentielle d'endommagement de fatigue avec cumulation non linéaire," *Revue Française de Mécanique*, 50–51, 1974; "A Differential Law for Non-Linear Cumulative Fatigue Damage," *Materials and Building Research, Annales de l'ITBTP*, HS No. 39, 1977, pp. 117–124.
- [29] Lemaitre, J. and Chaboche, J. L., *Journal de Mécanique Appliquée*, Vol. 2, No. 3, 1978, pp. 317–365.
- [30] Dubuc, J., Bui-Quoc, T., Bazergui, A., and Biron, A., "Unified Theory of Cumulative Fatigue Damage in Metal Fatigue," WRC Bulletin No. 62, 1971.
- [31] Chaboche, J. L., "Description thermodynamique et phénoménologique de la viscoplasticité cyclique avec endommagement," thèse Univ. Paris VI et publication ONERA No. 1978–3.
- [32] Chaboche, J. L., Kaczmarek, H., Raine, P., "Etude expérimentale et modélisation des

- effets d'interaction de l'érouissage et de l'endommagement dans l'acier 316L," *Recherche Aéronautique*, No. 1980-3.
- [33] Lemaitre, J. and Chaboche, J. L., "A Non-Linear Model of Creep Fatigue Damage Cumulation and Interaction," in *Mechanics of Visco-Plastic Media and Bodies*, Jan Hult, Ed., Springer Verlag, 1975, pp. 291-301.
 - [34] Bui-Quoc, T., *Journal of Engineering Materials and Technology, Transactions of ASME*, Vol. 101, 1979, pp. 337-343.
 - [35] Benallal, A., "Modélisation de creep-fatigue interaction of 2 $\frac{1}{2}$ Cr-1Mo steel at 550°C," International Symposium on Low Cycle Fatigue and Life Prediction, Firminy, France, 1980.
 - [36] Krempl, E., "On Phenomenological Failure Laws for Metals under Repeated and Sustained Loading (Fatigue and Creep)," Conference on Environmental Degradation of Engineering Materials, Blacksburg, Va., 1977.
 - [37] Ostergren, W. J. and Krempl, E., *Journal of Pressure Vessels and Technology, Transactions of ASME*, Vol. 101, 1979, pp. 118-124.
 - [38] Marco, S. M. and Starkey, W. L., *Transactions of ASME*, Vol. 76, 1954, pp. 627-632.
 - [39] Chaboche, J. L., "The Continuous Damage Mechanics: a Tool to Describe Phenomena before Crack Initiation," SMIRT-5 Conference, Berlin, 1979; *Nuclear Engineering and Design*, Vol. 64, 1981, pp. 233-247.
 - [40] Kachanov, L. M., *Izvestiia Akademii Nauk SSSR, Otdelenie Tekhnicheskikh Nauk*, No. 8, 1958, pp. 26-31.
 - [41] Rabotnov, Y. N., "Creep Rupture," in *Proceedings*, 12th International Congress on Applied Mechanics, 1968, Stanford-Springer, 1969.
 - [42] Hult, J. and Broberg, H., "Creep Rupture under Cyclic Loading," 2nd Bulgarian National Congress of Theoretical and Applied Mechanics, Varna, 1973.
 - [43] Janson, J. and Hult, J., *Journal de Mécanique Appliquée*, Vol. 1, No. 1, 1977.
 - [44] Polhemus, J. F., Spaeth, C. E., and Vogel, W. H. in *Fatigue at Elevated Temperatures, ASTM STP 520*, American Society for Testing and Materials, 1973, pp. 625-636.
 - [45] Radhakrishnan, V. M., *Engineering Fracture Mechanics*, Vol. 11, 1979, pp. 373-383.
 - [46] Dang Van, K. "Sur la résistance à la fatigue des métaux," *Sciences et Techniques de l'Armement*, Vol. 47, 3ème Fasc., 1973.
 - [47] Sorensen, A., Jr., *Journal of Basic Engineering, Transactions of ASME*, No. 68-WA/Met. 6, 1969, pp. 1-14.
 - [48] Radhakrishnan, V. M., *Experimental Mechanics*, 1978, pp. 292-296.
 - [49] Shanley, F. R., "A Theory of Fatigue Based on Unbending During Reversed Slip," The Rand Corporation Report, 1953, p. 350.
 - [50] Henry, D. L., *Transactions of ASME*, Vol. 77, 1955, pp. 913-918.
 - [51] Gatts, R. R., *Journal of Basic Engineering, Transactions of ASME*, Series D, Vol. 83, No. 4, 1961, pp. 529-540.
 - [52] Subramanyan, S., *Journal of Materials and Technology, Transactions of ASME*, 1976, pp. 316-321.
 - [53] Manson, S. S., "Some Useful Concepts for the Designer in Treating Cumulative Damage at Elevated Temperature," ICM 3, Cambridge, 1979, Vol. 1, pp. 13-45.
 - [54] Levaillant, C., Rezgui, B., and Pineau, A., "Effects of Environment and Hold Times on High-Temperature Low-Cycle Fatigue Behaviour of 316L Stainless Steel," Third International Congress on Mechanical Behaviour, Cambridge, 1979.
 - [55] Robinson, E. L., "Effect of Temperature Variation on the Long Time Rupture Strength of Steels," *Transactions of ASME*, Vol. 5, 1952.
 - [56] Taira, S., "Lifetime of Structures Subjected to Varying Load and Temperature," in *Creep in Structures*, N. J. Hoff, Ed., Academic Press, New York, 1962.
 - [57] Chaboche, J. L., Policella, H., and Savalle, S., "Application of the Continuous Damage Approach to the Prediction of High-Temperature Low-Cycle Fatigue," Conference sur les alliages à Haute Température pour Turbines à Gas, Liège, 1978.
 - [58] Plumtree, A. and Lemaitre, J., "Application of Damage Concepts to Predict Creep-Fatigue Failures," ASME Pressure Vessels and Piping Conference, Montreal, June 1978.
 - [59] Ellison, E. G. and Patterson, A. J. F., *Proceedings of the Institution of Mechanical Engineers*, Vol. 190, No. 12, 1976.
 - [60] Lagneborg, R., *Metallurgical Transactions*, Vol. 2, July 1971.
 - [61] Morishita, T., Miwa, K., Munakata, Y., Nomura, M., and Kan, S., "Thermal Fatigue of

- INCO 713 and IN 100 Gas Turbine Blades," Tokyo Joint International Gas Turbine Conference and Products Show, ISME, October 1971.
- [62] Jaske, C. E., Mindlin, H., and Perrin, J. S. in *Fatigue at Elevated Temperatures, ASTM STP 520*, American Society for Testing and Materials, 1973, pp. 365-376.
 - [63] Campbell, R. D., *Journal of Engineering for Industry, Transactions of ASME*, Nov. 1971, pp. 887-892.
 - [64] Rezgui, B., "Interaction fatigue fluage. Effet d'un temps de maintien sur la résistance à la fatigue d'un acier Z2 CND 17-13 (type 316L) à 600°C," Rapport CEA-R-4982, 1979.
 - [65] Chaboche, J. L., Dang-Yan, K., and Cordier, G., "Modelization of the Strain Memory Effect on the Cyclic Hardening of 316 Stainless Steel," SMIRT-5 Conference, Berlin, 1979.
 - [66] Halford, G. R., "Cyclic Creep-Rupture Behavior of Three High-Temperature Alloys," NASA TN D-5309, 1971.
 - [67] Cailletaud, G., Culie, J. P., and Kaczmarek, H., "Mechanical Description of Viscoplastic and Damage Behavior in Presence of Microstructural Instabilities Induced by Variable Temperature," Comm. Symposium IUTAM "Creep in Structures", Leicester, Sept. 80.
 - [68] Cailletaud, G. and Chaboche, J. L., "Macroscopic Description of the Micro-Structural Changes Induced by Varying Temperature: Example of IN 100 Cyclic Behavior," Conference ICM3, Cambridge, 1979.
 - [69] Hayhurst, D. R., *Journal of the Mechanics and Physics of Solids*, Vol. 20, No. 6, 1972, pp. 381-390.
 - [70] Lemaitre, J., "Damage Modelling for Prediction of Plastic or Creep-Fatigue Failure in Structures," Paper L5-1, SMIRT-5 Conference, Berlin, 1979.
 - [71] Sines, G., "Behavior of Metals under Complex Static and Alternating Stresses," in *Metal Fatigue*, G. Sines and J. L. Waisman, Eds., McGraw-Hill, New York, 1959, pp. 145-169.
 - [72] Murakami, S. and Ohno, N., "A Constitutive Equation of Creep Damage in Polycrystalline Metals," IUTAM Colloquium, Euromech 111, Marienbad, Tchécoslovaquie, 1978.
 - [73] Chaboche, J. L., "Le concept de contrainte effective appliqué à l'élasticité et à la viscoplasticité en présence d'un endommagement anisotrope," Colloque Euromech 115, Grenoble, 1979.
 - [74] Leckie, F. A. and Onat, E. T., "Tensorial Nature of Damage Measuring Internal Variables," IUTAM Symposium on Physical Non-Linearities in Structural Analysis, Senlis, France, 1980, Springer-Verlag ed.
 - [75] Sidoroff, F., "Description of Anisotropic Damage—Application to Elasticity," IUTAM Symposium on Physical Non-Linearities in Structural Analysis, Senlis, France, 1980, Springer-Verlag ed.
 - [76] Bui-Quoc, T., "Cumul du dommage en fatigue," in *La fatigue des matériaux et des structures*, Sherbrooke, 1978, Maloine ed., 1980.
 - [77] Chrzanowski, M., *International Journal of Mechanical Sciences*, Vol. 18, 1976, pp. 69-73.
 - [78] Antolovitch, S. D., "Aspects métallurgiques de la fatigue à haute température," in *La fatigue des matériaux et des structures*, Sherbrooke, 1978, Maloine ed., 1980.
 - [79] Brinkman, C. R., Strizak, J. P., and Booker, M. K., "Experiences in the Use of Strain-Range Partitioning for Predicting Time-Dependent Strain-Controlled Cyclic Lifetimes of Uniaxial Specimens of 2½ Cr-1Mo Steel, Type 316 Stainless Steel, and Hastelloy X," in *Characterization of Low-Cycle High-Temperature Fatigue by Strain-Range Partitioning*, AGARD CP-243, 1978.

An Evaluation of Four Creep-Fatigue Models for a Nickel-Base Superalloy

REFERENCE: Bernstein, H. L., "An Evaluation of Four Creep-Fatigue Models for a Nickel-Base Superalloy," *Low-Cycle Fatigue and Life Prediction, ASTM STP 770*, C. Amzallag, B. N. Leis, and P. Rabbe, Eds., American Society for Testing and Materials, 1982, pp. 105-134.

ABSTRACT: Four models for the creep-fatigue interaction were evaluated for their ability to predict fatigue behavior at 650°C (1200°F) of thermomechanically processed René 95, a nickel-base superalloy used for turbine disks. These models are the Strain-range-Partitioning Model, the Frequency-Separation Model, the Frequency-Modified Damage Function, and the Damage-Rate Model. The data base was divided into baseline and verification tests. The correlations of the baseline tests, having the smallest standard deviation of 0.18, were by the Frequency-Separation Model and the Frequency-Modified Damage Function. The other two models had standard deviations greater than 0.22. These standard deviations correspond to worst correlations of 3.6 and over 5.0 times the observed life. The ratios of the observed to the predicted life of the verification tests ranged from 5.2 by the Frequency-Modified Damage Function to 18 by the Frequency-Separation Model. Each of the models consistently overpredicted or underpredicted the lives of certain types of tests in the data base. The models did not account for the mean stresses observed in the fatigue tests. A method based upon the stress versus minimum creep rate and the cyclic stress-strain curves is suggested to indicate whether an environmental-fatigue interaction or a creep-environmental-fatigue interaction is present. For René 95, this method indicates an environmental-fatigue interaction.

KEY WORDS: René 95, crack initiation, low-cycle fatigue, high-temperature fatigue, strain-rate effects, nickel-base superalloys, creep-fatigue interaction

The purpose of this paper is to evaluate the ability of four prominent creep-fatigue models to predict the high-temperature low-cycle fatigue (HT-LCF) behavior of a nickel-base superalloy used for military-engine turbine disks.² HT-LCF constitutes a principal failure mode for disks, and in many cases limits the service life. For extension of this life and the design of lighter-weight disks, an accurate model to predict HT-LCF is required. Accuracy is required both on overprediction and underprediction—overprediction of the life

¹ Graduate Assistant, University of Cincinnati, Cincinnati, Ohio 45221; formerly with Systems Research Laboratories, Inc., Dayton, Ohio 45440.

² The terms HT-LCF and creep-fatigue are used interchangeably in this paper without implying a particular physical mechanism.

would be unsafe and underprediction would result in a heavier design than required.

No model for HT-LCF has yet gained widespread acceptance. The primary difficulty in predicting this behavior is accounting for the interaction of creep and/or environmental attack (from high-temperature oxidation) with the fatigue process.

Four models are evaluated in this paper:

- Strainrange-Partitioning Model (SRP) [1-4]³
- Frequency-Separation Model (FS) [5,6]
- Frequency-Modified Damage Function (FMDF) [7,8]
- Damage-Rate Model (DRM) [9-11]

These models, which have been applied previously with promising results, were developed mainly with materials having lower strength and higher ductility than the nickel-base superalloys used in turbine disks.

An advanced nickel-base superalloy—thermomechanically processed, cast and wrought René 95—was used to generate the data base. A series of fatigue tests—both continuous cycling tests at different frequencies and strainhold tests—was run at 650°C (1200°F), which is the operating temperature of this material. Each of the models was evaluated for its ability to both correlate and predict these tests, and then the models were compared.

This study is a continuation of previous investigations. Menon [12] evaluated the SRP and Frequency-Modified [13] Model using a smaller data base. Bernstein [14] made a preliminary evaluation of the four models using a somewhat larger data base. A detailed evaluation of the SRP Model by Hyzak and Bernstein [15] used the same data base as that in the present paper, with the exception of five tests. A detailed description of the fitting of the models to the data and a tabular listing of the data base are given in Ref 16.

The constitutive behavior of René 95 has been examined by Stouffer et al [17], and the complete fatigue program on the material has been presented by Conway and Stentz [18].

Material

René 95—a nickel-base superalloy used in jet-engine turbine disks—has high tensile strength, excellent creep resistance, and good ductility up to 650°C (1200°F). The alloy is strengthened primarily by the precipitation of a high-volume fraction of the intermetallic γ' , $\text{Ni}_3(\text{Al}, \text{Ti}, \text{Cb})$, as well as by solid-solution hardening and carbide formation. The particular form of René 95 used in this study was a forging that underwent a thermomechanical processing (TMP) treatment during the forging operation. This produced a duplex microstructure consisting of large, warm-worked grains (75 μm) surrounded by a grain boundary composed of fine, recrystallized grains (4 μm).

³ The italic numbers in brackets refer to the list of references appended to this paper.

René 95 is also available as a forging without TMP and as a powder-metal-lurgy product.

The principal alloying elements (in weight percent) are 14Cr, 8Co, 3.6W, 3.6Al, 3.5Mo, 3.5Cb, 2.5Ti, and 0.15C. A complete chemical composition is given in Ref 16. The processing and heat treatment of the René 95 is given in Ref 12. Microstructural characterization can be found in Refs 12 and 19–22.

Constitutive Behavior

Stress-Strain Behavior

The stress-strain behavior of René 95 has been studied by Stouffer [17,23]. At 650°C (1200°F) René 95 has a 0.2 percent tensile yield stress of 1207 MPa (175 ksi), an ultimate tensile stress of 1448 MPa (210 ksi), a tensile elastic modulus of 175×10^3 MPa (25.4×10^3 ksi), and a reduction in area of 12 percent. The creep behavior is shown in Fig. 1. Two minimum creep rate

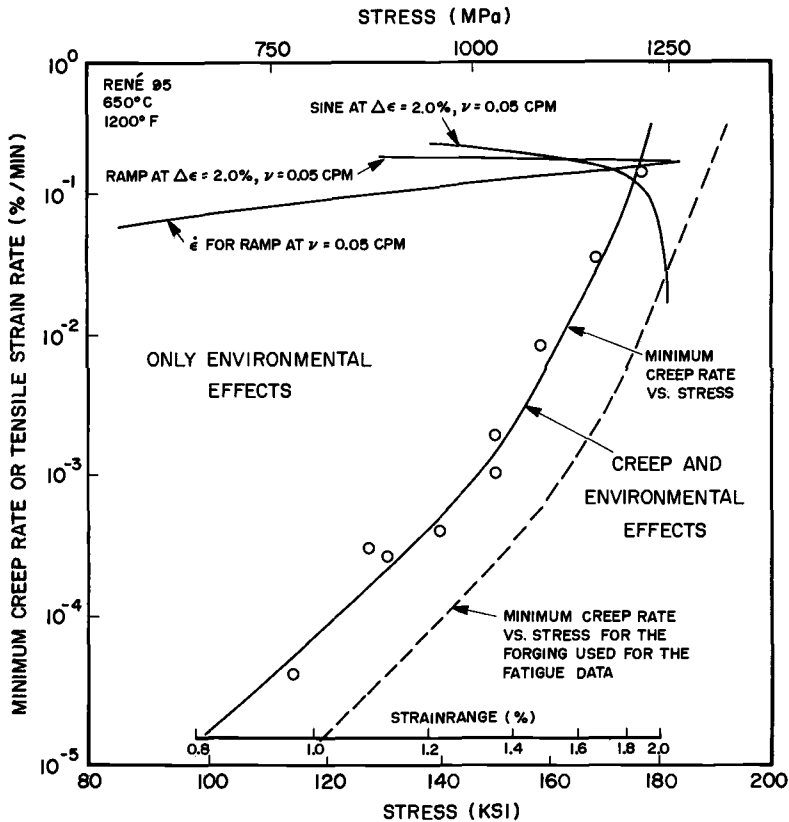


FIG. 1—Relationship between creep and fatigue based upon the minimum creep rate versus stress and the cyclic stress-strain curves.

curves are given: the solid curve for the forging used to produce the stress-strain data in Ref 17, and the dashed curve for the forging used for the fatigue tests and the data in Ref 23. Figure 1 is quite complicated and will be explained throughout this section.

The most significant aspect of the stress-strain behavior related to HT-LCF is the strain-rate sensitivity of the material. For strain-controlled tension tests run on a servohydraulic machine, similar stress-strain behavior to 1.2 percent strain was exhibited from strain rates of 50 to 0.05 percent/min. A strain-rate effect was observed only for a strain rate of 0.001 percent/min. This same behavior was also observed for the fatigue tests in which similar hysteresis loops were exhibited for continuous-cycling tests at frequencies of 0.05 cycles per minute (cpm) and 20 cpm.

This strain-rate sensitivity can be understood in relation to the creep behavior in Fig. 1. If a tension test were run under strain control at a rate of 0.001 percent/min, one would expect a maximum stress of 1000 MPa (145 ksi) from Fig. 1 because a creep test at this stress has a minimum creep rate of 0.001 percent/min. All the imposed strain in the tension test can be absorbed by creep deformation when the stress reaches this value. This idea was confirmed by tension tests run at strain rates of 0.001 and 0.05 percent/min, in which the maximum stress observed was 1014 MPa (147 ksi) and 1244 MPa (180 ksi), respectively. The tensile behavior to 1.2 percent strain at 50 and 0.05 percent/min was similar because insufficient stress was generated to cause creep at these strain levels and strain rates.

The possibility of strain-age-hardening influencing the stress-strain behavior was investigated. A series of cyclic stress-strain tests was run at frequencies from 0.05 to 20 cpm [16]. Similar hysteresis loops were observed at all frequencies. If strain-age-hardening was occurring, then the stress-range should have increased as the frequency was lowered instead of remaining the same. In addition, the tension tests run by Stouffer et al [17] did not exhibit any strain-age-hardening. Therefore it was concluded that strain-age-hardening was not present for the given test conditions.

These ideas can be extended to the fatigue behavior of René 95. In Fig. 1, a total strainrange scale has been drawn above the stress scale. The strainrange scale was calculated from the cyclic stress-strain curve. (This curve was determined from continuous-cycling fatigue tests at a frequency of 20 cpm). Each strainrange is placed above the peak tensile stress reached in the fatigue test; that is, a fatigue test at a strain range of 1.4 percent developed a stress of 1055 MPa, therefore the value of 1.4 percent is written above 1055 MPa.

A relationship between creep and fatigue can now be given by considering a fatigue test with a triangular waveform having a strain rate of 0.01 percent/min. At this rate a stress of 1100 MPa (160 ksi) is required to produce creep deformation. For developing this stress a strainrange of 1.5 percent or greater must be employed. At smaller strainranges little creep will occur because the stresses will not be sufficiently large. If the strain rate of the fatigue test is re-

duced, then creep will occur at smaller strainranges. If faster strain rates are employed, larger strainranges will be required to develop the stresses necessary to cause creep. Therefore creep deformation in a fatigue test depends upon a combination of strain rate and strain range.

This relationship provides insight into the circumstances under which a creep-environmental-fatigue interaction can take place. If the combination of strainrange and strain rate is sufficient to produce creep deformation, then a creep-fatigue interaction can be expected, with an environmental effect being present. If this combination is out of the creep regime, then only an environmental-fatigue interaction is possible. A creep-fatigue interaction cannot occur because creep is absent. It should be noted that the minimum creep rate is lower for some materials in vacuum than in air [24] including René 95 [25]; therefore smaller strain rates may be required to produce creep in vacuum than in air. In this sense, one may speak of a true creep-environmental-fatigue interaction.

In many test programs, the frequency is held constant for all strainranges, and the strain rate is allowed to vary. A curve is constructed in Fig. 1 for a triangular waveform of constant frequency of 0.05 cpm from the equation relating frequency ν , strain rate $\dot{\epsilon}$, and strainrange $\Delta\epsilon$:

$$\dot{\epsilon} = 2(\Delta\epsilon)\nu$$

It can be seen that using the dashed curve, creep does not occur for the 0.05-cpm triangular wave until a strainrange greater than 2.0 percent is reached. This result explains the similarity in the hysteresis loops for the 20-cpm and 0.05-cpm fatigue tests. Neither frequency produces creep deformation over the strainranges studied.

These concepts also help to explain the differences between the sine and ramp waveforms. The sine waveform has a continuously varying strain rate whose magnitude becomes smaller at the higher stress levels. This behavior is plotted in Fig. 1 for a total strainrange of 2.0 percent and a frequency of 0.05 cpm from the equations

$$\dot{\epsilon} = \pi\nu(\Delta\epsilon) \cos(2\pi\nu t)$$

$$\epsilon = \frac{1}{2} \Delta\epsilon \sin(2\pi\nu t)$$

where t is time. Because of the drooping nature of the sine curve, it encounters the creep curve before the ramp wave. Consequently, the sine wave should exhibit more creep effects than the ramp wave. Creep may not be the only reason for a difference between the ramp and sine waves, since environmental effects may be dependent upon strain rate, stress, and strainrange.

Finally, Fig. 1 shows that different deformation and failure mechanisms would be expected in a set of HT-LCF data that spans the creep and no-creep regimes. The figure provides a quantitative estimate of the location of these regimes and should aid in the planning of test matrices.

Cyclic Behavior

René 95 does not form a stable cyclic stress-strain curve. Under continuous cycling it initially hardens and then softens [17,26]. This softening continues until failure.

The most striking feature of tension-only and compression-only strain-hold tests is the large mean stresses that developed. The mean stress became greater as the hold period lengthened or as the strainrange decreased. The mean stresses for all the fatigue tests are shown in Fig. 2, and a description of the test conditions can be found in the following section on the experimental program. The mean stress develops rapidly during the first 10 percent of the test life and thereafter continues to increase, but at a slower rate. The mean stress does not stabilize, owing to the continuously softening nature of the material. Figure 3 is a plot of the peak tensile and compressive stresses for a tensile strain-hold test as a function of both percent of cyclic life and the logarithm of cycles. It can be seen that the stresses appear to reach an asymptotic value on a linear scale; whereas on a logarithmic scale, they are seen to be constantly decreasing. Since the stresses are decreasing at a logarithmic rate, they appear to reach an asymptotic value on a linear scale.

The lack of a stable cyclic stress-strain curve for René 95 meant that the values of the stresses and strains were changing throughout the test. To circumvent this problem in evaluating the models, the values of the stresses and strains at one half the fatigue life were used in the models to predict the life. The justification for this procedure would be that these values uniquely characterize the particular fatigue test. In addition, this procedure is used almost universally in the literature.

Graphical and tabular data on the cyclic behavior of the stresses for many of the fatigue tests in this paper have been reported in Ref 26.

Fatigue Behavior

Experimental Program

The LCF tests were performed using servohydraulic, closed-loop feedback machines. The test specimen was of the 6.35-mm (0.25-in.)-diameter hourglass geometry. The load and diametral strain were measured and converted by an analog computer into an equivalent axial strain, which was used to control the test. The specimen was heated by an induction coil. Further details of the test procedure are given by Slot [27] and Conway [28].

The test program was divided into two sections: baseline tests and verification tests. Baseline tests were used to obtain the constants in the models and to test the correlative ability of the models. Verification tests were of waveforms different from the baseline tests and were used to determine the ability of the models to predict tests not used in calculating the constants.

The waveforms used for the baseline tests consisted of continuous-cycling

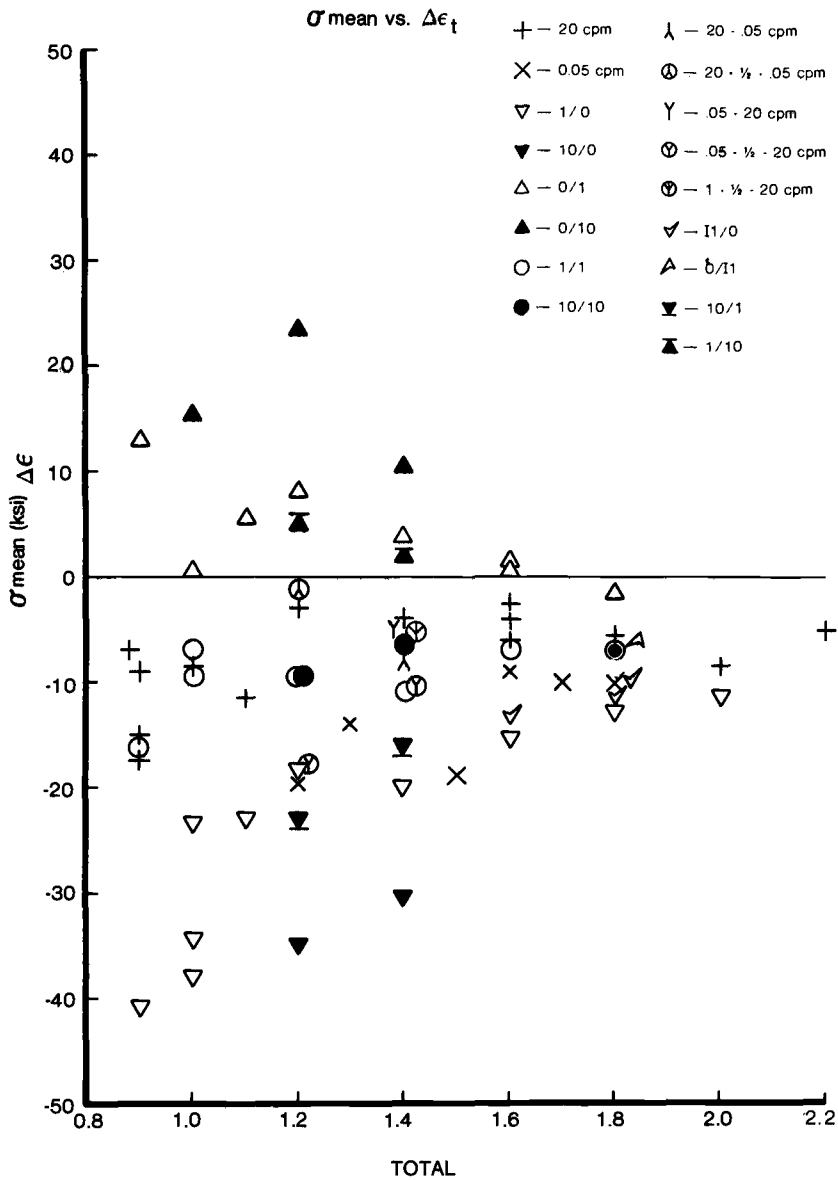


FIG. 2—Plot of mean stress as function of total strain range ($6.895 \times \text{ksi} = \text{MPa}$).

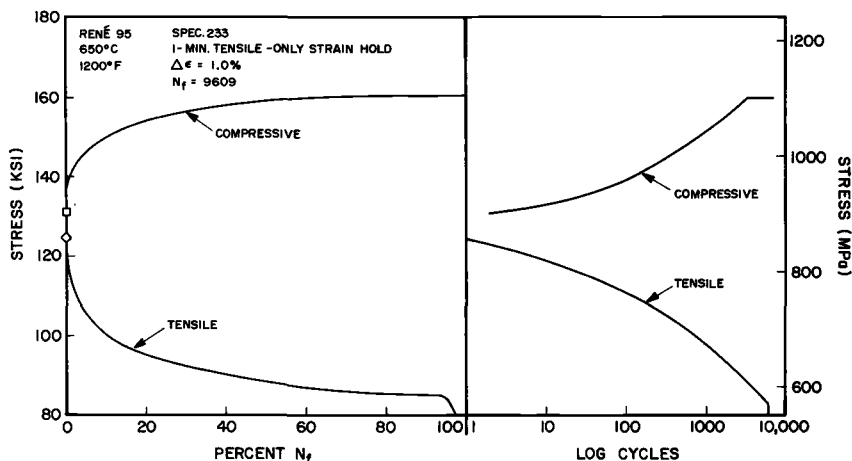


FIG. 3—Change of stress during a fatigue test.

tests and strain-hold tests. The continuous-cycling tests were run at two frequencies: 20 and 0.05 cpm. The strain-hold tests consisted of tensile and compressive strain-holds of 1 or 10 min. They are identified by a two-digit code x/y , where x is the amount of time spent in a tensile strain-hold and y is the amount of time spent in a compressive strain-hold.

The waveforms used for the verification tests consisted of unbalanced strain-hold tests, intermediate strain-hold tests, and dual-rate continuous-cycling tests. The unbalanced strain-hold tests were similar to the baseline strain-hold tests except that the strain was held on the tensile side for 1 min and on the compressive for 10 min, or the reverse. These tests are identified using the same code as the baseline strain-hold tests.

In the intermediate strain-hold tests, a 1-min hold period was placed between the peak tensile and compressive strains rather than at the peak strain. The purpose of this test was to determine whether there was an order effect when first plastic strain and then creep strain followed by more plastic strain was applied to the test specimen. The intermediate strain-hold tests are identified by the code I1/0 or 0/I1, I signifying intermediate hold.

In the dual-rate continuous-cycling tests, a positive strain rate which was different from the negative strain rate was employed. These tests were similar to the slow-fast (S/F) and fast-slow (F/S) tests used by Coffin [5]. The fast strain rate was 20 cpm, and the slow strain rate was either 1 cpm or 0.05 cpm. These tests are identified by a two-digit code, $x-y$ cpm, x being the positive strain rate and y being the negative strain rate. For example, a test having a positive strain rate of 0.05 cpm and a negative rate of 20 cpm is called a 0.05–20 cpm test.

On some of the dual-rate tests, the first quarter of the strain in the slow

rate was run at the fast rate in order to avoid spending a long period of time at a high tensile or compressive load which could result in creep. In these tests the strain rate was changed from the fast to the slow strain rate halfway between the peak tensile or compressive strain and the zero-strain level. These tests are identified by means of a " $\frac{1}{2}$ " between the strain rate—that is, 0.05- $\frac{1}{2}$ -20 cpm.

All testing was performed at 650°C (1200°F) at an *A*-ratio on strain of infinity. Further details on the test program can be found in Refs 16 and 18.

Failure Behavior

The lives of the baseline fatigue tests plotted as a function of the total strainrange and the inelastic strainrange are shown in Figs. 4 and 5, respectively. The most damaging waveform was the compressive strain-hold. The least damaging waveforms were the tensile strain-hold—especially at lower strainranges—and the 20-cpm tests. The transition fatigue life was 72 cycles.

As shown in Figs. 4 and 5, the fatigue life was sensitive to frequency, although the stress-strain behavior was not. The 0.05-cpm tests had shorter lives than the 20-cpm tests, but their hysteresis loops were similar. This behavior means that another form of time-dependent damage, such as environmental attack, is occurring.

The validation data are also plotted in Figs. 4 and 5, along with the baseline data. Based upon either the inelastic or total strainrange, the intermediate strain-hold tests had longer lives than the tension or compression strain-hold tests. Based upon these same strainranges, the unbalanced strain-hold tests had lives between those of the tension-only and compression-only strain-hold tests. Therefore, holding the strain only at the peak tensile or peak compressive stress produced the most severe effects upon test life.

The life of one of the dual-rate tests plotted as a function of the total or inelastic strainrange had a very short life. Specimen 252 (a 0.05-20 cpm test at 1.4 percent total strainrange) had a life of 194 cycles. This life is felt to be valid because the specimen had multiple crack-initiation sites, and a duplicate test had a life of 238 cycles. The reason for this short life is not known. Except for this specimen, the lives of the other dual-rate tests were similar to those of the 20-cpm tests when compared on the basis of total strainrange. All the dual-rate tests had shorter lives than the 20-cpm tests, when compared on the basis of inelastic strainrange.

An attempt was made to assess the experimental scatter inherent in the material. Five test conditions were replicated, and the scatter in test lives was a maximum of 36 percent.⁴ Although this limited number of replications is not statistically meaningful, based upon the author's experience the scatter did not appear to be much greater than ± 50 percent, or a factor of 1.5.

⁴ Scatter in test lives = [(longest life - mean life)/mean life] \times 100.

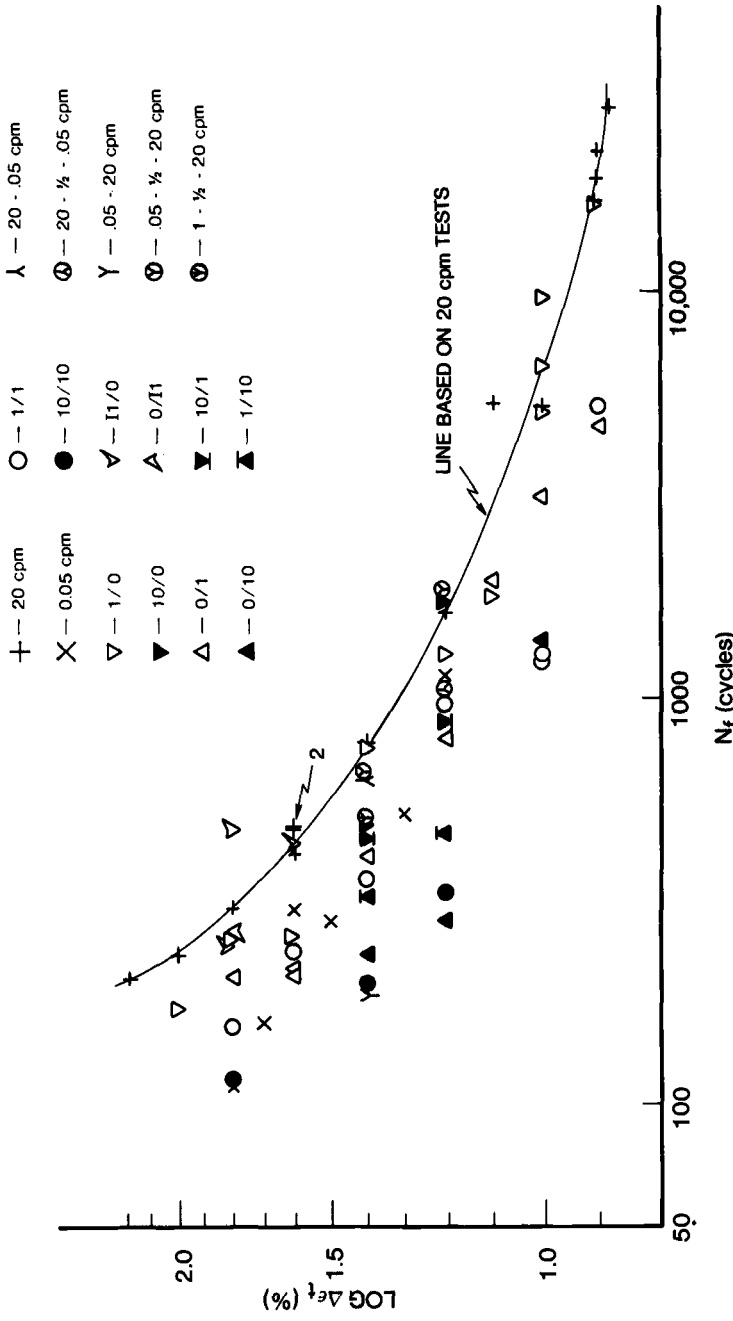


FIG. 4—Plot of total strain range as function of cycles to failure.

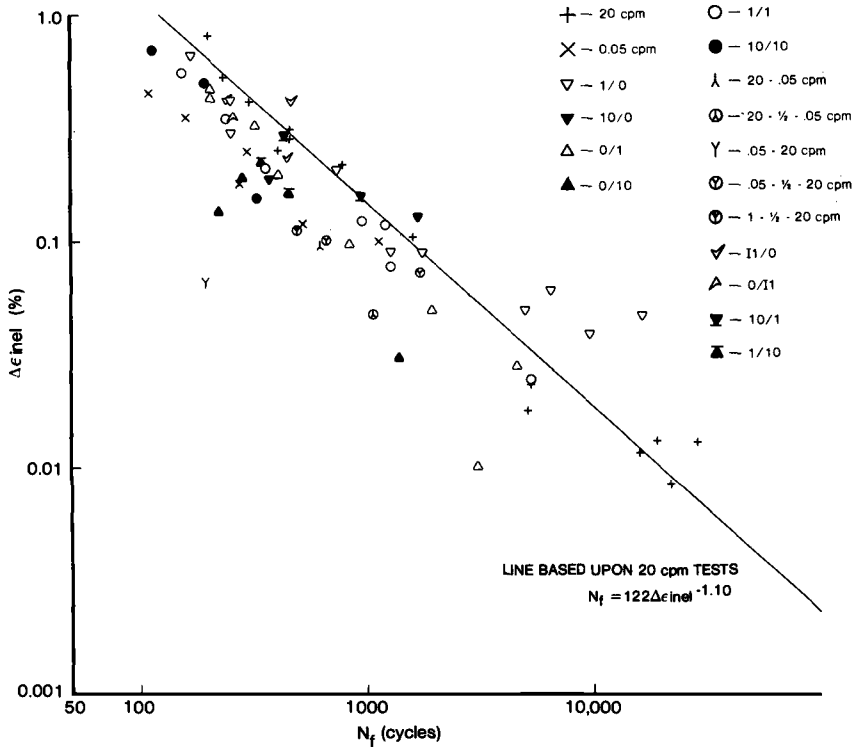


FIG. 5—Inelastic strainrange as function of cycles to failure.

Parameters Used for Evaluation of the Models

The predictive ability of a model was assessed using three different criteria concerning the ability of the model to (1) correlate the baseline data, (2) predict the verification data, and (3) avoid consistently overpredicting or underpredicting any test waveform.

The ability of the models to correlate the baseline data was determined using the scatter band of the predicted versus observed life. The scatter band was defined as the data point having the largest ratio of predicted to observed life or the reciprocal of this ratio if the ratio was less than one.

$$\text{scatter band} = \max \left\{ \begin{array}{ll} \frac{N_p}{N_f} & \text{if } N_p > N_f \\ \frac{N_f}{N_p} & \text{if } N_p < N_f \end{array} \right.$$

where N_p is the predicted life and N_f is the observed life. This is the conventional evaluation technique for models of creep-fatigue interaction. It mea-

sures the scatter of the extreme point. If the scatter band was two or less, then the model was considered to have correlated the data well.

The standard deviation was also used to evaluate the correlative ability of the models. It was defined as

$$\text{standard deviation} = \left(\frac{\sum (\log N_f - \log N_p)^2}{n - 1} \right)^{1/2}$$

where n is the number of data points.

The lives of the verification tests were predicted using constants in the model which were determined from the baseline tests. If the predicted life was within a factor of two of the observed life, then the model was considered to have been verified.

The life predictions of each model for the baseline tests were examined to determine whether any test waveforms were consistently overpredicted or underpredicted. This phenomenon was termed segregation because the data were segregated to one side or the other of the best-fit line. Segregation occurred because the model was not correctly taking into account the material behavior.

Models

Strainrange-Partitioning Model

The Strainrange-Partitioning (SRP) Model [1-4] extends the Manson-Coffin Law [29,30], which is valid at room temperature, to high temperature by considering the interaction of time-dependent inelastic (or creep) strains and time-independent inelastic (or plastic) strains. The equations of the SRP Model are

$$N_{ij} = C_{ij} (\Delta \epsilon_{\text{inel}})^{\beta_{ij}} \quad (1)$$

$$(N_f)^{-1} = \sum (f_{ij}/N_{ij}) \quad (2)$$

where ij represents the four strainranges pp , cp , pc , and cc . N_{ij} is the cycles to failure if $\Delta \epsilon_{\text{inel}}$ is all ij -strain; $f_{ij} = \Delta \epsilon_{ij} / \Delta \epsilon_{\text{inel}}$; and C_{ij} and β_{ij} are constants. Equation 2 is the interaction damage rule [2] and is used to predict the fatigue life N_f .

Two modifications were made to the SRP model after the analysis described in this paper had been completed. The first modification, called Ductility Normalized SRP [31], consisted of specifying the values of the constants in Eq 1 in a manner similar to that of the method of Universal Slopes [32]. Since sufficient tests were available to calculate these constants, it was not necessary to use the ductility-normalized equations.

In addition to specifying the constants, the ductility-normalized equations attempt to incorporate environmental effects into the SRP model. These effects are modeled by determining the creep-rupture ductility as a function of

the time to rupture in a creep test and using this function for some of the constants in Eq 1. However, the creep-rupture ductility of René 95 did not appear to be a function of the time to rupture. Consequently, this method could not be used.

The second modification [4] involved incorporating the effect of mean stresses into the model along the same lines as Morrow [33]. This modification required computing what the fatigue life would have been if the mean stress were zero and then determining the constants in Eq 1 using these computed lives. To predict the life of a test, Eq 2 is used to find the cycles to failure when no mean stress is present, and then a mean stress correction is made to these cycles. It is not known whether making these computations would have significantly influenced the overall results.

The SRP Model has a validity requirement that before a test point can be used to establish the constants in Eq 1, it must have 50 percent or more of its damage due to the particular strainrange of interest in which

$$\text{percent damage} = 100 \times N_f \times f_{ij} / N_{ij}$$

The purpose of this requirement is to ensure that the fatigue test contains a sufficient portion of the damage of interest so that the test is representative of this damage. Not all the René 95 data met this criterion. Although the intent of this requirement is appreciated, it was decided to attempt to apply the SRP model to the data. After this attempt was made it was found that data did provide an accurate evaluation of the model, as discussed in detail in Ref 15.

When Eqs 1 and 2 were fit to the fatigue data, as discussed in Ref 16, the following constants were determined: $C_{pp} = 0.777$, $C_{cp} = 1.40$, $C_{pc} = 0.429$, $C_{cc} = 0.130$, $\beta_{pp} = -1.10$, $\beta_{cp} = -0.882$, $\beta_{pc} = -0.870$, and $\beta_{cc} = -1.20$. The 0.05-cpm tests were not used to determine the constants, because these tests could not be directly partitioned from the individual test results.

All the tensile strain-hold tests with lives greater than 5000 cycles had negative values for N_{cp} because these tests lasted longer than pp -tests having the same inelastic strain range. According to Eq 2, if

$$N_f > \frac{N_{pp}}{f_{pp}}$$

then

$$N_{cp} < 0$$

It should be noted that all the cp -tests having negative values of N_{cp} also had large compressive mean stresses, which may have increased the life.

The SRP correlation of the baseline data is shown in Fig. 6 (see Appendix). The scatter band was 5.4 and the standard deviation was 0.23. The 0.05 cpm, 0/10, and long-life 1/0 tests were not well predicted. The predicted lives for

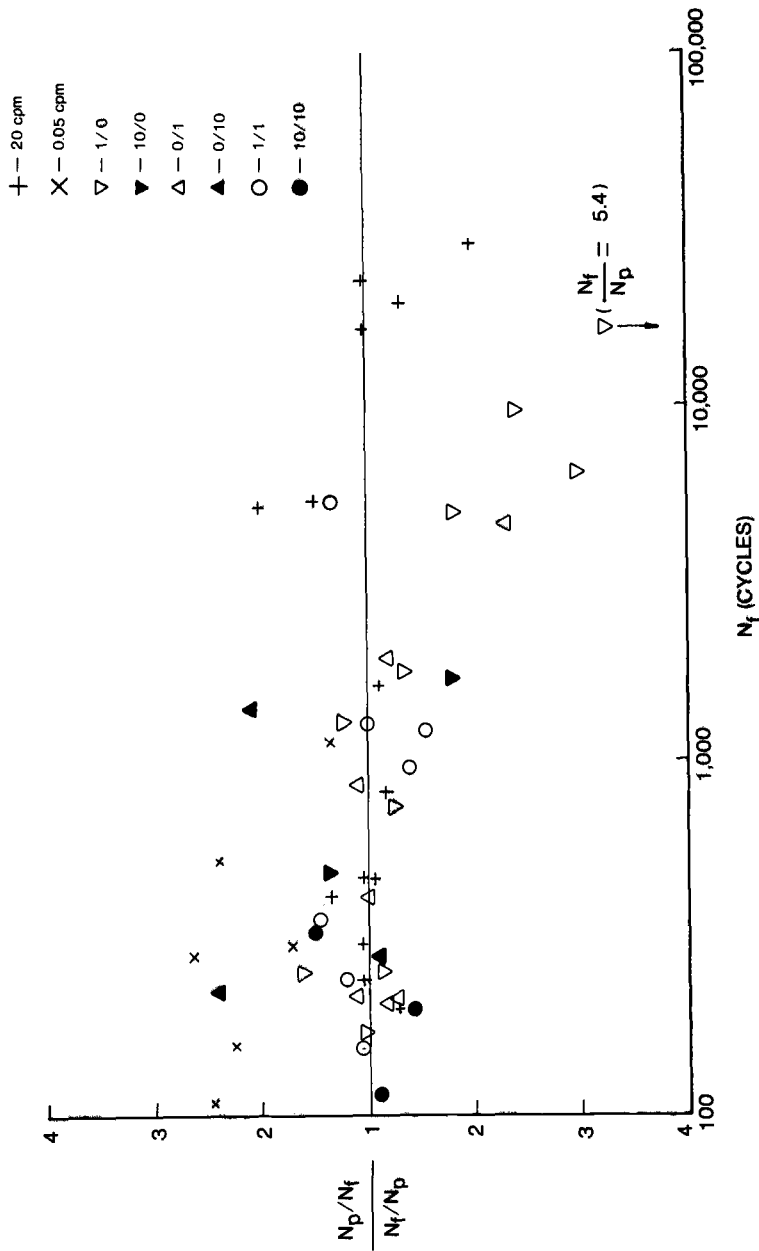


FIG. 6—Life predictions of baseline tests by the Strainrange-Partitioning Model.

some of these tests were either greater than two and one half times the observed life or less than one fifth the observed life.

The SRP predictions of the verification tests are given in Table 1. Except for the dual-rate tests, the verification tests were well predicted. The dual-rate tests presented special problems in partitioning the strains. In all these tests, anomalous behavior occurred when the strain rate switched from fast to slow. This behavior was similar to either stress relaxation or strain recovery, as discussed in Ref 16. Only two of the dual-rate tests could be partitioned, and only one was predicted well.

The SRP model segregated three test types: the 0.05 cpm, 0/10, and long-life tensile strain-hold tests. The 0.05 cpm and 0/10 tests were consistently overpredicted. All the tensile strain-hold tests having lives greater than 1700 cycles were underpredicted. These 0/10 and tensile strain-hold tests had large mean stresses. Although some 0/10 and 10/0 tests having large mean stresses were well predicted, it is felt that the mean stress was the major contributor to the poor predictions. The modification to the model to account for mean stress [4] should improve these predictions.

The consistent overprediction of the life of the 0.05-cpm tests indicates that the model encounters problems when used in a regime where creep is not the principal type of time-dependent damage. As discussed in a preceding section on stress-strain behavior, the strain rates associated with cycling at a frequency of 0.05 cpm are higher than the minimum creep rates for the given strain ranges tested. That a negligible amount of creep occurred is confirmed by the similarity between the 20-cpm and 0.05-cpm hysteresis loops. The SRP model is a deformation-based model; therefore it treats a 0.05-cpm test as a 20-cpm test, since the amount and type of deformation is similar. However, the life of the 0.05-cpm tests is shorter than that of the 20-cpm tests. Thus there must be another type of time-dependent damage taking place, most likely that of environmental attack caused by oxidation. Since the SRP model did not take this type of damage into account, it overpredicted the life of these tests.

Frequency-Separation Model

The Frequency-Separation (FS) Model [5,6] postulates that the basic parameters necessary to predict the creep-fatigue life are the inelastic strain-range $\Delta\epsilon_{\text{inel}}$, the tension-going frequency ν_t , and the loop-time unbalance ν_c/ν_t . These three parameters are combined in a power-law relationship to predict the cycles to failure:

$$N_f = C \Delta\epsilon_{\text{inel}}^\beta \nu_t^m \left(\frac{\nu_c}{\nu_t} \right)^k \quad (3)$$

where C , β , m , and k are constants. Thus the FS Model extends the Coffin-Manson Law by the addition of two frequency terms.

TABLE 1—Life predictions of verification tests.

Specimen	Type of Test	Total Strain Range, %	Observed Life, cycles	Strainrange-Partitioning Model	+ $\frac{\text{Observed Life}}{\text{Predicted Life}}$ or - $\frac{\text{Predicted Life}}{\text{Observed Life}}$		Damage-Rate Model
					Frequency-Separation Model	Frequency-Modified Damage Function	
251	20-0.05 cpm	1.4	639	2.08	-1.23	1.12	1.37
262	20-1/2-0.05 cpm	1.2	1086	^a	1.09	1.50	1.83
261	1-1/2-20 cpm	1.4	499	^a	3.45	1.79	2.29
252	0.05-20 cpm	1.4	194	6.09	17.88	5.22	8.92
260	0.05-1/2-20 cpm	1.4	646	^a	3.41	1.14	1.70
259	0.05-1/2-20 cpm	1.2	1731	^a	1.83	-1.41	-1.09
242	11-0	1.8	472	-1.64	-1.22	-2.04	-1.57
246	11-0	1.8	253	1.13	1.57	-1.11	1.22
244	11-0	1.6	447	1.02	1.44	-1.17	1.11
247	0-11	1.8	263	-1.32	-1.39	-1.02	1.25
227	10-1	1.4	455	-1.49	-1.34	-1.68	-1.19
223	10-1	1.2	945	-1.50	-1.41	-1.58	-1.27
226	1-10	1.4	349	1.17	-1.31	-1.12	1.31
225	1-10	1.2	464	1.23	-1.23	-1.00	1.42

^a Could not accurately partition.

The values of the constants in Eq 3 that yielded the best fit to the baseline data were $C = 0.456$, $\beta = -1.11$, $m = 0.121$, and $k = 0.183$.⁵ The predicted and observed lives of the baseline data are shown in Fig. 7. The scatter band was 3.6 and the standard deviation was 0.18. Of the baseline tests, only the tensile strain-hold tests were segregated. For observed lives of less than 1800 cycles, the lifetimes were consistently overpredicted; for lives greater than 1800 cycles, the lifetimes were all underpredicted. The probable reason for this behavior is that the longer-life tests had large compressive mean stresses.

The constants obtained for Eq 3 show that ν_t has less of an effect upon fatigue life than ν_c . ν_t is raised to the $m - k$ power, which is -0.06 , while ν_c is raised to the 0.18 power. This small influence of ν_t is contrary to the basic postulate of the model that ν_t is a major parameter which affects the fatigue life.

The FS Model was able to predict all the verification tests to within a factor of two except the slow-fast tests. The predicted and observed lives are given in Table 1. All the slow-fast tests were overpredicted, one by a factor greater than ten. The reason for this waveform being so poorly predicted is that the tension-going time had a negligible influence in the model. Thus the long tension-going time of the slow-fast waveform was ignored by the model, and the waveform was treated as a 20-cpm test, which would account for the consistent overprediction of this waveform.

The FS Model is one of three models proposed by Coffin which modify the Coffin-Manson relation by the addition of a frequency term. The other two models—a Frequency-Modified (FM) Model [13] and a Tension-Going Frequency-Modified (TGFM) Model [6]—were also examined. The FM Model makes use of the total cyclic frequency, while the TGFM Model employs the tension-going frequency. Neither model makes use of the loop-time unbalance term. The best-fit equations for the baseline data were found to be

$$\text{FM: } N_f = 0.6084 (\Delta\epsilon_{\text{inel}})^{-1.091} \nu^{0.1292}$$

$$\text{TGFM: } N_f = 0.4014 (\Delta\epsilon_{\text{inel}})^{-1.153} \nu_t^{-0.004253}$$

where ν is the total cyclic frequency. The scatter band for the FM Model was 6.2, and that for the TGFM Model was 5.8. Both of these models extensively segregated the data. Also, the exponent on the tension-going frequency is almost zero, which indicates the lack of importance of this term. Since both of these models were significantly inferior to the FS Model, they were not evaluated further.

Overall, the FS Model predicted the results of most of the baseline and verification tests well. Only the slow-fast tests, a few tensile strain-hold tests, and one compressive strain-hold test were poorly predicted; and only the tensile strain-hold tests were segregated. The concept that the tension-going frequency controls fatigue life did not appear to be applicable in the case of René 95 at 650°C (1200°F).

⁵ The units of the variables are in./in. for $\Delta\epsilon_{\text{inel}}$ and cpm for ν .

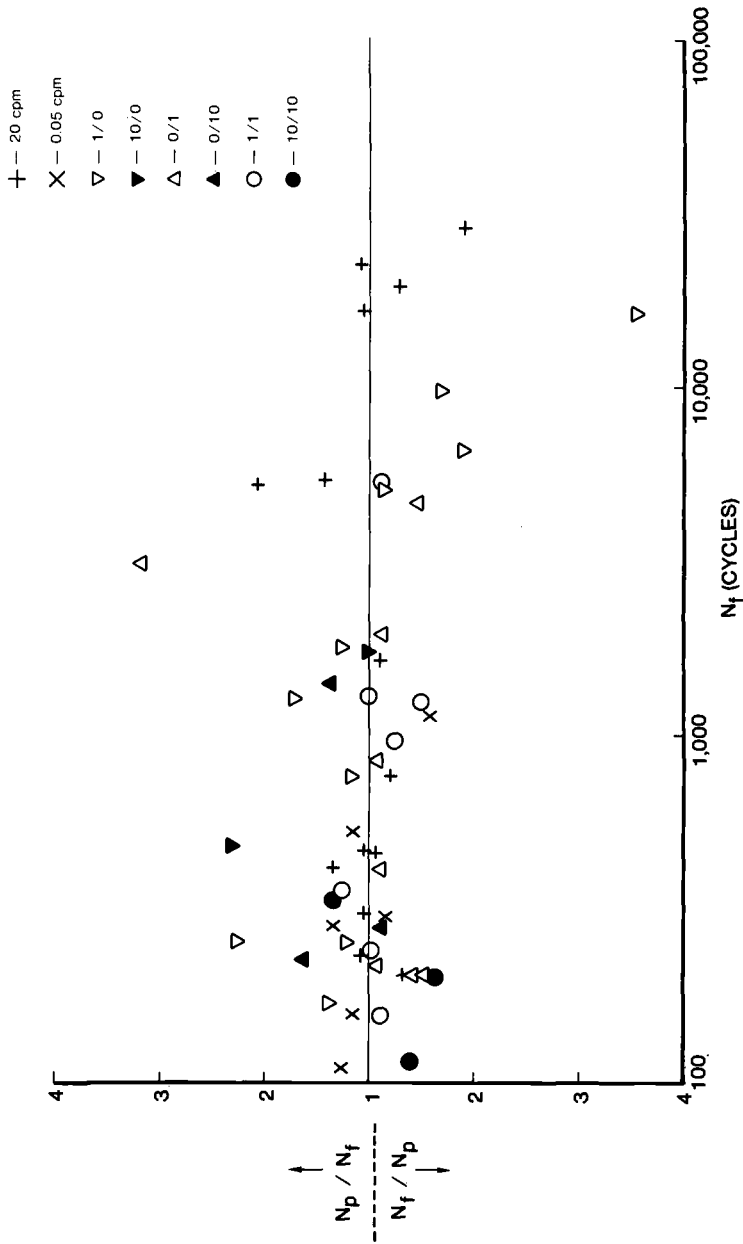


FIG. 7—Life predictions of baseline tests by the Frequency-Separation Model.

Frequency-Modified Damage Function

The Frequency-Modified Damage Function (FMDF) [7,8] is based upon the premise that LCF is controlled by the tensile hysteretic energy absorbed by the specimen. This energy is approximated by the damage function—the product of the inelastic strainrange, $\Delta\epsilon_{\text{inel}}$, and the peak tensile stress, σ_t . The life is predicted by using a power-law relationship between the damage function and the life:

$$N_f = C (\Delta\epsilon_{\text{inel}} \cdot \sigma_t)^\beta \quad (4)$$

where C and β are constants. In effect, what the FMDF has done is to modify the Coffin-Manson Law by the addition of the tensile stress to the inelastic strainrange. It should be noted that Eq 4, like the Coffin-Manson Law, is valid only for time-independent fatigue.

When time-dependent mechanisms are present, as in the creep-fatigue interaction, Eq 4 is modified by a frequency term which takes into account the time dependency:

$$N_f = C (\Delta\epsilon_{\text{inel}} \cdot \sigma_t)^\beta \nu^m \quad (5)$$

where m is a constant and ν is the frequency. The frequency term selected for use in Eq 5 is dependent upon the sensitivity of the material to different waveshapes. If the material is insensitive to waveshape, then the proper value for frequency in Eq 5 is the frequency of the entire cycle. If the material is waveshape sensitive, then a frequency term is chosen in Eq 5 to properly reflect this sensitivity.

Since it was not possible to determine in advance which frequency term would be appropriate for René 95, different terms were fitted to the baseline data [16]. The term which provided the best fit to the data with the least segregation was the total cyclic frequency. This frequency is reasonable because it reflects environmental attack, which is apparently the predominant type of time-dependent damage in the fatigue tests.

Life predictions for the baseline tests were made using $C = 162$, $\beta = -0.976$, and $m = 0.137$ and are shown in Fig. 8.⁶ The scatter band was 3.6 and the standard deviation was 0.18. Most of the tests were correlated to within a factor of two. One 20-cpm test, two compressive strain-hold tests, and three tensile strain-hold tests yielded correlations greater than a factor of two.

The life predictions for the verification tests are given in Table 1. All the tests except a I1/0 and a 0.05–20 cpm test were predicted to within a factor of two. The I1/0 test was predicted to 2.05, slightly above a factor of two. The 0.05–20 cpm test was underpredicted by a factor of 5.2. However, this test had a very short life and was badly predicted by all the models.

The FMDF segregated the tensile-only and compressive-only strain-hold

⁶ The units of the variables are in./in. for $\Delta\epsilon_{\text{inel}}$, ksi for σ_t and cpm for ν .

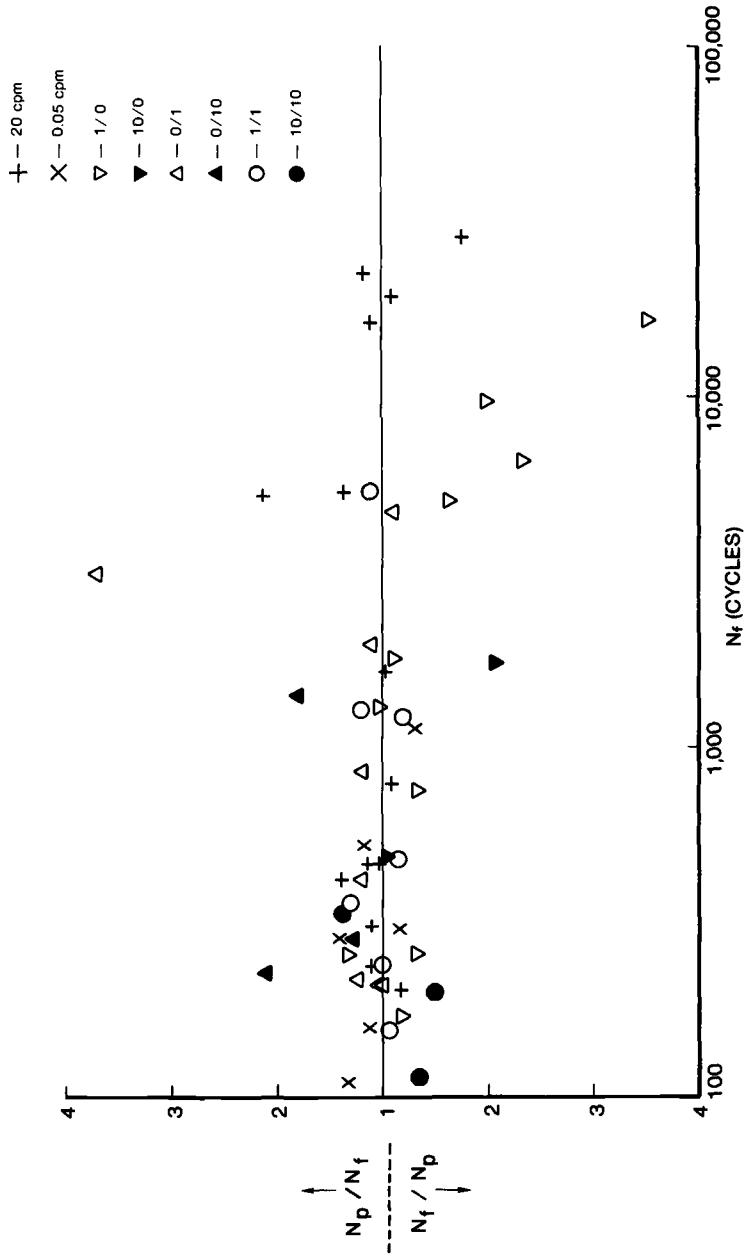


FIG. 8—Life predictions of baseline tests by the Frequency-Modified Damage Function.

tests. All the tensile strain-hold tests having lives greater than 1700 cycles were underpredicted, and all but one of the compressive strain-hold tests were overpredicted. The reason for this segregation is probably the mean stresses which these tests developed.

According to the FMDF, the life of a test should decrease with test frequency. Figure 9 is a plot of the baseline and validation tests where $\Delta \epsilon_{\text{inel}} \times \sigma_t$ is plotted as a function of life. It can be seen that the life does not always decrease with frequency. The 1/0 and 11/0 tests have a lower frequency than the 20-cpm tests; yet, in some cases, the 1/0 and 11/0 tests last longer than the 20-cpm tests. Also the 10/1 and 1/10 tests are not nearly so damaging as would be expected from their low frequency. On the other hand, the 0/10 tests are more damaging than their frequency terms would suggest.

In summary, the FMDF was able to correlate most of the baseline data and to predict all the validation tests except for two of the slow/fast tests. The model segregated two parts of the data base. Also, the test life did not always follow the expected behavior with respect to frequency.

Damage-Rate Model

The Damage-Rate Model (DRM) [9-11] is based upon the premise that LCF is primarily a process of crack propagation and cavity growth. Microcracks and cavities are assumed to be originally present in the virgin material, and the majority of the LCF life is spent growing these microcracks and cavities to a critical size at which time they link up and form a macrocrack. Once a macrocrack is formed, it propagates rapidly until fracture takes place.

The model postulates the following growth law for the microcracks and cavities:

$$\frac{da}{dt} = \begin{cases} aT |\epsilon_{\text{inel}}|^m |\dot{\epsilon}_{\text{inel}}|^k & \left\{ \begin{array}{l} \text{in the presence of} \\ \text{tensile stress} \end{array} \right. \\ aC |\epsilon_{\text{inel}}|^m |\dot{\epsilon}_{\text{inel}}|^k & \left\{ \begin{array}{l} \text{in the presence of} \\ \text{compressive stress} \end{array} \right. \end{cases} \quad (6)$$

$$\frac{dc}{dt} = \begin{cases} cG |\epsilon_{\text{inel}}|^m |\dot{\epsilon}_{\text{inel}}|^{k_c} & \left\{ \begin{array}{l} \text{in the presence of} \\ \text{tensile stress} \end{array} \right. \\ \alpha(-G) |\epsilon_{\text{inel}}|^m |\dot{\epsilon}_{\text{inel}}|^{k_c} & \left\{ \begin{array}{l} \text{in the presence of} \\ \text{compressive stress} \end{array} \right. \end{cases} \quad (7)$$

where a is crack length, c is cavity length, t is time, ϵ_{inel} is the inelastic strain, $\dot{\epsilon}_{\text{inel}}$ is the inelastic strain rate, and T , C , G , m , k , and k_c are constants. The law states that microcrack and cavity growth is a function of the inelastic strain and the inelastic strain rate. The microcrack is assumed to grow at different rates under compressive and tensile stresses. The cavity is assumed to shrink under a compressive load, but its size is not allowed to be less than the initial cavity size.

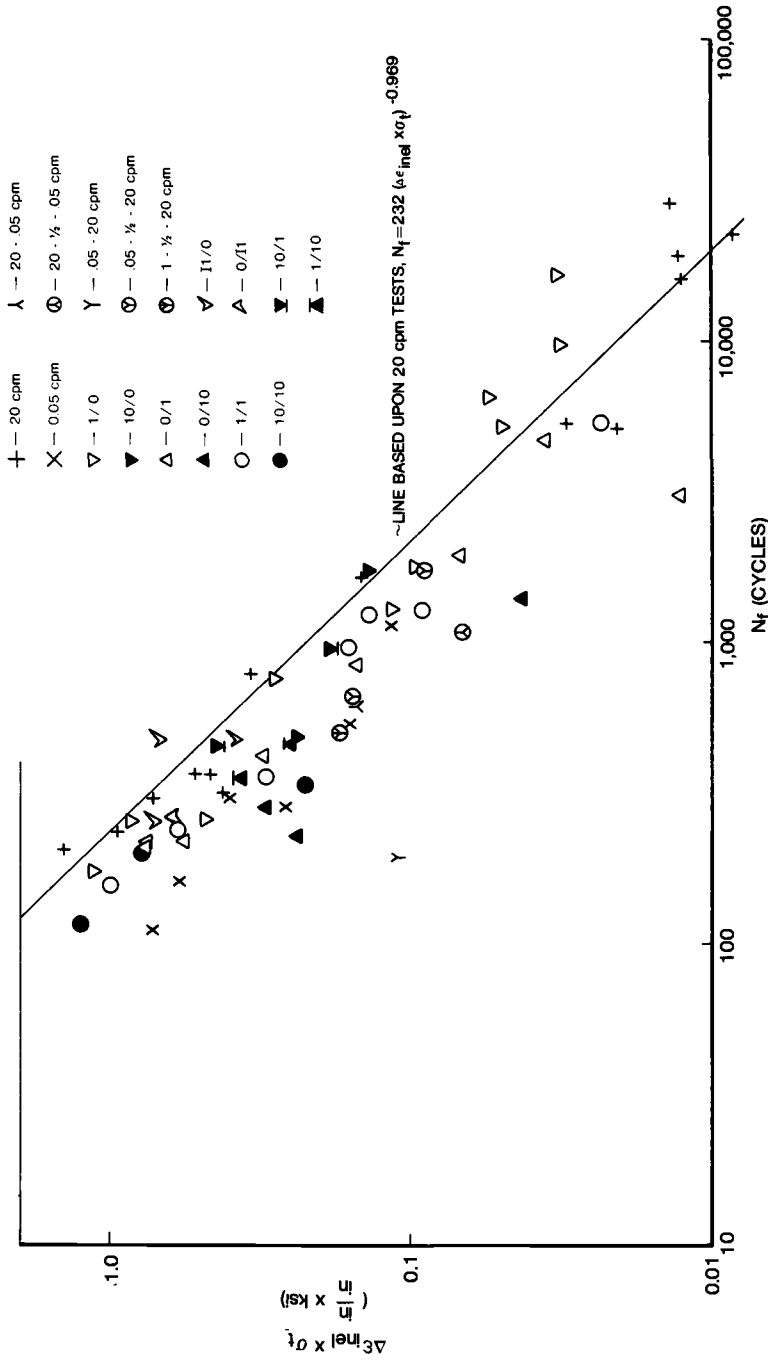


FIG. 9— $\Delta \epsilon_{in\epsilon l} \times \sigma_t$ as function of N_f ($6.895 \times \text{ksi} = \text{MPa}$).

The growth laws of Eqs 6 and 7 are integrated over the specimen life from the initial microcrack and cavity size to the critical crack and cavity size when a macrocrack is formed. The integration is performed over an ideal cycle⁷ in which the peak tensile and compressive stresses are equal and the inelastic strain rate is constant. The critical crack and cavity size which causes failure is determined from a microcrack and cavity-growth interaction equation

$$\frac{\ln a/a_0}{\ln a_f/a_0} + \frac{\ln c/c_0}{\ln c_f/c_0} = 1 \quad (8)$$

where a_0 is the initial crack size, a_f is the critical crack size, c_0 is the initial cavity size, and c_f is the critical cavity size. When Eqs 6 and 7 are integrated over such an ideal cycle and Eq 8 is used, the predictive equations of the DRM result. For continuous cycling at a constant frequency or strain rate:

$$N_f = \frac{m+1}{4A} \left(\frac{\Delta \epsilon_{inel}}{2} \right)^{-(m+1)} (\dot{\epsilon}_{inel})^{1-k} \quad (9)$$

where $A = [(C+T)/2] / [\ln(a_f/a_0)]$. For hold times

$$D_a = \frac{4A}{m+1} \left(\frac{\Delta \epsilon_{inel}}{2} \right)^{m+1} (\dot{\epsilon}_{inel})^{k-1} + |\epsilon_{inel \max}|^m \int_0^{t_t} \frac{2A}{1+C/T} |\dot{\epsilon}_{inel}|^k dt + |\epsilon_{inel \min}|^m \int_0^{t_c} \frac{2A}{1+T/C} |\dot{\epsilon}_{inel}|^k dt \quad (10)$$

$$D_c = G \int_0^{t_t} |\epsilon_{inel}|^m |\dot{\epsilon}_{inel}|^k dt - G \int_0^{t_c} |\epsilon_{inel}|^m |\dot{\epsilon}_{inel}|^k dt \quad (11)$$

$$N_f = \frac{1}{D_a + D_c} \quad (12)$$

where D_a is the damage caused by crack growth, D_c is the damage caused by cavity growth, t_t is the time spent in a tensile hold, t_c is the time spent in a compressive hold, $\epsilon_{inel \max}$ is the inelastic strain at the beginning of the tensile hold time, $\epsilon_{inel \min}$ is the inelastic strain at the beginning of the compressive hold time, and C/T is a constant. In Eq 10 the first term on the right-hand side is the damage caused by continuous cycling, the second term is the damage caused by a tensile hold, and the third term is the damage caused by a compressive hold. In Eq 11 the first term on the right-hand side is the damage

⁷ Strictly speaking, the integration should be performed over the actual cycle observed in the test. However, the DRM, as its authors presently propose it, makes use of the equations developed from integrating an ideal cycle. Use of the observed cycle instead of the ideal cycle would necessitate a modification to the model.

caused by a tensile hold, and the second term is the healing due to a compressive hold. For F/S (fast-slow) tests:

$$N_f = \frac{m+1}{4A} \left(\frac{\Delta \epsilon_{inel}}{2} \right)^{-(m+1)} \left[\frac{\dot{\epsilon}_{inel f}^{(k-1)}}{1+C/T} + \frac{\dot{\epsilon}_{inel s}^{(k-1)}}{1+T/C} \right]^{-1} \quad (13)$$

where $\dot{\epsilon}_{inel f}$ is the inelastic strain rate for the fast rate and $\dot{\epsilon}_{inel s}$ is the inelastic strain rate for the slow rate. For S/F (slow-fast) tests:

$$D_a = \frac{4A}{m+1} \left(\frac{\Delta \epsilon_{inel}}{2} \right)^{(m+1)} \left[\frac{\dot{\epsilon}_{inel s}^{(k-1)}}{1+C/T} + \frac{\dot{\epsilon}_{inel f}^{(k-1)}}{1+T/C} \right] \quad (14)$$

$$D_c = \frac{2G}{m+1} \left(\frac{\Delta \epsilon_{inel}}{2} \right)^{(m+1)} [\dot{\epsilon}_{inel s}^{(k_c-1)} - \dot{\epsilon}_{inel f}^{(k_c-1)}] \quad (15)$$

$$N_f = \frac{1}{D_a + D_c} \quad (16)$$

A detailed description of how the model was fitted to the fatigue data can be found in Ref 16.

Preliminary examination of metallographic sections of tensile strain-hold and S/F test specimens using a scanning electron microscope (SEM) revealed no evidence of cavity damage. Therefore Eqs 11 and 15, which take into account the cavity damage, were not used. This assumption of no cavity damage was justified by the life predictions which will be discussed later.

It should be noted that no constants need be determined in order to achieve a best fit for the strain-hold tests. Thus the strain-hold tests constitute verification tests for the DRM.

The constants used in DRM were $m = 0.2395$, $k_c = 0.8340$, $A = 1.650$, $k = 0.8705$, and $C/T = 2$.⁸ These constants were used in Eqs 9, 10, 13, and 14 to predict both the baseline and verification tests. Life predictions are presented in Fig. 10 and Table 1. The scatter band for the baseline tests was 5.1 and the standard deviation was 0.24.

In order to predict the lives of the strain-hold tests, only Eq 10 was used. It was assumed that no cavity growth occurred. This assumption was justified because the lives of these tests were either accurately predicted or underpredicted. If cavity growth did occur, then the lives would be expected to be overpredicted because the cavity growth was ignored.

The DRM was able to predict all the verification tests except two of the S/F tests, which were overpredicted by as much as 8.9 times the observed life. Equation 14 was used to predict these tests. An attempt was made to use Eq 15 to account for cavity growth. The value of G was determined for each test by equating the predicted life and the observed life. The values of G ranged from 18.7 to -0.2. Since no value of G which was similar for each of the S/F

⁸ The units used for the variables were in./in. for $\Delta \epsilon_{inel}$ and min^{-1} for $\dot{\epsilon}_{inel}$.

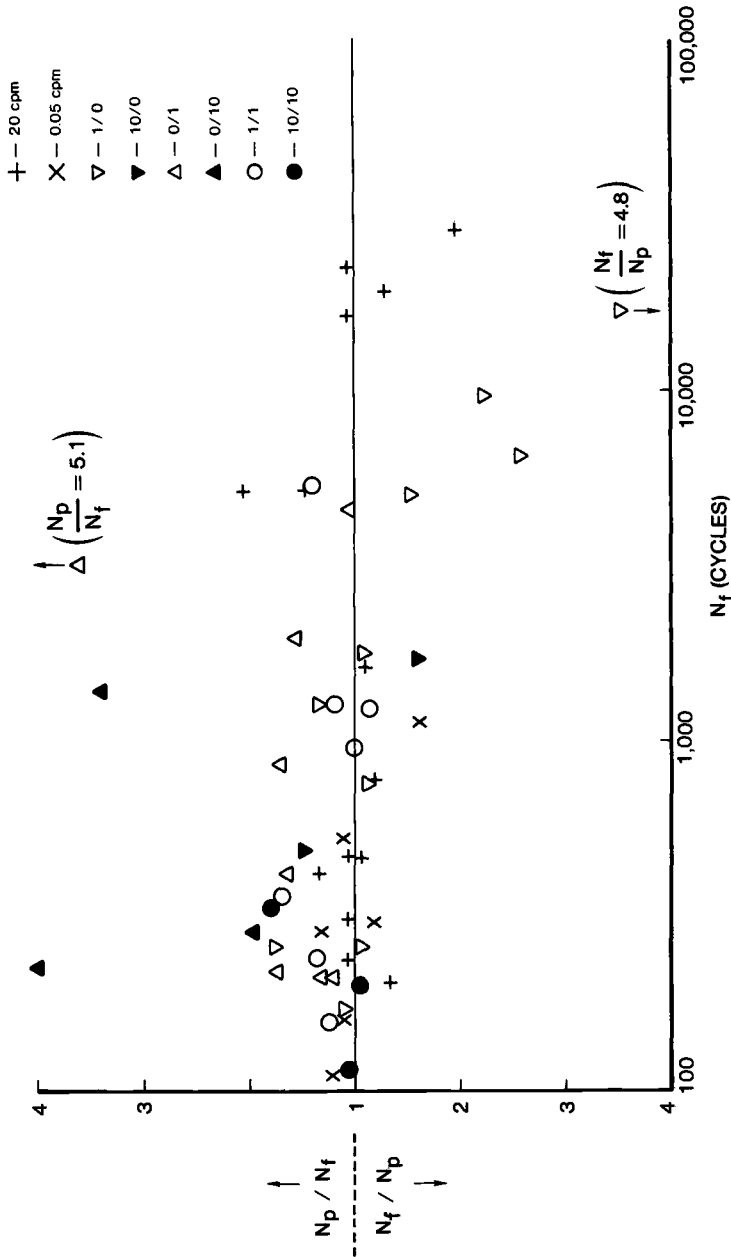


FIG. 10—Life predictions of baseline tests by the Damage-Rate Model.

tests could be obtained, the cavity-growth equation was assumed to be inappropriate and was not used to predict these tests.

The DRM segregated the tensile strain-hold and compressive strain-hold tests. All the tensile strain-hold tests having lives greater than 1700 cycles were underpredicted. As the lives became longer, the predictions became less accurate. The lives of all the compressive strain-hold tests were overpredicted. These predictions became worse as the length of the hold time was increased.

One possible reason for these strain-hold tests being segregated is that they were the only tests having large mean stresses. The DRM as used in this evaluation did not take into account mean stresses. The crack-growth law of Eq 6 was integrated over an ideal cycle in which the mean stress was zero. If the crack-growth law were integrated over a cycle containing mean stresses, then better life predictions might result.

A conceptual difficulty arises in the assumed crack-growth equation (6). The appropriate value of C/T used for René 95 was 2. This indicates that the crack growth under a compressive stress is twice as great as that under a tensile stress, contrary to what would be expected. This unusual result may be influenced by the presence of mean stresses.

Discussion

None of the models was able to correlate the baseline tests to within the desired scatter band of two. The models fell into two groups according to their correlative ability. The first group, composed of the FS and the FMDF Models, was able to correlate the baseline data to within a scatter band of 3.6 and a standard deviation of 0.18 (as done by both models). The second group, composed of the DRM and the SRP Models, correlated these data worse, having scatter bands of 5.1 and 5.4, respectively, and standard deviations of about 0.23.

Except for the S/F tests, all the models predicted the verification tests to within a factor of two. For the S/F tests, the FMDF Model yielded the best predictions, with a scatter band of 5.2, and the FS Model the worst, with a scatter band of 18. The DRM Model fell in the middle, having a scatter band of 9. It was possible to partition only one of the S/F tests, and the SRP Model's prediction of this test was a scatter band of 6.1. It is not understood why the S/F tests were so difficult to predict. Mean stresses were not present in these tests. An unusually short life occurred for one of these tests (which led to the majority of the poor predictions), but this life was confirmed by duplicate testing.

All the models segregated sections of the baseline data set to some extent. The data were segregated the least by the FS and the FMDF Models and most by the DRM and SRP Models. The FS Model had the wrong trend for the tensile strain-hold tests, overpredicting those tests having short lives and underpredicting those having long lives. The FMDF underpredicted the ten-

sile stain-hold tests having long lives and overpredicted all but one of the compressive strain-hold tests. The DRM also underpredicted the long-life tensile-hold tests and overpredicted all of the compressive strain-hold tests. The SRP Model underpredicted the long-life tensile strain-hold tests and overpredicted the 0/10 tests. It also overpredicted all of the 0.05-cpm tests. Thus the amount of segregation of the data by the models followed the same trend as the life predictions.

In general, those tests having large mean stresses were poorly predicted by all the models. However, some tests having large mean stresses were well predicted. Thus the influence of mean stress could not be conclusively determined. Nevertheless, the general trend was that the models did not account for mean stress effects.

It is noteworthy that the models employing frequency terms—the FS and the FMDF Models—were more successful in life prediction than those models dependent upon creep deformation to cause time-dependent damage—the SRP and DRM Models.⁹ As discussed previously, the frequency regime over which the testing was done produced negligible amounts of creep in the continuous-cycling tests, and the amount of creep during the strain-hold tests was usually small. Consequently, another type of time-dependent damage, such as environmental attack, would be expected to be important. Those models able to take into account other types of time-dependent damage by the use of a frequency term were able to predict the data better than those models which did not.

The Coffin-Manson equation [29,30] was also examined. The equation yielding the best fit to the baseline data was

$$N_f = 0.4070 (\Delta \epsilon_{\text{inel}})^{-1.151}$$

The scatter band was 5.8 and the standard deviation was 0.26. The data were extensively segregated by this equation. These results show that a more sophisticated model is needed to accurately predict the data.

It should be noted that the conclusions of this paper are limited to fatigue behavior similar to that of René 95. This behavior is characterized by small inelastic strains, small amounts of creep, and the presence of mean stresses. The models evaluated in this paper have been used with success for materials exhibiting other types of fatigue behavior.

Conclusions

1. No model was able to correlate the fatigue life of René 95 at 650°C (1200°F) to within the desired scatter band of two. The correlations and predictions are shown in Table 2.

⁹ The DRM is dependent upon creep deformation because the damage during a strain-hold period is controlled by the amount of stress relaxation that occurs. Although the ductility-normalized SRP equations have a term to account for environmental attack, this term was unable to be used for reasons explained in the section on the SRP model.

TABLE 2—*Correlations and predictions of the models.*

Model	Baseline Tests		Verification Tests
	Scatter Band	Standard Deviation	Scatter Band
Frequency-Modified Damage Function	3.6	0.18	5.2
Frequency-Separation Model	3.6	0.18	17.9
Damage-Rate Model	5.1	0.24	8.9
Strainrange-Partitioning Model	5.4	0.23	6.1
Coffin-Manson Equation	5.8	0.26	. . .

2. All the models segregated the baseline tests to some extent.

3. The models were unable to predict the fatigue life to within the desired scatter band because (1) mean stress was not properly taken into account, and (2) environmental attack, which appears to be the principal time-dependent damage for René 95 at 650°C (1200°F), was not properly taken into account by the Strain-Range Partitioning Model and the Damage Rate Model.

4. A method based upon the minimum creep rate versus stress and the cyclic stress-strain curves was presented to determine when an environmental-fatigue interaction or a creep-environmental fatigue interaction may be present. Essentially, the method states that if the imposed strain rate is greater than the minimum creep rate for the highest stress in the cycle, then no creep damage can take place and only environmental attack can occur. For René 95, this method indicates an environmental-fatigue interaction and little creep damage.

Acknowledgments

The author expresses his appreciation for the support of Dr. Noel Ashbaugh and Mr. Walter Tripp of Systems Research Laboratories, Inc., Mar-Test, Inc., for running the fatigue tests, and Dr. Theodore Nicholas of the Air Force Wright Aeronautical Laboratories/Materials Laboratory for funding this work under Contract No. F33615-76-C-5191. The author also acknowledges valuable discussions with Dr. Ashbaugh, Dr. Don Stouffer of the University of Cincinnati, Messrs. Ray Stentz and Joe Conway of Mar-Test, Inc., and Mr. Jim Berling of Materials-Behavior Research Corporation. Finally, the author thanks Mrs. Marian Whitaker and Mrs. Judith Paine for helping to type this paper.

APPENDIX

Reading the Graphs

The graph of the predicted and observed lives has been made in an unconventional manner in order to achieve a more meaningful display of the data. The observed life

is plotted logarithmically on the horizontal axis. The ratio of predicted to observed life or its inverse is plotted linearly on the vertical axis. When a perfect prediction is made, this ratio has a value of one. When the life is overpredicted, then the ratio of predicted to observed life is greater than one and is plotted above the perfect fit line of one. When the life is underpredicted, the ratio of observed to predicted life is greater than one and is plotted below the perfect fit line. Thus, unconservative predictions are above the perfect fit line, and conservative predictions are below it.

References

- [1] Manson, S. S., Halford, G. R., and Hirschberg, M. H., "Creep-Fatigue Analysis by Strainrange Partitioning," *Symposium on Design for Elevated Temperature Environment*, ASME, New York, 1971, pp. 12-28.
- [2] Manson, S. S. in *Fatigue at Elevated Temperatures*, ASTM STP 520, American Society for Testing and Materials, 1973, pp. 744-775. The interaction damage rule is postulated on pp. 751-753.
- [3] Manson, S. S., Halford, G. R., and Hirschberg, M. H., "Strainrange Partitioning-A Tool for Characterizing High-Temperature, Low-Cycle Fatigue," NASA TMX-71691, NASA-Lewis Research Center, Cleveland, Ohio, 1975.
- [4] Halford, G. R. and Nachtigall, A. J., "The Strainrange Partitioning Behavior of an Advanced Gas Turbine Disk Alloy, AF2-1DA," Paper No. 79-1192, presented at the AIAA/SAE/ASME 15th Joint Propulsion Conference, 18-20 June 1979.
- [5] Coffin, L. F., Jr., "The Concept of Frequency Separation in Life Prediction for Time-Dependent Fatigue," in *1976 ASME-MPC Symposium on Creep-Fatigue Interaction*, MPC-3, American Society of Mechanical Engineers, New York, 1976, pp. 349-364.
- [6] *Time-Dependent Fatigue of Structural Alloys*, ORNL-5073, Oak Ridge National Laboratory, Oak Ridge, Tenn., 1975, pp. 109-133.
- [7] Ostergren, W. J., *ASTM Standardization News*, Vol. 4, No. 10, 1976, p. 327.
- [8] Ostergren, W. J., "Correlation of Hold Time Effects in Elevated Temperature Low Cycle Fatigue Using a Frequency Modified Damage Function," in *1976 ASME-MPC Symposium on Creep-Fatigue Interaction*, MPC-3, American Society of Mechanical Engineers, New York, 1976, pp. 179-202.
- [9] Majumdar, S. and Maiya, P. S., "A Unified and Mechanistic Approach to Creep Fatigue Damage," ANL-76-58, Argonne National Laboratory, Argonne, Ill., January 1976.
- [10] Majumdar, S. and Maiya, P. S., "A Damage Equation for Creep-Fatigue Interaction," in *1976 ASME-MPC Symposium on Creep-Fatigue Interaction*, MPC-3, American Society of Mechanical Engineers, New York, 1976, pp. 323-336.
- [11] Majumdar, S. and Maiya, P. S., "Wave Shape Effects in Elevated-Temperature Low-Cycle Fatigue of Type 304 Stainless Steel," in *Inelastic Behavior of Pressure Vessel and Piping Components*, PVP-PB-028, American Society of Mechanical Engineers, New York, 1978, pp. 43-54.
- [12] Menon, M. N., "Life Prediction Techniques for Analyzing Creep-Fatigue Interaction in Advanced Nickel-Base Superalloys," AFML-TR-76-172, Air Force Materials Laboratory, Wright-Patterson AFB, Ohio, 1976.
- [13] Coffin, L. F., Jr., "The Effect of Frequency on High-Temperature, Low-Cycle Fatigue," in *Proceedings of the Air Force Conference on Fatigue of Aircraft Structures and Materials*, AFFDL-TR-70-144, Air Force Flight Dynamics Laboratory, Wright-Patterson AFB, Ohio, 1970, pp. 301-311.
- [14] Bernstein, H. L., "An Evaluation of Four Models for the Creep-Fatigue Interaction in René 95 at Twelve Hundred Degrees Fahrenheit," Masters thesis, University of Illinois, Urbana, Ill., 1978.
- [15] Hyzak, J. M. and Bernstein, H. L., "An Analysis of the Low Cycle Fatigue Behavior of the Superalloy René 95 by Strainrange Partitioning," in AGARD-CP-243, Advisory Group for Aerospace Research and Development, London, 1978, pp. 11-1 to 11-25.
- [16] Bernstein, H. L., "An Evaluation of Four Current Models to Predict the Creep Fatigue Interaction in René 95," AFML-TR-79-4075, Air Force Materials Laboratory, Wright-Patterson AFB, Ohio, 1979.

- [17] Stouffer, D. C., Papernik, L., and Bernstein, H. L., "An Experimental Evaluation of the Mechanical Response Characteristics of René 95," AFWAL-TR-80-4136, Air Force Wright Aeronautical Laboratories, Wright-Patterson AFB, Ohio, 1980.
- [18] Conway, J. B. and Stentz, R. H., "High Temperature LCF Data for Three High-Strength Ni-Base Superalloys," AFWAL-TR-80-4077, Air Force Wright Aeronautical Laboratories, Wright-Patterson AFB, Ohio, 1980.
- [19] Shamblen, C. E., Allen, R. E., and Walker, F. E., *Metallurgical Transactions*, Vol. 6A, November 1975, p. 2073.
- [20] Menon, M. N., "Metallographic Characterization of René 95 Forgings," AFML-TR-73-180, Air Force Materials Laboratory, Wright-Patterson AFB, Ohio, 1973.
- [21] Menon, M. N. and Reiman, W. H., *Metallography*, Vol. 8, 1975, p. 221.
- [22] Menon, M. N. and Reiman, W. H., *Journal of Materials Science*, Vol. 10, 1975, p. 1571.
- [23] Stouffer, D. C., "An Evaluation of the Monotonic Response of René 95 at 1200°F," AFOSR-TR-78-0905, Air Force Office of Scientific Research, Bolling AFB, D.C., 1978.
- [24] Cook, R. H. and Skelton, R. P., *International Metallurgical Reviews*, Vol. 19, 1974, p. 199.
- [25] Menon, M. N., *Journal of Materials Science*, Vol. 11, 1976, p. 984.
- [26] Bernstein, H., "The Stress Behavior of Three Advanced Nickel-Base Superalloys During High-Temperature, Low-Cycle Fatigue," AFWAL-TR-80-4075, Air Force Wright Aeronautical Laboratories, Wright-Patterson AFB, Ohio, 1980.
- [27] Slot, T., Stentz, R. H., and Berling, J. T. in *Manual on Low Cycle Fatigue Testing, ASTM STP 465*, American Society for Testing and Materials, 1969, pp. 100-128.
- [28] Conway, J. B., Stentz, R. H., and Berling, J. T., *Fatigue, Tensile, and Relaxation Behavior of Stainless Steels*, TID-26135, Oak Ridge National Laboratory, Oak Ridge, Tenn., 1975, pp. 14-31.
- [29] Coffin, L. F., Jr., *Transactions of ASME* 7, Vol. 76, 1954, p. 923.
- [30] Manson, S. S., "Behavior of Materials Under Conditions of Thermal Stress," NACA-TN-2933, NASA-Lewis Research Center, Cleveland, Ohio, 1953.
- [31] Halford, G. R., Saltsman, J. F., and Hirschberg, M. H., "Ductility Normalized-Strainrange Partitioning Life Relations for Creep-Fatigue Life Prediction," in *Proceedings of the Conference on Environmental Degradation of Engineering Materials*, Virginia Tech., Printing Dept., VPI and State Univ., Blacksburg, Va., 1977, pp. 599-612; also NASA TM-73737.
- [32] Manson, S. S., *Experimental Mechanics*, Vol. 5, No. 7, 1965, p. 193.
- [33] Morrow, J., "Fatigue Properties of Metals," Section 3.2, *Fatigue Design Handbook*, SAE Advances in Engineering, Vol. 4, 1968, pp. 21-29.

Damage Accumulation and Fracture Life in High-Temperature Low-Cycle Fatigue

REFERENCE: Radhakrishnan, V. M., "Damage Accumulation and Fracture Life in High-Temperature Low-Cycle Fatigue," *Low-Cycle Fatigue and Life Prediction, ASTM STP 770*, C. Amzallag, B. N. Leis, and P. Rabbe, Eds., American Society for Testing and Materials, 1982, pp. 135–151.

ABSTRACT: An analysis of the interaction of creep and fatigue is made based on the energy expended for the nucleation of damage at the advancing crack front. A rate equation is assumed for the damage nucleation, and the activation energy is taken as a function of the total mechanical energy at the crack tip. The analysis yields a relation in terms of J -integral which is applicable to both crack propagation and final failure. Raw data from various sources have been analyzed for different types of loading and compared with the theoretical prediction. The total energy in tension, which includes the tension-going strain rate, appears to be a good parameter for the prediction of fracture life in creep-fatigue interaction.

KEY WORDS: creep, fatigue, energy approach, damage function, crack propagation, life prediction

Interaction of creep and low-cycle fatigue has been the subject of much investigation during the last decade. Approaches based on damage summation [1,2],² strain range partitioning [3,4], and frequency modification [5,6] have been proposed and discussed in detail. Using the ASME Boiler and Pressure Vessel Code's damage summation equation given in the form

$$\alpha \Sigma t/t_r + \beta \Sigma N/N_f = D_{\text{total}} \quad (1)$$

Campbell [7] analyzed the experimental data on Type 304 stainless steel and found the damage to be minimum when the strain range is low or when the hold periods are long. The relation between creep damage, D_c , and the fatigue damage, D_f , is more nonlinear, and such nonlinear interaction relation is also reported by Janson [8]. Majumdar and Maiya [9] have analyzed the damage accumulation based on crack propagation and void formation.

¹ Metallurgy Department, Indian Institute of Technology, Madras, India.

² The italic numbers in brackets refer to the list of references appended to this paper.

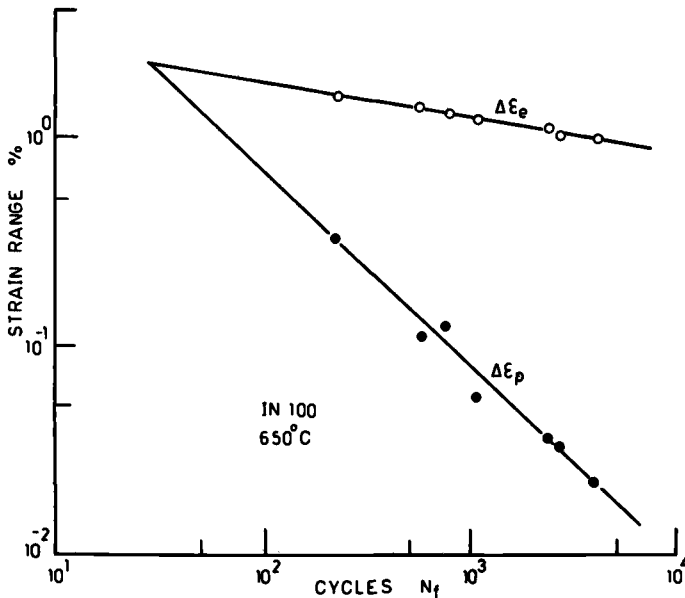


FIG. 1—Relative magnitudes of the elastic and inelastic strains in IN 100 alloy at 650°C.

In the analysis of the strain range partitioning method, the data collected and reported in Ref 10 clearly reveal that in many cases the elastic portion of the strain, $\delta\epsilon_{el}$, is either greater than or comparable to the inelastic strain range, $\delta\epsilon_{in}$, as shown by a typical example for IN 100 in Fig. 1. Therefore the analyses made are for the conditions beyond the transition fatigue life, N_t , as defined by Coffin [5], and hence the contribution to damage due to the elastic strain component cannot be neglected. At low temperatures when creep is negligible, there will be one-to-one correspondence between $\delta\epsilon_{el}$ and $\delta\epsilon_{in}$. Thus analysis and correlation based on $\delta\epsilon_{el}$ or $\delta\epsilon_{in}$ can be sufficient. At higher temperatures with creep deformation also present, however, there will not be one-to-one correspondence between $\delta\epsilon_{el}$ and $\delta\epsilon_{in}$, as shown in Fig. 2 [11] for turbine disk alloy AF2-1Da; therefore the elastic strain component must also be taken into consideration in the analysis.

In the interaction rule employed for SRP analysis, the damage contribution per cycle of any typical strain component, say $\delta\epsilon_{pp}$, for a given total inelastic strain, $\delta\epsilon_{in}$, is given by

$$\text{damage/cycle} = \frac{1}{N_{pp}^*} = \frac{\delta\epsilon_{pp}/\delta\epsilon_{in}}{N_{pp}} = \frac{F_{pp}}{N_{pp}} \quad (2)$$

where N_{pp} is the number of cycles obtained against the value $\delta\epsilon_{in}$ on the $\delta\epsilon_{pp}$ - N_f curve (Fig. 3a). This means that so long as the inelastic strain range $\delta\epsilon_{in}$ is fixed, the damage line will be the DD' line with a slope equal to unity (according to the relation $N_{pp}^* \delta\epsilon_{pp} = N_{pp} \delta\epsilon_{in} = \text{constant}$) and is not influenced

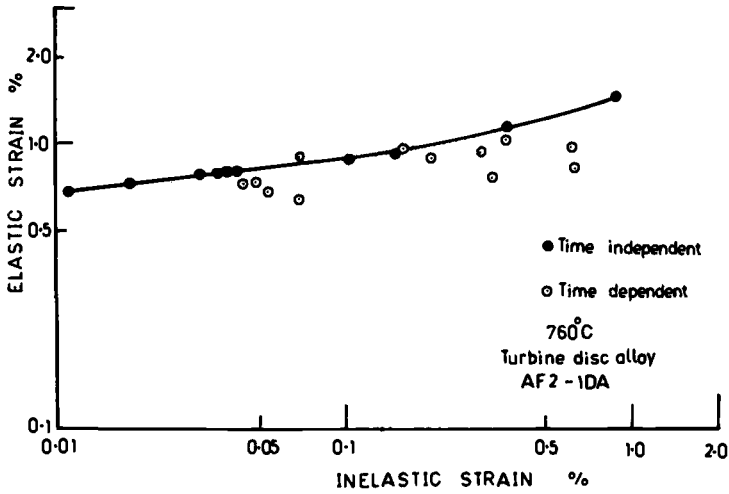


FIG. 2—Time-dependent and time-independent elastic and inelastic strain relation in turbine disk alloy AF2-1DA at 760°C.

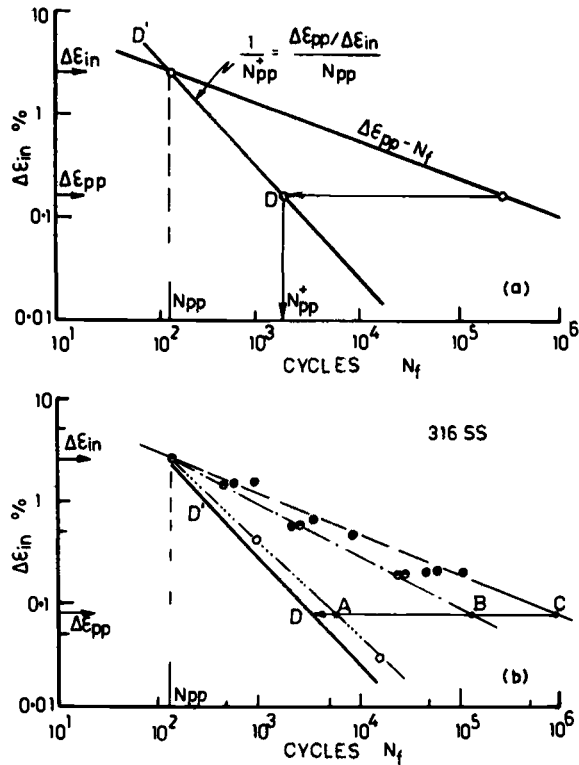


FIG. 3—Damage contribution of PP component in Type 316 stainless steel under different treated conditions in SRP method.

by the slope of the curve $\delta\epsilon_{pp}-N_f$. For a typical case of Type 316 stainless steel, different treatments, such as annealing, aging, and irradiation, give different $\delta\epsilon_{pp}-N_f$ lines with different slopes (Fig. 3b) [12]. Yet if the inelastic strain range $\delta\epsilon_{in}$ is fixed as shown, the damage contribution for a given $\delta\epsilon_{pp}$ -component will be the same in all three cases; that is, the damage contribution per cycle in all three materials will correspond to point $D(=1/N_{pp}^*)$.

Ostergren [13] proposed the hysteresis energy in the tensile portion as a basis for creep-fatigue analysis. Investigations carried out on René 95 and Inconel 718 alloys [14] showed better correlation with the hysteresis loop energy approach. Leis [15] and Fong [16] have also approached the problem of interaction of creep and fatigue from the energy standpoint. Bernstein [17] analyzed the creep-fatigue behavior of René 95 based on the different models currently in discussion and found that none of the models could predict all the verification tests to within a factor of two.

The damage due to creep-fatigue interaction has also been viewed from the standpoint of crack propagation [18,19], and the crack growth rate da/dN was correlated with the J -integral. The damage accumulation as envisaged in other approaches is the nucleation and propagation of a dominant crack up to the critical point, and even at elevated temperatures where creep-fatigue interaction will be more pronounced, an analysis based on damage nucleation and accumulation in the form of a dominant crack will be able to give a better understanding and method of life prediction. A model for damage accumulation in the form of crack growth based on the energy input is discussed in the following section.

A Model for Crack Growth

When a crack of length a forms on the surface of the material, the stress and strain just ahead of the crack are increased, and this enhanced effect is felt over a small highly strained volume represented by its width R_p . Beyond this highly strained volume of the material, the stress and strain will rapidly reduce to macrovalues applied away from the crack. The stress-strain concentration factors, K_σ and K_ϵ , are related to the theoretical stress concentration factor, K_t , by [20,21]

$$K_t^2 = K_\sigma K_\epsilon \quad (3)$$

If σ^* and ϵ^* are the stress and strain near the crack tip, it can be taken that

$$K_\sigma = \sigma^*/\sigma \text{ and } K_\epsilon = \epsilon^*/\epsilon \quad (4)$$

and in the case of fatigue it can be written as

$$K_t^2 = \frac{\delta\sigma^* \delta\epsilon^*}{\delta\sigma \delta\epsilon} = \frac{\delta\sigma^*(\delta\epsilon_{el}^* + \delta\epsilon_{pl}^*)}{\delta\sigma(\delta\epsilon_{el} + \delta\epsilon_{pl})} \quad (5)$$

where $\delta\sigma$ and $\delta\epsilon$ are the stress and strain range away from the crack, and $\delta\sigma^*$

and $\delta\epsilon^*$ are those at the crack tip. The product $\delta\sigma \delta\epsilon_{pl}$ is considered to represent the energy absorbed during each cycle as given by the area of the hysteresis loop, and the product $\delta\sigma \delta\epsilon_{el}$ represents the elastic energy. Hence the numerator in Eq 5 represents the energy δW^* at the crack tip, and the denominator represents the energy δW supplied away from the crack. Thus we can write

$$K_t^2 = \frac{\delta W^*}{\delta W} = \frac{(\delta W_{el}^* + \delta W_{pl}^*)}{(\delta W_{el} + \delta W_{pl})} \quad (6)$$

With the relation $K_t = 1 + 2\sqrt{a/\rho} \approx 2\sqrt{a/\rho}$, where a is the crack length and ρ is the crack-tip radius, we can write Eq 6 as

$$\delta W^* = \frac{4}{\rho} (\delta W \cdot a) \quad (7)$$

A plastic J -solution for a center crack strip of infinite extent is given by Shih and Hutchinson [22] and their solution in fatigue terminology can be written as

$$\delta J_p = k(3.85/n'\pi + n'\pi) (n' + 1)\delta W_p \cdot a \quad (8)$$

which can be approximated within 3 to 4 percent by the modified form [23]

$$\delta J_p = C_1(\delta W_p \cdot a) \quad (9)$$

where $C_1 = 1.96\sqrt{1/n'}$. Similarly the elastic δJ -solution can be given as

$$\delta J_e = C_2(\delta W_e \cdot a) \quad (10)$$

where $C_2 = 2\pi$. The total will be

$$\delta J = \delta J_e + \delta J_p = (C_2\delta W_e + C_1\delta W_p) \cdot a \quad (11)$$

In creep-fatigue the damage nucleation at the tip of the advancing crack could be in the form of microcrack or void growth contributed by point and line defects. Both the strain energy at the crack tip and the thermal energy will contribute to the damage nucleation ahead of the crack tip. The damage per unit volume of the material ahead of the crack nucleated per cycle can be given by a rate equation of the form

$$\frac{dD}{dN} = C_3 \exp \frac{-(Q - m' \log (\delta W^*/W_0))}{kT} \quad (12)$$

where Q is the activation energy, and m' and W_0 are constants. A similar da/dN dependence on the activation energy has been found to be valid in the case of high-temperature fatigue of aluminum [24]. Equation 12 can be re-written as

$$\frac{dD}{dN} = C_4 \left(\frac{\delta W^*}{W_0} \right)^m \exp (-Q/kT) \quad (13)$$

where $m = m'/kT$.

The damage takes place over a small highly strained volume, represented by its linear dimension R_p . In the case of elastic field this dimension can be identified as the width of the plastic zone given by

$$R_p \propto (E/\sigma_{ys}^2) J_e$$

where E is Young's modulus and σ_{ys} is the yield stress. In the case of high-temperature low-cycle fatigue, the width of the highly strained volume can be given by a similar type of relation:

$$R_p \propto (E/\sigma_{ys}^2) \delta J \quad (14)$$

The total damage in the volume of highly strained zone joins the crack, and the crack advances through a small distance da in the time dN . Hence the crack growth rate can be written as

$$\begin{aligned} R_p \cdot dD/dN &= da/dN = C_5 (E/\sigma_{ys}^2) (\delta J) (\delta W^*/W_0)^m \exp(-Q/kT) \\ &= C(C_1 \delta W_p + C_2 \delta W_e) (\delta W/W_0)^m (a)^{m+1} \exp(-Q/kT) \end{aligned} \quad (15)$$

In the above model, it is assumed that the damage nucleates only in the highly strained volume represented by its width R_p during the small interval dN . This damage joins the advancing crack at the end of the interval, thereby making the crack advance through a small distance da . When the value of the cyclic strain-hardening exponent n' is in the range of 0.1 to 0.15, the constants C_1 and C_2 will be nearly equal and Eq 15 can be given as

$$da/dN = C_6 (\delta W \cdot a)^{m+1} \exp(-Q/kT) \quad (16)$$

Under certain conditions of testing, as in vacuum, some of these damages may get healed. Under normal testing conditions with ambient air, such healing may not be possible. In addition, with hold times the crack front will be subjected to environmental attack. Hoffelner and Speidel [25] have reported that the crack propagation rate is two times higher in air than in vacuum for IN 738 LC alloy and IN 939 alloy at 850°C. The stress corrosion effect at the crack front in the above cases appears to be a mere multiplying effect; however, the effect may also depend on the time. In the simple case we can write Eq 16 in the form

$$da/dN = C_7 C_f (\delta J)^{m+1} \quad (17)$$

where C_7 is a temperature-dependent constant and C_f is a stress corrosion factor. The crack growth rate in high-temperature low-cycle fatigue is shown to be a function of δJ [18, 19], and the value of the exponent $(m + 1)$ is found to be around 1.3 to 1.7.

After rearranging and integrating, we obtain

$$\frac{1}{ma_0^m} [1 - (a_0/a_f)^m] = C_7 C_f (\delta W)^{m+1} \cdot N_f \quad (18)$$

where a_0 is the length of the crack at the time of initiation and a_f its final length. Assuming the variation of a_f under different loading to be marginal and $a_0 \ll a_f$, we obtain

$$C_f(\delta W)^{m+1} \cdot N_f = \text{constant} \quad (19)$$

The left-hand side of the relation gives the energy input during the tensile portion of the cycle.

Wave Shape Analysis

In the case of a balanced hysteresis loop with no creep effect, the energy associated with the J -integral will be W_e and W_p corresponding to δJ_e and δJ_p respectively (Fig. 4). This energy term will be

$$\begin{aligned} \delta W &= \delta W_e + \delta W_p \\ &= \frac{\delta \sigma}{2} \delta \epsilon_{el} + [(1 - n')/(1 + n')] \frac{\delta \sigma}{2} \delta \epsilon_{pl} \end{aligned} \quad (20)$$

The second term, corresponding to the plastic region, depends on the cyclic strain-hardening exponent n' .

The case of unbalancing in the hysteresis loop comes in when there is a hold period either in tension or compression or when the tension-going frequency is different from the compression-going frequency. The need to consider wave shape effects has been recognized in recent life-prediction techniques. The general approach is either to separate the hysteresis loop into components of fully reversed strain elements (as is employed in SRP method) or to consider tensile-going and compression-going frequencies separately (as has been proposed by Coffin [26,27] and Ostergren [28]). In such a case, the contribution to damage due to creep also comes into the picture. Tomkins and Wareing [29] have taken the creep damage as an effect in reducing the crack length to cause instability. In the analysis presented, the entire energy term can be looked upon as three components, W_e , W_p , and W_{creep} , the latter being due to the tensile stress σ_t and the displacement ϵ_{creep} . It is generally agreed that intergranular cavitation and triple point cracks at high temperatures are produced by tensile (not compressive) axial stresses, and that they are also enhanced by lowering the strain rate [30]. Hence Eq 20 can be extended to creep region and be written as

$$\delta W = \frac{\delta \sigma}{2} \delta \epsilon_{el} + \frac{1 - n'}{1 + n'} \frac{\delta \sigma}{2} \delta \epsilon_{pl} + \sigma_t \delta \epsilon_c \quad (21)$$

where $\delta \epsilon_{el} + \delta \epsilon_{pl} + \delta \epsilon_c = \text{total strain}$. The third term need not necessarily be due to creep under constant stress hold. When the frequency is low, the creep effect will come in. Thus the strain rate will play a part, and in such a case the energy term can be given as

$$\delta W = \sigma_t \delta \epsilon_{el} + \frac{1 - n'}{1 + n'} \sigma_t \delta \epsilon_{pl} + [\sigma_t \delta \epsilon_c] \left(\frac{\dot{\epsilon}_t}{\dot{\epsilon}_r} \right)^q \quad (22)$$

where $\dot{\epsilon}_r$ is the reference strain rate (for example, when the creep contribution is zero) and $\dot{\epsilon}_t$ is the actual strain rate during the tensile portion. The exponent q is a constant. The cyclic strain-hardening exponent n' refers to Fast-Fast (FF) cycling. Since the tensile portion of the energy is considered in the analysis, tests CC (creep-creep) and CP (creep-plasticity) can be considered similar and tests PP (plasticity-plasticity) and PC (plasticity-creep) will be similar, except for the mean stress effect. Typical energy evaluations are shown schematically in Fig. 4.

Under certain conditions of high-temperature low-cycle fatigue, some materials are more prone to environmental stress corrosion than to creep damage. Low strain rate alone will not be a sufficient condition for creep damage to take place. The stress induced must also be sufficiently high enough to introduce the creep phenomenon. Materials that are environmental-corrosion sensitive will have accelerated crack growth rate with or with-

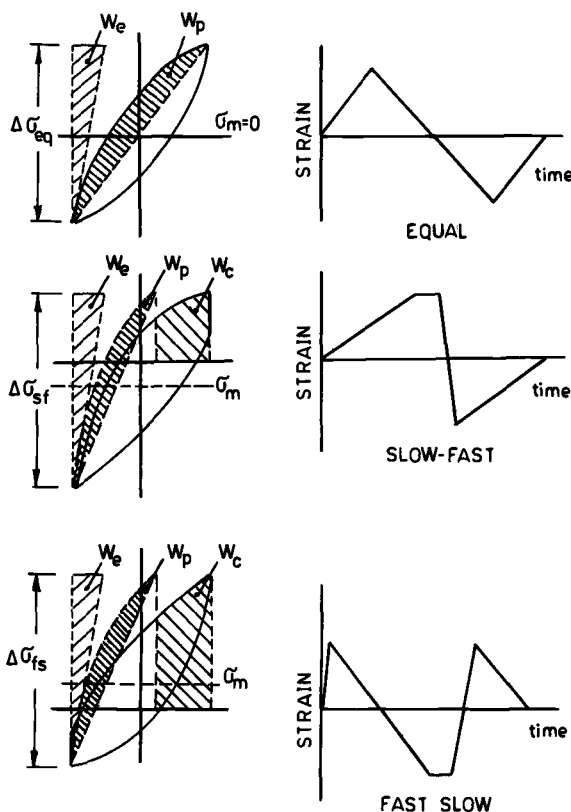


FIG. 4—Schematic energy separation in creep-fatigue interaction.

out the aid of the creep damage. When the stress or strain is held constant at the peak value, or when the material is subjected to a low strain rate, the crack front will be attacked by corrosion and the crack zone will experience a stress corrosion effect. Under such a case the failure life can be given as

$$N_f \propto C_f^{-1} (\delta W)^{-(m+1)} \quad (23)$$

where C_f is the corrosion factor. Whether this factor is a simple multiplying factor or is a function of the time of exposure of the material during each cycle, depends on whether the protective layer that forms at the crack front because of corrosion is going to be stable during each cycle or will break down immediately after formation, thereby continuously exposing the crack-front to stress corrosion attack. When the hold time involved is small, C_f can be taken as a simple multiplying factor.

Case Study and Discussion

Continuous Cycling (Fast-Fast)

When the cycling is continuous and symmetrical at a constant strain rate, the first two terms in Eq 21 will be valid because there is no creep effect, and the total energy will be

$$\delta W = \sigma_t \delta \epsilon_{el} + \frac{1 - n'}{1 + n'} \sigma_t \delta \epsilon_{pl} \quad (24)$$

If the hysteresis loop is available, the energy can be evaluated or for computation purposes Eq 24 can be approximated as

$$\delta W = (\sigma_t \delta \epsilon_{total})$$

so that

$$(\sigma_t \delta \epsilon_{total})^{m+1} \cdot N_f = \text{constant} \quad (25)$$

where σ_t is the tensile stress.

Typical relations between tensile total energy δW_t and the cycles to failure for 800 and 800 H nickel alloys are shown in Fig. 5 (raw data from Ref 31). Even when the stress or strain is held constant for a duration in tension or in compression, if the temperature is not high enough to cause creep damage in the small interval of time, then Eq 25 will be valid for cases of continuous cycles (●), tension hold (◐), compression hold (◑), or tension and compression hold (○). Such a typical correlation at a comparatively low temperature where the creep damage or relaxation effect may be negligible is shown in Fig. 6 for chromium-molybdenum steel [12] under Fast-Slow, Slow-Fast, and Slow-Slow conditions of testing.

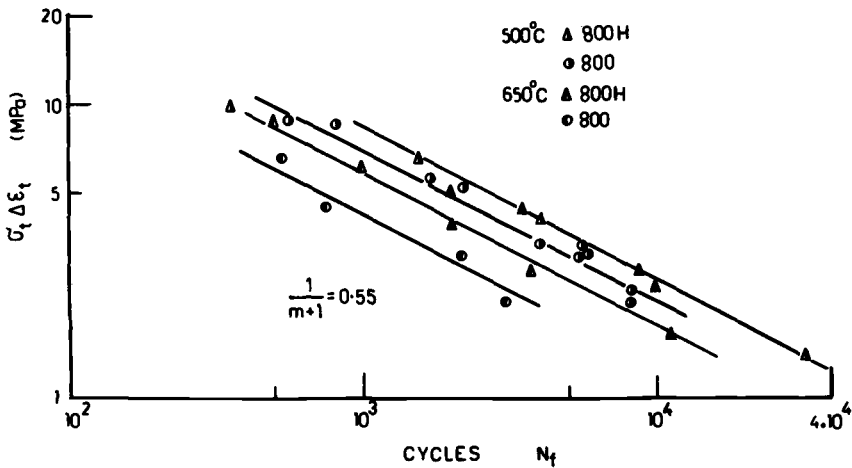


FIG. 5—Relation between δW_t and N_t for 800 and 800 H nickel-base alloys in FF type of loading. Data from Ref 31.

Slow-Fast Cycling (CP type).

In the case of slow-fast cycling, the tensile-going strain rate $\dot{\epsilon}_t$ will be smaller than the compression-going strain rate $\dot{\epsilon}_{com}$ which will correspond to the normal fast-fast cycling. In this case creep strain will be introduced in the total strain range, and the energy is computed as shown in Fig. 4. The total tensile energy term responsible for the damage accumulation can be written as

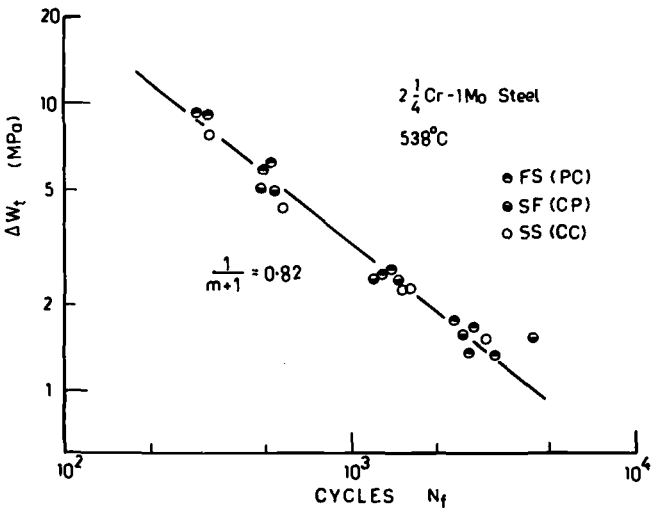


FIG. 6—Relation between δW_t and N_t for chromium-molybdenum steel at 538°C in PC, CP, and CC type of loading. Data from Ref 12.

$$\delta W_t = \sigma_t \delta \epsilon_{el} + \frac{1 - n'}{1 + n'} \sigma_t \delta \epsilon_{pl} + \sigma_t \delta \epsilon_c \left(\frac{\dot{\epsilon}_r}{\dot{\epsilon}_t} \right)^q$$

For a given pattern of slow-fast cycling, where n' refers to cyclic strain-hardening exponent under FF condition, the relation

$$(\delta W_t)^{m+1} N_f = \text{constant}$$

will be valid. Typical relations for FF (●) and SF (⊖) loading conditions for Waspaloy are shown in Fig. 7 [32]. On the log-log plot, the FF and SF give two straight-line relations, the slopes of which are the same, equal to $1/(1 + m)$. If the data of SF are to be compared with those of FF (so that a single relation will emerge), then the strain rate effect must be taken into consideration, as shown in the above relation. Typical experimental results on Inconel 718 alloy and René 95 alloy are shown in Fig. 8 (raw data from Ref 14).

The SF loading gives rise to two considerations. The tensile strain rate $\dot{\epsilon}_t$ will be smaller than $\dot{\epsilon}_r$ (the reference FF strain rate), and so the damage owing to δW_t will be greater than that owing to FF loading. The SF loading will also introduce a mean compressive stress which will reduce the value of σ_t . However, the net effect will still be large enough to cause failure at a lower number of cycles. In general we can say that the fatigue life will be governed by the net effect of these two opposing forces.

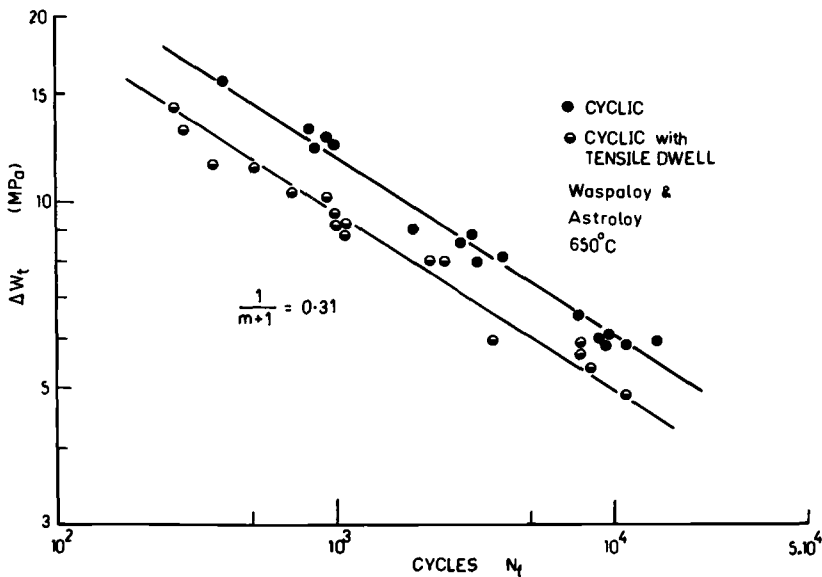


FIG. 7—Relation between δW_t and N_f for Waspaloy and Astroloy in FF and SF type of loading. Data from Ref 32.

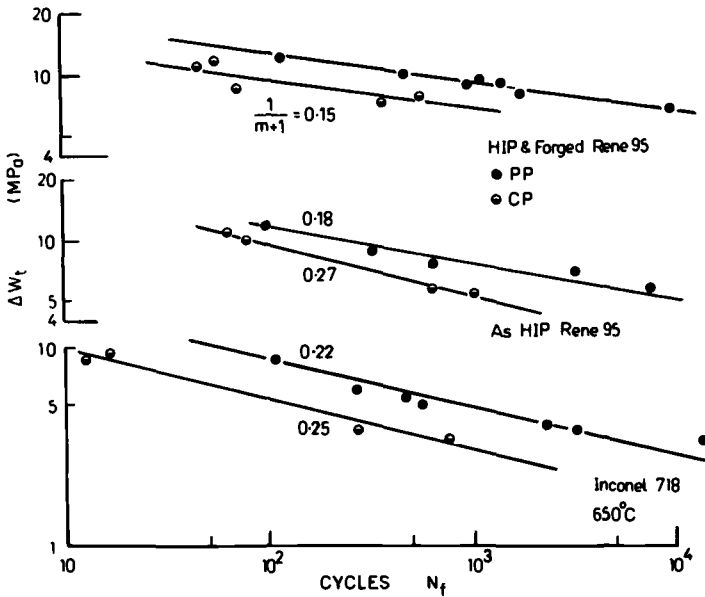


FIG. 8—Relation between δW_t and N_f for Inconel 718 alloy and René 95 alloy in PP and CP type of loading. Data from Ref 14. $N_f = (\times 10)$.

Fast-Slow (FS) Cycling

It is assumed in the analysis that the damage accumulation takes place during the tensile portion of the cycling. Hence fast-slow cycling data will be similar to the FF cycling data. Typical results of turbine disk alloy AF2-1DA

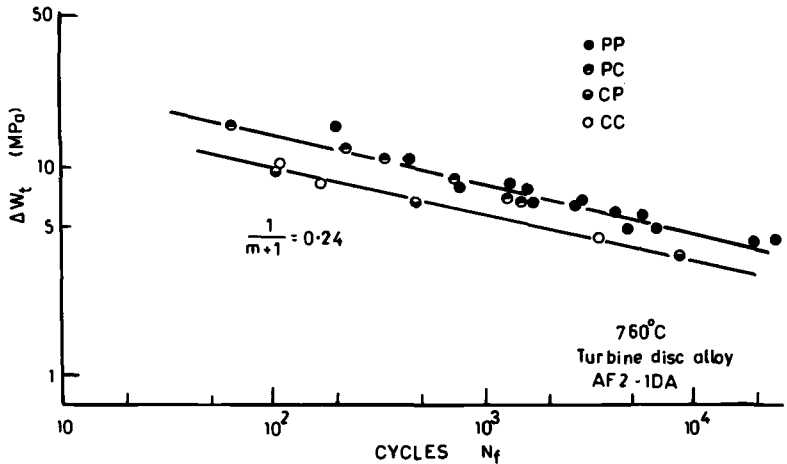


FIG. 9—Relation between δW_t and N_f for turbine disk alloy AF2-1DA in PP, PC, CP, and CC type of loading. Data from Ref 11.

are shown in Fig. 9 (raw data from Ref 11), where the FF and FS data fall on one line and the SF and SS data fall on another. It should be noted, however, that even though FS may be similar to FF, FS will introduce a tensile mean stress and the total strain range will also be increased. Thus the energy absorbed will be slightly higher in the case of FS than in FF, depending on the mean stress level. Typical results of MAR M002 alloy at temperatures of 850 and 1040°C are shown in Fig. 10 (raw data from Ref 33). It can be noted that at 850°C the creep effect appears to be negligible, and therefore all the points fall on the same line. As the temperature is increased, creep effect is more pronounced. Thus there is difference between FF-FS and SF-SS data at 1040°C.

Corrosion Effect

In the investigations carried out by Bernstein [17] on René 95 alloy at 650°C it was observed that the hysteresis loops for frequencies of 20 and 0.05 cpm were similar, thereby indicating that the material was not very sensitive to strain rate at that temperature. Tests were carried out with 1 and 10 min hold periods at peak stress or strain. Some tests were also carried out at some intermediate strain level (before the strain reached its peak value).

This material appears to be very sensitive to environment, the tests having

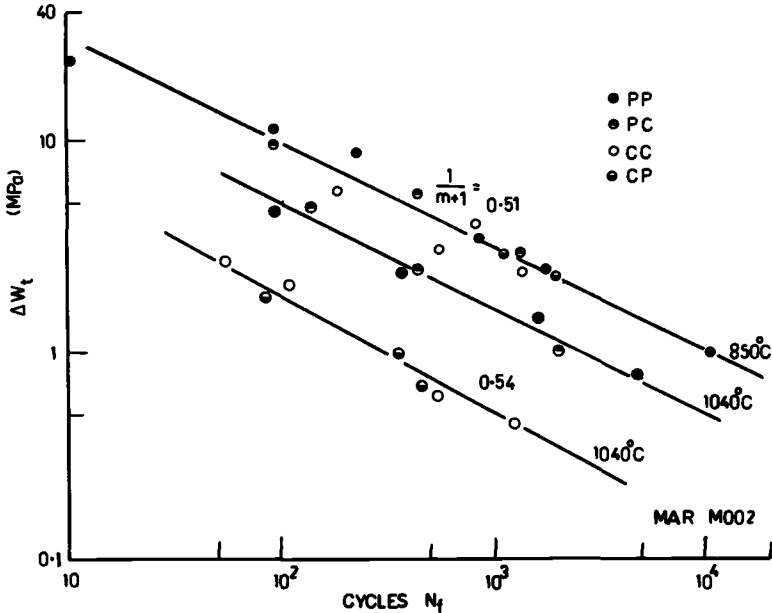


FIG. 10—Relation between δW_t and N_f for MAR M002 alloy in PP, PC, CP, and CC type of loading at 850 and 1040°C. Data from Ref 33.

been carried out in air, and the creep damage appears to be negligible. In such a case the life can be given by

$$C_f(\delta W_t)^{m+1} \cdot N_f = \text{constant}$$

In the experimental analysis, the 20-20 (FF) tests and the intermediate strain-hold tests (I1-0, 0-I 1) will offer little (or similar) conditions for stress corrosion. Other tests—namely 0.05–0.05 (SS), 1-min hold, 10-min hold, etc.—will offer more time for stress corrosion at the peak values of the stress and strain. Thus the first three fall into one category and the others fall under a category where corrosion is more severe than in the first. The raw data reported in Ref 17 were analyzed based on this premise, with the corrosion factor $C_f = 1$ for the first category and $C_f = 2.5$ for the other cases; correlations were made between tensile work $\delta W_t (= \sigma_t \delta \epsilon_{\text{total}})$ and N_f . The results are shown in Fig. 11. For the first three tests the correlation is very good, with a scatter band of only ± 1.4 . The correlation in the second category can be said to be good because the scatter band is within the recognized limits of ± 2 . Even this scatter may be because a common C_f -factor of 2.5 is taken for all the cases. René 95 alloy is a typical example where stress corrosion plays a dominant role at 650°C, creep damage is rather negligible, and the model presented and discussed here can be successfully applied.

Concluding Remarks

If fatigue resistance of different materials are compared on the basis of the inelastic strain range, higher strength materials will exhibit lower strength. On the other hand, if results are plotted in terms of the saturation stress range, then the higher strength materials will exhibit better fatigue behavior. In order to combine the influence of both stress and strain, the energy parameter combining both stress and strain ranges will be best.

In the analysis presented, the total energy is partitioned into elastic, plastic, and creep. The macroscopic elastic strain energy is also taken into consideration, since it will also aid the accumulation of damage at the crack front. For the calculation only the tensile portion is considered, as damage accumulation normally occurs only during tensile excursion. Compressive stresses will try to close the crack. Even in normal fatigue crack propagation analysis, the crack closure effect has been recognized and the effective stress intensity factor is used to describe the crack growth rate. In the partitioned strain energy, the plastic strain energy refers to fast-fast balanced cycling. The hold time and frequency influence will be taken care of by the energy term associated with creep effect. If the creep effect is negligible and stress corrosion effect is more pronounced, then the corrosion factor C_f can be introduced to evaluate the failure life.

In all these cases, if the hysteresis loop is available for any particular type of loading, then these energy quantities can be directly computed. The effect

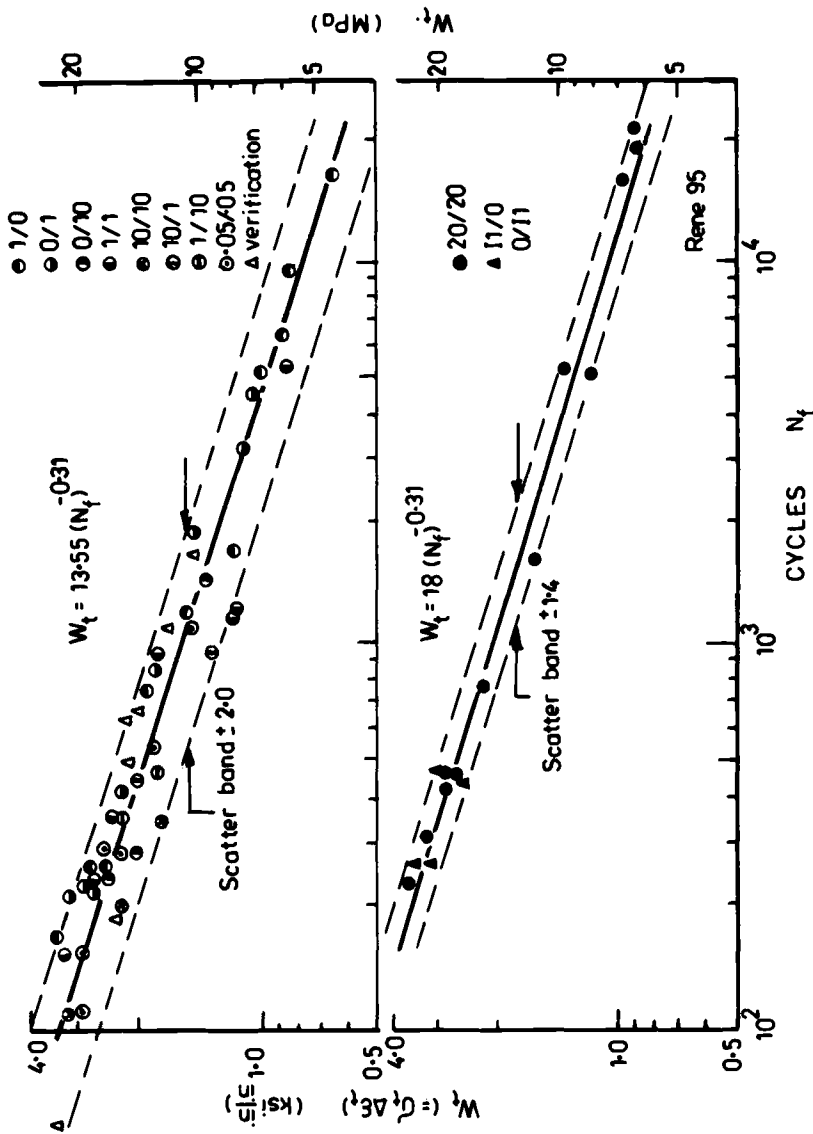


FIG. 11—Relation between δW_f and N_f for René 95 alloy under different hold conditions at 650°C. Data from Ref 17.

of hold either in tension or compression will introduce a mean stress which will alter the value of σ_t . Though FS cycling may be similar to FF cycling, the former will increase σ_t in addition to increasing the value of the total strain range. In that respect FS may be more damaging than FF cycling.

In the analysis, the slope of da/dN versus δJ is given by the exponent $(1 + m)$ on the log-log plot. With increasing temperature, the value of m will decrease. A similar tendency has been observed by Huang and Pelloux [19]. The slope of δW_t versus N_t on the log-log plot is likely to increase with increase in temperature. This is observed in the case of MAR M002 alloy. At low temperatures when the creep effect is negligible, the interrelation between the exponents of da/dN versus δJ and δW versus N_t is discussed in Ref 34. At high temperatures with different combinations of loading conditions, experimental data to examine the behavior of da/dN versus δJ and δW_t vs N_t for a particular material are rather limited. The analysis carried out with the available data, however, shows that the total tensile energy may prove to be a useful parameter to predict the fracture life in creep-fatigue condition. This parameter appears to be more attractive, as computation of the total tensile energy will be easier once the hysteresis loop for any particular loading is available.

Acknowledgments

Sincere thanks are due Prof. Dr. A. J. McEvily for his constant support and encouragement. The financial support by the Air Force Office of Scientific Research (Contract No. F49620-79-C-004) is gratefully acknowledged.

References

- [1] Chaboche, J. L., Policella, H., and Kaczmarek, H. in *Advisory Group for Aerospace Research and Development (AGARD) Conference Proceedings*, No. 243, 1978, p. 4.1.
- [2] Ostergren, W. J. and Krempl, E., "A Linear Uniaxial Damage Accumulation Law for Creep-Fatigue Interaction," ASME Paper 78-PVP-63, American Society of Mechanical Engineers, 1978.
- [3] Manson, S. S., Halford, G. R., and Hirschberg, M. H. in *Symposium Design for Elevated Temperature Environment*, American Society of Mechanical Engineers, 1971, p. 12.
- [4] Manson, S. S. in *Fatigue at Elevated Temperature*, ASTM STP 520, American Society for Testing and Materials, 1973, pp. 744-774.
- [5] Coffin, L. F., Jr., in *Fatigue at Elevated Temperature*, ASTM STP 520, American Society for Testing and Materials, 1973, pp. 5-36.
- [6] Coffin, L. F., Jr., in *Proceedings*, Institute of Mechanical Engineers, Vol. 188, 1974, p. 109.
- [7] Campbell, R. D., *Journal of Engineering Industry, Transactions of ASME*, Vol. 93, 1971, p. 887.
- [8] Janson, Jan, *Engineering Fracture Mechanics*, Vol. 11, 1979, p. 397.
- [9] Majumdar, S. and Maiya, P. S., *Journal of Engineering Materials and Technology, Transactions of ASME*, Vol. 102, 1980, p. 159.
- [10] *Characterization of High-Temperature Low-Cycle Fatigue by SRP Method*, AGARD Conference Proceedings, No. 243, 1978.
- [11] Halford, G. R. and Nactigall, A. J., "The Strain Range Partitioning Behaviour of an Advanced Gas Turbine Disc Alloy AF2-IDA," presented at AIAA/SAE/ASME 15th Joint Propulsion Conference, Las Vegas, June 1979.

- [12] Brinkman, C. R., Strizak, J. P., and Booker, M. K. in *AGARD Conference Proceedings*, No. 243, 1978, p. 15.1.
- [13] Ostergren, W. J. in *Proceedings*, ASME-MPC Symposium on Creep-Fatigue Interaction, MPC-3, Dec. 1976, p. 179.
- [14] Shahani, V. and Popp, H. G. "Evaluation of Cyclic Behaviour of Aircraft Turbine Disc Alloys," NASA-CR-159433, June 1978.
- [15] Leis, B. N., *Journal of Pressure Vessel Technology, Transactions of ASME*, Vol. 98, 1977, p. 524.
- [16] Fong, J. T., *Journal of Pressure Vessel Technology, Transactions of ASME*, Vol. 96, 1975, p. 214.
- [17] Bernstein, H., "An Evaluation of Four Models to Predict the Creep-Fatigue Interaction in René 95," Technical Report AFML-TR-79-4075, June 1979.
- [18] Taira, S., Ohtani, R., and Komatsu, T., *Journal of Engineering Materials and Technology, Transactions of ASME*, Vol. 101, 1979, p. 162.
- [19] Huang, J. S. and Pelloux, R. M., *Metallurgical Transactions*, Vol. 11A, 1980, p. 899.
- [20] Neuber, H., *Journal of Applied Mechanics, Transactions of ASME*, Vol. 28, 1961, p. 544.
- [21] Gowda, C. V. B., Topper, T. H., and Leis, B. N. in *Proceedings*, International Conference on Mechanical Behaviour of Materials, Vol. II, 1971, p. 187.
- [22] Shih, C. F. and Hutchinson, J. W., *Journal of Engineering Materials and Technology, Transactions of ASME*, Vol. 98, 1976, p. 289.
- [23] Kaisand, L. R. and Mowbray, D. F., *Journal of Testing and Evaluation*, Vol. 7, No. 5, 1979, p. 270.
- [24] Jeglic, F., Niessen, P., and Burns, D. J. in *Fatigue at Elevated Temperatures, ASTM STP 520*, American Society for Testing and Materials, 1973, pp. 139-147.
- [25] Hoffelner, W. and Speidel, M. O. in *Proceedings*, International Conference on High Temperature Alloys in Aggressive Environments, The Netherlands, Oct. 1979.
- [26] Coffin, L. F., Jr., "Time Dependent Fatigue of Structural Alloys," ORNL Report No. 5073, Oakridge National Laboratory, Tenn., June 1977, p. 37.
- [27] Coffin, L. F., Jr., in *Proceedings*, ASME-MPC Symposium on Creep-Fatigue Interaction, MPC-3, Dec. 1976, p. 349.
- [28] Ostergren, W. J., *Journal of Testing and Evaluation*, Vol. 4, 1976, p. 327.
- [29] Tomkins, B. and Wareing, J., *Metal Science Journal*, Vol. 11, 1977, p. 414.
- [30] Perry, A. J., *Journal of Materials Science*, Vol. 9, 1974, p. 1016.
- [31] Taraneshi, H. and McEvily, A. J., "On Fatigue Crack Initiation and Propagation at Elevated Temperature," presented at International Conference on Fracture-5, France, April 1978.
- [32] Cowles, B. A., Sims, D. L., and Warren, J. R., "Evaluation of the Cyclic Behaviour of Aircraft Turbine Disc Alloys," NASA CR-159409, Oct. 1978.
- [33] Antunes, V. T. A. and Hancock, P. in *AGARD Conference Proceedings*, No. 243, 1978, p. 5.5.
- [34] Radhakrishnan, V. M., *Fatigue of Engineering Materials and Structures*, Vol. 3, No. 1, 1980, p. 75.

M. Mottot,¹ P. Pétrequin,¹ C. Amzallag,² P. Rabbe,²
J. Grattier,³ and S. Masson³

Behavior in Fatigue-Relaxation of a High-Creep Resistant Type 316L Stainless Steel

REFERENCE: Mottot, M., Pétrequin, P., Amzallag, C., Rabbe, P., Grattier, J., and Masson, S., "Behavior in Fatigue-Relaxation of High-Creep Resistant Type 316L Stainless Steel," *Low-Cycle Fatigue and Life Prediction, ASTM STP 770*, C. Amzallag, B. N. Leis, and P. Rabbe, Eds., American Society for Testing and Materials, 1982, pp. 152-168.

ABSTRACT: In order to predict long-term behavior of a high-creep resistant low-carbon Type 316L stainless steel under low-cycle fatigue with long hold times, a series of tests of fatigue relaxation was undertaken at 550, 600, 650, and 700°C for medium strain ranges ($\Delta\epsilon_t = 0.7, 1.2$, and 1.6 percent). Hold times up to 5 h were introduced at the maximum tensile strain. It has been shown that a reduction of fatigue life occurred, generally associated with intergranular cracking when hold times increased. A maximal effect was observed at 600°C.

Different methods for extrapolating results for very long hold times, such as those encountered on fast breeder reactor components (~ 1000 h) were proposed. These methods were based on a time-temperature equivalence comparable to those used for extrapolating creep rupture data. A correlation between reduction of fatigue life with the amount of stress relaxation during hold times was also used. Predictions by these methods are compared with ASME N47 fatigue design curves.

KEY WORDS: creep fatigue interaction, Type 316 stainless steel, high temperature design, stress relaxation

Nomenclature

- A Coefficient in primary creep equation
- B Coefficient in creep rupture equation, MPa
- C Coefficient in secondary creep rate equation, MPa
- C_e, C_p Coefficients in fatigue life equations
- F_R Fatigue life reduction factor
- K' Strain-hardening coefficient

¹ Commissariat à l'Energie Atomique, Division de Metallurgie et d'Etudes des Combustibles Nucléaires, Saclay, France.

² Creusot Loire, Centre de Recherches d'Unieux, Firminy, France.

³ Electricité de France, Centre de Recherches des Renardières, Moret Sur Loing, France.

m, p	Exponents in fatigue life equations
n	Exponent in creep rupture equation
n'	Cyclic strain-hardening exponent
N_d	Design fatigue life
$N_{F,0}$	Number of cycles to failure in continuous cycling
$N_{F,TH}$	Number of cycles to failure with tensile hold times
$\frac{N_{F,TH}}{N_{F,0}}$	Linear fatigue damage
P	Time-temperature equivalence parameter
q	Stress exponent in primary creep equation
q'	Stress exponent in secondary creep equation
r	Time exponent in primary creep equation
T	Temperature, °C
T_H	Length of hold time, min
t	Time, h
t_R	Time to rupture, h
ϵ	Strain, m/m
$\dot{\epsilon}$	Strain rate, m/m/s
$\Delta\epsilon_e$	Elastic strain range, %
$\Delta\epsilon_t$	Total strain range, %
$\Delta\epsilon_p$	Plastic strain range, %
σ	Stress, MPa
σ_a	Stress amplitude, MPa
σ_{tmax}	Tensile stabilized stress in continuous cycling or at the beginning of hold time, MPa
σ_{tmin}	Tensile stress amplitude at the end of a hold time, MPa
$\frac{\sigma_{tmin}}{\sigma_{tmax}}$	Relative relaxed stress
$\frac{\sigma_{tmax} - \sigma_{tmin}}{\sigma_{tmax}}$	Relative amount of stress relaxation

The problem of creep-fatigue interaction on austenitic stainless steels has received considerable attention during the past decade [1-5].⁴ In particular, with the development of liquid-metal fast breeder reactors (LMFBRs), the need to know the consequences of creep-fatigue interaction has been accentuated. Effectively, several components of LMFBRs are subjected to creep and fatigue loadings; creep loading occurs during normal operation and fatigue loading occurs during startup and arrest transients.

In order to evaluate possible component life reductions resulting from creep-fatigue interaction, usually low-cycle fatigue tests are carried out with hold times. For austenitic stainless steels, these hold times are more detri-

⁴The italic numbers in brackets refer to the list of references appended to this paper.

mental when they are introduced in the tensile part of the fatigue cycle. However, to avoid excessive experimental times these tests are generally conducted at relatively high strains (0.5 to 2 percent) and short hold times (less than 48 h). When compared with the strain ranges and hold times encountered in actual service (less than 0.3 percent and about 1000 h) the results imply that a considerable degree of extrapolation is needed for the prediction of the long-term behavior of the materials.

The present work on a Type 316L stainless steel that is used for fast breeder reactor components is a cooperative effort among three laboratories involved in fast breeder reactor development in France. The purpose is to generate data and to propose extrapolation methods for establishing design curves for creep-fatigue interaction.

Material

The steel studied in this work is a Type 316L stainless steel used for nuclear applications [6]. It is characterized by a relatively high nitrogen content and good tensile and creep properties which are very close to those of conventional Type 316 stainless steel [7]. Only one cast was used throughout the experiments; its composition is given in Table 1.

The test material was received in the form of a 30-mm-thick plate that had been twice annealed at 1070°C and water quenched. It had an austenitic microstructure with some ferrite stringers (less than 0.5 percent) and an ASTM grain size number of 4 to 6. All test specimens were machined in the longitudinal direction.

Testing Procedures

The mechanical properties of the material were fully determined by tension, creep, low-cycle fatigue, and low-cycle fatigue with hold time tests. In this paper only low-cycle fatigue tests, with and without hold times, are reported in detail.

Creep tests were conducted at 550, 600, 650, and 700°C. From these tests average creep deformation and creep rupture properties were determined.

Low-cycle fatigue tests were conducted in air on push-pull strain-controlled machines at $R\epsilon = -1$ with axial extensometry and resistance furnace heating in all three laboratories. Particular attention was given to axial alignment of specimens and clamping devices (misalignment less than 0.03 mm). Specimens were cylindrical type and measured 8 to 10 mm in gage length and 38 to 64 mm² in cross section. They were all finished by fine turning to a roughness average value of 0.8 μm .

Axial strains were measured by attaching extensometers either directly on the calibrated cylindrical part of the specimens or on the shoulders of the specimens. In the latter case, which was generally adopted for avoiding rupture under the extensometer knives, a calibration factor, as determined experi-

TABLE 1—*Chemical composition.*

C	S	P	Si	Mn	Ni	Cr	Mo	N	B	Co	Cu	Ti	Nb
0.023	0.006	0.029	0.40	1.70	12.12	17.44	2.45	0.076	0.003	0.23	0.17	<0.01	<0.01

mentally and by computation at each temperature, was used to calculate the actual strain range applied to the gage length. Round-robin tests were successfully conducted to check the validity of testing procedures in the three laboratories.

Low-cycle fatigue tests were performed at 20, 450, 550, 600, 650, and 700°C using constant strain rates of 1.5 to $4 \times 10^{-3} \text{ s}^{-1}$, depending on the laboratory, and strain ranges between 0.4 and 3 percent. Tests with hold times in the tensile part of the cycle were conducted at 550, 600, 650, and 700°C with strain ranges of 0.7, 1.2, and 1.6 percent and hold times of 1, 3, 10, 30, 90, and 300 min.

The number of cycles to failure, N_F , was defined as the number of cycles leading to a reduction of the maximum load by 25 percent. The symbols used for analyzing results are given in the section on Nomenclature.

Results

Creep Results

Primary creep was described by

$$\epsilon = A\sigma^q t^r \quad (1)$$

secondary creep rate by

$$\dot{\epsilon} = \left(\frac{\sigma}{C} \right)^{q'} \quad (2)$$

and creep rupture by

$$t_R = \left(\frac{\sigma}{B} \right)^n \quad (3)$$

These equations were fitted to experimental data points using the least squares method at the different temperatures. Creep rupture strengths obtained were close to the average creep strength of Type 316 stainless steel [6].

TABLE 2—Average creep properties of Type 316L stainless steel.

T, °C	Primary Creep Equation $\epsilon = A\sigma^q t^r$			Secondary Creep Rate Equation $\dot{\epsilon} = \left(\frac{\sigma}{C} \right)^{q'}$		Creep Rupture Equation $t_R = \left(\frac{\sigma}{B} \right)^n$	
	A	q	r	C	q'	B	n
550	1.45×10^{-13}	3.87	0.403	1011	10.15	665	-12
600	5.69×10^{-14}	4.31	0.467	663	10.15	537	-10
650	2.60×10^{-14}	4.75	0.570	449	9.2	465	-7.5
700	1.33×10^{-14}	5.19	0.713	309	8.5	386	-6

The results of the creep experiments are summarized in Table 2.

Low-Cycle Fatigue Results

Fatigue resistance and cyclic-hardening stress-strain curves were determined using the usual relationships

$$\Delta\epsilon_t = C_e N^{-p} + C_p N^{-m} \quad (4)$$

and

$$\sigma_a = K' \left(\frac{\Delta\epsilon_p}{2} \right)^{n'} \quad (5)$$

Results are summarized in Table 3.

Creep-Fatigue Results

Low-cycle fatigue tests with hold time were performed at 550, 600, 650, and 700°C; this paper concentrates on those at 550 and 600°C because they were more numerous.

Effect of Hold Time on Cyclic Stress-Strain Curve—Significant cyclic hardening occurred in continuous cycling. It remained important when hold times were introduced, but at 600°C a slight decrease in hardening occurred with increase in hold time over 10 min (Fig. 1). Similar behavior had been observed by Rezgui [8] on Type 316L stainless steel. This effect was more complicated at 550°C, since a supplementary hardening appeared for short hold times, but for hold times greater than 30 min a decrease in hardening finally occurred. This behavior is illustrated in Fig. 2, where stresses in tests with hold time normalized to stresses in continuous cycling are plotted against hold time duration.

Effect of Hold Time on Fatigue Resistance—Introduction of hold time in tension reduced fatigue life at 600, 650, and 700°C. At 550°C a transitory increase in fatigue resistance occurred for short hold times. For longer hold

TABLE 3—Average continuous fatigue properties of Type 316L stainless steel.

T, °C	Cyclic Stress-Strain Curve		Fatigue Life Curve			
	$\sigma_a = K' \left(\frac{\Delta\epsilon_p}{2} \right)^{n'}$		$\Delta\epsilon_t = (C_e \times N_F^{-p}) + (C_p \times N_F^{-m})$			
	K'	n'	C _e	p	C _p	m
550	462	0.340	1.33	0.16	17.14	0.47
600	469	0.332	1.20	0.14	8.22	0.37
650	394	0.218	1.00	0.12	21.83	0.51
700	363	0.225	1.07	0.14	20.57	0.52

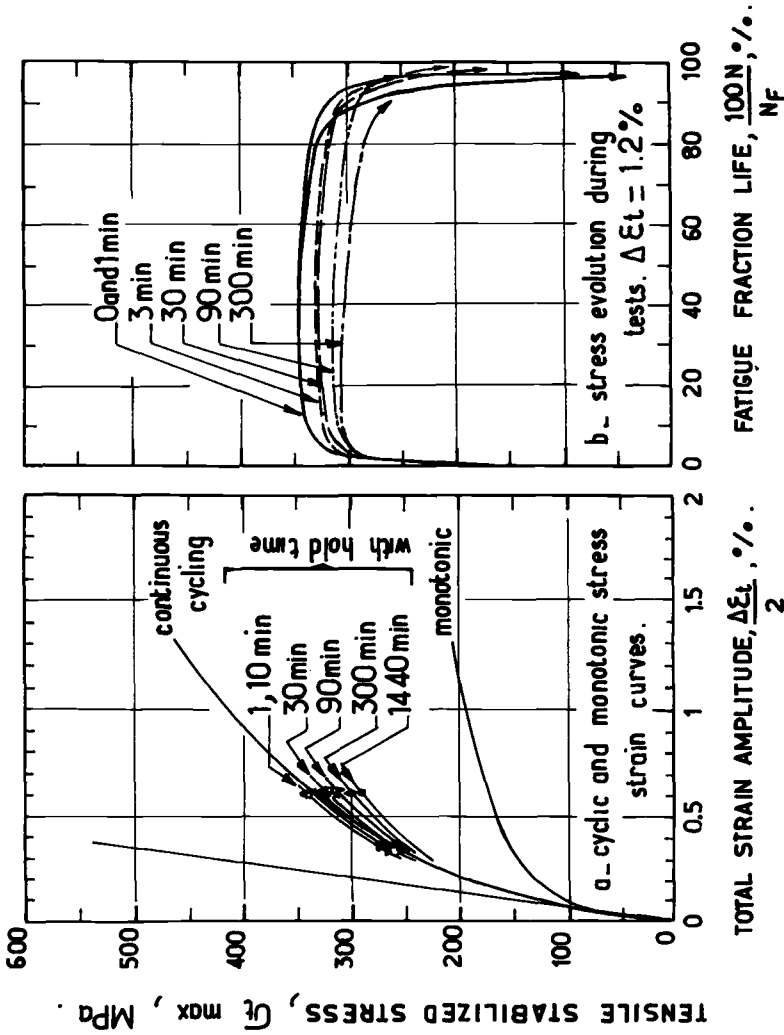


FIG. 1—Effect of hold time on cyclic hardening of Type 316L stainless steel at 600°C.

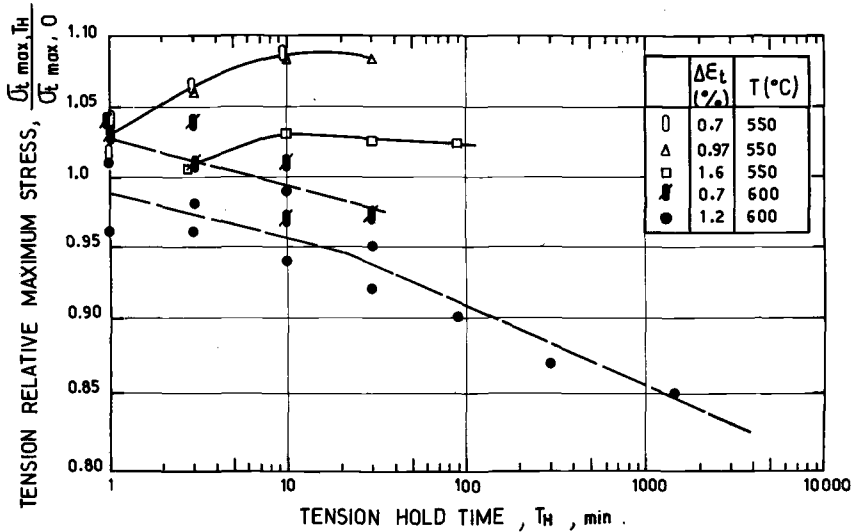


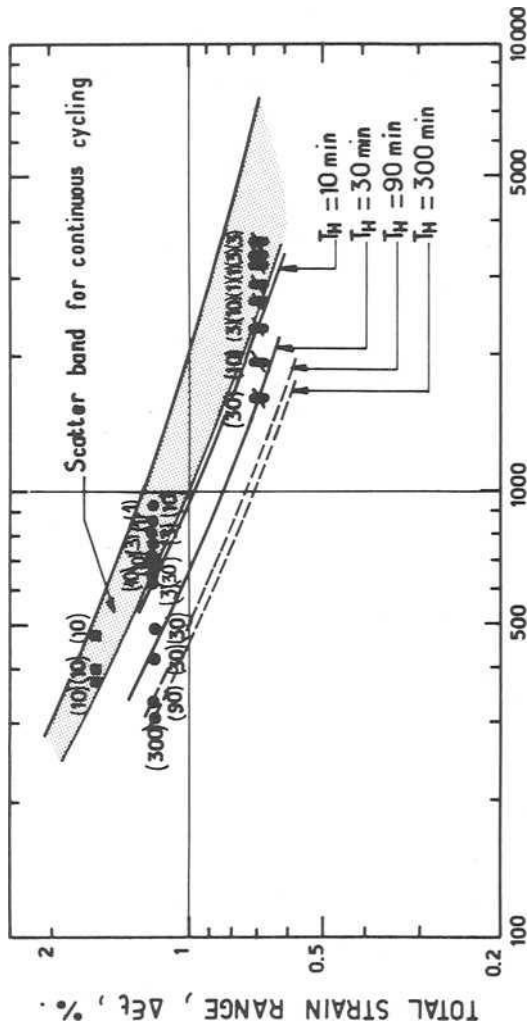
FIG. 2—Effect of hold time on maximum tensile stress of Type 316L stainless steel at 550 and 600°C.

times (longer than 30 min), the general trend of decreasing fatigue life when increasing hold time also occurred at 550°C.

Figure 3 illustrates the steel behavior at 600°C. It can be seen that, owing to scatter in results, the reduction in fatigue life becomes important and noticeable only for hold times greater than 10 min.

In order to summarize the results, a reduction factor F_R , defined as the ratio of fatigue life with hold time to fatigue life without hold time, was introduced. Figure 4 plots this reduction factor F_R against hold time T_H for different temperatures. The decrease in F_R is quicker at high temperatures (650 to 700°C) for short hold times, but seems to be lesser than that at 550°C and 600°C for longer hold times. It can be noticed that only at 600°C is the relationship between F_R and T_H not strain range dependent. A further point is that the F_R versus T_H plot is quasi-linear for long T_H -values on the log-log diagram; the slopes of these linear relationships are close together at 550 and 600°C and decrease in absolute value at 700°C. At 600°C there is no significant increase of F_R between 90 and 300 min of hold time, but results are too scarce to allow us to predict a hold time saturation effect.

Effect of Hold Time on Fracture Appearance—After testing, the fracture surfaces of all specimens were examined using scanning electron microscopy. It appeared that at 550 and 600°C, where reduction of fatigue life occurred, the rupture was mainly intergranular. Similar behavior is described in Ref 9. At 650 and 700°C the rupture was essentially transgranular, which indicates that, for the steel tested here, a change in damage mechanism under creep fatigue condition occurs at and above 650°C. This is the main reason why only results at temperatures below 650°C are discussed in this paper.



FATIGUE LIFE, N_f , cycles.

FIG. 3—Effect of tension hold time on fatigue life of Type 316L stainless steel at 600°C.

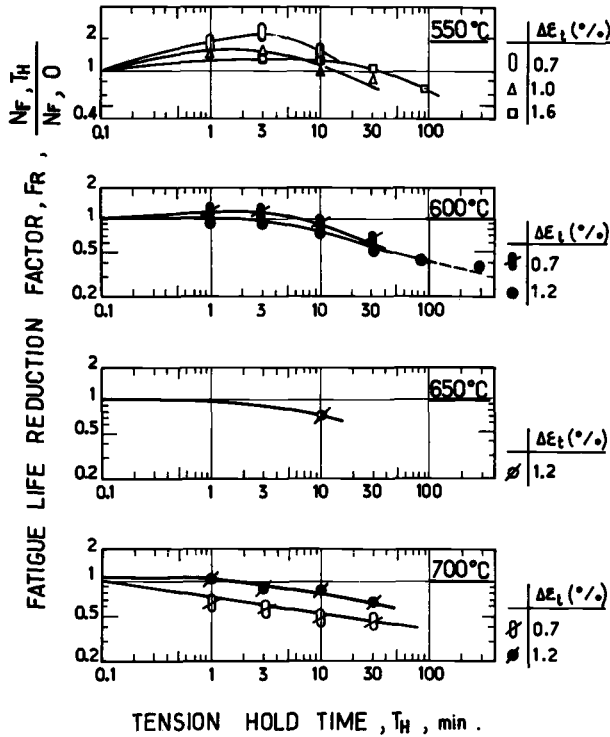


FIG. 4—Effect of tension hold time on fatigue life of Type 316L stainless steel at different temperatures.

Stress Relaxation Behavior

During hold time, stress relaxation occurs. For a given test, the amount of stress relaxation is practically constant. At the beginning, during cyclic hardening, a slight increase in stress relaxation occurs. During the central part of the test, where maximum stress remains constant, the amount of stress relaxation does not vary. The amount of stress relaxation increases with increasing hold time and strain range. These results are in good agreement with those given by Conway et al [10]. In order to account for the change in cyclic hardening due to hold times, stress during relaxation was normalized to tensile stabilized stress, σ_{tmax} , and a relationship between normalized stress and time was obtained.

As creep strains during stress relaxation are always less than 0.3 percent, primary creep laws were used since, for this steel, the onset of secondary creep is always at strains greater than 0.5 percent. From creep data, stress relaxation curves for different tests were calculated in the following manner. During stress relaxation, elastic strains are transformed in creep strains and stress decreases following

$$\frac{d\sigma}{dt} = -E \frac{d\epsilon}{dt} \quad (6)$$

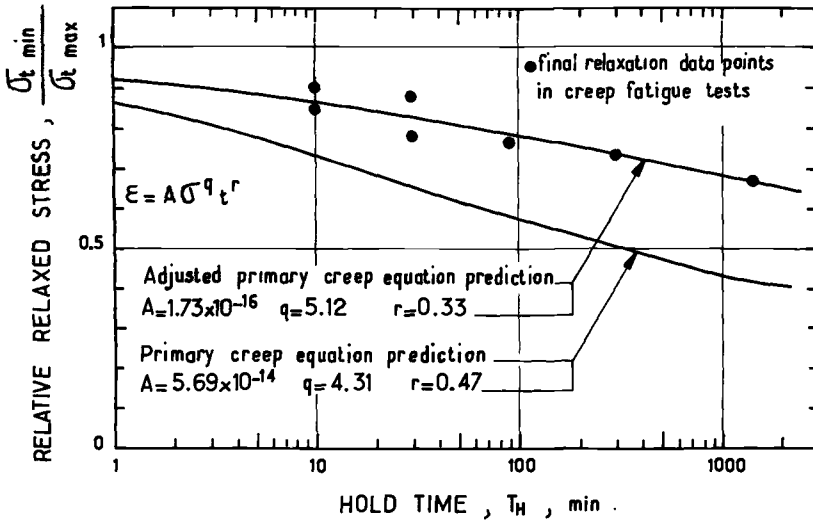


FIG. 5—Prediction of cyclic stress relaxation from primary creep equation for Type 316L stainless steel at 600°C.

From the primary creep equation (1), we have

$$\frac{d\epsilon}{dt} = A\sigma^q t^{r-1} \quad (7)$$

From Eqs 1, 6, and 7, eliminating ϵ for time-hardening rule or t for strain-hardening rule, relaxation curves can be numerically calculated. Figure 5 shows that stress relaxation computed by this method is significantly greater than actual stress relaxation. Corrected coefficients for primary creep equation were determined to describe more accurately cyclic stress relaxation. Corrected coefficients are given in Fig. 5; only results with time-hardening rule are presented, since they gave the best agreement between calculated and experimental data. It can also be shown that the use of normalized stress leads to a good description of stress relaxation for a given strain range, eliminating initial stress variations due to different lengths of hold time, since all the final normalized relaxed stresses for different hold times are practically on the same curve.

Linear Damage Cumulation

Linear damages were calculated for the different tests at 550 and 600°C in the following manner. Fatigue damage is evaluated by

$$\sum \frac{1}{N_F} = \frac{N_{F,TH}}{N_{F,0}} = F_R$$

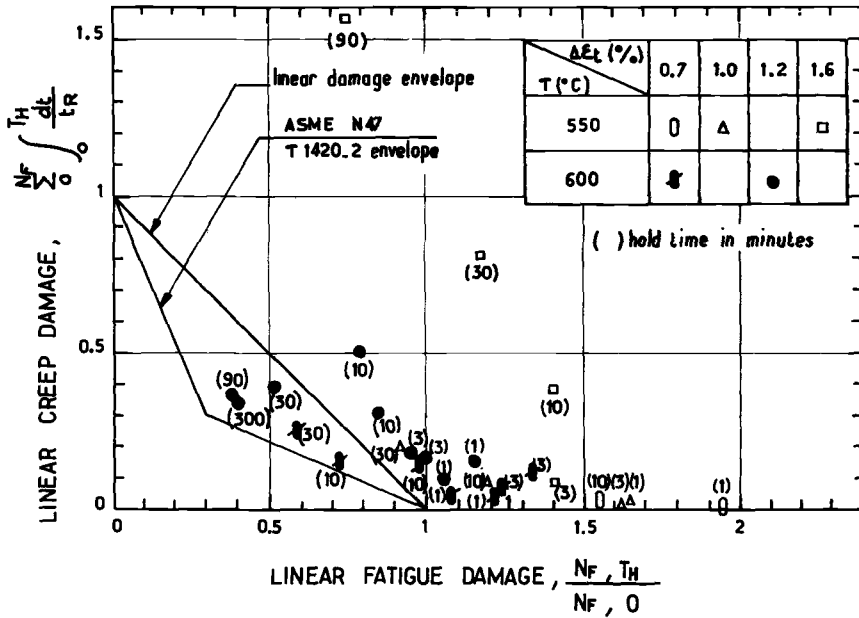


FIG. 6—Creep-fatigue linear damage diagram of Type 316L stainless steel at 550 and 600°C.

and creep damage is given by

$$\sum \frac{t}{t_R} = \sum_{i=1}^{N_f} \int_0^{T_H} \frac{dt}{t_R} \approx N_f \int_{\sigma_{\max}}^{\sigma_{\min}} \frac{dt}{t_R(\sigma)}$$

where t_R is given by Eq 3, σ_{\max} is obtained from the cyclic-hardening curve (Eq 5), and numerical integration along the stress relaxation curve is calculated as described previously. This method of computation of damage in creep fatigue interaction is compared with other methods in Ref 11. Results are given in Fig. 6. It appears that at 600°C total linear damage occasionally falls below the linear damage envelope, but is above the bilinear limit given by ASME N47 T1420-2 for austenitic stainless steels [12].

Discussion

The major problem in creep fatigue interaction evaluation for design purposes is how to extrapolate experimental results obtained with short hold times (less than 5 h) and relatively high strain ranges (greater than 0.7 percent) to practical situations with long hold times (1000 h) and low strain ranges (0.3 percent). The fatigue resistance curve at 600°C with 1000-h hold time was determined using three different methods: (1) direct extrapolation

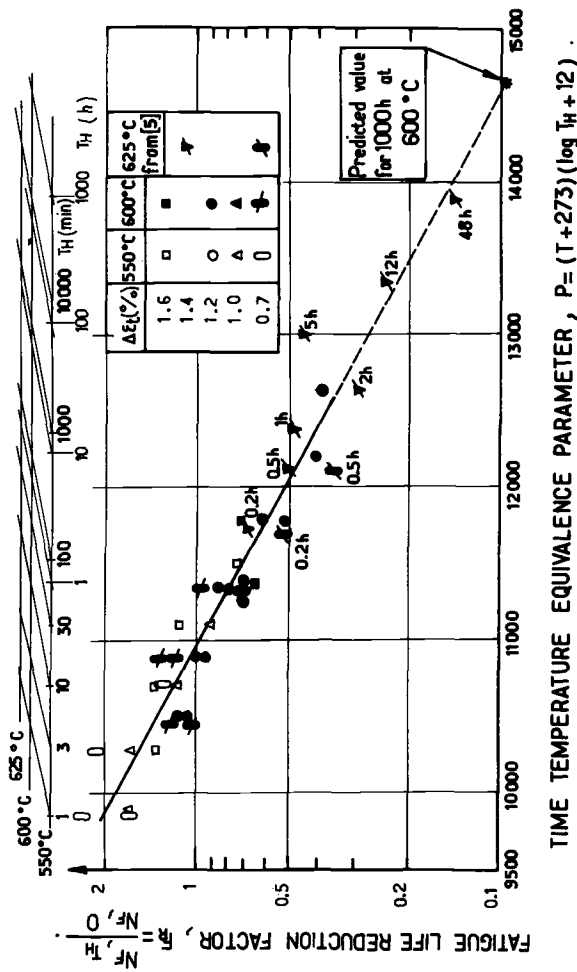


FIG. 7—Application of time-temperature equivalence for predicting fatigue life reduction factor of Type 316L stainless steel.

using time-temperature equivalence, (2) direct extrapolation using stress relaxation correlation, and (3) computation method using linear damage rule.

Direct Extrapolation Using Time-Temperature Equivalence

Figure 4 shows the relation between F_R and T_H in log-log scale at different temperatures. A time-temperature equivalence similar to the Larson-Miller parameter was employed for creep rupture data extrapolation, with longer time being replaced by higher temperature. As stated earlier, owing to the change in damage mechanisms, only results at 550 and 600°C in this study were employed. Some recently published data by Wood et al [5] obtained on a similar stainless steel were included for determining time-temperature equivalence. A parameter $P \approx (T + 273)(12 + \log T_H)$ was found efficient in describing the relation between F_R and P . This approach is given in Fig. 7. It is worthwhile noticing that in the aforementioned temperature range there is practically no effect of the strain range in this correlation.

Stress Relaxation Correlation

If we take into consideration that creep deformation and creep rupture characteristics are interrelated, it appears that a correlation must exist between creep damage and the amount of stress relaxation, creep damage increasing with the amount of stress relaxation. In Fig. 8, the correlation between the reduction factor F_R and the amount of stress relaxation during a cycle is shown as estimated lines drawn through data points. The formulation derived previously for calculating the amount of stress relaxation associated with a long hold time was used, and the reduction factor and the fatigue life were determined from the correlation. In Fig. 8, that approach appeared to be strain range dependent in the experimental field.

Linear Damage Method

From the experimental data described previously, it is possible, for a given strain range, to compute cyclic stress and fatigue life in continuous cycling, to determine the stress relaxation during hold time, and, from creep rupture properties, to evaluate total creep damage. Using the bilinear limit for total damage given by ASME N47 T1420-2, the life in fatigue can be determined. This approach was used to predict fatigue life including different hold times.

Table 4 gives results of life reduction by the three different approaches for 1000-h hold time at 600°C. Good agreement between the three methods is reached for higher strain range (1.2 percent). But for lower strain ranges, the stress relaxation correlation and the linear damage method predict an increase in life reduction that is not given by the time-temperature equivalence approach which is strain range independent. It appears that the evaluation of the effect of strain range for estimating fatigue life reduction in creep-fatigue tests is an essential point which needs further study.

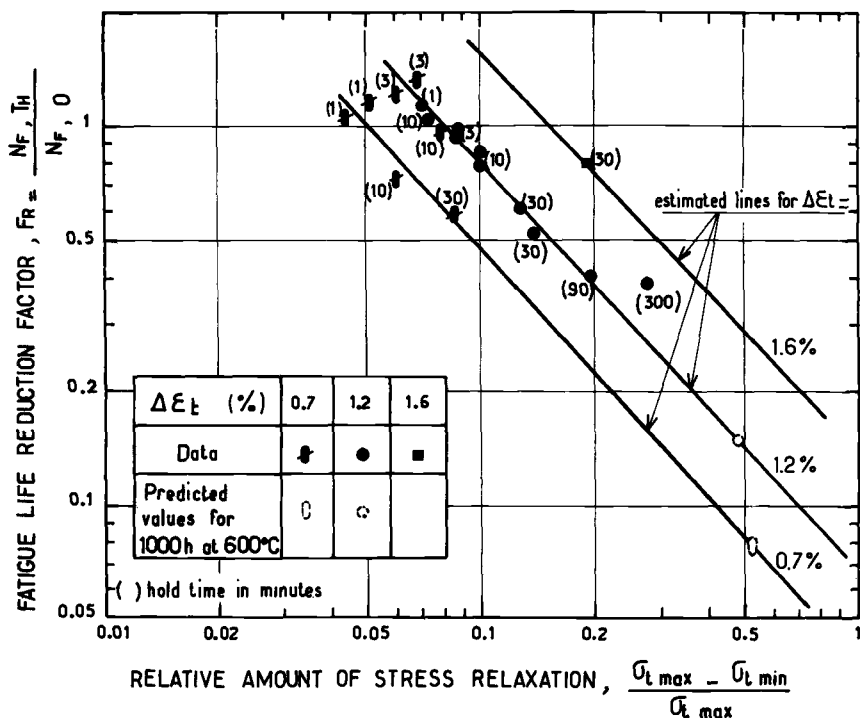


FIG. 8—Application of stress relaxation correlation for predicting fatigue life reduction factor for Type 316L stainless steel at 600°C.

These approaches for predicting fatigue life under creep-fatigue loading were compared with the ASME N47 T1430 design curve. For this purpose, reduction factors were calculated by different methods and applied to mean fatigue resistance curves, and finally a dividing factor of 20 on number of cycles or of 2 on strain range was introduced. The results are given in Fig. 9. The linear damage method leads to the most detrimental effect of hold time and gave results comparable with the ASME N47 T1430 design curve but slightly less pessimistic. Results obtained by time-temperature equivalence were significantly less pessimistic owing to the fact that this method was strain range independent.

TABLE 4—Predicted fatigue life reduction factor by different methods for 1000 h at 600°C.

Prediction Method	Total Strain Range, %		
	1.2	0.7	0.2
Time-temperature equivalence	0.095	0.095	0.095
Stress relaxation correlation	0.15	0.08	...
Computation of creep damage	0.116	0.056	0.021

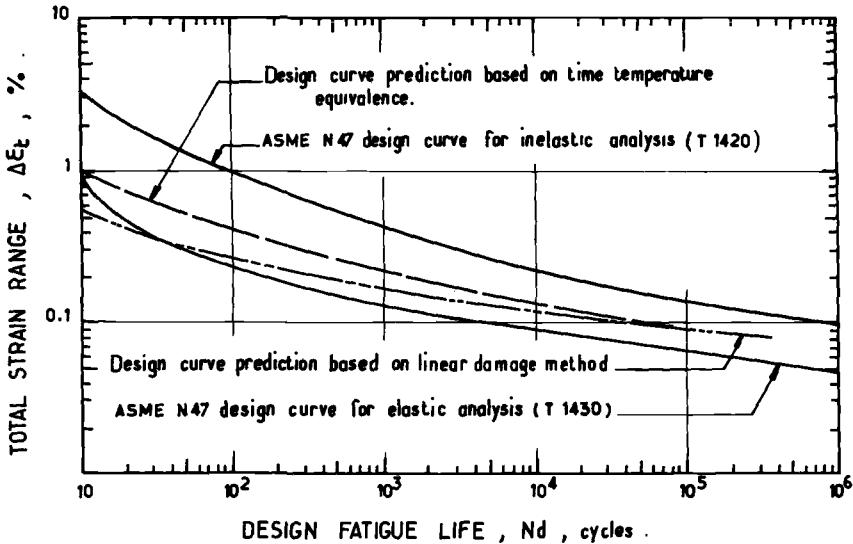


FIG. 9—Comparison of different prediction methods. Design fatigue lifes curves including hold time effects for Type 316L stainless steel at 600°C.

Conclusions

The following conclusions are drawn from this study of creep-fatigue interaction in a Type 316L stainless steel:

1. Creep fatigue interaction leads to a reduction in fatigue life at temperatures from 500 to 700°C.

2. Fatigue life reduction under creep-fatigue loading is associated with intergranular fracture below 650°C. At higher temperatures, fatigue life reduction also occurs, but is not associated to intergranular fracture.

3. At 600°C, life reduction was found independent of strain range in the experimental work.

4. A time-temperature equivalence using a parameter $P = (T + 273)(12 + \log T_H)$ can be used to correlate results at temperatures below 650°C. This parameter appeared to be strain range independent in the experimental field.

5. A correlation between reduction of life and amount of stress relaxation was established.

6. Computation of linear creep damage and stress relaxation correlation methods predicts a reduction of fatigue life with decreasing strain range. This does not occur for time-temperature equivalence.

7. The three different methods (time-temperature equivalence, amount of stress relaxation correlation, and linear damage method) used to predict fatigue life reduction for 1000-h hold time at 600°C were in good agreement for

strain range of ~ 1 percent. The number of cycles to rupture is in that case divided by 10 compared with continuous cyclic life.

8. Clarification of the effect of strain range on reduction of fatigue life in creep fatigue is needed.

9. It appeared that the ASME N47 T1430 design curve for elastic analysis at 600°C was conservative compared with extrapolations made by different methods.

Acknowledgments

This research was "Delegation générale à la Recherche Scientifique et Technique". The authors gratefully acknowledge Dr. A. A. Tavassoli for his help in writing the manuscript. Gratitude is also expressed to Mrs. N. Cortay, who prepared figures and drawings.

References

- [1] Berling, J. T. and Conway, J. B., *First International Conference on Pressure Vessel Technology*, Delft, 1969, p. 1233.
- [2] Brinkman, C. R., Korth, G. E., and Hobbins, R. R., *Nuclear Technology*, Vol. 16, Oct. 1972, p. 297.
- [3] Weeks, R. W., Pierks, D. R., and Cheng, C. F., "ANI Low-Cycle Fatigue Studies, Program, Results and Analysis," Argonne National Laboratory, ANL-8009, Nov. 1973.
- [4] Brinkman, C. R., Sikka, V. K., and King, R. T., *Nuclear Technology*, Vol. 33, April 1977, p. 76.
- [5] Wood, D. S., Wynn, J., Baldwin, A. B., and O'Riordan, P., "Some Creep Fatigue Properties of Type 316 Steel and Weld Metal at 625°C," UKAEA Report ND-R 418 (R), Nov. 1979.
- [6] Weisz, M., Berge, P., and Rabbe, P., *Matériaux et Techniques*, Sept.-Oct. 1977, p. 477.
- [7] RAMSES 40702, Caractéristiques et contraintes admissibles de l'acier, Z4 CND 18-12 CN (316 CN), First Edition, Commissariat à l'Energie Atomique, April 1978.
- [8] Rezgui, B., "Interaction fatigue fluage. Effet d'un temps de maintien sur la résistance à la fatigue d'un acier Z2 CND 17-13 (type 316L) à 600°C," Thesis, CEA Report, CEA-R-4982, Oct. 1979.
- [9] Levaillant, C., Rezgui, B., and Pineau, A. in *Mechanical Behavior of Materials*, ICM3, Vol. 2, Cambridge, Aug. 1979, p. 163.
- [10] Conway, J. B., Stentz, R. H., and Berling, J. T., "Fatigue, Tensile, and Relaxation Behaviour of Stainless Steels," TID-26135.
- [11] Weisz, M., Petrequin, P., Rezgui, B., and Tortel, J., "A Method of Evaluation of Creep-Fatigue Interaction for Elastic Analysis," to be presented at International Conference in Mechanical Behavior and Nuclear Applications of Stainless Steel at Elevated Temperatures (NETS), 20-22 May 1981, Varese, Italy.
- [12] *ASME Boiler and Pressure Vessel Code*, Case N-47-16 (1592-16), July 1979.

Assessment of High-Temperature Low-Cycle Fatigue Life of Austenitic Stainless Steels by Using Intergranular Damage as a Correlating Parameter

REFERENCE: Levaillant, C. and Pineau, A., "Assessment of High-Temperature Low-Cycle Fatigue Life of Austenitic Stainless Steels by Using Intergranular Damage as a Correlating Parameter," *Low-Cycle Fatigue and Life Prediction*, ASTM STP 770, C. Amzallag, B. N. Leis, and P. Rabbe, Eds., American Society for Testing and Materials, 1982, pp. 169-193.

ABSTRACT: Strain-controlled continuous fatigue and creep-fatigue experiments are reported for two types of 316 steel tested at 600°C (1112°F). It is shown that, although the continuous fatigue properties of the two materials are very similar, the one containing a controlled amount of nitrogen exhibits a better creep-fatigue resistance than the other alloy. Detailed measurements of intergranular damage made either on the fracture surfaces or in the bulk of creep-fatigue specimens indicate that the susceptibility of the materials to the effect of tensile hold times can be related to their propensity to intergranular cracking. A stress relaxation-propagation reduction factor per cycle correlation is proposed in order to account for the detrimental effect of tensile hold times on the fatigue life. This correlation relies upon experimental results on austenitic stainless steels published in the literature. It is shown that the proposed approach, derived largely from the quantitative measurement of intergranular damage, holds some promise for predictive purposes.

KEY WORDS: austenitic stainless steels, tensile hold low-cycle fatigue, intergranular damage measurements, crack propagation, life prediction

There are many experimental studies in the literature dealing with creep-fatigue properties of 304 and 316 type austenitic stainless steels (for example, [1-9]).² These studies were conducted in order to evaluate the fatigue resistance of these structural materials whose use is anticipated for the fabrication of sodium-cooled fast reactors.

It has been shown that for these stainless steels, hold periods at maximum tensile strain seriously reduce fatigue life while compressive hold periods or

¹ Centre des Matériaux, École Nationale Supérieure des Mines de Paris, France.

² The italic numbers in brackets refer to the list of references appended to this paper.

equal tension-compression hold times have little or less effect on endurance (for example, [1,5,10,11]). Most of these experiments were performed at strain ranges (≈ 0.5 to 2 percent) and at temperatures [$\approx 600^\circ\text{C}$ (1112°F)] which are higher than those anticipated in service. These experimental conditions are chosen in order to produce results in a reasonable length of time. At present there is no generally accepted method that can be used to extrapolate the short-term data to the service situation. This is a major area of concern.

To deal with this problem, several approaches such as the frequency-modified approach [12], the strain-range partitioning model [13], the Ostergren approach [14] and, in this conference, the time-temperature equivalence approach [9] have been proposed. These models are essentially phenomenological, and they give no insight into the fundamental aspects of the creep-fatigue mechanisms. Other models, more closely related to the creep-fatigue micromechanisms have also been proposed ([7,15,16]). Although the details of these models are very different from each other, they assume essentially that creep damage accelerates the fatigue crack growth rate. In this respect, it is rather surprising to note that, although it seems to be well accepted that the acceleration in crack growth rate originates from intergranular damage, very few experimental studies dealing with this important aspect of the problem have been reported.

The present study is an attempt to show that quantitative measurements of intergranular damage made on creep-fatigue specimens can be used to model creep-fatigue interactions. Towards this end, the present work is an extension of a preliminary study [17] performed on one of the materials, VIRGO steel, which is a Type 316 stainless steel. A number of short-term tests performed at 600°C (1112°F) on two types of austenitic stainless steels are reported, with emphasis placed on indicating how the results derived either from our study or from other studies published in the literature can be used to extrapolate short-term data.

Experimental Procedures

Two materials were investigated. Their composition and conventional tensile properties are given in Tables 1 and 2, respectively. VIRGO steel is essentially a 316 low-carbon steel, while ICL 167 steel is a 316 steel with a con-

TABLE 1—Chemical composition (weight percent).

	C	S	Si	Mn	Ni	Cr	Mo
VIRGO (316L)	0.033	0.022	0.44	1.55	13.6	16.4	2.12
ICL 167	0.021	0.007	0.41	1.74	12.3	17.2	2.40
	N	B	Co	Cu	P		
VIRGO (316L)	0.025	0.0012	0.18	0.07	0.022		
ICL 167	0.080	0.0032	0.21	0.15	0.030		

TABLE 2—Tensile properties at 600°C (1112°F).

	E , 10^3 MPa	0.2 percent Yield Stress, MPa	UTS, MPa	Elongation, %	Reduction of Area, %
VIRGO (316L)	144	116	377	49	74
ICL 167	144	159	404	41	67

trolled nitrogen content. The creep properties of these two materials have been extensively investigated [18,19]. These studies have shown that ICL 167 steel exhibits a better creep resistance than VIRGO steel.

All specimens were cut in the longitudinal direction of rolled plates, with a thickness of 15 mm for VIRGO steel and a thickness of 32 mm for ICL 167 steel. The materials were investigated in the as-received condition, which corresponds to an annealing treatment at 1110°C (2012°F) and water-quench for VIRGO steel, and a double-annealing treatment at 1070°C (1958°F) and water-quench for ICL 167 steel. In these materials, the grain size was about 50 μm , although ICL 167 steel contained a few larger grains (≈ 200 μm).

Low-Cycle Fatigue (LCF) Tests

All tests were run at 600°C (1112°F) using a servohydraulic machine in the axial strain control mode. Cylindrical specimens whose gage length was 12 mm and diameter was 8 mm were employed. These specimens were heated in a radiation furnace specially constructed for the experiments. Two types of tests were conducted [1]. Continuous cycling was performed with a triangular fully reversed wave shape ($\dot{\epsilon}_t = 4 \cdot 10^{-3} \text{ s}^{-1}$) [2]. Creep-fatigue tests were carried out by superimposing a tensile hold time at the maximum tensile strain corresponding to continuous cycling. The tests conducted on VIRGO steel were performed under constant plastic strain amplitude. This was achieved by periodic manual adjustment of the total strain. The tests performed on ICL 167 steel were conducted under constant total strain amplitude. The tests dealing with ICL 167 steel are part of a cooperative program between several laboratories including CEA, EDF, CLU and CDM.³ The LCF properties of VIRGO steel have already been partially reported [17]. This material has also been extensively investigated by Rezgui [20].

Metallography and Fractography

Optical microscopy observations were used to measure the percentage of cracked grain boundaries in specimens subjected to superimposed tensile hold times. This quantity, hereafter named "bulk damage", was defined as

³ CEA, Commissariat à l'Energie Atomique; EDF, Electricité de France, CLU, Laboratoire de Creusot-Loire (Unieux); CDM, Centre des Matériaux, École des Mines de Paris-Cooperative program "Groupe de Travail Matériaux".

the ratio between the length of damaged grain boundaries per unit of area on a section plane parallel to the specimen axis and the average length of grain boundaries per unit of area. The procedure used for these measurements is described elsewhere [17]. The fracture surfaces were examined using scanning electron microscopy (SEM).

Results

Mechanical Tests

The results of the LCF tests are given in Table 3. In this table we have included some of the results obtained by Rezgui [20] on VIRGO steel and some of the results obtained on ICL 167 in the cooperative program pre-

TABLE 3—LCF tests results at 600°C (1112°F).

NOTES: $\sigma_{t,max}$ = Maximum tensile stress.

$\sigma_R = \sigma_{t,max} - \sigma_{t,min}$.

$\sigma_{t,min}$ = Minimum tensile stress.

Material	Specimen	$\Delta\epsilon_t$, %	$\Delta\epsilon_p$, %	T_h , min	N_f , cycles	$\sigma_{t,max}$, MPa	σ_R , MPa
VIRGO 316L	54	2.48	1.96	0	348	376	0
	18	2.02	1.52	0	298	361	0
	17	1.68	1.20	0	434	342	0
	14	1.42	0.98	0	795	317	0
	19	1.00	0.60	0	1631	287	0
	20	0.74	0.40	0	3288	245	0
	R60 ^a	2.47	1.96	3	305	370	35
	56	2.46	1.96	10	146 ^a	358	52
	55	2.45	1.96	30	122	350	84
	57	2.31	1.86	200	66 ^a	324	113
	21	1.26	0.88	3	671	276	29
	22	1.23	0.88	10	410	249	34
	23	1.25	0.88	30	273	264	45
	58	1.51	1.14	100	125 ^a	268	75
ICL 167 SP	SP16	1.60	1.09	0	438	367	0
	SP15	1.60	1.10	0	498	363	0
	SP 6	1.20	0.73	0	704	340	0
	SP12	1.20	0.74	0	942	333	0
	SP 7	0.70	0.31	0	3312	269	0
	SP14	0.67	0.29	0	6170	256	0
	SP17	1.60	1.14	30	375	334	64
	SP 8	1.20	0.74	3	634	329	33
	SP11	1.20	0.75	10	944	324	35
	SP13	1.22	0.77	10	692	323	42
	SP10	1.20	0.78	30	651	300	39
	183 ^b	1.17	0.76	30	484	316	40
	187 ^b	1.18	0.76	30	413	324	43
	188 ^b	1.18	0.80	90	332	309	59

^aData from Rezgui [20].

^bData from Groupe de Travail Matériaux [9,21].

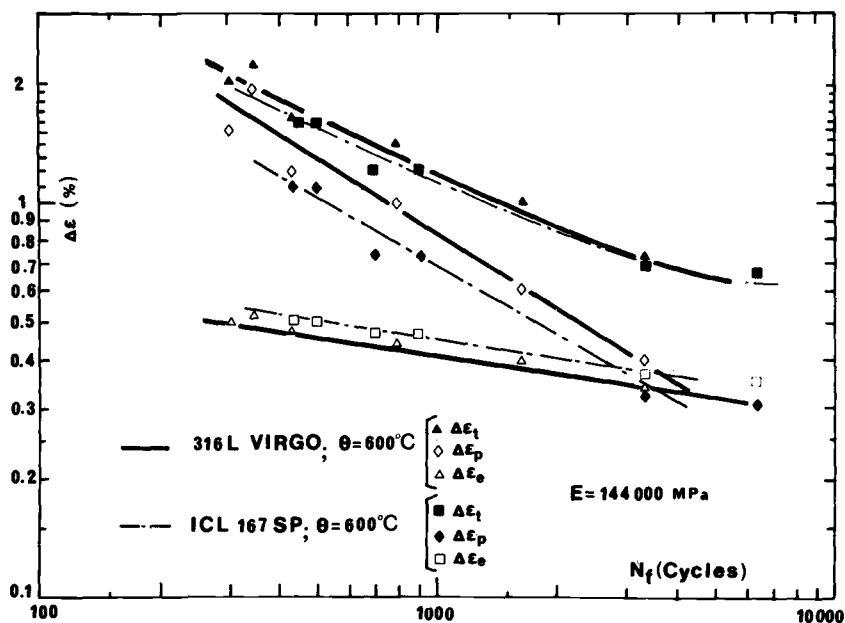


FIG. 1—Continuous cycling fatigue life versus strain range at 600°C (1112°F).

viously mentioned [9,21]. Figure 1 shows the variation of the number of cycles to failure, N_f , as a function of the applied strain range for continuous cycling fatigue tests. It is observed that within the range of fatigue lives investigated in this study, fatigue lives at a given total strain range are very similar for the two steels. ICL steel exhibits a lower endurance in terms of the plastic strain component, $\Delta\epsilon_p$, which is balanced by a higher strength leading to a higher elastic component, $\Delta\epsilon_e$.

Figure 2 summarizes the effect of tensile hold times on the fatigue life. In this figure, the test conditions were selected so that the two materials exhibited approximately the same fatigue life for continuous cycling. The results obtained on ICL steel are given in terms of the total strain range, $\Delta\epsilon_t$, while those obtained on VIRGO steel are reported in terms of the plastic strain range, $\Delta\epsilon_p$, since, as indicated previously, different testing procedures were used for the two materials. Table 3 gives the values of $\Delta\epsilon_t$ and $\Delta\epsilon_p$ for both materials. Figure 2 shows that at $\Delta\epsilon_t = 1.20$ percent, which corresponds to $\Delta\epsilon_p \approx 0.88$ percent, ICL steel exhibits a better resistance to the detrimental effect of tensile hold times on the fatigue life than VIRGO steel. At higher strain amplitude, the same behavior difference is observed.

Fractography

Continuous Fatigue—Scanning electron microscopy observations showed that fracture is transgranular in specimens tested under continuous fatigue.

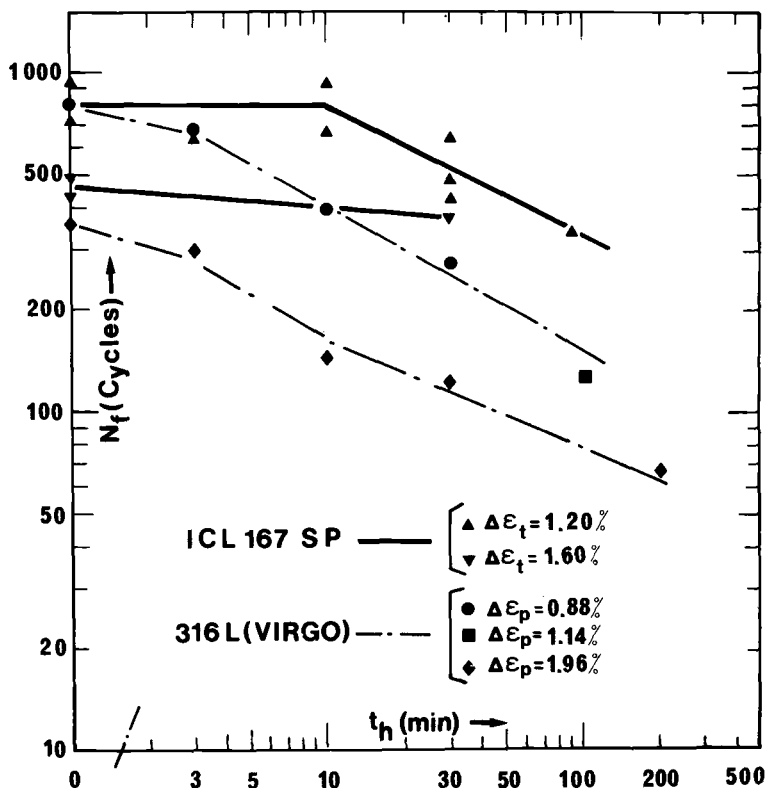


FIG. 2—Influence of tensile hold time on fatigue endurance at 600°C (1112°F).

In these specimens Stage I crack initiation occurs along crystallographic facets of about 20 μm depth. On these facets no striation could be observed. After this initiation stage fatigue striations are observed as illustrated in Fig. 3. Striation spacing was measured as a function of the crack length along the crack path in accordance with a procedure already used by other investigators [22,23,24]. Eleven specimens were examined (4 on VIRGO steel at 600°C, 3 on ICL steel at 600°C, 4 on ICL steel at 550°C). The details of the results are given elsewhere [17,25]. Here we shall only underline that the two alloys behave similarly when they are compared at the same plastic strain range. A recent study by Wareing and coworkers [26] has shown that at a temperature close to 600°C a one-to-one relationship exists between striation spacing and macroscopic crack growth rate. The striation spacing therefore can be used to derive an LCF crack propagation relation; this can be written as

$$\frac{da}{dN} = A (\Delta\epsilon_p)^{1.5} a^{1.45} \quad (1)$$

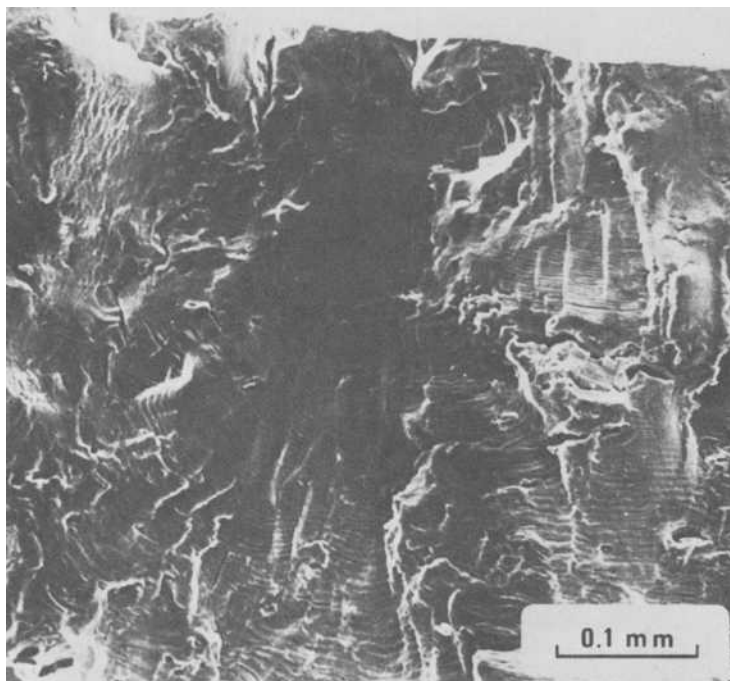


FIG. 3—Scanning electron microscopy; fracture surface of a continuous cycling fatigue specimen; VIRGO steel; Specimen 54; $\Delta\epsilon_p = 1.96$ percent; 600°C .

where

$$\begin{aligned} a &= \text{crack length in } \mu\text{m}, \\ da/dN &= \text{crack growth rate in } \mu\text{m/cycle}, \\ \Delta\epsilon_p &= \text{plastic strain range in percent, and} \\ A &= 7.07 \cdot 10^{-4}. \end{aligned}$$

This experimental relationship is valid for crack length larger than a critical value a_s , which is a decreasing function of the applied strain range, as shown schematically in Fig. 4. For crack length between $a_0 = 20 \mu\text{m}$, which corresponds to the end of Stage I cracking, and a_s , it was found that the striation spacing ($=da/dN$) was almost constant whatever the applied strain range. Thus, in this domain,

$$\frac{da}{dN} \approx 0.27 \mu\text{m/cycle for } a_0 < a < a_s. \quad (2)$$

These experimental crack propagation relationships result from the best fit of eleven da/dN versus a curves.

The number of cycles spent in crack propagation, N_p , can be calculated

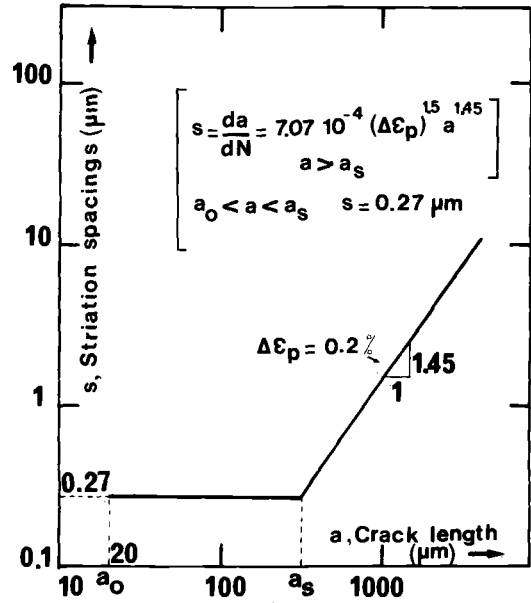


FIG. 4—Schematic representation of the results of striation spacing measurements.

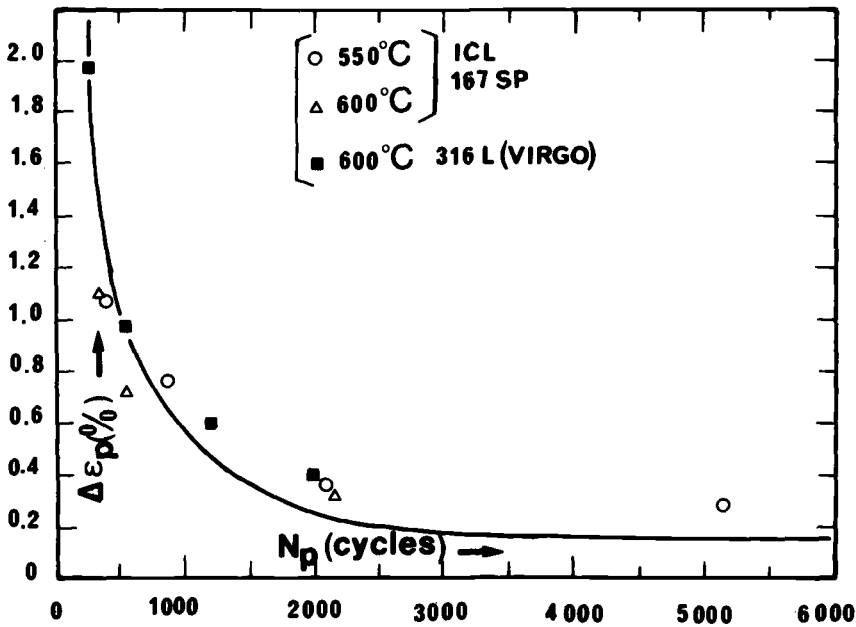


FIG. 5—Number of cycles for crack propagation, N_p , calculated from integration of Eqs 1 and 2 (plain curve) and calculated from striation spacing measurements at 550 and 600°C for ICL steel and at 600°C for VIRGO steel.

either using Eqs 1 and 2 or by numerical integration of the experimental striation spacing curves. Results reported in Fig. 5 show the number of cycles for propagation as a function of the applied strain range. The curve derived from integration of Eqs 1 and 2 is given by

$$N_p = 721 \Delta\epsilon_p^{-1.0345} - 103\Delta\epsilon_p^{-1.5} - 74 \quad (3)$$

where $\Delta\epsilon_p$ is given in percent.

In this integration the final crack length was taken as 2000 μm . This corresponds approximately to the length of the main crack observed in the specimens whose cycling was stopped after a 25 percent decrease in the stabilized stress range. This experimentally determined N_f is very close to the rupture life. This procedure for determining N_f was adopted in order to avoid rubbing damage of the fracture surfaces during the last cycles. Figure 5 indicates that the data points obtained by the integration of each striation spacing versus crack length curve fit well with the proposed relationship [3].

Creep-Fatigue—Scanning electron microscopy observations showed that tensile hold times promote intergranular rupture. Figure 6 illustrates that the fracture surface of the specimens tested with superimposed hold time shows areas covered with striations and areas of intergranular cracking. The amount of intergranular rupture, D_S , was measured on fracture surfaces.

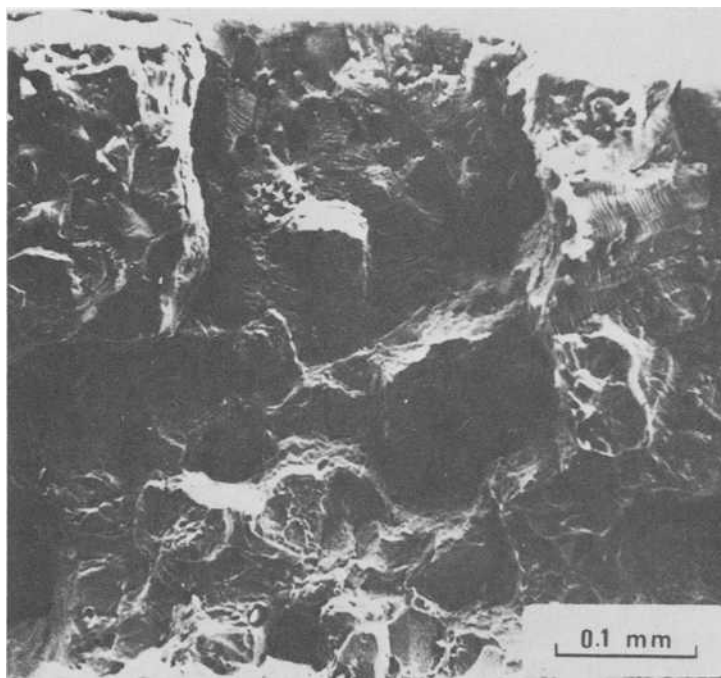


FIG. 6—Scanning electron microscopy; fracture surface of a creep-fatigue specimen; VIRGO steel; Specimen 55; $\Delta\epsilon_p = 1.96$ percent; $T_h = 30$ min; 600°C .

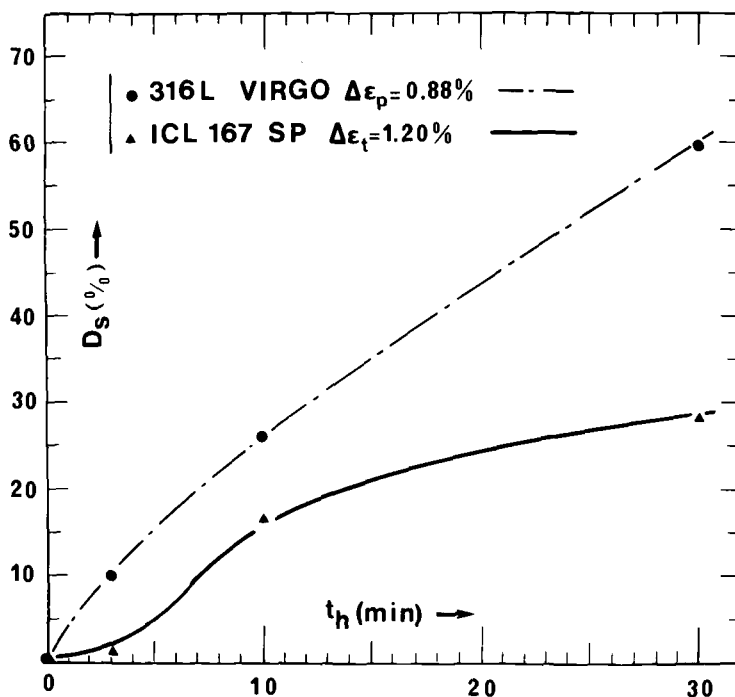


FIG. 7—Influence of hold time of the amount of intergranular rupture measured on the fracture surface, D_s , at 600°C.

Figure 7 indicates that the intergranular fraction D_s increases with hold time. The propensity to intergranular fracture is more pronounced for VIRGO steel than for ICL steel. This difference can be associated with the different hold time fatigue lives already mentioned. The greater susceptibility of VIRGO steel to intergranular cracking was confirmed by optical micrography of longitudinal sections of specimen and short Stage I cracks density measurements [25].

Quantitative Assessment of Grain Boundary Damage—Figure 8 is an optical micrograph illustrating the presence of cracked grain boundaries in a VIRGO creep-fatigue specimen. Observations were made away from the crack rupture surface, as described previously [17]. Preliminary results giving the percentage of cracked grain boundaries measured in the bulk of VIRGO specimens have already been reported [17]. Similar measurements were conducted on specimens of ICL steel, which allowed a quantitative comparison of the microstructural behavior of the two alloys. Figure 9 indicates that the amount of intergranular bulk damage, D_m , measured at failure, increases much more rapidly with increasing hold time in VIRGO steel than in ICL steel.

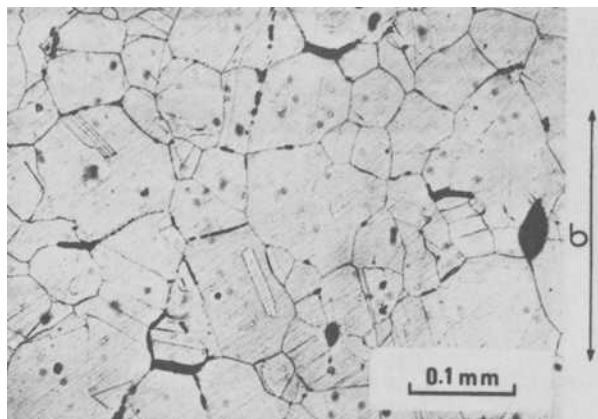


FIG. 8—Optical micrograph illustrating intergranular bulk damage in a creep-fatigue specimen; VIRGO steel; Specimen 55; $\Delta\epsilon_p = 1.96$ percent; $T_h = 30$ min; 600°C . The direction of applied stress is indicated by the arrow.

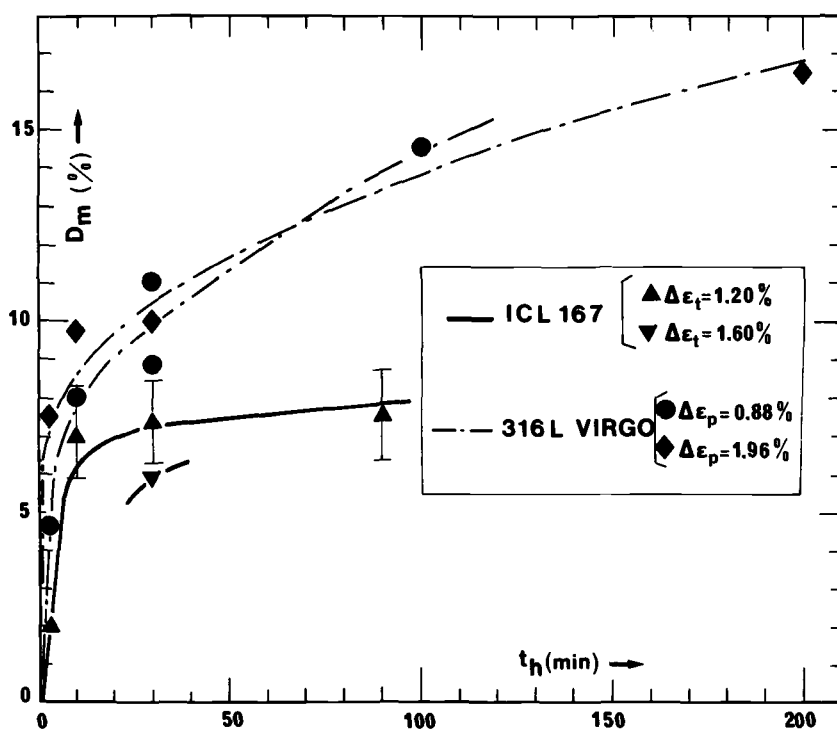


FIG. 9—Influence of hold time on intergranular bulk damage, D_m , measured at failure. Typical scatterband is indicated on the curve corresponding to ICL steel tested at $\Delta\epsilon_t = 1.20$ percent. Test temperature $\approx 600^\circ\text{C}$.

It is worth mentioning that experiments on VIRGO steel [17] showed that the amount of intergranular bulk damage increased roughly linearly with the number of cycles applied to the specimens. This means that a constant damage, D_c , may be attributed to each cycle; that is,

$$D_c = \frac{D_m}{N_f} \quad (4)$$

where

D_m = intergranular bulk damage measured at failure, and
 N_f = number of cycles to failure.

If we assume that this result is also valid for ICL steel, the difference between the two materials is still larger in terms of D_c as a function of hold time, as shown in Fig. 10. This is owing to a better creep-fatigue resistance of ICL steel as compared to VIRGO steel.

Discussion

All the experimental results of our study clearly indicate that the detrimental effect of tensile hold times on LCF life is closely related to intergranular fracture. Similar conclusions have also been reached by others [7,8], at least

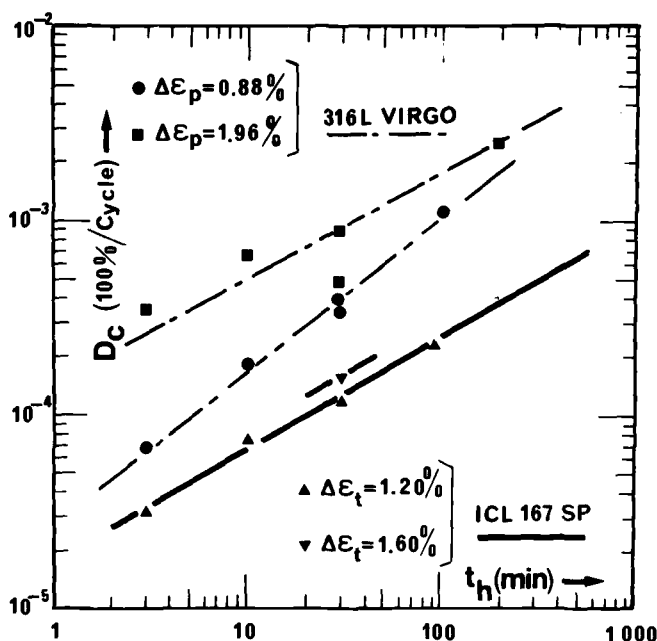


FIG. 10—Influence of hold time on intergranular bulk damage per cycle, D_c . Test temperature = 600°C.

qualitatively. The measurements made in the present study can be used to quantitatively model creep-fatigue interactions using intergranular damage as a correlating parameter.

The first part of this discussion introduces a model based on the effect of intergranular damage on crack growth rate. The second part applies the present approach to various results in the literature. The last part is an insight into predictive methods which can be derived from our approach.

Part I—Relation between Intergranular Damage and the Reduction in Fatigue Life

It is well known that the fatigue life, either in continuous cycling or in creep fatigue, can be divided into a crack initiation stage and a crack propagation stage. In a previous study [17], SEM observations of the gage length surface of specimens tested with tensile dwell times showed that the number of cycles spent into crack initiation, N_i , was much reduced as compared to pure fatigue conditions. It is felt that this reduction is mainly due to the occurrence of intergranular surface cracking and to the effect of oxidation. Therefore it was assumed that under the extreme conditions of large hold times ($>10^2$ h) all of the fatigue life is spent in crack propagation, so that

$$N_t \approx N_p$$

With this assumption, which is obviously conservative, one is left with the problem of modeling the effect of creep damage associated with intergranular rupture on the fatigue crack growth rate. It should be mentioned that models in terms of crack propagation rate have already been introduced by several authors [15,17] in order to take into account the effect of hold time on fatigue life.

In our approach, parts of which have been already presented [27], the crack propagation rate in continuous fatigue is taken as a reference, and a damage function \mathcal{J} is introduced to express the crack growth rate acceleration due to intergranular cracking. The crack propagation rate under creep fatigue conditions is expressed as

$$\left(\frac{da}{dN} \right)^{CF} = \left(\frac{da}{dN} \right)^{PF} \times \mathcal{J}(D, D_c) \quad (5)$$

where CF refers to creep fatigue and PF refers to pure fatigue conditions.

As a general rule, two parameters, D which is the cumulated intergranular bulk damage and D_c which is the intergranular bulk damage of a given cycle, are necessary to fully characterize the state of damage. For cycling with a constant dwell time throughout all the fatigue life:

$$D_c = \frac{dD}{dN} = \text{constant so that } D = D_c N \quad (6)$$

The bulk damage parameter, D_c , is preferred to the local rupture surface percentage of intergranular cracking, D_s , because the latter parameter is not necessarily characteristic of the creep or relaxation part of the cycle but results from the interaction between a growing fatigue crack and intergranular damage. Actual mechanisms of interactions between a crack and intergranular damage in the region ahead of the crack tip are not known. Consequently, at the present time, only empirical correlations may provide information on the damage function \mathcal{G} .

Our aim is to correlate the damage per cycle, D_c , to its detrimental effect on LCF endurance. The reduction of the crack propagation stage due to hold periods is expressed by

$$R = \frac{N_p^{\text{PF}} - N_p^{\text{CF}}}{N_p^{\text{PF}}} \quad (7)$$

Since $N_p^{\text{CF}} \approx N_f^{\text{CF}}$,

$$R \approx \frac{N_p^{\text{PF}} - N_f^{\text{CF}}}{N_p^{\text{PF}}} \quad (8)$$

The contribution of each creep-fatigue cycle to this reduction is given by

$$i_c = \frac{R}{N_f^{\text{CF}}} \quad (9)$$

where i_c is referred to as the propagation reduction factor per cycle (PRFC). i_c was calculated using Eq 3 to evaluate N_p^{PF} . Figure 11 shows that a very good correlation is obtained between the PRFC i_c and the bulk damage per cycle D_c . It is worth noting that this correlation is independent of strain range, hold time, and material. This correlation can be written with a correlation coefficient equal to 0.976 as

$$i_c = k D_c^p \quad (10)$$

where $k = 22.2$ and $p = 1.208$.

This experimental correlation combined with integration of Eq 5 can be used to derive the damage function (see Appendix):⁴

⁴It is worth mentioning that this formulation of the damage function \mathcal{G} can also be used to take into account the effect of sequential tests conducted at a constant strain range and including cycles with different hold times. These sequential tests might be of some practical importance for reducing the total duration of experiments. For example, a certain number of cycles (N_1) including large dwell time (T_1) followed by shorter cycles (N_2) with hold time (T_2) leading to failure could be applied. From these tests the number of cycles to failure corresponding to T_1 , which is unknown, can be determined by integrating Eq 5, which gives D_c corresponding to T_1 , and by using Eq 10. However, it should be kept in mind that this procedure can only be applied if the fracture modes remain unchanged. Moreover, because the microstructure in stainless steels can be modified with time, sequential tests have also some limitations, namely these tests do not fully reproduce the complex interaction between cyclic straining and transgranular or intergranular carbide precipitation.

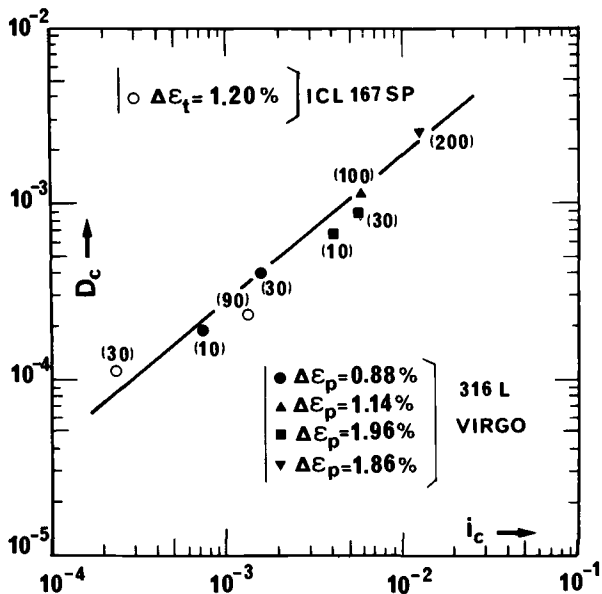


FIG. 11—Correlation between intergranular bulk damage per cycle, D_c , and the PRFC i_c parameter. Test temperature = 600°C. The numbers indicate the hold time in minutes.

$$\mathcal{J}(D, D_c) = \frac{1}{(1 - kD_c^{p-1}D)^2} \quad (11)$$

Equation 11 cannot be directly used to predict fatigue life unless D_c is related to the mechanical creep or relaxation behavior of the material. One way of dealing with this problem is to relate the fatigue life directly to a damage parameter which can be calculated from stress relaxation. In a previous study [16], McLean and one of the authors have shown that grain boundary sliding could be this parameter. Here we have attempted to derive directly a correlation between D_c and the amount of stress relaxation taking place every cycle, σ_R . The results are shown in Fig. 12. In this figure, σ_R is defined as

$$\sigma_R = \sigma_{t,\max} - \sigma_{t,\min} \quad (12)$$

where $\sigma_{t,\max}$ is the tensile stress at the beginning of hold period, and $\sigma_{t,\min}$ is the tensile stress at the end of dwell period.

It is worth noting that this $\sigma_R - D_c$ correlation is neither hold-time nor strain-range dependent, at least within the limits investigated in this study. However, it is clearly material dependent. For a given stress relaxation, σ_R , VIRGO steel suffers more intergranular damage, D_c , than ICL steel. This situation is likely associated with the higher creep resistance of ICL steel as compared to VIRGO steel. This suggests that creep damage is not uniquely

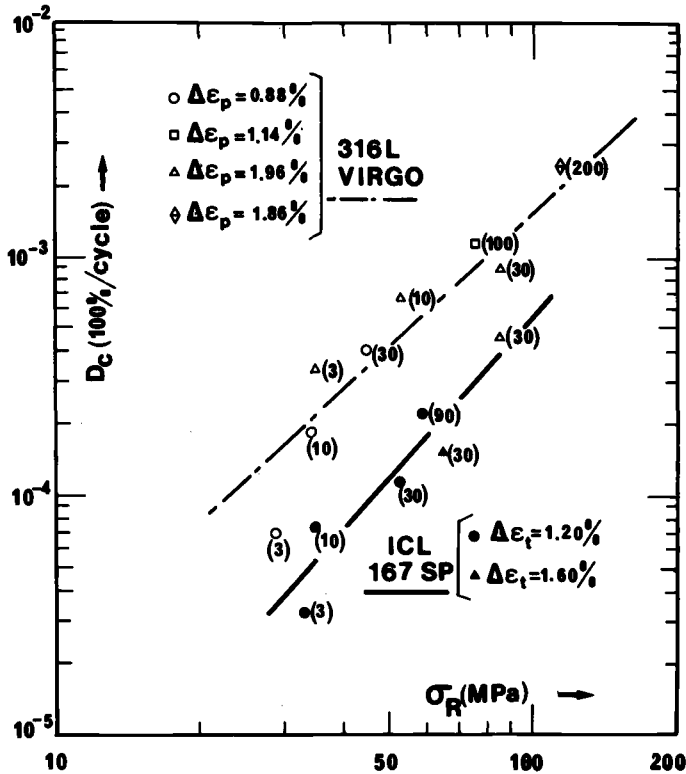


FIG. 12—Variation of the intergranular bulk damage per cycle, D_c , as a function of the amount of stress relaxation σ_R . Test temperature = 600°C. The numbers indicate the hold time in minutes.

dependent on σ_R . Other factors, including in particular chemistry and aging effects, are known to strongly influence the creep resistance of austenitic stainless steels and likely their creep-fatigue properties.

If we combine the two correlations, a purely mechanical and macroscopic relationship is found between stress relaxation σ_R and PRFC i_c , as shown in Fig. 13:

$$i_c = j\sigma_R^q \quad (13)$$

where j and q are material-dependent constants.

Part II—Application to Literature Data on Austenitic Stainless Steels

It is worth comparing the present results to extensive data on 316 and 304 stainless steels available in the literature. For this purpose the values of i_c were determined by calculating N_p^{PF} with Eq 3 for all materials. For 316 stainless steels, the various σ_R versus i_c data points are shown in Fig. 14. Results of Brinkman and coworkers [4] obtained on annealed material at 593°C (1100°F) are included for three strain range levels and hold times

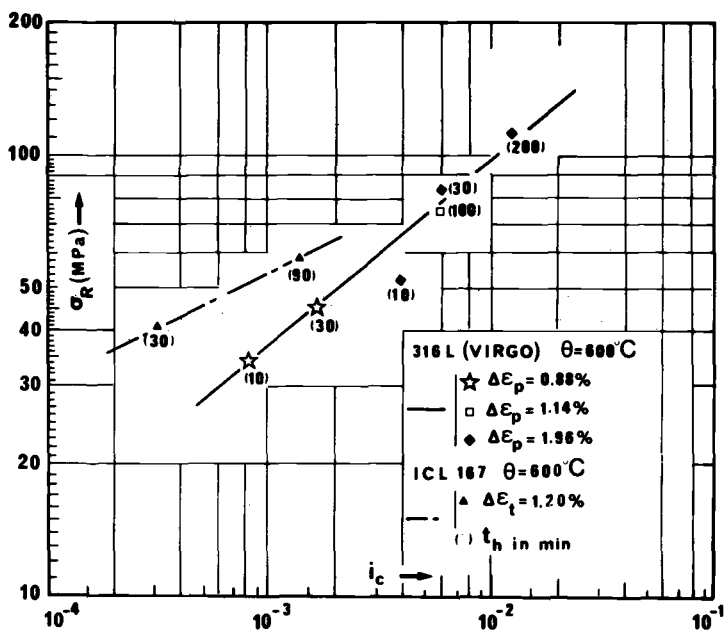


FIG. 13—Correlation between the amount of stress relaxation σ_R and the PRFC i_c parameter.

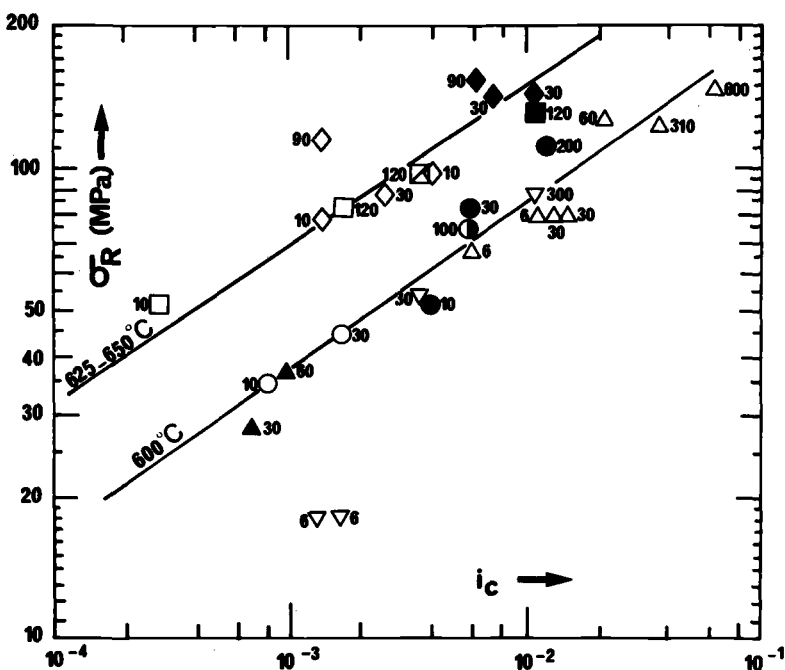


FIG. 14—Application of the σ_R - i_c correlation to literature data on 316 stainless steels in the range of 593 to 650°C. Data obtained on VIRGO steel are included. All reported tests refer to annealed material. The numbers indicate the hold time in minutes. The meanings of the symbols are given in Table 4.

TABLE 4—Symbols used in Fig. 14.

Symbol	$\Delta\epsilon$, %	(p) = plastic (t) = total	Reference	Temperature, °C
○	0.88	(p)	this study; VIRGO steel	600
⊙	1.14	(p)		
●	1.96	(p)		
△	2.0	(t)	4	593
▽	1.0	(t)		
▲	0.5	(t)		
◇	1.25	(t)	8	625
◆	1.98	(t)		
□	0.45	(t)	6	650
⊠	0.58	(t)		
■	0.88	(t)		

reaching 10 h in one case. These data fit the VIRGO steel curve. Data obtained at 625°C (1157°F) and 650°C (1202°F) [3,6,8] give another σ_R - i_c curve, indicating that a given stress relaxation σ_R is more damaging in terms of i_c -parameter at 600°C than at 650°C.

For 304 stainless steels, a certain number of the results of the literature [2,4,5,7,11] obtained in the temperature range of 538 to 650°C (1000 to

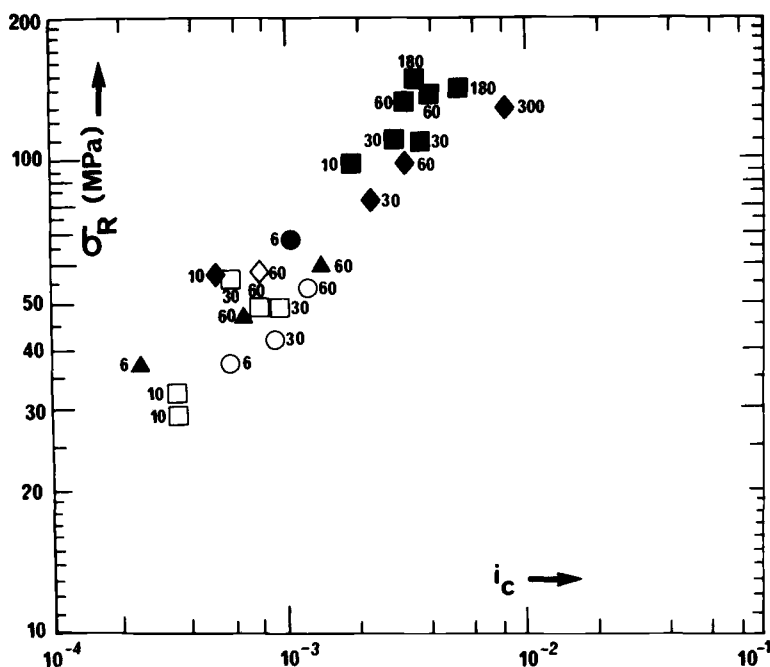


FIG. 15—Application of the σ_R - i_c correlation to a number of results published in the literature on 304 stainless steels in the range of 538 to 650°C. The numbers indicate the hold time in minutes. The meanings of the symbols are given in Table 5.

TABLE 5—Symbols used in Fig. 15.

Symbol	$\Delta\epsilon_t$, %	Reference	Temperature, °C	Material Conditions	Remarks
◇	1	7	593	Heat 845; aged at 593°C for 1000 h	stress relaxation is calculated from Table 4 [7]
▲	1	4	593	aged at 400 to 410°C for 3096 to 8760 h	
○	1	11	593	Heats 597, 414, 380, 796; annealed or aged; Table 2 [11]	the results related to Heat 813 exhibiting an increased resistance to creep-fatigue are not included
●	2				
□	0.5	2	650	annealed	
■	2				
◆	2.2	5	538	annealed	stress relaxation is calculated from Table 2 [5]

1202°F) are shown in Fig. 15. These results suggest a smaller temperature dependence of the σ_R - i_c curve as compared to 316 stainless steels. The slope of σ_R - i_c curve is higher for 304 steels, however, as shown in Fig. 16 where the comparison between 304 and 316 stainless steels is made. In this figure scatter bands encompassing all the results are drawn.

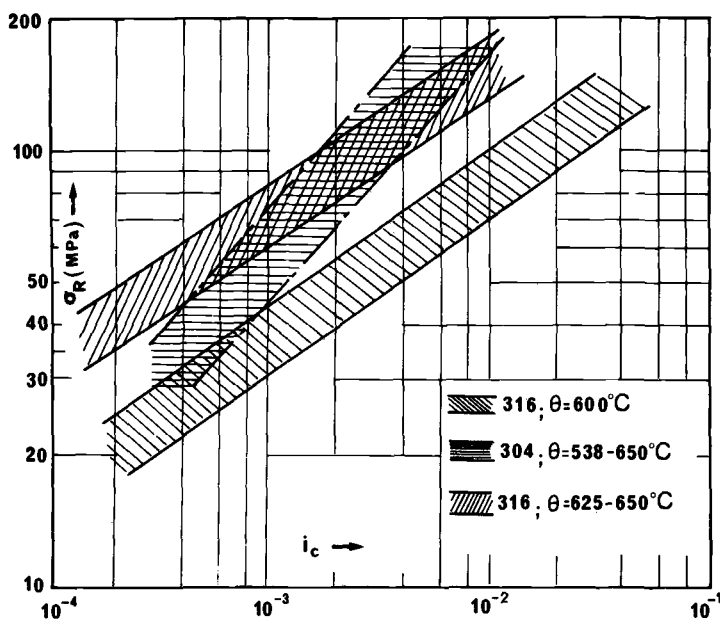


FIG. 16—Comparison between 316 and 304 type steels.

It appears that the present σ_R - i_c approach is appropriate for austenitic stainless steels exhibiting a propensity to intergranular cracking. It should be emphasized, however, that in some cases, as for instance in one of the five heats of 304 steel investigated by Brinkman and Korth [11], hold times have less of an effect on LCF life, although the relaxation behavior does not greatly change. It is clear that the stress relaxation σ_R is essentially a correlating parameter based on numerous experiments, but it does not indicate intrinsically the material susceptibility to intergranular fracture. In particular the occurrence of intergranular cracking is a prerequisite condition for applying the proposed approach.

Part III—Application to the Prediction of Long-Term Behavior

The σ_R - i_c correlation may conceivably be used to predict fatigue lives of components in actual service conditions with large dwell periods (10^2 to 10^3 h) and low strain ranges ($\Delta\epsilon_t \approx 0.5$ percent). Prediction does not mean extrapolation on the σ_R - i_c curve of a given material, because increasing hold time increases the stress relaxation σ_R but decreasing strain range decreases the stress relaxation, so that the two trends are opposite. If we assume as a working hypothesis that the σ_R - i_c correlation remains valid for long-term conditions, the stress relaxation must be known to calculate the fatigue life N_p^{CF} through i_c . But at the present time, no data of stress relaxation for large dwell time are available. In order to illustrate the predictive ability of the present approach, the stress relaxation curves were calculated using a creep strain hardening law fitted on creep tests conducted on annealed VIRGO material [18] at 600°C (1112°F). Two extreme conditions were assumed in order to define the maximum tensile stress at the beginning of the dwell time. It is experimentally observed that the incorporation of hold times into continuous cycling lowers the cyclic stress-strain curve (Table 3). Under extreme conditions corresponding to very long hold times it can be assumed that, at a given strain rate and a given temperature, the monotonic tensile curve is a lower bound for the cyclic curve. Conversely the cyclic stress-strain curve corresponding to pure fatigue can be used as an upper bound.

Fatigue lives corresponding to these two assumptions were calculated for 5, 50, and 500 h hold times at 600°C (Fig. 17). They are compared with the pure fatigue endurance curve, N_f^{PF} , and with the pure fatigue propagation curve, N_p^{PF} , calculated from Eq 3 where the plastic strain range was inferred from the pure fatigue cyclic stress-strain curve. In these calculations, the monotonic and the pure fatigue cyclic stress-strain curves determined at a strain rate of about $4 \times 10^{-3} \text{ s}^{-1}$ were used.

Figure 17 shows that all the calculated curves tend towards the N_p^{PF} curve at a small strain range. This is associated with the assumption that for long hold times $N_i^{CF} \approx 0$. It is equally observed that the calculations made with the cyclic stress-strain curve lead to much lower lives. This is not an unex-

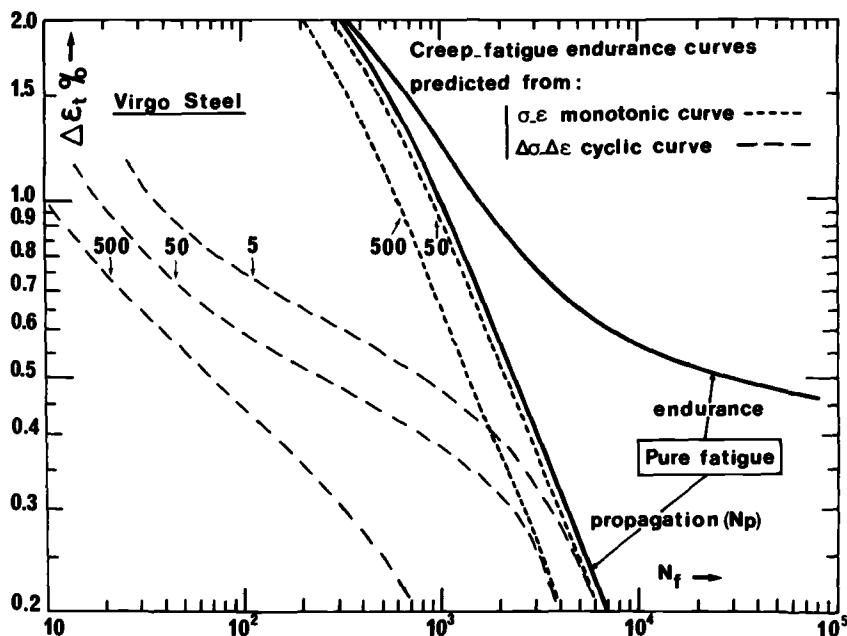


FIG. 17—Predictions of fatigue life for large hold times using two different assumptions for calculating stress relaxation. Temperature = 600°C. The numbers indicate the hold time in hours.

pected result; since the stress relaxation, σ_R , is larger, the higher the maximum tensile stress. It should be noticed that the difference in fatigue life resulting from the two bounds used for the maximum tensile stress decreases with decreasing strain range. This situation corresponds to the fact that the difference between the cyclic stress-strain curve and the monotonic curve decreases with decreasing strain. Finally there exists a large difference between the two sets of curves calculated either from the monotonic curve or from the cyclic stress-strain curve.

This difference is pronounced at high strain levels, but is smaller at lower strain ranges. In the absence of other experiments it is difficult to assert which assumption is more realistic. It is interesting to note, however, that for predictive purpose the stress relaxation σ_R is a parameter of practical interest because it is characteristic of a stabilized cycle, the measurement of which does not necessarily imply tests to failure but can be continuously monitored.

The curves shown in Fig. 17 indicate a large reduction in the number of cycles to failure due to creep-fatigue interaction. This reduction is largely associated with the assumption dealing with crack initiation ($N_i^{CF} = 0$). However, this effect is important essentially at a small strain range. For large strain ranges, such as those usually used in laboratory tests, a simplified expression for i_e could be used by replacing the numbers of cycles for propaga-

tion by the fatigue lives; that is,

$$i_c = \frac{N_p^{PF} - N_t^{CF}}{N_p^{PF} \times N_t^{CF}} \simeq \frac{N_t^{PF} - N_t^{CF}}{N_t^{PF} \times N_t^{CF}} = \frac{1}{N_t^{CF}} - \frac{1}{N_t^{PF}} \quad (14)$$

It is felt that this simplification must be avoided for strain ranges corresponding more closely to service conditions because it is not conservative.

Limitations

1. Creep-fatigue loading involves many factors. Clearly our model is strictly applicable for tests with tensile hold at the maximum strain limit and for a given strain rate ($\dot{\epsilon} \approx 10^{-3} \text{ s}^{-1}$). A modification in strain rate and test temperature could eventually change the values of the coefficients determined in our correlations.

2. More fundamentally, the correlation found between the magnitude of stress relaxation and intergranular damage implies that the strain rate is not an important factor in producing tensile hold time damage. This presumably arises from the fact that, in fatigue-relaxation tests, at least at high strain levels and for relatively small dwell periods, intergranular cavity growth is essentially controlled by the creep strain taking place during relaxation at every cycle. In other words, in those conditions intergranular cavity growth is very similar to hole growth processes in ductile rupture which are governed by plastic deformation at a given stress triaxiality. In the creep literature (for example, [28]) the models developed for the growth of intergranular cavities predict that at high strain rate the cavity growth rate is proportional to the cavity size and strain rate. Thus the correlation established between σ_R and D_c is in broad agreement with the results of these models. However, at smaller strain amplitudes and for longer hold times other micromechanisms of cavity growth could operate. Clearly further work is needed to derive an extrapolation procedure which takes into account the damage mechanisms responsible for the reduction in the tensile hold time fatigue life. Nevertheless, it is felt that the correlation determined between the intergranular damage and i_c -parameter can be very useful to continuously monitor the damage in a specimen or in a component subjected to creep-fatigue conditions including very long hold times.

Summary

1. When tensile hold time periods are introduced into LCF tests, progressively larger reductions in cyclic life are observed as the hold time is increased. This reduction in fatigue endurance is attributed to the reduction of the periods of both crack initiation and crack propagation.

2. The acceleration in crack growth is related to intergranular rupture taking place every cycle during dwell period.

3. It is possible to correlate the relative reduction in fatigue life and intergranular damage.

4. The intergranular damage per cycle is directly related to stress relaxation which takes place during hold times. The susceptibility to intergranular rupture is also material dependent.

5. A new approach based partly on the effect of intergranular damage on fatigue crack growth rate and partly on the effect of oxidation and intergranular rupture on crack initiation is proposed for the prediction of the fatigue life of components subjected to creep-fatigue loading.

Acknowledgments

This work was performed under SCSIN Contract No. 293 341 and CEA Contract No. SA.7.387. Thanks are due Mr. Weisz and Mr. Petrequin from CEA for many fruitful discussions. We wish to thank Mr. R. Locicero from the École des Mines for his assistance in the experiments.

APPENDIX

Identification of the Damage Function $\mathcal{G}(D, D_c)$

$$\left(\frac{da}{dN}\right)^{CF} = \left(\frac{da}{dN}\right)^{PF} \times \mathcal{G}(D, D_c)$$

For periodic cycling:

$$D = D_c N \text{ with } D_c = \text{constant}$$

Then

$$\frac{da}{\left(\frac{da}{dN}\right)^{PF}} = \mathcal{G}(D, D_c) \frac{dD}{D_c}$$

If we assume that during the propagation stage a crack grows from the same a_0 to the same a_f as in pure fatigue whereas D increases from 0 ($N^{CF} = 0$) to $D_m = D_c \times N_f^{CF}$, it follows that

$$N_p^{PF} = \int_{a_0}^{a_f} \frac{da}{\left(\frac{da}{dN}\right)^{PF}} = \frac{1}{D_c} \int_{D=0}^{D=D_m} \mathcal{G}(D, D_c) dD$$

Hence

$$N_p^{PF} = \frac{N_f^{CF}}{D_m} \times G(D_m, D_c)$$

with

$$g(D, D_c) = \frac{\delta G(D, D_c)}{\delta D}$$

and

$$G(0, D_c) = 0$$

From

$$i_c = \frac{N_p^{PF} - N_t^{CF}}{N_p^{PF} \times N_t^{CF}} = k D_c^p$$

we obtain

$$\frac{G(D_m, D_c)}{D_m} - 1 = \frac{G(D_m, D_c)}{D_m} N_t^{CF} \times k D_c^p = G(D_m, D_c) k D_c^{p-1}$$

Then

$$G(D, D_c) = \frac{D}{1 - k D_c^{p-1} D}$$

with

$$G(0, D_c) = 0$$

and

$$g(D, D_c) = \frac{\delta G}{\delta D} = \frac{1}{(1 - k D_c^{p-1} D)^2}$$

References

- [1] Dawson, R. A. T., Elder, W. J., Hill, J. G., and Price, A. T. in *Proceedings*, International Conference on Thermal and High Strain Fatigue, Metals and Metallurgy Trust, London, 1967, pp. 239-269.
- [2] Berling, J. T. and Conway, J. B. in *Proceedings*, First International Conference on Pressure Vessel Technology, Delft, ASME, 1970, Part II, pp. 1233-1246.
- [3] Conway, J. B., Berling, J. T., and Stentz, R. H. in *Proceedings*, International Conference on Thermal Stresses and Thermal Fatigue, Gloucestershire, 1969, pp. 89-108.
- [4] Brinkman, C. R., Korth, G. E., and Hobbins, R. R., *Nuclear Technology*, Vol. 16, Oct. 1972, pp. 297-302.
- [5] Jaske, C. E., Mindlin, H., and Perrin, J. S. in *Proceedings*, International Conference on Creep and Fatigue in Elevated Temperature Applications, Philadelphia, Sept. 1973, pp. 163.1-163.7.
- [6] Udoguchi, T., Asada, Y., and Ichino, I. in *Proceedings*, International Conference on Creep and Fatigue in Elevated Temperature Applications, Philadelphia, Sept. 1973, pp. 211.1-211.9.
- [7] Maiya, P. S. and Majumdar, S., *Metallurgical Transactions A*, Vol. 8, Nov. 1977, p. 1651-1660.
- [8] Wareing, J., *Metallurgical Transactions A*, Vol. 8, May 1977, pp. 711-721.
- [9] Mottot, M., Petrequin, P., Amzallag, C., Rabbe, P., Grattier, J., and Masson, S., this publication, pp. 152-168.
- [10] Wareing, J., Tomkins, B., and Sumner, G. in *Fatigue at Elevated Temperatures*, ASTM STP 520, American Society for Testing and Materials, 1972, pp. 123-138.
- [11] Brinkman, C. R. and Korth, G. E., *Metallurgical Transactions*, 1974, Vol. 5, pp. 792-794.

- [12] Coffin, L. F. in *Fatigue at Elevated Temperatures*, ASTM STP 520, American Society for Testing and Materials, 1972, pp. 5-34.
- [13] Manson, S. S. in *Fatigue at Elevated Temperatures*, ASTM STP 520, American Society for Testing and Materials, 1972, pp. 744-782.
- [14] Ostergren, W., *Journal of Testing and Evaluation*, 1976, Vol. 4.
- [15] Tomkins, B. and Wareing, J., *Metal Science Journal*, Vol. 11, 1977, p. 414.
- [16] MacLean, D. and Pineau, A., *Metal Science Journal*, July 1978, pp. 313-316.
- [17] Levaillant, C., Rezgui, B. and Pineau, A. in *Proceedings*, Third International Conference on Mechanical Behaviour of Materials, Cambridge, England, Aug. 1979, Miller and Smith Eds., Vol. 2, pp. 163-173.
- [18] Groupe de Travail Matériaux, Document No. 4, 1975.
- [19] Calvet, J. N. and Birault, M., Commissariat à l'Energie Atomique, Internal Report, 1979.
- [20] Rezgui, B., Commissariat à l'Energie Atomique, Report R4982, 1979.
- [21] Groupe de Travail Matériaux, Internal Reports, 1979-1980.
- [22] Maiya, P. S. and Busch, D. E., *Metallurgical Transactions*, Vol. 6A, 1975, pp. 1761-1766.
- [23] Yamaguchi, K., Kanazawa, K., and Yoshida, S., *Materials Science and Engineering*, Vol. 33, 1978, pp. 175-181.
- [24] Wareing, J. and Vaughan, H. G., *Metal Science Journal*, Oct. 1977, pp. 439-446.
- [25] Masuda, C., Levaillant, C. and Pineau, A., to be published.
- [26] Wareing, J., Vaughan, H. G., and Tomkins, B., UKAEA, Northern Division Report N.D.R. 447(S), Sept. 1980; also presented at the fall meeting of the Metallurgical Society, AIME, Milwaukee, 16-20 Sept. 1979.
- [27] Clavel, M., Levaillant, C., and Pineau, A., presented at the fall meeting of the Metallurgical Society, AIME, 16-20 Sept. 1979.
- [28] Svensson, L. E. and Dunlop, G. L., *International Metals Review*, Vol. 26, 1981, pp. 109-131.

Cumulation of High-Temperature Low-Cycle Fatigue Damage in Two-Temperature Tests

REFERENCE: Reuchet, J., Réger, M., Rezai-Aria, F., and Rémy, L., "Cumulation of High-Temperature Low-Cycle Fatigue Damage in Two-Temperature Tests," *Low-Cycle Fatigue and Life Prediction, ASTM STP 770*, C. Amzallag, B. N. Leis, and P. Rabbe, Eds., American Society for Testing and Materials, 1982, pp. 194-211.

ABSTRACT: The cumulation of damage in high-temperature low-cycle fatigue is investigated for a cast cobalt-base superalloy MarM509, by using two-temperature testing. The two temperature levels [600 and 900°C (873 and 1173 K)] are taken as representative of low and high temperature behavior. At low temperatures crack initiation is crystallographic, while at high temperatures MC carbides are preferentially oxidized, giving rise to early initiation. Testing is conducted at a constant plastic strain range ($\Delta\epsilon_p/2 = 0.2$ percent), and the remaining fatigue life is determined at one temperature after cycling at the other temperature for a definite amount of the expected life. The fatigue lives so obtained exhibit a large deviation from Miner's rule, particularly when the first cycling is carried out at the higher temperature. A detailed metallographic study using a replication technique shows that this deviation was related to the differences in the microcracking process at each temperature. More quantitatively, an estimate of the life to initiation is defined using a potential drop technique, which has shown that conservative predictions can be made from the application of Miner's rule to the initiation period.

KEY WORDS: high-temperature low-cycle fatigue, cobalt-base superalloy, cumulative damage rules, crack initiation

A number of papers dealt with the definition of fatigue damage using either a mechanical or metallurgical approach, especially in the field of isothermal creep-fatigue testing. Only a few studies, however, examine the problem of thermal fatigue damage, which many components suffer under service conditions. In this case one has to deal not only with the interaction of fatigue with creep and oxidation damage (as in high-temperature fatigue), but also with the effect of temperature variation. At the present time the most successful method has been that of Spera [1],² who considered thermal fatigue similar to a process of cumulative creep. On the other hand, a very

¹ Centre des Matériaux de l'Ecole des Mines de Paris, Evry, France.

² The italic numbers in brackets refer to the list of references appended to this paper.

attractive method is to treat the relevant damage as equivalent to that induced under isothermal fatigue conditions. This was actually done (mainly for steels) by Taira [2], who tried to define an equivalent temperature from the temperature dependence of the Manson-Coffin law, and by Halford and Manson [3], who applied the strain-range partitioning method. However, linking thermal and isothermal loading requires the use of cumulative damage rules that can properly account for the temperature dependence of cyclic damage. A simple and relevant way to investigate this problem is to carry out sequential fatigue testing at two temperatures.

This is the object of the present paper, which reports preliminary results obtained on a cast cobalt-base superalloy MarM509 used for guide vanes in gas turbines. Based on detailed study of low-cycle isothermal fatigue, two temperatures were studied [600 and 900°C (873 and 1173 K)]. At the first temperature, oxidation which occurred did not much affect the fatigue life, which is the same as at room temperature. At the higher temperature, creep and oxidation damage may intervene in reducing the fatigue life with respect to that observed at 20 and 600°C, as previously pointed out [4]. Therefore a constant plastic strain range was used, and the influence of previous cycling for a definite amount of expected life at each temperature on the residual life at the other temperature was investigated.

After reviewing the basic alloy behavior at both temperatures, the results of two-temperature tests will be presented with metallographic examinations of the various specimens. These observations will be discussed with reference to the mechanisms of crack initiation and the respective importance of crack initiation and crack propagation periods in the overall life.

Experimental Procedure

Two heats were used in this study; their compositions are given in Table 1. Specimens were taken from cylindrical castings of 20 mm diameter. The as-cast alloy was given a heat-treatment at 1230°C (1503 K) for 6 h, and for the casting conditions used the average grain size was in the range of 0.5 to 2 mm. The corresponding microstructure is that of a face-centered-cubic (fcc) matrix with a few percent of two kinds of interdendritic carbides: (1) coarse-textured $M_{23}C_6$ carbides, which are rich in chromium and nickel, and (2) the so-called "chinese script" MC carbides, which contain mainly tantalum [5-7]. These MC carbides are nearly platelets which delineate the secondary arm spacing of about 60 μm (Fig. 1). So far as high-temperature fatigue is concerned, these are the most important microstructural features.

An investigation of the temperature dependence of the fatigue behavior was previously carried on Heat 1 using hourglass-shaped specimens with a diameter of 5 mm and a radius of curvature of 30 mm. Results have been partly reported in the range of 20 to 900°C (293 to 1173 K) using induction heating for continuous saw-tooth push-pull cycling under air [4]. All these tests were

TABLE 1—Alloy composition (weight percent).

	C	Ni	Cr	W	Ta	Zr	Ti	Fe	B	P	S	Mn	Si	Co
Heat 1	0.59	10	23.7	7	3.57	0.45	0.19	0.19	0.005	...	0.003	0.1	0.1	balance
Heat 2	0.59	11	23.2	6.95	3.31	0.30	0.22	0.17	0.008	0.005	0.003	balance

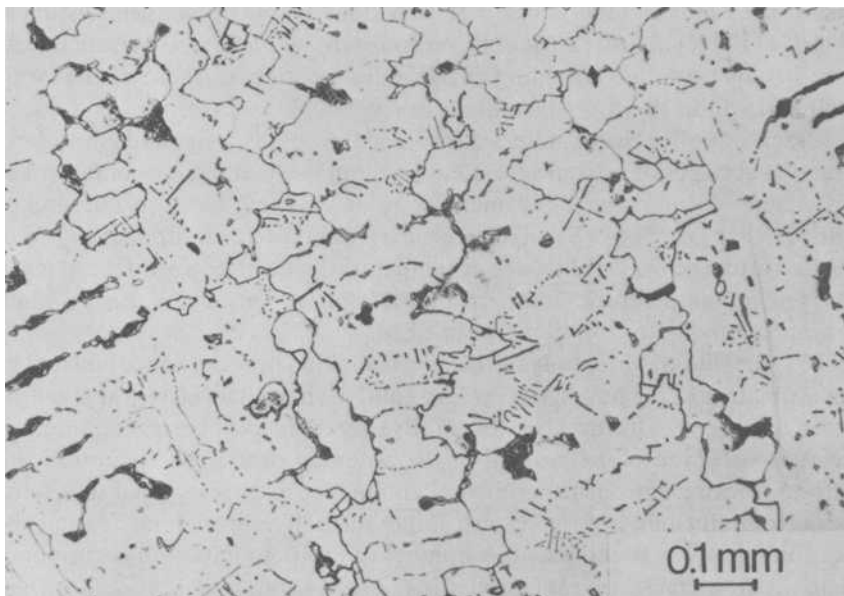


FIG. 1—Microstructure of the as-cast heat-treated condition.

carried out on a modified screw-driven tension testing machine, under total constant diametral plastic strain control, which recorded continuously the load and from time to time the stress-strain hysteresis loops.

These first results were completed by tests on Heat 2 in the range of 20 to 1100°C (293 to 1373 K) using the same wave shape, but with axial strain control of cylindrical specimens 8 mm in diameter and 12 mm in gage length. In this case a radiation furnace was used. Within the experimental accuracy, variation in the results from both heats and strain controls was found to be negligible. Accordingly, in the reference life curves, the specific mode of control will not be referred to.

For the two temperature tests of interest here, only Heat 2 and axial strain control were used. A nearly constant total strain rate $\dot{\epsilon}_t$ was used; this was for a plastic strain amplitude $\Delta\epsilon_p/2 = 0.2$ percent, $5 \cdot 10^{-4} \text{ s}^{-1}$ at 900°C (1173 K) and 10^{-3} s^{-1} at 600°C (873 K). These two temperatures were selected because they can be taken as representative of the high and low temperature behavior in a Manson-Coffin plot of the fatigue life as a function of the plastic strain range. As definitions vary among the literature, it is worth noting that the fatigue life was conventionally defined as corresponding to the onset of a rapid decrease in the tensile load, which corresponds to the existence of a fatigue crack typically in the range of 1 to 2 mm. Thus specimens are still suitable for various metallographic examinations. One has to emphasize that in the case of a pre cycling at 600°C, some dynamic aging occurs, and a thermal treat-

ment of 15 min at 1100°C (1373 K) was done before subsequent testing at 900°C (1173 K) in order to avoid alterations in the cyclic stress-strain behavior. In this way, the hardening curves were identical to those of the virgin material within the experimental accuracy.

Crack initiation sites and crack propagation paths were studied on both fracture surfaces of broken specimens and longitudinal sections of unbroken specimens, using either light microscopy or scanning electron microscopy (SEM). In the case of two temperature level tests, specimen surfaces were replicated after the first cycling at one temperature and after the final cycling at the second temperature. Standard plastic replicas were made using a shadowing technique for examination in SEM.

This metallographic study of the microcracking process was completed by an estimation of the number of cycles to initiation from an electrical potential drop technique. This number was arbitrarily defined as corresponding to a relative variation of 0.1 percent of the potential drop. This definition was chosen because for our experimental equipment it corresponded to a fairly good reproducibility of the results. Experimentally, through replicating and sectioning, it was found that this number of cycles to initiation corresponds actually to a crack size range roughly 0.2 to 0.3 mm in depth.

Results and Discussion

Isothermal Fatigue Behavior

From an extensive study of the isothermal fatigue behavior of MarM509 [4], one can classify the test temperatures between 20 and 1100°C (293 and 1373 K) into two ranges with respect to a Manson-Coffin plot of the fatigue life under continuous cycling in air versus the plastic strain range. Below, say, 650°C (823 K) there is no temperature dependence of the fatigue life. Above 650°C (823 K) there is a strong reduction of the number of cycles to failure. These two different behaviors can be typified by 600 and 900°C (873 and 1173 K). The corresponding experimental points are given in Fig. 2, together with the points obtained at room temperature. There is a break in the Manson-Coffin curves at large strain ranges. But, neglecting this domain, one can see that the slope of these curves is slightly temperature dependent about -0.5 at 600°C and room temperature and higher at 900°C (≈ -0.8), and that the main feature is the reduction in fatigue life from 20 to 600°C to 900°C of a factor of about 7 for a strain range $\Delta\epsilon_p/2$ about 0.2 percent. (Further details on the mechanical characterization are given in Ref 4.)

A detailed metallographic study has enabled us to show that this transition in the fatigue fracture law is linked with a change in the microcracking process, for both initiation and propagation. The crack initiation is mainly crystallographic at low temperatures. Crystallographic facets can be observed on the fracture surface (Fig. 3). In this case ($\Delta\epsilon_p/2 = 7 \cdot 10^{-4}$ at 20°C) there is a definite correspondence between the slip markings on the gage

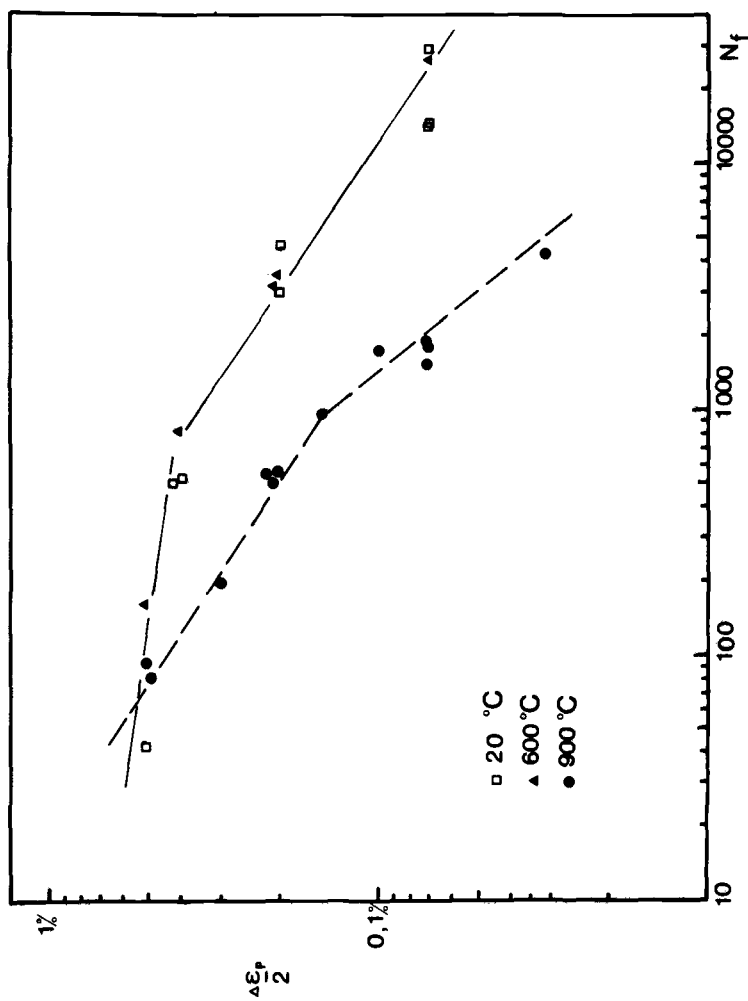


FIG. 2—Variation of the number of cycles to failure N_f with the plastic strain range $\Delta \epsilon_p / 2$.

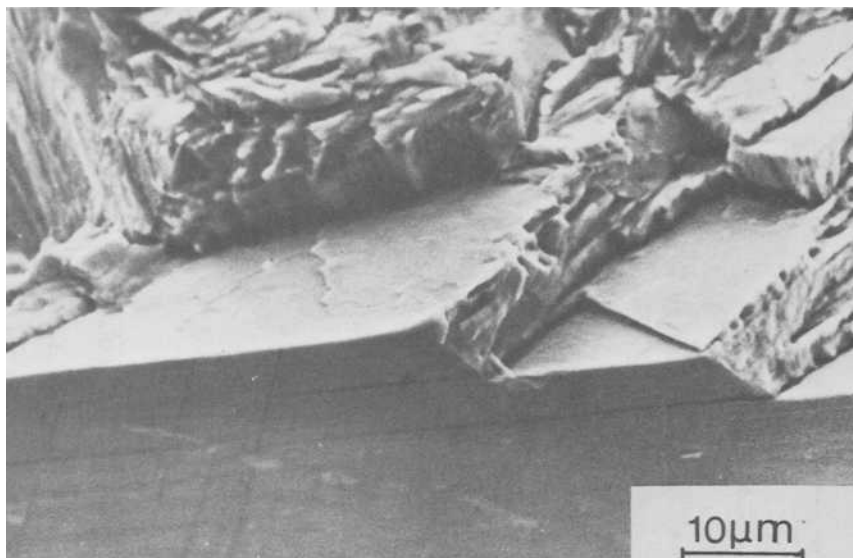


FIG. 3—Crack initiation at low temperature; facets on the fracture surface (temperature = 20°C, $\Delta\epsilon_p/2 = \pm 7 \cdot 10^{-4}$, SEM).

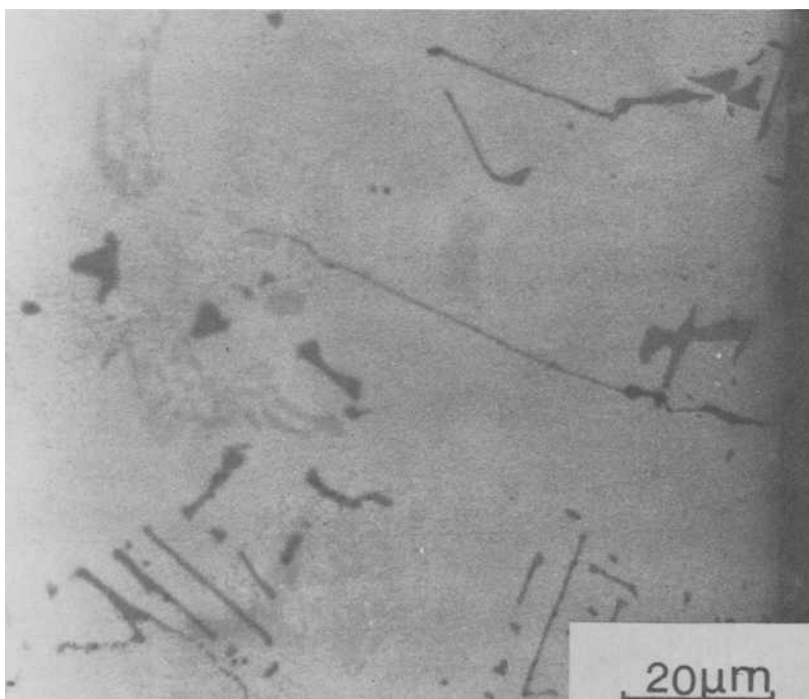


FIG. 4—Crack initiation at low temperature; longitudinal section showing Stage I growth from the specimen surface (temperature = 600°C, $\Delta\epsilon_p/2 = \pm 0.2$ percent, the stress axis is vertical).

length and the facets on the fracture surface as seen in wrought alloys [8]. This result is confirmed by observations on longitudinal sections of specimens (Fig. 4) (with a vertical stress axis). This secondary crack obtained for $\Delta\epsilon_p/2 = 0.2$ percent at 600°C shows that if Stage I crack growth is mainly transcrystalline and transdendritic, the actual path may be connected with broken carbides. For strain ranges not low enough, it is thus suspected that in some instances carbide cracking below the surface may play some role in the initiation process. At high temperatures the initiation of cracks is completely modified by the occurrence of oxidation, as shown in Fig. 5 for $\Delta\epsilon_p/2 = 0.2$ percent at 900°C. The observation of the specimen gage length after interrupted testing reveals a preferential oxidation of MC carbides. Longitudinal sections confirm that this preferential oxidation of the free surface connected MC carbides is the origin of microcracking (Fig. 6).

In addition, the Stage II crack propagation was found to be different because of longitudinal sectioning. Up to 650°C (823 K) the fatigue cracks propagate either in the matrix dendrites or along carbides in the interdendritic regions. At higher temperatures, cracks have essentially an interdendritic path, mostly along MC carbides, which is presumably caused by the influence of oxidation.

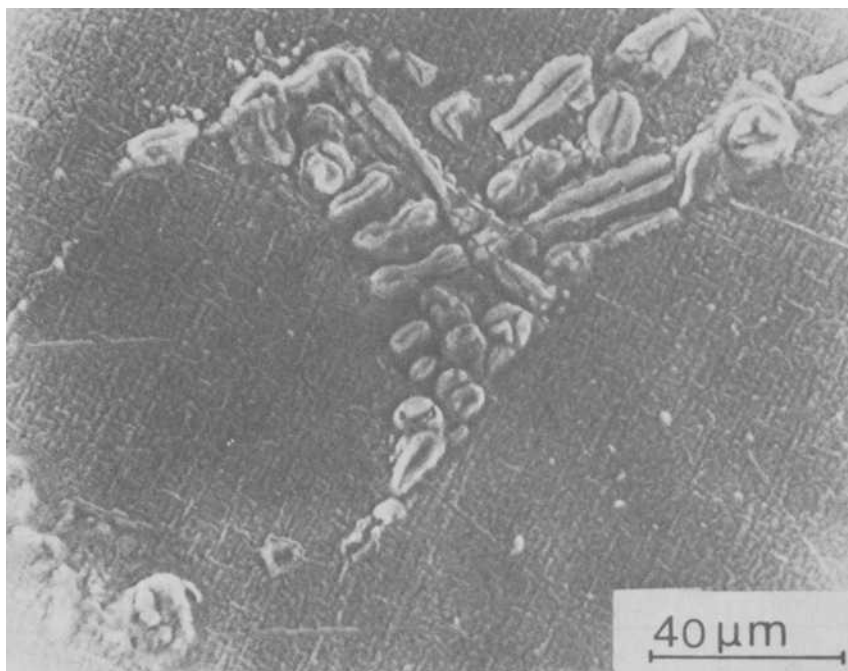


FIG. 5—Crack initiation at high temperature ($\Delta\epsilon_p/2 = \pm 0.2$ percent, temperature = 900°C); oxidation of the MC carbides at the surface.

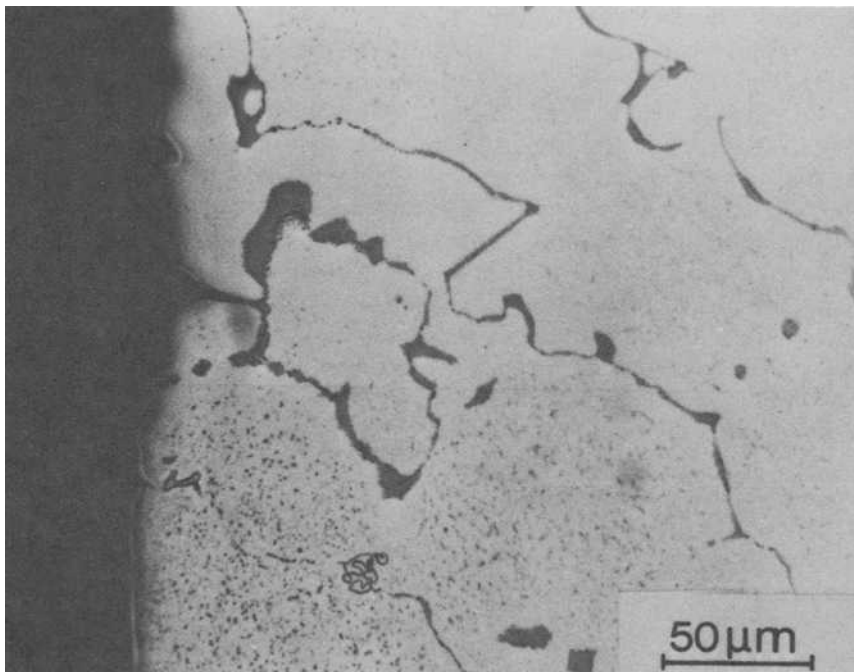


FIG. 6—Crack initiation at high temperature ($\Delta\epsilon_p/2 = \pm 0.2$ percent, temperature = 900°C); longitudinal section showing crack initiation by oxidation of the carbides connected with the free surface (vertical stress axis).

Two-Temperature Level Tests

From these observations on the transition of both crack initiation mechanisms and fatigue lives, we decided to investigate the damage cumulation at 600 and 900°C , typical low and high temperatures. This study was limited to a single plastic strain range $\Delta\epsilon_p/2 = 0.2$ percent. Since for sequential fatigue testing it is necessary to have good reference values, three tests were completed for each temperature. The results are given in Table 2 with 90 percent confidence intervals; for this strain level, the fatigue life was about 3360 cycles at 600°C and 440 cycles at 900°C .

TABLE 2—Test results for a plastic strain range of $\Delta\epsilon_p/2 = 0.2$ percent.

Temperature, $^\circ\text{C}$	N_f	Number of tests for N_f	N_i	Number of tests for N_i	N_i/N_f
600	3358 ± 308	3	1905 ± 503	5	≈ 0.57
900	442 ± 157	3	142 ± 18	4	≈ 0.32

^a N_f is the conventional number of cycles to failure, as defined in the text. N_i is the number of cycles to crack initiation, as inferred from the potential drop technique. All these values are given with error bounds corresponding to a 90 percent confidence interval.

Sequential fatigue tests were conducted at the two temperatures. A first cycling was made at T_1 with n_1 cycles, and the remaining life, n_2 cycles, was determined at the temperature T_2 ; T_1 and T_2 being respectively 600 and 900°C. If N_{t1} and N_{t2} are the expected life at each temperature level, the damage as defined by Miner at the first level is $D_1 = n_1/N_{t1}$ and the remaining life actually observed, n_2 , corresponds to a damage $D_2 = n_2/N_{t2}$. According to Miner's rule, the sum of D_1 and D_2 should be unity; therefore we have reported the test results in this classical form of observed cycles normalized to the expected life at each temperature level (Fig. 7). As usual for tests under two stress levels at a single temperature, Miner's rule did not apply to our results, even within the experimental scatter that cannot be avoided with sequential testing. In particular, when cycling is carried out first at 900°C, the remaining life at 600°C is much lower than that predicted by Miner's rule. It is worth noting that only 10 cycles at 900°C, which corresponds to only 0.2 percent of the expected life, reduce the final life at 600°C to 55 percent of the expected value. Precycling at 600°C yields a smaller deviation from Miner's rule. Despite the small number of tests carried out and within the experimental scatter, it appears that the final life at 900°C is nearly unaffected by pre-cycling for less than about 55 percent of the expected life when Miner's rule is nearly verified for higher amounts of precycling.

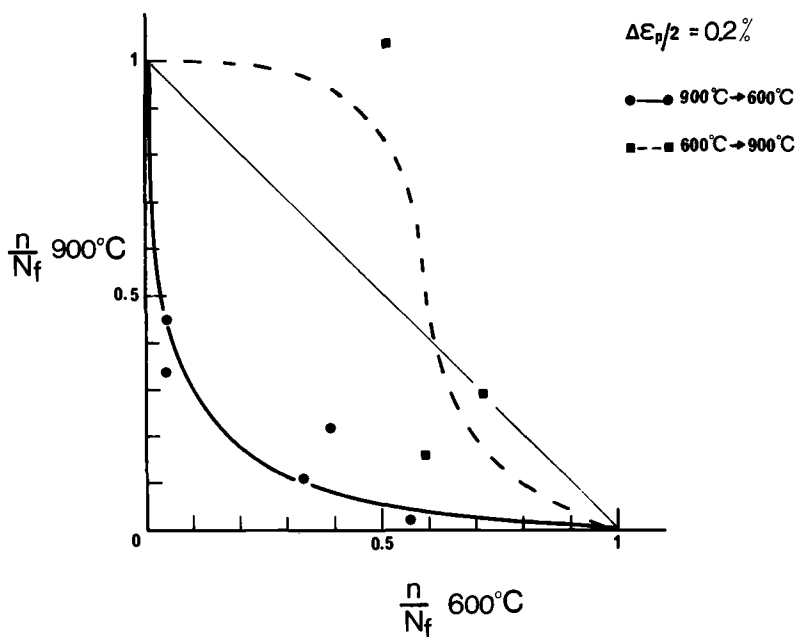


FIG. 7—Variation of the remaining life with the amount of precycling as normalized to the reference life at each temperature.

Thus the results obtained on this material showed clearly that Miner's rule is not obeyed whatever the precycling temperature, low or high. However, life predictions according to this rule are largely unconservative when cycling is first carried out at high temperatures.

Two major reasons may account for this large deviation from Miner's law. Firstly, in low cycle fatigue the number of cycles to failure encompasses both a crack initiation period usually considered as including Stage I crack growth, and a Stage II crack propagation period. The importance of the crack growth period is well known to increase in the high-temperature range [4,9]. Secondly, there is a complex interaction between the microcracking mechanisms at each temperature, which renders a linear cumulative damage rule unsound.

Therefore to rationalize the observed behavior we used extensive metallographic observations of the cracking process during fatigue cumulation, and we tried to estimate the number of cycles to crack initiation.

Metallographic Examinations for Sequential Tests

During the two temperature level tests, replicas of the gage length were taken after cycling at the first temperature, T_1 , and after the final cycling at T_2 . Observing these replicas by SEM enabled us to study how microcracks initiated at one temperature have evolved at the second temperature.

All the obtained replicas were not studied in a quantitative manner. However, two examples of sequential observations are illustrated in Fig. 8, which can be taken as representative. In these diagrams the surface crack length is plotted as a function of Miner's damage; that is, $\Sigma n/N_f = n_1/N_{f1}$ after the first cycling and $\Sigma n/N_f = (n_1/N_{f1}) + (n_2/N_{f2})$ after the final cycling. The results are shown for a specimen given 200 cycles at 900°C ($n/N_f = 0.45$) and then 150 cycles at 600°C ($\Sigma n/N_f \approx 0.50$), and for a second specimen given 2370 cycles at 600°C ($n/N_f = 0.70$) and then 130 cycles at 900°C ($\Sigma n/N_f \approx 1$). As the primary object of Fig. 8 is to illustrate the evolution of individual cracks, all the cracks of the histogram could not be represented and are thus typified by a number of cracks in each class interval. The straight lines joining two points refer to the same crack. From these lines, three kinds of behavior can be observed. Firstly, the main crack after precycling at T_1 is still the main crack or at least one of the largest cracks after cycling at T_2 . Secondly, most of the secondary cracks formed at T_1 exhibited a slow evolution at T_2 or eventually stayed dormant. Thirdly, the final cycling at T_2 may produce new cracks that did not exist after precycling.

The same conclusions applied whether the first temperature was 600 or 900°C. Nevertheless, there are differences in the relative importance of every class of crack and the total number of cracks, as can be inferred by comparing both diagrams of Fig. 8. In particular the proportion of newly initiated

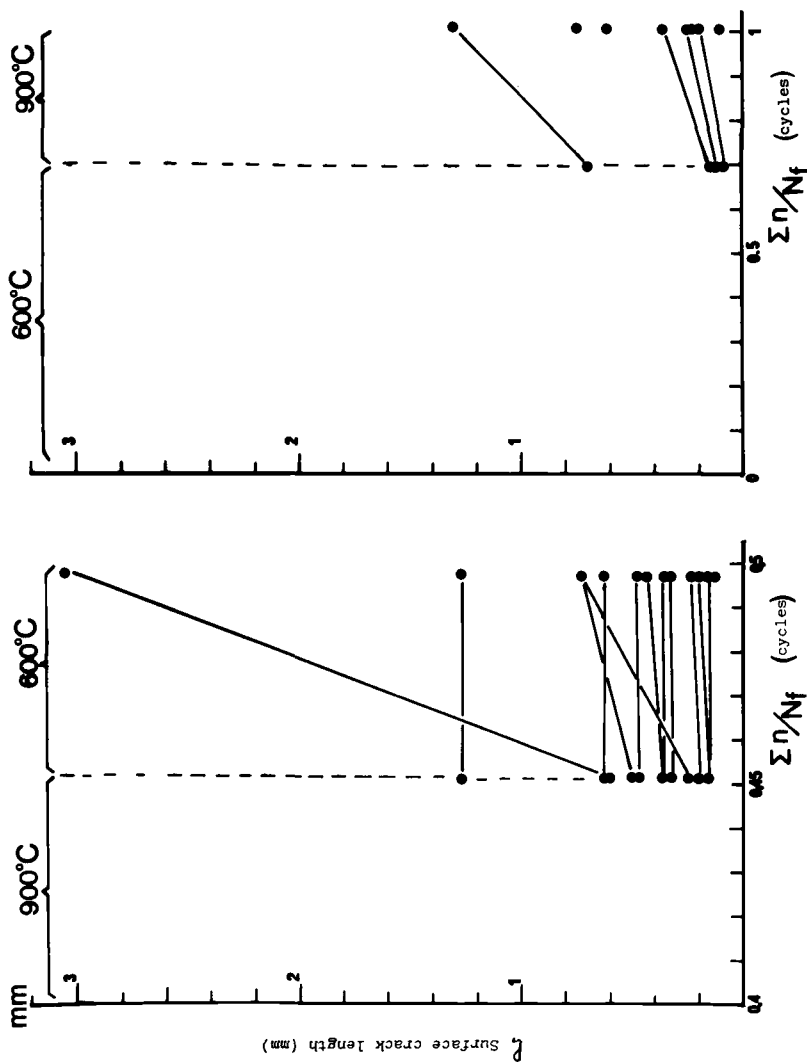


FIG 8—Variation of the surface length of individual cracks as a function of Miner's damage for the two senses of cycling. Experimental details are given in the text.

cracks is much higher with final cycling at 900 than at 600°C. But the more striking difference is in the density of microcracks per unit area formed during the first temperature level: at 600°C this density is about $3 \cdot 10^{-2} \text{ mm}^{-2}$ when it reaches 0.8 to 2 mm^{-2} at 900°C (more than an order of magnitude higher).

Strictly speaking all these observations are relevant to the propagation period of the overall life. However, the propagation is largely determined by the initiation mechanisms, which are physically different at each temperature along crystallographic planes at 600°C and along preferentially oxidized MC carbides at 900°C. Therefore cycling at 600°C for a period shorter than the number of cycles to initiation, which can be defined as corresponding to the transition between Stage I and Stage II crack growth, does not seem likely to be effective in reducing the initiation period at 900°C. In fact an early initiation at the latter temperature is expected owing to the oxidation of carbides, which should give rise to a large density of new cracks inside the carbides. This qualitative behavior is associated on a quantitative viewpoint with a much higher crack density at 900 than at 600°C. For microcracks smaller than some unknown critical size, there should be a competition between the small density of microcracks initiated at 600°C and those then initiated at 900°C; the latter cracks may be shorter but are much more numerous, and presumably may grow at a higher rate.

Precycling at 900°C induced a rapid oxidation of MC carbides, which gave rise to microcrack formation inside the carbides. As for the former case of cycling at 600°C and then at 900°C, there should be a competing process of possible initiation sites, but the large density of microcracks initiated at the highest temperature should prevail over those newly formed at 600°C and must yield a reduction in the initiation period. This mechanism is illustrated in Fig. 9 by the observation of a two temperature test where only 50 cycles were carried out at 900°C. For this amount of cycles all the initiated surface cracks are contained inside the oxidized carbide aggregate. Figure 10 refers to a secondary crack where an initial microcrack contained in a MC carbide at 900°C extends into the matrix during subsequent cycling at 600°C.

Therefore, because of the mechanisms of crack initiation and the large differences in microcrack density, a strong influence is expected on the remaining initiation period when cycling is carried out first at 900°C, and a much weaker influence is expected in the opposite case. However, as soon as the microcrack size exceeds some critical value—that is, in the propagation period—the same kind of interaction is expected whatever the temperature sequence, provided the interaction of microcracks remains of minor importance.

Definition of a Crack Initiation Period and Its Application to Life Prediction

These metallographic observations yield a physical understanding of the deviation from Miner's rule. However, it is necessary to estimate the respec-

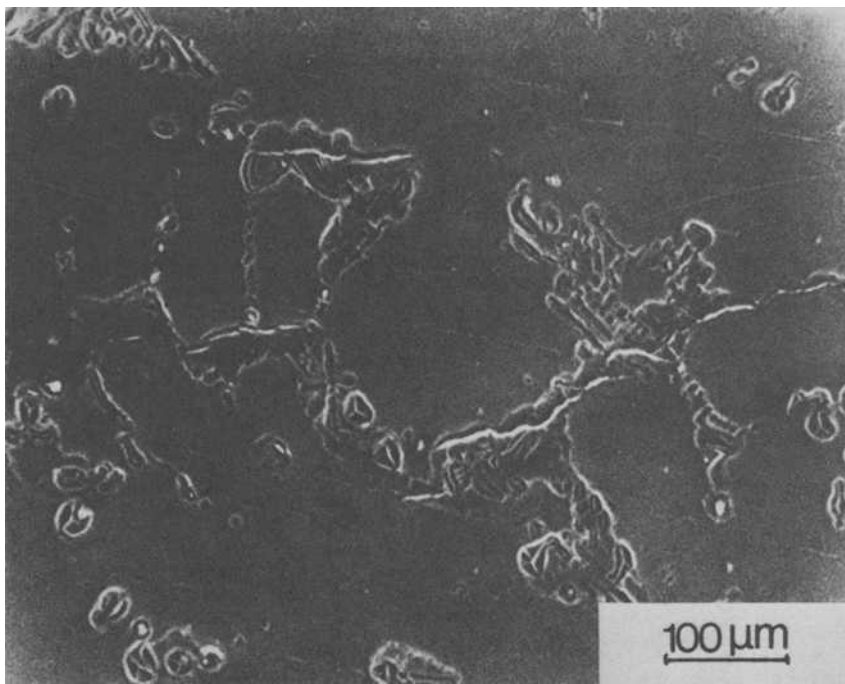


FIG. 9—Evolution of microcracks during sequential testing after 50 cycles at 900°C; all cracks are limited to the carbide size.

tive importance of the initiation and propagation periods. In fact the conventional fatigue life corresponds to the existence of main cracks about 1 to 2 mm in depth. This may be an initiation criterion for a designer but not for a metallurgist who is looking for cracks on the order of 0.1 mm in depth (which is often roughly the size of a microstructural feature such as a grain size or a dendrite arm spacing or a carbide size in the present case). It is generally difficult to determine directly the number of cycles corresponding to such a size. However, using a potential drop technique, we found that a conventional initiation period could be defined that corresponds to crack sizes of about 0.2 to 0.3 mm in depth, with sufficient reproducibility. The corresponding values for the reference tests at a strain range $\Delta\epsilon_p/2 = 0.2$ percent are given in Table 2 with a 90 percent confidence interval. This initiation period at 600°C is about 1900 cycles for a fatigue life of 3360 cycles (that is, 57 percent of the total life) and at 900°C is only 140 cycles against 440 cycles that is, 32 percent of the total life). Therefore the propagation period becomes dominant at the higher temperature, and the difference in overall fatigue life results in part from variations in the propagation period, but mostly from a reduction of the initiation period within a factor of 13.

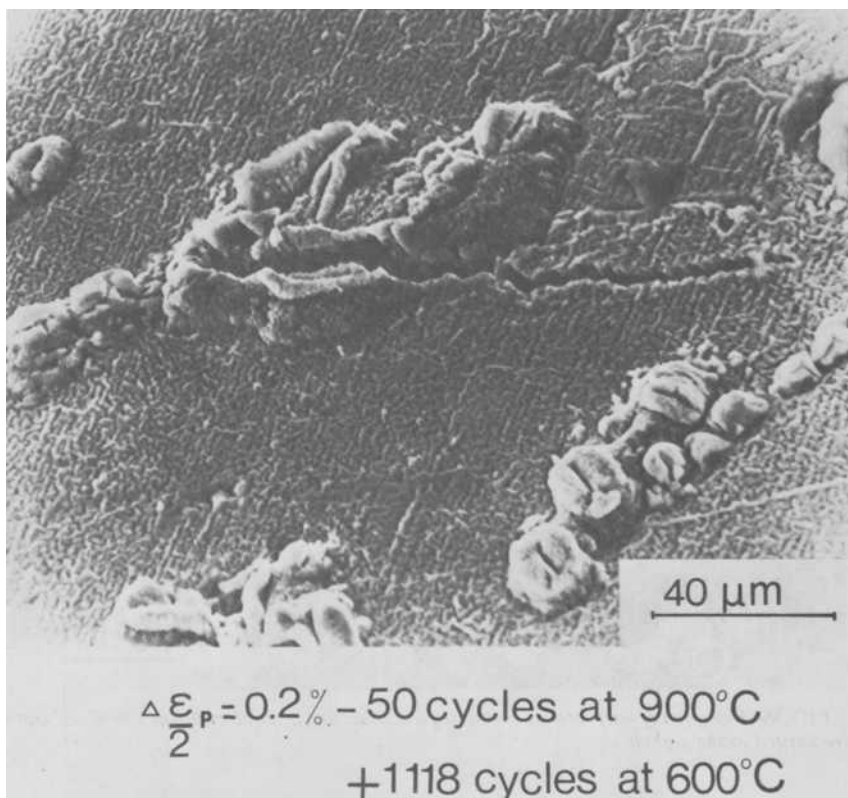


FIG. 10—Evolution of microcracks during sequential testing after 50 cycles at 900°C (Fig. 9) and after 1118 further cycles at 600°C; a secondary crack extends from the carbide into the matrix.

Taking into account the relative importance of initiation and propagation, one may reasonably consider that the deviation from Miner's rule is partly owing to the importance of the crack propagation period.

In addition, we determined this number of cycles to initiation for all the two temperature level tests. The corresponding initiation lives are reported in Fig. 11 using initiation cycles normalized to the expected life to initiation; that is, similar to Fig. 7 for initiation instead of total fatigue life. But in contrast to the previous case, the remaining initiation life obtained at 600°C after a first cycling at 900°C is within the experimental accuracy, in good agreement with Miner's rule. Despite its simplicity, the linear damage rule accounts for the influence of carbide oxidation and of a very large density of initiation sites on the subsequent initiation life at 600°C. On the other hand, the linear damage rule is not obeyed in the case of a precycling at 600°C, and the initiation life at 900°C does not seem to be altered. This behavior is in good agreement with the inferences made from the metallographic study.

Thus in all cases Miner's rule even if not obeyed yields a conservative pre-

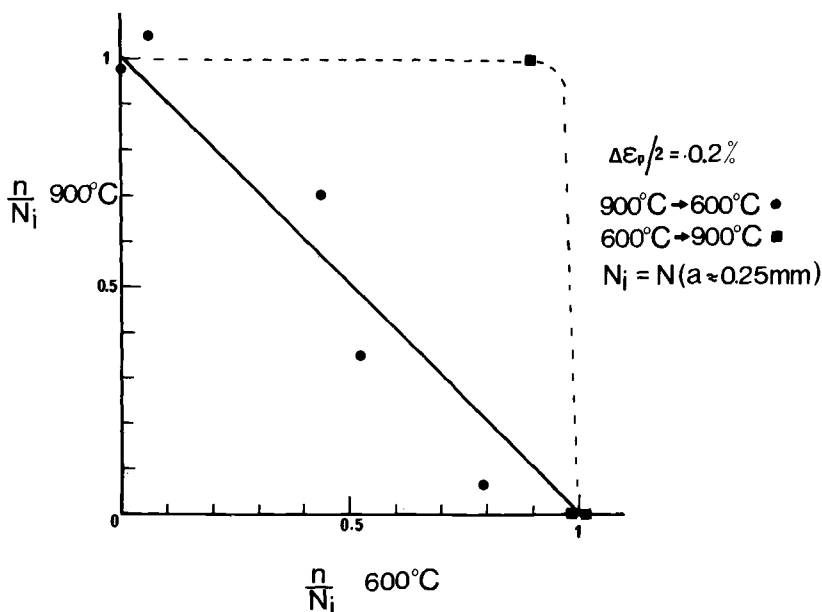


FIG. 11—Variation of the remaining life to initiation with the amount of precycling as normalized to the reference life to initiation at each temperature.

diction for the number of cycles to initiation so defined. However, it must be emphasized that there is a large modification of the remaining period of propagation after a previous cycling, and in all the cases this period was found smaller than that predicted from Miner's rule as applied to the crack propagation periods.

The applicability of Miner's rule as a predictive method that accounts for the temperature dependence of low-cycle fatigue damage has been checked as illustrated in Fig. 12. When the overall life N_f is predicted from the damage rule as applied to the expected total lives at 600 and 900°C, one observes good agreement with the experimental values when cycling first at 600°C, but the prediction is largely unconservative after precycling at 900°C since it can overestimate the fatigue life by a factor of 6. The overestimation is larger the higher the number of cycles at 900°C. One must remember, however, the strong reduction in the crack propagation period after previous cycling. Thus in order to obtain a reliable and conservative prediction it seems reasonable to neglect the crack propagation period. Therefore one may try to estimate the overall life N_f by assuming N_f to be equal to N_i and by then applying a linear cumulative rule to the expected initiation lives at each temperature. As shown in Fig. 12, the prediction of N_f is now conservative within an error of 10 percent, and at most the underestimation of life is within a factor of 2 for a precycling at 900°C. This implies that in order to make a reliable prediction of the remaining life under various temperature

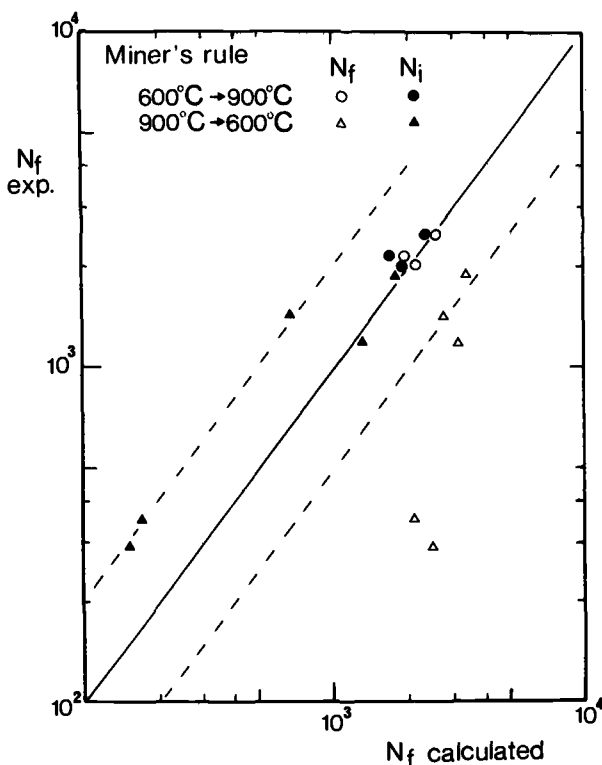


FIG. 12—Comparison between the observed experimental life and that predicted from the application of Miner's rule either to the total life N_t or to the initiation period N_i .

loadings, the actual resistance to low-cycle fatigue damage to consider is not the overall life but merely the initiation period.

Conclusions

The present study has examined the cumulation of low-cycle fatigue damage in the superalloy MarM509 under sequential testing at two temperature levels [600 and 900°C (873 and 1173 K)] where the initiation mechanisms are very different, mainly by crystallographic cracking at 600°C and by carbide oxidation at 900°C.

A large deviation from the linear cumulative damage rule was observed, especially for a precycling at 900°C. This behavior was qualitatively explained by a study of the initiation mechanisms and the microcracking process. The importance of the higher crack density at the higher temperature has been emphasized.

By using a potential drop technique for determining the number of cycles to initiation, Miner's rule was found to apply for the initiation period for a

precycling at 900°C. On the other hand, this initiation period seems to be unaltered by previous cycling at 600°C.

These results showed that for the cumulation of damage at various temperatures, the resistance to low-cycle fatigue damage to consider is not the conventional fatigue life, but the duration of the initiation period.

This study is in agreement with the common idea that high-temperature low-cycle fatigue is more damaging than low-temperature fatigue, for a same strain level. However, in the particular material studied, this effect seems to result mainly from an oxidation effect rather than from a creep-fatigue interaction.

References

- [1] Spera, D. A. in *Fatigue at Elevated Temperatures, ASTM STP 520*, American Society for Testing and Materials, 1972, pp. 648-657.
- [2] Taira, S. in *Fatigue at Elevated Temperatures, ASTM STP 520*, American Society for Testing and Materials, 1972, pp. 80-101.
- [3] Halford, G. R. and Manson, S. S. in *Thermal Fatigue of Materials and Components, ASTM STP 612*, D. A. Spera and D. F. Mowbray, Eds., American Society for Testing and Materials, 1976, pp. 239-254.
- [4] Reuchet, J., and Rémy, L., *Fatigue of Engineering Materials and Structures*, Vol. 2, 1979, pp. 51-62.
- [5] Coutsouradis, D., Drapier, J. M., Dupont, C., Habraken, L., and Leroy, V., *Cobalt*, Vol. 41, 1968, pp. 199-213.
- [6] Biss, V., *Journal of Testing and Evaluation*, Vol. 5, 1977, pp. 217-223.
- [7] Reuchet, J., and Rémy, L., unpublished work, Centre des Matériaux, Evry, France, 1978.
- [8] Chalant, G. and Rémy, L., *Acta Metallurgica*, Vol. 28, 1980, pp. 75-88.
- [9] Skelton, R. P., *Materials Science and Engineering*, Vol. 32, 1978, pp. 211-219.

Low-Cycle Fatigue Damage Mechanisms in Body-Centered-Cubic Materials

REFERENCE: Magnin, T. and Driver, J. H., "Low-Cycle Fatigue Damage Mechanisms in Body-Centered-Cubic Materials," *Low-Cycle Fatigue and Life Prediction, ASTM STP 770*, C. Amzallag, B. N. Leis, and P. Rabbe, Eds., American Society for Testing and Materials, 1982, pp. 212-226.

ABSTRACT: The mechanisms of low-cycle fatigue damage of two high-purity ferritic alloys, Fe-3Si and Fe-26Cr-1Mo, have been investigated at room temperature using both polycrystal and single crystal specimens. The cyclic stress-strain behavior and the fatigue crack initiation mechanisms are shown to be sensitive to the applied strain rate and the crystal orientation. In the case of single crystals, high strain rates ($\geq 10^{-3} \text{ s}^{-1}$) give rise to large cyclic stress asymmetries and crystal shape changes. In bicrystals and polycrystals the cyclically induced grain distortions lead to intergranular crack initiation. Low cyclic strain rates favor the formation of persistent slip bands and hence transgranular crack initiation and reduced fatigue lives. These results are interpreted as a consequence of the asymmetry of dislocation motion in the body-centered-cubic (bcc) lattice.

Other unusual features of the cyclic deformation of bcc alloys, such as the softening and hardening behavior at low amplitudes and deformation banding, are described and discussed.

KEY WORDS: fatigue, high strain, ferritic alloys, crack initiation mechanisms, cyclic hardening, polycrystals, bicrystals, single crystals

Although the behavior of different materials during cyclic deformation has been widely studied in recent years, surprisingly little attention has been paid to the specific mechanisms of fatigue damage in body-centered-cubic (bcc) materials, and, in particular, to iron-based ferritic alloys. It is well known, from monotonic tests, that the mechanical response of such materials is very sensitive to the strain rate (or the temperature) and the presence of alloying elements both interstitial and substitutional. Furthermore, bcc crystals are known to exhibit an asymmetric behavior in tension and compression [1].² These characteristics are expected to strongly influence the

¹ Ecole des Mines de Saint-Etienne, Saint-Etienne, France.

² The italic numbers in brackets refer to the list of references appended to this paper.

cyclic stress-strain response, the specific damage mechanisms, and the fatigue resistance of the material. In this context several recent studies have examined the cyclic plasticity of high-purity niobium [2,3], molybdenum [4,5] and iron [3,6,7] single crystals.

This paper presents results of room-temperature cyclic plastic deformation tests on two different iron-based, essentially single-phase substitutional ferritic alloys, namely Fe-3Si and Fe-26Cr-1Mo. The respective influences of strain amplitude and strain rate on these different materials are described. The asymmetrical mechanical behavior of the grains (that is, the stress asymmetry and the shape changes) is examined by means of tests on oriented single and bicrystals. Finally, the different modes of fatigue crack initiation observed in polycrystalline silicon-iron and iron-chromium are discussed in terms of the basic mechanisms that govern the cyclic plasticity of these ferritic alloys.

Experimental Procedure

The compositions, in weight percent, of the two steels are as follows: (1) Fe-(25.5 to 26.1)Cr-(0.94 to 1.15)Mo, containing about 15 ppm carbon and 25 ppm nitrogen; and (2) Fe-(2.5 to 3)Si, containing 30 ppm carbon and 10 ppm nitrogen. Single crystals of the Fe-Si and Fe-Cr alloys were grown by controlled solidification in horizontal furnaces. Some Fe-26Cr-Mo bicrystals were produced either by controlled solidification using two seed crystals or by electron beam welding two oriented single crystals [8].

The single crystal fatigue specimens, with a square cross section of side 4 mm and a gage length of 10 mm, were obtained by spark cutting. After the appropriate heat treatment they were brazed into threaded shoulders and electropolished before testing.

The different heat treatments used to control the interstitial content, and, in the case of the cylindrical polycrystalline specimens, to ensure a relatively fine grain size, were as follows: (1) Fe-3Si (polycrystal), annealed 16 h at 800°C *in vacuo*, grain size $\approx 60 \mu\text{m}$; (2) Fe-3Si (single crystal), annealed 16 h at 1200°C *in vacuo*; (3) Fe-26Cr-1Mo (polycrystal), annealed 800°C *in vacuo* 16 h, then 30 min at 950°C in argon and water quenched, grain size $60 \mu\text{m}$; and (4) Fe-26Cr-1Mo (single crystal), annealed 1200°C *in vacuo* 16 h and slow cooled, then solution treated at 950°C for 30 min in argon and water quenched.

Symmetrical tests in tension-compression were carried out at constant strain rate (in the range of $2 \cdot 10^{-6}$ to $2 \cdot 10^{-1} \text{ s}^{-1}$) under total strain control using a servo-hydraulic machine. The strain was measured with a strain gage extensometer mounted directly on the gage length. Liquid metal grips were used for specimen positioning and alignment. Further details of the testing techniques have been published elsewhere [9].

Results

Cyclic Stress-Strain Response

The changes in the cyclic stress levels at $\dot{\epsilon}_T = 2 \cdot 10^{-3} \text{ s}^{-1}$ of the polycrystal Fe-Si and Fe-Cr alloys are shown in Figs. 1a and 1b as a function of the cumulative plastic strain ϵ_{pcum} ($= 2N\Delta\epsilon_p$) for two different strain amplitudes ($\Delta\epsilon_T/2 = \pm 0.2$ percent and ± 0.6 percent). Both alloys show somewhat similar behavior: at high plastic strain amplitudes ($\Delta\epsilon_p \sim 10^{-2}$) the usual rapid hardening is followed by a slight softening; conversely, at low plastic strain amplitudes ($\Delta\epsilon_p \sim 10^{-3}$), the annealed alloys initially soften, then, in certain cases, may harden before saturation. It should be noted, however, that the softening phase is relatively short for silicon-iron and prolonged for Fe-26Cr. This unusual initial softening behavior has also been observed on low-carbon steels [10] and Fe-30ppm C single crystals cycled at $\Delta\epsilon_p$ -values between 4×10^{-4} and 6×10^{-3} [3]. Similar effects are observed on all the iron-chromium single crystals, but only on certain orientations of the silicon-iron crystals.

Typical cyclic hardening curves of the $\langle 100 \rangle$ and $\langle 011 \rangle$ Fe-Si and the $\langle 100 \rangle$ Fe-Cr crystals, at the same total strain amplitude, are illustrated in Figs. 2a to 2c and demonstrate the following important features:

1. At low strain amplitudes all the Fe-Cr crystals soften then harden, as in the case of the polycrystalline Fe-Cr (Fig. 2a).

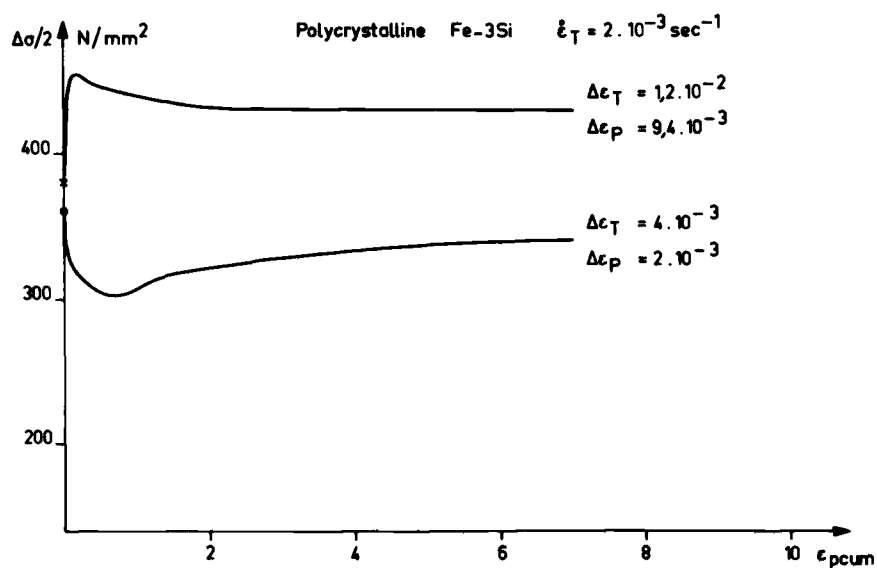


FIG. 1a—Variation of the peak cyclic stress of Fe-3Si with cumulative plastic strain at $\dot{\epsilon}_T = 2 \cdot 10^{-3} \text{ s}^{-1}$.

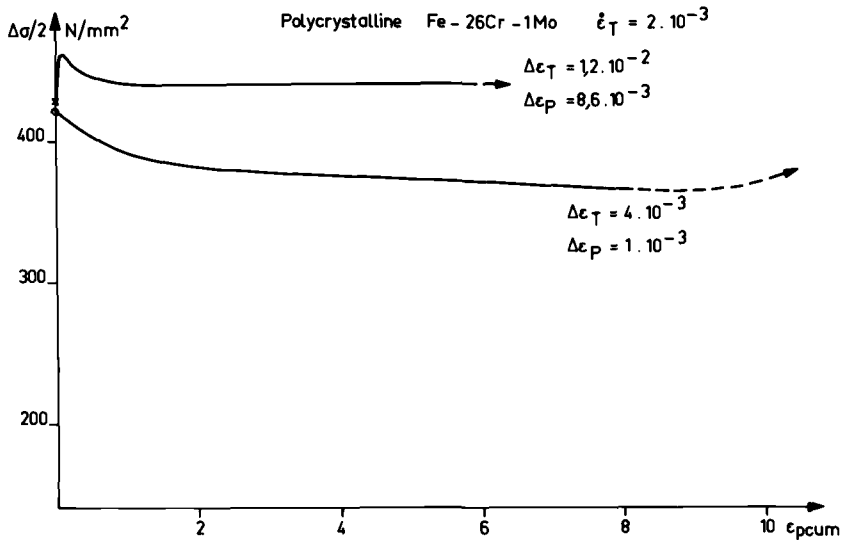


FIG. 1b—Variation of the peak cyclic stress of Fe-26Cr-1Mo with cumulative plastic strain at $\dot{\epsilon}_T = 2 \cdot 10^{-3} \text{ s}^{-1}$.

2. The Fe-3Si crystals either harden normally (Fig. 2b) or soften then harden—for example, the $[112]$ orientation [11]. In one particular case, however, namely the $[001]$ orientation for which the plastic strain amplitude was very small (6×10^{-4}), neither significant hardening nor softening was detected (Fig. 2c).

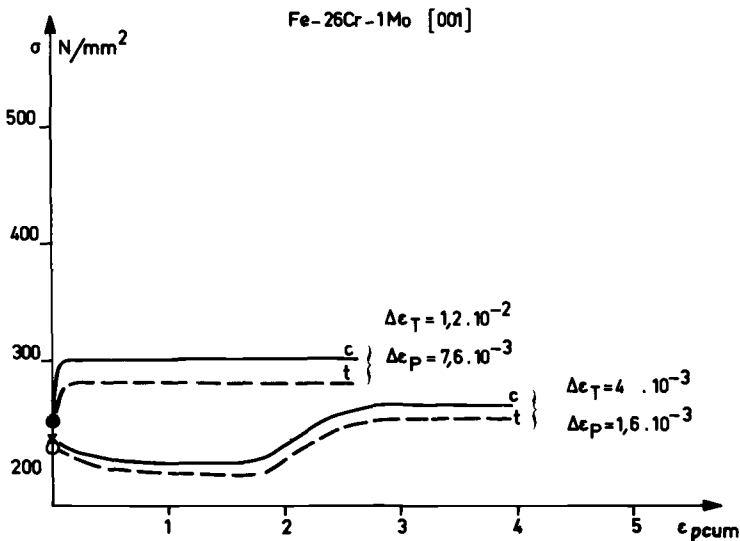


FIG. 2a—Variation of the cyclic tensile and compressive stresses of Fe-26Cr-1Mo $[001]$ single crystals with $\epsilon_{p \text{ cum}}$, $\dot{\epsilon}_T = 2 \cdot 10^{-3} \text{ s}^{-1}$.

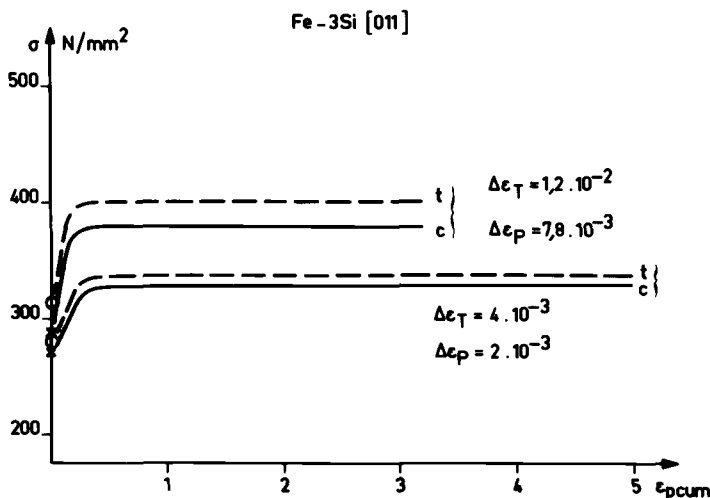


FIG. 2b—Variation of the cyclic tensile and compressive stresses of Fe-3Si [011] single crystals with ϵ_{pcum} , $\dot{\epsilon}_T = 2 \cdot 10^{-3} \text{ s}^{-1}$.

3. A stress asymmetry between tension and compression is frequently observed.

The low strain amplitude softening of the Fe-Cr crystals, extending over cumulative plastic strains of 2 or 3, is usually followed by a hardening phase, so that saturation is only attained for ϵ_{pcum} values of 3 or higher. Furthermore, only the final plateau appears to be a stable state. If cycling is stopped

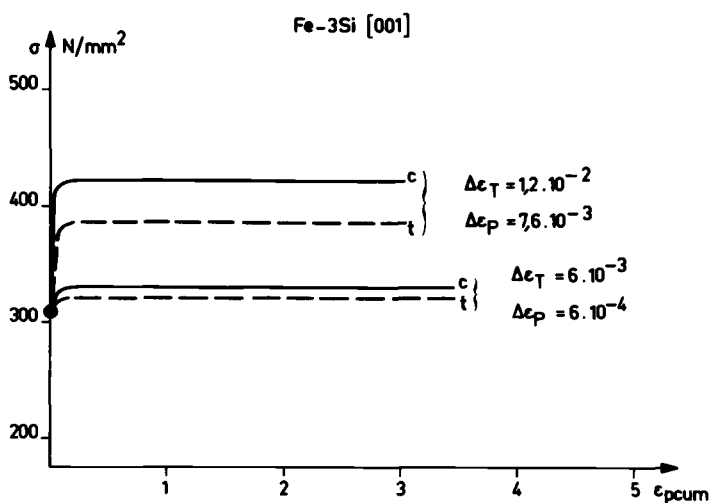


FIG. 2c—Variation of the cyclic tensile and compressive stresses of Fe-3Si [001] single crystals with ϵ_{pcum} , $\dot{\epsilon}_T = 2 \cdot 10^{-3} \text{ s}^{-1}$.

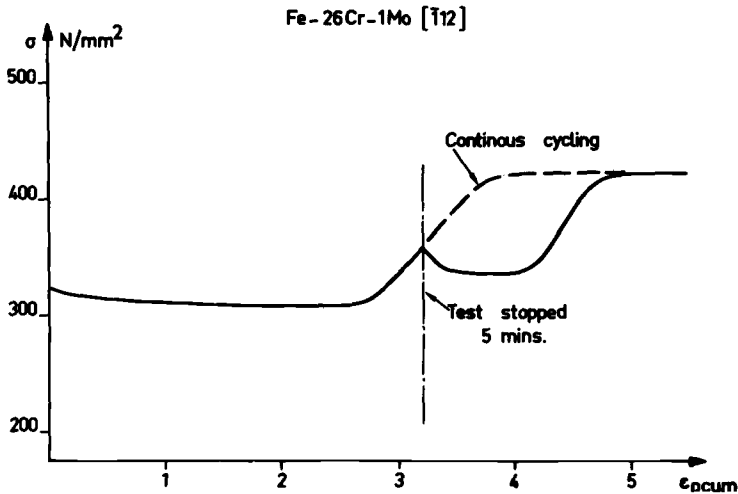


FIG. 3—Cyclic softening and hardening of a Fe-26Cr-1Mo $[112]$ crystal during interrupted and continuous cycling ($\Delta\epsilon_T = 4 \cdot 10^{-3}$; $\dot{\epsilon}_T = 2 \cdot 10^{-3} \text{ s}^{-1}$).

briefly for a few minutes during the hardening phase (Fig. 3), then restarted, softening re-occurs and the hardening is retarded, for several hundreds of cycles, to higher $\epsilon_{p \text{ cum}}$ values. Interrupting a test, when saturation is reached, only affects the subsequent peak stresses for 2 or 3 cycles before saturation is regained. It should also be pointed out that softening is sensitive to strain rate, being more pronounced at high strain rates. This softening is not related to Luders band formation, at least in single crystals, since homogeneous slip is observed throughout the specimen gage length after the first few cycles. As discussed later we attribute the softening and hardening to dislocation interstitial interactions.

The fact that the $[001]$ Fe-3Si crystals do not harden at very low plastic strain amplitudes leads to a discontinuity in the cyclic stress-strain curves (Fig. 4). In this figure, hardening is insignificant at $\Delta\epsilon_p \leq 6 \cdot 10^{-4}$ for strain rates $\dot{\epsilon}_T \sim 2 \cdot 10^{-3} \text{ s}^{-1}$. A similar absence of hardening at $\Delta\epsilon_p \sim 5 \cdot 10^{-4}$ has been reported for niobium single crystals [5] and pure iron single [6] and polycrystals [10], and may well be general to all bcc metals at low temperatures (or high strain rates). At low strain rates of $\sim 10^{-5} \text{ s}^{-1}$ (Fig. 4), the cyclic stress-strain curves become more conventional and the low plastic strain anomaly disappears. These stress effects at low strains and high strain rates are considered to be related to the relative mobility of edge and screw dislocations in the bcc lattice [5,6] and, according to Mughrabi et al [3], can directly control the fatigue limit of bcc metals and alloys.

The stress asymmetry of certain crystals, clearly shown in Figs. 2a to 2c and 4, depends upon the crystal orientation, the plastic strain amplitude, and the cyclic strain rate. The orientation effects have been previously shown

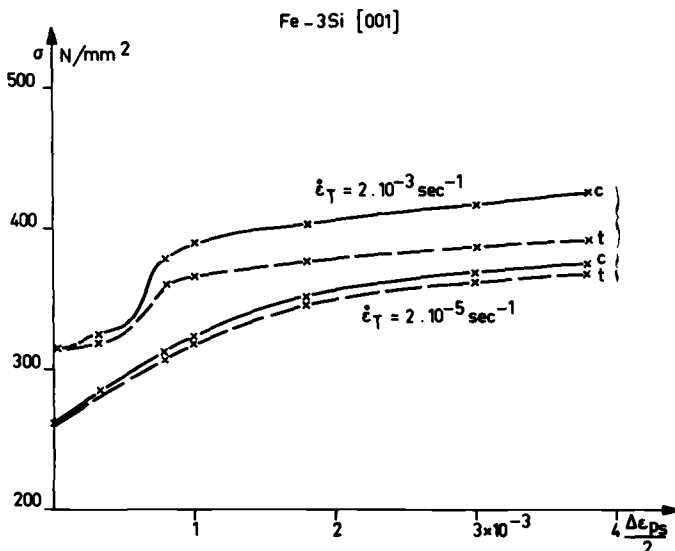


FIG. 4—Saturation stresses of Fe-3Si [001] crystals as a function of the plastic strain amplitude at two strain rates.

[9,12] to be related quite simply to the sense of slip on the active slip systems when slip occurs on systems which do not exhibit two-fold symmetry—that is, on systems other than $\{110\} \langle 111 \rangle$. Thus for the [001] Fe-Cr single crystals in tension, slip occurs on four well-defined $\{112\} \langle 111 \rangle$ systems in the easy, twinning sense; in compression, since the $\{112\}$ planes are oriented for slip in the hard, or anti-twinning sense, very wavy noncrystallographic slip is observed. Under symmetrical cyclic strain the peak stresses of the [001] Fe-Cr and Fe-Si crystals are significantly higher in compression than in tension. For the [011] crystals the opposite behavior is observed, slip being easier in compression (planar slip on $\{112\} \langle 111 \rangle$ in the twinning sense) than in tension (wavy slip in the anti-twinning sense). This slip asymmetry typical of the plastic deformation of bcc lattices, which gives rise to stress asymmetry in symmetrical strain control, will cause *strain* asymmetry in symmetrical load control. Figures 5a and 5b illustrate this behavior for the case of [001] and [011] Fe-3Si crystals. In Fig. 5a the [001] crystal deforms more easily in tension than in compression and thus, when cycled at constant load, will elongate slightly at each cycle (the loop shifts to the right). Since stress asymmetry is a permanent effect (Figs. 2a to 2c and 4), over thousands of cycles very large elongations are possible. The [011] crystals cycled at the same stress level will, on the other hand, contract in length since slip is easier in compression (Fig. 5b). The asymmetry is also clearly revealed by the shape of the hysteresis loops in load control: pointed in compression for [001] and in tension for [011]. The pointed part of the loop corresponds to the stress sense

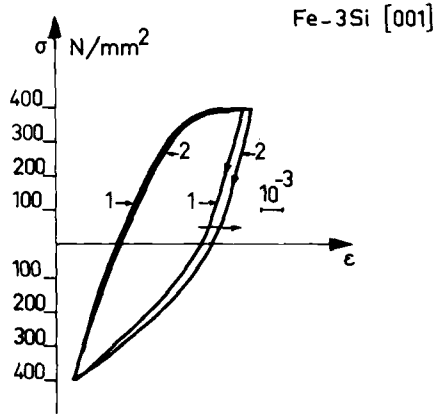


FIG. 5a—Typical shapes of the saturation cyclic hysteresis loops of Fe-3Si [001] single crystals under symmetric load control (0.5 Hz).

for which σ is highest in symmetrical strain control—that is, the hard sense of shear.

It should also be noted that the cyclic stress asymmetry is reduced at low strain amplitudes (Figs. 2a to 2c and 4) and low strain rates (Fig. 4).

Influence of Strain Rate—Strain-rate effects are particularly important during the cyclic plastic deformation of bcc metals at relatively low temperatures. As a general rule high strain rates lead to high cyclic flow stresses, large stress and slip asymmetries, but relatively lower amounts of cyclic hardening. An example of the influence of strain rate on the cyclic stress-strain curves of the polycrystalline Fe-26Cr alloy is shown in Fig. 6. The saturation stresses are significantly higher at strain rates $\sim 10^{-2}$ than 10^{-5} s^{-1} ; the effect is particularly marked at low strain amplitudes and relatively minor at large

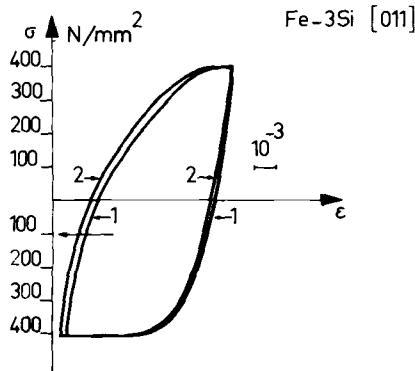


FIG. 5b—Typical shapes of the saturation cyclic hysteresis loops of Fe-3Si [011] single crystals under symmetric load control (0.5 Hz).

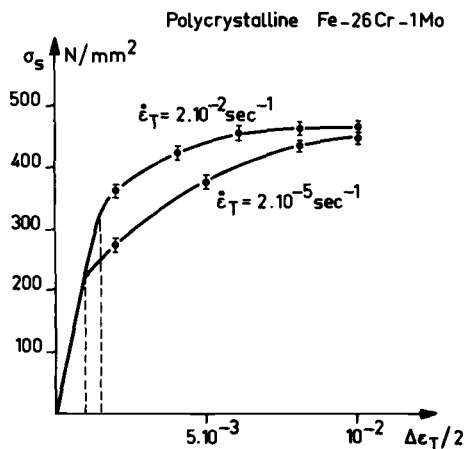


FIG. 6—Influence of strain rate on the saturation cyclic stresses of polycrystalline Fe-26Cr-1Mo.

strain amplitudes. Similar results are obtained on single crystals (see, for example, Fig. 4). In addition, the amount of cyclic hardening, compared with the initial yield stress, is higher at low strain rates than at the higher strain rates. The influence of strain rate on the saturation stresses, particularly at low strain amplitudes, together with the disappearance of the low strain "plateau" region (Fig. 4), implies that strain rate would have a pronounced effect on the fatigue limits of bcc materials [6].

Finally, as previously noted, decreasing the strain rate decreases the stress asymmetry, as shown in Fig. 4. This behavior has been described by the authors in further detail [9] and is owing to the influence of the strain rate on the ability of dislocations to change slip planes when stressed in different senses.

Crystal Shape Changes—The operation of different slip systems in tension and compression leads to mass displacements that are different in tension and compression—that is, to a change in shape of the crystal when deformed cyclically under symmetrical strain control. The grain shape change per cycle is relatively small (typically in the range of 10^{-4} to 10^{-3}), but, since the process is continuous throughout cycling, becomes significant over large numbers of cycles. The shape changes of cyclically deformed bcc crystals have been studied in detail on niobium [2,5], iron [7], and Fe-26Cr-1Mo [9,13]. An example of the change in cross section of an initially square section [011] Fe-26Cr crystal at $\epsilon_{pcum} = 2$ is shown in Fig. 7. Maximum diametral plastic strains on the order of 0.3 or higher are frequently encountered. The shape changes can be related quantitatively to the slip systems that operate in tension and compression and depend sensitively on the crystal orientation. Finally, it is important to note that, yet again, the strain rate and the strain amplitude have

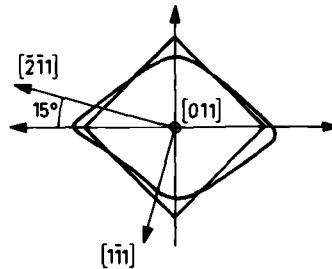


FIG. 7—Cross-sectional shape change of an Fe-26Cr-1Mo [011] crystal cycled under symmetrical strain control at $\Delta\epsilon_T = 1.2 \cdot 10^{-2}$ ($\epsilon_{pcum} = 2$; $\dot{\epsilon}_T = 2 \cdot 10^{-3} \text{ s}^{-1}$).

a pronounced effect on the phenomenon; for a given value of ϵ_{pcum} *shape change is large at high strain rates* ($\geq 10^{-3} \text{ s}^{-1}$) *and high plastic strains* ($\sim 10^{-3}$), but can be very small at low strain rates and very small plastic strains [5,7,9,13].

Crack Initiation Mechanisms

The large crystal shape changes that take place during cyclic straining of bcc materials (at high $\dot{\epsilon}_T$ and $\Delta\epsilon_p$) can be expected to influence the fatigue crack mechanisms of polycrystals. To relate the single crystal behavior to that of polycrystalline material we have studied the influence of strain rate on cyclically deformed oriented bicrystals of the Fe-26Cr-1Mo alloy.

The bicrystals were oriented so that the stress axis was contained in the boundary plane and the individual grains had orientations $A = [31, 33, 89]$ and $B = [10, 21, 97]$ (misorientation 15 deg). For both grains the boundary plane was close to {011}. Tests were performed at a strain amplitude $\Delta\epsilon_T/2 = 10^{-2}$ and at two different strain rates, $2 \cdot 10^{-3}$ and $2 \cdot 10^{-5} \text{ s}^{-1}$. Both grains were orientated so that slip on the {112} <111> and {123} <111> systems was easier in tension than in compression. Consequently at $\dot{\epsilon}_T = 2 \cdot 10^{-3} \text{ s}^{-1}$ the bicrystal exhibited a stress asymmetry, $\sigma_e > \sigma_c$, but exhibited an insignificant stress asymmetry at $\dot{\epsilon}_T = 2 \cdot 10^{-5} \text{ s}^{-1}$ in agreement with the single-crystal results.

At the lower strain rate, homogeneous slip and profuse cross-slip was observed by optical microscopy throughout both crystals and no extra slip was detected in the boundary region, indicating the absence of large plastic incompatibilities. Continued cycling led to transgranular crack initiation without any apparent effect on the grain boundary (Fig. 8a). At the higher strain rate, planar slip was observed in the grains and additional slip systems were clearly visible within about 0.1 mm of the boundary. After continued cycling, the region adjacent to the grain boundary became extremely rumpled and eventually intergranular cracks developed at the boundary (Fig. 8b). The fact that the prominent surface relief effects were only observed near the boundary at high strain rates means that they were caused by

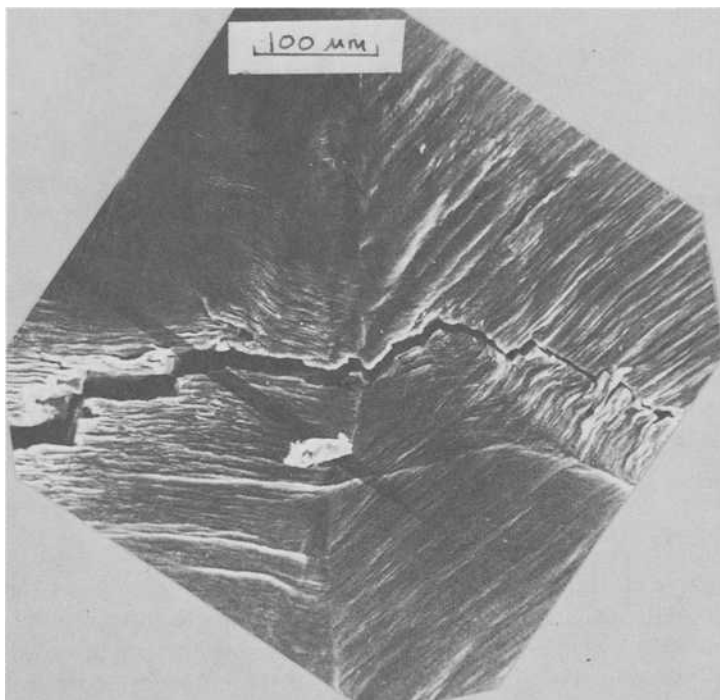


FIG. 8a—Fatigue crack initiation modes in an Fe-26Cr-1Mo bicrystal (SEM of the specimen surface); transgranular at $\dot{\epsilon}_T = 2 \cdot 10^{-5} \text{ s}^{-1}$.

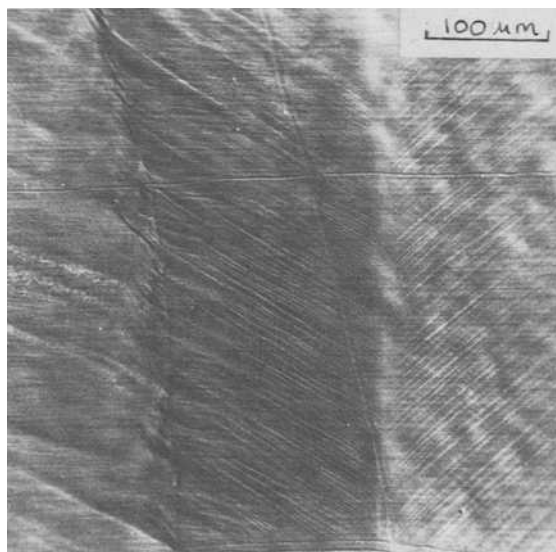


FIG. 8b—Fatigue crack initiation modes in an Fe-26Cr-1Mo bicrystal (SEM of the specimen surface); intergranular at $\dot{\epsilon}_T = 2 \cdot 10^{-3} \text{ s}^{-1}$.

the grain shape changes during cycling and not by the well-known monotonic elasto-plastic boundary incompatibilities. (Furthermore the elasto-plastic incompatibilities of grains A and B were calculated to be relatively small, as confirmed by the absence of boundary secondary slip at low strain rates).

The single crystal and bicrystal results are also in very good agreement with the crack initiation modes observed on polycrystal Fe-30 ppm C [13], Fe-3Si, and Fe-26Cr-1Mo. In all cases fatigue crack initiation was intergranular at high strain rates ($\dot{\epsilon}_T$ on the order of 10^{-2} s^{-1}) and transgranular at low strain rates.

Other examples of the influence of strain rate on the crack initiation mechanisms of α -Fe [14], Fe-Si, and Fe-26Cr have been reported [9]. The critical strain rate at which the transition from transgranular to intergranular initiation occurs depends upon the alloy composition, the strain amplitude, and the grain size [13].

Transgranular fatigue crack initiation, an example of which is shown in Fig. 8a, usually occurs along the intrusions and extrusions formed in association with the persistent slip bands (PSB). Mughrabi [3] has suggested that PSB formation in high-purity bcc materials would be rather difficult owing to the particular dislocation substructure developed during fatigue of bcc metals. PSBs would only be likely to form under conditions of low strain rates (or high temperatures) and significant interstitial contents. Our results on all these steels are in good agreement with this suggestion; intrusions and extrusions favoring transgranular crack initiation occur predominantly at low strain rates. Well-defined PSBs are not observed at high strain rates in any of the steels.

Since PSB formation promotes fatigue crack initiation, it is therefore understandable that fatigue lifetimes at low strain rates should be lower than those at high strain rates. In fact the fatigue lifetimes of Fe-Cr polycrystals at $\dot{\epsilon}_T \sim 10^{-4} \text{ s}^{-1}$ are about half those at $\dot{\epsilon}_T \sim 10^{-2} \text{ s}^{-1}$. It is also probable that this difference in fatigue resistance would be appreciably higher if intergranular cracking caused by crystal shape changes did not intervene at high strain rates.

PSB formation is not the only mechanism of transgranular crack formation in bcc materials. Strain localization can also occur in deformation bands such as kink bands or shear bands. In single crystals these bands are easily distinguishable from the PSBs, since they do not follow the trace of the primary slip plane. They have been observed as kink-like bands in niobium [15] and iron [3] and as shear bands for particular crystal orientations in Fe-3Si and Fe-26Cr-1Mo [11]. In the latter cases, the conditions for shear band formation could be related to a critical amount of cyclic hardening, and consequently shear bands only formed in crystals oriented within $\sim 20^\circ$ of $\langle 111 \rangle$. Fatigue lives were drastically reduced when shear band formation occurred. It seems reasonable to suggest that this type of failure mechanism could also occur in polycrystalline material.

Discussion and Conclusions

The results have clearly shown that bcc materials exhibit specific cyclic stress-strain behavior and fatigue crack initiation mechanisms which can be related to the detailed mechanisms of slip in bcc materials. Both the monotonic and cyclic plastic deformation of bcc alloys are characterized by the particular slip geometry and by the pronounced dependence on strain rate and solute elements.

For example, cyclic softening (often followed by hardening) of the annealed, essentially single-phase alloys is a common feature at low strain amplitudes. Cyclic hardening and softening are essentially related to the change in dislocation density and substructure caused by cyclic deformation. These factors can be approximately described by the athermal internal stress component σ_i of the flow stress σ :

$$\sigma = \sigma_i + \sigma^*(\dot{\epsilon}, T)$$

where σ^* , the effective stress, describes the stress required to move the dislocation through short-range obstacles.

Cyclic hardening and softening are both related to changes in σ_i [5,6,9], σ^* remaining constant at a given strain rate and temperature.

We propose that the initial softening, observed particularly in Fe-Cr, is owing to the liberation, during the first few cycles, of mobile dislocations from interstitial-substitutional solute atom complexes. Unlike a tension test, however, this phase can last for large cumulative plastic strains at low strain amplitudes (and relatively high strain rates), since the dislocation-dislocation interactions which harden the material are relatively rare events caused by the low dislocation density under these conditions, as observed by TEM [16]. Hardening follows when either secondary systems are activated or when the screw components cross-slip to increase the dislocation density and hence the internal stress σ_i . Single crystal Fe-Cr may be more prone to this softening behavior than Fe-Si, since during annealing carbon and chromium atoms tend to attract each other and form with the dislocations strongly bound C-Cr complexes or very fine precipitates unlike the mutually repulsive carbon and silicon atoms. The slight initial softening in polycrystalline Fe-Si may also be caused by segregation effects at the grain boundaries.

This behavior means that even under well-defined laboratory testing conditions the saturation flow stress, σ_s , is difficult to define. In service conditions where loading into the plastic region is rarely periodic but random (and occurs more frequently at low ϵ_p values) the σ_s values will be very poorly defined.

The asymmetrical slip that accommodates the plastic strain in bcc metals is a direct consequence of the special structure of the dislocations in the bcc lattice. The threefold symmetry of the $\langle 111 \rangle$ screw dislocations leads to

asymmetric slip, and hence the observed crystal shape changes during cyclic stressing. It now seems well established that the shape changes which bcc crystals undergo during cyclic deformation can promote intergranular cracking. This type of cracking will obviously be accelerated by the presence of impurity elements which embrittle the grain boundary. Nevertheless, it is important to realize that boundary embrittlement is not a necessary condition for intergranular fatigue crack initiation in bcc materials. This failure mechanism is a direct result of the slip asymmetry characteristic of these materials, particularly at high strain rates and strain amplitudes.

The pronounced influence of strain rate on both the cyclic stress-strain behavior and the crack nucleation mechanisms is also a consequence of the dislocation core structure. Glide only occurs when a stressed sessile screw dislocation adopts, by a thermally activated process, a glissile configuration. The process is strain-rate dependent, so that changing the strain rate changes both the effective stress and the relative mobilities of the edge and screw components. At high cyclic strain rates (or low temperatures) plastic deformation is governed by the movement of relatively immobile screw dislocations, as shown by recent transmission electron microscopy studies [6,16]. Thus high cyclic strain rates are associated with (1) high cyclic flow stresses, (2) large stress asymmetries, and (3) large crystal shape changes.

This study has concentrated on two high-purity single-phase ferritic alloys. It is probable, however, that the proposed basic mechanisms, in many ways specific to bcc alloys, would apply to less pure multiphase industrial steels.

Further studies should examine the cyclic behavior of industrial ferritic steels in the light of the specific mechanisms proposed from the single-crystal studies. It would be particularly interesting to specify in greater detail the role of the interstitial and substitutional elements and the influence of temperature.

Acknowledgments

The authors thank Dr. H. Mughrabi and Dr. F. Guiu for several useful discussions and for kindly providing manuscripts prior to publication.

References

- [1] Christian, J. W. in *Proceedings*, Second International Conference on the Strength of Metals and Alloys, Asolimar, Calif., ASM, 1970, pp. 31-70.
- [2] Neumann, R., *Zeitschrift für Metallkunde*, Vol. 66, 1975, pp. 26-32.
- [3] Mughrabi, H., Ackermann, F., and Herz, K. in *Fatigue Mechanisms*, ASTM STP 675, Jeffrey T. Fong, Ed., American Society for Testing and Materials, 1979, pp. 69-97.
- [4] Etemad, B. and Guiu, F., *Scripta Metallurgica*, Vol. 8, 1974, pp. 931-936.
- [5] Anglada, M. and Guiu, F. in *Proceedings*, Fifth International Conference on the Strength of Metals and Alloys, Aachen, P. Haasen, Ed., Pergamon, 1979, pp. 1237-1242.
- [6] Mughrabi, H., Herz, K., and Stark, X., *Acta Metallurgica*, Vol. 24, 1976, pp. 659-668.

- [7] Mughrabi, H. and Wüthrich, Ch., *Philosophical Magazine*, Vol. 33, 1976, pp. 963-984.
- [8] Cyrille, M., Rieux, P., and Passet, P. in *Second International Colloquium on Electron Beam Welding and Melting*, Avignon, France, 1978, pp. 107-112.
- [9] Magnin, T. and Driver, J. H., *Materials Science and Engineering*, Vol. 39, 1979, pp. 175-185.
- [10] Lukas, P. and Polak, J. in *Work Hardening in Tension and Fatigue*, A. W. Thompson, Ed., AIME, New York, 1977, pp. 177-205.
- [11] Magnin, T. and Driver, J. H. in *Proceedings*, Fifth International Conference on the Strength of Metals and Alloys, Aachen, P. Haasen, Ed., Pergamon, 1979, pp. 1213-1218.
- [12] Magnin, T., Driver, J. H., and Rieu, J., *Mémoires Scientifiques de la Revue de Métallurgie*, Vol. 75, No. 5, 1978, pp. 293-300.
- [13] Magnin, T. and Driver, J. H. in *Proceedings*, ICF 5, Cannes, D. Francois, Ed., Pergamon, 1981, pp. 307-313.
- [14] Mughrabi, H., *Zeitschrift für Metallkunde*, Vol. 66, 1975, pp. 719-724.
- [15] Donner, M., DiPrimio, J. C., and Salkovitz, E. I., *Acta Metallurgica*, Vol. 21, 1973, pp. 1547-1559.
- [16] Magnin, T., Fourdeux, A., and Driver, J. H., *Physica Status Solidi (A)*, Vol. 65, 1981, pp. 301-314.

Effect of Discontinuities on Low-Cycle Fatigue Behavior of NiMoV Rotor Forging Steel

REFERENCE: Miller, G. A., Shih, T-T., Reemsnyder, H. S., and Swenson, C. E., "Effect of Discontinuities on Low-Cycle Fatigue Behavior of NiMoV Rotor Forging Steel," *Low-Cycle Fatigue and Life Prediction, ASTM STP 770*, C. Amzallag, B. N. Leis, and P. Rabbe, Eds., American Society for Testing and Materials, 1982, pp. 227-253.

ABSTRACT: An assessment of the effects of discontinuities and a gaseous environment on the low-cycle fatigue behavior of NiMoV generator rotor forging steel is presented. Discontinuities were positioned near the notch root in blunt-notch compact tension specimens machined from trepanned core bars. These specimens were subjected to cyclic loading with two maximum stress/yield-stress ratios, 0.95 and 1.37. For tests conducted in air, discontinuities reduced the average crack initiation and propagation cycles by factors of as much as 6 and 1.5, respectively. The discontinuity influence was greater at the low cyclic load. Hydrogen reduced the cycles for crack propagation in discontinuity-free specimens by as much as a factor of 2 but had less influence on initiation. In specimens containing discontinuities, the crack propagation interval was shorter in hydrogen than in air, thus indicating the existence of a discontinuity-environment interaction. The variability in cycles to crack initiation from specimen to specimen was reduced by taking into account the initiation criterion as well as the discontinuity size and location with respect to the notch. The relation between discontinuities, cracks, and the service performance of generator rotors is discussed.

KEY WORDS: testing (fatigue), stress concentration, crack initiation, crack propagation, environment, discontinuities, low-cycle fatigue, ultrasonics

Nomenclature

- a* Crack length
- B* Specimen thickness
- d* Distance from notch surface to discontinuity

¹ Research Engineer and Principal Scientist, respectively, Research Department, Bethlehem Steel Corporation, Bethlehem, Pa. 18016.

² Senior Engineer, Research and Development Center, Westinghouse Electric Corporation, Pittsburgh, Pa. 15235.

³ Senior Engineer, Advanced Reactor Division, Westinghouse Electric Corporation, Madison, Pa. 15663.

K_t	Fatigue notch factor
K'_t	Specific value of K_t for a given specimen
K_t	Elastic stress concentration factor
l_o	Discontinuity length parallel to notch surface
N_a	$N_t - N_c - N_i$
N_c	Cycles from first crack detection to crack emergence on specimen side-surfaces
N_t	Cycles to end of test
N_i	Cycles to first crack detection
P_{\max}	Maximum load per cycle
P_r	Load range
R	Keyhole notch radius
S_{\max}	Maximum nominal stress per cycle
S_r	Nominal stress range
W	Specimen width
α	Parameter expressing local stress near notch root
$\sigma_{\log N_t}$	Standard deviation of the logarithms of life

With the development of fracture mechanics and nondestructive testing techniques, realistic and safe nondestructive inspection standards for power generator rotor forgings can be established [1].⁴ Current rotor acceptance practice involves deciding whether discontinuities can be tolerated, must be removed, or necessitate rejection of the forging. With improvements in ultrasonic testing methods, smaller indications can be resolved than was previously possible. The nature of the discontinuity distribution is such that the smaller indications, presumably representing small discontinuities, are more numerous than the larger ones of obvious concern. The possibility of the interaction of many small discontinuities to cause premature crack initiation has raised questions regarding the adequacy of the present acceptance procedures.

A cooperative program was undertaken by Bethlehem Steel Corporation and Westinghouse Electric Corporation to provide information concerning the effects of discontinuities on the reliability of generator rotor forgings. The program consisted of two phases. The first phase characterized the population of ultrasonic indications in bore core bars. The core bars were taken from large 4-pole generator forgings made from 3300-mm (130-in.)-diameter ingots weighing about 3.18×10^5 kg (350 ton). The number of signals, the signal amplitude, discontinuity location, and the number of groups of discontinuities were recorded. Metallographic results of this phase of the pro-

⁴The italic numbers in brackets refer to the list of references appended to this paper.

gram showed that an ultrasonic indication or cluster of indications can represent either an individual discontinuity or, what is more often the case, a discontinuity composite in which a number of microporosities and/or sulfide inclusions were near or adjacent to each other forming an irregularly shaped mass. In strict usage we are here defining a "cluster" as two or more *ultrasonic* indications within 2.5 mm (0.1 in.) of the same depth and separated by less than 12 mm (0.5 in.) in their common plane. Since the cluster was viewed in terms of its function as a discontinuity, however, we will use the latter term. Although the practical output from this first program phase was determination of specific locations within the core bars where fatigue specimens containing discontinuities could be prepared, we also gained insight into the complexities of the relation between discontinuities and ultrasonic indications.

In the second program phase we studied the effect of discontinuities on the low-cycle fatigue behavior of bore core bar material from large NiMoV rotor forgings. The effect of hydrogen on fatigue life was also studied, because hydrogen gas is currently used as a cooling medium in large generator rotors. The focus of the present paper is the comparison of fatigue results on specimens having discontinuities with those in which no discontinuities were present. Some discussion is devoted to the effect of discontinuities on the service performance of generator rotors.

Experimental Work

Materials

Specimens tested in this program were taken from trepanned bore core bars of five vacuum-cast NiMoV generator rotor forgings identified as A, B, C, D, and F. The highest and lowest levels of chemical composition, tensile properties, and impact energy of these core bars are given in Table 1. Tension and impact specimens were oriented so that the longitudinal axis and direction of crack growth were parallel to the respective tangential and radial directions in both core bar and rotor forging. The core bars had a bainitic microstructure containing globular sulfides (Fig. 1).

Specimen locations in the core bars were selected so that they contained no discontinuities (DF), "small discontinuities" (SD), or "large discontinuities" (LD). (A depth-corrected ultrasonic signal amplitude was used to give a qualitative index to discontinuity size.) Large discontinuities are represented by ultrasonic indication D2D177 (Fig. 2a). Examples of small discontinuities are given by sonic indications D2B167 and D2B139 in Figs. 2b and 2c, respectively.

TABLE 1—Chemical composition, mechanical properties, and impact energy of NiMoV rotor forging core bar material.^a

Core Bar	Chemical Composition, % by weight									
	C	Mn	P	S	Si	Ni	Cr	V	Mo	O ₂
highest	0.31	0.41	0.012	0.023	0.28	3.76	0.10	0.15	0.41	0.0022
lowest	0.18	0.32	0.007	0.009	0.25	3.50	0.06	0.12	0.27	0.0016

Core Bar	Mechanical Properties ^b			
	0.2 % Offset Yield Strength, ksi	Tensile Strength, ksi	Elongation in 1.4-in. Gage Length, %	Reduction in Area, %
highest	85.2	106.1	23.7	65.2
lowest	71.8	93.0	14.6	30.7

Core Bar	Charpy Impact Energy Absorption, ^c ft·lb			
	Test Temperature, °F			
	−50	0	75	212
highest	15.3	28.0	70.0	118.5
lowest	5.0	8.7	21.3	57.5

^a 1 in. = 25.4 mm; 1 ksi = 6.89 MPa; 1 ft·lb = 1.36 J.^b Tabulated mechanical properties represent the average of results of four cylindrical specimens from a given core bar.^c Tabulated energy values represent the average of results for at least two V-notch specimens at a given test temperature.

Fatigue Specimens and Tests

Low-cycle fatigue tests were performed on keyhole (blunt) notch compact tension specimens, (Fig. 3) for which the elastic stress concentration factor K_t was 2.1 [2]. The specimens were oriented in the CR direction;⁵ that is, the crack grows in the radial direction with respect to the parent rotor. For those specimens containing discontinuities, ultrasonic data were used to locate the notch root as close to the discontinuity as possible, that is, in the range of 0 to 1.3 mm (0 to 0.05 in.). In most cases the positioning technique was successful. In a few instances, however, a postfracture metallographic examination using optical and/or scanning electron microscopy did not reveal a discontinuity in the fracture plane even though pretest ultrasonic inspection showed indications to be present. The missing discontinuity may have been removed during machining of the keyhole notch or may have been located out of the fracture plane.

The fatigue tests were conducted in three laboratories on electrohydraulic

⁵ ASTM Test for Plane-Strain Fracture Toughness of Metallic Materials (E 399).

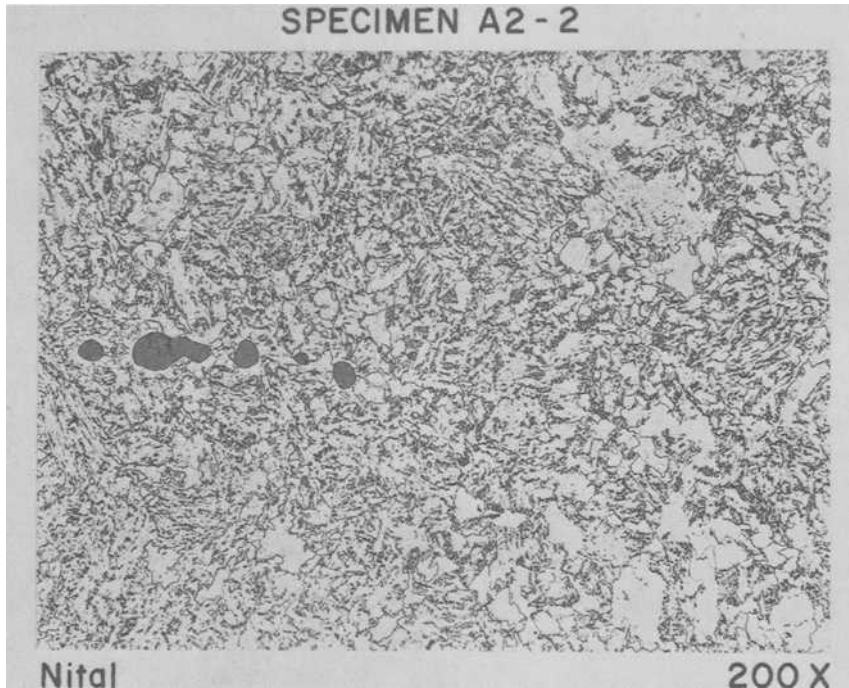


FIG. 1—Bainitic microstructure of NiMoV rotor forging core bar.

testing systems under sinusoidal tension-tension loading at a test frequency of 3 Hz. The cyclic loads were selected to give fatigue lives which were shorter and longer than that for a generator rotor in service. The maximum cyclic loads of 20.0 and 28.9 kN (4500 and 6500 lb) resulted in ratios of the nominal stress/yield stress of 0.95 and 1.37, respectively. The maximum nominal stress was computed from Eq 1 where P_{\max} is the maximum load, and W , B , and a are respectively specimen width, thickness, and crack length in Fig. 3.

$$S_{\max} = \left[\frac{3(W + a)}{W - a} + 1 \right] \frac{P_{\max}}{B(W - a)} \quad (1)$$

The minimum cyclic load was 1/10 of the maximum load for all tests. The number of loading cycles required to initiate a fatigue crack was determined by visual examination of the notch radius with a $\times 50$ telemicroscope positioned to look directly into the slot. Once the crack had emerged on the side surface, crack length was determined by measurements on both sides of the specimen. Failure was defined as either complete separation (high load) or crack extension of 5 mm (0.2 in.) beyond the notch root (low load).

For the tests carried out in a 34.5 kPa (5 psig) hydrogen gas environment, visual detection of crack initiation was made through a viewport in the environment chamber. Since a small portion of the notch root was not visible

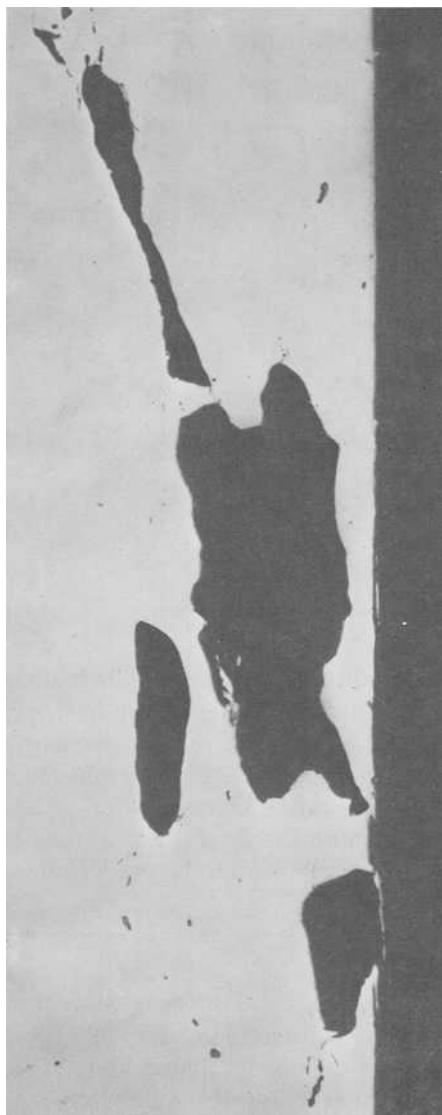


FIG. 2a—Example of discontinuities in core bar D2; D2D177; $\times 50$.

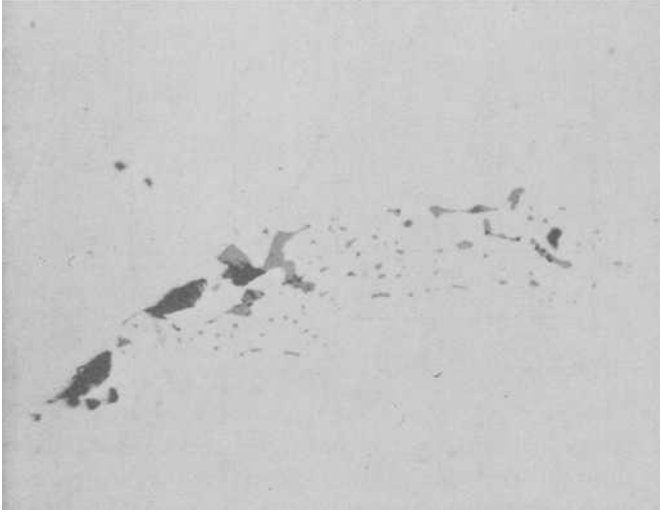


FIG. 2b—Example of discontinuities in core bar D2; D2B167; $\times 100$.

through the viewport, it was necessary to periodically disassemble the environmental chamber in order to view the entire notch root. The chamber was then reassembled and purged with nitrogen for about 30 min. After purging, the chamber was again filled with hydrogen gas and the fatigue test was resumed. Once crack initiation occurred, the test was not interrupted again and the crack length was measured from only one side of the specimen. After

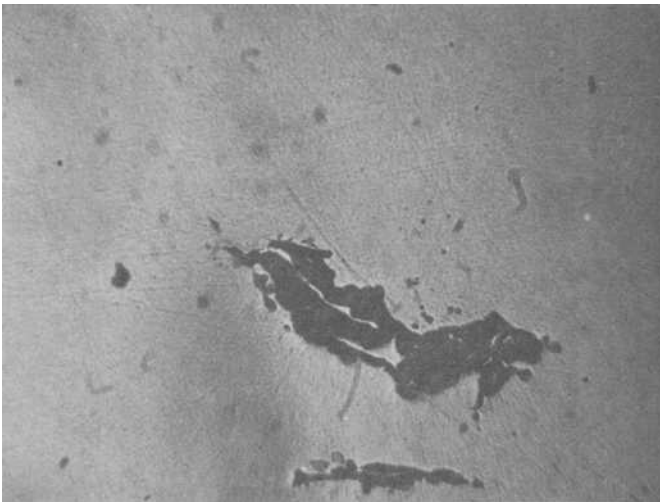


FIG. 2c—Example of discontinuities in core bar D2; D2B139; $\times 50$.

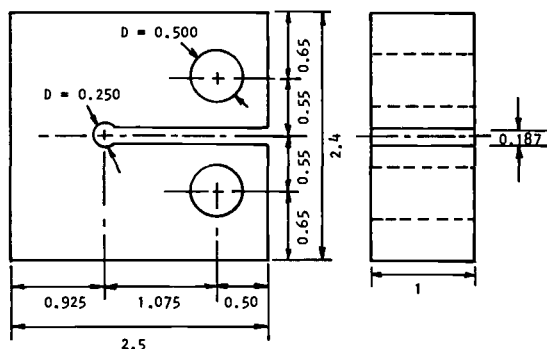


FIG. 3—Keyhole (blunt) notch compact tension specimen (dimensions in inches; 1 in. = 25.4 mm).

the crack emerged from the notch root to the specimen surface the rate of crack growth in this environment was so fast that the test frequency had to be reduced to 0.1 Hz to facilitate taking data on crack length versus cycles.

In the test program 22 discontinuity-free DF specimens, 8 SD specimens with small discontinuities, and 36 LD specimens with large discontinuities were assigned randomly to the treatment combinations (load, environment). Fatigue tests in ambient air were performed by the three participating laboratories, whereas those in hydrogen gas were run at only one laboratory.

Test Results

Figures 4 and 5 and Tables 2 and 3 present (1) cycles to first crack detection, N_i , (2) the *additional* cycles from first detection until the crack emerged⁶ to the specimen side-surface, N_c , and (3) cycles to failure, N_f .

As seen in Tables 2 and 3, differences in the experimental results obtained by the three laboratories are not very great. With the assumption that $(N_i + N_c)$ and N_f follow a log normal distribution, a t -test [3] at the 5 percent significance level was used to compare the differences in average cycles between Bethlehem and Westinghouse (LRA). The comparison showed that for two levels of cyclic load and either discontinuity-free or large-discontinuity specimens, the null hypothesis—that is, no differences in interlaboratory initiation and failure cycles—could not be rejected. Statistical comparisons of intralaboratory data showed that the effects of discontinuities and environment on low-cycle fatigue behavior were significant. Average fatigue life (antilog of $\log \bar{N}_f$) along with the cyclic intervals for initiation ($N_i + N_c$) and propagation ($N_f - N_i - N_c$) are presented in Figs. 4 and 5 for the low- and high-load tests, respectively.

⁶ Bethlehem's criterion of emergence was the cycles necessary to reach a total notch root crack length of 23 mm (0.9 in.) or 90 percent of the specimen thickness, whereas Westinghouse used the cycles for first contact of the crack with a side surface. Results for discontinuity-free materials, Tables 2 and 3, show little influence of this difference in emergence criteria.

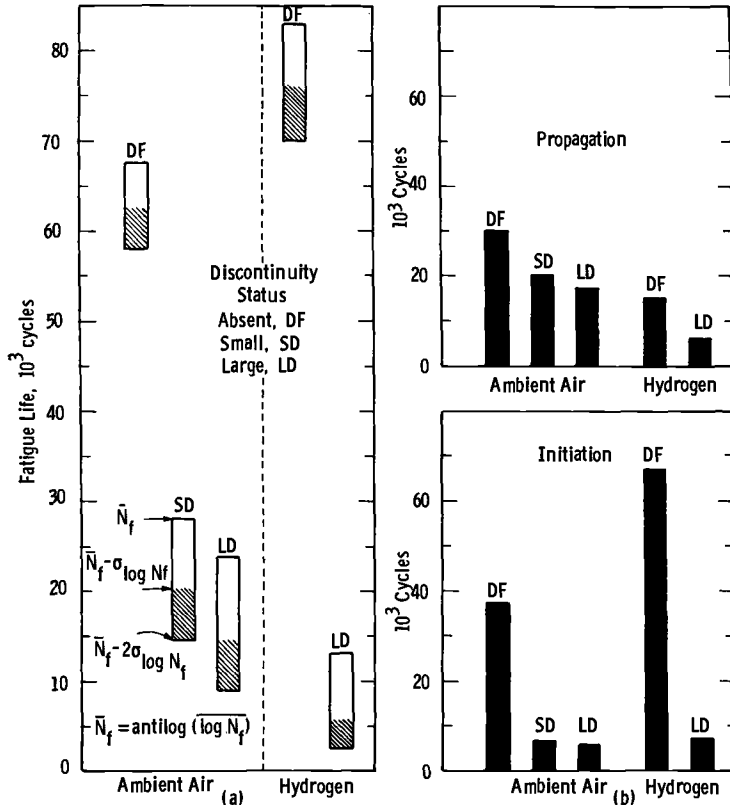


FIG. 4—Effect of discontinuities and environment on low-cycle fatigue life at a maximum cyclic load of 4500 lb (1 lb = 4.45 N). (a) Fatigue life. (b) Average initiation and propagation cycles.

Results of Low-Load Tests

Results in Fig. 4a show that for low-load tests in air the average fatigue life decreased progressively from 67 500 to 27 800 to 23 800 cycles as the discontinuity status changed from discontinuity-free (DF) to small discontinuities (SD) to large discontinuities (LD). Intragroup variability of tests in air as expressed by $\sigma_{\log N_f}$, the standard deviation of $\log N_f$, increased from 0.033 to 0.137 to 0.212 for the same progression in discontinuity status. For tests performed in hydrogen gas the average fatigue life and standard deviation of $\log N_f$ were respectively 83 000 cycles and 0.037 for DF specimens and 13 200 cycles and 0.363 for LD specimens.

Results in Table 2 show that for low-load tests of DF specimens in air about 50 percent of the fatigue life was spent in crack initiation. Discontinuities decreased the average cycles to crack initiation by factors of about 5 and 9 for air and hydrogen tests, respectively. For DF specimens the results in hy-

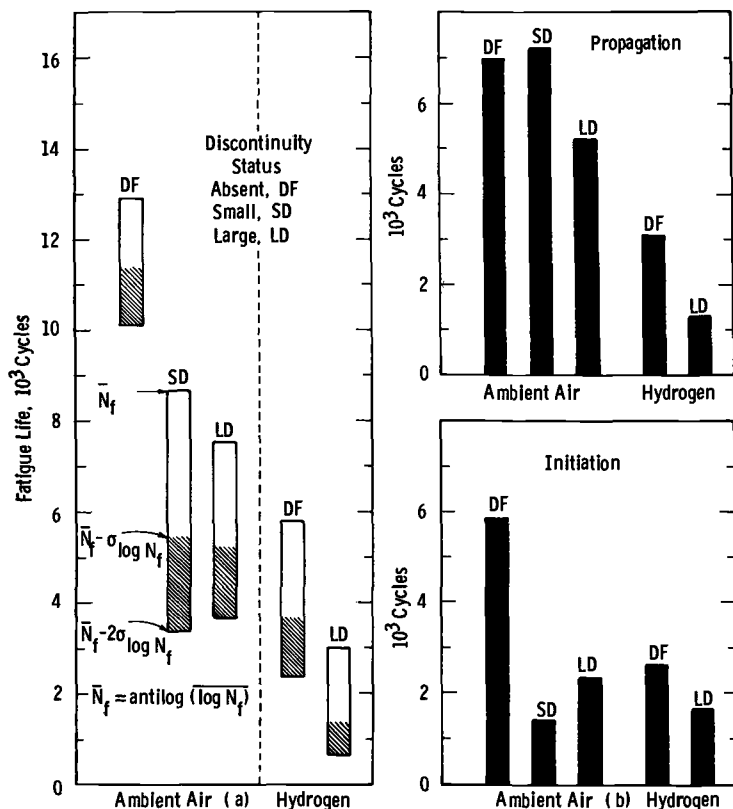


FIG. 5—Effect of discontinuities and environment on low-cycle fatigue life at a maximum cyclic load of 6500 lb (1 lb = 4.45 N). (a) Fatigue life. (b) Average initiation and propagation cycles.

drogen exhibited a longer initiation period than for the air tests. Propagation cycles were slightly reduced by the presence of the discontinuity and/or by hydrogen gas. Propagation cycles for discontinuity-containing specimens in hydrogen are about half the value for tests in air.

Results of High-Load Tests

Results in Fig. 5a show that for high-load tests in air the average fatigue life (antilog of $\log \bar{N}_f$) decreased progressively from 12 900 to 8600 to 7500 cycles as the discontinuity status changed from DF to SD to LD. For the same progression in discontinuity status the standard deviation of $\log N_f$ varied from 0.053 to 0.202 to 0.158. In the hydrogen environment the average fatigue life and standard deviation of $\log N_f$ were 5800 cycles and 0.198 for DF specimens and 3000 cycles and 0.328 for LD specimens.

Results in Table 3 and Fig. 5b show that for high-load tests of DF speci-

mens in either environment about 50 percent of life was spent initiating the crack. Discontinuities decreased the average cycles to initiation in air and hydrogen by factors of about 3 and 1.6, respectively. As observed for the low-load tests, the average propagation cycles were reduced by the presence of discontinuities and/or hydrogen. Also, for DF specimens average propagation cycles in hydrogen were about half the value for air tests at high cyclic load.

Effect of Hydrogen Gas

Results presented in Table 4 show the effect of hydrogen on first detection of initiation and on propagation both along and away from the notch. Tabulated data are the ratios of average cycles (hydrogen/air) for a particular stage of cracking. The effect of hydrogen on cycles for first crack detection is not consistent. The N_i -ratio decreased in going from DF to LD specimens at low load, whereas the opposite was true at high load. Moreover, at low load hydrogen did not reduce the initiation period. Crack propagation along the notch root was adversely affected by hydrogen, and there was a large hydrogen-discontinuity interaction since the N_c -ratio is a factor of 3 to 5 less for LD than for DF specimens. Propagation of the through-thickness crack in the vicinity of the notch, as represented by the N_a -ratio, exhibited the same trend as for N_c .

Discussion

The test data and analyses are discussed in terms of (1) effect of discontinuities in air, (2) hydrogen influence on discontinuity-free material, (3) discontinuity-environment interaction, (4) sources of variation in results, and (5) discontinuities and generator rotor performance.

Effect of Discontinuities in Air

Results in Figs. 4 and 5 and Tables 2 and 3 show that the presence of discontinuities can reduce average fatigue life (failure cycles) in air by as much as a factor of 3. The reduction in life is on about the same order of magnitude whether the discontinuities are large or small and is greatest at the low cyclic load. The reduction in fatigue life is caused primarily by a reduction in the cycles for first crack detection. When a discontinuity was present, average N_i -values were reduced by as much as a factor of 6, whereas average propagation cycles were reduced at most by a factor of 1.6. The propagation result is consistent with previous work, which showed that small discontinuities have little effect on the rate of crack growth [4,5], and that spherical discontinuities as large as 6.3 mm ($\frac{1}{4}$ in.) diameter do not significantly affect the growth rate in a specimen 25.4 mm (1 in.) thick [6].

TABLE 2—Low-cycle fatigue results for NiMoV keyhole notch compact specimens tested with a maximum cyclic load of 4500 lb.^a

Specimen	Discontinuity Free				Small Discontinuities				Large Discontinuities			
	Initiation (N_i), cycles	Propagation Along Notch (N_c), cycles	Failure (N_f), ^b cycles	Failure (N_f), ^b cycles	Specimen	Initiation (N_i), cycles	Propagation Along Notch (N_c), cycles	Failure (N_f), ^b cycles	Specimen	Initiation (N_i), cycles	Propagation Along Notch (N_c), cycles	Failure (N_f), ^b cycles
Bethlehem, Ambient Air												
C310	33 150	21 150	60 500	60 500	B2B1	5 500	14 400	24 300	F1B79	7 000	15 500	27 200
C37	29 000	26 500	61 300	61 300	B2D10	5 000	21 900	29 200	F1B600	5 000	19 950	34 500
D312	36 145	33 655	71 700	71 700	D1D84	19 800	21 200	42 000	F2B69	0 ^d	9 900	31 500
D35	30 000	34 000	67 700	67 700	C1B34	4 000	14 750	20 000	F2B92	10 000	17 850	12 400
									C1D3	500	15 800	18 000
									D1D119	30 000	20 600	53 500
Westinghouse (LRA), Ambient Air												
C34	62 500	6 563	74 500	74 500	F2D61	5 000	5 625	18 000
C38	45 000	17 188	65 500	65 500	D1B28	14 500	10 313	29 000
D36	31 000	29 375	72 500	72 500	C1D105	5 250	22 500	30 000
									F1B305	0 ^d	6 250	12 000
									F2B96	3 000	2 813	13 000

Westinghouse (R&D), Ambient Air											
D311	40 000	25 000	68 000	F1D529	20 000	9 688	38 000
Average ^c	37 160	21 911	67 542	...	6 831	17 720	27 785		6 425	11 214	23 784
Westinghouse (R&D), Hydrogen Gas											
C311	75 000	7 188	83 500	F2B87	4 500	1 250	6 000
C36	60 000	13 750	82 500	C1D114	5 000	1 250	7 500
								F2B62	5 000	1 250	7 000
								D1D146	15 000	1 563	17 000
								B1D31	15 000	3 125	18 200
Average ^c	67 082	9 942	82 998	F1D581	5 000	...	54 000
									7 086	1 570	13 164

^a 1 in. = 25.4 mm; 1 lb = 4.45 N.^b Failure is defined as crack extension 0.2 in. beyond the notch root.^c Antilogarithm of the average value of log N .^d Excluded from average.

TABLE 3—Low-cycle fatigue results for NiMoV keyhole notch compact specimens tested with a maximum cyclic load of 6500 lb.^a

Discontinuity Free				Small Discontinuities				Large Discontinuities			
Specimen	Initiation (N_i), cycles	Propagation Along Notch		Specimen	Initiation (N_i), cycles	Propagation Along Notch		Specimen	Initiation (N_i), cycles	Propagation Along Notch	
		(N_c), cycles	Failure (N_f) ^b cycles			(N_c), cycles	Failure (N_f) ^b cycles			(N_c), cycles	Failure (N_f) ^b cycles
Bethlehem, Ambient Air											
C32	7 000	3 430	12 700	B2D7	300	5 600	6 000	F1B255	1 ^d	4 250	5 900
C35	8 289	1 831	13 000	B1B9	750	1 350	5 700	F1B131	1 050	350	5 600
D33	3 000	8 430	13 200	D1D69	2 500	4 800	11 300	F2B82	1 ^d	2 810	4 700
D32	5 000	5 200	14 500	D1B92	7 000	5 590	14 500	F2B81	4 250	2 220	15 500
								C1D53	1 000	6 170	7 900
								D1B31	2 000	5 690	10 800
Westinghouse (LRA), Ambient Air											
C33	8 000	3 000	15 200	F1D501	3 100	3 000	7 100
C39	5 000	...	10 200	F2B115	2 300	1 750	6 200
D37	5 500	5 000	12 900	C1D75	1 500	4 250	5 800
								F1B268	6 800	4 000	11 200
								D1B84	4 000	4 250	10 200

Westinghouse (R&D), Ambient Air											
D34	7 500	2 500	11 900	F2B89	2 000	2 000	5 800
Average ^c	5 884	3 745	12 869		1 409	3 773	8 652		2 352	2 815	7 547
Westinghouse (R&D), Hydrogen Gas											
C312	2 000	...	4 100	C1B44	700	125	900
C31	2 000	...	3 900	F1B237	1 000	375	4 100
D38	4 000	1 250	7 200	C1B173	5 500	500	8 600
D39	3 000	5 500	10 000	F1D565	1 000	1 125	2 300
								D1B13	3 300	500	4 000
								F2B105	1 800	313	2 400
Average ^c	2 632	2 622	5 824		1 684	400	2 980

^a 1 in. = 25.4 mm; 1 lb = 4.45 N.
^b Failure is defined as a complete separation.
^c Antilogarithm of the average value of log *N*.
^d Excluded from average.

TABLE 4—*Environment and discontinuity influence on initiation and propagation phases of low-cycle fatigue life.^a*

Maximum Cyclic Load, lb	First Crack Detection ($N_{i\text{hydrogen}}/N_{i\text{air}}$)		Propagation Along Notch ($N_{c\text{hydrogen}}/N_{c\text{air}}$)		Propagation Away from Notch ($N_{a\text{hydrogen}}/N_{a\text{air}}$) ^b	
	Discontinuity Status ^c					
	DF	LD	DF	LD	DF	LD
4500	1.82	1.10	0.45	0.14	0.76	0.11
6500	0.45	0.71	0.71	0.14	0.63	0.23

^a 1 lb = 4.45 N.^b $N_a = N_t - (N_i + N_c)$.^c Discontinuity free, DF; large discontinuities, LD.

Hydrogen Influence on Discontinuity-Free Material

The effect of hydrogen on the fatigue life of discontinuity-free material was not consistent. At the low cyclic load, life was slightly increased by the presence of hydrogen, whereas at the high cyclic load the opposite effect occurred. The cycles to first crack detection followed this same trend. The increased initiation interval for DF specimens tested in hydrogen as opposed to air, might be due to the larger average crack length at first detection, namely 7.6 versus 2.1 mm (0.300 versus 0.082 in.). This explanation, however, cannot be used to rationalize the apparent increase in life at low cyclic load. Propagation results are consistent with other work [7] showing that hydrogen causes a reduction in the propagation cycles.

Discontinuity-Environment Interaction

Results presented in Tables 2 and 3 reveal a discontinuity-environment interaction. The reduction in life due to the presence of discontinuities is greater in hydrogen than in air, and it is also greater at low than at high cyclic load. Data presented in Table 4 show that the discontinuity-environment interaction involves crack propagation both along and away from the notch, but not crack initiation.

Sources of Variation in Results

Results presented in Figs. 4 and 5 show a fairly wide variation in the cycles to initiation for a particular treatment combination (load level, discontinuity status, environment). There was also variability in the crack length at first detection. Since the precision of predictive models and the ability to resolve differences in average effects depend on the variability in cycles to crack initiation, it is important to minimize this variability by identifying and removing the sources of variation.

In the present program the definition of initiation was identified as a possible source of variation. For example, consider the case of discontinuity-free specimens. The standard deviation of cycles to first crack detection exceeds that for total life by about a factor of two or more. If initiation is defined in terms of the number of cycles to form a crack that intersects a side surface or extends 23 mm (0.9 in.) along the notch, the variability in cycles to crack initiation for DF specimens in ambient air is comparable to that for failure.

In specimens containing discontinuities another source of variation is the discontinuity itself. Variability for SD and LD specimens is greater than for DF specimens and depends on the size, shape, and location of the discontinuity as well as the definition of initiation. For example, Specimens C1D3 and F2B69 (Fig. 6) had large discontinuities located near the notch and relatively short cyclic periods for crack initiation. On the other hand, for Specimen D1D119 (Fig. 6) the discontinuity was far from the notch, and both the initiation and failure cycles were greater than for the other LD specimens tested at the same loads.

Discontinuity location is important because the local stress field decays with distance from the notch. An estimate of the effect of distance is based on the parameter α :

$$\alpha = \frac{1}{6} \left[2 + \left(\frac{R}{R+d} \right)^2 + 3 \left(\frac{R}{R+d} \right)^4 \right] \quad (2)$$

where

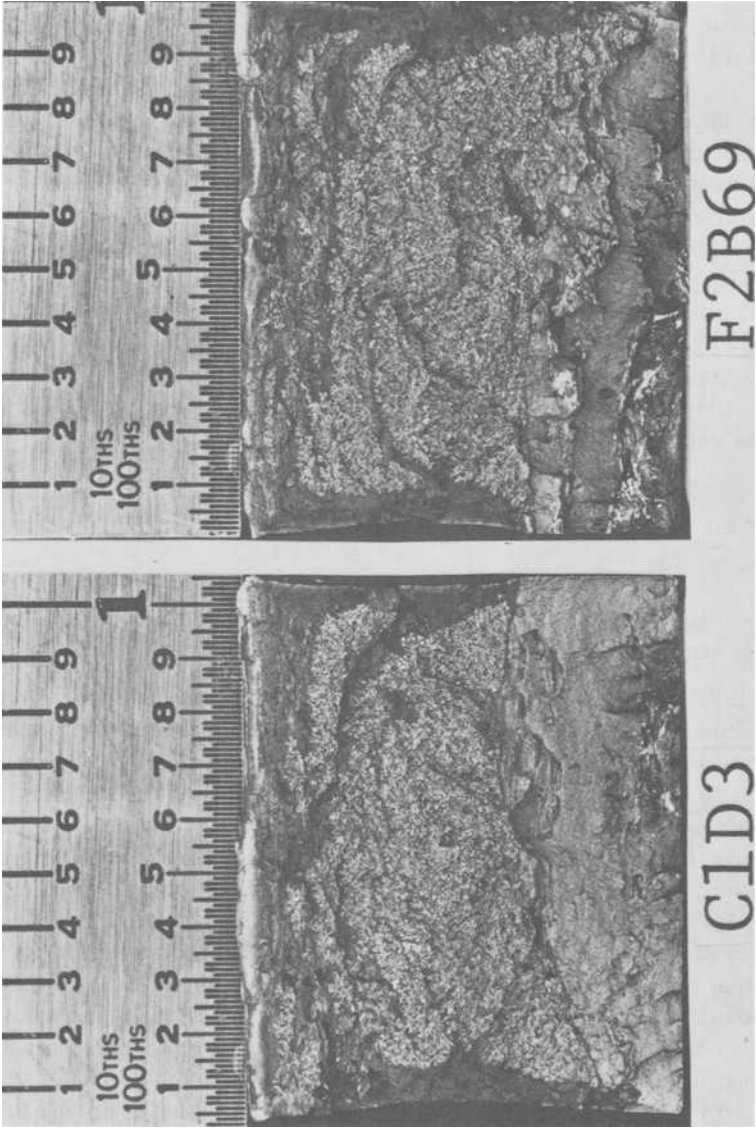
R = keyhole notch radius, and

d = distance from notch surface to discontinuity.

In Eq 2, α describes the decrease in local stress as the distance from a circular notch increases [8]. The discontinuity length parallel to the notch surface, l_o , is important because it reduces the amount of crack extension required to satisfy the emergence criterion of initiation. An increase in the product αl_o reflects either an increase in discontinuity size or a decrease in distance from the notch root. This product quantifies the effects of both discontinuity size and location on cycles to crack initiation $N_i + N_c$ (Fig. 7).

Values of d and l_o were obtained from $\times 10$ photographs of the fracture surface of the specimen. Given the roughness of the fracture surface plus the irregular nature of the discontinuity itself, the determination of d and l_o were approximate. However, the data generated at both low and high cyclic loads (Fig. 7) exhibit a fairly well-defined trend that $(N_i + N_c)$ decreases as the product αl_o increases. Moreover, the trend suggests that there is a vertical asymptote—that is, a limit to the decrease in $N_i + N_c$ —as the notch acuity or product αl_o increases. This result is consistent with previous work by others [9,10].

SD Specimen B1B9 is considered to be an outlying observation since its initiation period was much less than expected based on the trends depicted in



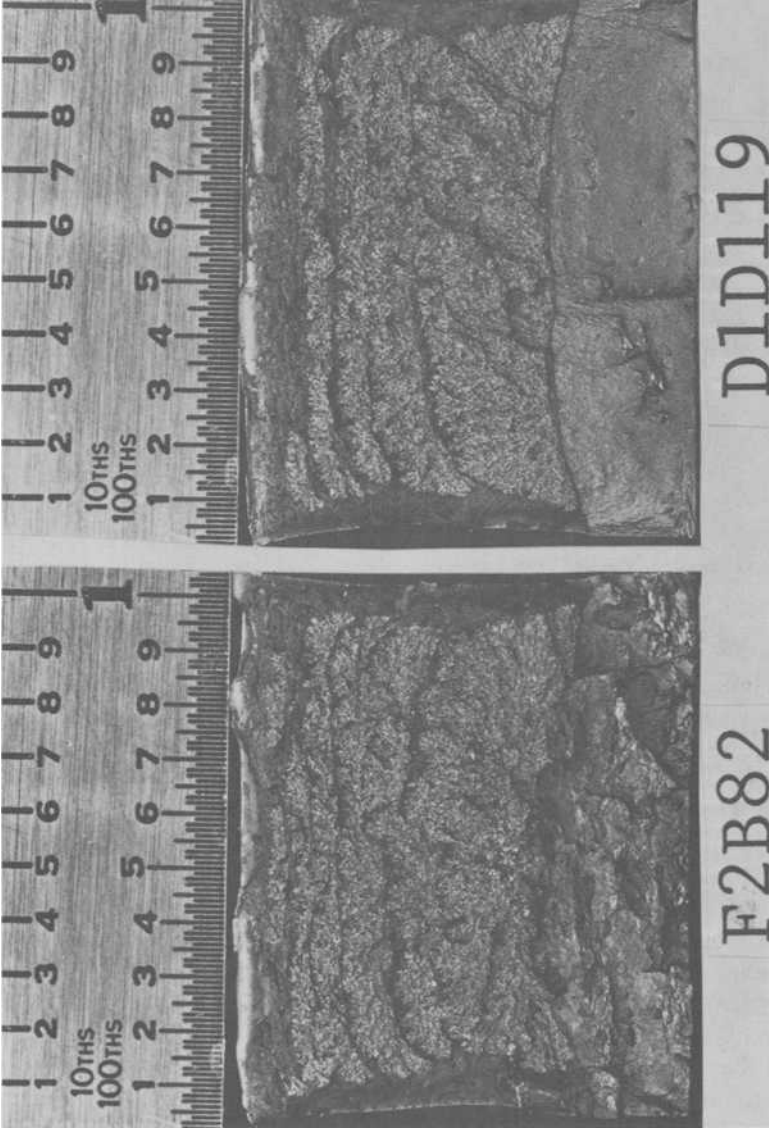


FIG. 6—Fracture surfaces of Specimens C1D3, F2B69, F2B82, and D1D119.

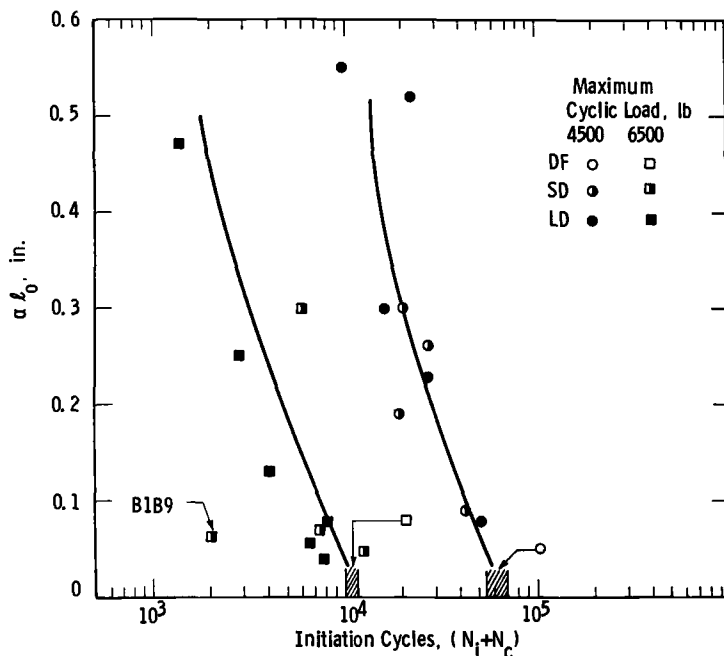


FIG. 7—Discontinuity size and location parameter of $\alpha\ell_0$ versus cycles to crack initiation ($N_i + N_c$) (1 in. = 25.4 mm; 1 lb = 4.45 N).

Fig. 7. One explanation is that the $\times 10$ photographs used for determining d and ℓ_0 failed to reveal the true nature of the discontinuities in B1B9. Support for this view is provided by the scanning electron microscope photographs of the fracture surface (Fig. 8) which revealed the presence of several manganese sulfide (MnS) particles lying within about 0.3 mm (0.01 in.) from the notch surface. Their presence could increase the product $\alpha\ell_0$ and thus could account for the short initiation period of Specimen B1B9.

In the case of Specimens D1D84 (Table 2) and F2B81 (Table 3) a second crack observed along the notch root probably contributed to the increased cycles for initiation. For Specimen F1D581 (Table 2) there is no explanation for the inordinately long propagation interval, which was 16 to 30 times longer than those for the other specimens of this group.

Finally, a comparison of the data presented in Figs. 4, 5, and 7 demonstrates the importance of recognizing that what might seem to be an acceptable estimate of variability contains sources which make it in fact an inflated estimate. That is, one should make a determined attempt to identify and eliminate such sources. Thus, accounting for variability due to initiation criteria and to discontinuity size and location with respect to the notch root reduced the range in initiation cycles by a factor of 2 or more.

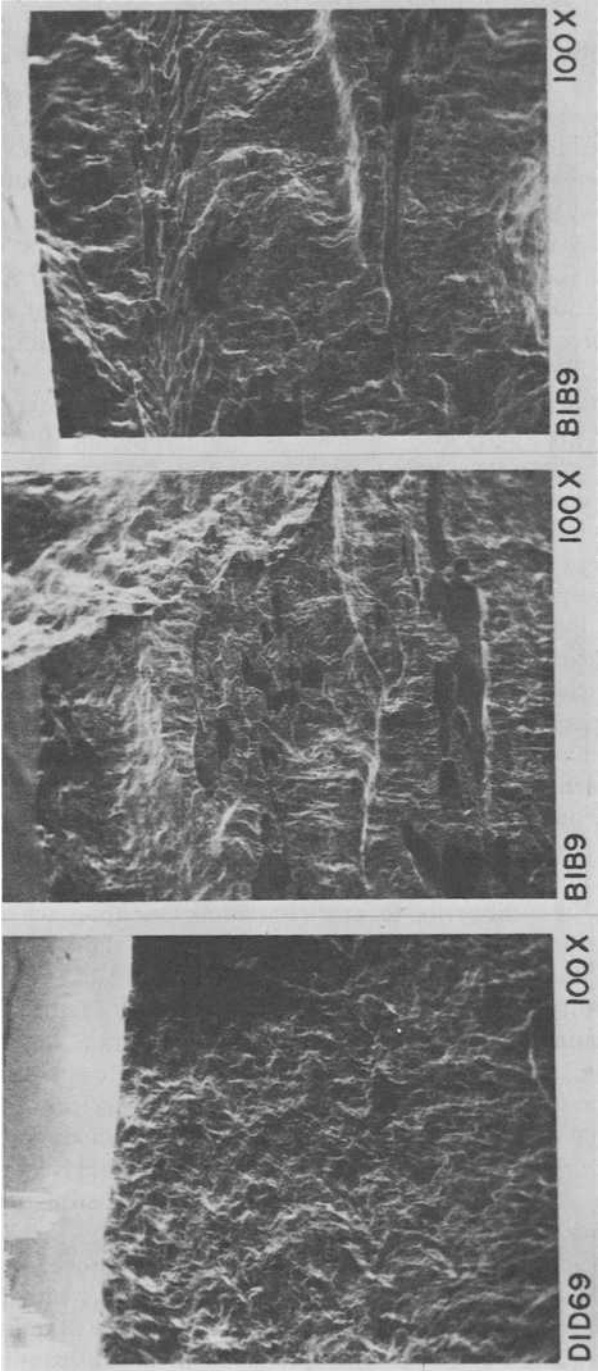
Discontinuities and Generator Rotor Performance

To examine the applicability of the present findings to the assessment of generator rotor reliability, consider the following design example [11]. A generator operating at a nominal tangential bore stress of 345 MPa (50 ksi) accumulates 14 600 cycles of fluctuating tangential stress in a 40-year life of daily startup and shutdown. If the bore surface of this generator contains a discontinuity assumed to be equivalent to a crack 2.5 mm (0.1 in.) deep (radial) by 25.4 mm (1 in.) long that escaped detection during inspection, it would take about 25 000 cycles [11] to grow this crack in air from its initial size to the critical flaw size. Thus, in air, a rotor containing an isolated crack similar in size to discontinuity F2B82 (Fig. 6) would not fail in nearly twice the service life.

On the other hand, based on the results of Table 4, hydrogen could accelerate crack growth by about a factor of 7 and failure in 10 years would be predicted. Service experience indicates, however, that even hydrogen-cooled generators do not fail after 10 years of exposure to normal operating conditions. This fact can probably be attributed to a combination of factors: (1) the absence of hydrogen at the bore, (2) the severity of the initial discontinuity not being as great as the crack assumed in the design example, and (3) the possibility that even under conditions of daily startup and shutdown the service cycles do not accumulate as fast as expected. The presence of hydrogen in an appreciable concentration on the bore surface is unlikely [11] because this gas would first have to react with the rotor material and then diffuse through a minimum of 127 mm (5 in.) of steel at temperatures only slightly above ambient.

Since the preceding discussion suggests that discontinuities are *not* initially equivalent to the assumed 2.5 by 25.4 mm (0.1 by 1 in.) crack, the important question is how one can make a quantitative estimate of the effect of discontinuities on the cyclic period for crack initiation. One approach involves using the fatigue notch factor K_t , that is, the ratio of the unnotched fatigue strength to the notched fatigue strength. It is assumed that in the presence of a discontinuity there is a value of K_t , namely K'_t , that can be estimated. For each discontinuity-containing specimen in this program, the procedure for determining K'_t involved using the value of $(N_i + N_c)$ to enter the plot in Fig. 9 in order that a value of the product $K'_t S_r$ could be selected for the specimen. K'_t was obtained by dividing the product by S_r determined from Eq 1 using P_r instead of P_{max} . The plot in Fig. 9 was developed from Neuber's rule [12], incremental step data for core bar A, and cyclic stress-strain parameters estimated from tensile properties [13,14].

For each specimen containing a discontinuity this procedure was used to determine K'_t . The resulting values range from 1.8 to 3.1 with the maximum value of K'_t being about 50 percent greater than K_t . The average value of K'_t increases in going from: air to hydrogen, small to large discontinuity, or high



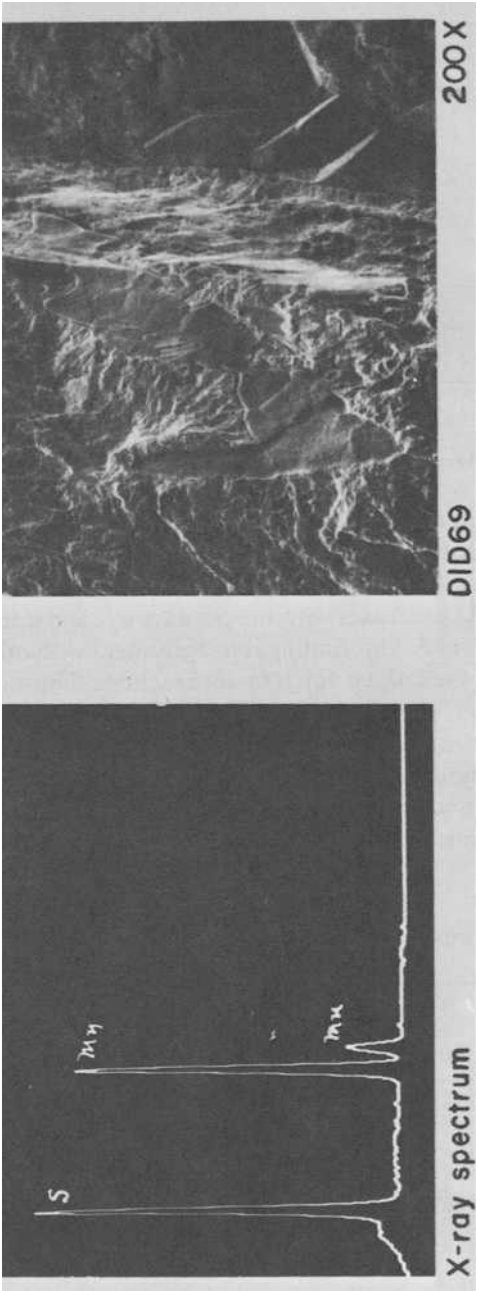


FIG. 8—Scanning electron fractography of SD Specimens B1B9 and D1D69.

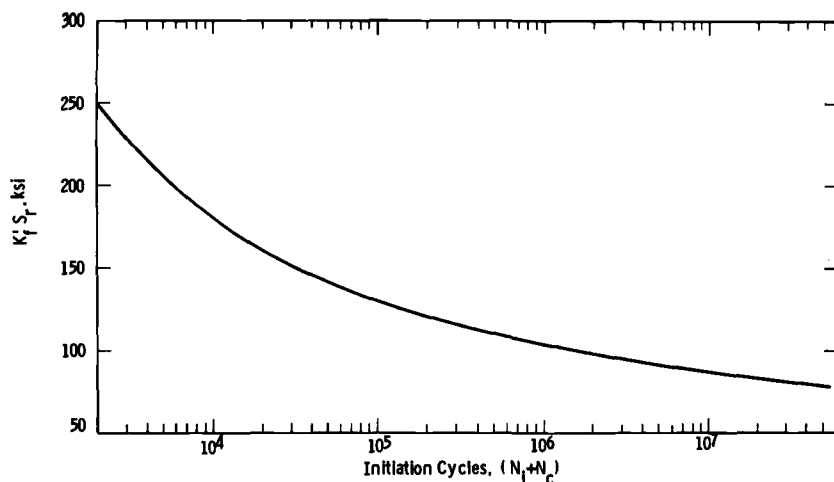


FIG. 9— $K'_t S_r$ versus cycles to crack initiation ($N_i + N_c$) ($1 \text{ ksi} = 6.89 \text{ MPa}$).

to low cyclic maximum load (Table 5). K'_t can also be used to estimate the effects of discontinuity size and location on crack initiation, as shown by ambient air data in Fig. 10. Excluding SD Specimen B1B9, which was discussed previously, K'_t increases with the product αl_0 and appears to reach a limiting value of about 3. This finding is in agreement with other work [9,10] which suggests that the fatigue notch factor reaches a limiting value, regardless of notch severity.

Although the uncertainty of any prediction method is affected by factors such as the means used to detect and measure discontinuities, given the size and location of a discontinuity, information such as that in Figs. 9 and 10 could be used to estimate the effect of that discontinuity on fatigue behavior.

TABLE 5—Fatigue stress concentration factors for discontinuities.^a

NOTE—Tabulated values represent the average and (range) in K'_t for a given treatment combination.

Maximum Cyclic Load, lb	Environment	Discontinuity Status ^b	
		SD	LD
4500	ambient air	2.35 (2.2 to 2.46)	2.51 (2.13 to 3.04)
4500	hydrogen gas	...	2.86 (2.48 to 3.12)
6500	ambient air	2.12 (1.82 to 2.59)	2.17 (1.96 to 2.81)
6500	hydrogen gas	...	2.58 (2.08 to 3.13)

^a $1 \text{ lb} = 4.45 \text{ N}$.

^b Small discontinuities, SD; large discontinuities, LD.

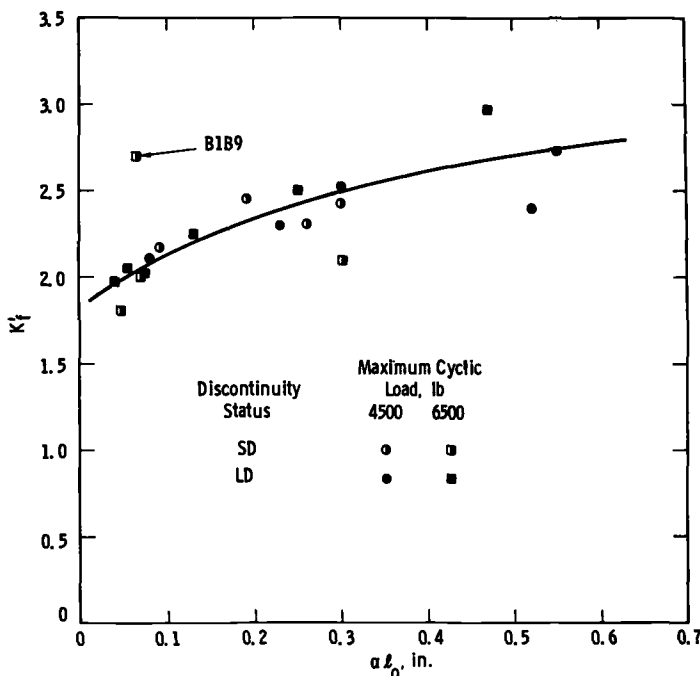


FIG. 10—Fatigue notch factor K'_t versus discontinuity size-location parameter αL_o (1 in. = 25.4 mm; 1 lb = 4.45 N).

To illustrate the use of the method, return to the design example with $K'_t = 3$ and $S_r = 345$ MPa (50 ksi). $K'_t S_r$ would then be 1035 MPa (150 ksi) and the cycles to crack initiation predicted from Fig. 9 would be about 30 000 or more than twice the life estimate based on daily startup and shutdown. This illustration supports the view that an isolated near-bore surface discontinuity should not, in general, be regarded as equivalent to a crack.

Conclusions

The influence of discontinuity presence and size and of environment—that is, ambient air or hydrogen gas—on the low-cycle fatigue behavior of NiMoV generator rotor forging material was evaluated. Blunt-notch compact tension specimens 25.4 mm (1 in.) thick were subjected to cyclic maximum loads of 20.0 and 28.9 kN (4500 and 6500 lb) and corresponding cyclic minimum loads of 2.0 and 2.9 kN (450 and 650 lb). Specific findings of the investigation were as follows:

1. For tests carried out in air, discontinuities reduced the average crack initiation and propagation cycles by as much as factors of 6 and 1.5, respectively. The reduction was greater for specimens tested at the low cyclic load.

2. For discontinuity-free specimens, cycles to initiation and failure were decreased by the presence of hydrogen at the high load. No explanation was found for the opposite trend at low load. Propagation cycles were reduced by the presence of hydrogen at both load levels.

3. The more deleterious effect of discontinuities on life in a hydrogen atmosphere as opposed to air attests to the existence of a significant discontinuity-environment interaction, which primarily affected propagation in the vicinity of the notch.

4. Variability in cycles to initiation was dependent on the initiation criterion and exceeded that for cycles to failure. Specimens with discontinuities exhibited greater variability than those without them. Taking into account discontinuity size and location with respect to the notch reduced the variability of test data by a factor of 2 or more.

5. In the presence of a discontinuity, the fatigue notch factor K'_t exceeded the elastic stress concentration factor K_t of the discontinuity-free blunt-notch by as much as 50 percent.

6. Based on the strain-cycle fatigue model for estimating the effects of discontinuities on the service performance of generator rotors, an isolated near-bore surface discontinuity should not, in general, be regarded as equivalent to a crack.

Acknowledgments

The technical support in terms of facilities and laboratory personnel provided by both the Westinghouse Electric and Bethlehem Steel Corporations is gratefully acknowledged. Helpful discussions with H. C. Smith, G. S. Hartman, R. F. Cappellini, H. Darlington, B. S. Mikofsky, W. G. Clark, Jr., and G. A. Clarke are appreciated. Special thanks are due T. R. Sharron, P. J. Barsotti, and D. W. Peters for their untiring efforts in all phases of the program.

References

- [1] Clark, W. G., Jr., *Journal of Engineering for Industry, Transactions of ASME*, Vol. 94, Feb. 1972, pp. 291-298.
- [2] Wilson, W. K., "Elastic-Plastic Analysis of Blunt Notched CT Specimens and Applications," ASME Paper No. 74-PVP39, presented at Pressure Vessels and Piping Conference, Miami Beach, Fla., June 1974.
- [3] Crow, E. L., Davis, F. A., and Maxfield, M. W., *Statistics Manual*, Dover Publications, New York, 1960, pp. 45-46.
- [4] Bucci, R. J., Clark, W. G., Jr., and Paris, P. C. in *Stress Analysis and Growth of Cracks, ASTM STP 513*, American Society for Testing and Materials, 1972, pp. 177-195.
- [5] Shih, T.-T. and Clarke, G. A. in *Fracture Mechanics, ASTM STP 677*, American Society for Testing and Materials, 1979, pp. 125-143.
- [6] Clark, W. G., Jr. in *Fracture Mechanics, ASTM STP 677*, American Society for Testing and Materials, 1979, pp. 303-319.
- [7] Clark, W. G., Jr., *Hydrogen Damage in Metals*, American Society for Metals, 1974, pp. 149-164.

- [8] Timoshenko, S. P. and Goodier, J. M., *Theory of Elasticity*, 2nd ed., McGraw-Hill, New York, 1970, p. 80.
- [9] Reemsnyder, H. S. in *Structural Steel Design*, 2nd ed., L. Tall, Ed., Ronald Press, New York, 1974, pp. 530-531.
- [10] Lawrence, F. V., Mattos, R. J., Higashida, Y., and Burk, J. O. in *Fatigue Testing of Weldments*, ASTM STP 648, American Society for Testing and Materials, 1978, pp. 134-158.
- [11] Greenberg, H. D., Wessel, E. T., Clark, W. G., Jr., and Pryle, W. H., "Critical Flaw Sizes for Brittle Fracture of Large Turbine Generator Rotor Forgings," Westinghouse Scientific Paper 69-1D9-MENTL-P2, 1 Dec. 1969.
- [12] Neuber, H., *Journal of Applied Mechanics, Transactions of ASME*, Vol. 28, Dec. 1961, pp. 544-550.
- [13] Landgraf, R. W. in *Achievement of High Fatigue Resistance in Metals and Alloys*, ASTM STP 467, American Society for Testing and Materials, 1970, pp. 3-36.
- [14] *The Fatigue Design Handbook*, Section 3.2, Society of Automotive Engineers, 1968, pp. 22-24.

Application of Low-Cycle Fatigue Test Results to Crack Initiation from Notches

REFERENCE: Truchon, M., "Application of Low-Cycle Fatigue Test Results to Crack Initiation from Notches," *Low-Cycle Fatigue and Life Prediction, ASTM STP 770*, C. Amzallag, B. N. Leis, and P. Rabbe, Eds., American Society for Testing and Materials, 1982, pp. 254–268.

ABSTRACT: Fatigue crack initiation tests were carried out on notched specimens, with K_t values ranging from 1.4 to 4.2, made of a large variety of steels. The paper describes the application of the critical location approach to these tests on the basis of low-cycle fatigue data obtained on smooth specimens under Neuber control straining or under conventional reverse straining ($R_\epsilon = (\epsilon_{\min}/\epsilon_{\max}) = -1$).

KEY WORDS: fatigue crack initiation, low-cycle fatigue, Neuber's rule

Fatigue crack initiation from notches has been a subject of active interest over the last 20 years [1–22].² Problems such as correlation between smooth and notched specimen test data and prediction of crack initiation were examined during this period by different methods. Initially, notches were accounted for in current fatigue design by means of a fatigue strength reduction factor K_t , depending on the elastic stress concentration factor, but it was not unique owing to size effects and local plasticity effects [1–4]. More recently, in the case of sharp stress raisers, some authors [5–9] used fracture mechanics concepts to correlate the results. Another point of view, which has prevailed during the last 10 years, is based on the fact that equal fatigue damage will take place in a smooth specimen or at the root of a notch, provided the metal at the critical location experiences the same stress-strain history [10–22]. This hypothesis has been the basis for further developments ranging from the improvement of the K_t -approach (indirect approach) [10–18] to cycle-by-cycle calculations of the damage at the critical location (direct approach) [19–22].

In this paper we are only concerned with the indirect approach, since it has proven to be successful in predicting initiation from notches [10–17] and

¹Research Engineer, IRSID, Saint Germain en Laye, France.

²The italic numbers in brackets refer to the list of references appended to this paper.

correlating smooth and notched specimen data [18]. The aim of this work was to apply this approach to a large variety of steels, and to investigate the crack initiation phenomenon in a large domain of number of cycles.

Experimental Conditions

The experimental work was divided into three different parts:

1. *Fatigue crack initiation tests* to obtain the basic data necessary to make the correlation between initiation and low-cycle fatigue. The notch severity was varied, with K_t -values ranging from 1.39 to 4.22.

2. *Conventional low-cycle fatigue (LCF) tests* to derive the Manson-Coffin curve and the cyclic stress-strain curve for the materials of this study.

3. *LCF tests under Neuber control*: that is, the product $\Delta\sigma \times \Delta\epsilon$ is kept constant during the test at each strain reversal.

Materials

This work was conducted on four steels. The chemical compositions are given in Table 1.

The following heat-treatments were applied to these materials:

35 CD4	850°C, 45 min, oil-quenched 550°C, 4 h, air
XC 38	850°C, 30 min, water-quenched 600°C, 30 min, air
E 36	normalized to 900°C, 2 h 30 min, air
AISI 316	1100°C, 1 h, water-quenched

In these conditions, the materials exhibited the mechanical properties given in Table 2.

Specimens

The specimens used for the crack initiation tests are shown in Fig. 1. They were three-point-bend specimens with 15 mm thickness and different notch root radii in order to make the K_t -values vary from 1.39 to 4.22. Particular care was brought to the finishing operation of the notch root. Automatic

TABLE 1—Chemical composition of the steels investigated.

Material	C	Mn	Si	Cr	Mo	P	S	Ni	Cu	Co	N
35 CD4	0.339	0.620	0.270	1.12	0.235	0.0147	0.006
XC 38	0.403	0.657	0.167	0.022	0.037
AISI 316	0.069	1.76	0.46	17.5	2.22	0.034	0.006	11.5	0.104	0.26	0.0414
E 36	0.191	1.43	0.435	0.222	0.0142	0.006

TABLE 2—*Mechanical properties of the steels investigated.*

Material	σ_y , N/mm ²	Ultimate Tensile Strength, N/mm ²	Elongation to Rupture, %	Reduction of Area, %
35 CD4	1005	1100	16.5	62
XC 38	525	750	19	63
E 36	350	547	33	72
AISI 316	250	575	72	75

grinding achieved the same conditions of metal surface at the critical point in notched and smooth specimens—that is, similar roughness and machining striations normal to the crack plane.

Except for the case of the high-strength steel 35 CD4, it was found impossible to carry out tests on specimens with $K_t = 1.39$ because of gross plasticity which developed within the ligament. This explains why only two K_t values were investigated.

For the LCF tests, smooth specimens with a cylindrical central part were used. In these tests the longitudinal strain was controlled.

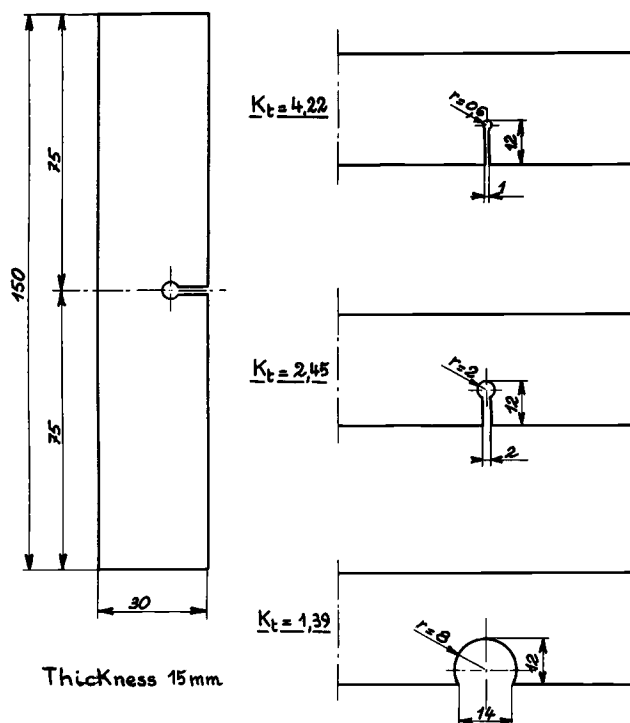


FIG. 1—Notched specimens for fatigue crack initiation tests.

Mode of Loading for Initiation Tests

Tests on the notched specimens were carried out with the loading equipment as shown in Fig. 2. This device was designed to allow for quick positioning of the specimens relative to the rollers, and also to electrically insulate the specimen from the load frame. The tests on the notched specimens were carried out at constant amplitude, with an R -ratio of 0.1 and a frequency of 30 Hz.

Detection of Crack Initiation

For both the notched and the smooth specimens in the Neuber control mode, we used an a-c potential-drop method [18,23].

Notched Specimens—Figure 3 shows a specimen instrumented with the a-c leads and potential probes. Figure 4 shows a typical record of the potential-drop signal during a crack initiation life test. Initiation was chosen as the moment when the signal began to leave its plateau. It has been shown [18] that such a criterion corresponds to a crack area of approximately 1 mm^2 .

Smooth Specimens—It should be emphasized here that crack initiation observations were performed only in the LCF tests under Neuber control conditions. The observation system was the same as that used for the notched specimens. The potential measurement probes were placed across the central part of the specimen.

Figure 5 shows the variations of the potential-drop signal during a strain cycle. This signal was found to vary substantially during cycling, but the am-

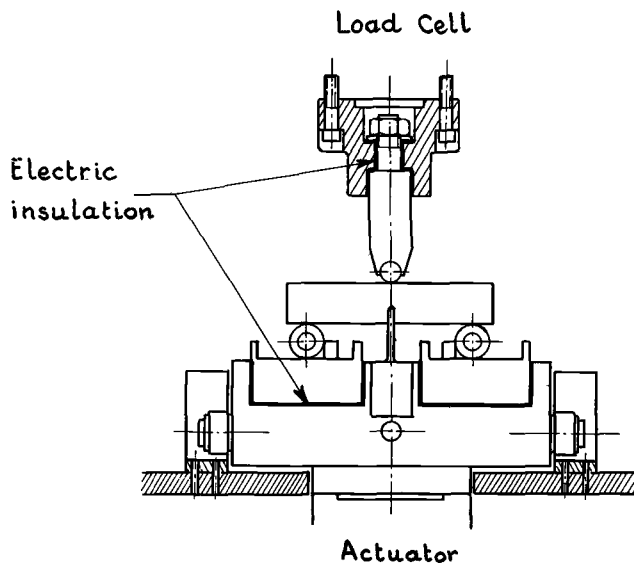


FIG. 2—Experimental setup for notched specimens.

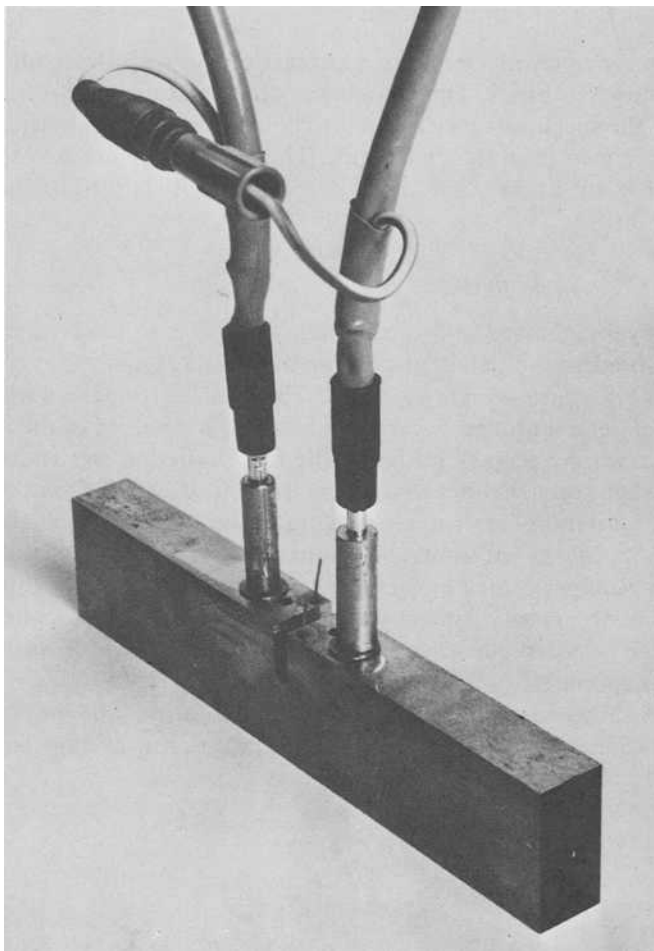


FIG. 3—Notched specimen instrumented for the detection of crack initiation.

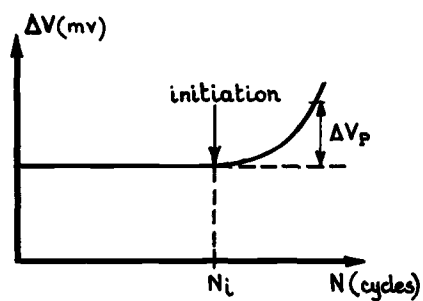


FIG. 4—Definition of initiation from the a-c potential-drop record.

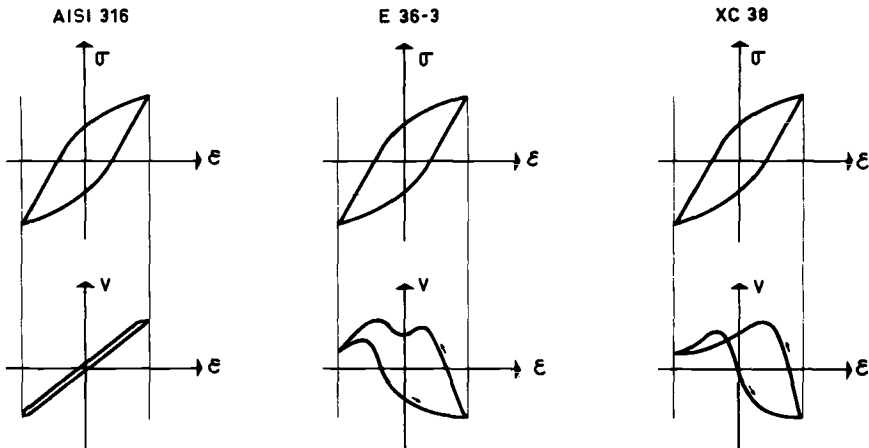


FIG. 5—Typical records of the a-c potential-drop (signal within a strain cycle).

plitude of this variation varied from one material to another. This point has been discussed in Ref 23, where it is explained that such an effect is due to the magnetic properties of the material and their alternations with stressing and yielding.

This potential-drop signal was recorded during the test, as shown in Fig. 6, and initiation was found to occur when the shape of the potential-drop cycle began to change. It was checked that this point always corresponded to the existence of a macroscopic crack within the specimen (less than 1 mm wide).

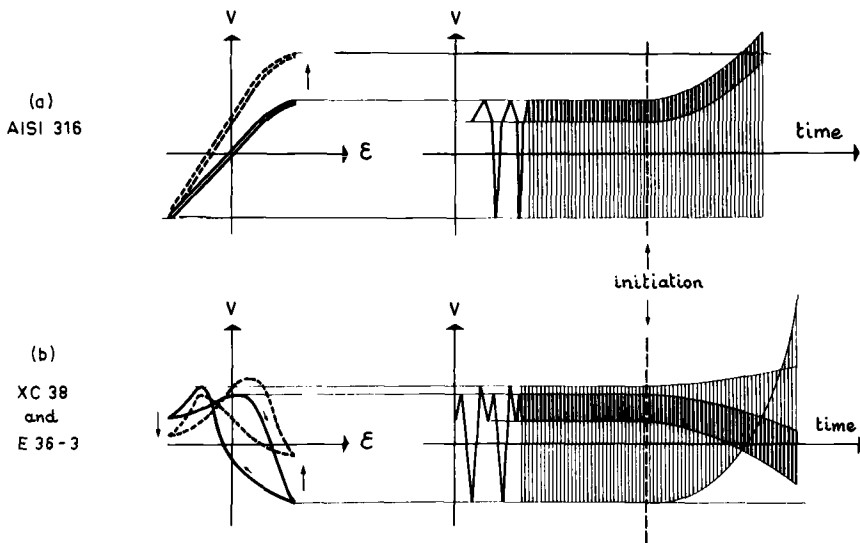


FIG. 6—Definition of the initiation point on smooth specimens from the a-c potential-drop record.

Fatigue Crack Initiation Results

Figure 7 shows the crack initiation data. The amplitude of nominal stress as applied to the specimens is plotted as a function of the number of cycles to crack initiation in the range of 10^3 to 10^7 cycles. The amplitude of nominal stress refers to that in the ligament of the specimen. It is determined assuming a linear distribution of stress within the ligament [1]; that is;

$$\sigma_{\text{nom}} = \frac{6 M_b}{B L^2}$$

where M_b is the bending moment, and B and L are the thickness and ligament width of the specimen, respectively.

These diagrams show the influence of notch severity on crack initiation.

Application of LCF to Correlate with Crack Initiation Data

As mentioned previously, we used the critical location approach together with Neuber's rule [24], which gives an approximate means of approaching the local stress-strain history at the notch root [10-18]. We rearranged the Neuber relation to determine K_f^{EP} , the elasto-plastic fatigue strength reduction factor, from the "local" quantities $\Delta\sigma$ and $\Delta\epsilon$, and the nominal stress amplitude $\Delta\sigma_{\text{nom}}$:

$$K_f^{\text{EP}} = \frac{\sqrt{E \Delta\sigma \Delta\epsilon}}{\Delta\sigma_{\text{nom}}}$$

In this investigation it is assumed that the quantity $\sqrt{E \Delta\sigma \Delta\epsilon}$ is a criterion for the crack initiation at notches. If this criterion applies, K_f^{EP} should be constant whatever the nominal loading. This is examined in the present paper.

The quantity $\sqrt{E \Delta\sigma \Delta\epsilon}$ can be calculated by the help of basic LCF data in two different ways (see below).

Analysis with Conventional LCF Data

These data refer to tests carried out with $R_e = (\epsilon_{\text{min}}/\epsilon_{\text{max}}) = -1$. They give (1) the number of cycles to failure as a function of the strain amplitude $\Delta\epsilon$; and (2) the cyclic stress-strain curve

$$\left(\frac{\Delta\sigma}{2}, \frac{\Delta\epsilon}{2} \right)$$

These data are given in numerical form in Appendix I.

On the other hand, from each test on a notched specimen with a nominal stress amplitude $\Delta\sigma_{\text{nom}}$, a number of cycles to initiation is derived. Taking this number of cycles to initiation as a starting point (Fig. 8), it is possible to derive the local amplitudes of stress and strain from the above LCF data.

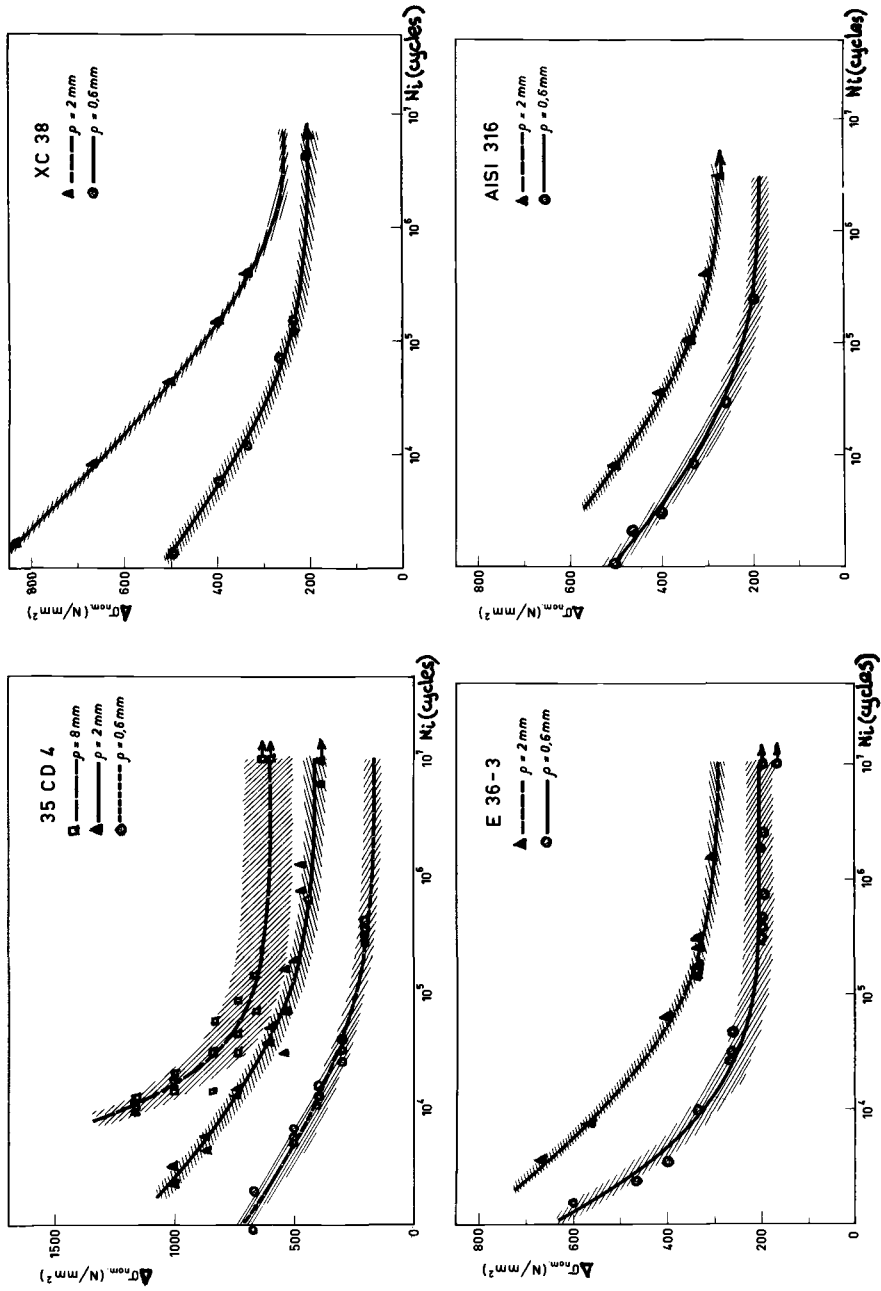


FIG. 7—Fatigue crack initiation results as a function of notch severity.

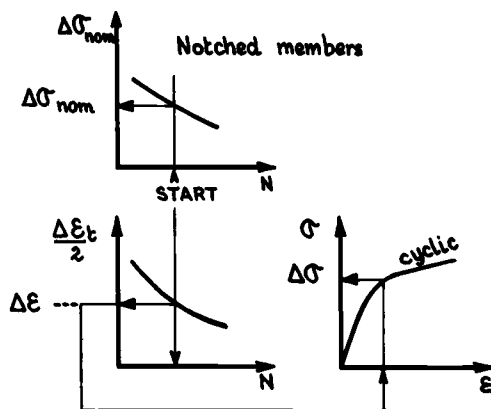


FIG. 8—Derivation of K_f^{EP} from conventional LCF data and fatigue crack initiation results.

With the three quantities, it is now possible to calculate K_f^{EP} as the ratio of the local quantity $\sqrt{E \Delta \sigma \Delta \epsilon}$ and the nominal stress amplitude.

Analysis with LCF Data under Neuber Control

The second way to evaluate K_f^{EP} is to use the so-called “Neuber simulation” for the generation of the LCF data. In this type of test the product $\Delta \sigma \times \Delta \epsilon$ is kept constant. Appendix II gives a description of the experimental technique used to control the machine. Figure 9 summarizes the results of the Neuber simulation tests. They are presented in diagrams where the preset quantity $\sqrt{E \Delta \sigma \Delta \epsilon}$ is given as a function of the number of cycles to initiation.

These Neuber simulation tests differ from the conventional LCF tests in that they take into account the effects of local mean strain and local stress transients. Indeed, for all materials in this investigation, when tests under Neuber control were carried out in the manner described in Appendix II, a transient mean stress appeared in the early stage of cycling (less than 5 percent of the number of cycles to initiation) and the stress-strain hysteresis loop stabilized at $R_\epsilon = (\epsilon_{\min}/\epsilon_{\max}) \sim 0.5$ and zero mean stress, in the domain of low-cycle fatigue (that is, $N_i \leq 10^5$ cycles).

Derivation of K_f^{EP} and Comments

Figure 10 gives the variations of K_f^{EP} as a function of $\Delta \sigma_{\text{nom}}$. In the first analysis, K_f^{EP} values are calculated according to the procedure described in Fig. 8. In the second, Neuber control test data of Fig. 9 are used to determine the quantity $\sqrt{E \Delta \sigma \Delta \epsilon}$ corresponding to a given number of cycles to initiation.

According to Fig. 10, it is obvious that K_f^{EP} values obtained by the two analyses differ substantially for some materials. This can be attributed to (1)

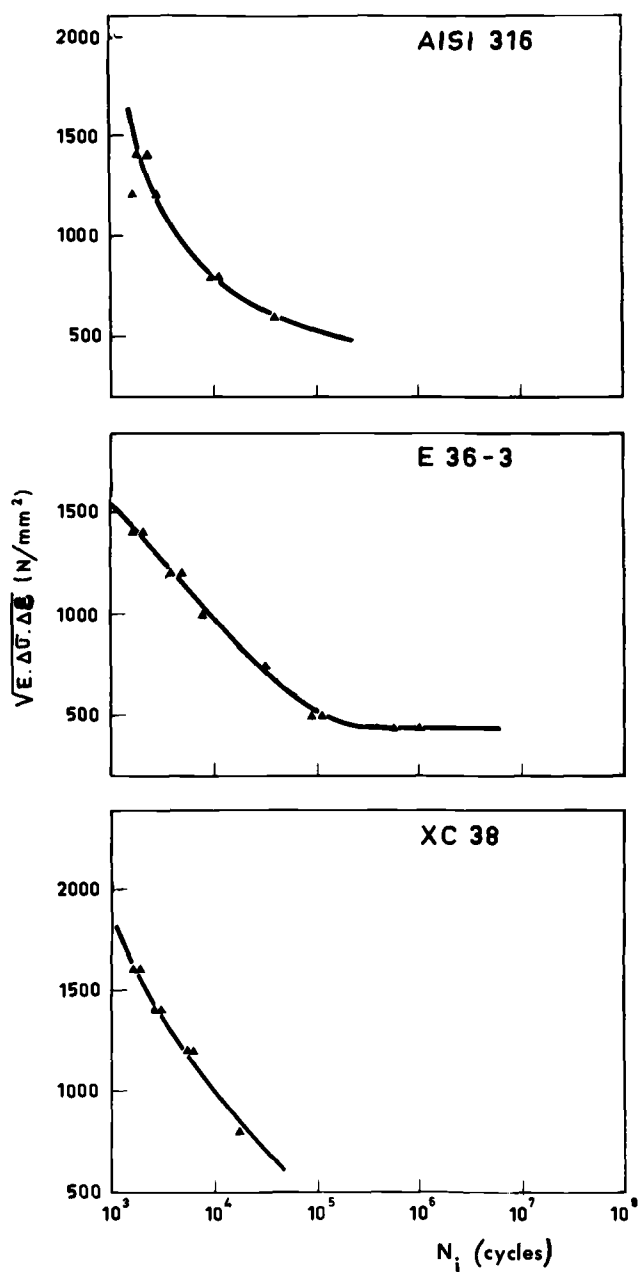


FIG. 9—LCF results presented according to Neuber's rule.

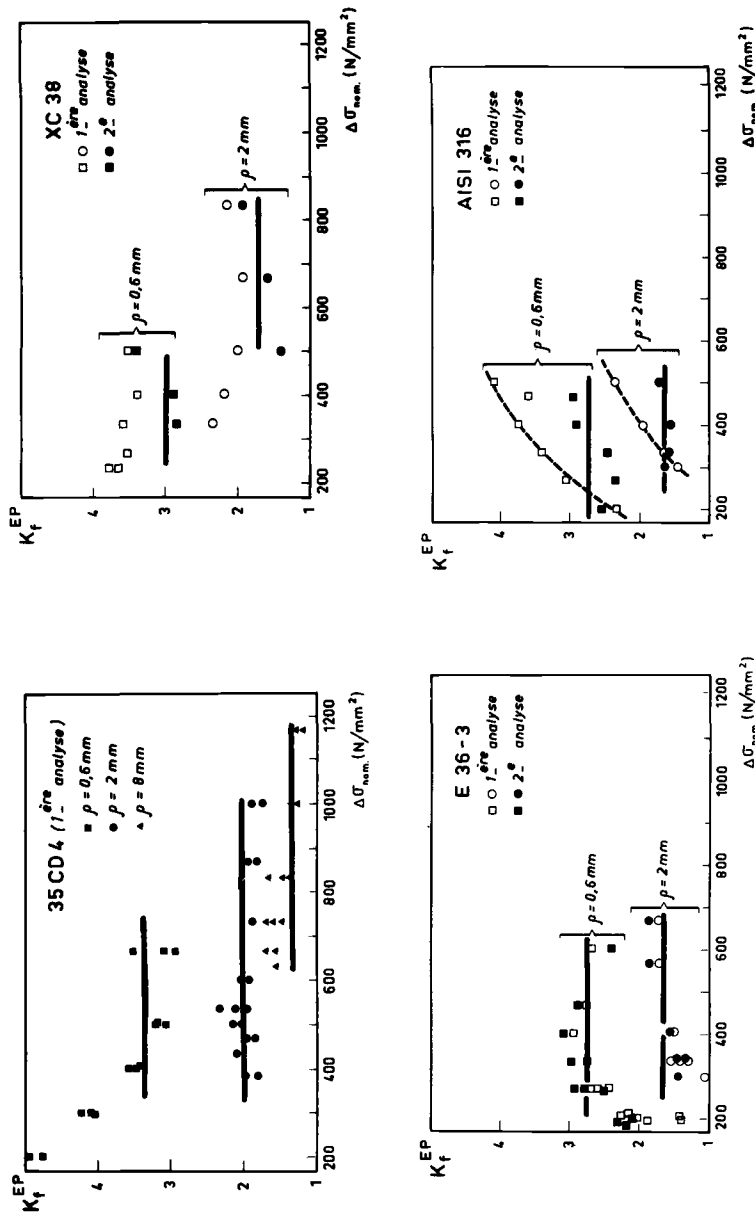


FIG. 10—Fatigue strength reduction factor values obtained by the two approaches.

the definition of crack initiation in the smooth specimens and (2) the local stress-strain history.

Definition of Crack Initiation in the Smooth Specimens—As it is a pertinent statement that the criterion from crack initiation must be the same for smooth and notched specimens [19], the conventional LCF test data fall out of this requirement because they were run up to specimen separation. According to Manson [25] and Pineau [26], 10 to 20 percent can be spent in propagating a crack in a smooth specimen when its total life is between 10^3 and 10^5 cycles. In a previous investigation [18] on high-strength steels, this parameter had not been found to be important, because the LCF smooth specimens broke by sudden failure with a crack size similar to that which was used to define initiation in the notched specimens. The same feature appeared in the case of steel XC 38. However, this approximation cannot be allowed when the material ductility increases. This is thought to be a major source of error in the case of the first analysis when applied to steels AISI 316 and E 36.

Local Stress-Strain History—In the procedure shown in Fig. 8, the influence of mean strains and/or stresses is not accounted for. Examples in the literature [19–20] show that neglecting this effect can induce incorrect prediction of crack initiation at notches. In this regard the second procedure, which is based on Neuber simulation tests, meets this requirement because it reproduces, at least approximately, the strain history at the notch root [14].

LCF experiments reported in Ref 27 show that the cyclic properties and resistance to failure of the 316 steel were greatly dependent on strain history. This is a second reason why K_f^{EP} is about constant when the second procedure is used, while it was increasing with the first one.

With regard to the effect of mean stress, it was shown earlier that the mean stress at the notch root was zero, even for the Neuber simulation tests. In this respect, the damage parameter used in this investigation coincides with the one Smith et al [11] proposed to account for the mean stress effect. Such is not the case for high-cycle fatigue, which is beyond the scope of the present paper, where this must be accounted for by using the appropriate damage parameter and the appropriate smooth specimen data.

Conclusion

Fatigue crack initiation tests with notched specimens and LCF tests were carried out. LCF data with unnotched specimens were used to analyze the fatigue crack initiation data. This was done according to Neuber's rule. In this way it was possible to derive an elasto-plastic fatigue strength reduction factor K_f^{EP} which is able to account for local plasticity effects on the fatigue crack initiation phenomenon. Its amount depends on the notch severity and the mechanical properties of the material.

LCF smooth specimens were strained according to Neuber's rule in order to simulate the local strain history. This procedure improved the correlation between LCF and notched specimen data by defining a fatigue strength reduction factor that is almost constant in the low-cycle fatigue regime.

APPENDIX I

LCF Properties of the Steels Investigated

$$R_{\epsilon} = \frac{\epsilon_{\min}}{\epsilon_{\max}} = -1$$

35 CD4

Cyclic stress-strain law:

$$\frac{\Delta\sigma}{2} = 861 \left(\frac{\Delta\epsilon_p}{2} \right)^{0.13}$$

Manson-Coffin curve:

$$\frac{\Delta\epsilon_t}{2} = \frac{\Delta\epsilon_e}{2} + \frac{\Delta\epsilon_p}{2} = 0.63 (2N)^{-0.072} + 78.25 (2N)^{-0.675}$$

XC 38

Cyclic stress-strain law:

$$\frac{\Delta\sigma}{2} = 650 \left(\frac{\Delta\epsilon_p}{2} \right)^{0.104}$$

Manson-Coffin curve:

$$\frac{\Delta\epsilon_t}{2} = 0.64 (2N)^{-0.091} + 97.2 (2N)^{-0.686}$$

AISI 316

Cyclic stress-strain law:

$$\frac{\Delta\sigma}{2} = 489 \left(\frac{\Delta\epsilon_p}{2} \right)^{0.39}$$

Manson-Coffin curve:

$$\frac{\Delta\epsilon_t}{2} = 1.42 (2N)^{-0.223} + 23.5 (2N)^{-0.434}$$

E-36-3

Cyclic stress-strain law:

$$\frac{\Delta\sigma}{2} = 366 \left(\frac{\Delta\epsilon_p}{2} \right)^{0.22}$$

Manson-Coffin curve:

$$\frac{\Delta \epsilon_t}{2} = 0.54 (2N)^{-0.12} + 43.9 (2N)^{-0.533}$$

Units: σ in N/mm², ϵ in %, N = number of cycles to failure.

APPENDIX II

Description of the Neuber Simulation Test Technique

Neuber's rule [13,14] is a method of approximately determining the local stress-strain behavior of material at the root of a notch. For a nominal loading in the elastic range, the local stress and strain amplitudes follow the relation

$$\sqrt{E \Delta \sigma \Delta \epsilon} = K_f \cdot \Delta \sigma_{\text{nom}}$$

where K_f depends on the sharpness of the notch.

In order to simulate this behavior on smooth specimens, it is necessary to control the product $\Delta \sigma \times \Delta \epsilon$. This is now possible with computerized fatigue machines. At IRSID, a minicomputer PDP 11/03 was coupled to a servohydraulic MTS machine of 250-kN capacity.

Description of the Control Program

The program is called DSDE. It was written to control the product $\Delta \sigma \times \Delta \epsilon$ during the LCF test on a smooth specimen. The inputs of the computer are the stress and strain at the specimen. At each strain reversal, the computer generates a strain ramp (increasing or decreasing) which is the command of the machine. During the i th reversal, which begins at the point $(\sigma_i; \epsilon_i)$, the quantity Q is computed at any time as

$$Q = (\sigma - \sigma_i)(\epsilon - \epsilon_i)$$

When Q reaches the preselected value of the constant $C1$ at the point $(\sigma_{i+1}; \epsilon_{i+1})$, the command is reversed and Q is computed again, taking $(\sigma_{i+1}; \epsilon_{i+1})$ as a new origin. $C1$ is computed from the input parameters K_f and $\Delta \sigma_{\text{nom}}$:

$$C1 = \frac{1}{E} (K_f \cdot \Delta \sigma_{\text{nom}})^2$$

$C1$ works throughout the test, except for the first reversal. Indeed, DSDE takes into account the load ratio R of the nominal loading. During the first reversal, Q is compared with the constant $C2$, which is defined by

$$C2 = \frac{1}{E} \left(\frac{K_f \Delta \sigma_{\text{nom}}}{1 - R} \right)^2$$

References

- [1] Peterson, R. E., *Stress Concentration Factors*, Wiley-Interscience, New York, 1974.
- [2] Neuber, H., *Theory of Notch Stresses*, J. W. Edwards, Ann Arbor, Mich., 1946.
- [3] Kuguel, R., "The Highly Stressed Volume of Material as a Fundamental Parameter in the Fatigue Strength of Metal Members," Report No. 169, University of Illinois, Urbana, June 1960.

- [4] Neuber, H., "Theoretical Determination of Fatigue Strength at Stress Concentration," Technical Report AFML-TR-68-20, April 1968.
- [5] Forman, R. G., *Engineering Fracture Mechanics*, Vol. 4, 1972, pp. 333-345.
- [6] Jack, A. R. and Price, A. T., *International Journal of Fracture Mechanics*, Vol. 6, No. 4, Dec. 1970.
- [7] Jack, A. R. and Price, A. T., *Acta Metallurgica*, Vol. 20, July 1972, pp. 857-866.
- [8] Barsom, J. M. and McNicol, R. C. in *Fracture Toughness and Slow-Stable Cracking*, ASTM STP 559, American Society for Testing and Materials, 1974, pp. 183-204.
- [9] Heckel, K. and Wagner, R., *International Journal of Fracture*, Vol. 11, 1975, pp. 135-140.
- [10] Topper, T. H., Wetzel, R. M., and Morrow, JoDean, *Journal of Materials*, Vol. 4, No. 1, March 1969, pp. 200-209.
- [11] Smith, K. N., Watson, P., and Topper, T. H., *Journal of Materials*, Vol. 5, No. 4, Dec. 1970, pp. 767-778.
- [12] Morrow, JoDean, Wetzel, R. M., and Topper, T. H. in *Effects of Environment and Complex Load History on Fatigue Life*, ASTM STP 462, American Society for Testing and Materials, 1970, pp. 74-91.
- [13] Stadnick, S. J. and Morrow, JoDean in *Testing for Prediction of Material Performance in Structures and Components*, ASTM STP 515, American Society for Testing and Materials, 1972, pp. 229-252.
- [14] Leis, B. N., Gowda, C. V. B., and Topper, T. H. in *Cyclic Stress-Strain Behavior*, ASTM STP 519, American Society for Testing and Materials, 1973, pp. 133-150.
- [15] Leis, B. N., Gowda, C. V. B., and Topper, T. H., *Journal of Testing and Evaluation*, Vol. 1, No. 4, July 1973, pp. 341-348.
- [16] Leis, B. N. and Topper, T. H., *Nuclear Engineering and Design*, Vol. 29, 1974, pp. 370-383.
- [17] Gowda, C. V. B., Topper, T. H., and Leis, B. N., "Crack Initiation and Propagation in Notched Plates Subjected to Cyclic Inelastic Strains," in *Proceedings*, ICM Conference, Kyoto, 1971, Vol. 2, pp. 187-198.
- [18] Baus, A., Lieurade, H-P., Sanz, G., and Truchon, M. in *Flaw Growth and Fracture*, ASTM STP 631, American Society for Testing and Materials, 1977, pp. 96-111.
- [19] Leis, B. N., "An Approach for Fatigue Crack Initiation Life Prediction with Applications to Complex Components," in *Proceedings*, 9th ICAF Symposium, Darmstadt, Germany, 9-13 May 1977.
- [20] Dowling, N. E., Brose, W. R., and Wilson, W. K., "A Discussion of the Local Strain Approach to Notched Member Fatigue Life Prediction," Westinghouse Research Report No. 76-1E7-PALFA-P1, Feb. 1976.
- [21] Chaboche, J. L., *Revue Française de Mécanique*, Nos. 50 and 51, pp. 71-82.
- [22] Chaboche, J. L. and Stolz, C., *Revue Française de Mécanique*, No. 52, 1974, pp. 37-47.
- [23] Marandet, B., Lagge, G., Pinard, J., and Truchon, M., "Détection de l'amorçage et suivi de la propagation d'une fissure par variation du potentiel électrique en régime alternatif," IRSID Report 549, June 1978.
- [24] Neuber, H., *Journal of Applied Mechanics*, Vol. 28, No. 4, 1961, p. 544.
- [25] Manson, S. S., *Pressure Vessels and Piping—Design and Analysis*, Vol. 1, ASME, 1972, p. 157.
- [26] Pineau, A. and Petrequin, P., "La fatigue plastique oligocyclique," in *La fatigue des matériaux et des structures*, C. Bathias and J. P. Bailon, Eds., PUM, 1980, Montreal.
- [27] Amzallag, C., Rabbe, P., Gallet, G., and Lieurade, H-P., "Influence des conditions de sollicitation sur le comportement en fatigue oligocyclique d'aciers inoxydables austénitiques," Rapport IRSID, RPC 9, Oct. 1976.

H. Nowack,¹ D. Hanschmann,¹ J. Foth,¹ G. Lütjering,²
and G. Jacoby³

Prediction Capability and Improvements of the Numerical Notch Analysis for Fatigue Loaded Aircraft and Automotive Components

REFERENCE: Nowack, H., Hanschmann, D., Foth, J., Lütjering, G., and Jacoby, G., "Prediction Capability and Improvements of the Numerical Notch Analysis for Fatigue Loaded Aircraft and Automotive Components," *Low-Cycle Fatigue and Life Prediction, ASTM STP 770*, C. Amzallag, B. N. Leis, and P. Rabbe, Eds., American Society for Testing and Materials, 1982, pp. 269–295.

ABSTRACT: Because they combine minimum experimental expenses with a maximum flexibility regarding their application areas and objectives, numerical notch analysis methods have attained special importance among the presently available crack initiation life prediction methods.

The first part of this study gives the results of an evaluation program in which the prediction capability of the numerical notch analysis concept using the Neuber approach for the consideration of the notches was investigated. The loading histories considered are standard flight loading histories (TWIST and FALSTAFF), automotive histories, and simple, systematically varied loading histories. The test specimens were center notched and angle type, and the materials were high-strength aluminum alloys, Ti6-4, and others. The test results showed satisfactory predictions in many cases; however, unacceptable deviations occurred, especially under long-term random loading, after high peak loads, and under a high amount of compressive loads.

The second part of this study investigates the reasons for the deviations in the predictions. The main reasons are (1) inadequate consideration of the sequence effects on the damage accumulation, and (2) differences in the stress states and crack initiation processes at the stress raisers of the notched specimens and at the unnotched specimens.

A new damage evaluation procedure is proposed that is based on these test results. A more adequate definition of the crack initiation stage is attempted and a consideration of short cracks is provided.

KEY WORDS: crack initiation life behavior, variable amplitude loading, prediction methods, damage evaluation, sequence effects, small cracks

¹ Department Head and Research Fellows, respectively, Deutsche Forschungs- und Versuchsanstalt für Luft- und Raumfahrt (DFVLR), Institut für Werkstoff-Forschung, Köln, West Germany.

² Professor, Technische Universität Hamburg-Harburg, Hamburg, West Germany.

³ Professor, Schenck AG, Darmstadt, West Germany.

In order to achieve a higher efficiency of light-weight constructions, improved fatigue life prediction methods, which are more reliable, more flexible, and less expensive than the conventional methods (as, for example, the Palmgren-Miner hypothesis [1]⁴ are required.

An important step in damage analysis methods development was the special consideration of stress concentrations present at specimens and components and the local stresses and strains at these stress raisers (local approach) [2,3]. The crack initiation stage and the crack propagation stage are separately considered.

An important basis of the local approach for the crack initiation stage is the idea of Crews and Hardrath, the "Companion Specimen Method" [4]. The local stresses and strains are determined by the combined experimental operation of the notched specimen or component (for which the prediction has to be made, and where the local strains are measured at the root of the notch) and an unnotched specimen (where the local strains are applied to determine the corresponding local stresses). It is assumed that the notch root material and the unnotched specimen behave in a similar manner and show the same crack initiation life behavior (equivalence criterion). Because of its large experimental expense, the companion specimen method is not practical in its basic form. Derivatives of the method, however, have attained special importance, especially the experimental notch simulation method (Neuber control method) [5] in which the notched specimen (or component) is replaced by the utilization of an equation derived by Neuber (Neuber hyperbola) [6] or by other equations [7]. The material stress-strain response and the damage accumulation are simulated on an actual (unnotched) specimen, which should yield quite realistic results within the boundaries of the aforementioned equivalence. This method is applied in the present study, especially in a consideration of the nonlinear damage accumulation in the crack initiation stage.

The most practical derivative of the companion specimen method is the numerical notch analysis. Only basic material input data are required and crack initiation life predictions can be made for arbitrary loading histories and specimen geometries (provided that the actual notch factor is known). The basic principles of the method have often been described [8,9]. The special features of the analysis types considered in the present study are briefly outlined later.

In this paper the numerical analysis is considered in its standard format and with various modifications that have been proposed in the literature to improve the quality of its predictions. It is shown that a comparison of the predictions of the numerical analyses with actual test results for different types of automotive and standard flight histories and different high-strength materials (aluminum alloys, Ti6-4) gives unsatisfactory predictions in several

⁴ The italic numbers in brackets refer to the list of references appended to this paper.

cases. Systematic tests on unnotched specimens show that inadequate consideration of the sequence effects that occur under consecutive cycles with varying amplitudes and mean stresses, which lead to considerable deviations from a linear damage accumulation scheme, is a main cause of the unsatisfactory predictions. An approach that more accurately accounts for the sequence effects is described.

Very short cracks appear in the course of the fatigue life much earlier than they can be detected by engineering nondestructive testing methods. These short cracks and their behavior significantly influence the whole damage accumulation process in the crack initiation stage. During the last 3 to 5 years analysis concepts have been formulated to account for the behavior of very short cracks at stress raisers [10,11]. Some of these approaches even neglect the crack-free part of the fatigue life, and the whole fatigue damage analysis is based on crack propagation. The advantages of approaches where short cracks are included, and where the significance of the severe stress field around such small cracks and their opening behavior is considered, are outlined in the last part of this study. The still-existing difficulties in applying these concepts from a practical point of view are also discussed.

Investigation Program

The investigation program included three main parts:

1. An analysis evaluation program.
 - (a) Series of tests with different loading histories, specimen types, and materials were run and the occurrence of engineering-size cracks was observed.
 - (b) Crack initiation life predictions were made with the numerical notch analysis method.
 - (c) Results from (a) and (b) were compared in order to gain insight into the prediction capabilities.
2. A test program that investigated the causes for the deviations between the actual and predicted crack initiation life data. Its main objectives were:
 - (a) A systematic experimental evaluation of the sequence effects under variable amplitude loading by applying simple systematically varied strain histories on unnotched specimens.
 - (b) The application of the experimental notch analysis method for comparative considerations.
 - (c) A careful observation of the initiation of short cracks at notches as well as at unnotched specimens in order to identify the actual crack initiation mechanism more clearly.
3. The integration of the results of the second part of the study into the notch evaluation schemes.

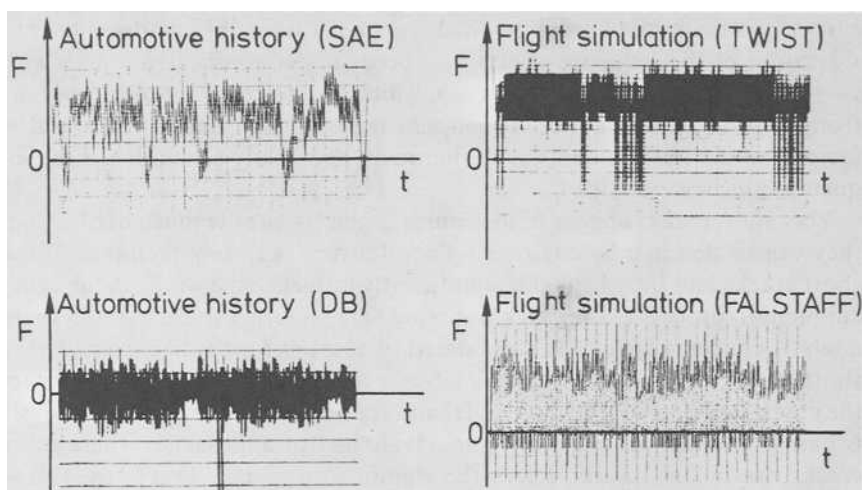


FIG. 1—Loading histories as applied in the tests.

Notch Analysis Evaluation Program

Experimental Program

The loading histories applied in the present study are shown in Fig. 1. The monotonic and cyclic properties of the investigated materials are given in Table 1 in the manner proposed in Ref 12, so that they can immediately be used for the application of the numerical notch analysis methods.

The size and shape of the 4.7 and 10 mm thick specimens are given in Fig. 2. The crack initiation life behavior was determined with the notched specimens (Figs. 2a to 2c); the unnotched specimen type (Fig. 2e) served for the generation of the basic material and notch analysis input data. The notched specimen type of Fig. 2c ($K_t \sim 3.3$) and the specimen types of Fig. 2d ($K_t \sim 1.3$) and Fig. 2e ($K_t \sim 1.0$) were applied for basic crack initiation mechanism studies. The elastic strain distributions along the net sections of these specimen types as determined by finite-element analyses are shown in Fig. 3.

TABLE 1—Monotonic and cyclic properties of the investigated materials.

Material	2024-T3	7075-T6	7475-T761	GkAlSi7Mg _{wa}	TiAl6V4
Monotonic Properties					
Modulus of elasticity (E), N/mm ²	72 500	71 000	70 000	69 000	120 350
Yield strength ($\sigma_{0.2}$), N/mm ²	315	470	457	190	1046
Ultimate strength (σ_B), N/mm ²	475	532	510	230	1069
Cyclic Properties					
Strain-hardening exponent (n')	0.136	0.154	0.0514	0.0682	0.137
Strength coefficient (K')	960	276.36	620	354	1797

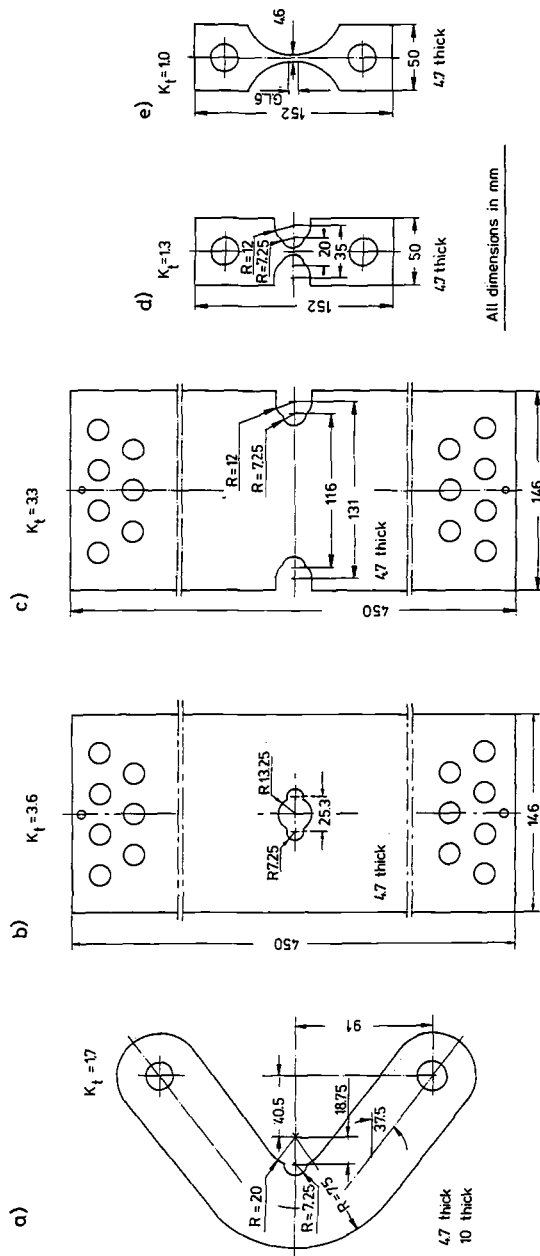


FIG. 2—Specimens.

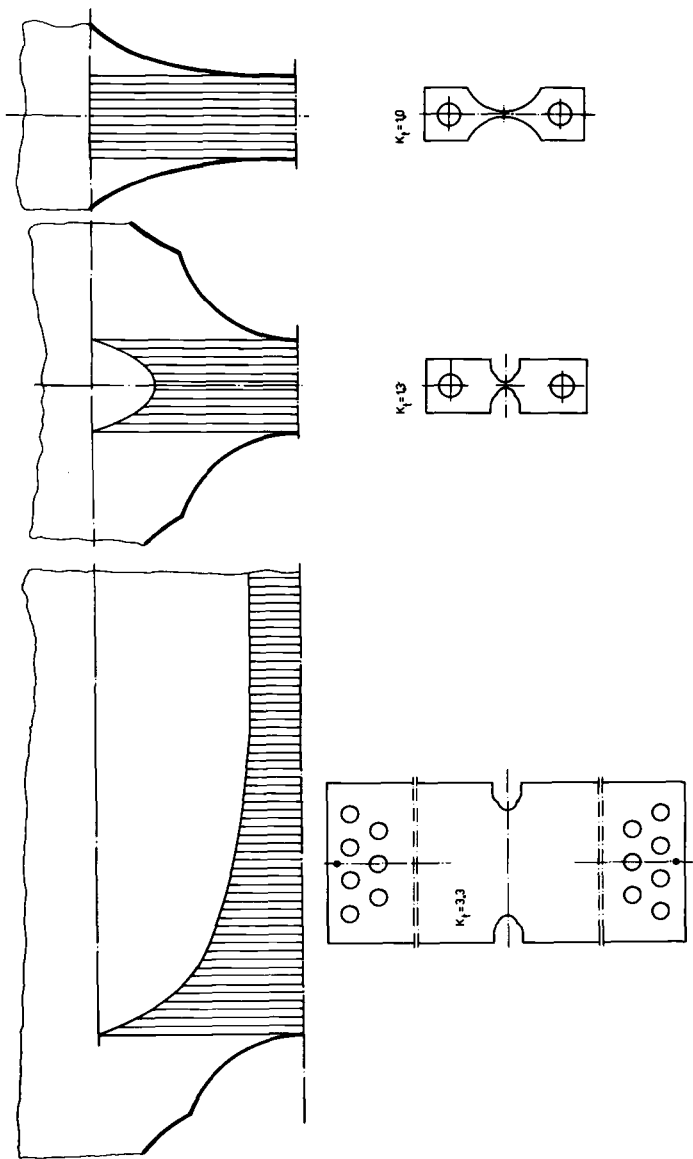


FIG. 3—Finite-element analysis of the net section stresses.

As the yield stress of the material was exceeded at the stress concentrations, the elastic-plastic deformations along the net section of the specimens were experimentally determined by applying a special grid technique, where the displacements between the nodal points of an engraved grid (line spacing 0.1 mm) were measured both in the loading direction and transverse to the loading direction (Fig. 4).

The orientation of all specimens was such that the cracks propagated in the rolling direction.

All tests were performed on 400 and 20 kN computer-controlled servohydraulic testing machines. The computer generated the loading histories for the tests and changed the loading input on-line by the aid of a special memory matrix routine (EKOR, Schenck AG) until the actual loading on the specimens was accurate (within ± 2 percent). (Because of this special software a serious source of errors in variable-amplitude testing was eliminated.) A second main function of the computer was the control of the Neuber control tests [9].

For the observation of the crack initiation in the tests, two different methods were applied:

1. *A high-resolution recording method*—the notch root and the side surfaces of the specimens were observed by at least four microscopes; cracks of a size less than 10 μm could be identified, and their growth was followed during the course of the tests. A special mapping procedure was applied in which the locations and the actual lengths of the growing microcracks were documented. For certain cycle numbers a separate sheet of transparent paper was used. By the superposition of these transparent sheets a reconstruction of the whole crack initiation process became possible.

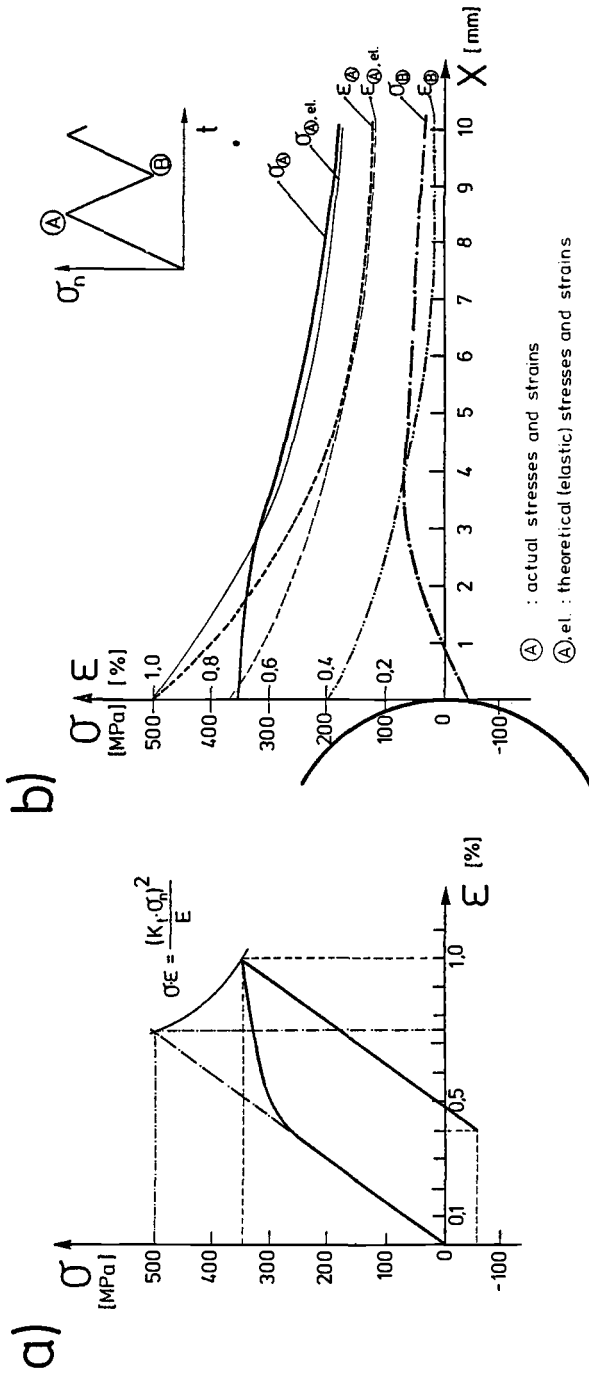
2. *A routine method for the detection of cracks of an engineering size*—this consisted of one microscope (magnification $\times 100$) and a special crack initiation monitoring device similar to that in Ref 13.

Computerized Notch Analysis

The notch analysis method was used in a basic format and in various modifications. The basic format included:

1. A straight-line element simulation of the stress-strain response of the material, based on the stabilized cyclic material properties (Table 1) and a detailed consideration of the material memory effect under variable-amplitude loading [14] (Module I).

2. The transformed Neuber equation [5] [for the consideration of the notches (Module II)], whereby the elastic K_t -value was normally used in the equation (only in a very few cases the fatigue notch factor after [15] or after [16] was applied). The intersections of the σ - ϵ curve with the Neuber hyper-



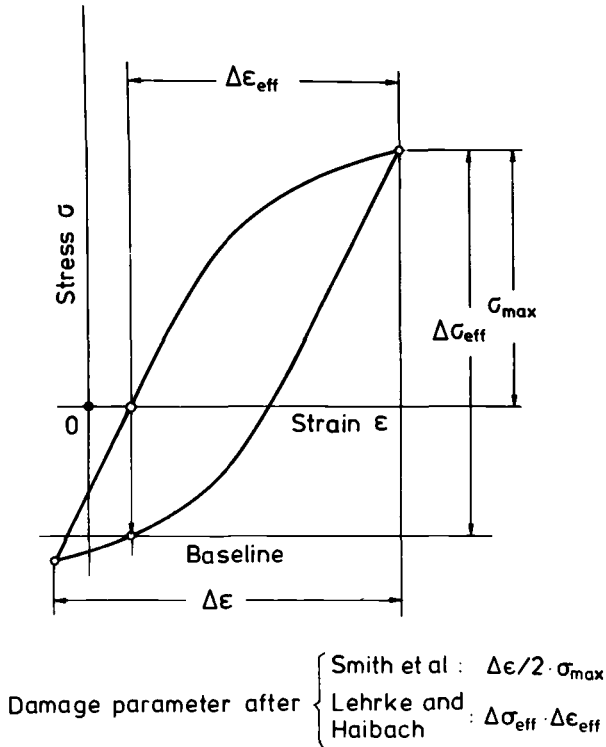


FIG. 5—Definition of damage parameters.

bolas were always iteratively determined with a high accuracy in order to avoid any unrealistic shifts in the σ - ϵ behavior.

3. For the damage evaluation (Module III), the Rainflow counting method, a damage evaluation per hysteresis loop on the basis of constant-amplitude crack initiation life data using the Smith et al damage parameter (Fig. 5) to account for the mean stress effect on linear damage accumulation, and—as a criterion for the end of the crack initiation stage—a sum of the individual damage amounts of unity.

The modifications of the numerical notch analysis method which were investigated here were mainly different damage calculation schemes in Module III:

1. The utilization of constant-amplitude crack initiation life curves, whereby the curves were extended below the endurance limit of the material for the evaluation of the damage partitions.

2. The use of the Haibach/Lehrke damage evaluation concept [17] instead of the Smith et al concept. In this concept the damage increments per cycle are calculated using a variable base line, which depends on the magni-

tude of the highest compressive loads in the loading history (Fig. 5). So long as no plastic deformations occur in the compressive direction the base-line remains unchanged for the subsequent loading events. However, when compressive plastic deformations actually occur which lead to a shift of the up-going branch of the overall hysteresis loop into the compressive direction, the base-line moves down. This leads to higher damage amounts per hysteresis loop not only for the instantaneous hysteresis loop but also for all following hysteresis loops. The procedure represents a load sequence dependent damage evaluation. Haibach et al reason that small cracks have to be assumed as being present very early in the fatigue life. These cracks open and close. As soon as a plastic deformation into compression occurs the residual stress field in the material surrounding the small cracks (the essential cause for crack closure) is rebuilt due to the plasticity, and the crack opening level is decreased; this leads to higher effective stress intensities at the crack tip and from that to higher crack rates. (Although this model is not complete, the idea to consider the load sequence effects explicitly has been a significant development in notch analysis.)

Comparison of Predictions and Actual Behavior

For an illustrative comparison of the predicted and the actual test results a plot-procedure as proposed by W. Schütz (IABG, Germany) is applied: a log-normal plot of the ratios of the predicted values, N_{pred} , by the actual test values, N_{test} . In such plots two essential features can be distinguished: the mean value of the $N_{\text{pred}}/N_{\text{test}}$ values [which shows the general trend in the predictions (overprediction or underprediction)] and the scatter range of the $N_{\text{pred}}/N_{\text{test}}$ values (which is a main indication of the uncertainties due to a certain method). Both parameters are expressions of limitations in the physical quality of a prediction method.

Figure 6 compares five different materials (Al 2024, Al 7075, Al 7475, G_kAlSi7Mg_{wa} (cast aluminum alloy), Ti6-4) and four different loading histories (SAE, DB, TWIST, FALSTAFF). The Smith et al damage parameter concept and straight-line elongated crack initiation life curves from strain-controlled constant-amplitude tests with unnotched specimens were used for the damage evaluation.

It can be observed that the $N_{\text{pred}}/N_{\text{test}}$ values group around 1 with a slight tendency to overpredict the actual crack initiation life behavior. It was found that decreasing the stress levels or increasing the number of small stress variations between higher peak loads caused a tendency to overpredict the actual crack initiation life behavior.

Figure 7 shows the crack initiation life behavior as predicted using the Haibach et al damage calculation scheme. In this case the predictions were all conservative. The magnitude of the compressive peak loads in the loading history proved to be the most essential controlling variable for the trend in the predictions. All loading histories investigated exhibited high compressive

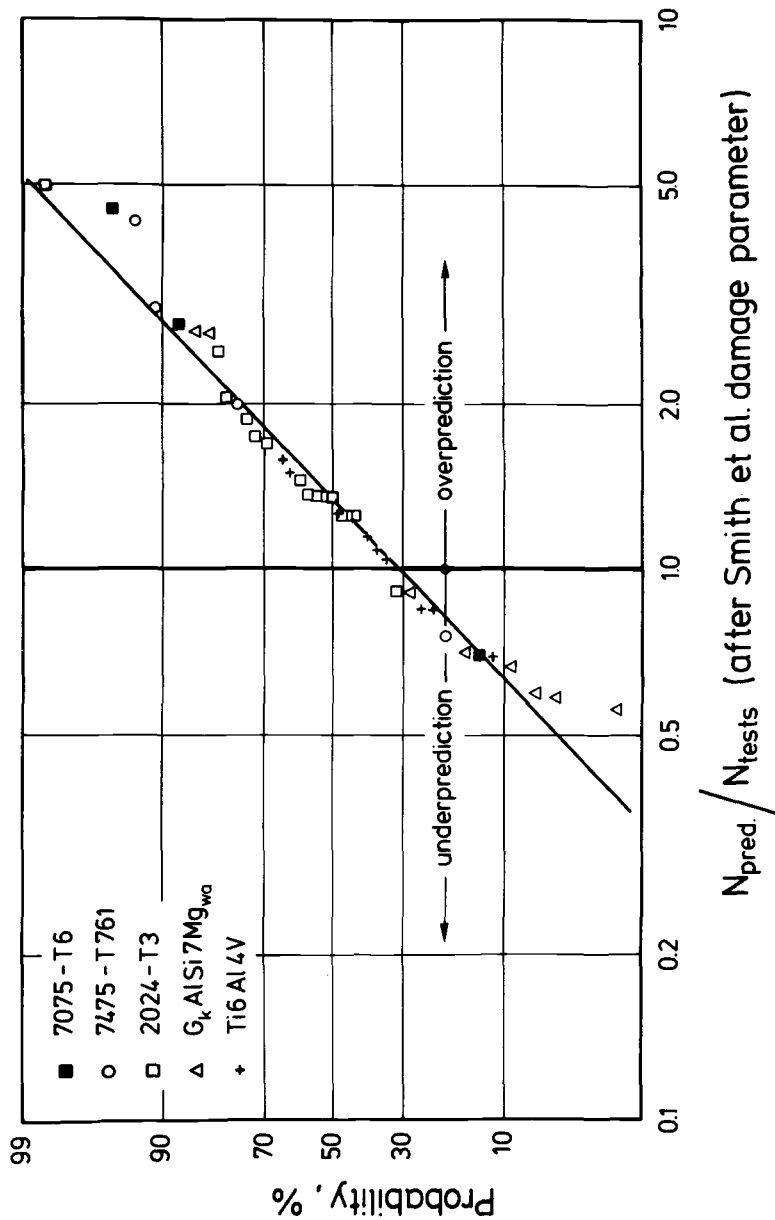


FIG. 6—Crack initiation life predictions using the Smith et al damage parameter concept.

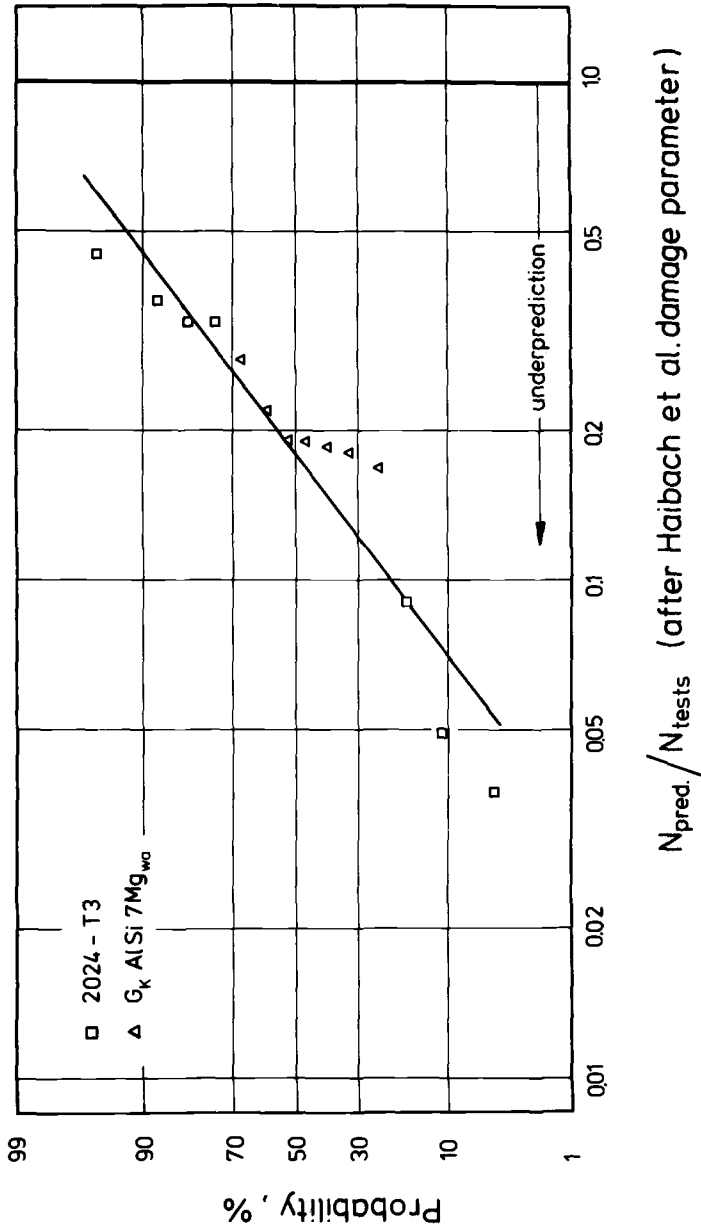


FIG. 7—Crack initiation life predictions using the Haibach et al damage parameter concept.

loads, such that the base-line for the damage parameter evaluation was actually shifted into the compressive direction, which led to conservative predictions in all cases. One can, however, easily imagine that loading histories may exist where the compressive loads are not so high that the position of the base-line is shifted into compression. In these cases the predictions fall closer to those predicted by the Smith et al damage evaluation concept. From that it follows that the whole scatter range in the predictions may become quite large.

When all the prediction results are considered it must be concluded that the quality of the predictions remains unsatisfactory. Improvement of this situation required a more detailed evaluation of the phenomena and mechanisms of the damage accumulation processes, which was tried by the testing and evaluation program described in the following sections.

Analysis of Damage Accumulation Process

Evaluation of Sequence Effects

A systematic evaluation of the load sequence effects that cause a nonlinear damage accumulation becomes rather difficult if loading and geometry parameters vary in a complicated manner. Thus unnotched specimens were taken and simple strain histories were applied (in strain-controlled tests) that consisted of two types of cycles only, which were combined as indicated in Figs. 8 to 10. Constant-amplitude tests, where only one of the two cycle types was applied, were also performed as a basis for damage calculations. Figures 8 to 10 show the experimentally determined crack initiation life behavior and the predicted behavior following the Smith et al and the Haibach et al damage evaluation concepts. The Smith et al damage parameter calculations represent a simply linear damage evaluation scheme. In all cases overpredictions can be observed; obviously considerable sequence effects occur that cause the smaller cycles to damage significantly more than in a constant-amplitude test.

The Haibach et al damage parameter calculations lead to satisfactory predictions only for the 1-1 sequence. For the other histories a significant underestimation of the actual behavior occurs (Figs. 8 and 10) or a considerable overprediction (Fig. 9). The overprediction is close to the Smith et al damage parameter predictions. If all prediction results are considered, the complete range in the predictions between under- and overpredictions is quite large, larger than for the Smith et al damage parameter concept, a tendency which has already been mentioned.

The experimental results in Figs. 8 to 10 show the following important phenomena tendencies. The small cycles inserted in a 1-1 sequence at the top reduced the initiation life (expressed as the number of complete cycles until crack initiation of ~35 percent). If the same damaging effect of the small cy-

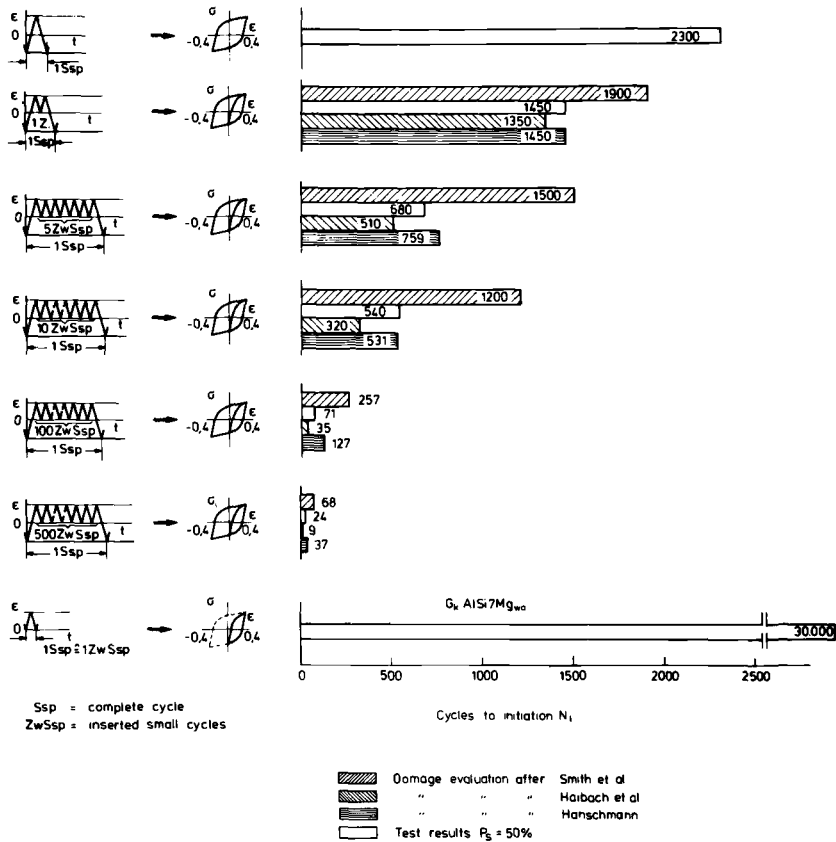


FIG. 8—Predicted and actual crack initiation life behavior under simple program loading history for $G_kAlSi7Mg_{wa}$.

cles in the 1-1 sequence is assumed to become effective in the 1-5 and 1-10 sequences (according to a linear damage calculation scheme), initiation life values of 585 and 340, respectively, should have been observed for the $G_kAlSi7Mg_{wa}$ alloy, and 290 and 170, respectively, for the 2024-T3 alloy. The actual initiation life values, however, are 680 and 540, respectively, for the $G_kAlSi7Mg_{wa}$ alloy, and 472 and 344, respectively, for the 2024-T3 alloy. From these results and from those in Fig. 9, where the small cycles are inserted below and which show the same trend, it can be seen that the damaging effect of a small cycle decreases as the number of consecutive small cycles following one large cycle is increased, and, also, that the type of material influences how much the damaging effect of the small cycles decreases as their number is increased.

Based on the experiences from these and similar basic studies on unnotched specimens a straightforward engineering approach to the problem

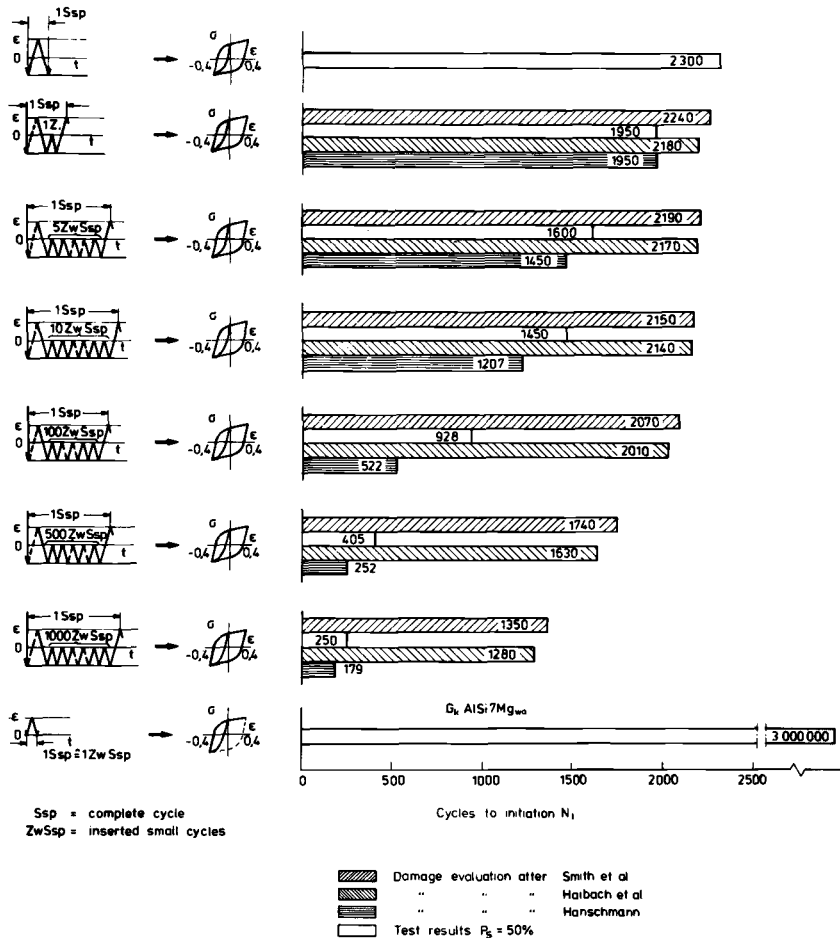


FIG. 9—Predicted and actual crack initiation life behavior under simple program loading history for $G_kAlSi7Mg_{wa}$.

of sequence effects was attempted; this will be described in the following section.

New Damage Evaluation Concept

The observations and influencing factors the new damage evaluation concept considered were:

1. The sequence effects usually increased the damage as compared to a linear damage law. They depended on the type of material investigated and

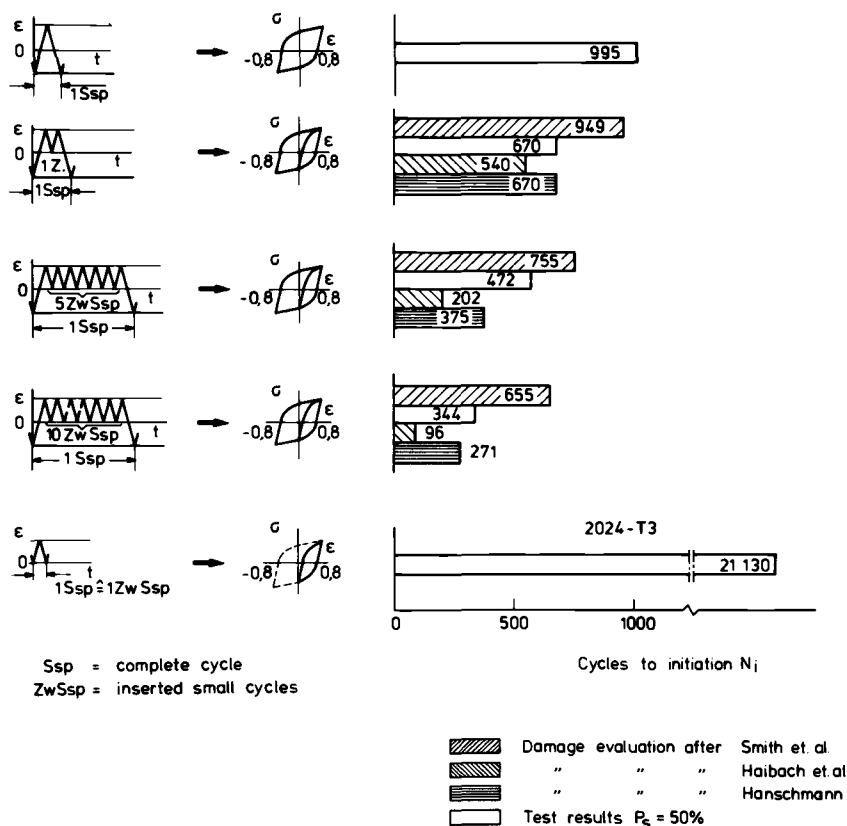


FIG. 10—Predicted and actual crack initiation life behavior under simple program loading history for 2024-T3.

decreased as the cycle number after high load (which caused the sequence effects) increased.

2. The application of the simple linear Smith et al damage parameter concept led to a lower overall scatterband in the prediction results than the utilization of the Haibach et al parameter. The Smith et al parameter offered a more suitable basis for damage calculation schemes.

The damage evaluation scheme found to represent the observed trends in the actual crack initiation life behavior best was

$$D_i = D_{S.P.(h,p,l)} + \Delta D_i \quad (1)$$

where i is the instantaneous cycle number, D_i is the instantaneous damage, $D_{S.P.i}$ is the instantaneous damage partition after the Smith et al parameter-based damage evaluation scheme, and ΔD_i is the additional damage caused by the sequence effects.

$$\Delta D_i = f \left(\text{MSP}, \exp [D_{\text{S.P.}(h.p.l.)}, D_{\text{S.P.}(i-1)}, D_{\text{S.P.}i}], \frac{1}{f(k)} \right) \quad (2)$$

where MSP is a material constant indicating the sensitivity of the material to sequence effects, $D_{\text{S.P.}(h.p.l.)}$ is the damage due to the foregoing highest peak load which caused the main (first-order) sequence effects after the Smith et al parameter, $D_{\text{S.P.}(i-1)}$ is the damage due to the second-last cycle after the Smith et al parameter (to consider second-order sequence effects that may occur between $D_{\text{S.P.}(i-1)}$ and $D_{\text{S.P.}i(i)}$), and $f(k)$ is a functional expression of the number of smaller cycles k after the foregoing high peak load that caused the first-order sequence effects.

Based on a large amount of test results, including those in Figs. 8 to 10, the following equation for ΔD_i was empirically derived for high-strength aluminum alloys:

$$\Delta D_i = \frac{\text{MSP} \left[2 \ln \frac{D_{\text{S.P.}i}}{D_{\text{S.P.}(h.p.l.)}} + 2 \ln \frac{D_{\text{S.P.}i}}{D_{\text{S.P.}(i-1)}} \right]}{\sqrt{K \cdot D_{\text{S.P.}(h.p.l.)} \cdot D_{\text{S.P.}i}}}$$

The application of this damage calculation procedure, which was originally proposed by Hanschmann [9], on simple block histories is shown in Figs. 8 to 10.

When the proposed damage calculation scheme is applied to predict the crack initiation life behavior under the automotive histories, the results shown in Figs. 11 to 13 are achieved. It can be seen that the overall scatter band in the predictions becomes less.

In order to further investigate the quality of the proposed prediction method the Neuber-control method was applied—that is, whole notch histories were applied on unnotched specimens until crack initiation. The results of the application of this method, where the damage realistically occurs on the unnotched specimens, were very close to the predictions of the proposed damage evaluation concept. This indicates that the new concept may be a substantial improvement of the damage evaluation module of the numerical crack initiation life analysis regarding the consideration of sequence effects.

At this stage of the study two points were found necessary to be considered in more detail.

1. The results of the Neuber-control method underestimated (so far as the 50 percent value of the scatter band of all results is considered) the actual life of the notched specimen. A similar tendency was found previously in constant-amplitude tests, where the same strain history was applied at the notch root of a notched specimen and at unnotched specimens [3]. The unnotched specimens also showed a shorter life than the crack initiation life of the notch; that is, the occurrence of an engineering crack of a length of ~ 0.5 mm at the side surface of the notched specimens was taken as the end of the crack

DB-loading history

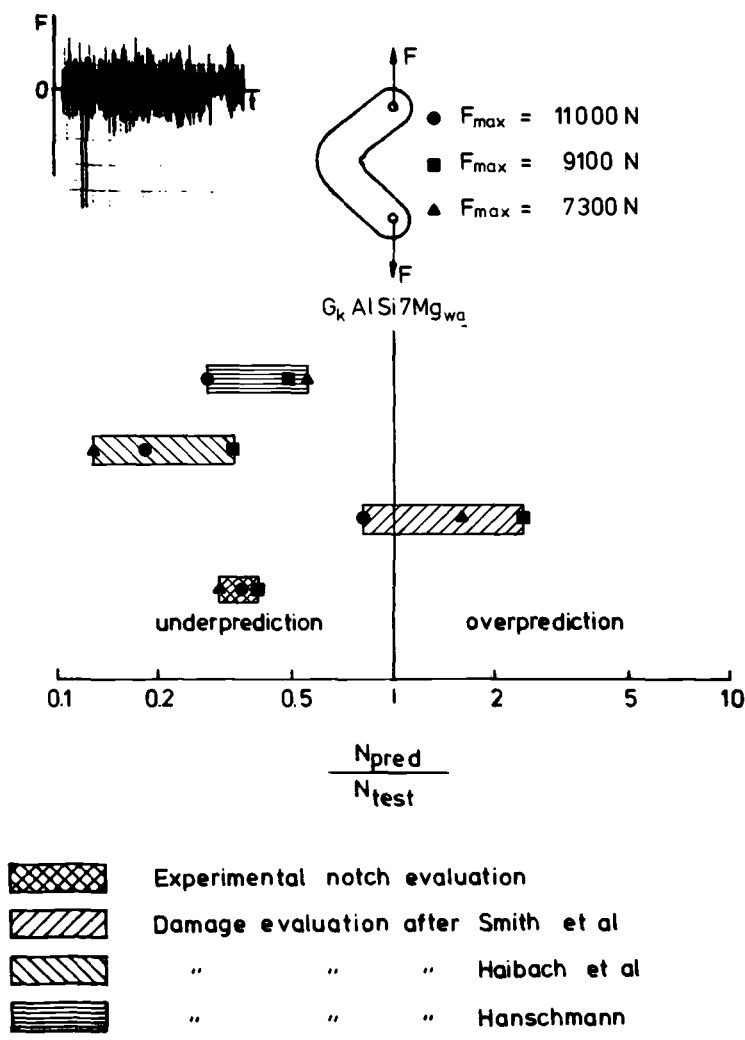


FIG. 11—Crack initiation life predictions using different damage evaluation concepts and after the Neuber-control method.

SAE-loading history

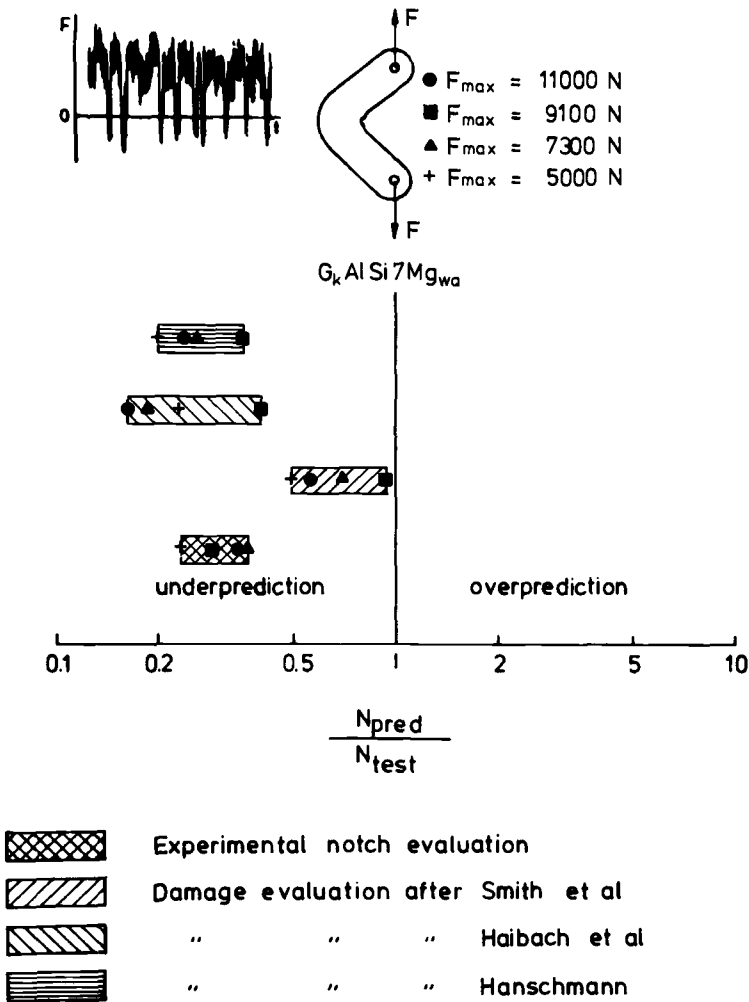


FIG. 12—Crack initiation life predictions using different damage evaluation concepts and after the Neuber-control method.

initiation period. These results also clearly indicated that the equivalence between a notch root and an unnotched specimen with the same strain histories was not satisfactorily fulfilled for the aforementioned convenient crack initiation criterion. Therefore the crack initiation process at the notch root and at the unnotched specimens had to be considered in more detail (see next section).

Automotive history (SAE)

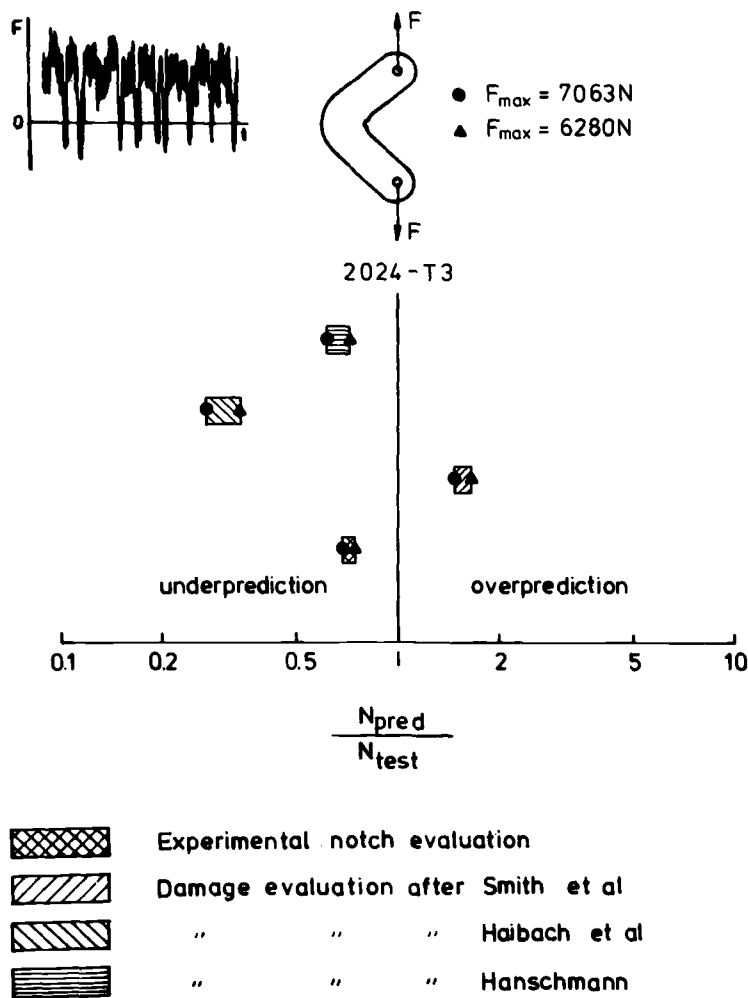


FIG. 13—Crack initiation life predictions using different damage evaluation concepts and after the Neuber-control method.

2. Another essential characteristic of the present crack initiation life prediction concept is that it does not explicitly account for cracks. Studies of sequence effects in the crack stage have shown that especially high positive peak loads cause crack retardation; thus the crack life is elongated. This is in contrast to the observations made in the crack initiation stage, where high peak loads usually increased the damage of the following low loads. Residual stresses and the deformation fields surrounding the crack are mainly responsible for the sequence effects in the crack stage. As soon as a crack grows so large that these stress and deformation mechanisms become predominant, they must be considered in the damage analysis or errors will result.

The crack initiation and propagation is considered in more detail in the next section.

Initiation of Cracks at Notches and at Unnotched Specimens

For the evaluation of the crack initiation behavior at notches where a stress gradient is present and at unnotched specimens with a uniform stress distribution, a constant-amplitude loading was applied at the $K_t = 3.3$ specimen in Fig. 2c; this loading was tension-tension with a maximum net section stress of 160 N/mm^2 and $R = 0.25$, and led to a complete failure of the specimens after $N \sim 10^5$ cycles. The strain history at the notch root showed significant plasticity at the beginning of the loading and then remained nearly elastic (compare Fig. 4). The same strain history was applied on an unnotched specimen (Fig. 2e) and, also, at the notch of the specimen type in Fig. 2d, which shows a similar elastic stress gradient immediately at the notch as the specimen type in Fig. 2c.

Experimental Crack Initiation Behavior

Figure 14 shows the initiation process of cracks at the notch surfaces of the $K_t = 3.3$ specimens as it was observed by optical microscopes. Four essential stages could be distinguished. In Stage I small cracks started at various places at the notch, especially at the hard iron-silicon particles present in the 2024 alloy that fail when the shear forces of the piled-up dislocations at the particles exceed a certain limit. So long as the crack size does not exceed 60 to 80 μm the small cracks start and behave independently, and there are no certain indications which later path the macrocrack will follow. In Stage II the small cracks further grow and other new cracks develop. The end of Stage II can be defined as that cycle number when the surface path of the later macrocrack can be identified (as a sequence of individual cracks of sizes between 100 μm and 300 to 400 μm). The transition from Stage II to Stage III represents a certain limit behind which macrocrack propagation mechanisms become obviously predominant. During Stage III the initiated crack grows through the whole notch surface and into the interior of the

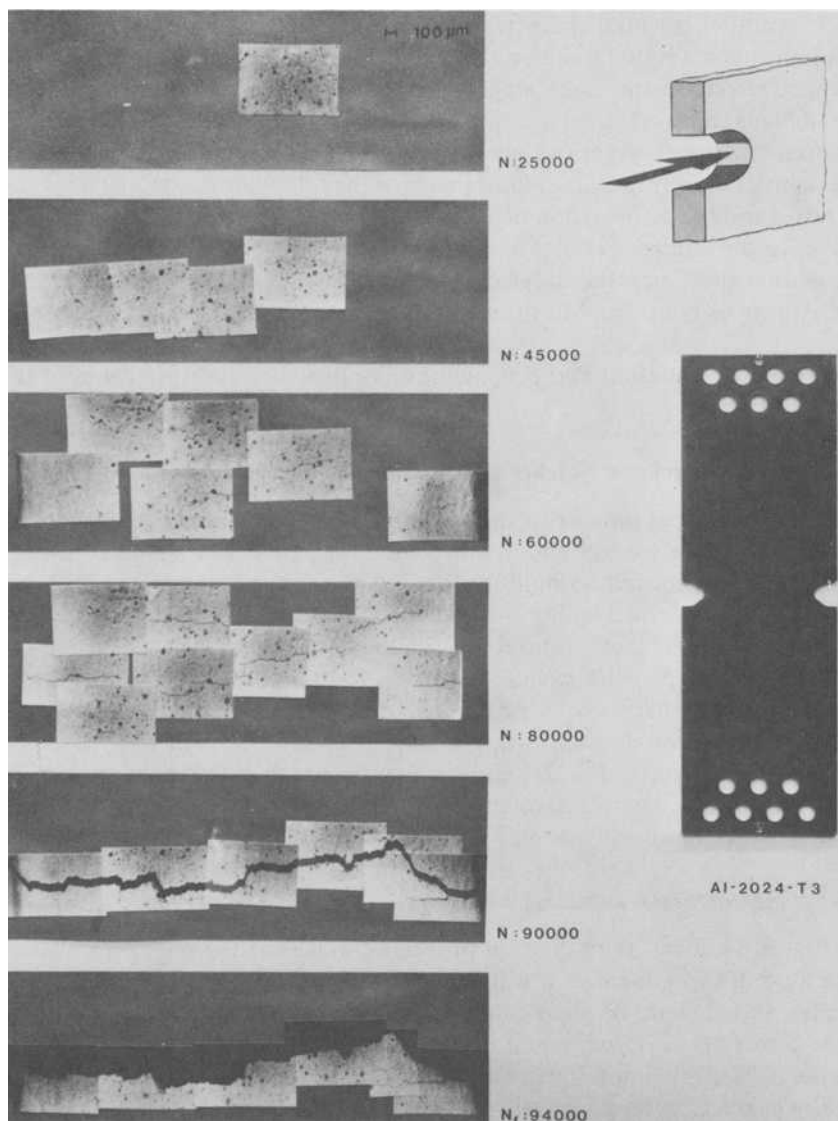


FIG. 14—Crack initiation at a notch.

specimen. When the crack reaches one edge of the notch, Stage III is defined to be ended. During Stage IV the crack propagates as a through crack clearly visible at the side surfaces of the specimen. It can immediately be seen that the convenient technical crack initiation criterion (a crack of ~ 0.5 mm length at the specimen side surface) marks a rather late state of the whole damage process. At the end of Stage IV the specimen separates by complete failure.

The crack initiation processes at the specimen type in Fig. 2*d* and at the unnotched specimen type in Fig. 2*e* show qualitatively similar stages; however, the cycle numbers for the individual stages (especially for Stage III) are different and a significant Stage IV could not be observed. Figure 15 plots the observed lengths of the predominant cracks and the scatter bands against the cycle numbers. It can be seen that the Stage III period is extremely short for the unnotched specimen. The reason for this is the high uniform stress field along the whole cross section of the specimen compared with the other (notched) specimen types, where the stresses decrease behind the specimen surface (stress gradient) (compare with Figs. 3 and 4) and where higher cycle numbers have to be applied in order to reach a similar crack size.

In summary, significant differences in the trends of the fatigue behavior of specimens with a gradient at the notch and without a gradient (unnotched specimen) occurred as soon as Stage I was ended. The formation and propagation of the macrocrack were highly accelerated for the unnotched specimens. The results indicate that equivalence considerations of notches and unnotched specimens where the same surface strain histories are applied require a careful consideration of the individual crack initiation processes.

Analysis of Short Crack Behavior

As previously mentioned, several fracture mechanics based methods have been proposed that consider the behavior of short cracks at notches [10,11]. These analyses explicitly include both (1) the notch stress field, and (2) the small crack stress field within the notch stress field, for the calculation of the stress-intensity factors.

These analyses show that, because of its notch field, a crack starting at a notch surface is propagated by a different stress-intensity variation than a crack of the same size starting at a flat surface. At the notched specimen types in Figs. 2*c* and 2*d* the notch field influences play a significant part. Unfortunately a satisfactory quantitative evaluation of the crack propagation behavior for the specimens in the present study was not possible for several reasons:

1. Presently available continuum mechanics analyses consider cracks that start immediately as completely through cracks. Actually they begin as notch surface cracks—that is, their shape is first the envelope of several individual small cracks. Later a roughly half-elliptical crack shape develops. The extension of the elliptical crack into the interior of the specimen is influenced by the notch field. In tests with the specimen type in Fig. 2*c* the short axis of the ellipse became about 0.3 to 0.4 times the long axis, the visible surface crack at the notch. The crack front propagated up to about $\frac{2}{3}$ of the notch field extension into the interior of the specimen until the cracks became visible as side surface cracks. The assumption that completely through cracks are present only from the beginning is not valid in the present case. Exact solu-

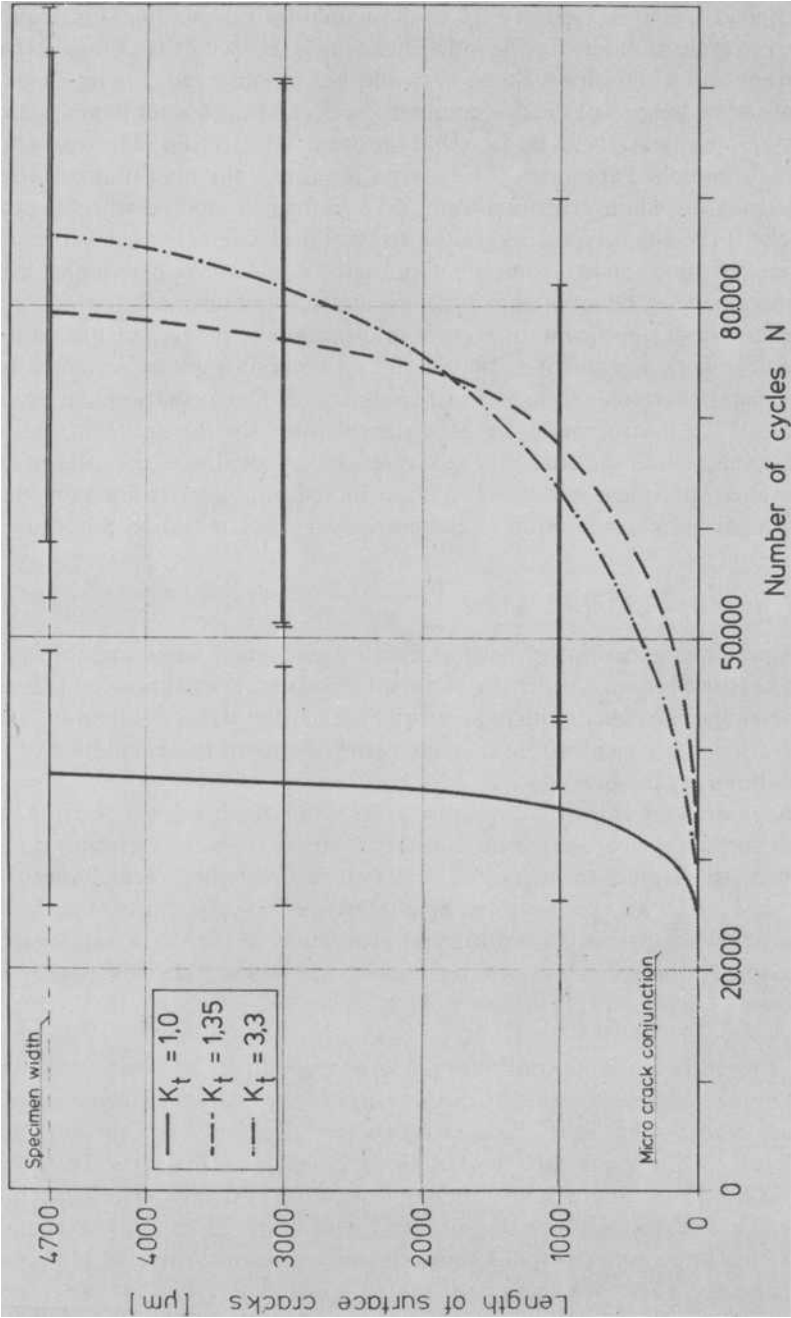


FIG. 15—Crack formation and propagation of cracks at the notch and at the unnotched specimen.

tions for thicker walled test pieces (also common in engineering design) have to be developed until realistic short-cracks in notches' analyses become possible.

2. The specimen type in Fig. 2*d* spent nearly 100 percent of its total life with surface cracks significantly smaller than the specimen width. Because the nominal stresses that had to be applied to the specimens in order to obtain the same notch surface strain history as for the specimen type in Fig. 2*c* were high, the specimens always failed rather quickly after the crack had passed through the main part of the notch field. Exact fracture mechanics solutions for this situation are not available at present; besides, the high net section stress requires elastic-plastic solutions.

3. As previously mentioned, the crack initiation and propagation behavior of the unnotched specimen differ from that of the notched specimens. The cracks (which start as individual small surface cracks that later join together) do not meet a decreasing notch stress field as they propagate. In order to achieve the same strains as at the notch surfaces on the notched specimens the nominal stresses had to be made high enough so that gross yield occurred only from the beginning of the test. Once Stage II was passed failure occurred rather quickly. For an adequate description of the crack propagation behavior elastic-plastic fracture mechanics has to be applied (for example, the approximate J -integral solution given in Ref 11).

These considerations show clearly that equivalence between unnotched specimens and the notch root of notched specimens becomes rather poor the longer the cracks grow. An acceptable limit for the validity of the equivalence may be the end of Stage II (when the first macrocrack forms as a conjunction of individual small surface cracks).

Sequence Effects

As previously mentioned, sequence effects significantly influence the damage accumulation. The aforementioned test results showed that sequence effects mainly increased the damage in the crack initiation stage. In the crack stage, however, sequence effects due to high peak loads considerably decrease the crack propagation. The crack closure behavior that becomes clearly visible when COS-measurements are performed across the crack [18,19] must be considered the main cause of the crack retardation behavior. COS-measurements were also performed for the specimen type in Fig. 2*c* and for the unnotched specimens down to (surface) crack lengths of 0.5 mm. The results showed that crack closure and crack-retarding sequence effects are present at least down to the end of Stage II of the crack initiation process, and that they have to be considered in an adequate crack initiation life analysis.

Summary and Conclusions

In the present investigation the prediction capability of the conventional notch analysis for the crack initiation stage was considered. Based on (1) numerous comparisons of the predicted and the actual crack initiation life behavior under different types of service loading histories, and (2) cumulative damage studies with unnotched specimens and with simple program histories, a damage calculation scheme has been suggested that considers load sequence effects on the damage accumulation. In order to more clearly define the influence of the initiation of small cracks on the damage accumulation the crack initiation was investigated in more detail. The investigations led to the following results:

1. The main causes of the unsatisfactory results of the conventional notch analyses (large scatter bands in the predictions) are inadequate consideration of the sequence effects and the neglect of the different initiation behavior of small cracks at notches and at unnotched specimens. A main cause for the differences in the initiation processes is the different stress-strain fields in the vicinity of a notch and along the cross section of an unnotched specimen. In order to generate the same strains on unnotched specimens as at the notch of notched specimens the cross section of the unnotched specimen has to be loaded much higher; this leads to extremely high crack propagation rates and from that to a short life in the crack stage as soon as small cracks have started. Conventional engineering definitions of the crack initiation stage at notched specimens (a crack length of ~ 0.5 mm at the specimen side surface) do not adequately consider this behavior.

2. The ability of fracture mechanics to describe the behavior of small cracks is still rather limited, especially when the variety of possible crack initiation sites of real components is considered. Until satisfactory solutions become available a reasonable compromise from an engineering point of view may be to use the unnotched specimen data for the crack initiation life predictions, because there is some safety built in in the predictions.

3. Load sequence effects increased the damage in the crack initiation stage in all cases considered in the present study. The proposed modified damage evaluation concept adds a damage portion to each damage amount calculated on the basis of the conventional Smith et al damage parameter. The additional damage portion is material and sequence dependent. The material dependence of the sequence effects may be determined with simple block program tests on unnotched specimens. These tests can be performed in conjunction with other tests in which the basic input data for the application of the numerical crack initiation life analysis are generated. The notch analysis modified by the new damage evaluation concept led to satisfactory results. This is of special interest because many engineers in various technical application areas are quite familiar with the conventional notch analysis concepts and can easily modify their own computer programs.

4. In the crack stage sequence effects due to high peak loads also decrease the damage. Since the proposed damage evaluation concept only accounts for increased damage amounts per cycle, the predictions become more conservative, which may be tolerable from an engineering viewpoint at present.

Acknowledgments

This investigation was financially supported by Deutsche Forschungsgemeinschaft (DFG). The experimental program was mainly performed by K. H. Trautmann and J. Strunck. A fruitful collaboration with Dr. Rohwer, Dr. Geier, and Dr. Marci took place regarding the continuum and fracture mechanics aspects of the investigation.

References

- [1] Schütz, W. and Zenner, H., *Zeitschrift für Werkstofftechnik*, Vol. 4, 1973, pp. 25-33, 97-102.
- [2] Leis, B. N. in *Proceedings*, 9th ICAF Symposium, Darmstadt, May 1977, ICAF-Doc. No. 960, pp. 3.4/1-47.
- [3] Nowack, H., Hanschmann, D., and Trautmann, K. H. in *Proceedings*, International Symposium on Low Cycle Fatigue Strength and Elasto-Plastic Behaviour of Materials, Stuttgart, Oct. 1979, pp. 331-354.
- [4] Crews, J. H. and Hardrath, H. F., *Experimental Mechanics*, Vol. 23, 1966, pp. 313-320.
- [5] Wetzel, R. M., "Smooth Specimen Simulation of Fatigue Behaviour of Notches," T&A.M. Rep. No. 295, University of Illinois, Urbana, 1967.
- [6] Neuber, H., *Journal of Applied Mechanics, Transactions of ASME*, Vol. 28, 1961, pp. 544-550.
- [7] Seeger, T. and Heuler, P., *Journal of Testing and Evaluation*, Vol. 8, 1980, pp. 199-204.
- [8] Wetzel, R. M., Ph.D. thesis, University of Waterloo, Ontario, Canada, 1971.
- [9] Hanschmann, D., Ph.D. thesis, *Technische Hochschule Aachen*, West Germany, 1981.
- [10] Dowling, N. E. in *Fracture Mechanics, ASTM STP 677*, American Society for Testing and Materials, 1979, pp. 247-273.
- [11] El Haddad, M. H., Dowling, N. E., Topper, T. H. and Smith, K. N., *International Journal of Fracture*, Vol. 16, 1980, pp. 15-30.
- [12] Landgraf, R. W. in *Proceedings*, International Symposium on Low Cycle Fatigue Strength and Elasto-Plastic Behaviour of Materials, Stuttgart, Oct. 1979, pp. 285-300.
- [13] Schütz, D., "Residual Stresses in Notches Produced by Variable Operational Loads and their Importance for the Application of the Linear Cumulative Damage Hypothesis," RAE Library Translation No. 1800, 1975.
- [14] Conle, A., Nowack, H. and Hanschmann, D., "The Effect of Engineering Approximations on Fatigue Life Evaluation for Variable Amplitude Loading," in *Proceedings*, 8th ICAF Symposium, Lausanne, June 1975, ICAF-Doc. No. 801.
- [15] Conle, A. and Nowack, H., *Experimental Mechanics*, Vol. 17, 1977, pp. 57-63.
- [16] Topper, T. H., Wetzel, R. N. and Morrow, JoDean, *Journal of Materials*, Vol. 4, 1969, pp. 200-209.
- [17] Haibach, E. in *Proceedings*, International Conference on Applications of Computers in Fatigue, Warwick, April 1978, pp. 11.1-25.
- [18] Elber, W. in *Damage Tolerance in Aircraft Structures, ASTM STP 486*, American Society for Testing and Materials, 1971, pp. 230-242.
- [19] Nowack, H., "Ein Beitrag zur Untersuchung der Schadensakkumulation auf der Grundlage biharmonischer Belastungsabläufe," DLR-Forschungsbericht No. 71-23, Ed. DFVLR, Köln-Porz, West Germany, 1971.

Low-Cycle Fatigue Behavior of Thick High-Strength Steel Plates for Pressure Vessels

REFERENCE: D'Haeyer, R. and Simon, P., "Low-Cycle Fatigue Behavior of Thick High-Strength Steel Plates for Pressure Vessels," *Low-Cycle Fatigue and Life Prediction, ASTM STP 770*, C. Amzallag, B. N. Leis, and P. Rabbe, Eds., American Society for Testing and Materials, 1982, pp. 296-310.

ABSTRACT: In this study of low-cycle fatigue, the following steels were evaluated: (1) two reference steels used in pressure vessel construction, A 543, Grade B (200 mm thickness) and St 52-3 (50 mm thickness); these steels were also studied after heat treatments simulating heat-affected zones of weldments with heat inputs ranging from 10 to 150 kJ/cm; (2) one structural steel, St E47 (50 mm thickness), after either normalization or quench-tempering treatment in order to compare two characteristic values of the yield strength/ultimate tensile strength ratio; and (3) fifteen experimental steels (28 mm thickness) in a thermal condition simulating the water quenching at the core of a plate 200 mm thick, this quenching being followed by a tempering.

Smooth and notched specimens were fatigue tested at 20 and 350°C under completely reversed tension-compression. The imposed diametral strain range was controlled to a constant value throughout each test.

Results were compared with ASME design curves and showed sufficient performances in all cases, so that the choice of the steel may be based upon another use property or economical argument. Nevertheless, differences between steel fatigue properties were studied by statistical methods as a function either of the tensile properties or of the chemical composition in the case of quenched and tempered steels. Concerning these last correlations, the influence of chromium at 350°C was particularly noted.

KEY WORDS: low-cycle fatigue, high-strength steel, pressure vessel, quenched and tempered steel

Nomenclature

- N Fatigue life, number of cycles to failure
- a Fatigue strength exponent, slope of $\log \Delta\sigma$ - $\log 2N$ plot
- b Fatigue ductility exponent, slope of $\log \Delta\epsilon_p/2$ - $\log 2N$ plot
- c Exponent, slope of $\log \Delta\epsilon_{td}$ - $\log N$ plot, plain specimens
- c^E Exponent, slope of $\log \Delta\epsilon_{td}^E$ - $\log N$ plot, notched specimens

¹ Ingénieur Civil, Centre de Recherches Métallurgiques (CRM), Liege, Belgium.

σ'_f	Fatigue strength coefficient, intercept of $\log \Delta\sigma$ - $\log 2N$ plot
ϵ'_f	Fatigue ductility coefficient, intercept of $\log (\Delta\epsilon_{pl}/2)$ - $\log 2N$ plot
$\Delta\epsilon_{el}\{_{1000}^{100}\}$	Elastic longitudinal strain range for a life of $\{_{1000}^{100}\}$ cycles (plain specimens)
$\Delta\epsilon_{pl}\{_{1000}^{100}\}$	Plastic longitudinal strain range for a life of $\{_{1000}^{100}\}$ cycles (plain specimens)
$\Delta\epsilon_{td}\{_{1000}^{100}\}$	Total longitudinal strain range for a life of $\{_{1000}^{100}\}$ cycles (plain specimens)
$\Delta\epsilon_{td}\{_{1000}^{100}\}$	Total diametral strain range for a life of $\{_{1000}^{100}\}$ cycles (plain specimens)
$\Delta\epsilon_{td}^E\{_{1000}^{100}\}$	Total diametral strain range for a life of $\{_{1000}^{100}\}$ cycles (notched specimens)
$\Delta\sigma$	Stress range
C	Coefficient, intercept $\log \Delta\epsilon_{td}$ - $\log N$ plot (plain specimen)
C^E	Coefficient, intercept $\Delta\epsilon_{td}^E$ - $\log N$ plot
R_e	Tensile offset yield point, MPa
R_m	Ultimate tensile strength, MPa
A	Gage length at fracture, %
Z	Reduction in area at fracture, %
ν_e	Poisson's ratio (elastic strain range)
ν_p	Poisson's ratio (plastic strain range)

This work is part of an important collective research program studying use properties of thick high-strength steel plates for pressure vessels.² The project aim was to allow the making of less heavy-weight vessels by reducing the wall thicknesses and by increasing the steel yield stress. Therefore the fatigue behavior of new steels had to be compared with that of classical materials having the same use.

This paper is a comparison of materials by means of classical low-cycle fatigue tests. In addition, a statistical study was carried out in order to better understand the steel behavior.

Experimental Studies

Materials

Various chemical compositions and a quenching and tempering treatment were used to obtain the desired levels of mechanical properties in the exper-

² Research carried out with a financial grant from IRSIA (Institut pour l'Encouragement de la Recherche Scientifique dans l'Industrie et l'Agriculture) and CECA (Communauté Européenne du Charbon et de l'Acier).

imental steels. The main characteristics of all the tested steels are given in Table 1. Most of the steels contained about 0.5 percent molybdenum (Table 2).

Concerning the microstructures, the following comments can be given. All the heat-treated steels except C (normalized) have a bainitic structure (tempered bainite in experimental steels). The steel St 52-3, as-received, shows a classical ferrite-pearlite microstructure, whereas the index C (St E47 normalized) presents a composite microstructure wherein some bainitic areas are dispersed in the ferrite.

Test Specimens and Extensometers

Drawings of the smooth and notched specimens configurations are given in Fig. 1. The theoretical elastic stress concentration factor k_t is equal to 1.68 for the notched specimens. All specimens were cut in the rolling direction. The tests were strain controlled by means of devices measuring the diametral deformation of the specimen (Fig. 1).

Procedure

Smooth and notched specimens were fatigue tested at 20 and 350°C under completely reversed tension-compression. All tests were carried out with a sine strain-time wave form, the frequency being 0.4 Hz. Until rupture (N cycles), during each test, $\Delta\epsilon_{td}$ (see Nomenclature) was controlled and $\Delta\sigma$ was recorded. After the test, a conservative value of $\Delta\sigma$ was chosen to describe the test (value of $\Delta\sigma$ at half life or minimum value if this minimum exists). From a classical analysis of hysteresis loop (Fig. 2), plastic and elastic strains were further calculated.

In the case of smooth specimens, longitudinal strains were also calculated by

$$\Delta\epsilon_{tl} = \frac{\Delta\epsilon_{td}}{\nu_p} + \left(1 - \frac{\nu_e}{\nu_p}\right) \frac{\Delta\sigma}{E}$$

where

$\Delta\epsilon_{tl}$ = longitudinal total strain,

$\Delta\epsilon_{td}$ = diametral total strain,

$\Delta\sigma$ = stress range, MPa,

E = Young's modulus, MPa,

ν_e = Poisson's ratio (elastic strain range), and

ν_p = Poisson's ratio (plastic strain range).

From the sets of measurements of $\Delta\epsilon_{td}$, $\Delta\sigma$ and N , the classical parameters describing low-cycle fatigue relationships were determined. These relationships are summarized in Fig. 3 for the case of a smooth specimen. Figure 3 also suggests the fact that these different formulas are not quite mathemati-

TABLE 1—Chemical and mechanical properties.

Index	Grade	Plate thickness (mm)	Welding simulation heat input (kJ/cm)	Thermal state	C	10 ⁻² %				(// RD) 20°C				(// RD) 350°C			
						Mn	Cr	Ni	Re (MPa)	Rm (MPa)	A (%)	Z (%)	Re (MPa)	Rm (MPa)	A (%)	Z (%)	
A	A543-grB	200	-	as received					639	781	21,2	76,0	549	672	15,6	61,1	
AB	A543-grB	200	25	annealed : 20 h at 600°C					620	756	17,6	76,0	528	652	15,4	62,3	
AC	A543-grB	200	25	annealed : 40 h at 600°C					607	749	20,1	75,4	517	637	16,0	65,8	
AD	A543-grB	200	150	quenching + tempering : 16 h at 620°C + annealing : 20 h at 600°C	17,5	25	175	348	697	812	19,2	74,2	581	697	15,7	65,7	
AE	A543-grB	200	150	annealing : 20 h at 600°C					633	756	20,6	75,0	538	656	14,7	63,7	
B	St 52-3	50	-	as received					322	525	30,0	66,0	210	496	26,0	59,0	
BG	St 52-3	50	10	annealing : 4 h at 570°C	20	136	3	2	328	523	25,9	67,3	208	497	12,5	57,9	
BH	St 52-3	50	25	annealing : 4 h at 570°C					326	527	23,9	68,6	206	481	17,1	56,4	
C	St E47	50	-	normalized	18	159			62 453	706	21,0	51,4	431	684	19,8	65,4	
D	St E47	50	-	quenched + tempered					686	781	18,5	68,1	605	714	18,0	53,5	
E		28			18	51	57	292 592	726	22,2	64,4	525	659	19,5	65,2		
G		28			17	142	16	290 563	745	19,4	58,7	502	661	19,1	60,4		
H		28			11	46	58	302 554	666	20,8	63,9	481	609	21,8	57,0		
K		28			11	45	145	203 531	647	18,1	59,2	457	570	13,6	55,4		
L		28			12	50	136	297 570	688	14,2	58,4	480	586	14,9	61,3		
M		28			12	58	138	383 618	762	19,6	65,9	543	661	16,9	61,3		
O		28			10	45	186	199 531	643	19,7	68,9	538	674	15,0	57,5		
P		28			9	41	190	303 573	678	20,4	60,3	470	572	16,6	70,8		
R		28			12	49	186	381 521	717	21,3	64,6	474	645	18,0	57,5		
S		28			13	71	48	196 476	591	21,2	61,6	405	553	21,5	60,4		
T		28			11	78	58	294 479	643	21,0	61,6	427	583	19,0	54,4		
U		28			11	99	143	194 533	650	18,1	51,6	451	569	13,0	53,5		
W		28			12	89	145	294 540	708	17,7	54,8	480	623	17,9	54,6		
X		28			11	138	19	292 458	661	23,7	58,4	416	592	26,6	62,5		
Z		28			11	141	17	468 587	769	24,4	59,4	531	663	24,9	66,9		

x : + 0,18 % A

TABLE 2—Typical composition of tested steels and Japanese reference steels.

Mo	C	Mn	Cr	Ni	Index
0	0,18	1,60	0	0,60	C and D
	0,20	1,40	0	0	B, BG, BH
	0,26	0,80	0	0	SB 46
0,50	0,12	0,45	0,50	3	H
	0,14	0,60	1	0,15	SCMV 2 (1Cr-0,5 Mo)
			1,25	0,15	SCMV 3 (1,25Cr-0,5 Mo)
			1,40	2	K
				3	L
				4	M
			1,90	2	O
				3	P
				4	R
		0,80	0,50	2	S
				3	T
			1,40	2	U
				3	W
		1,40	0,15	3	X
				5	Z
	0,18	0,45	0,50	3	E
		1,40	0,15	3	G
		0,25	1,75	3,5	A, AB, AC, AD, AE (A 543B)
1	0,12	0,50	2,25	0,16	SCMV 4 (2,25 Cr-1 Mo)

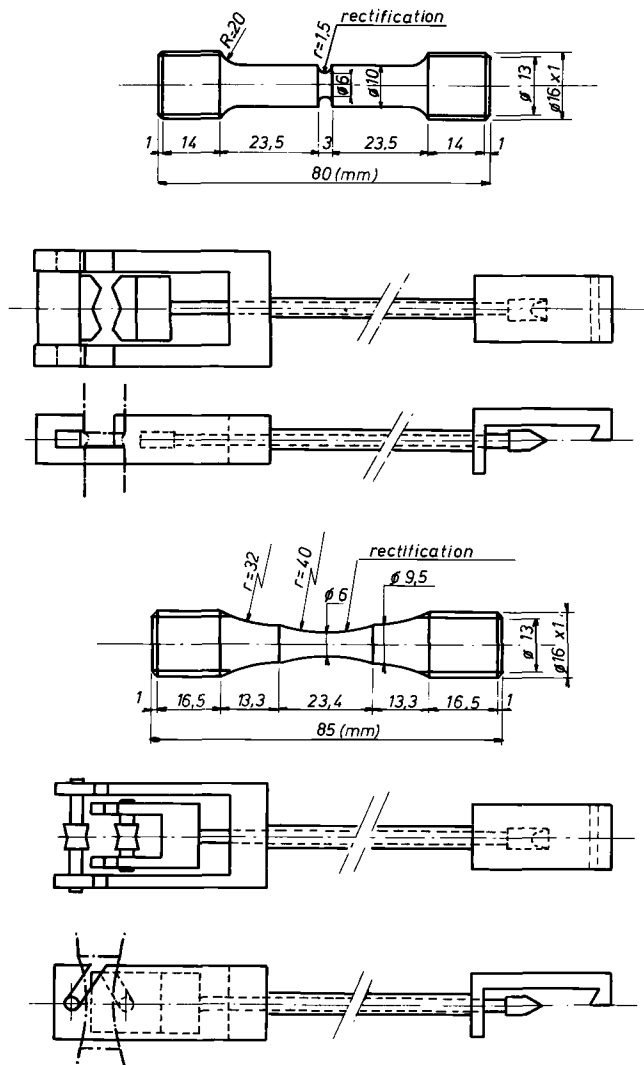


FIG. 1—Types of test specimens and extensometers.

cally compatible. If one admits that ϵ_{pl} and ϵ_{el} are given by relations of the kind $\epsilon = CN^k$ then the function $\Delta\epsilon_{td}$ cannot have the same form.

In the case of notched specimens, only measured quantities were used in the study.

Results

Characteristic values of the results can be found in Table 3 (for explanations of symbols, see Nomenclature). The test results on smooth specimens

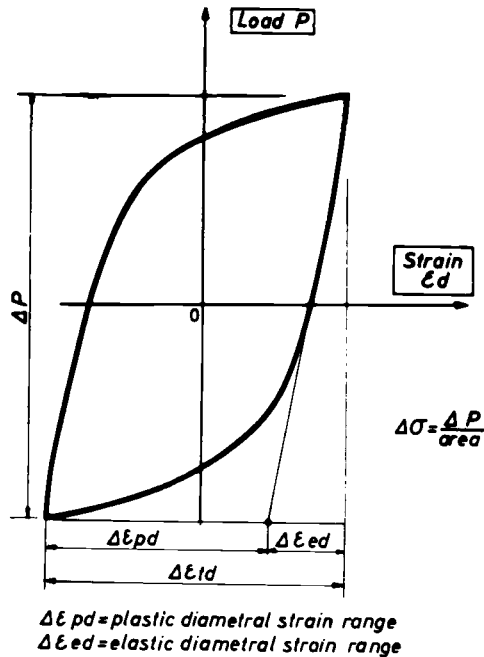


FIG. 2—Parameters of the hysteresis loop.

are summarized in Figs. 4 and 5 for test temperatures of 20 and 350°C, respectively. Obviously, it was interesting to compare the performances of these new steels with those of steels currently used in pressure vessel construction. We tested reference steels and compared the results with ASME design curves [1] and with values published in the literature, namely the values given by the NRIM (National Research Institute for Metals, Tokyo) laboratory [2] for steels SB 46, SCMV2, SCMV3, and SCMV4 (nomenclature in accordance with the Japanese standards).³

As shown in Figs. 4 and 5, the comparison with ASME design curves is carried out by following some rules: on the one hand, the cycles numbers are divided by a factor of 20; on the other hand, the strains are divided by a factor of 2. These 2 and 20 factors are consistent with those given in the criteria for the ASME Code. Then the worst case is considered and compared with the design curves. Figures 4 and 5 show that scatter bands corresponding to our results are above the ASME curves, so that sufficient performances are obtained.

Concerning the comparison to NRIM results, the following comments can be made. At 20°C, our results agree with those obtained with steels SB 46, SCMV2, and SCMV3, whereas results for steel SCMV4 seem to be lower. At

³The italic numbers in brackets refer to the list of references appended to this paper.

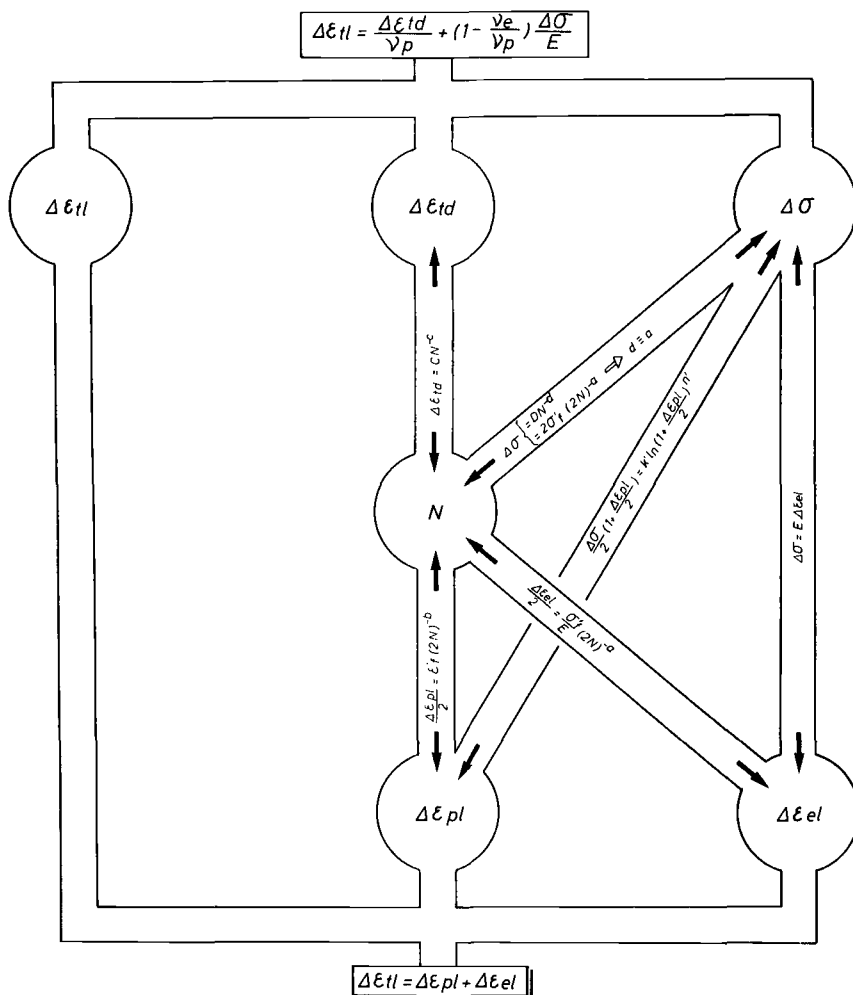


FIG. 3—Analysis of a strain-controlled test on smooth specimen.

350°C, the lower limit of our scattering band roughly separates NRIM results at 300 and 400°C.

The experimental steels having yield points ranging from 475 to 590 MPa (20°C) show, from the low-cycle fatigue point of view, a behavior as good as that of ductile steels normally used in pressure vessel construction, which have yield points of about 330 MPa (20°C) (steels St 52-3, SB 46, SCMV2, and SCMV3). However, several factors have to be kept in mind:

1. The obtainment of a given level of performance does not mean that no difference exists between steels; these differences will be examined subsequently.

TABLE 3—*Diametral strains.*

Steel	Smooth - 20°C		Smooth - 350°C		Notched - 20°C		Notched - 350°C	
	$\Delta\epsilon_{td} 100$ 10^{-4}	$\Delta\epsilon_{td} 1000$ 10^{-5}	$\Delta\epsilon_{td} 100$ 10^{-4}	$\Delta\epsilon_{td} 1000$ 10^{-5}	$\Delta\epsilon_{td} 100$ 10^{-4}	$\Delta\epsilon_{td} 1000$ 10^{-5}	$\Delta\epsilon_{td} 100$ 10^{-4}	$\Delta\epsilon_{td} 1000$ 10^{-5}
1.A	340	<u>1071</u>	298	977	158	224	127	216
2.AB	325	959	269	865	158	254	120	211
3.AC	343	1001	285	865	160	207	123	223
4.AD	334	1020	311	961	106	171	79	178
5.AE	334	1020	256	857	155	218	111	198
6.B	<u>364</u>	1050	330	892	<u>169</u>	<u>394</u>	<u>146</u>	<u>321</u>
7.BG	329	930	<u>206</u>	773	145	237	85	201
8.BH	291	920	273	754	151	240	87	156
9.C	295	918	269	754	106	210	90	163
10.D	324	947	293	794	110	155	96	167
11.E	315	1018	269	830	131	227	106	183
12.G	308	1016	241	731	92	216	70	160
13.H	336	<u>914</u>	295	826	106	185	84	<u>105</u>
14.K	<u>231</u>	961	<u>386</u>	967	127	267	108	249
15.L	318	1042	297	952	142	239	132	240
16.M	339	1021	314	917	128	209	119	197
17.O	339	1068	379	1003	122	218	131	209
18.P	330	1007	363	<u>1030</u>	92	<u>115</u>	98	137
19.R	308	970	323	789	87	172	90	186
20.S	338	1040	269	863	98	247	86	213
21.T	333	1070	252	742	129	167	88	115
22.U	281	978	261	900	128	191	105	171
23.W	<u>231</u>	953	266	803	113	183	101	204
24.X	304	1003	242	<u>699</u>	<u>67</u>	202	53	<u>105</u>
35.Z	255	967	258	764	75	119	<u>45</u>	142

□ → max.

○ → min.

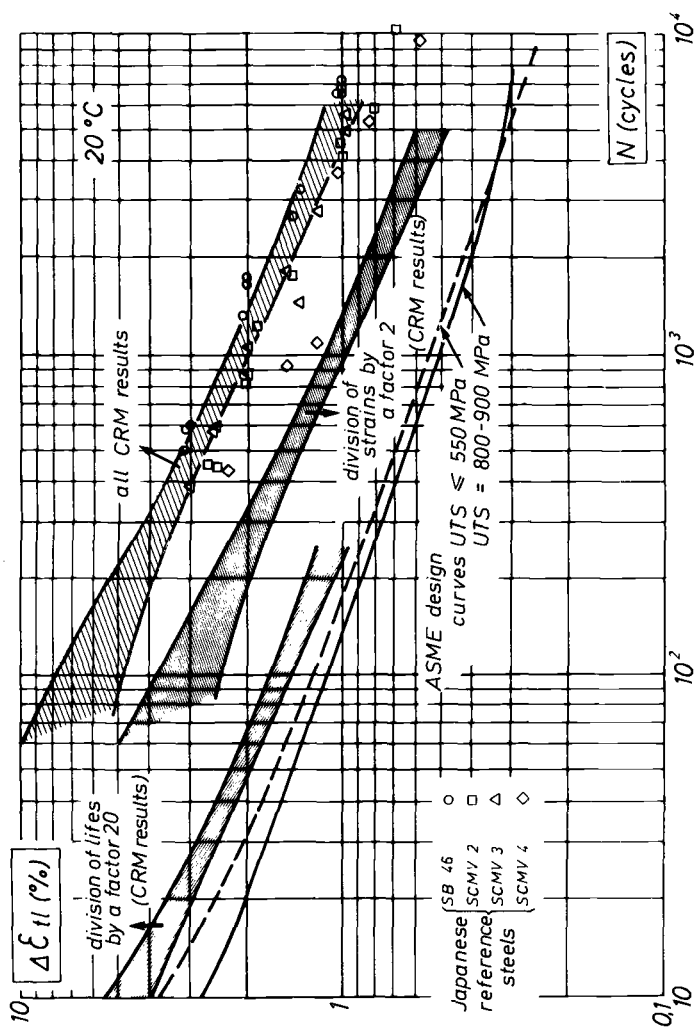


FIG. 4—Comparison of obtained results with ASME design curves and existing data.

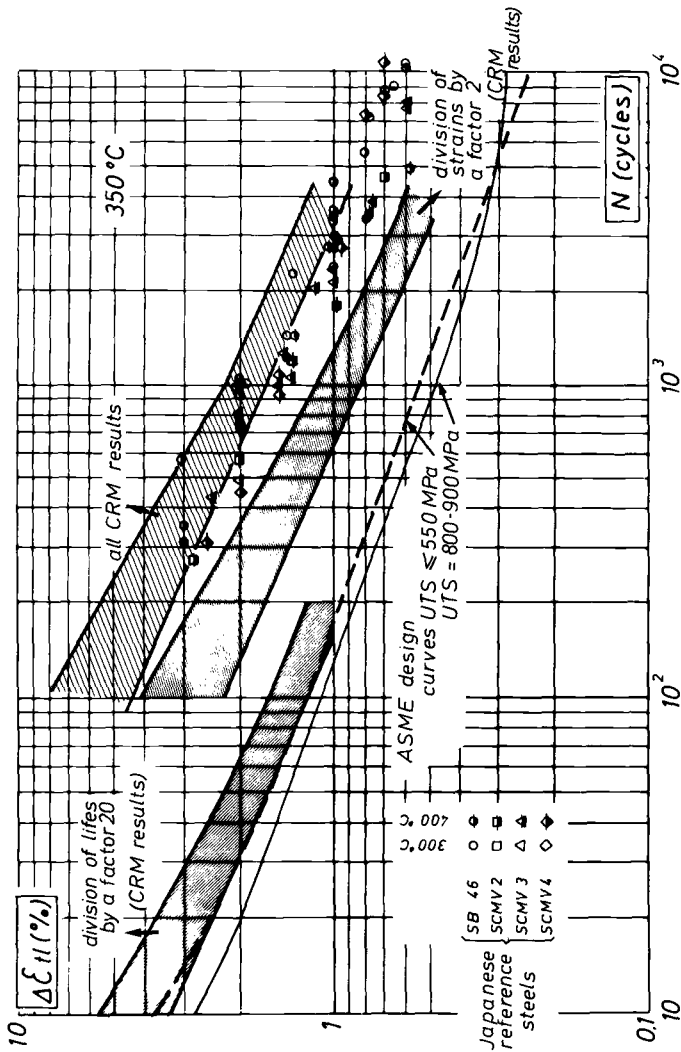


FIG. 5—Comparison of obtained results with ASME design curves and existing data.

2. In the case of steels submitted to a welding simulation (with the Gleeble machine) and showing good low-cycle fatigue performances after the treatment, actual welding may induce lower performance.

3. Although the tested steels represent a wide range of chemical compositions (Table 2), in most cases the microstructure was bainitic (excepted for indexes B and C). This could explain why the obtained results are situated in a relatively narrow range.

4. This comparison is based upon results of smooth specimens submitted to strain-controlled tests only.

Concerning the test results on notched specimens at both temperatures, Fig. 6 shows that the different performances are less grouped than the corresponding ones on smooth specimens, since the scatter band is broader in the case of notched specimens.

Here the ductile steel B (St 52-3) shows a significantly better behavior (drawn separately on Fig. 6), but this advantage disappears after welding simulation at the Gleeble machine (steels BG and BH having performances inside the scatter band). This leads us to attempt an analysis of the observed differences within the scattering band of results as a function of tensile properties.

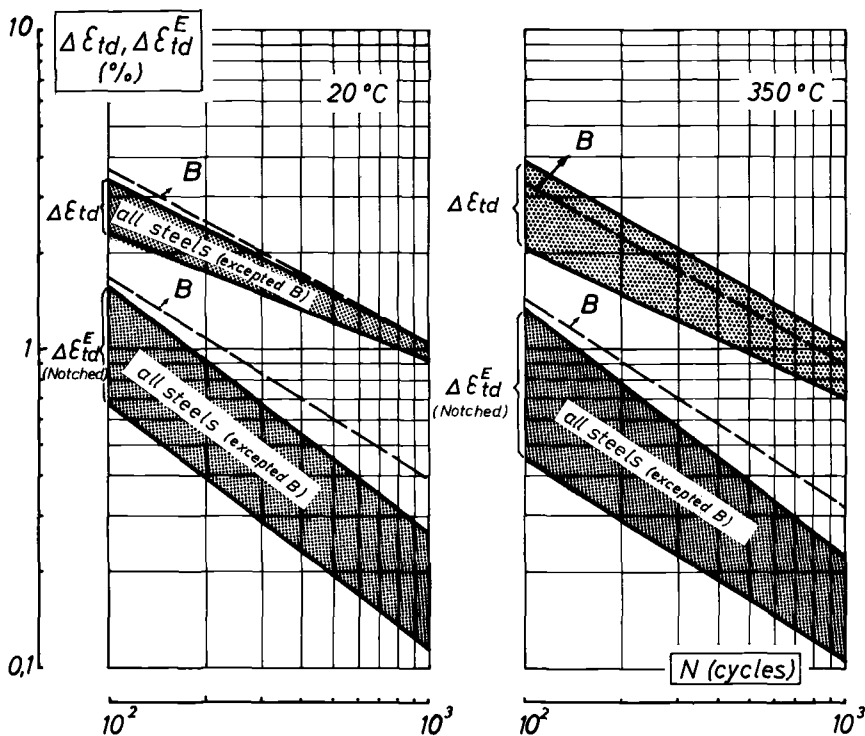


FIG. 6—Comparison of results on smooth and notched specimens.

Statistical Analysis of Low-Cycle Fatigue Performances as a Function of Tensile Properties

The statistical study on the whole set of steels gives few results but, if only the quenched and tempered steels are considered, good relations can be found. The data for other types of steels were not numerous enough to make a statistical analysis. Such a situation is shown in Fig. 7, which also explains the differences within the scattering band of Fig. 6. Figure 7 clearly shows the existence of two different tendencies, on the one hand for quenched and tempered steels, on the other hand for the other tested steels.

The statistical study on quenched and tempered steels is summarized in Table 4. Table 4 is presented in the following manner: (1) every fatigue property is described by a line of the table; (2) the influence of a tensile property is seen in a row; (3) if a tensile property influences a given fatigue property, the case at the intersection of the corresponding line and row contain an arrow; this arrow indicates a positive or negative influence; and (4) the correlation coefficients are also given. Table 4 shows that better correlations are obtained by considering the values of different parameters corresponding to lives of 100 and 1000 cycles rather than classical parameters.

The influence of the test temperature on the values of correlation coefficients will also be noted: better results are obtained at 350°C for diametral and longitudinal total strains (notched and smooth specimens) than at 20°C.

As stated in previous work [3,4], Table 3 also shows that diametral and longitudinal total strains, as well as longitudinal plastic strain corresponding to a life of 1000 cycles, are relatively constant at 20°C but not at 350°C. The

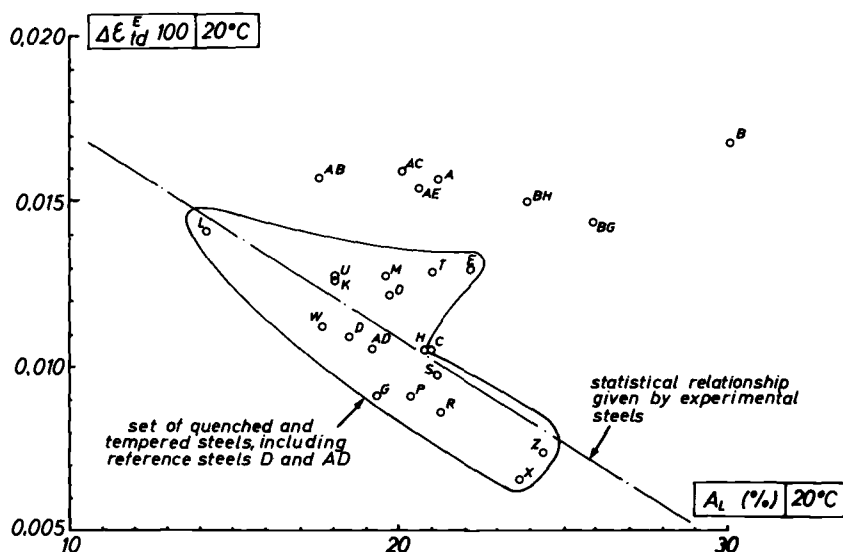


FIG. 7—Behavior of notched specimens as a function of fracture elongation.

TABLE 4—Summary of the correlations between fatigue properties and tension test properties.

		Quenched and tempered steels									
		Tests at 20°C					Tests at 350°C				
		r	R _e	R _m	A	Z	r	R _e	R _m	A	Z
$\Delta \epsilon_{eL}$ $= \frac{\Delta \sigma}{E}$	a	0.821			✱		-				
	σ_f^1	0.916		✱			0.688			✱	
	$\Delta \epsilon_{eL} 100$	0.918		✱	✱		0.788			✱	
	$\Delta \epsilon_{eL} 1000$	0.987*		✱			0.707			✱	
$\Delta \epsilon_{pL}$	b	0.568				✱	-				
	ϵ_f^1	0.591				✱	-				
	$\Delta \epsilon_{pL} 100$	0.694				✱	0.779			✱	✱
	$\Delta \epsilon_{pL} 1000$	-	constant value				0.844			✱	✱
$\Delta \epsilon_{tL}$	$\Delta \epsilon_{tL} 100$	0.620					0.758			✱	✱
	$\Delta \epsilon_{tL} 1000$	-	constant value				0.840			✱	✱
$\Delta \epsilon_{td}$	c	0.577				✱	-				
	C	0.623				✱	-				
	$\Delta \epsilon_{td} 100$	0.620				✱	0.768			✱	✱
	$\Delta \epsilon_{td} 1000$	-	constant value				0.846			✱	✱
$\Delta \epsilon_{td}^E$	c ^B	-					-				
	C ^E	-					-				
	$\Delta \epsilon_{td}^E 100$	0.693			✱		0.814			✱	
	$\Delta \epsilon_{td}^E 1000$	0.485			✱		0.677			✱	

*with n and K in the relationship

r = coefficient of correlation

variations at 350°C depend on both the fracture elongation A and the reduction of area Z .

Statistical Analysis of Low-Cycle Fatigue Performances as a Function of Chemical Composition

This analysis was carried out in the same way as the mechanical one. In particular, it was limited to experimental steels. It can be summarized in the following manner. At 20°C, the study shows only a few correlations: positive influences of nickel and manganese on elastic properties and a negative influence of manganese on lives of notched specimens. (One also knows the influence of manganese on the appearance of banding microstructures.) At 350°C, the chromium influence systematically appears. Increase of chromium content improves total and plastic strains of smooth specimens, while elastic properties slightly decrease. The amount of chromium influence at 350°C can be estimated by the relationship $\Delta \epsilon_{pl 100} = 0.0124$ (chromium in percent) + 0.0435 ($r = 0.776$).

Influence of the Ratio "Yield Stress to Tensile Strength"

The statistical study shows little influence of this ratio, but the direct comparison of C and D steels indicates that a low YS/UTS ratio is better at 20°C in the case of a notch.

Concluding Remarks

Which are the best steels from the low-cycle fatigue point of view? Answering this question is rather difficult because (1) the answer changes according to the chosen criterion: values at 100 cycles or 1000 cycles, presence of notch, behavior after welding, test temperature, etc.; and (2) stress-controlled tests would give another classification.

In fact, no tested steel shows very significant advantages with regard to the others. For example, the ductile steel St 52-3 shows better results with notched specimens, but this advantage tends to disappear after the welding simulation. Within the class of steels having higher yield points, few differences are observed. However, steels X and Z frequently show lower results (Table 3).

Concerning the relations between mechanical properties and fatigue, it was mainly found that the ultimate elongation A and the reduction of area Z are related to the fatigue results obtained in strain-controlled tests. This is not surprising. However, details of the statistical study show that (1) there is no correlation between A and Z ; and (2) there is a negative influence of A on the behavior of notched specimens (Table 4, Fig. 7) that is not counterbalanced by a positive influence of Z . This should be related to the particular heat treatment given to the considered steels.

More details of this study can be found in the complete report [5] published by the European Community for Steel and Coal (ECSC).

Acknowledgments

The authors express their acknowledgments to Mr. J.-C. Herman, Research Metallurgist at CRM, for fruitful discussions concerning the microstructural aspects of this study.

References

- [1] ASME Boiler and Pressure Vessel Code, Section III, Nuclear Power Plant Components, 1974.
- [2] *Transactions of the National Research Institute for Metals*, Vol. 20, 1978, p. 184. Relevant sections are Section 6—Elevated Temperature Fatigue Properties of a 0.25 C Steel Plate for Boilers (SB46); Section 7—Elevated Temperature Fatigue Properties of an 1Cr-0.5Mo Steel Plate for Pressure Vessel (SCMV2); Section 8—Elevated Temperature Fatigue Properties of 1.25Cr-0.5Mo Steel Plates for Pressure Vessels (SCMV3); and Section 9—Elevated Temperature Fatigue Properties of 2.25Cr-1Mo Steel Plates for Pressure Vessels (SCMV4).
- [3] Raske, D. T. and Morrow, J. D. in *Manual on Low-Cycle Fatigue Testing*, ASTM STP 465, American Society for Testing and Materials, 1969, pp. 1–26.
- [4] Gallet, G. and Lieurade, H. P., *Revue de Métallurgie*, Jan. 1978, pp. 37–49.
- [5] D'Haeyer, R. and Bragard, A., "Tôles de forte épaisseur pour réservoirs soumis à pression—Partie fatigue," Rapport EUR 6331 FR., ECSC publication.

Low-Cycle Fatigue Behavior of Welded Joints in High-Strength Steels

REFERENCE: Lieurade, H.-P. and Maillard-Salin, C., "Low-Cycle Fatigue Behavior of Welded Joints in High Strength Steels," *Low-Cycle Fatigue and Life Prediction, ASTM STP 770*, C. Amzallag, B. N. Leis, and P. Rabbe, Eds., American Society for Testing and Materials, 1982, pp. 311-336.

ABSTRACT: Low-cycle fatigue tests are carried out on different types of welded joints in structural steels. The low-cycle fatigue strength of welded joints depends on the weld geometry and the weld toe quality. The influence of these parameters and the role of the microstructure on low-cycle fatigue are discussed. For cruciform joints, the weld toe ground increases the low-cycle fatigue strength. The butt joints present a higher fatigue strength, and this fatigue strength increases when the weld reinforcement decreases. Submerged arc welded butt joints (presenting small reinforcement) have the same low-cycle fatigue strength as as-rolled base metal. The test results are expressed as a function of different fatigue notch factors.

KEY WORDS: low-cycle fatigue, welded joints, surface finish, notch factor, yield strength

In recent years, the low-cycle fatigue strength of construction steels in the as-welded conditions has called for particular attention owing to the use of these steels in metal structures such as pressure vessels and earth-moving equipment. In these types of structures, intermittent loading can lead to local plastic strains, which results in reduced service life. The use of high-strength steels in these structures is thus of particular interest.

In their bibliography devoted to the low-cycle fatigue strength of welded joints, Diez and Salkin [1] observe that most of the research done in this area concerns heat-treated ground welds containing very few defects and that it would be interesting to have a closer simulation of the real conditions under which welded joints are used.² Since their review, few studies have been conducted in this area [2-8]. Accordingly, the present study deals with different types of joints in the as-welded conditions subjected to controlled strain experiments. These types of joints have also been characterized in the case of long fatigue lives [9-12].

¹ Engineer, Institut de Recherches de la Sidérurgie Française, Saint-Germain-en-Laye, France.

² The italic numbers in brackets refer to the list of references appended to this paper.

TABLE 1—Chemical compositions.^a

Grade ^b	C	Mn	Si	P	S	Ni	Cr	V	Al	N	Cu	Mo	Sn
E 355	0.16	1.46	0.36	0.022	0.023	0.20	0.15	...	0.034	...	0.25	0.03	0.02
E 36	0.21	1.38	0.22	0.026	0.015	0.08	0.006	0.013
A 70	0.20	1.41	0.38	0.092	0.012	0.10	0.03	0.15	0.04	0.014	0.180	0.01	...

^a In percent.^b AFNOR specification.

Materials

The examined joints are made of structural steel plates in the annealed condition. The steels are AFNOR E 355, E 36, and A 70 types. The chemical compositions of these steels are given in Table 1. The E 355 steel is also characterized after a heat treatment simulating the structure of a heat-affected zone (HAZ) caused by welding. The chosen treatment consists of quenching in a 2 g/dm³ aqueous solution of methyl cellulose after holding for 10 min at 1250°C in a salt bath.

The mechanical properties of the steels in the normalized and heat-treated conditions are given in Table 2. Table 3 gives the parameters n , k , n' , and k' of the monotonic and cyclic stress-strain curves determined for the E 355 steel (Fig. 1).

Experiments

Test Specimens

The nominal sections of the specimens are indicated in Table 4.

Cruciform Joints (Fillet Welds)—Two stiffeners are welded perpendicularly to the rolling direction (Fig. 2a). Manual arc welding is carried out in two different ways: (1) in the vertical position (Fig. 2b), and (2) in the flat position; in this case, the toe of the weld is lightly ground. This grinding eliminates microdefects caused by welding (Fig. 2c).

Butt Joints—The weld is perpendicular to the rolling direction (Fig. 3a). Two types of welding are carried out: (1) manual arc welding leading to a convex bead (Fig. 3b), and (2) submerged arc welding leading to a flat bead (Fig. 3c).

Test Setup

The tests are conducted on an electrohydraulic machine of ± 400 kN under total strain amplitude control, $\Delta\epsilon_t/2$. This strain is related to the base metal.

TABLE 2—Mechanical properties.

Grade of Steel	Yield Strength (Y), N/mm ²	Ultimate Tensile Strength (UTS), N/mm ²	Elongation, %	Reduction of Area, %
E 355, annealed	400	570	32	74
E 355, HAZ simulation	570	760
E 36	420	570	28	55
A 70	515	660	24	54

TABLE 3—Parameters of the monotonic and cyclic stress-strain curves for E 355 steel.

Grade of Steel	n	k , N/mm ²	Y , N/mm ²	n'	k' , N/mm ²
E 355, annealed	0.28	1300	350	0.18	1100
E 355, HAZ simulation	0.11	1000	470	0.19	1500

The frequency of the sinusoidal strain cycle is set between 0.01 and 0.1 Hz, so that there is no heating of the specimen. The load versus time curve is recorded.

Strain Transducers

The strain is controlled by two strain transducers connected in full bridge in order to observe the average strain on the two sides of the specimen. For cruciform joints, the knives of the transducers are positioned on each side of the weld. The gage length—that is, the distance between the knives—is equal to 50 mm (Fig. 4). For butt joints the specimen has two calibrated parts (Fig. 5*a*); one is in the base metal (used for strain control), the other contains the weld. At this level, the resultant strain is also recorded (Fig. 5*b*).

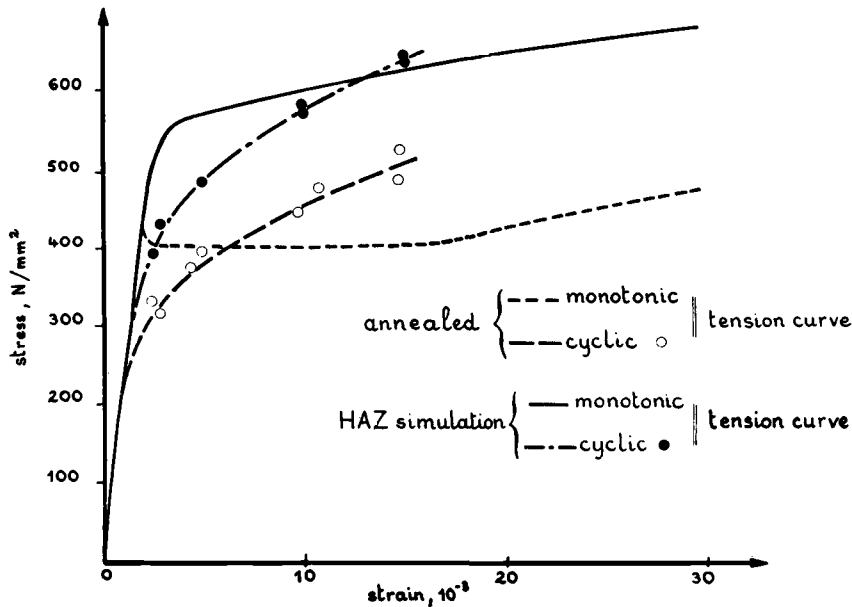


FIG. 1—Monotonic and cyclic stress-strain curves for E 355 steel.

TABLE 4—Constants of fatigue-life relationships.

Grade of Steel	Specimen	Welding	Surface Finish	Nominal Section	$\frac{\sigma'_t}{E}$, %	b	r^2	
							(Correlation Coefficient)	c
E 355, HAZ simulation	base metal	. . .	ground	ϕ 8	0.59	-0.10	0.97	65
								-0.64
E 355, annealed	base metal	. . .	ground	ϕ 9	0.43	-0.09	0.99	31
			as-rolled	14 by 40	0.52	-0.12	0.97	74
	butt joints	manual arc welding	as-welded	14 by 50	0.47	-0.12	0.97	63
		submerged arc welding	as-welded	14 by 50	0.47	-0.12	0.98	73
E 36	cruciform joints	vertical position	as-welded	12 by 60	0.44	-0.12	0.97	21
		flat position	after grinding the weld toe	12 by 60	0.44	-0.10	0.91	26
A 70	cruciform joints	vertical position	as-welded	12 by 50	0.51	-0.12	0.98	29
		flat position	after grinding the weld toe	12 by 50	0.47	-0.10	0.97	29

$$\frac{\Delta \epsilon_e}{2} = \frac{\sigma'_t}{E} (2 N_i)^b$$

$$\frac{\Delta \epsilon_i}{2} = \frac{\sigma'_t}{E} (2 N_i)^b + \epsilon'_t (2 N_i)^c$$

$$\frac{\Delta \epsilon_p}{2} = \epsilon'_t (2 N_i)^c$$

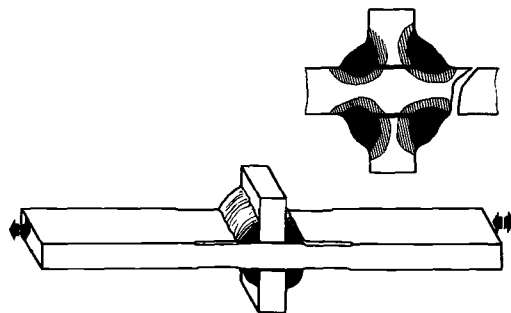


FIG. 2a—Welded joints—cruciform joints.

Stiffener

A device is used to prevent the flat specimens from buckling. It is held on the specimen by means of bolts. Teflon plates are inserted to facilitate the sliding of the specimen (Fig. 5c).

Results

Available Results

In each case, we dispense with the following results: (1) a load versus time recorded chart, and (2) load plotted as a function of total strain.

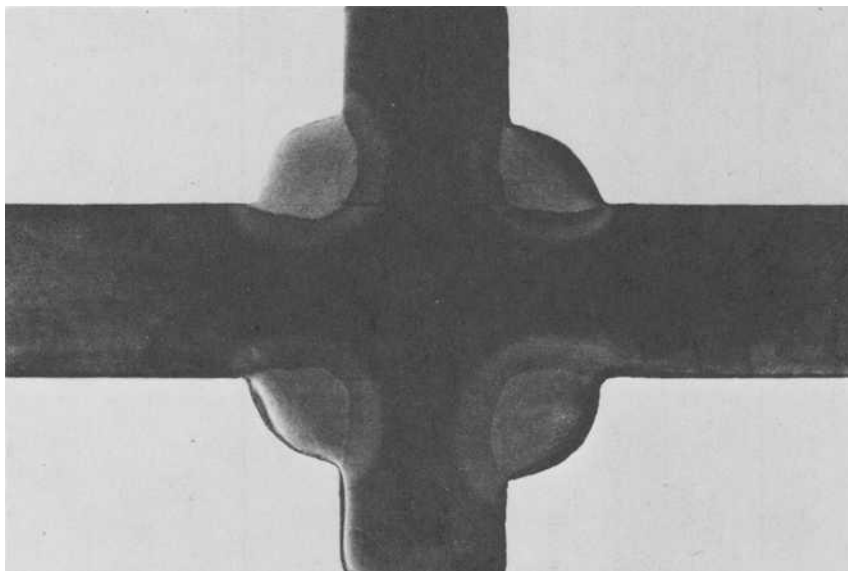


FIG. 2b—Welded joints—cruciform joints—as-welded.

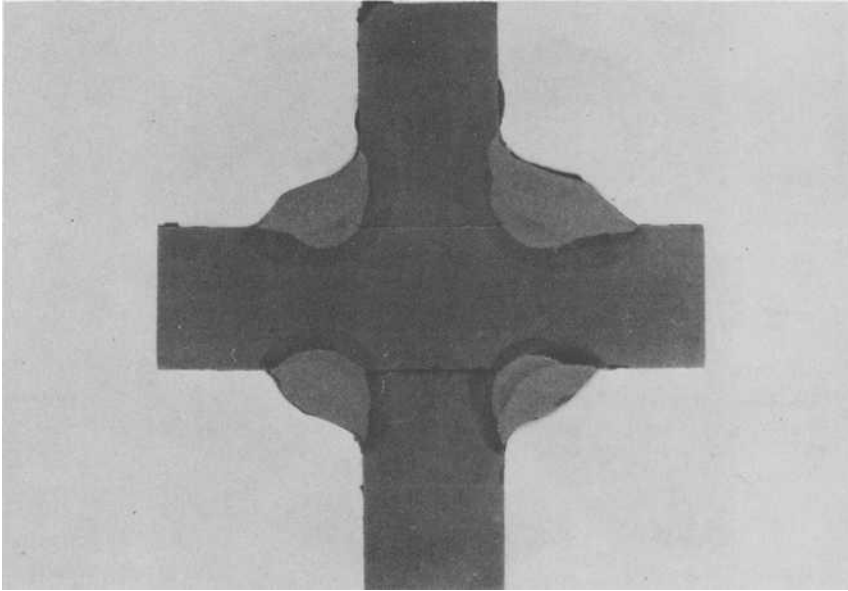


FIG. 2c—Welded joints—cruciform joints—after grinding the weld toe.

Presentation of Results

Stress and Strain—The nominal stress and elastic strain can be calculated by

$$\frac{\Delta\sigma_{\text{nom}}}{2} = \frac{\Delta F}{2} \cdot \frac{1}{S_{\text{nom}}}$$

$$\frac{\Delta\epsilon_{\text{nom}}}{2} = \frac{1}{E} \cdot \frac{\Delta\sigma}{2}$$

where

ΔF = load range,

S_{nom} = nominal section of the plate, and

E = Young's modulus.

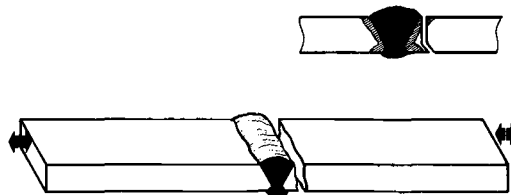


FIG. 3a—Welded joints—butt joints.

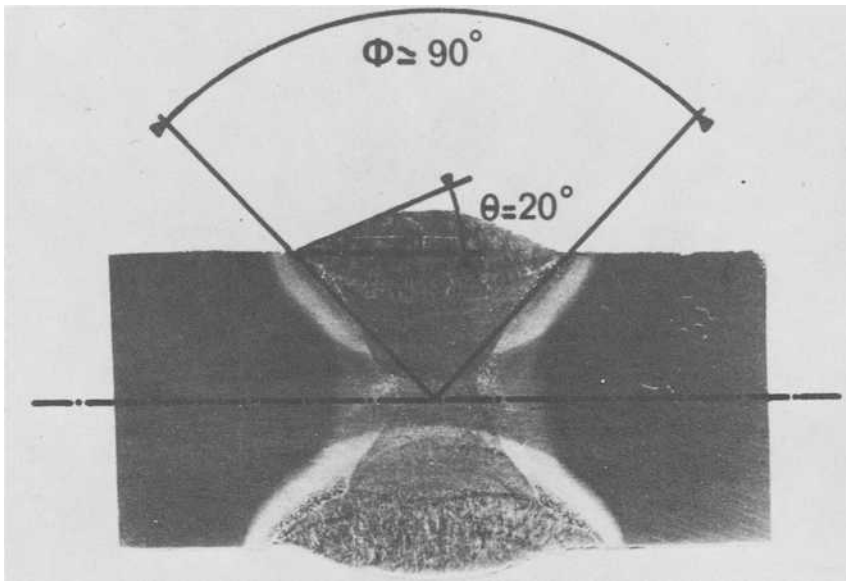


FIG. 3b—Welded joints—butt joints—manual arc welding.

For cruciform joints, the strain of the joint is heterogeneous. Manual arc welding leads to a very convex bead (Figs. 2b and 2c), and if the local strain at the toe of the weld is neglected, it is possible to assume that the central part made of the flange and the joints undergo only elastic strain. The nominal plastic strain can be then calculated by

$$\frac{\Delta \epsilon_{p \text{ nom}}}{2} = \frac{\Delta \epsilon_p}{2} \cdot \frac{1}{l_{\text{nom}}}$$

where

$\Delta \epsilon_p$ = gage length variation, and

l_{nom} = length outside of the joint within the base of the transducer.

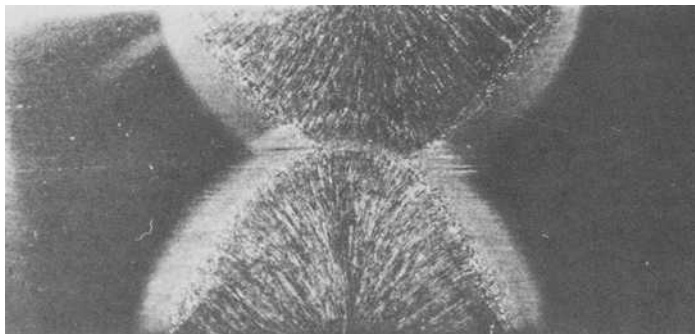
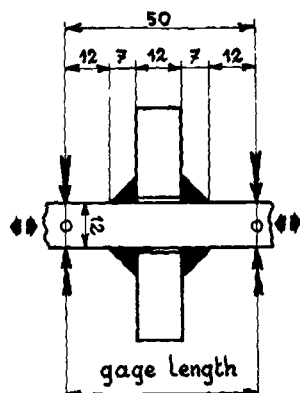


FIG. 3c—Welded joints—butt joints—submerged arc welding.



→: Knives of the transducers

FIG. 4—Gage length on the cruciform joints.

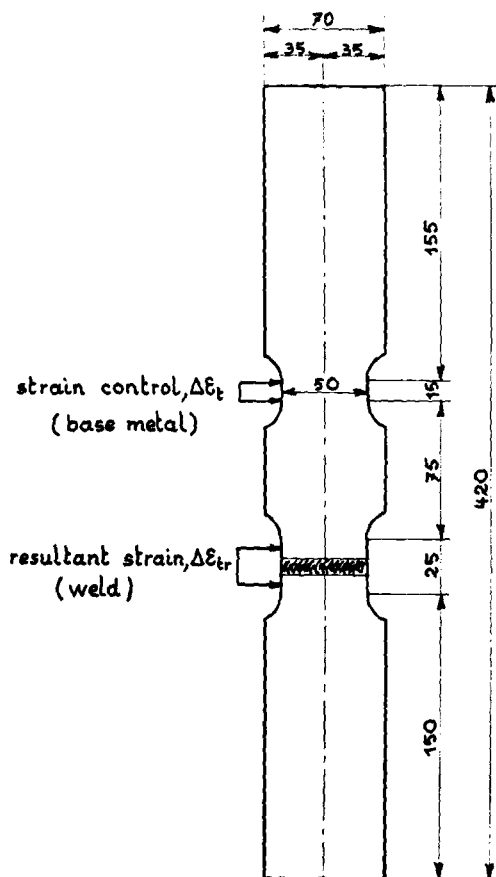


FIG. 5a—Fatigue test on butt joints—specimen.

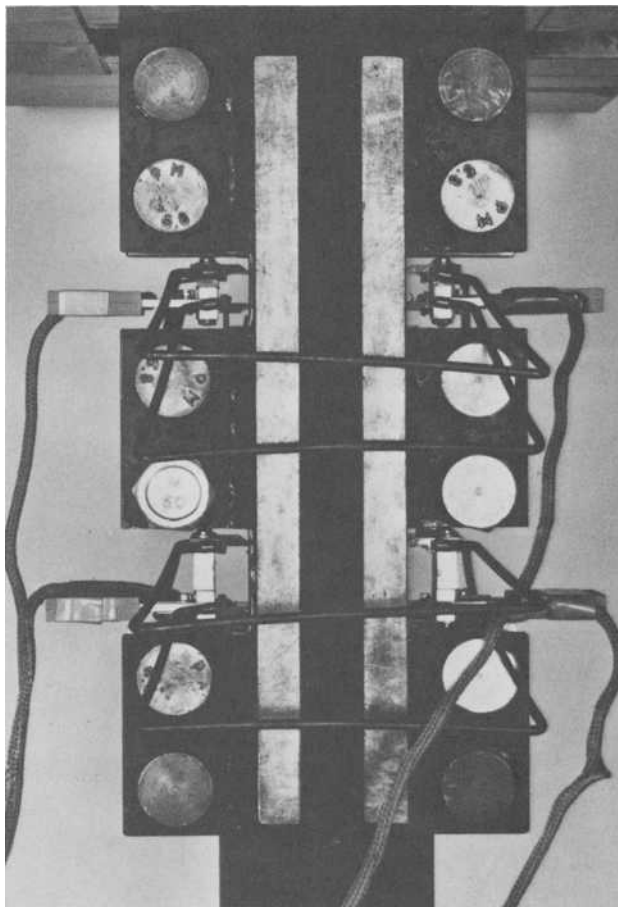


FIG. 5b—Fatigue test on butt joints—transducer setup.

For butt joints, the weld reinforcement is too progressive and not important enough for us to assume that the weld does not deform plastically. The specimen, then, has two calibrated parts and the nominal plastic strain is calculated for the part in the base metal.

Variation in Stress Amplitude as a Function of the Number of Cycles—Since the controlled strain is the average of the strain on the two sides of the specimen, stress amplitude is a function of the number of cycles dependent on the location of crack initiation (Fig. 6a). Stress distribution without crack is shown in Fig. 6b. If the crack appears between the blades of the transducers that control the strain, the stress amplitude drops (Fig. 6c, Example I). If the crack appears outside of this zone and symmetrically on the specimen (case of butt joints), there is no variation in stress amplitude (Fig. 6d, Example II). If

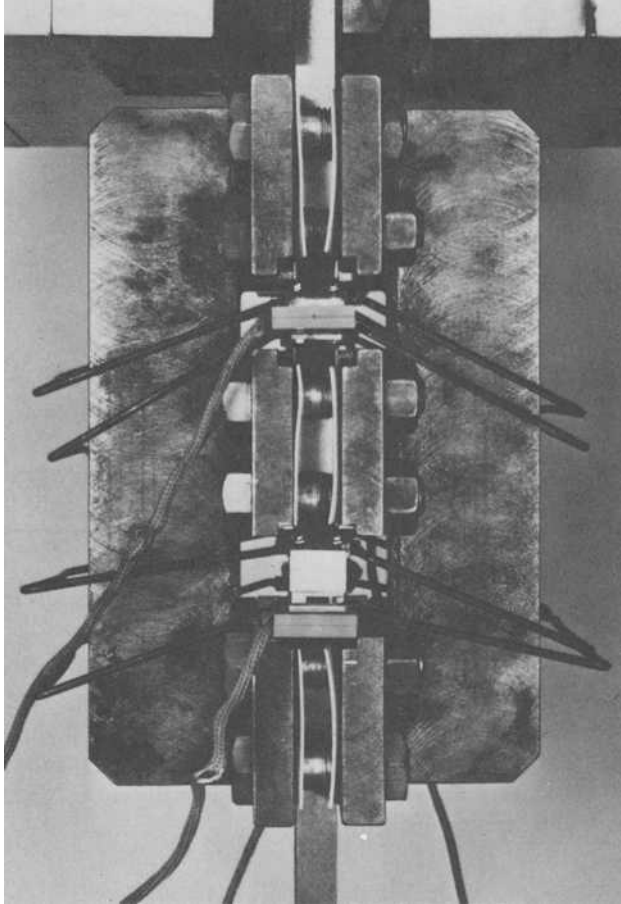


FIG. 5c—Fatigue test on butt joints—stiffener setup.

the crack forms outside of the transducers and is not symmetrical, the stress amplitude can increase (Fig. 6e, Example III).

Failure Criterion—The failure criterion chosen should be applicable to each case described in the preceding paragraph. The chosen criterion corresponds to the appearance of a crack smaller than 5 percent of the nominal section. In the case of a load variation, this change is considered as representative of the existence of a crack. When there is no load variation, the strain recorded at the weld increases rapidly with the appearance of a crack (Fig. 7). This change allows us to determine the number of cycles corresponding to the initiation of the crack.

The reference cycle is chosen at half life. For this cycle, stress and strain amplitudes are calculated; the results are given in Table 5. Taking these crite-

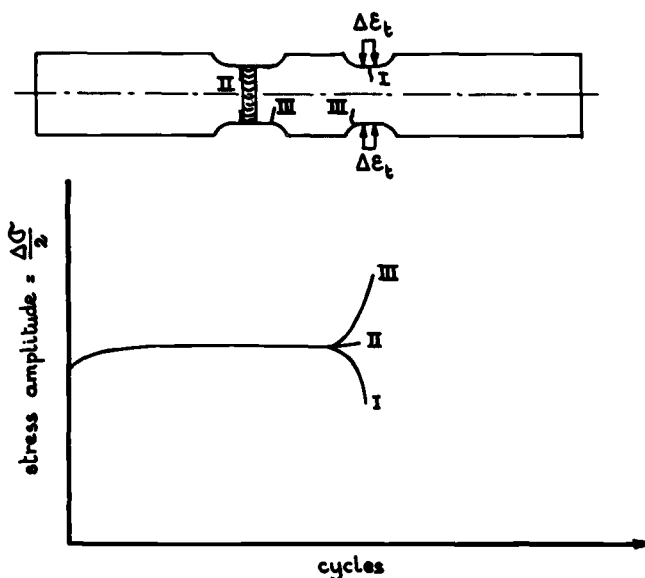


FIG. 6a—Variation in stress amplitude versus N as a function of crack initiation location.

ria into account, we can plot nine strain amplitude versus life curves. Figures 8a, 8b, and 8c give the total, plastic, and elastic strain amplitudes versus life curves determined with ground specimens for the E 355 steel in the annealed and the heat-treated conditions and the total strain amplitude versus life curves for all other tests. Parameters σ'_t/E and b of the elastic line and ϵ'_t and c of the plastic line are grouped in Table 4.

Analysis of Results

E 355 and E 36 steels have similar metallographic structure and mechanical properties. Therefore it can be assumed that in the annealed and heat-treated conditions, these steels present nearly similar low-cycle fatigue properties. For E 355 and E 36 steels several experimental parameters characterizing the notch acuity of the different specimens tested (as-rolled or as-welded) can be derived using the test data. For this derivation, characteristics of the tested specimens (indexed "nom") are compared with reference characteristics determined on ground specimens (without index). The used reference characteristics correspond to the heat-treated E 355, if the crack initiation occurs in the HAZ of the tested specimens, and to the annealed E 355, if the crack initiates in the base metal or in the weld metal having the same hardness as the base metal.

From low-cycle fatigue strength curves ($\Delta\epsilon-N_i$) and from the cyclic stress-strain curve, the strain and stress amplitudes corresponding to a given fatigue life have been derived (Fig. 9).

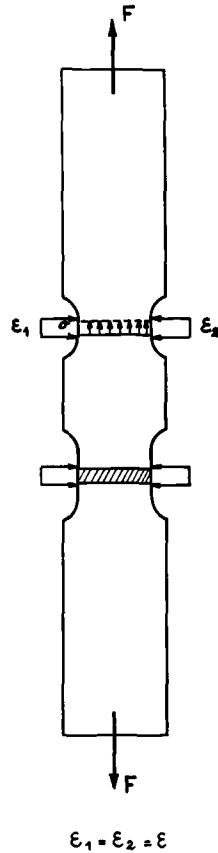


FIG. 6b—Variation in stress amplitude versus N as a function of crack initiation location—stress distribution without crack.

Elastic Strain Range (Long Fatigue Lives)

Elastic stress concentration factor (K_t)—The factor K_t was determined by Mattos and Lawrence [13] on butt welded joints using an elastic finite-element computer program. The geometry of the joint is then defined by different parameters and in particular by the ratio r/t (r = local radius at weld toe; t = plate thickness) and by the angles θ and ϕ (Fig. 3b).

Fatigue notch factor (K_f)—This factor is conventionally defined as the ratio of the endurance limit obtained on plain specimens, $\Delta\sigma$, over that obtained on notched specimens, $\Delta\sigma_{\text{nom}}$; for the investigated joints [9–11], the endurance limit is obtained for $2 \cdot 10^6$ cycles.

$$K_f = \frac{\Delta\sigma}{\Delta\sigma_{\text{nom}}}$$

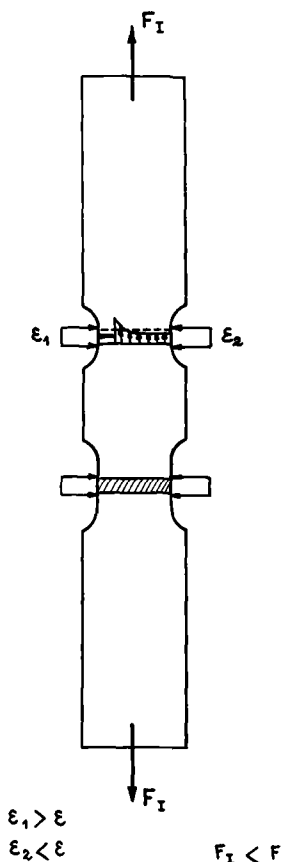


FIG. 6c—Variation in stress amplitude versus N as a function of crack initiation location—Example I.

where

$\Delta\sigma/2$ = endurance limit of the E 355 ground specimens, and
 $\Delta\sigma_{\text{nom}}/2$ = endurance limit of the studied specimens.

Fatigue notch factor according to Peterson—Peterson proposes a relationship between K_t , K_f and a parameter a that depends upon the metal:

$$K_f^P = 1 + \frac{K_t - 1}{1 + \frac{a}{r}}$$

In fact, as pointed out by Mattos and Lawrence [13], K_f^P is also a function of r/t . This function goes through a maximum corresponding to a critical value of r/t . Since in an as-welded joint the radius r at the toe is not constant along

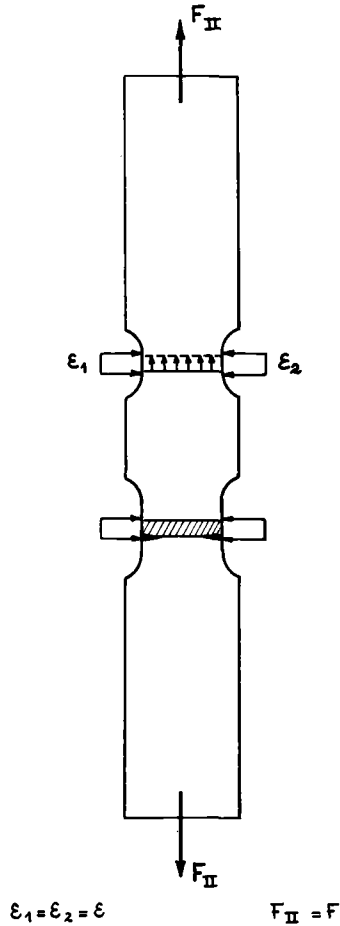


FIG. 6d—Variation in stress amplitude versus N as a function of crack initiation location—Example II.

the weld bead, the maximum value of K_f^P is a conservative estimate for the fatigue crack initiation life.

Plastic Strain Range (Short Fatigue Lives)

Strain concentration factor (K'_ϵ)— K'_ϵ is the ratio of the total strain amplitudes obtained for a given fatigue life for the reference specimens and for the tested specimens (Fig. 9):

$$K'_\epsilon = \frac{\Delta\epsilon}{\Delta\epsilon_{\text{nom}}}$$

Stress concentration factor (K'_σ)—The notch acuity of the investigated joints can also be expressed in terms of stress by using the stress concentration factor K'_σ (text continues on page 332):

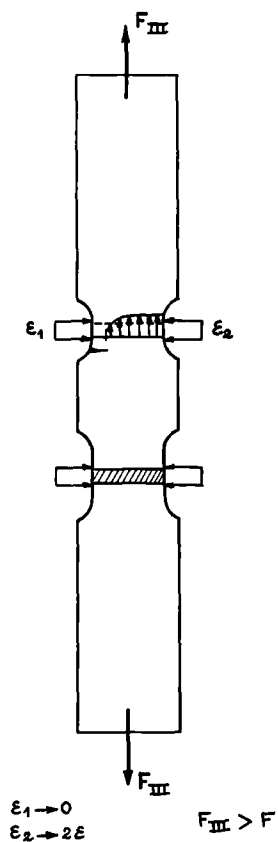


FIG. 6e—Variation in stress amplitude versus N as a function of crack initiation location—Example III.

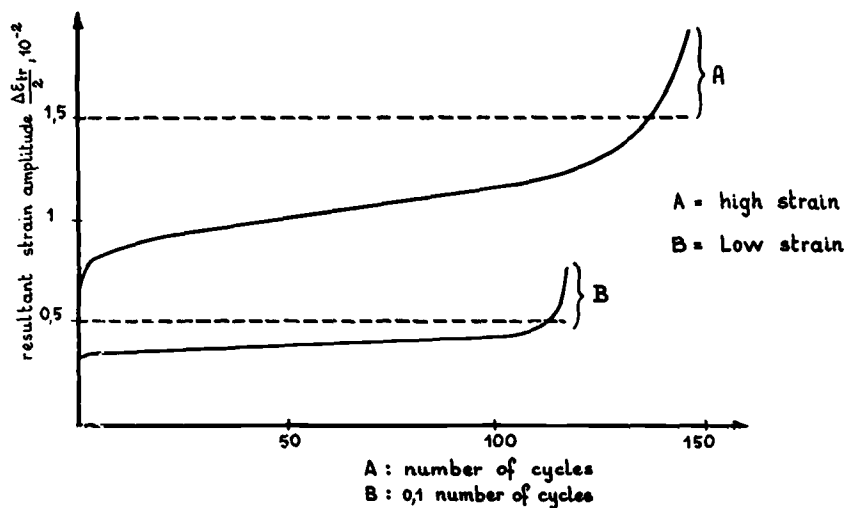


FIG. 7—Variation in strain amplitude as the weld joint versus N .

TABLE 5a—Low-cycle fatigue results (base metal in E 355 steel).

E 355	$\frac{\Delta \epsilon_t}{2}$, %	$\frac{\Delta \epsilon_e}{2}$, %	$\frac{\Delta \epsilon_p}{2}$, %	$\frac{\Delta \sigma}{2}$, N/mm ²	N_i
HAZ simulation ground specimens	1.509	0.311	1.198	641	235
	1.504	0.308	1.196	635	310
	1.009	0.281	0.728	578	556
	1.010	0.278	0.732	572	600
	0.506	0.236	0.270	486	1926
	0.509	0.236	0.273	485	2784
	0.304	0.208	0.096	429	16186
	0.261	0.191	0.070	393	19692
Annealed ground specimens	1.520	1.287	0.233	480	245
	1.000	0.779	0.221	455	660
	0.500	0.316	0.184	380	3760
	0.310	0.152	0.158	325	16800
	0.500	0.313	0.187	385	3330
Annealed as-rolled specimens	1.475	0.236	1.239	486	183
	1.483	0.254	1.229	524	176
	0.978	0.216	0.762	445	540
	1.083	0.231	0.852	476	364
	0.503	0.193	0.310	397	1828
	0.452	0.183	0.269	377	1408
	0.294	0.154	0.140	317	6780
	0.258	0.162	0.096	333	5030

TABLE 5b—Low-cycle fatigue results (butt joints in E 355 steel).

E 355	$\frac{\Delta \epsilon_{t \text{ nom}}}{2}$, %	$\frac{\Delta \epsilon_{e \text{ nom}}}{2}$, %	$\frac{\Delta \epsilon_{p \text{ nom}}}{2}$, %	$\frac{\Delta \sigma_{\text{nom}}}{2}$, N/mm ²	$N_{i \text{ nom}}$	Localization of Crack Initiation ^a
Manual arc welded	1.490	0.237	1.253	488	115	J, BM
	1.500	0.235	1.265	484	130	J, BM
	0.994	0.215	0.779	443	294	J, BM
	0.994	0.216	0.778	444	297	J
	0.512	0.185	0.327	381	1230	J, BM
	0.512	0.185	0.327	381	1240	J, BM
	0.250	0.146	0.104	300	4000	BM
	0.250	0.154	0.096	317	4950	BM
Submerged arc welded	1.481	0.229	1.252	472	154	J
	1.465	0.233	1.232	480	205	BM
	1.002	0.213	0.789	439	410	J
	0.953	0.211	0.742	435	525	BM
	0.502	0.187	0.315	385	1340	BM
	0.516	0.182	0.334	374	1640	BM
	0.263	0.154	0.109	317	6060	J, BM
	0.269	0.148	0.121	306	6425	BM
	0.256	0.153	0.103	315	7200	BM

^a J = welded joint; BM = base metal.

TABLE 5c—Low-cycle fatigue results (cruciform joints in E 36 steel).

E 36	$\frac{\Delta \epsilon_t \text{ nom}}{2}$, %	$\frac{\Delta \epsilon_e \text{ nom}}{2}$, %	$\frac{\Delta \epsilon_p \text{ nom}}{2}$, %	$\frac{\Delta \sigma \text{ nom}}{2}$, N/mm ²	$N_{i \text{ nom}}$	Localization of Crack Initiation ^a
As-welded	0.118	0.116	0.020	225	46 520	J
	0.179	0.131	0.048	255	17 000	J
	0.198	0.137	0.061	267	13 150	J
	0.200	0.140	0.060	273	9 316	J
	0.203	0.140	0.063	272	7 911	J
	0.208	0.140	0.068	273	10 570	J
	0.271	0.147	0.144	285	4 460	J
	0.400	0.180	0.220	349	1 379	J
	0.400	0.186	0.214	362	1 315	J
	0.400	0.179	0.221	349	1 789	J
	0.406	0.172	0.234	335	1 751	J
	0.435	0.185	0.250	360	820	J
	0.500	0.190	0.310	370	563	J
	0.580	0.216	0.364	420	388	J
	0.650	0.203	0.447	394	452	J
	0.656	0.208	0.448	404	503	J
	0.662	0.203	0.459	394	592	J
	0.662	0.207	0.455	403	465	J
	1.000	0.220	0.780	428	99	J
	1.018	0.229	0.789	446	110	J
After grinding the weld toe	1.020	0.233	0.787	454	165	J
	1.027	0.226	0.799	439	108	J
	0.186	0.144	0.042	280	33 000	J
	0.197	0.148	0.049	288	9 776	J
	0.206	0.158	0.048	307	7 345	J
	0.206	0.154	0.052	299	8 150	J
	0.271	0.154	0.117	300	8 170	J
	0.294	0.169	0.125	328	2 200	BM
	0.335	0.167	0.168	325	5 520	J
	0.397	0.190	0.207	370	1 667	J
	0.400	0.178	0.222	346	1 890	BM
	0.406	0.192	0.214	374	1 375	BM
	0.467	0.198	0.269	385	2 120	J
	0.500	0.207	0.293	403	1 195	J
	0.594	0.216	0.378	420	495	J
	0.633	0.220	0.413	428	658	J
	0.662	0.214	0.448	417	797	J
	1.018	0.229	0.789	445	134	J
	1.023	0.237	0.786	462	150	J

^aJ = welded joint; BM = base metal.

TABLE 5d—Low-cycle fatigue results (cruciform joints in A 70 steel).

A 70	$\frac{\Delta \epsilon_t \text{ nom}}{2}$, %	$\frac{\Delta \epsilon_o \text{ nom}}{2}$, %	$\frac{\Delta \epsilon_p \text{ nom}}{2}$, %	$\frac{\Delta \sigma_{\text{nom}}}{2}$, N/mm ²	$N_{i \text{ nom}}$	Localization of Crack Initiation ^a
As-welded	0.191	0.161	0.030	333	10 489	J
	0.195	0.160	0.035	331	7 768	J
	0.196	0.157	0.039	327	8 670	J
	0.202	0.166	0.036	344	4 664	J
	0.203	0.166	0.037	344	3 970	J
	0.206	0.159	0.047	331	9 400	J
	0.394	0.213	0.181	443	829	J
	0.397	0.210	0.187	435	1 018	J
	0.397	0.211	0.186	437	1 010	J
	0.398	0.209	0.189	435	1 188	J
	0.406	0.210	0.196	435	1 097	J
	0.409	0.211	0.198	437	795	J
	0.650	0.240	0.410	499	260	J
	0.650	0.240	0.410	499	256	J
	0.650	0.244	0.406	507	214	J
	0.654	0.248	0.406	516	344	J
	0.656	0.238	0.418	494	225	J
	0.997	0.268	0.729	557	101	J
	1.014	0.270	0.744	560	99	J
	1.017	0.263	0.754	547	94	J
After grinding the weld toe	1.017	0.275	0.742	572	76	J
	1.022	0.275	0.747	571	92	J
	1.024	0.274	0.750	568	118	J
	0.191	0.162	0.029	335	13 875	J
	0.194	0.165	0.029	343	13 466	BM
	0.197	0.167	0.030	347	18 622	BM
	0.197	0.166	0.031	345	14 576	BM
	0.197	0.166	0.031	345	12 506	J
	0.200	0.160	0.040	328	13 817	J
	0.203	0.170	0.033	432	11 928	BM
	0.397	0.209	0.188	433	1 530	J
	0.400	0.217	0.183	451	1 397	J
	0.400	0.220	0.180	456	1 137	J
	0.403	0.211	0.192	437	1 591	J
	0.411	0.217	0.194	451	1 738	BM
	0.642	0.248	0.394	515	372	J
	0.645	0.250	0.395	520	388	J
	0.650	0.250	0.400	520	325	BM
	0.656	0.244	0.412	507	384	J
	0.658	0.235	0.423	488	377	J
	0.660	0.247	0.413	513	276	J
	0.999	0.277	0.722	575	140	BM
	1.003	0.272	0.731	565	147	J
	1.009	0.285	0.724	592	94	BM
	1.011	0.274	0.737	569	88	BM
	1.016	0.272	0.744	565	117	J

^a J = welded joint; BM = base metal.

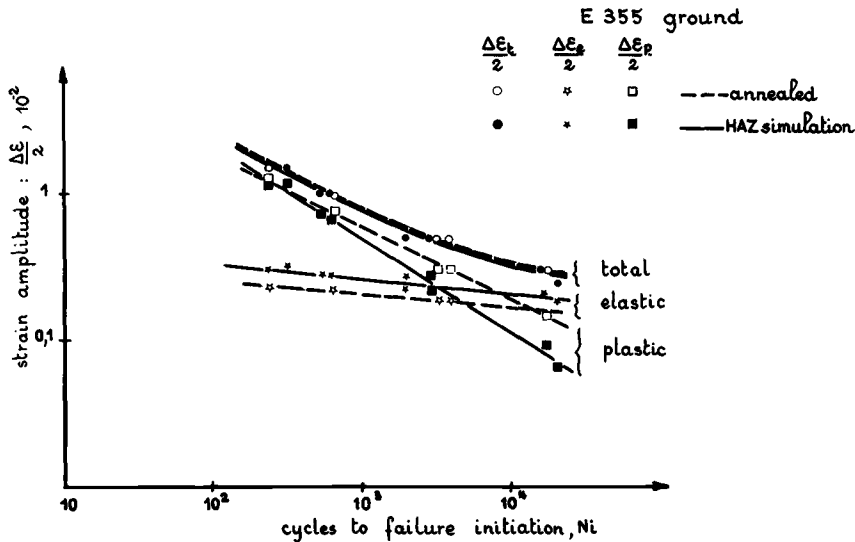


FIG. 8a—Strain amplitude life curves—base metal (ground specimens).

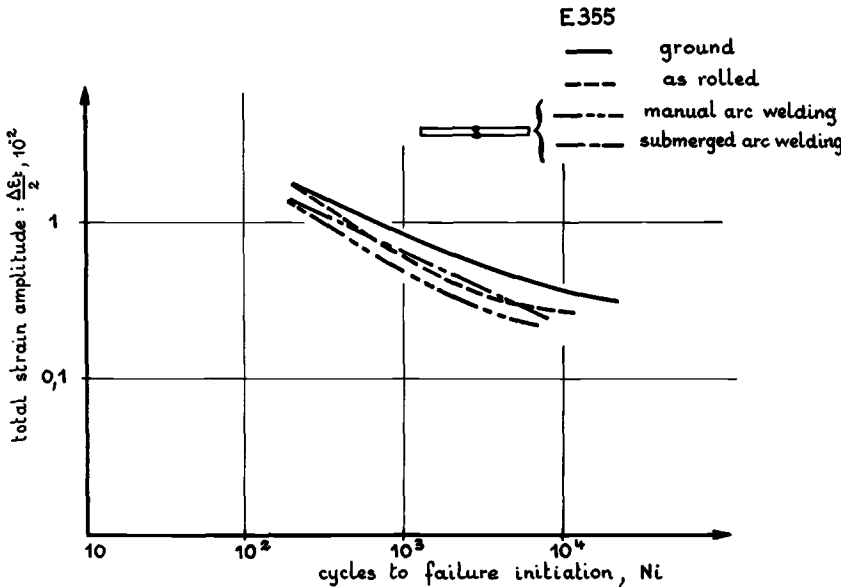


FIG. 8b—Strain amplitude life curves—comparison between butt joints and base metal.

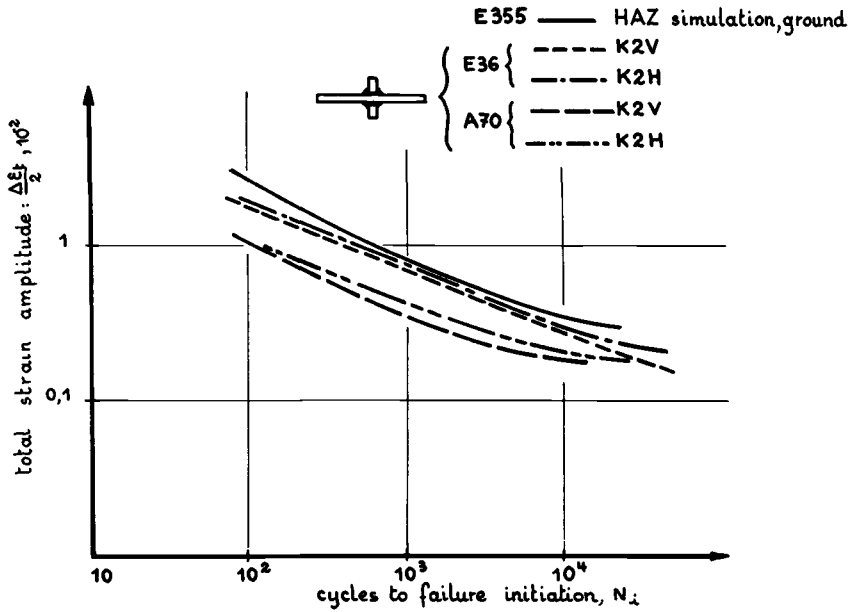


FIG. 8c—Strain amplitude life curves—comparison between cruciform joints and base metal.

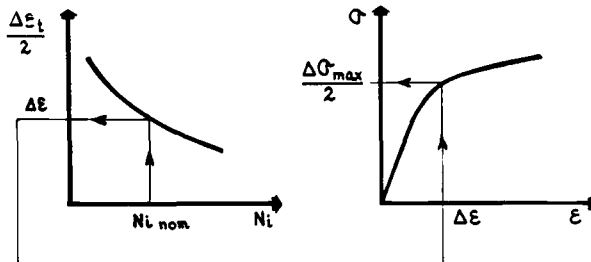


FIG. 9—Derivation of the local strain and stress conditions ($\Delta \sigma$, $\Delta \epsilon$) using smooth specimen properties.

$$K'_{\sigma} = \frac{\Delta\sigma}{\Delta\sigma_{\text{nom}}}$$

where $\Delta\sigma$ and $\Delta\sigma_{\text{nom}}$ correspond to the stable cycle for a given fatigue life (Fig. 9).

Application of Neuber's rule—Using Neuber's hypothesis [14], it is possible to define

$$K_t^{\text{EP}} = \sqrt{\frac{\Delta\epsilon \cdot \Delta\sigma}{\Delta\epsilon_{\text{nom}} \cdot \Delta\sigma_{\text{nom}}}}$$

This expression relates the local strain and stress conditions ($\Delta\sigma$, $\Delta\epsilon$) to the nominal conditions ($\Delta\sigma_{\text{nom}}$, $\Delta\epsilon_{\text{nom}}$) applied to the plate. For the short fatigue lives, the variations of K'_ϵ , K'_σ and K_t^{EP} as functions of N_i are limited. These parameters are then calculated for $N_i = 2000$ cycles.

Discussion of Results

Notch Effect

The notch effect was studied from results obtained from E 355 and E 36 steels. Table 6 gives the values of the different concentration factors.

Long Fatigue Life Range—In only one case (butt joint made by manual arc welding) are estimates available for the theoretical value of K_t and for the level K_t^{P} deduced from Peterson's analysis. These estimates, respectively 2.05 to 1.85, are substantially lower than the K_t -level deduced from endurance limits (2.85). The difference observed can be explained by the difficulty, during calculation, of taking into account the microgeometry of the weld toe as well as the presence of residual stresses caused by the welding operation.

Short Fatigue Life Range—A very substantial drop in the stress or strain concentration factors is observed compared with those calculated in the endurance range; the ratio K_t/K_t^{EP} varies between 1.6 and 2.4. This observation shows that the deformation ability of the metal increases with the plastic strain amplitude level to which the metal is subjected.

The level of K_t^{EP} is intermediate between those of K'_ϵ and K'_σ ; in fact,

$$K_t^{\text{EP}} = \sqrt{K'_\epsilon \cdot K'_\sigma}$$

In the cyclic strain-hardening range, stress and strain amplitudes are related by

$$\frac{\Delta\sigma}{2} = k' \left(\frac{\Delta\epsilon_p}{2} \right)^{n'}$$

For this reason, in the case of butt joints, where the crack initiation occurs in a zone comparable with the base metal,

$$K'_{\sigma} = (K'_\epsilon)^{n'}$$

TABLE 6—*Static and fatigue notch factors.*

	Base Metal, As-Rolled	Butt Joints		Cruciform Joints	
		Manual Arc Welded	Submerged Arc Welded	Vertical Position	Flat Position
K_t	...	2.05
K_f	1.55	2.85	2.2	3.9	2.4
K_f^P	...	1.85
K_f^e	1.4	1.7	1.4	1.7	1.65
K_f^a	1.1	1.2	1.1	1.5	1.35
K_f^{EP}	1.25	1.4	1.25	1.6	1.5

Surface Conditions

The results show that the initiation life is much shorter in the as-rolled conditions than in the ground conditions (Fig. 8b). Within the low-cycle fatigue range, this drop expressed in terms of strain is still about 40 percent ($K'_\epsilon = 1.4$). It is due, on one hand, to the detrimental nature of the surface defects and of the scale effect (ratio of useful sections between unmachined and machined specimens) in the case of as-rolled specimens and, on the other hand, to the beneficial effect of strain hardening during machining in the case of ground specimens.

Bead Geometry

Butt Joints (Fig. 8b)—In the low-cycle fatigue range, no significant difference is observed between the behavior of the joints obtained by submerged arc welding and of the as-rolled plate; K'_σ , K'_ϵ and K'_f ^{EP} are the same for both. This accounts for the fact that, owing to the small reinforcement of the bead many failures have been observed in the base metal. In the case of manual arc welding, the increase is about 10 percent for K'_σ and 20 percent for K'_ϵ compared with submerged arc welding (Table 6). It may be noted that this difference is clearly smaller than in the endurance range; there the increase of K_f is on the order of 30 percent (Table 6).

Cruciform Joints (Fig. 8c)—The drop in the low-cycle fatigue properties of cruciform joints is substantially greater than that observed in the case of butt joints. This is because of the increase in the transition angle at the bead. The improvement obtained with weld toe grinding leads to a drop of about 10 percent in K'_σ (Table 6). Nevertheless, the grinding effect is clearly smaller than in the case of long fatigue lives; the drop of K_f is on the order of 40 percent (Table 6).

Role of Microstructure

Heat Treatment—The cyclic tensile curves of E 355 steel in the annealed condition and in the heat-treated condition are very different (Fig. 1). The cyclic yield strength, Y' , increases from 350 to 470 N/mm², whereas the strain-hardening coefficients, n' , are similar (Table 3).

These differences result in a major shift of the elastic line ($\Delta\epsilon_e-N_i$) and of the plastic line ($\Delta\epsilon_p-N_i$). The annealed condition, more ductile, leads to a higher resistance to cyclic plastic strain amplitudes, whereas the heat-treated condition entails better behavior under high stress cyclic conditions (Fig. 8a).

On the other hand, the total strain curves, $\Delta\epsilon_t-N_i$, practically coincide. In the studied fatigue life range, there is a compensation of the elastic and plastic behaviors for E 355 steel.

Steel Grade—In the case of fillet weld specimens, the low-cycle fatigue strength expressed in terms of strain is found to be lower for A 70 steel than for E 36 steel (Fig. 8c). This representation method shows that the higher ductility of E 36 steel enables the welded joints to support slightly higher

strains for any given fatigue life. If the low-cycle fatigue strength is expressed in terms of stress (Fig. 10), however, we observe an advantage for A 70 steel, for which fatigue strength increases with strain amplitude.

This behavior, observed for short fatigue lives, is different from long fatigue lives ($N > 10^6$ cycles), where the fatigue properties are comparable for both steels [9].

Conclusion

The results of low-cycle fatigue tests ($N < 10^4$ cycles) on base metal and welded joints have made it possible to elucidate the following points:

1. The fatigue reduction factor, as an expression of the notch acuity, is considerably reduced for the low-cycle fatigue range compared with the endurance range ($K_f \approx 2K'_\sigma$). Thus the ability of the metal to adapt to localized defects increases with the applied strain amplitude.
2. For short fatigue lives ($N_i < 10^4$ cycles) and for a given fatigue life:
 - (a) Strain amplitudes are about 30 percent higher in the machined conditions than in the as-rolled conditions.

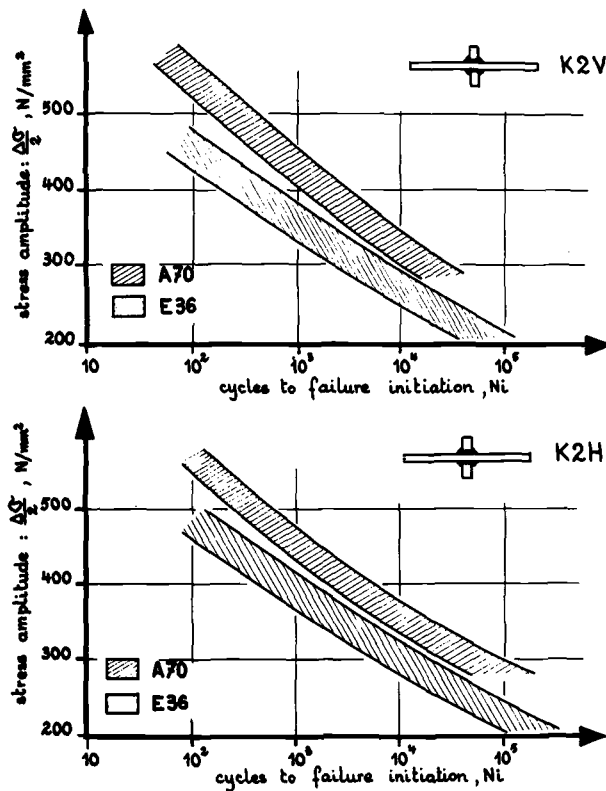


FIG. 10—Stress amplitude life curves (cruciform joints).

- (b) For butt joints, the results show major difference in behavior depending on the welding process. Submerged arc welding leads to strain amplitudes more than 20 percent higher than those obtained by manual arc welding. These differences are explained by the bead profile and by the microgeometry at the bead toe.
- (c) The effect of the toe grinding in the case of cruciform joints leads to an improvement in stress (about 10 percent), clearly smaller than that observed in the endurance range (>40 percent).
- (d) The simulated HAZ metal does not show any difference in low-cycle fatigue strength when compared with the annealed metal.
- (e) For cruciform joints, the increase in the yield strength of the base metal improves the low-cycle fatigue strength expressed in terms of stress. For a given strain, the fatigue life increases with ductility.

Acknowledgments

This work was supported by the European Coal and Steel Community (ECSC) under Contracts 6210.45.1/10, 6210-45-3/301, and 7210.KD/303.

References

- [1] Diez, J.-M. and Salkin, R.-V., CNRM Report D/1976 0124/30, Centre National de Recherches Metallurgiques, Belgium.
- [2] Serensen, S.-V. and Machutov, N.-A., IIW Report XIII, No. 635-71, International Institute of Welding.
- [3] Harrison, J.-D., *Report Series*, The Welding Institute, 1974, Part 1, No. C 215/6/68.
- [4] Harrison, J.-D. in *Proceedings*, Conference on Fatigue of Welded Structures, Vol. 2, Paper 12, The Welding Institute, 1971, pp. 194-207.
- [5] Harrison, J.-D., *Report Series*, The Welding Institute, 1974, Part 1, No. C 215/11/69.
- [6] Harrison, J.-D., *Report Series*, The Welding Institute, 1974, Part 1, No. C 215/21/71.
- [7] Fall, H.-W., Brugioni, D.-L., Randall, M.-D., and Monroe, R.-E., *Welding Research Supplement*, April 1962, pp. 145s-153s.
- [8] Iida, K., Ochiai, O., Kawai, T., Hiradawa, K., Fujisawa, K., and Okasawa, T., *The Sumitomo Search*, No. 17, May 1977, pp. 1-17.
- [9] Bastenaire, F., Lieurade, H.-P., and Regnier, L., *Revue de Metallurgie*, Nov. 1979, pp. 709-725.
- [10] Lieurade, H.-P. and Rabbe, P., *Revue de Metallurgie*, April 1976, pp. 333-358.
- [11] Lieurade, H.-P., *Métaux, Corrosion, Industrie*, No. 609, May 1976, pp. 185-200.
- [12] European Coal and Steel Community, ECSC Contract No. 6210-45, Report EUR 5357e, 1975.
- [13] Mattos, R.-J. and Lawrence, F.-V., SP-424, Society of Automotive Engineers.
- [14] Neuber, H., Technical Report AFML TR 68-20, Air Force Materials Laboratory, April 1968.

Growth of Short Cracks During High Strain Fatigue and Thermal Cycling

REFERENCE: Skelton, R. P., "Growth of Short Cracks During High Strain Fatigue and Thermal Cycling," *Low-Cycle Fatigue and Life Prediction, ASTM STP 770*, C. Amzallag, B. N. Leis, and P. Rabbe, Eds., American Society for Testing and Materials, 1982, pp. 337-381.

ABSTRACT: Research in high-temperature fatigue usually concerns either crack initiation and endurance of smooth specimens in high strain fatigue (HSF) or the growth of long cracks in the nominally elastic regime described by linear elastic fracture mechanics. This review shows that the relatively unfamiliar growth rates in HSF can be linked to those in stress-intensity controlled growth, and so can be used satisfactorily for predicting component failure. Either a strain-based intensity parameter or a J-integral method may be used, and several examples are given. Integrated HSF growth rates are also shown to be consistent with smooth specimen endurance from (1) striation measurements, (2) direct measurement, and (3) the predictions of the shear decohesion model.

Empirical HSF growth relations are summarized and the effects of temperature, environment, tension dwells, and microstructural damage are assessed in several alloys. The greatest correction that has to be made to the experimental and theoretical growth relations arises from the accelerating effects of creep during dwell.

KEY WORDS: high temperature alloys, thermal cycling, thermal shock, thermomechanical test, high strain fatigue, cyclic crack growth relation, linear elastic fracture mechanics, strain intensity, J-integral, creep-fatigue interaction, tension dwell, frequency, total endurance, integrated endurance, striation spacing, growth models, crack tip opening displacement, transgranular and intergranular crack, microstructural damage, aging, environment, laboratory specimen, component, plastic strain range

Components in power-generating plants experiencing a heating and cooling cycle during routine operation vary over three orders of magnitude in thickness: from fuel-element cladding tubes in nuclear reactors (~0.5 mm), to vanes and blades of gas turbines (5 mm), and ending with cast valve chests and casings and rotor forgings in conventional turbine plants (100 to 300 mm). The rate at which plants can be brought up to full load is limited by the transient thermal stresses developed across certain regions [1,2].² As will be

¹ Materials Division, Central Electricity Research Laboratories, Central Electricity Generating Board, Leatherhead, Surrey, England.

² The italic numbers in brackets refer to the list of references appended to this paper.

seen, the service cycle experienced by the more massive components is essentially strain controlled [1-3].

However large or small the component, if the magnitude of successive thermal cycles produces reversed yield at the surface (or at the root of a stress-raising notch or groove) a small fatigue crack will initiate after a characteristic number of cycles. The crack then propagates through a plastic zone defined by the notch geometry [4] and temperature gradient. This is the high strain fatigue (HSF) growth stage. Ultimately the crack will emerge from such local plasticity, and its progress is then described by linear elastic fracture mechanics (LEFM) [4]. In rotating components, cracks cannot be allowed to propagate far from the surface, and so use of initiation data in design [5] is appropriate. Since the early work of Walker [6] on low-alloy steels, many subsequent studies have been undertaken on creep-fatigue initiation behavior, many tests lasting up to six years [3,7]. However, in large static components, great economic savings can result if it can be shown that relatively deep cracks discovered during service operation will become dormant, thus allowing that component to continue in use. If we could describe convincingly the complete crack growth pattern, an important practical link would be achieved between the major disciplines of HSF and LEFM.

There is an increasing tendency for the presence of defects either to be allowed for at the design stage or to be assessed when disclosed during construction or operation. Thus stress intensity at the tip of a crack starting from a notional defect must be kept below threshold or one must be able to estimate crack progress during service cycles [8]. In laboratory determinations, the propagation relation, valid for intermediate-range stress intensities [9],

$$\frac{da}{dN} = C \Delta K^m \quad (1)$$

(where da/dN is cyclic growth rate, ΔK is the range of stress intensity, m lies in the range of 2 to 4, and C is a constant) was quickly applied at high temperature. Some of the earliest results were on Type 304 and Type 316 stainless steels [10,11]. It is not intended to review all subsequent work in this regime except to note that tensile dwell periods are now being incorporated, causing an increase in cyclic growth rate [12-14]. The application of fracture mechanics techniques to high-temperature crack growth in many structural alloys has recently been discussed by Sadananda and Shahinian [15].

For a simple, ductile, high-temperature alloy of yield strength ~ 150 to 200 MPa it is impossible to initiate a surface fatigue crack without general cyclic yield. In a push-pull specimen, valid LEFM data are only obtainable at crack depth/specimen width (a/W) ratios in excess of 0.1 to 0.2—that is, when there are the first indications of a compliance change—and crack growth may then proceed for zero width of hysteresis loop. After the initiation stage

in smooth specimens, there is thus a significant technological range involving crack propagation under reversed plasticity—that is, HSF. This region constitutes an important but neglected chapter in the study of high-temperature fatigue deformation. It is of course embraced by the total failure of a smooth specimen, but comparatively few attempts have been made to monitor the growth stage. Tomkins et al [16] suggest the reasons as (1) experimental difficulties and (2) lack of analytical solutions for short cracks in elasto-plastic stress-strain fields. As for (1), however, growth increments of 0.02 to 0.05 mm can readily be detected using the d-c potential drop technique [17].

The empirical crack growth relations that have been established in thermal and HSF are not currently familiar; perhaps this is because investigators have not expressed their results usefully for design assessment purposes. The subject has only received passing mention in two previous reviews of HSF [18,19], and it is hoped that the present contribution will give some idea of the cyclic growth rates involved.

In this review, theoretical and experimental HSF growth relations are first identified with total endurance data and then compared with propagation rates in the LEFM regime. The data are then used to describe crack growth in two instances of thermal stressing which arises from deformation that is *contained*.

Data Requirements and Laboratory Simulation of the Service Cycle

A typical strain-controlled cycle arising from heating and cooling the surface of a thick structure has been discussed previously [20] and is shown in Fig. 1. The main points to note are that during the steady running period, the residual tension stress relaxes from R to R' so that creep damage is introduced, and that the loop width attenuates for increasing distances into the yield zone, shown shaded in Fig. 1a. If external stresses are imposed, the loop width increases [21] and conversely, if cooling is sufficiently slow, the tension-going phase $R'S$ disappears [22].

Crack growth in the system of Fig. 1 can be measured in the laboratory as follows:

1. If the variation of stress intensity across the section is known, the growth of long cracks (that is, in region B) can be measured on standard specimens at several temperatures. This forms the *LEFM* test (Eq 1).
2. The stress gradient near the surface is ignored. A smooth specimen, representing the surface at A , is temperature and strain cycled concurrently in the push-pull mode (Fig. 1b). This is a *thermomechanical* test.
3. A simpler form of 2 above is to perform the test isothermally at the maximum temperature, assuming this to be the most damaging. This is the *HSF* test. In types 2 and 3 a shallow starter notch can be introduced, and testing continued under fully reversed net section plasticity.
4. For crack growth across the whole section, whether on thin or thick

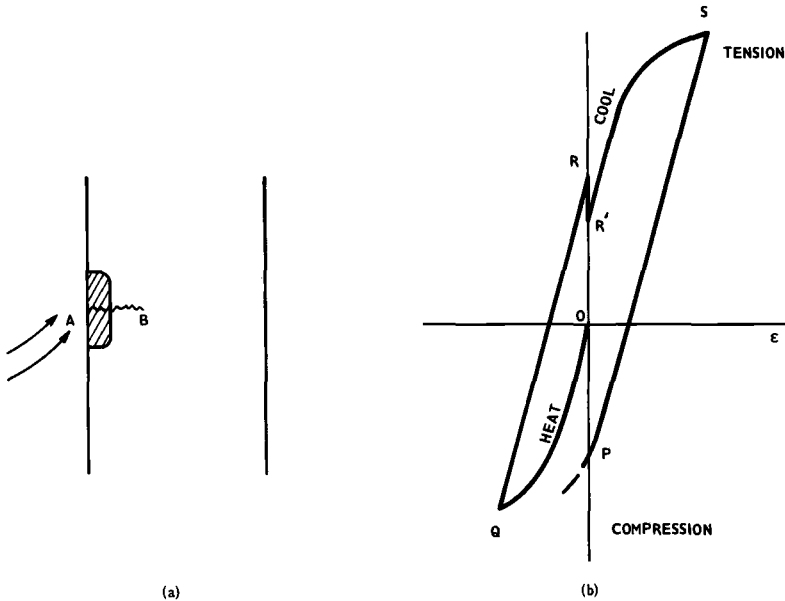


FIG. 1—Heating and cooling the surface of a structure (a) leads to hysteresis loop (b).

specimens, a *thermal shock* test is employed [21]. Once the crack has emerged from the region of reversed plasticity, growth is retarded because of the stress gradient.

Only the thermal shock test (4) simulates the whole process from nucleation to propagation deep into the structure. On the other hand, tests of types 1 to 3 are convenient simplifications of crack initiation and growth across a whole component. Type 3 is often simplified even further by introducing the dwell at peak tension (compare Fig. 1), thus producing conservative data [7].

Theoretical and Experimental HSF Crack Growth Rates Compared with Total Endurances

Shear Decohesion Model

An analysis by Tomkins [23] considered HSF crack advance per cycle to take place by irreversible shear decohesion of material on 45-deg planes immediately ahead of the crack tip. The length of the intense deformation zone D was given by

$$D = \sqrt{2} \left[\sec \left(\frac{\pi \sigma}{2T} - 1 \right) \right] a \quad (2)$$

where σ is the maximum applied stress and T is the flow stress of heavily cycled material. The amount of decohesion δ was originally given [23] by

$\delta = D \epsilon_p$ where ϵ_p is the bulk plastic strain range (that is, width of hysteresis loop at zero stress), but was later [24,25] modified to

$$\delta = \int_0^{\epsilon_p} D \epsilon_p d\epsilon \quad (3)$$

From Eqs 2 and 3 the cyclic growth rate was derived for $\sigma/T < 0.5$:

$$\frac{da}{dN} = \frac{\pi^2}{8} \left(\frac{\sigma}{T} \right)^2 \frac{\epsilon_p}{1 + 2\beta} a \quad (4)$$

β is the cyclic-hardening exponent obtained during steady-state cycling of a plain specimen and is given by

$$\Delta\sigma = k \epsilon_p^\beta \quad (5)$$

where $\Delta\sigma = 2\sigma$ is the stress range and k is a constant.

Equation 4 may thus be expressed alternatively

$$\frac{da}{dN} = \frac{\pi^2}{8} \left(\frac{k}{2T} \right)^2 \frac{\epsilon_p^{2\beta+1}}{1 + 2\beta} a \quad (6)$$

This equation has aroused much interest because it may be integrated [23] to give a form of the Coffin relation

$$\epsilon_p N_f^\alpha = \text{constant} \times \ln \left(\frac{a_f}{a_0} \right) \quad (7)$$

whose slope α is identified with $1/(1 + 2\beta)$. The terms a_0 and a_f are initial crack length ($\sim 10 \mu\text{m}$) and final crack length (~ 0.75 specimen width), respectively.

The theory has subsequently been developed to cater for grain boundary creep damage that builds up during dwells at high temperature [26–28], to explain observed striation spacings [29,30], and to establish links between crack-tip opening displacement (CTOD) ϕ and da/dN . An expression for CTOD under elasto-plastic conditions is given [31] by

$$\phi = \frac{A_1(1 - \nu^2)\pi\sigma^2 a}{ET} + \frac{A_1 2(1 - \nu_1^2)\pi\sigma\epsilon_p a}{(1 + \beta)} \quad (8)$$

where ν and $\nu_1 = 0.3$ and 0.5 , respectively (elastic and plastic Poisson's ratio), E is Young's modulus, and $A_1 = 0.5$ for plastic relaxation at $\pm 45^\circ$. Each of these aspects will be discussed. Since the creation of new crack surface by shear decohesion is common to both HSF and LEFM [31], Eq 8 can be used in both regimes to describe crack growth.

Experimental Growth Relations

In one of the first high-temperature studies on crack growth at 600°C it was observed for Type 316 steel [32,33] that cracks initiated at grain bounda-

ries (Stage I) but then accelerated perpendicular to the alternating stress in a transgranular manner (Stage II). Ripple (nowadays called striation) spacings were identified with cyclic crack growth rate, and provided that a was “small compared with the specimen diameter” the following growth relation applied:

$$\frac{da}{dN} = B a \tag{9}$$

B is a constant measuring fractional growth per cycle and it depends on plastic strain range. When $a/W > 0.1$, a deviation from linearity under strain-controlled cycling has since been observed in other high-temperature alloys [16,34–37].

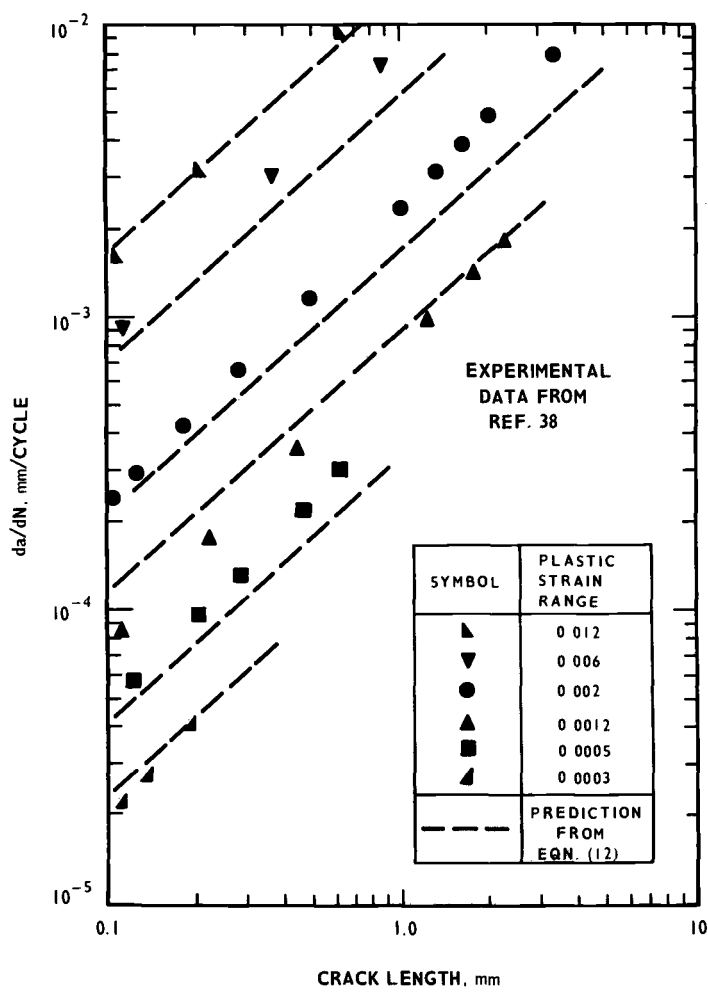


FIG. 2—Experimental crack growth rates for 20Cr-25Ni-Nb at 750°C in air.

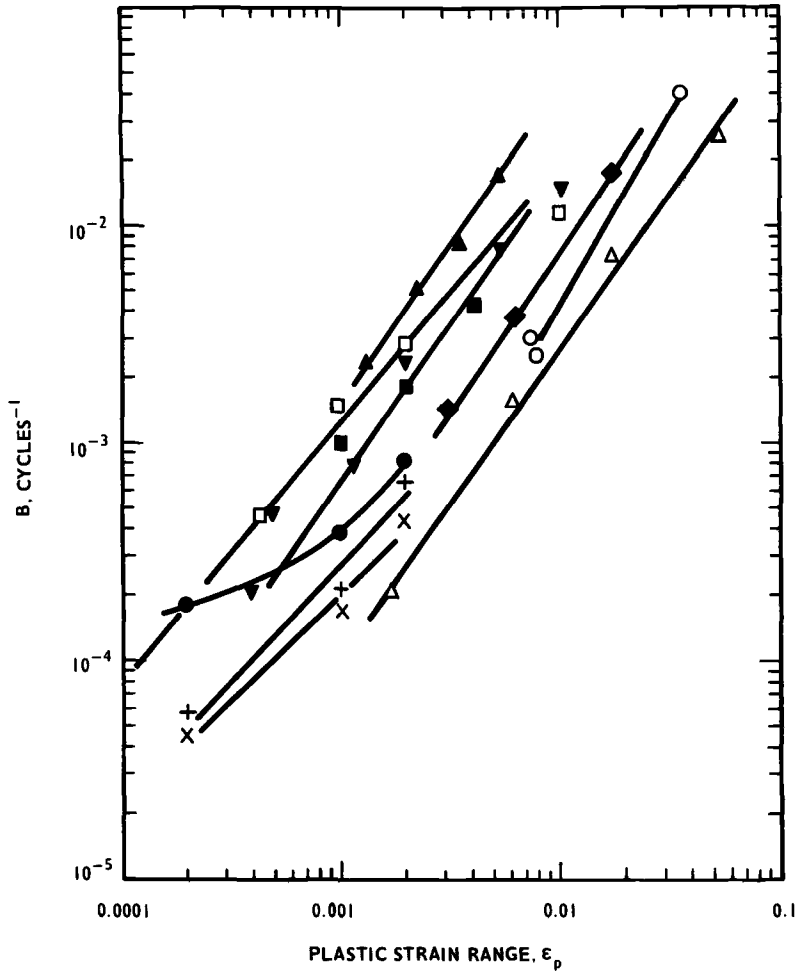


FIG. 3—Variation of growth rate with plastic strain.

Figure 2 shows some crack growth data of Wareing [38] on 20Cr-25Ni-Nb stainless steel at 750°C . The variation of B with plastic strain range is shown in Fig. 3 for this and other high-temperature materials for which growth data are available [17,38-46]. It is clear that Eq 9 can be written more generally:

$$\frac{da}{dN} = C \epsilon_p^n a \quad (10)$$

where C and n are constants for a given material. Comparing this experimental relation with Eqs 6 and 7, we thus have $n = 1 + 2\beta = 1/\alpha$. Some examples at high temperature are given in Table 1; it is seen that the term $1 + 2\beta$ generally overestimates the experimental exponent n given by the slopes of Fig. 3 and also the reciprocal Coffin slope $1/\alpha$ (Eq 7). It is emphasized that the data of Fig. 3 and Table 1 refer to *continuous cycling* tests mostly carried out in air at a reversed strain rate of $\sim 10^{-3} \text{ s}^{-1}$.

The results of Fig. 3 together with Eq 9 can thus be used to predict near-surface crack growth rates in high-temperature components. Unfortunately much of the data is at rather large values of plastic strain and, further, this parameter cannot often be computed for use in engineering assessments. This is especially true for thermal transients where ϵ_p , the bulk section plastic strain, becomes zero at the edge of the yield zone (Fig. 1a) and yet cracks propagate beyond this [21]. Perhaps a more acceptable practical method is to relate the term B in Eq 9 to *total* strain range ϵ_t . This is done in Fig. 4 which also includes further results [47,48], some with dwell. The data should not be extrapolated to lower strains because oxide blocking (q.v.) sometimes rapidly decelerates the crack [17].

The linear increase in da/dN with crack depth a (Eqs 2 and 6) is based on Dugdale's [49] model for the spread of the plastic yield zone. There have, however, been several cases [17,20,41,42,45,46,50-52] where crack growth rates obey the relation

$$\frac{da}{dN} = Ba^Q \quad (11)$$

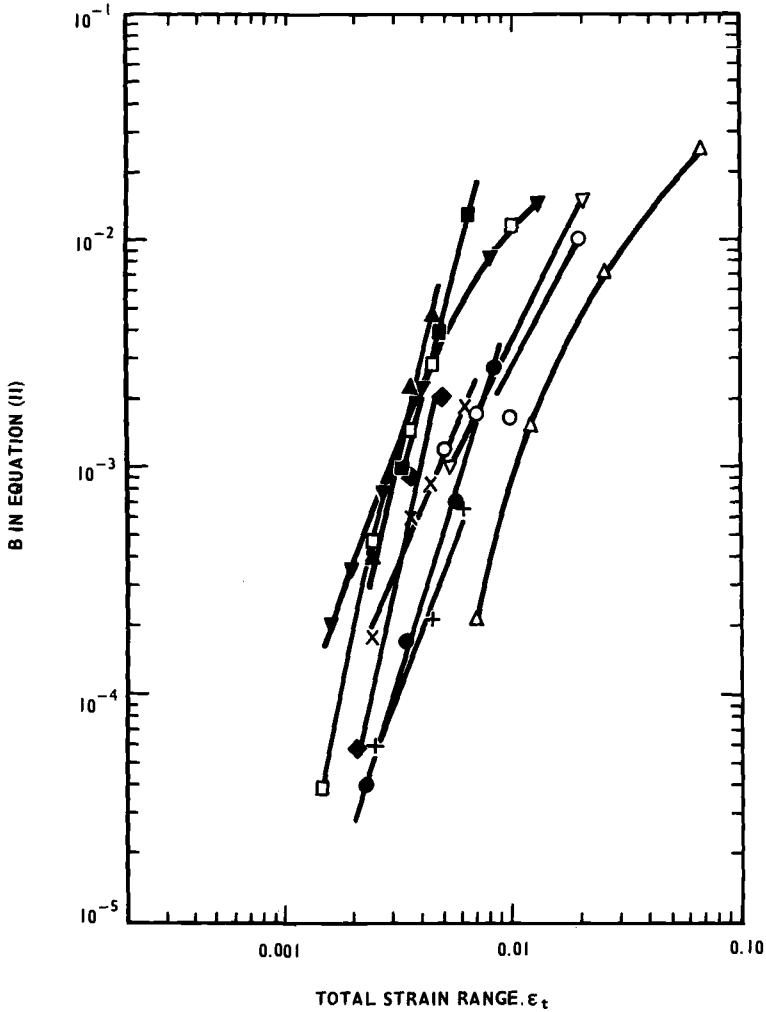
where $Q > 1$. Values of Q are summarized in Table 2 and some examples of growth rates given in Fig. 5.

A semi-empirical approach [46] accounting for Eq 11 regarded crack propagation as increments of successive reinitiation by determining each in-

TABLE 1—Comparison of constants for crack growth (n) cyclic stress-strain (β) and slope of Coffin plot (α).

Material	Temperature, °C	n	$1 + 2\beta$	$1/\alpha$	Reference
20Cr-25Ni-Nb	750	1.52	1.54	1.15	38
Type 316 steel	625	1.35	1.48	1.30	38
Hastelloy X	760	1.28	1.45	1.38	39
Type 321 steel	700	1.5	...	1.67	41
Type 321 steel	490	0.98	1.57	1.63	45
A286	593	0.7	1.20 ^a	1.03	44
½Cr-Mo-V	550	1.0	1.56	1.0	46
9Cr-1Mo	525	1.2	1.50	1.12	46
Type 301 steel	200	1.80	2.0	2.17	42

^a Calculated from Ref 33.



ALLOY	°C	REF.	NOTES	ALLOY	°C	REF.	NOTES
+ 9Cr1Mo	500	40	AIR	◆ ½CrMoV	550	20	STEAM & DWELL
● ½CrMoV	550	17	VACUUM	▼ 20Cr25NiNb	750	38	
x ½CrMoV	550	17	VAC & DWELL	□ TYPE 316	625	38	WELD
▲ ½CrMoV	550	17	AIR & DWELL	○ TYPE 304	593	47	
■ ½CrMoV	550	17	AIR & DWELL	▼ INCOLOY 800	700	48	
BAINITIC				Δ ZIRCALOY 2	350	43	

FIG. 4—As for Fig. 3 in terms of total strain.

TABLE 2—Deviations from exponential growth law (Eqs 9 and 11).

Material	Temperature, °C	Q	Environment	Remarks	Reference
½Cr-Mo-V	550	2.3	vacuum	continuous cycling	17
½Cr-Mo-V	550	2.3	air	continuous cycling, $\epsilon_p < 0.001$	17
½Cr-Mo-V, fine-grained bainitic	550	2.3	air	with dwell	17
½Cr-Mo-V	550	1.5	air	with dwell	17
½Cr-Mo-V	550	1.5	vacuum	with dwell	17
½Cr-Mo-V	550	1.5	steam	with dwell	20
½Cr-Mo-V, coarse-grained bainitic	550	2.9	air	with dwell	53
20Cr-25Ni-Nb	750	1.3	vacuum	continuous cycling	50
Type 316 Steel	625	1.6	vacuum	continuous or with dwell	40
Type 316 Steel	600	1.5	air	continuous cycling	51
Type 321 Steel	700	1.3	air	continuous cycling	41
Type 321 Steel	490	2.2	air	circumferential notch	45
MAR M509	900	1.8	air	continuous cycling	52
9Cr-1Mo	550	1.9	vacuum	with dwell	40

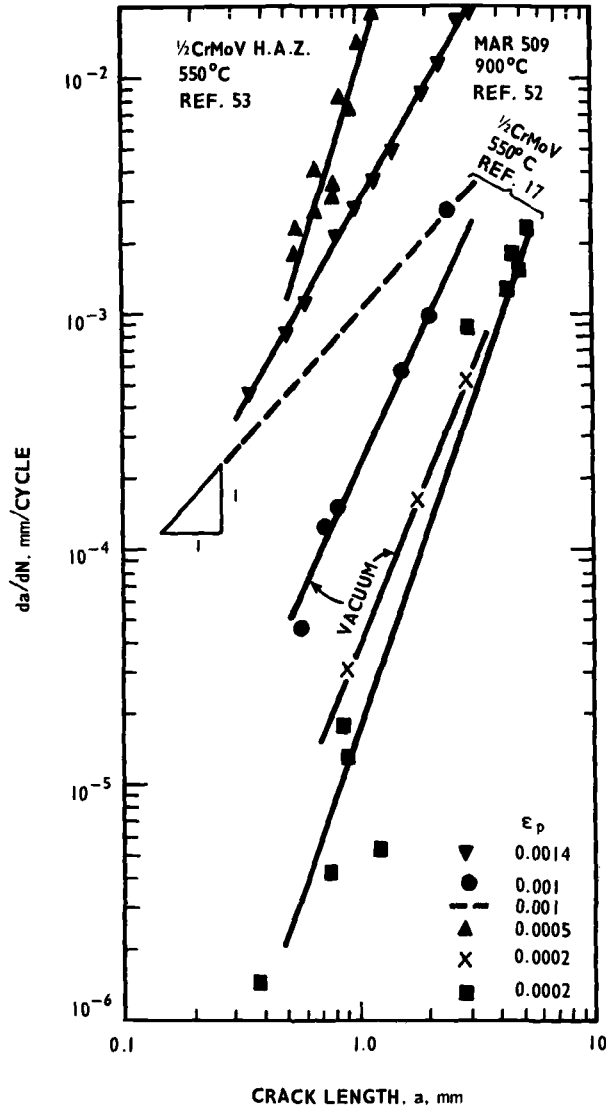


FIG. 5—Span of crack growth rates. Compare slopes in Fig. 2.

crease in crack-tip strain concentration. The resulting expression for crack growth was

$$\frac{da}{dN} = d \left[\frac{\epsilon_p}{K'} \left(\frac{4a^{1-n}}{G} \right)^{1/\gamma+\beta} \right]^{1/\alpha} \quad (12)$$

where d , K' , G , and γ are constants. Equation 12 can thus predict $Q > 1$ from the identity $Q = (1 - n)/(\gamma + \beta)\alpha$ via changes in the experimental

slope α [54]. Figure 2 shows some calculated growth rates according to Eq 12 [46] compared with experimental values [38].

The nonlinear growth relation (Eq 11):

(1) is not caused by compliance changes. Figure 5 shows that the effect occurs well before a/W values of 0.1 to 0.2. Typical values of W are 5 to 16 mm.

(2) does not arise from different modes of crack detection, namely potential drop against visual detection, as suggested by Yamaguchi and Kanazawa [41]. For rectangular specimens there is a one-to-one correspondence in depth.

(3) is not a geometry effect. The growth rate of a semielliptical crack in a cylindrical specimen is generally half that of a straight-fronted crack of equivalent depth [29, 40], provided the crack depth is less than the specimen radius, when they become identical.

Integrated Endurances from Crack Growth Data

In order to develop an integrated approach to life assessment, it is necessary to demonstrate that HSF crack growth rates are consistent with smooth specimen endurances. It has been shown [38, 39, 55] that the integrated Eq 9, namely

$$\ln \left(\frac{a_t}{a_0} \right) = B(N_t - N_0) \quad (13)$$

gives good predictions of smooth specimen total endurance. Initial crack length a_0 at cycles N_0 is taken as $\sim 10 \mu\text{m}$, and N_0 is neglected in comparison with N_t , the cycles to failure. Figure 6 shows Eq 13 plotted for Type 316 steel at 625°C [38]. Below a plastic strain of 0.0016 there is a considerable short fall in the integrated and actual endurance, and this difference may be attributed either to a finite number of cycles of initiation in smooth specimens or to a much lower growth rate in the early stages [30]. Other data for exceptionally smooth specimens ($0.0075 \mu\text{m}$ surface roughness) of Type 304 steel at 593°C have shown [36, 47], by striation measurements, that most of the life was spent in crack initiation. However, when Stage II cracking occupies most of the life, as clearly is the case with shallow starter notches, satisfactory estimates of total endurances can be made, including integration of the nonlinear equation 11 [41, 50, 51].

Wareing and Vaughan [29] counted striations in conjunction with direct measurement and found that striation spacing S increased linearly with crack depth:

$$S = Aa \quad (14)$$

The constant A depends on plastic strain range and was thus identified with B ($=S/a$) of Eq 9. The results are shown in Fig. 7. A similar integration (above $\epsilon_p = 0.0016$) for Type 316 steel at 625°C gave endurances in close agreement with experiment (Fig. 6).

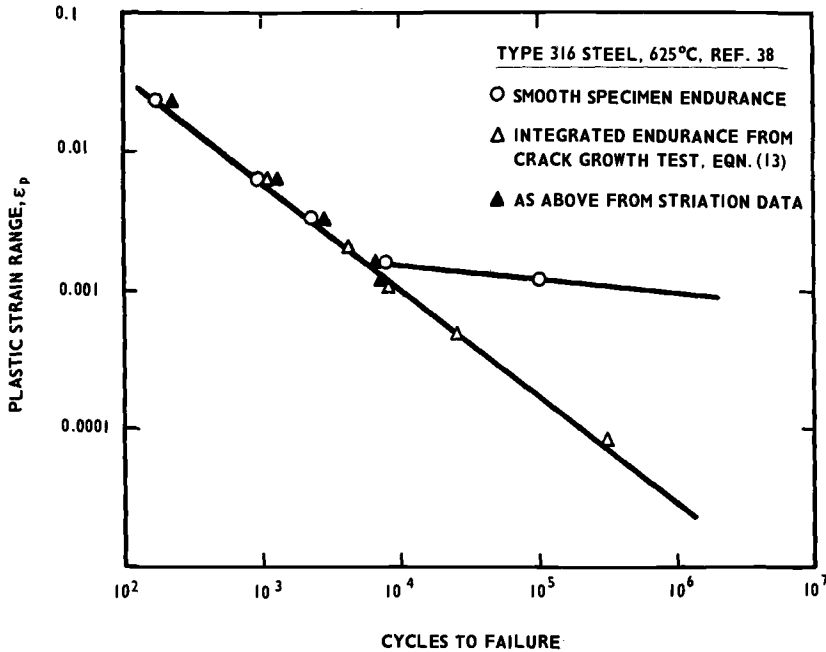


FIG. 6—Total endurance and integrated crack growth endurance compared.

The coincidence of striation spacing and crack growth increment was not always observed, however. Below $\epsilon_p = 0.0016$, several cycles were required to produce one spacing [29], while at the largest growth rates ($10 \mu\text{m}/\text{cycle}$; that is, $S = 10 \mu\text{m}$) striations of $0.5 \mu\text{m}$ separation were often seen within the larger ones. At 400°C on Type 316 steel, Wareing and Vaughan [30] found that striation spacing exceeded da/dN at *all* plastic strain ranges in the range of 0.001 to 0.006. Arguments as to whether striations represent CTOD or incremental growth at high temperature and the precise contribution of oxidation appear undecided [16]. Figure 7 shows that Eq 4 underestimates observed growth rates and that striation spacings are better given by the CTOD relation (Eq 8). To obtain the best agreement, the value of T in the intense plastic zone (Eqs 4 and 8) is taken from known relaxation data [29].

Transition to LEFM Regime

It has been shown that either an integration of experimental and theoretical expressions for da/dN or summing striations can give a satisfactory account of small, smooth specimen endurance. However, in many instances (for example, a peak thermal transient in relatively thin components) plastic strain rapidly falls to zero beneath the surface, whereas cracks can penetrate to the midsection [21]. Clearly Eq 10 cannot then be used. We require a transitional approach to the LEFM region (where indeed striations have

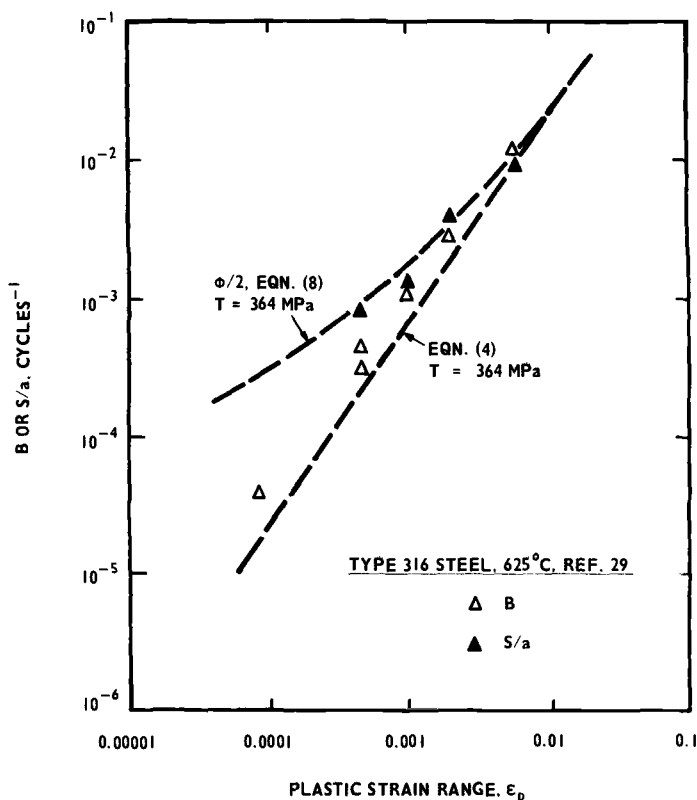


FIG. 7—Comparison of observed crack growth rates, striation spacings, and theoretical predictions.

been observed at high temperature [40,56] so that behavior across the whole component can be described.

J-Integral Approach

The J-integral is more usually applied to deep cracks and is a measure of the potential energy available for crack extension. By considering the area of the hysteresis loop, Dowling [57] has derived an approximate expression for J in the HSF regime by applying for a thumbnail crack in a push-pull specimen:

$$J = \left(3.2 \frac{\sigma^2}{2E} + 5.0 \frac{\sigma \epsilon_p}{1 + \beta} \right) a \quad (15)$$

Crack growth rates were measured at room temperature in 7.6-mm-diameter specimens of A533B steel and, using the above equation, were compared with growth rates obtained in elastic-plastic tests on compact tension specimens ($W = 25$ and 50 mm) and, in the linear elastic range, on very large ($W = 200$ mm) compact tension specimens of the same steel for which J is

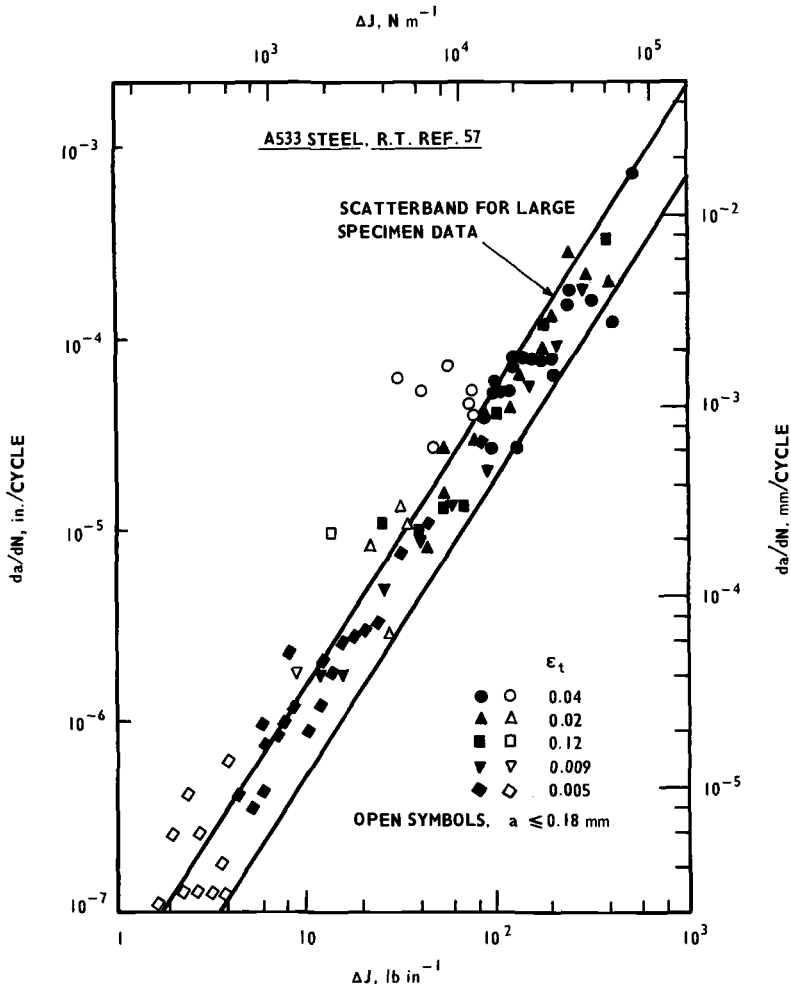


FIG. 8—Comparison of short crack data with long crack results.

well characterized [58,59]. The results are given in Fig. 8. The correlation (for a wide range of sizes from near-surface to deep cracks) is satisfactory over several orders of magnitude of growth rate. A very similar expression, derived from Eq 8, is given [16] by

$$J = \frac{\pi \sigma^2 a}{E} + \frac{2\pi \sigma \epsilon_p a}{1 + \beta} \quad (16)$$

which can be expressed alternatively as

$$\Delta J = \Delta K^2 \left[\frac{1}{E} + \frac{2\epsilon_p}{\sigma(1 + \beta)} \right]$$

in terms of the cyclic range. A similar comparison to that of Fig. 8 for Type 304 steel at room temperature shows [16] that HSF data somewhat exceed the LEFM data, with high plastic strains emerging at the top of the scatter-band; nevertheless, the method is acceptable for engineering assessment.

Strain-Based Intensity Factor

Following Boettner et al. [60] crack growth rates at high temperature have been expressed in terms of a strain intensity ($\Delta K_\epsilon = \Delta K/E$). Thermo-mechanical and thermal shock tests have been conducted on conventionally cast cobalt and nickel based superalloys and on a directionally solidified nickel-based alloy [61-64]. The results can be expressed as

$$\frac{da}{dN} = C_1 \Delta K_\epsilon^m \quad (17)$$

by analogy with Eq 1. The index m was typically ~ 3.4 for a nickel-based alloy cycled from 980°C and ~ 6 for the cobalt-based alloy cycled from 900°C [61]. The temperature variation of da/dN with ΔK disappears when plotted in terms of $\Delta K/E$ [14].

Solomon [65] proposed that when plastic strain occurs, the strain intensity is $\epsilon_t \sqrt{\pi a}$ where ϵ_t is the total strain range given by

$$\epsilon_t = \epsilon_p + \epsilon_e \quad (18)$$

where ϵ_e is the elastic strain range. Haigh and Skelton [66] showed that Solomon's [65] room-temperature data on 1018 steel could be better fitted by the relation

$$\Delta K_\epsilon = (\epsilon_p + q\epsilon_e) \sqrt{\pi a} \quad (19)$$

The term $(\epsilon_p + q\epsilon_e)$ describes the strain range for which the crack is open as shown in Fig. 9 and evidence for $q = 1/2$ was given [66]. The term $(\epsilon_p + 1/2\epsilon_e)$ is called the *equivalent elastic strain* and upon multiplication by E one has an *equivalent stress* σ_{eq} (Fig. 9), giving rise to $\sigma_{eq} \sqrt{\pi a}$, the *equivalent stress intensity*.

Equation 19 is able to correlate growth rates in HSF [17] with those under LEFM conditions [67]. Some results for $1/2\text{Cr-Mo-V}$ steel at 550°C under vacuum are reproduced in Fig. 10. Generally the spread of results in the HSF regime is contained within an upper limit set by tension-compression testing in LEFM ($R = -1$, where $R = \text{minimum stress}/\text{maximum stress}$) and a lower limit for the tension-only mode ($R = 0$). A similar comparison is made in Fig. 11 for some recent tests at Central Electricity Research Laboratories (CERL) on Type 316 steel at 625°C in air and an upper-bound value of Eq 1 is quoted.

There are common features between the J relations (Eqs 15 and 16, and Eq 19) which can be expressed, respectively, as

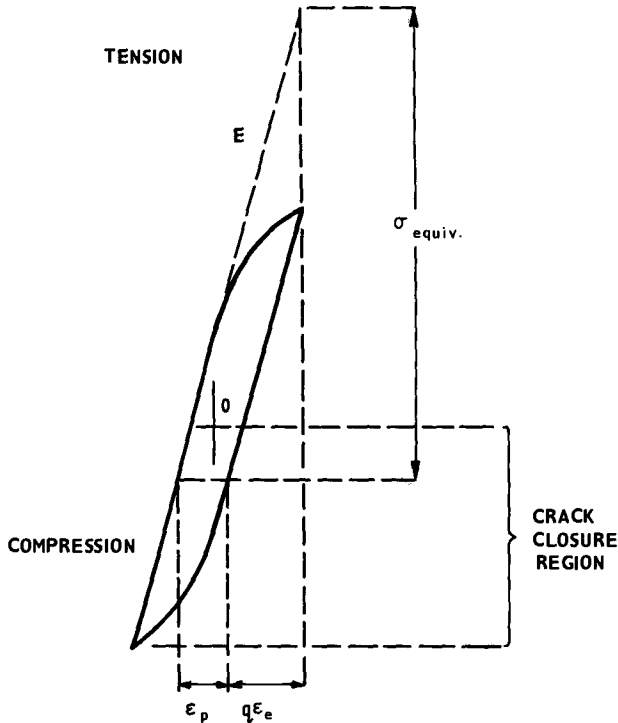


FIG. 9—Definition of equivalent stress and strain.

$$\Delta K = (\Delta J E^*)^{1/2} \quad (20)$$

and

$$\Delta K = \sigma_{eq} (\pi a)^{1/2} \quad (21)$$

where E^* is an effective modulus. Equivalent stress intensities for Type 316 steel at 625°C under vacuum [40] (Eq 21) are compared in Fig. 12 with ΔK calculated according to Eq 20. In the latter relation the stress *range* $\Delta\sigma$ has been used as an operational definition of cyclic J [59], but it can be seen (Fig. 12) that the method gives more scatter than the strain-based intensity relation. However, both methods may be used for cracks of *any* depth, thus overcoming the difficulties of Eq 10 discussed previously.

Effect of Frequency and Dwell

It is emphasized that all work mentioned hitherto concerns transgranular cracking. It is shown in this and the next section that the onset of intergranular cracking depends on strain rate, temperature, microstructural effects (including damage accumulated during the test), and environment. Indeed,

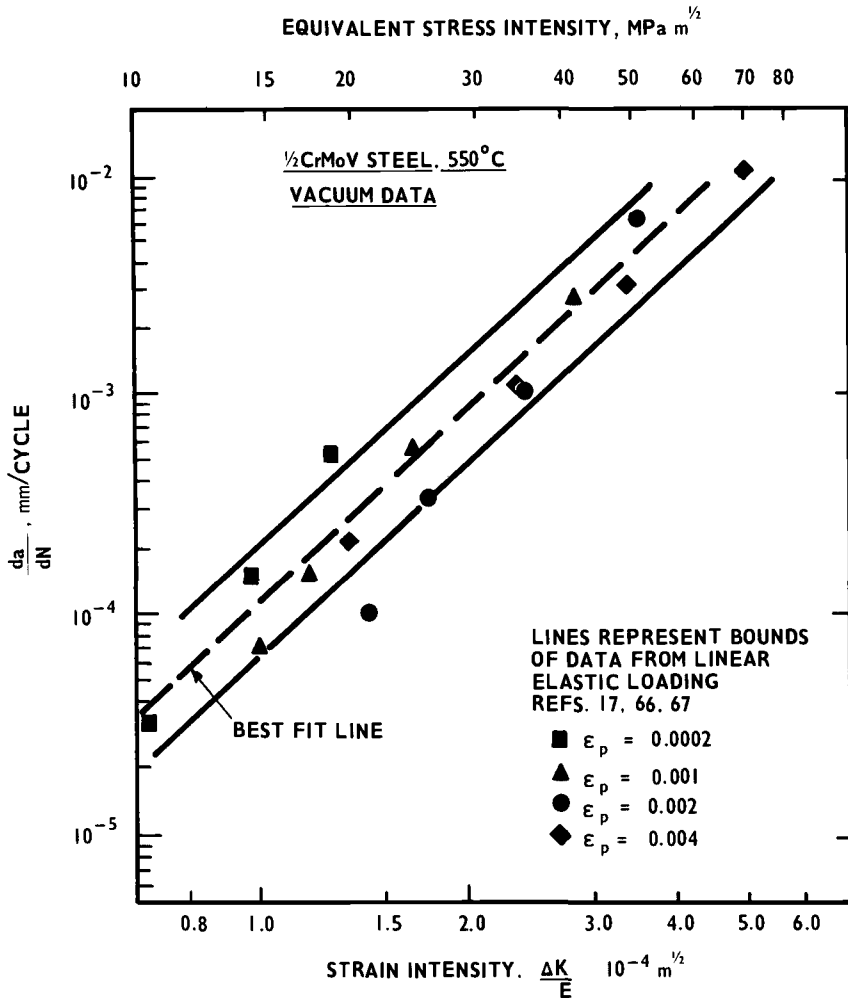


FIG. 10—Comparison of HSF and LEFM crack growth data. Continuous cycling at 10^{-2} to 10^{-3} Hz.

three-year reverse bend tests on ferritic steel incorporating a 16-h dwell have shown final failure to be induced by internal creep damage rather than by the growth of a surface crack [7]. One of the severest tests for the crack growth models is in accounting for the effect of creep damage induced by low strain rates or tensile dwells. After a summary of experimental trends, Eqs 1 to 21 are re-examined for the case of dwell.

Experimental Observations in HSF and LEFM Growth

It is now well established in the LEFM regime at high temperature that as the frequency of testing is reduced below 1 Hz the cyclic growth rate da/dN

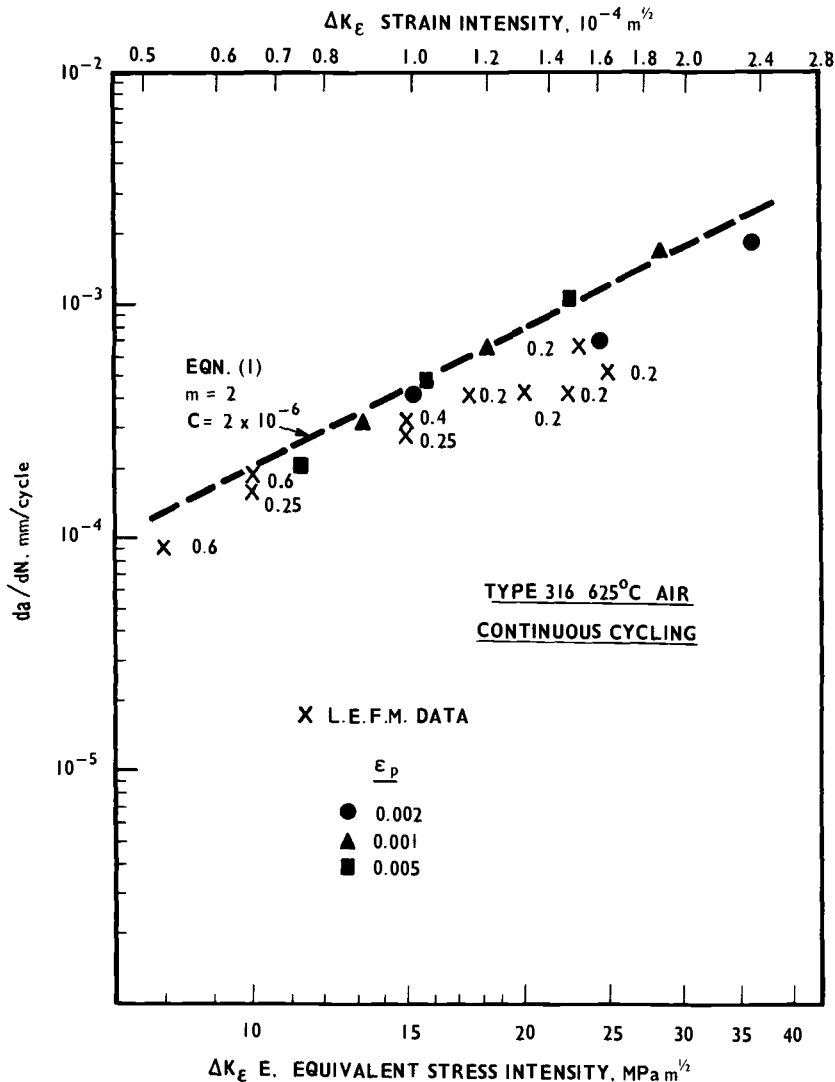


FIG. 11—As for Fig. 10. Numbers denote R-value.

increases. This has been shown, for example, in Type 304 steel in air at 538°C [68] and in low-alloy ferritic steels at 550°C [69]. Intergranular damage is apparent at frequencies below 10^{-3} Hz [13, 70], and over the frequency range of 1 to 10^{-3} Hz an order of magnitude increase in da/dN is typical [13]. When tension dwells are introduced, two orders of magnitude increase are often observed; some results are summarized in Fig. 13 [71–75].

A similar but not so pronounced effect is also found in HSF, reflecting the well-known reduction of endurance with increasing dwell time. Yamaguchi

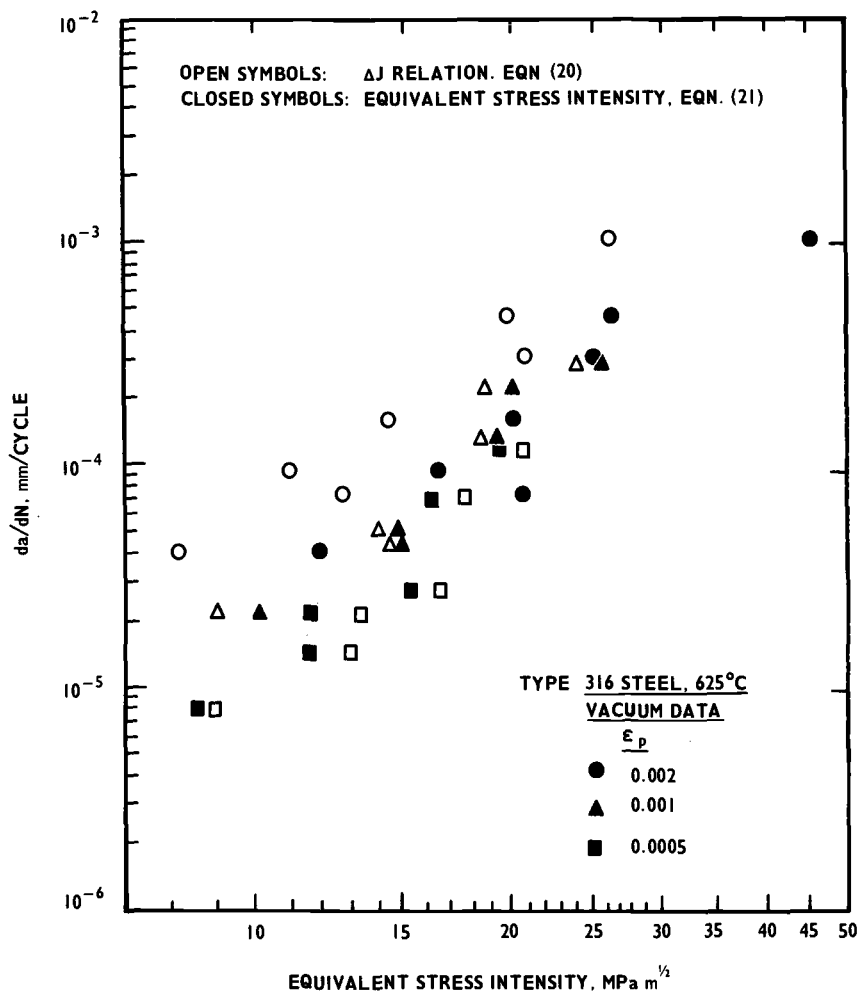
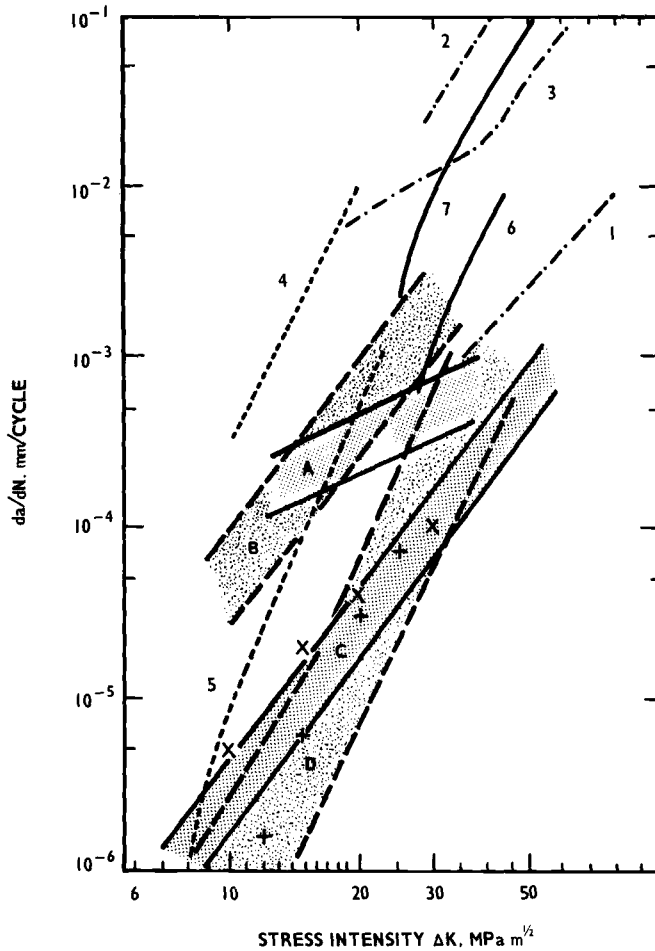


FIG. 12—Equivalent stress intensity and ΔJ methods compared at high temperature.

and Kanazawa [41] found that upon lowering the strain rate from $6.7 \times 10^{-3} s^{-1}$ to $6.7 \times 10^{-5} s^{-1}$ in Type 321 steel at $700^\circ C$ there was a factor 8 increase in da/dN . Solomon and Coffins' [35,44] data on A286 at $593^\circ C$ are replotted in Fig. 14. Growth rates in both air and vacuum increased as the testing frequency was reduced, and the effect was greater in air than in vacuum. This is discussed further in the section on Effect of Temperature, Environment, and Microstructure.

Other work does not show such large strain rate variations: that of Min and Raj [76] shows none at all for crack growth in aged Type 316 steel at $625^\circ C$ in the range of 7×10^{-4} to $8 \times 10^{-6} s^{-1}$ and the same applies to 20Cr-



593°C

1. 316, C.W., AIR VACUUM REF. 14
2. AS ABOVE, 1 MIN. DWELL
3. AS ABOVE, AIR REF. 12
4. FIG. 18 DATA, $R = -1$
5. AS ABOVE, 10^{-2} Hz, REF. 40
6. 1CrMoV, 565°C. VACUUM. 1 MIN. DWELL. REF. 71
7. AS ABOVE, 30 MIN. DWELL
- x 316, 649°C, ARGON, REF. 72
- + 304, 538°C, SODIUM, REF. 73

SCATTER BAND

- A. 1CrMoV, AIR 550°C, REF. 70
- B. 316, AIR, 600°C REF. 74
- C. 1CrMoV, VACUUM, 550°C, REF. 70
- D. 316, VACUUM, HELIUM, SODIUM
~ 600°C, REF. 74, 75

FIG. 13—Dwell and environmental effects in LEFM regime.

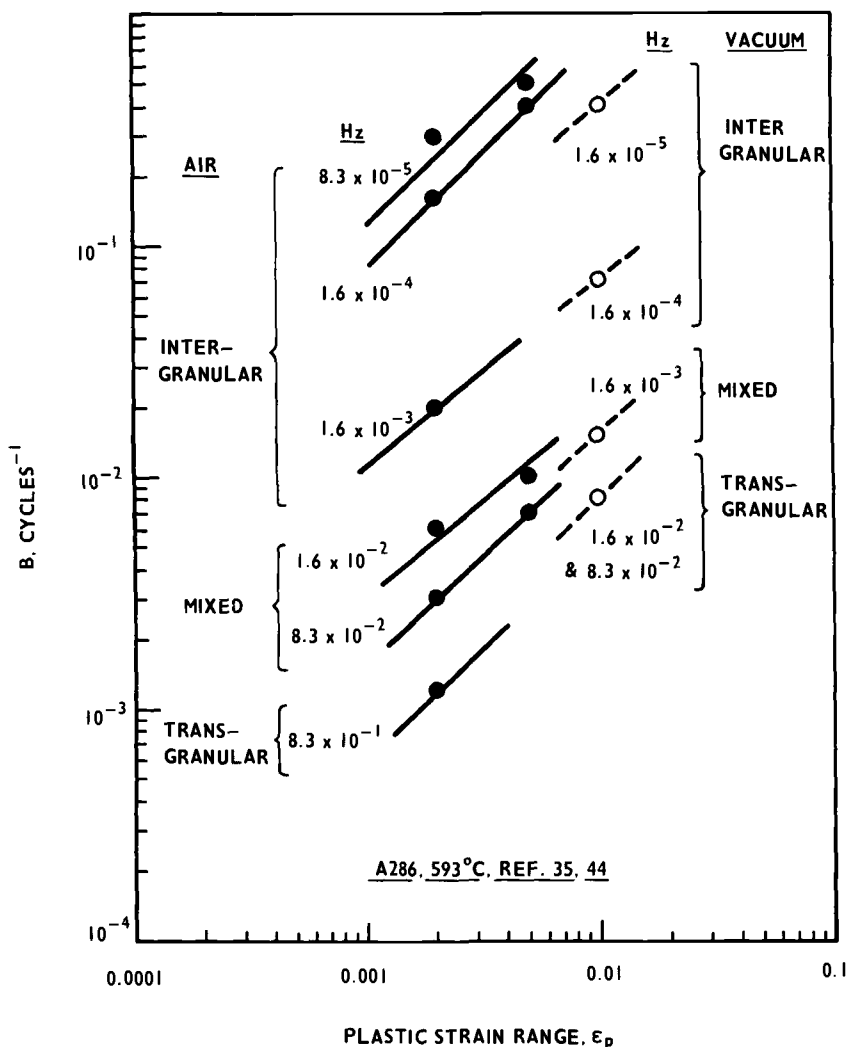


FIG. 14—Frequency effect and cracking mode in high-temperature alloy.

25Ni-Nb steel at 750°C in several environments [50]. In ferritic steel $\frac{1}{2}$ -h dwells cause an increase in crack growth rate compared with continuous cycling, but the effect is not large [17] (Figs. 4 and 22). Other crack growth results on this steel [17] show no increase in da/dN for a 7-h tensile dwell over $\frac{1}{2}$ -h dwell data. Also, despite heavy cavitation damage introduced during prior creep-fatigue on a plain specimen, subsequent propagation with dwell from a small starter notch (Fig. 15) was only ~ 2 to 3 times faster than that obtained in virgin material [17].

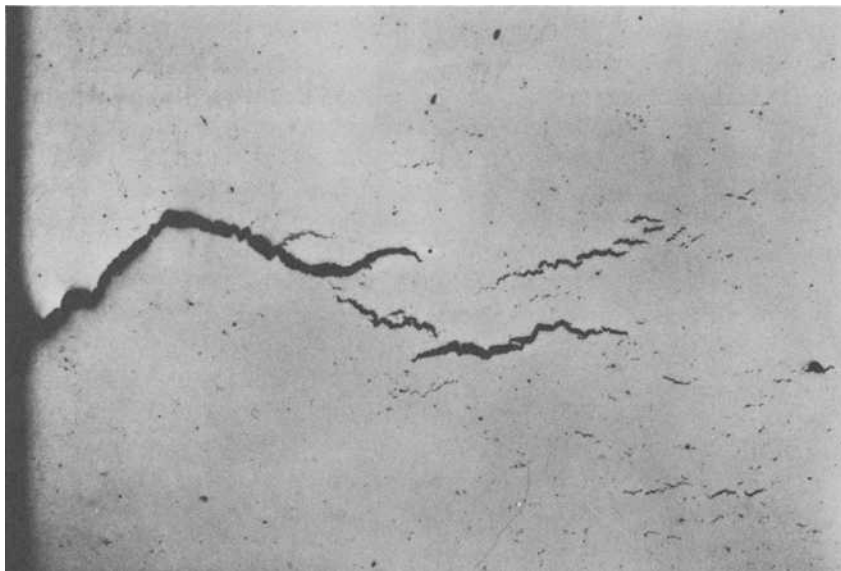


FIG. 15—HSF crack growth with dwell revealing prior creep-fatigue damage. $\frac{1}{2}$ Cr-Mo-V steel at 550°C , unetched, $\times 12$.

Integrated Endurances

It has been shown previously that the dwell effect is not so pronounced in HSF as in LEFM. Nevertheless, when reversed strain rates are $<10^{-4} \text{ s}^{-1}$ or when tensile dwells are introduced, difficulties are encountered in calculating integrated endurances using Eq 9 or 11. Even taking a_0 at the fairly high value of 0.02 to 0.05 mm the calculated cycles always exceed plain specimen endurances [17,50]. Below a depth of, say, 0.2 mm, crack growth rates are thus greater than those given by Eq 9 or 11 [17]. Reuchet and Rémy [52] found that for MAR M509 alloy at 900°C integration of Eq 11 with $Q = 1.8$ and $a_0 = 0.06 \text{ mm}$ gave a cyclic life of 3900 cycles compared with a plain specimen endurance of 1700 cycles. They suggested that a linear growth law applies for undamaged material, but that as cracking proceeds into cumulatively cavitated regions the relation becomes

$$\frac{da}{dN} = Ba (1 + qf) \quad (22)$$

where q is a constant and f is the volume fraction of cavities which for alloy MAR M509 at 900°C developed as $(\text{time})^{4/3}$, that is, $N^{4/3}$ [52]. Thus the value of B in Eq 9 effectively increases with time. Upon integrating Eq 22 instead, a propagation life of only 1350 cycles was predicted.

These authors' introduction of a damage parameter can be extended generally. Equation 22 becomes

$$\frac{da}{dN} = Ba (1 + gN^p) \quad (23)$$

where g and p are constants. Upon integration and neglecting N_0 we find

$$\ln \left(\frac{a}{a_0} \right) = B \left(N + \frac{gN^{p+1}}{p+1} \right) \quad (24)$$

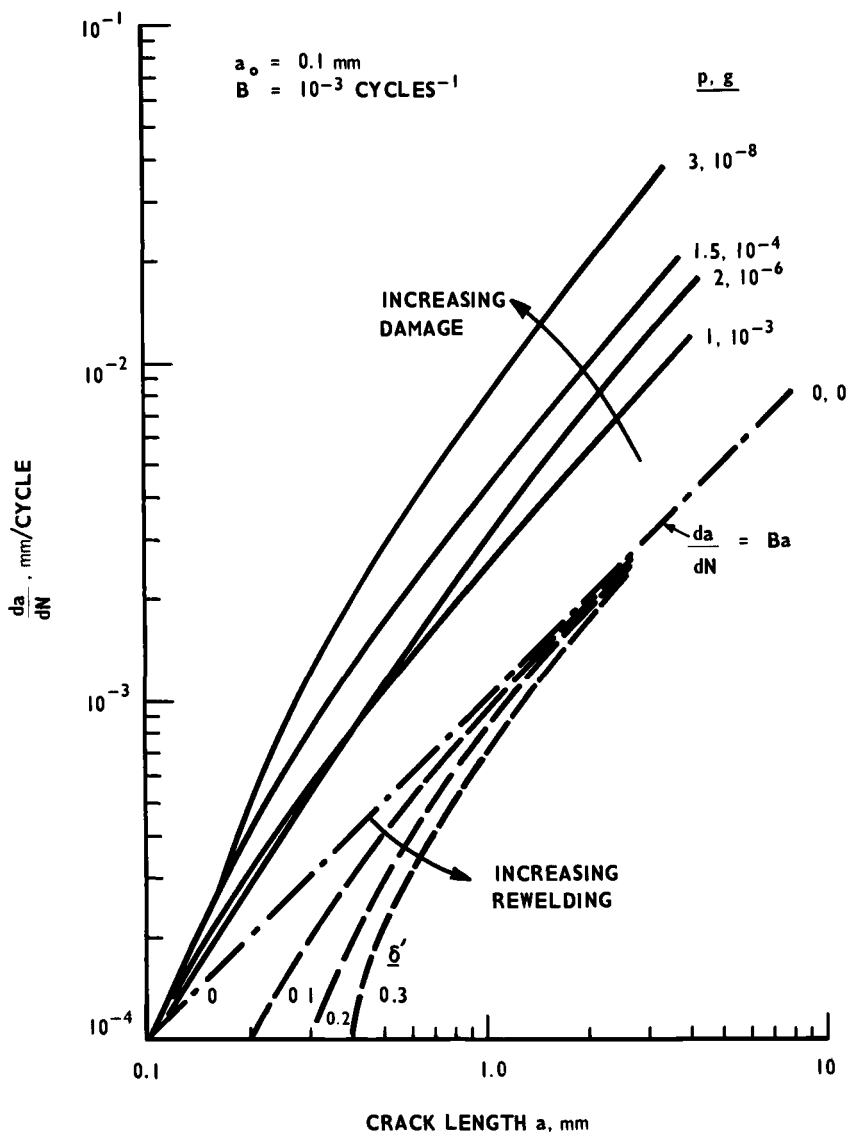


FIG. 16—Modifications to exponential growth law.

Using these equations, the variation of da/dN with a is shown in Fig. 16 for linear time-dependent and other forms of damage. This approach can explain apparent Q values > 1 (Fig. 5), and moreover is physically based in that for many materials, the damage can be detected microscopically [52,77].

A "lower bound" approach [25,26,31] supposes that once cavitation occurs extensively throughout the material the intense deformation zone D at the crack tip extends to the back face of the specimen or component, so that $D = \sqrt{2} (W - a)$ where W is the component width. The growth rate then becomes

$$\frac{da}{dN} = \epsilon_p \frac{D}{\sqrt{2}} = \epsilon_p (W - a) \quad (25)$$

which integrates to

$$\epsilon_p N_f = \ln \left(\frac{1}{1 - a_f/W} \right) \quad (26)$$

for $a_0 \ll a_f < W$. Equation 26 gives a slope of -1 on a Coffin plot; although it provides a failure line that is approached as tensile dwell times increase in several materials [25-27,31], it is not clear why the increase in growth rate with depth a (Eq 4) should disappear when the flow band meets the opposite face. Equation 25 predicts a deceleration which is not observed in push-pull tests.

The striation method is of limited help in tests at low frequency or with tensile dwells, because with intergranular cracking, little trace of cyclic crack progress is left [41,78,79]. (In Type 304 steel at 593°C, however, striations were present for compression, or equal tension and compression dwells [79].) This breakdown in continuum advance suggests an unstable state (that is, when the CTOD is on the order of the particle or cavity spacing ahead of the crack). This condition is given [27,28,80] by

$$\phi/2 = \lambda - p \quad (27)$$

where λ is the particle spacing and p is the particle diameter. It was shown that the corresponding reduction in flow stress $T(1 - [P/\lambda]^2)$ leads only to a second-order increase in ϕ [27]. When Eq 27 is used with Eq 8 a critical crack depth a_f is predicted; substituting this in the integrated form of Eq 4 enables an endurance for the onset of unstable growth to be calculated.

High-temperature experiments were conducted on two casts of Type 316 steel with different carbide spacings [28]. Even with dwell times, striations were observed up to 0.05 or 0.3 mm crack depth, depending on cast. Thereafter only ridge markings some 20 μm apart were observed. Figure 17 indicates the general lowering of predicted endurance with decreasing values of $\lambda - p$ in line with experimental trends as the dwell time was increased. In

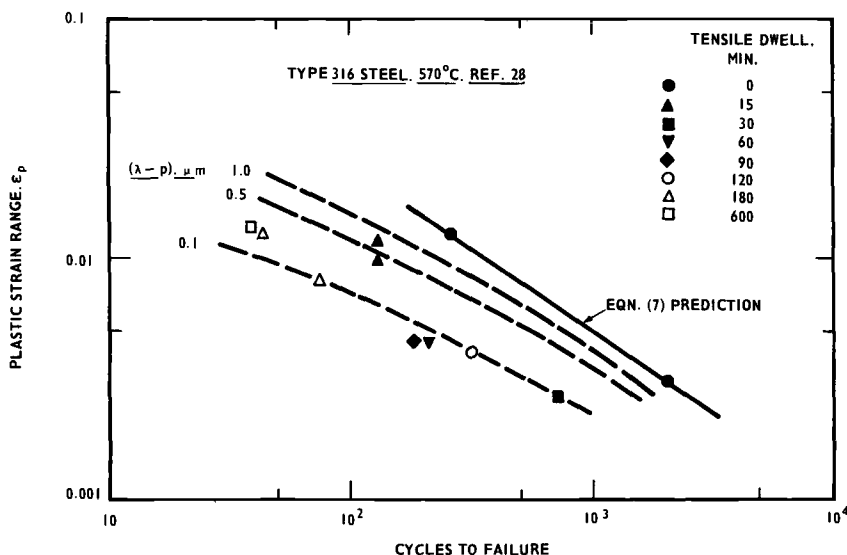


FIG. 17—Prediction of unstable growth (Eqs 7, 8, and 27) and effect of increasing dwell.

one cast the cavity spacing coincided with the particle spacing ($\sim 0.1 \mu\text{m}$), but in the second cast was an order of magnitude greater [28].

This model can account for a cast-to-cast variation in creep-fatigue endurance. However, the lower bound a_f is small, typically $\sim 0.1 \text{ mm}$ for $\epsilon_p = 0.01$ (compare $0.75W$ for continuous cycling), and, since the second-stage crack growth through cavitated material is rapid, really is a criterion for initiation in an engineering-sized component.

Equivalent Stress Intensity

The solid points *A* in Fig. 18 denote the equivalent stress intensity (Eqs 19 and 21) plotted against da/dN for 12.7-mm-diameter HSF specimens of solution-treated Type 316 steel at 625°C for cycles containing a ½-h tension dwell in vacuum [40]. The solid points *B* represent crack growth rates versus ΔK for single-edge-notched specimens in the LEFM range tested at $R = -1$ under the same conditions [53]. Why is there a remarkable lack of correlation?

During stress relaxation in the HSF dwell period, an additional bulk plastic strain ϵ_{pr} is generated. The effect upon ϕ and hence ΔK is not obvious from Eq 8. If relaxation is regarded as an unloading phase, ϵ_{pr} should be subtracted from ϵ_p in Eq 19. The effect of this is to displace the data along the ΔK axis, shown by the hollow points in Fig. 18. A further correction is to reduce the LEFM data by a factor 2 along the da/dN axis to allow for the difference in curved and straight crack fronts [29,40]. Even so, the data do not overlap.

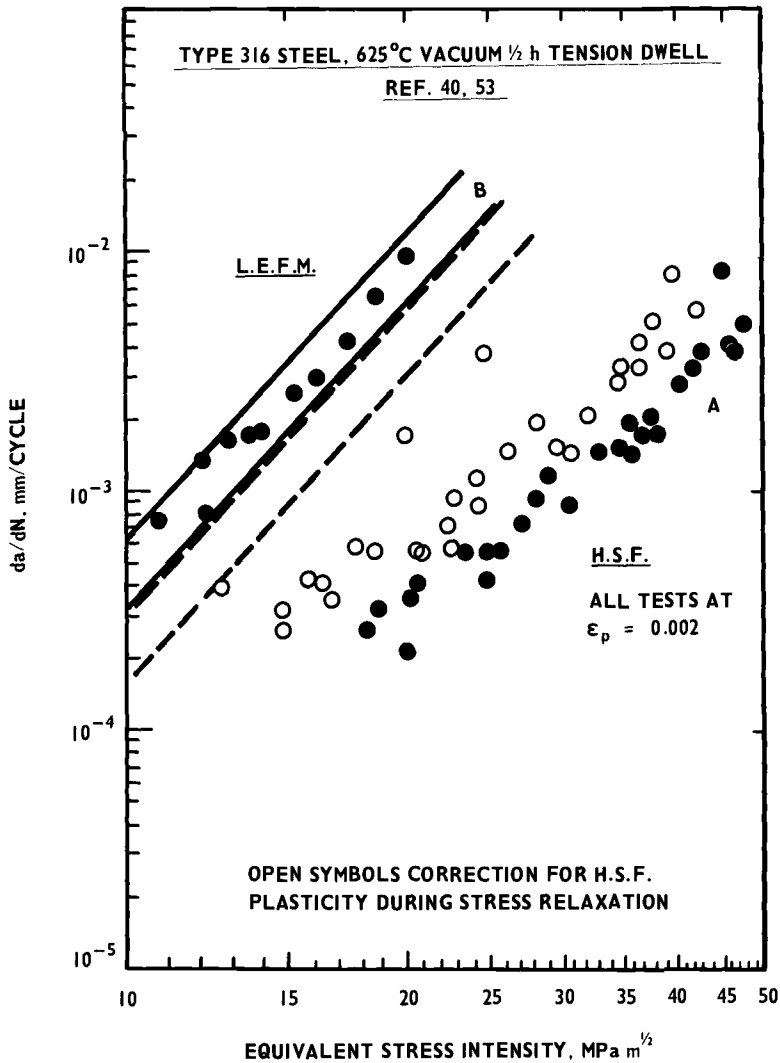


FIG. 18—HSF and LEFM data compared for case of dwell.

The very large increases in growth rate produced by tension dwells in LEFM (Fig. 13) may be owing to differences in creep damage in a highly constrained plastic zone (LEFM) compared with the HSF case. The correction for plastic strain during relaxation is still required for those materials (for example, 9Cr-1Mo) that show no creep-fatigue interaction either in crack growth [40] or in total endurances [81]. As an interim measure, however, the equivalent stress-intensity method provides lower bound crack growth data. HSF results are given in Fig. 19 for tests at 550°C with $\frac{1}{2}$ -h tension dwell in air on $\frac{1}{2}$ Cr-Mo-V steel in several heat treatments. Tests with $\frac{1}{2}$ -h

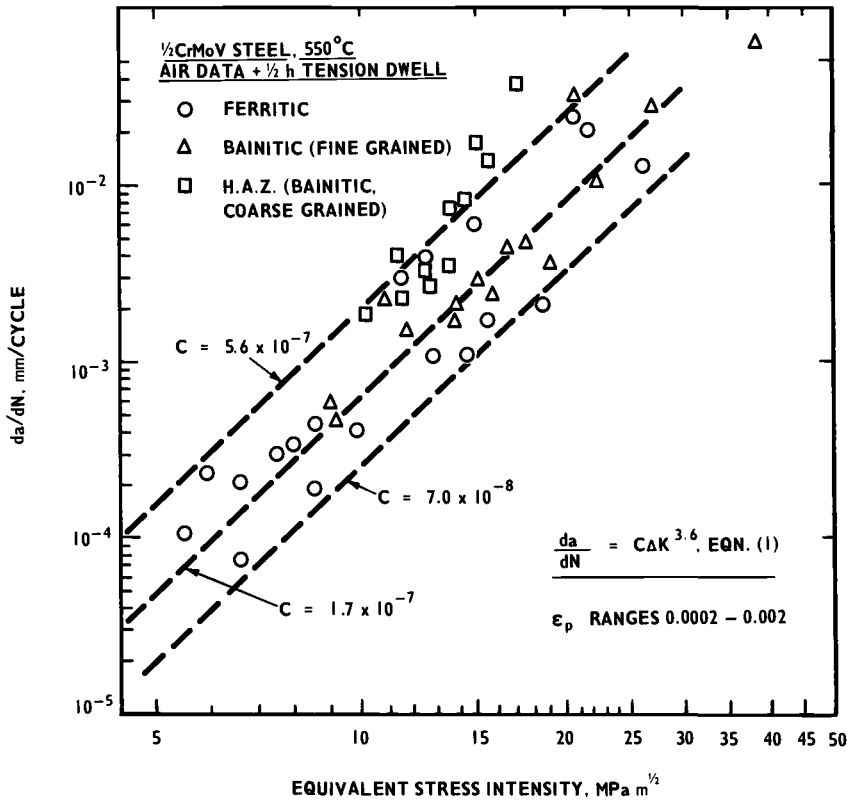


FIG. 19—Equivalent stress intensity data for a ferritic steel; HSF dwell tests.

dwell in the LEFM range are now in progress at CERL to establish an upper bound for this material.

Effect of Temperature, Environment, and Microstructure

It is convenient to consider the interrelated contributions to crack growth of microstructural changes and temperature/atmosphere separately, pointing out the alterations which can be made to the basic growth model to accommodate these effects.

Temperature

The predictions of Eq 6 are generally upheld experimentally. With increasing temperature it is found that T and β (Eq 6) both decrease; thus the integrated form (Eq 7) predicts a gradual reduction in endurance in accord with experiment [26].

Experiments conducted in air at frequencies $>10^{-2}$ Hz in the LEFM regime away from the threshold have generally shown a fourfold increase in propagation rate between room temperature and 500 to 600°C for low-alloy ferritic steels [69] and austenitic steels [14,82]. An order of magnitude difference occurs between room temperature and 850°C for Udimet 700 [15].

Very similar variations arise in the HSF regime. Figure 20 indicates the variation of the constant B in Eq 9 with temperature for several alloys [45,83,84]. The 0.16C steel gave a maximum propagation rate at the *intermediate* temperature of 300°C, which is surprising in view of the well-known increase in fatigue strength with strain-aging at this temperature [85].

Most temperature *cycling* experiments have been carried out on superalloys. Heating and quenching a cobalt-base alloy X-40 between 1075°C and room temperature produced growth rates about twice those observed for a maximum temperature of 975°C [86]. Figure 21 indicates the variation in uniform growth rate over the range of 2.5 to 7.5 mm observed in tapered disk

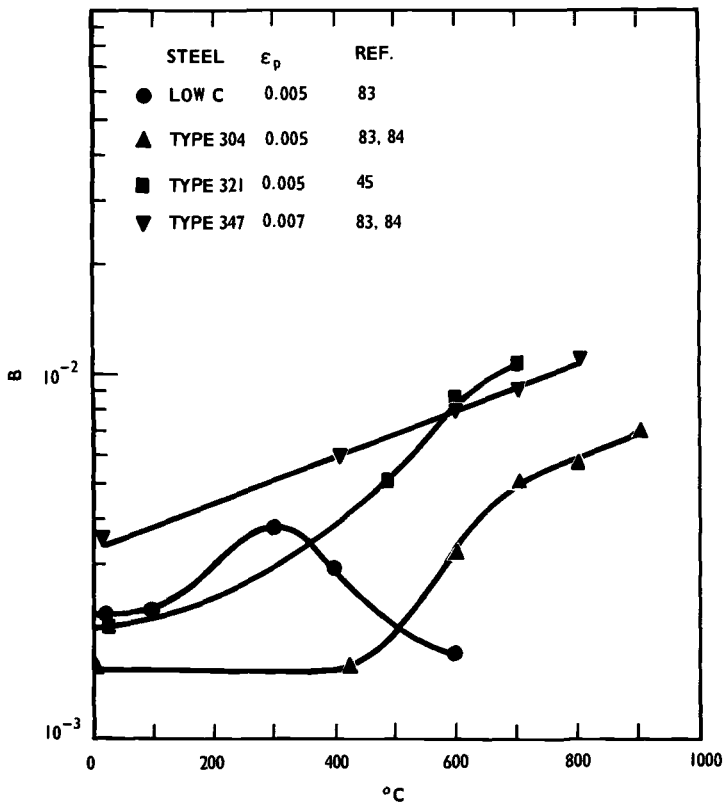


FIG. 20—Variation of crack growth rate with temperature given by B (Eq 9).

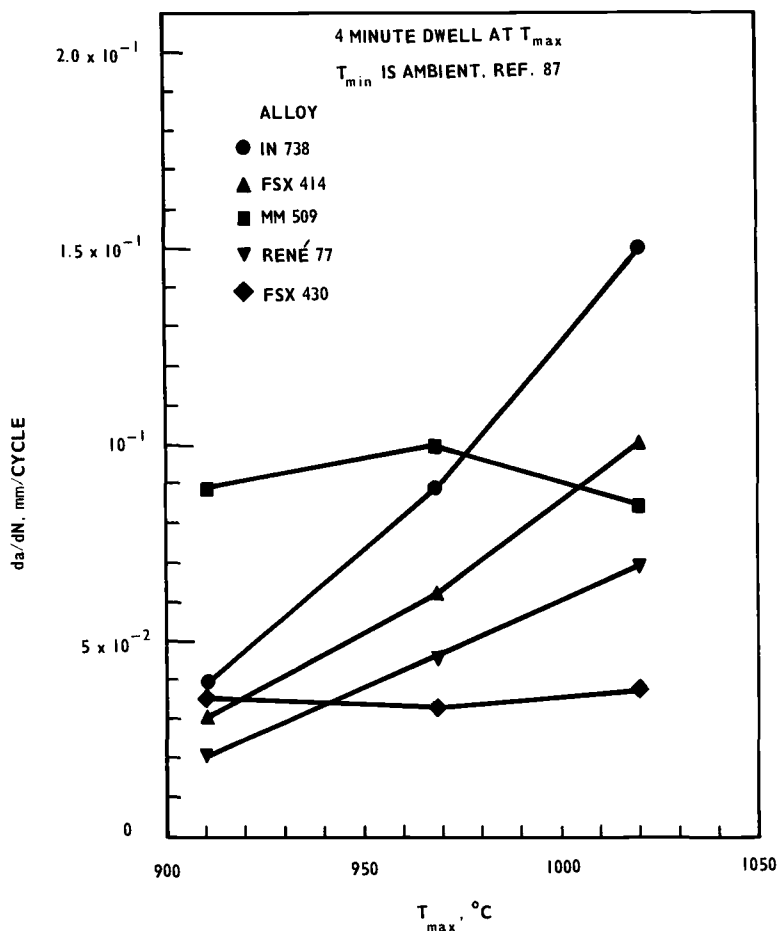


FIG. 21—Variation of steady crack growth (over 2.5 to 7.5 mm) with maximum temperature in thermal shock of several alloys.

experiments on several alloys [87] and its increase with increase in maximum temperature. These rates are rather higher than those discussed heretofore. An increase in dwell time from 4 to 16 min caused further crossovers in propagation rate [87]. In similar materials it has been shown that changes in growth rate may sometimes reflect a transition in cracking mode [61].

Amongst the ferritic alloys, during thermomechanical cycling of $\frac{1}{2}$ Cr-Mo-V steel in vacuum between 250 and 550°C ($\epsilon_p = 0.001$), crack growth rates were one third those for continuous cycling isothermally at 550°C at the same plastic strain [20]. In air tests, Koizumi and Okazaki [88] found very little difference in growth rates for 12Cr-Mo-V-W steel thermomechanically cycled between 300 to 550°C and 350 to 600°C at several strain ranges. The

latter data for example were unified as Eq 17, with $C_1 = 1.79 \times 10^{-3}$ and $m = 2.23$ when the growth rate was in mm cycle^{-1} . In contrast to Eq 19, the total strain ϵ_t was used to describe ΔK_e .

The temperature effect on crack growth clearly contains a contribution from oxidation, although it persists in vacuum. A threefold increase in propagation rate has been observed for Type 316 steel over the range of 0 to 600°C under LEFM conditions and is due to the variation of E with temperature [14].

Environment

One advantage of HSF crack growth rate experiments is that changes in atmosphere made during the test are immediately followed by changes in propagation rate, which eliminates specimen-to-specimen scatter. Thus in 20Cr-25Ni-Nb steel at 750°C, da/dN increased in the order, vacuum, air and CO_2 for all crack lengths [50]. Since smooth specimen total endurance in CO_2 are enhanced [89], initiation and very early growth must be inhibited by CO_2 [50]. Similarly (and rather surprisingly) in tests on Type 316 steel at 625°C and 6×10^{-4} Hz, growth rates in pure argon exceeded those in air [40]. At higher frequencies growth rates in air were about four times those in vacuum [40] (see Fig. 22 and compare also Figs. 11 and 12), and this factor also applies to A286 tested at 600°C [35,44] (Fig. 14).

At high plastic strains, oxidation contributes directly to cyclic growth either by strain-enhanced oxidation and subsequent metal loss at the crack tip [90] or by diffusion of oxygen ahead of the tip [74]. For the first case, the environmental effect may thus be expressed as

$$\left(\frac{da}{dN}\right)_{\text{total}} = \left(\frac{da}{dN}\right)_{\text{vacuum}} + M \times \left(\frac{da}{dN}\right)_{\text{surface loss}} \quad (28)$$

The second term in Eq 28 is a "mechanical" component while the third term represents cyclic metal loss at the crack tip. Surface metal loss rate itself increases with applied total strain in a $\frac{1}{2}\text{Cr-Mo-V}$ steel reverse-cycled in air at 550°C [90]. The magnification factor M in Eq 28 thus arises from the increase in strain concentration at the tip. If oxygen penetration is more significant, the last term is replaced by $2\sqrt{Dt}$ where t is the cycle time and D is a fatigue-enhanced diffusion coefficient [74]. In Solomon and Coffin's work on A286 [35,44] intergranular cracking occurred at 10^{-3} Hz in air, but was delayed until 10^{-4} Hz in vacuum (Fig. 14). This may be strong evidence for intergranular penetration, but it should be noted that changes in *strain range* (vacuum tests being conducted at greater ϵ_p , Fig. 14) sometimes cause a transition in fracture mode [7].

At low plastic strains in ferritic steels crossover effects sometimes occur so that crack growth rates in air and steam become less than those in vacuum [17,20]. This is shown in Fig. 22. The reasons for this unexpected benefit of

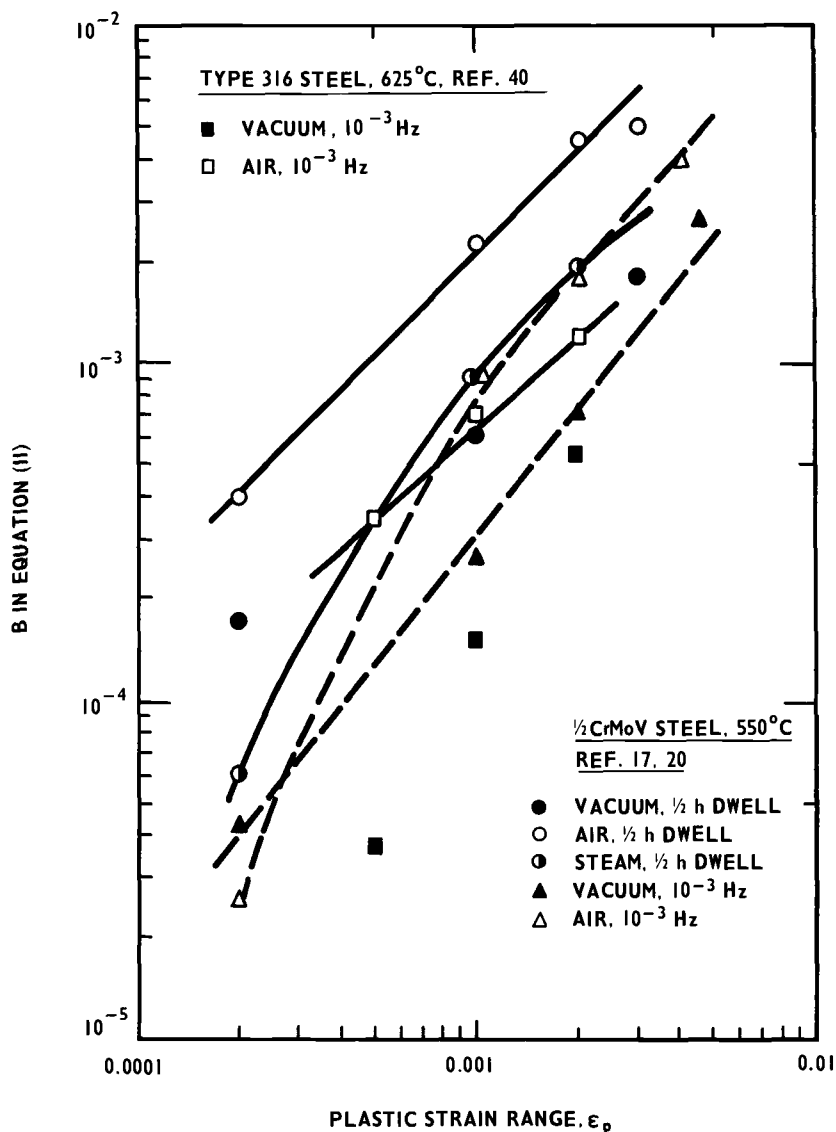


FIG. 22—At low strains in a ferritic steel growth rates in vacuum exceed those in oxidizing environments.

oxidation are (1) crack closure is prevented, interfering with the mechanism of advance, (2) crack-tip strains are thus too low to cause oxide spalling and subsequent metal attack, and (3) when the crack is sealed with oxide, the oxygen diffusion path to the tip is increased (and similarly with cation diffusion).

There is no crossover for Type 316 steel (Fig. 22). Because little bulk oxide is formed at the tip, the threshold value (at $R = -1$) in air and vacuum at

625°C is about 8 MPa m^{1/2} in both cases [40]. In contrast, the threshold of low alloy ferritic steel at 550°C is 15 MPa m^{1/2} in air compared with 10 MPa m^{1/2} under vacuum [67], again at $R = -1$. Vacuum/air crossovers can occur at midrange stress intensities, but this is due to crack branching in air reducing the effective ΔK [91].

At crack lengths >3 mm in HSF (Fig. 5) or for $\Delta K > 50$ MPa m^{1/2} in LEFM (Fig. 13) there is little difference between growth rates in inert and oxidizing environments in ferritic [70] and austenitic steels [72,73,75]. At a plastic strain of 0.01 striation measurements on Type 316 steel at 600°C confirm [92] that at low crack lengths propagation rates in air are three times those in vacuum but are similar beyond $a/W = 0.06$. At large CTOD values therefore the environmental component can be neglected. Excepting possibly the high-vacuum work of Coffin and Solomon [35,44], the order of magnitude difference in growth rates at midrange stress intensities is not reproduced in HSF (Figs. 4, 5, and 22). This is not surprising since (1) the CTOD is significant under reversed plasticity (Eq 8), and (2) the effect may be masked by creep damage ahead of the crack which occurs independently of environment.

Environmental effects can be included in Eq 6, for example, by allowing the cyclic stress-strain properties at the tip to increase under carburization conditions or by supposing [27] that oxidation raises the amount of crack surface created each cycle to its theoretical limit of $\frac{1}{2}$ CTOD. The most satisfactory explanation of $Q > 1$ in Eq 11 and Table 2 is to assume that partial rewelding [74] occurs at the crack tip. If the cyclic recohesion is $\delta'B$ independent of crack depth, which is reasonable because the crack is fully closed at peak compression, then Eq 9 becomes

$$\frac{da}{dN} = Ba \left(1 - \frac{\delta'}{a} \right) \quad (29)$$

This is shown plotted for $B = 10^{-3}$ and several values of δ' in Fig. 16. The initial slope Q increases as δ' increases, the effect diminishing at large crack depths. Tomkins has suggested [93] that vacuum data can be used as baseline only if recohesion does not occur.

Microstructure

The effects of creep, temperature, and environment upon crack growth are ultimately controlled by the microstructure, and are manifested by variations in the indices Q and m in Eqs 1 and 11 (Table 2 and Figs. 5 and 13). It follows that if the microstructure changes from its initial state during a long-term test, this should be attended by corresponding changes in crack growth rate.

In the LEFM range Lloyd [13] has shown that a transgranular crack, obeying Eq 1 with $m = 2.8$ in solution-annealed Type 316 steel at 625°C,

suddenly accelerated, proceeding intergranularly with $m = 10$. This was caused by aging during the first-stage (4500 h), leading, it was suggested, to a critical particle dispersion (Eq 27) and subsequent unstable growth. If the material was pre-aged, intergranular cracking occurred at the outset. Similar behavior in aged Type 316 steel was observed in HSF [76] where the transition occurred at a critical crack depth (that is, CTOD according to Eq 27). However, this crack depth was at $a/W \sim 0.13$ where, as discussed previously, deviations occur. Further criticisms are that the plastic strain (~ 0.008) increased during the test and was rather large, as were the datum growth rates (2 to 7×10^{-2} mm cycle $^{-1}$). Nevertheless, a significant demonstration was that a prolonged compressive dwell restored crack growth rates to the datum.

This healing effect, also reported for Type 304 steel at 593°C after tensile dwells [94], is generally accepted to be caused by the sintering of cavities. A related phenomenon was noted by Lloyd [13]: when the frequency was increased from 10^{-4} to 1 Hz, crack growth immediately fell from enhanced intergranular to the transgranular rate obtained previously at 1 Hz on a separate specimen, showing that the mechanism of advance depends only on the currently applied strain rate, ignoring previous damage. This device was

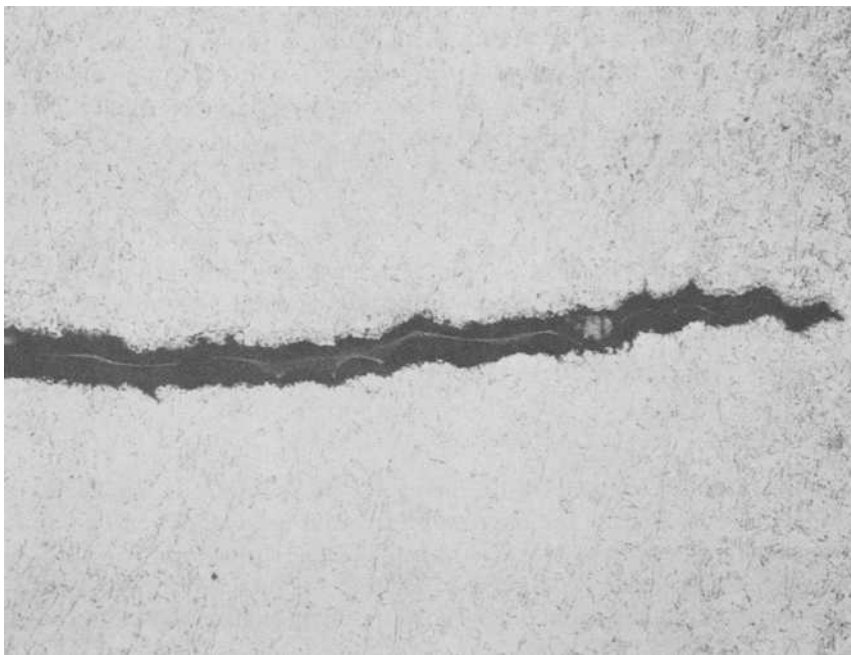


FIG. 23—LEFM transgranular crack growth at 10^{-2} Hz despite prior creep-fatigue damage. $\frac{1}{2}$ Cr-Mo-V steel at 550°C, etched, $\times 45$.

used in HSF [41] to leave striation markers in Type 316 steel at 700°C using an intermittent strain rate of $7 \times 10^{-3} \text{ s}^{-1}$ because the rate of interest ($6 \times 10^{-5} \text{ s}^{-1}$) left no intergranular growth history. Even with prior creep exposure of 3000 h at 538°C and 162 MPa, subsequent fatigue cracking in Type 304 steel was transgranular at 0.6 Hz [82]. Similar effects occur in $\frac{1}{2}\text{Cr-Mo-V}$ steel at 550°C for, despite prior HSF damage of 500 cycles at $\epsilon_p = 0.002$ and $\frac{1}{2}$ -h tension dwell, subsequent propagation at 10^{-2} Hz in LEFM at an average ΔK of $16 \text{ MPa m}^{1/2}$ at $R = 0$ was transgranular (Fig. 23) [53]. This contrasts sharply with the experiment of Fig. 15, where HSF testing with dwell reveals prior damage.

In *severely* damaged material fatigue cracking is always intergranular and unstable [80]. Figure 24 indicates widespread cavitation induced on prior austenite boundaries of a $\frac{1}{2}\text{Cr-Mo-V}$ steel quenched from 1250°C and tempered at 700°C, simulating an HAZ. Cavities arise from rapid precipitation of TiS and MnS during cooling and subsequent dissolution in ferrite during tempering [95]. Taking $(\lambda - p) = 5 \times 10^{-4} \text{ mm}$ from Fig. 24, it may be shown from Eqs 8 and 27 that the critical crack length for unstable propagation with $\epsilon_p = 0.0005$ is 0.4 mm. Thus the HSF experimental growth rates with $\frac{1}{2}$ -h dwell (Fig. 5) were unstable and occurred along the prior austenite

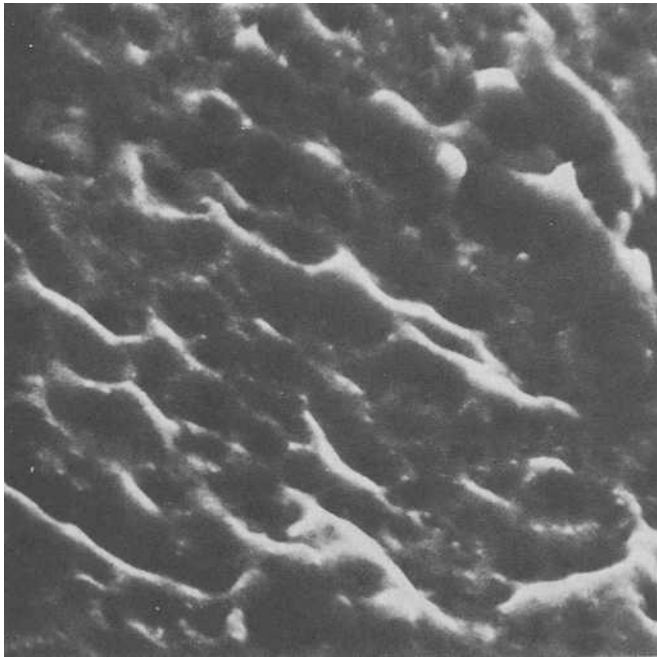


FIG. 24—Cavitation on prior austenite boundaries of quenched and tempered $\frac{1}{2}\text{Cr-Mo-V}$ steel ($\times 1.6K$ approximately).

boundaries. At room temperature, fatigue cracks in this material proceed by ductile striations [96] within the scatterband of low-alloy steel propagation rates [97].

There is now evidence that aging of Type 316 steel suppresses the switch to intergranular cracking observed at low strain rates in solution-treated material, for LEFM growth rates at 593°C on aged material were transgranular and unaffected by dwell [98]. In HSF, a strain rate of $4 \times 10^{-6} \text{ s}^{-1}$ or a 1-h tension dwell both left evidence of ductile striations—that is, transgranular growth—for a closely spaced distribution of precipitates which inhibited grain boundary sliding [99]. However, it is clear from experiments in which a transition occurred [13,76] that the CTOD as well as applied strain rate is important in defining the type of cracking.

Discussion

From the results of this and the previous section it is seen that the effects of creep damage, temperature, microstructure, and environment can be incorporated into *empirical* expressions. However, for developing *models* of crack growth, only temperature can be treated satisfactorily. At present, the effects of creep damage and microstructural changes are only predicted as an instability condition for growth and not as an increase in growth rate. The influence of environment is less clear; initiation and propagation may be affected differently and mechanical properties at the crack tip may be altered. Oxidizing environments are generally aggressive, either by metal loss at the crack tip or by oxygen penetration ahead of it. Beneficial effects of environment include crack sealing by oxide at low strains and rewelding in inert atmospheres.

Conclusions and Application of the Data

The HSF crack growth method yields information more quickly than a conventional endurance test, since several steps at different plastic strain ranges may be accomplished on one specimen [17]. The method also elucidates the cycles required for initiation at a smooth surface; recent results on 2¼Cr-1Mo steel, for example, have shown [100] that an unexpected decrease in endurance with *compression* dwells [101] is accompanied by an increase in HSF growth rate. Integrated HSF growth rates are identified with smooth specimen total endurances and furthermore can be reasonably linked, for continuous cycling at least, with growth rates in the LEFM range. We now show that short crack growth data in the range of 10^{-6} to $10^{-2} \text{ mm cycle}^{-1}$ can prove useful in design and failure assessment.

Short crack growth data are relatively new and their use has been overshadowed by other approaches using total endurance data, which have been taken to represent crack initiation in large components. For example, a “rule of thumb” for continuous cycling in HSF is that a plastic strain range of 0.01

gives 1000 cycles endurance. As an extension of this rule, the HSF growth relations may be used to calculate propagation rates at small depths. For example, B in Eqs 9 and 11 is numerically equal to the growth rate at 1 mm depth. Thus it may be seen in general from Fig. 3 that at this depth a plastic strain range of 0.01 produces a growth rate of about 0.01 mm with each cycle.

For a Type 321 steel stud fixing assembly which in operation would suffer a stress "well beyond that covered by present design codes", Bolton et al confirmed by subsequent metallography [102] that crack propagation from a thread root occupied most of the experimental life. This is one example where Eq 11 could be used directly, environmental, microstructural, temperature, and dwell effects being incorporated into the terms B and Q , thus providing more information on crack depth with cycles than is possible from a total endurance value.

In the LEFM regime, these variables are similarly accounted for in the terms C and m (Eq 1). The values C and m also apply over the whole range from HSF to LEFM when it can be demonstrated that there is a smooth link in crack growth rates (Figs. 10 and 11). There is thus a practical benefit in expressing da/dN as a single relation rather than by Eqs 11 and 17 separately.

As an example of the use of the data, we consider the steep temperature gradients set up over a small distance in the deliberate on-load water quenching of superheater tubes to remove ash deposits [103]. Thermal fatigue cracks initiate and propagate, and it is required to show that these arrest at some depth. The following calculation is based on experimental results for repeated quenching from 625°C of a Type 316 tube of 4.5 mm wall thickness [21]. After establishing an equivalent stress profile across the section using cyclic stress-strain data, the superposition method [104] is used to establish the corresponding variation in equivalent stress intensity. The crack growth rate at each depth is found from Eq 1 with $C = 3.2 \times 10^{-6}$ and $m = 2$ [40] (Fig. 11). Experimental growth rates and predictions are compared in Fig. 25, where it is seen that the crack arrests before reaching the outer surface. By integrating the curves, predicted crack depth can be given alternatively against the number of cycles. It has been shown [21] that the method gives conservative predictions compared with experiment.

An example for massive components is in the region ahead of a heat relief groove of tip radius ρ in a turbine rotor, where cracks form after high-temperature operation [105]. The basic service cycle is as shown in Fig. 1, but growth data for peak tensile dwell will be (conservatively) taken. For a temperature transient of, say, 120°C in the metal and stress concentration K_t , the elastic strain at the root of a groove is found and hence, from cyclic stress-strain data for 1Cr-Mo-V steel [3], the equivalent strain (Table 3). The stress ahead of the groove decays owing to the parabolic temperature transient [21] and the notch itself [106]. Taking both fields into account and a cyclic yield stress of 250 MPa at 550°C [3], we obtain the variation of equivalent stress intensity with distance given in Fig. 26. Taking the best fit line for

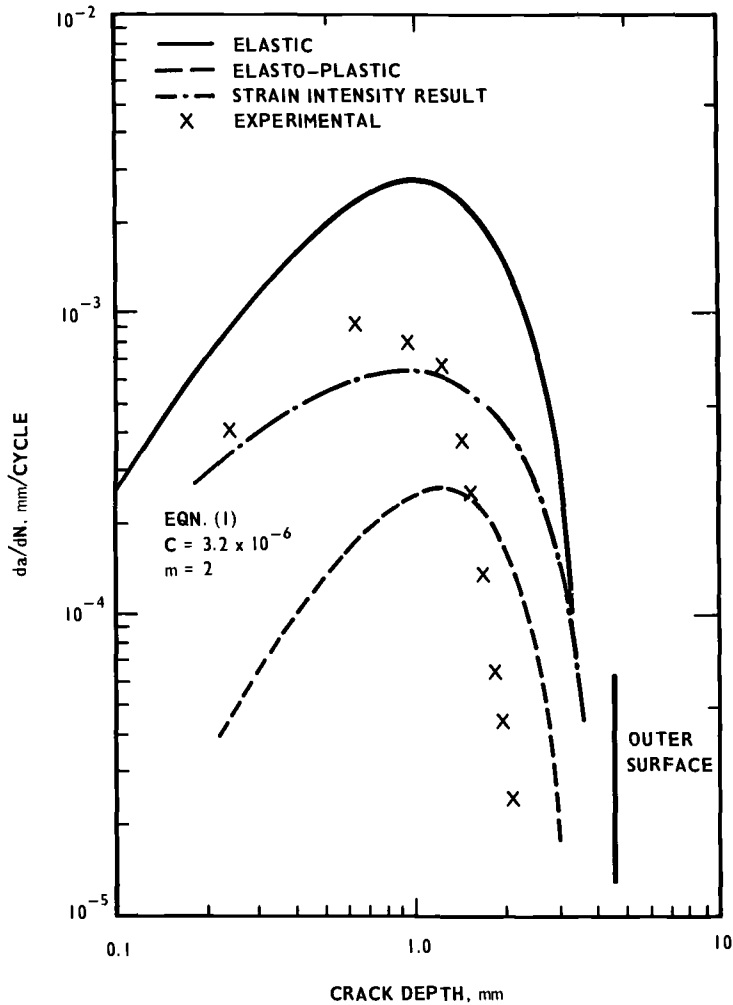


FIG. 25—Predicted and experimental growth rates in 316 tube repeatedly quenched from 625°C [21].

TABLE 3—Integrated cycles for ΔK variations in Fig. 26.

K_t	$\frac{1}{2}\epsilon_o + \epsilon_p$ Surface Value	Propagation Cycles 0.1 to 10 mm
2.0	0.00187	7260
2.5	0.00277	1584
3.0	0.00388	681

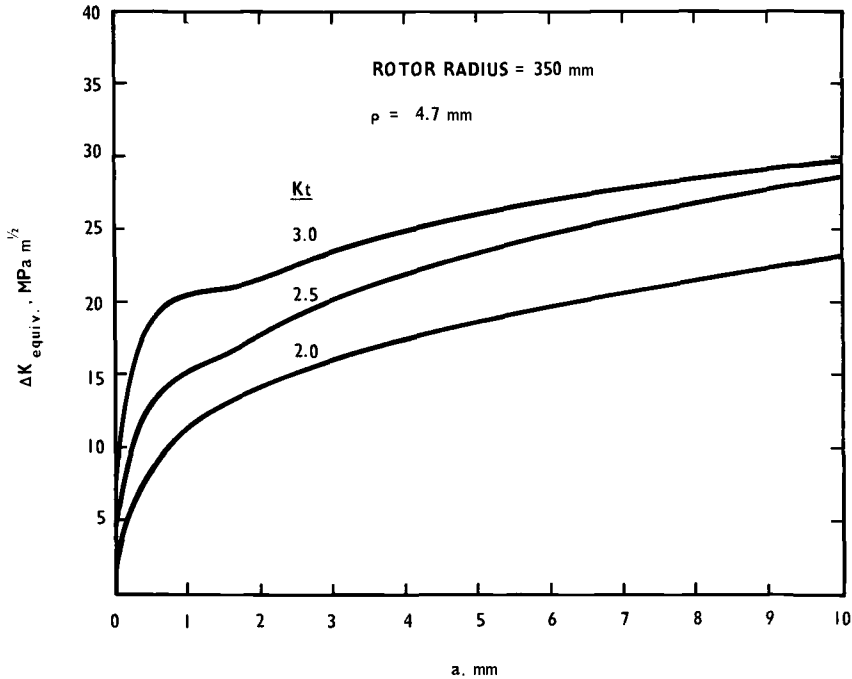


FIG. 26—Equivalent stress intensity at distance a ahead of groove tip for an assumed temperature difference in turbine rotor.

bainitic material (Fig. 19) as Eq 1 with $C = 1.7 \times 10^{-7}$ and $m = 3$ when da/dN is in mm cycle^{-1} , we obtain the integrated cycles for crack growth from 0.1 to 10 mm given in Table 3.

Thus a single crack growth relation, based on HSF and LEFM data, can be used to describe propagation across the complete section. While the method has practical advantages, further work, especially in the case of the low-alloy ferritic steels, is required to define an upper bound for growth in the combined creep/fatigue cycle.

Acknowledgments

The author is indebted to Mr. G. D. Branch for several discussions. The work was carried out at the Central Electricity Research Laboratories, and the paper is published by permission of the Central Electricity Generating Board.

APPENDIX

Modification to Growth Laws

Figure 16 indicates how the basic exponential growth law is affected by creep damage ahead of the crack and by rewelding at the tip. It can be shown that oxide attack at

the tip, given by Eq 28, also increases the slope Q in Eq 11. The last term in Eq 28 can be rewritten, for $\frac{1}{2}\text{Cr-Mo-V}$ steel at 550°C , as

$$\left(\frac{da}{dN}\right)_{\text{surface loss}} \times \left[\left(2\sqrt{\frac{a}{\rho}}\right)^{2\gamma/\gamma+\beta} \right]^3$$

where γ is a cyclic stress-strain constant ~ 0.45 [46] and ρ is the crack tip radius. The cubic term arises because surface metal loss rates vary as ϵ_t^3 for this material [90], and in the above equation the Neuber relation has been used to relate surface conditions with those at the tip. If $(da/dN)_{\text{surface loss}}$ is identified with an early crack growth rate (for example, 10^{-4} mm cycle $^{-1}$ at 0.1 mm depth in Fig. 16), an increase in slope very similar to the "increasing damage" lines is obtained.

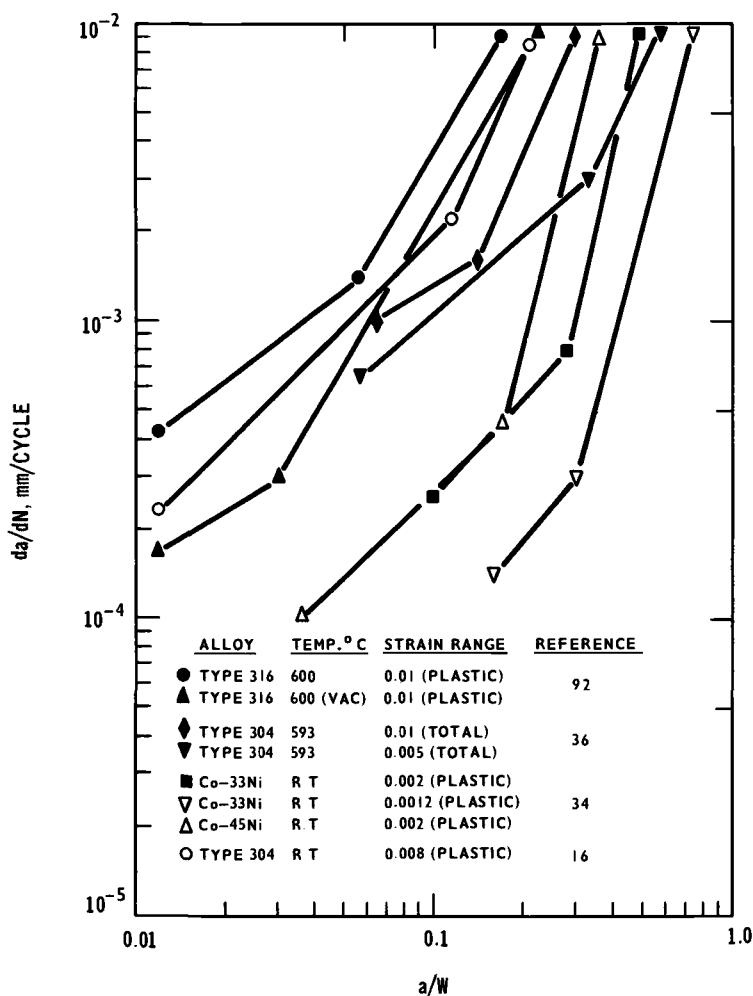


FIG. 27—Beyond a certain crack depth, crack growth rates deviate from an exponential growth relation.

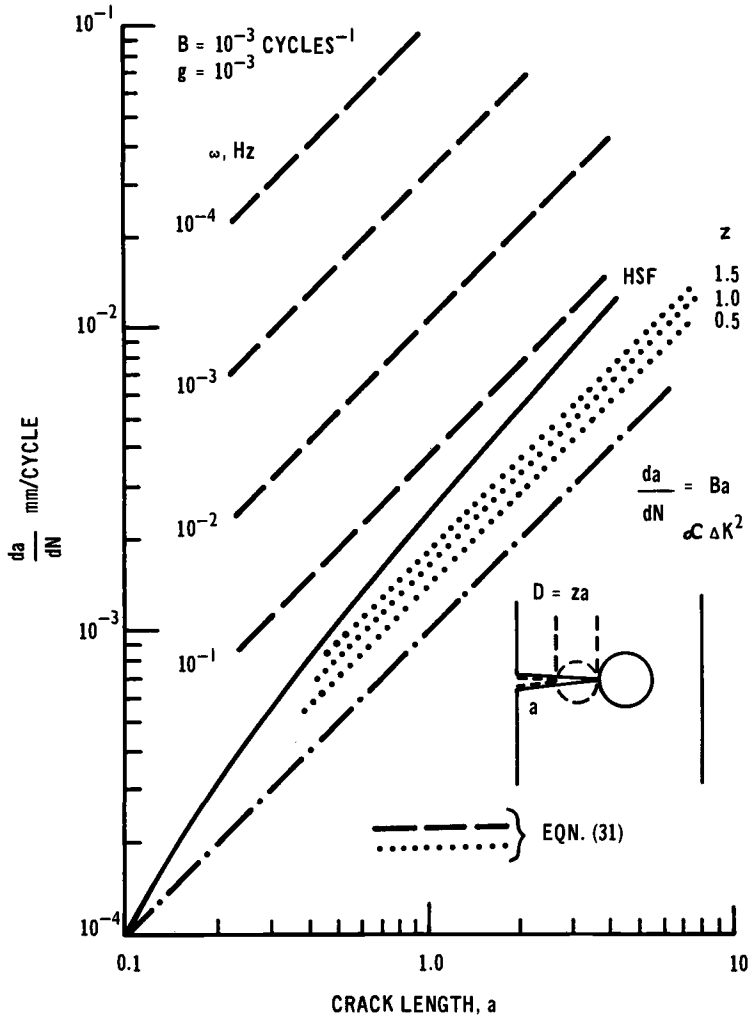


FIG. 28—Creep damage modification in LEFM regime; compare Fig. 16.

Figure 27 illustrates the deviation, mentioned previously, from an exponential growth law in HSF, generally in the a/W range of 0.06 to 0.3, depending on the strain range. The relation $da/dN = Ba$ (Eq 9) is equivalent to $da/dN \propto \Delta K^2$ (that is, $m = 2$ in Eq 1). It thus follows that values of $Q > 1$ in Eq 11, either for the a/W values shown in Fig. 27 or for those implied in Table 2, give rise to $m > 2$ in Eq 1. Therefore the rewelding and oxidation corrections apply equally in the LEFM regime, so that increased slopes in Eq 1 can be considered basically as a ΔK^2 relation modified by an ever-changing value of C .

However, unlike the case of Eq 23 where creep damage builds up from the outset, in LEFM it can only occur in the intense deformation zone D (Fig. 28). By considering the time taken for the crack to traverse the zone, a similar expression for LEFM is

$$\frac{da}{dN} = Ba \left[1 + \frac{gD}{\left(\frac{da}{dt}\right)} \right] \quad (30)$$

Putting $D = za$ and $da/dt = (da/dN)\omega$ where ω is the frequency, we find upon rearranging and solving for da/dN :

$$\frac{da}{dN} = \frac{a}{2} \left(B + \sqrt{B^2 + \frac{4Bzg}{\omega}} \right) \quad (31)$$

Putting $g = 10^{-3}$, we plot this in Fig. 28 for (1) several values of z when $\omega = 1$, and (2) several values of ω when $z = 1$. It is seen that an order of magnitude increase in cyclic growth rate is predicted for two orders of magnitude decrease in frequency; this is generally observed [68] (Fig. 13). Compared with HSF (Fig. 16) no increase in slope is predicted in Fig. 28. This is reasonable because as the plastic zone D expands, more cycles should be available for damage, but this is offset by an increase in crack growth rate for that zone size. By assuming a linear decrease in plastic strain in the zone ahead of the crack tip we may incorporate an *average* damage factor g_{av} in Eq 31. This alters the absolute magnitude of da/dN , but does not change the frequency effect or slope.

References

- [1] Dawson, R. A. T. and Neill, D. A. in *Thermal Stress and Thermal Fatigue*, D. J. Littler, Ed., Butterworths, London, 1971, pp. 439-452.
- [2] Timo, D. P. in *Thermal Stress and Thermal Fatigue*, D. J. Littler, Ed., Butterworths, London, 1971, pp. 453-469.
- [3] Thomas, G. and Dawson, R. A. T. in *Engineering Aspects of Creep*, Institution of Mechanical Engineers, London, 1980, Vol. 1, Paper C335/80, pp. 167-173.
- [4] Coffin, L. F. in *Fatigue at Elevated Temperatures*, ASTM STP 520, American Society for Testing and Materials, 1973, pp. 5-34.
- [5] *Cases of ASME Boiler and Pressure Vessel Code*, Case N47-12, Class 1, "Components in Elevated Temperature Service," American Society of Mechanical Engineers, 1977.
- [6] Walker, C. D. in *Proceedings*, International Joint Conference on Creep, Institution of Mechanical Engineers, 1963, Vol. 178, Part 3A, pp. 3-49-3-56.
- [7] Batte, A. D., Murphy, M. C., and Stringer, M. B., *Metals Technology*, Vol. 5, 1978, pp. 405-413.
- [8] Griffiths, J. R. and Oates, G., *Metal Science*, Vol. 11, 1977, pp. 285-292.
- [9] Paris, P. C. and Erdogan, F., *Journal of Basic Engineering*, Transactions of ASME, Series D, Vol. 85, 1963, pp. 528-534.
- [10] James, L. A. and Schwenk, B., *Metallurgical Transactions*, Vol. 2, 1971, pp. 491-496.
- [11] Shahinian, P., Smith, H. H., and Watson, H. E., *Journal of Engineering for Industry*, Transactions of ASME, Series B, Vol. 93, 1971, pp. 976-980.
- [12] Shahinian, P., *Journal of Pressure Vessel Technology*, Transactions of ASME, Series J, Vol. 98, 1976, pp. 166-172.
- [13] Lloyd, G. J., *Metal Science*, Vol. 13, 1979, pp. 39-47.
- [14] Sadananda, K. and Shahinian, P., *Metallurgical Transactions A*, Vol. 11A, 1980, pp. 267-276.
- [15] Sadananda, K. and Shahinian, P. in *Fracture Mechanics*, N. Perrone et al, Eds., University Press of Virginia, Charlottesville, 1978, pp. 685-703.
- [16] Tomkins, B., Sumner, G., and Wareing, J. in *International Symposium on Low Cycle Fatigue Strength and Elasto-Plastic Behaviour of Materials*, Deutscher Verband für Material Prüfung, Berlin, 1979, pp. 495-507.
- [17] Skelton, R. P., *Materials Science and Engineering*, Vol. 32, 1978, pp. 211-219.
- [18] Coffin, L. F. in *Proceedings*, Institution of Mechanical Engineers, Vol. 188 9/74, 1974, pp. 109-127.

- [19] Pineau, A. and Petrequin, P. in *La Fatigue des Matériaux et des Structures*, J. P. Bailon and C. Bathias, Eds., Montreal University Press, 1980, pp. 107-161.
- [20] Skelton, R. P., *Materials Science and Engineering*, Vol. 35, 1978, pp. 287-298.
- [21] Skelton, R. P. in *3rd International Conference on Mechanical Behaviour of Materials*, Vol. 2, Pergamon Press, Elmsford, N.Y., 1979, pp. 13-22.
- [22] Tomkins, B. in *International Conference on Fatigue Testing and Design*, Vol. 1, Society of Environmental Engineers, London, 1976, paper 17.1.
- [23] Tomkins, B., *Philosophical Magazine*, Vol. 18, 1968, pp. 1041-1066.
- [24] Tomkins, B., *Philosophical Magazine*, Vol. 23, 1971, pp. 687-703.
- [25] Tomkins, B., in *Corrosion Fatigue*, National Association of Corrosion Engineers, Houston, 1972, pp. 303-311.
- [26] Wareing, J., Tomkins, B., and Sumner, G. in *Fatigue at Elevated Temperatures, ASTM STP 520*, American Society for Testing and Materials, 1973, pp. 123-138.
- [27] Tomkins, B. and Wareing, J., *Metal Science*, Vol. 11, 1977, pp. 414-424.
- [28] Wareing, J., Vaughan, H. G., and Tomkins, B. in *Creep-Fatigue-Environment Interactions*, AIME, New York, 1980, pp. 129-150.
- [29] Wareing, J. and Vaughan, H. G., *Metal Science*, Vol. 11, 1977, pp. 439-446.
- [30] Wareing, J. and Vaughan, H. G., *Metal Science*, Vol. 13, 1979, pp. 1-8.
- [31] Tomkins, B., *Journal of Engineering Materials and Technology, Transactions of ASME, Series H*, Vol. 97, 1975, pp. 289-297.
- [32] Price, A. T. and Elder, W. J., *Journal of the Iron and Steel Institute*, Vol. 204, 1966, pp. 594-598.
- [33] Dawson, R. A. T., Elder, W. J., Hill, G. J., and Price, A. T. in *Thermal and High Strain Fatigue*, The Metals and Metallurgy Trust, London, 1967, pp. 239-269.
- [34] Chaland, G. and Rémy, L., *Acta Metallurgica*, Vol. 28, 1980, pp. 75-88.
- [35] Solomon, H. D. and Coffin, L. F. in *Fatigue at Elevated Temperatures, ASTM STP 520*, American Society for Testing and Materials, 1973, pp. 112-122.
- [36] Maiya, P. S., *Scripta Metallurgica*, Vol. 9, 1975, pp. 1277-1282.
- [37] Maiya, P. S. and Busch, D. E., *Metallurgical Transactions A*, Vol. 6A, 1975, pp. 1761-1766.
- [38] Wareing, J., *Metallurgical Transactions A*, Vol. 6A, 1975, pp. 1367-1377.
- [39] Huang, J., Pelloux, R. M., and Runkle, J., *Metallurgical Transactions A*, Vol. 11, 1980, pp. 899-904.
- [40] Skelton, R. P. in *Time and Load Dependent Degradation of Pressure Boundary Materials*, IAEA Meeting, Innsbruck, Report IWG-RRPC-79/2, 1979, pp. 73-87.
- [41] Yamaguchi, K. and Kanazawa, K., *Metallurgical Transactions A*, Vol. 10A, 1979, pp. 1445-1451.
- [42] Baudry, G. and Pineau, A., *Materials Science and Engineering*, Vol. 28, 1977, pp. 229-242.
- [43] Solomon, H. D., *Nuclear Technology*, Vol. 29, 1976, pp. 86-93.
- [44] Solomon, H. D., *Metallurgical Transactions*, Vol. 4, 1973, pp. 341-347.
- [45] Kunio, T., Iwamoto, K., and Kanazawa, K. in *Fracture 1969: Proceedings, 2nd International Conference on Fracture, Brighton*, Chapman and Hall, London, 1969, pp. 655-666.
- [46] Skelton, R. P., *Fatigue of Engineering Materials and Structures*, Vol. 2, 1979, pp. 305-318.
- [47] Maiya, P. S., *Scripta Metallurgica*, Vol. 9, 1975, pp. 1141-1146.
- [48] Ermi, A. M., Nahm, H., and Moteff, J., *Materials Science and Engineering*, Vol. 30, 1977, pp. 41-48.
- [49] Dugdale, D. S., *Journal of the Mechanics and Physics of Solids*, Vol. 8, 1960, pp. 100-104.
- [50] Skelton, R. P., *Materials Science and Engineering*, Vol. 19, 1975, pp. 193-200.
- [51] Yamaguchi, K., Kanazawa, K., and Yoshida, S., *Materials Science and Engineering*, Vol. 33, 1978, pp. 175-181.
- [52] Reuchet, J. and Rémy, L., *Fatigue of Engineering Materials and Structures*, Vol. 2, 1979, pp. 51-62.
- [53] Skelton, R. P., unpublished work.
- [54] Coffin, L. F., *Metallurgical Transactions*, Vol. 3, 1972, pp. 1777-1788.
- [55] Tomkins, B., Sumner, G., and Wareing, J. in *Fracture 1969: Proceedings, 2nd International Conference on Fracture, Brighton*, Chapman and Hall, London, 1969, pp. 712-724.
- [56] Mills, W. J. and James, L. A., *Fatigue of Engineering Materials and Structures*, Vol. 3, 1980, pp. 159-175.
- [57] Dowling, N. E. in *Cyclic Stress-Strain and Plastic Deformation Aspects of Fatigue Crack Growth, ASTM STP 637*, American Society for Testing and Materials, 1977, pp. 97-121.

- [58] Dowling, N. E. and Begley, J. A. in *Mechanics of Crack Growth*, ASTM STP 590, American Society for Testing and Materials, 1976, pp. 82-103.
- [59] Dowling, N. E. in *Cracks and Fracture*, ASTM STP 601, American Society for Testing and Materials, 1976, pp. 19-32.
- [60] Boettner, R. C., Laird, C., and McEvily, A. J., *Transactions, Metallurgical Society of AIME*, Vol. 233, 1965, pp. 379-387.
- [61] Rau, C. A., Gemma, A. E., and Leverant, G. R. in *Fatigue at Elevated Temperatures*, ASTM STP 520, American Society for Testing and Materials, 1973, pp. 166-178.
- [62] Mowbray, D. F., Woodford, D. A., and Brandt, D. E. in *Fatigue at Elevated Temperatures*, ASTM 520, American Society for Testing and Materials, 1973, pp. 416-426.
- [63] Leverant, G. R., Strangman, T. E., and Langer, B. S., *Superalloys: Metallurgy and Manufacture*, 3rd International Symposium, Seven Springs, Pa., 1976, pp. 285-295.
- [64] Gemma, A. E., Langer, B. S., and Leverant, G. R. in *Thermal Fatigue of Materials and Components*, ASTM STP 612, American Society for Testing and Materials, 1976, pp. 199-213.
- [65] Solomon, H. D., *Journal of Materials*, Vol. 7, 1972, pp. 299-306.
- [66] Haigh, J. R. and Skelton, R. P., *Materials Science and Engineering*, Vol. 36, 1978, pp. 133-137.
- [67] Skelton, R. P. and Haigh, J. R., *Materials Science and Engineering*, Vol. 36, 1978, pp. 17-25.
- [68] James, L. A. in *Fifth National Symposium on Fracture Mechanics*, ASTM STP 513, American Society for Testing and Materials, 1973, pp. 218-229.
- [69] Haigh, J. R., *Engineering Fracture Mechanics*, Vol. 7, 1975, pp. 271-284.
- [70] Haigh, J. R., Skelton, R. P., and Richards, C. E., *Materials Science and Engineering*, Vol. 26, 1976, pp. 167-174.
- [71] Ellison, E. G. and Harper, M. P., *Journal of Strain Analysis*, Vol. 13, 1978, pp. 35-51.
- [72] Mahoney, M. W. and Patton, N. E., *Nuclear Technology*, Vol. 23, 1974, pp. 290-296.
- [73] James, L. A. and Knecht, R. L., *Metallurgical Transactions A*, Vol. 6A, 1975, pp. 109-116.
- [74] Marshall, P. in *The Influence of Environment on Fatigue*, Institution of Mechanical Engineers and The Society of Environmental Engineers, London, 1977, pp. 27-36.
- [75] Priddle, E. K., Walker, F., and Wiltshire, C. in *The Influence of Environment on Fatigue*, Institute of Mechanical Engineers and the Society of Environmental Engineers, London, 1977, pp. 137-144.
- [76] Min, B. K. and Raj, R., *Acta Metallurgica*, Vol. 26, 1978, pp. 1007-1022.
- [77] Day, M. F. and Thomas, G. B., *Metal Science*, Vol. 13, 1979, pp. 25-33.
- [78] Wood, D. S., Slattery, G. F., Wynn, J., Connaughton, M. D., and Lambert, M. E. in *The Influence of Environment on Fatigue*, Institution of Mechanical Engineers and the Society of Environmental Engineers, London, 1977, pp. 11-20.
- [79] Cheng, C. Y. and Diercks, D. R., *Metallurgical Transactions*, Vol. 4, 1973, pp. 615-617.
- [80] Lloyd, G. J. and Wareing, J., *Journal of Engineering Materials and Technology, Transactions of ASME*, Series H, Vol. 101, 1979, pp. 275-283.
- [81] Wood, D. S., Baldwin, A. B., and Williamson, K. in *Time and Load Dependent Degradation of Pressure Boundary Materials*, IAEA Meeting, Innsbruck, Report IWG-RRPC-79/2, 1979, pp. 88-101.
- [82] James, L. A., *Journal of Engineering Materials and Technology, Transactions of ASME*, Series H, Vol. 98, 1976, pp. 235-241.
- [83] Taira, S., Fujino, M., Sakon, Y., and Maruyama, S., *Journal of the Society for Materials Science, Japan*, Vol. 23, 1974, pp. 632-639.
- [84] Taira, S., Maruyama, S. and Fujino, M., *Journal of the Society for Materials Science, Japan*, Vol. 24, 1975, pp. 227-233.
- [85] Forrest, P. G., *Journal of the Iron and Steel Institute*, Vol. 200, 1962, pp. 452-457.
- [86] Woodford, D. A. in *3rd International Conference on Mechanical Behaviour of Materials*, Vol. 2, Pergamon Press, Elmsford, N.Y., 1979, pp. 33-42.
- [87] Woodford, D. A. and Mowbray, D. F., *Materials Science and Engineering*, Vol. 16, 1974, pp. 5-43.
- [88] Koizumi, T. and Okazaki, M., *Fatigue of Engineering Materials and Structures*, Vol. 1, 1979, pp. 509-520.
- [89] Skelton, R. P., *Metal Science*, Vol. 8, 1974, pp. 56-62.
- [90] Skelton, R. P. and Bucklow, J. I., *Metal Science*, Vol. 12, 1978, pp. 64-70.

- [91] Scarlin, R. B. in *Fracture 1977: International Conference on Fracture 4*, University of Waterloo Press, Canada, Vol. 2, 1977, pp. 849-857.
- [92] Levaillant, C., Rezgui, B., and Pineau, A. in *3rd International Conference on Mechanical Behaviour of Materials*, Vol. 2, Pergamon Press, Elmsford, N.Y., 1979, pp. 163-172.
- [93] Tomkins, B., *Metal Science*, Vol. 14, 1980, pp. 408-417.
- [94] Majumdar, S. and Maiya, P. S. in *3rd International Conference on Mechanical Behaviour of Materials*, Vol. 2, Pergamon Press, Elmsford, N.Y., 1979, pp. 101-109.
- [95] Middleton, C. J., *Philosophical Transactions of the Royal Society*, London, A295, 1980, p. 305.
- [96] Andrew, R. C., Weston, G. M., and Ritter, J. C., *Metal Science*, Vol. 13, 1979, pp. 78-82.
- [97] Richards, C. E. and Lindley, T. C., *Engineering Fracture Mechanics*, Vol. 4, 1972, pp. 951-978.
- [98] Michel, D. J. and Smith, H. H. in *ASME-MPC, Symposium on Creep-Fatigue Interaction*, American Society of Mechanical Engineers, New York, 1976, pp. 391-415.
- [99] Maiya, P. S. and Majumdar, S., *Metallurgical Transactions A*, Vol. 8A, 1977, pp. 1651-1660.
- [100] Teranishi, H. and McEvily, A. J. in *International Symposium on Low Cycle Fatigue Strength and Elasto-Plastic Behaviour of Materials*, Deutscher Verband für Materialprüfung, Berlin, 1979, pp. 25-38.
- [101] Brinkman, C. R., Strizak, J. P., Booker, M. K., and Jaske, C. E., *Journal of Nuclear Materials*, Vol. 62, 1976, pp. 181-204.
- [102] Bolton, W. K., Suhr, R. W., and Wilkinson, P. R. in *Creep and Fatigue in Elevated Temperature Applications*, Vol. 1, Institution of Mechanical Engineers, London, 1975, pp. 191.1-191.9.
- [103] Newton, J. D., *Journal of the Australian Institute of Metals*, Vol. 21, 1976, pp. 94-102.
- [104] Buchalet, C. B. and Bamford, W. H. in *Mechanics of Crack Growth, ASTM STP 590*, American Society for Testing and Materials, 1976, pp. 385-402.
- [105] Kuwabara, K. and Nitta, A., CRIEPI Report E 277001, Tokyo, 1977, pp. 1-23.
- [106] Kalderon, D. in *Proceedings*, Institution of Mechanical Engineers, Vol. 186, 31/72, 1972, pp. 341-377.

Prediction of Fatigue Life of Smooth Specimens of SG Iron by Using a Fracture Mechanics Approach

REFERENCE: Starkey, M. S. and Irving, P. E., "Prediction of Fatigue Life of Smooth Specimens of SG Iron by Using a Fracture Mechanics Approach," *Low-Cycle Fatigue and Life Prediction, ASTM STP 770*, C. Amzallag, B. N. Leis, and P. Rabbe, Eds., American Society for Testing and Materials, 1982, pp. 382-398.

ABSTRACT: Studies have been made of factors influencing fatigue life of smooth specimens of SG iron. It is shown that nodule size does not influence fatigue life, whereas pore size exerts a strong influence. Microcrack growth commenced from the pores within a few percent of the life of the specimen, for lives up to 10^5 reversals. Using an experimentally determined expression for microcrack growth, and approximating the defects to small cracks, fatigue lives for a variety of starting defect shapes and sizes have been calculated. Calculated lives agree with the experimentally determined lives within a factor of four. It is shown that fatigue life is predominantly controlled by pores (owing to their larger size and more rapid crack initiation) rather than by nodules. The variation in observed fatigue lives can be related to the variation in pore size within the iron.

KEY WORDS: casting defects, crack initiation, crack growth, J integral, life prediction, microshrinkage porosity, SG irons, short cracks, fatigue life

Nomenclature

- a Half the surface crack length
- c Crack depth
- C Fatigue crack growth rate coefficient
- E Young's modulus
- J Path independent line integral
- Δj Range of J
- J_{SURF} J of crack where it intersects the specimen surface
- J_{TIP} J at the crack tip

¹Metallurgist and Section Head, respectively, Materials Engineering Department, GKN Technology Ltd., Wolverhampton, England.

ΔK	Stress intensity range
m	Fatigue crack growth rate exponent
N	Number of applied cycles
N_f	Number of cycles to failure
R	Stress ratio, minimum stress/maximum stress
$\Delta\epsilon$	Strain range
ϵ_p	Plastic strain
σ	Applied stress

The fatigue life of smooth test specimens is generally divided into crack initiation and crack growth. Where plastic strain predominates, at short lives, crack growth accounts for the major part of cycles to failure. At long lives, elastic strain is dominant, as are the cycles occupied by crack initiation [1,2].² The division between the two extremes becomes less distinct the closer the crack initiation process is examined, and it is now apparent that at all but the longest lives microcrack growth takes up a substantial part of total fatigue life [3,4].

Factors influencing the growth of such microcracks have recently become of interest from a fracture mechanics viewpoint as there is now evidence [5-7] that short cracks (typically $<100\ \mu\text{m}$) behave differently from long cracks, even though the nominal applied stress intensity range, ΔK , may be the same in both cases. Growth of cracks in smooth specimens will encompass both short and long crack behavior.

The smooth specimen fatigue behavior of cast irons is somewhat different than that of other materials, because cast irons contain shrinkage pores and graphite precipitates. These are of a larger size (50 to $200\ \mu\text{m}$) than defects found in forged materials, and their presence is liable to accelerate crack initiation and early growth. The evidence as to the magnitude and circumstances of their effect is somewhat conflicting.

Ikawa and Ohira [8] compared the properties of irons with different graphite morphologies and found that grey irons with sharp ended graphite flakes had inferior fatigue properties to SG irons in which the graphite is present as spheroids which have a reduced stress concentration. Gilbert [9] has shown that in SG irons under tensile load, graphite nodules at the surface can separate from the matrix at the graphite/matrix boundary or at the primary/secondary graphite interface. Thus the nodules act as spherical voids and many workers [10-12] have shown that cracks initiate at nodules under such circumstances. On the other hand Palmer [13], Ostensson [14], and Testin [15] have illustrated that pores can also contribute to crack initiation.

²The italic numbers in brackets refer to the list of references appended to this paper.

In previous work [16] the authors made an examination of the effects of nodules and micropores on the fatigue life of smooth specimens of SG iron. Thirty cylindrical specimens were cut from cast blocks of different nodule count and tested at two fully reversed strain amplitudes, 0.005 and 0.0018, resulting in lives of about 10^3 and 10^5 reversals respectively. In these castings, nodule size was found to have no effect on fatigue life. Failure origins were identified and found to be microshrinkage pores in 90 percent of the specimens tested. Additionally, replica studies were made of crack initiation and early growth in a few specimens. It was found that crack growth from these micropores occupied nearly all of life in the majority of specimens examined. From the replicas it was possible to measure crack growth rates; and, using a similar analysis to Dowling [17], these were successfully correlated with ΔJ , an elastic-plastic parameter, rather than with the linear elastic ΔK .

In the present work the authors have used a finite-element analysis to determine J for small semi-elliptical cracks similar in shape to the crack-initiating pores, in an elastic uniaxially loaded cylinder. J expressions used previously have been refined and crack growth rate constants calculated. Specimen life has been predicted by integration of these crack growth laws.

Materials

Five casts of spheroidal graphite cast iron were kindly supplied by the British Cast Iron Research Association. Three casts were of BS 2789 grade 370/17 with an annealed, fully ferritic structure, and two were of grade 700/2 with an as-cast, pearlitic structure. Chemical analyses of these irons are given in Table 1 and mechanical properties in Table 2. Their microstructures are shown in Fig. 1.

Nodule counts and size distributions were determined using a Quantimet. Nodule count was found to vary between 100 and 200 nodules per mm^2 . The observed two-dimensional size distributions were converted to three-dimensional size distributions using the Schwartz-Saltykov method [18]. The resulting histogram for the cast containing the largest nodules is given in Fig. 2a. The micropores found to have initiated fatigue failures in these irons were also measured; a histogram of their sizes (longest axis) is shown in Fig.

TABLE 1—Chemical composition of cast irons (weight percent).

SG Iron Code	C	Si	Mn	S	P	Mg
Pearlitic irons						
A	3.52	2.09	0.37	<0.01	0.016	0.053
B	3.57	2.24	0.33	<0.01	0.017	0.057
Ferritic irons						
C	3.56	2.02	0.34	<0.01	0.017	0.058
D	3.56	2.13	0.34	<0.01	0.017	0.058
E	3.57	2.18	0.34	<0.01	0.017	0.057

TABLE 2—*Monotonic mechanical properties of cast irons.*

SG Iron Code	Ultimate Tensile Strength, MN m ⁻²	0.2% Proof Stress, MN m ⁻²	Reduction in Area, (%)
Pearlitic irons			
A	800	443	7.7
B	844	455	5.6
Ferritic irons			
C	373	243	31.9
D	379	245	26.8
E	412	248	25.3

2b. These pores were intersected by the machined specimen surface. They were long and narrow, with their longer dimension generally perpendicular to the specimen surface. The ratio of depth to half surface length of these pores ranged from 0.5 to 7.0, with an average of 4.3. Similar microshrinkage porosity defects were found in polished metallographic sections of large SG iron axle housings.

The pores found can be seen to be much larger than the graphite nodules (Fig. 2). The majority of the nodules have diameters from 20 to 60 μm , whilst the pores have lengths from 60 to 150 μm . The majority of the micropores in the commercial castings were similar in size to those found in the tested laboratory castings, but a few were much larger, up to 300 μm in length.

Strain amplitude versus fatigue life curves generated for the ferritic and pearlitic irons are given in Figs. 3a and 3b respectively. The testing methods that were used are described fully in Ref 16. The ferritic irons have a fatigue limit of 0.0012 strain, corresponding to a stress amplitude of 200 MN m⁻² whilst the pearlitic irons have a fatigue limit of 0.0015 strain or 250 MN m⁻².

Techniques Used for Fatigue Life Prediction

In all but one of the specimens replicated, fatigue crack growth from the micropores was found to start almost immediately. It should be possible to predict the lives observed for all the tested specimens by integration of the crack growth expression previously determined [16]; namely

$$\frac{dc}{dN} = C(\Delta J)^m \quad (1)$$

where C and m are constants for the material, c is the crack depth, and N is the number of constant-amplitude cycles applied. As an approximation, the pores can be assumed to be crack-like defects and the expression integrated between starting pore size and final crack length. In order to carry out this integration expressions are needed for the line integral J and for the pore sizes and shapes observed. The pore shapes were extremely complex but a

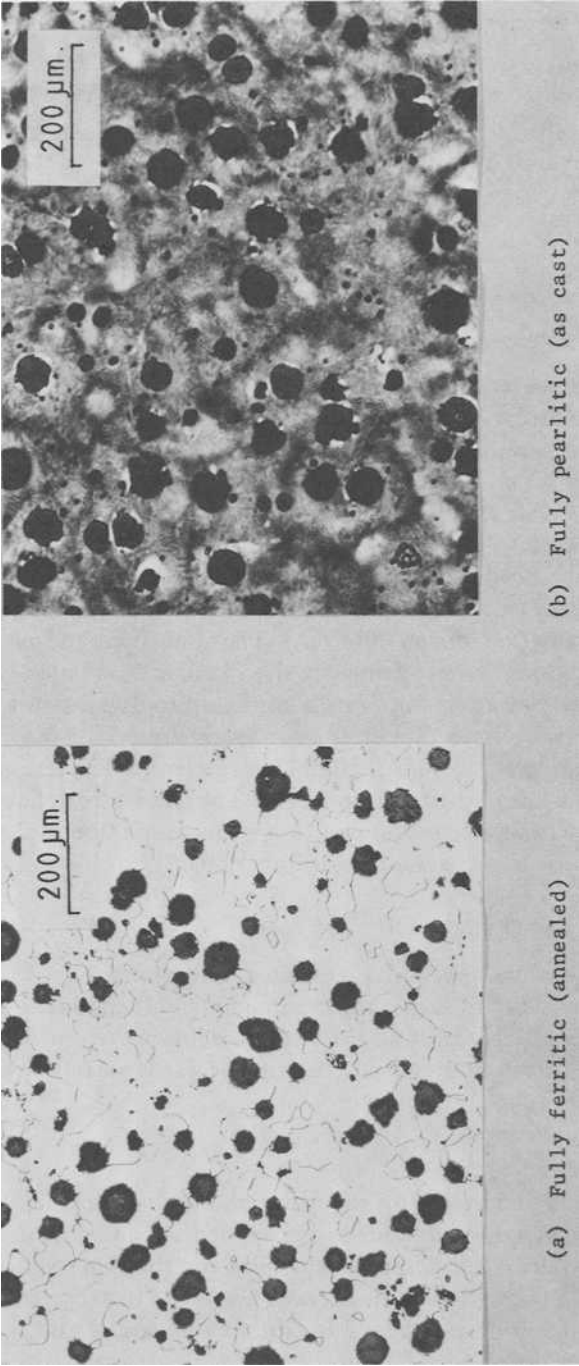


FIG. 1—Typical etched microstructures.

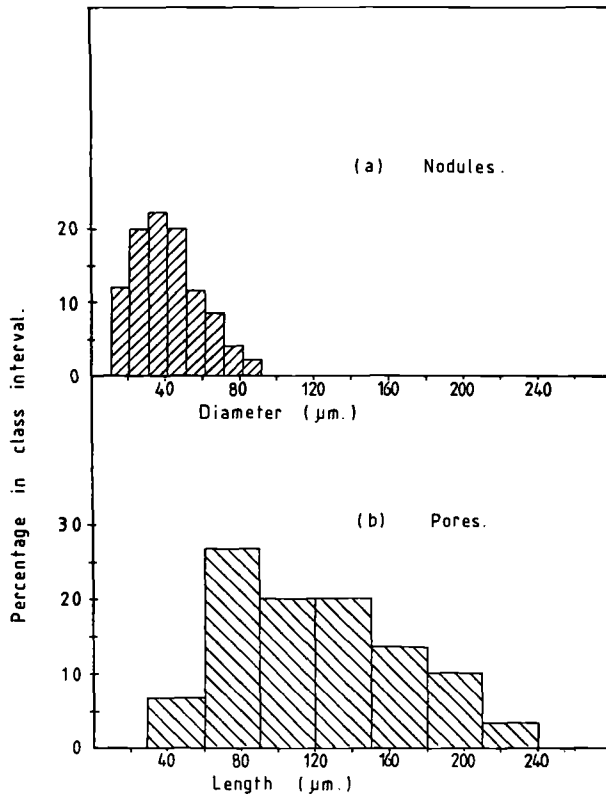


FIG. 2—Histograms of defect sizes.

semi-ellipse was thought to be a reasonable approximation to most of them. The values of the constants C and m in the crack growth rate expressions are also needed.

The MARC finite-element package [19] was used to evaluate J at the crack tip and at the specimen surface of small semi-elliptical cracks in elastically loaded cylindrical specimens. This program calculates the change in strain energy at a point on the crack front due to a very small increment of crack growth, while keeping the applied load constant [20]. The J -integral was derived from this value by dividing it by the incremental change in crack area.

For a through-crack in elastic loading:

$$J = \frac{\pi \sigma^2 a}{E} \quad (2)$$

Geometry constants for these elastically loaded semi-elliptical cracks were obtained by dividing the J -values from the MARC analysis by the above expression for a through-crack. The results are shown in Figs. 4a and 4b. As

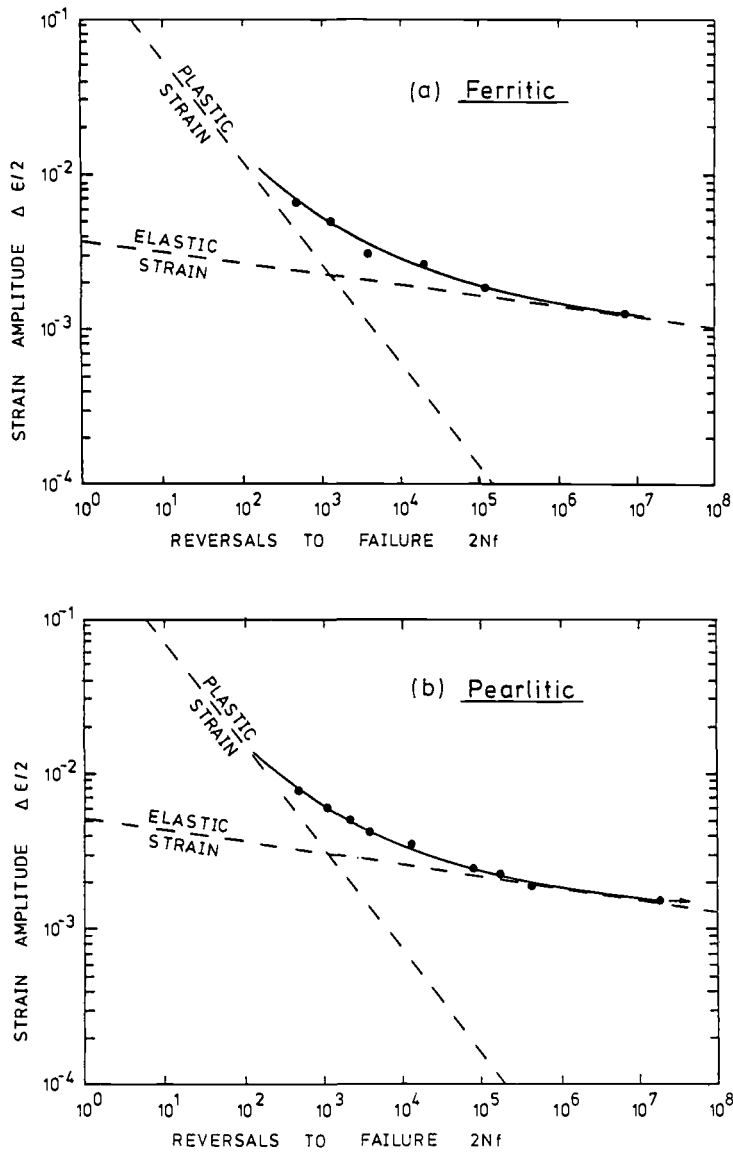


FIG. 3—Strain versus fatigue life curves for irons.

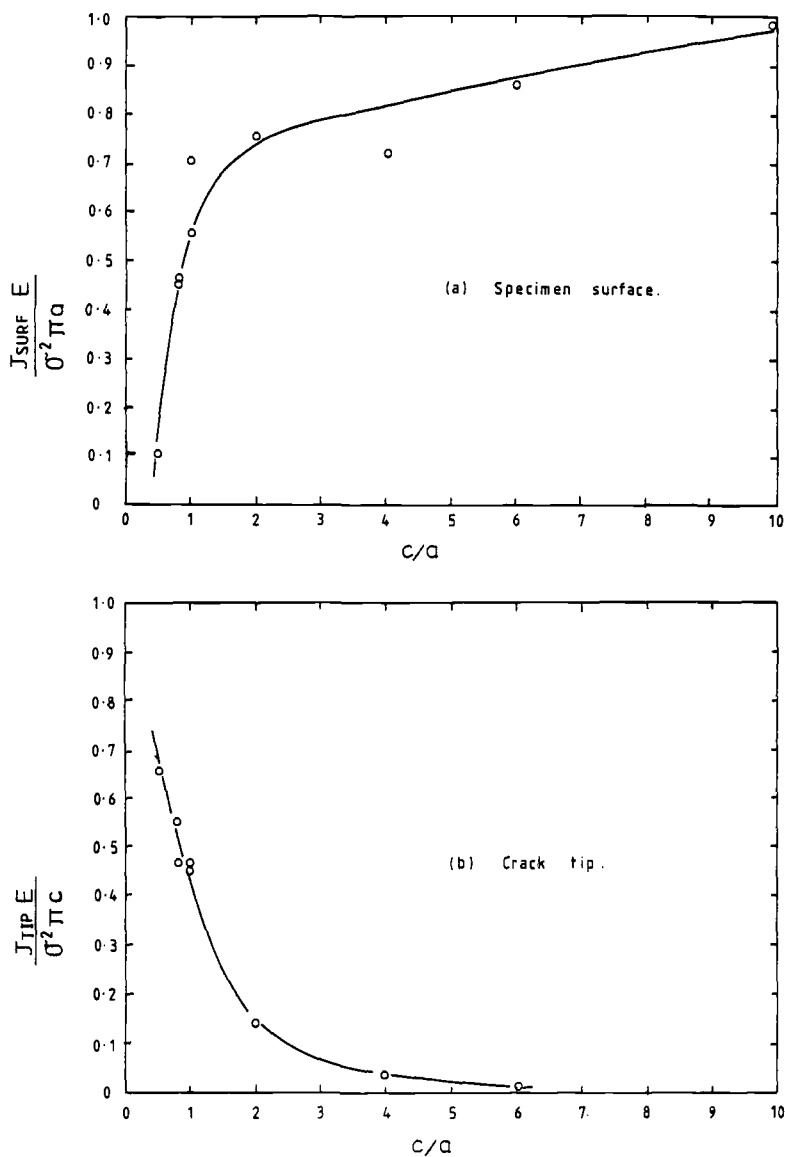


FIG. 4—Geometry constants for J of a small semi-elliptical surface crack in an axially loaded cylinder (elastically calculated).

the ratio of crack depth c to half surface length a increases, J at the specimen surface will approximate to J of a through-crack.

Most of the specimens were tested at strains high enough to cause substantial plasticity, and so these elastically calculated J -solutions are no longer valid. The cyclic strain hardening exponent for these irons was found to be 0.142. For such a material Shih and Hutchinson [21] have derived an estimate for J of a through-crack which includes a plasticity term

$$J = \pi a \left[\frac{1.377\sigma^2}{E} + 2.94\sigma \epsilon_p \right] \quad (3)$$

It was assumed that the geometry correction factors calculated for elastic loading are also applicable to plastic loading, and both the elastic and plastic components of this expression were modified by the geometry constants derived by the finite-element analysis.

Measurements were made of the surface length and depth of numerous small heat-tinted cracks in the tested specimens. From this it was established that cracks growing from the pores adopt a stable c/a ratio of 0.82 at short lengths.

For this crack shape

$$J = \frac{2.30\sigma^2 c}{E} + 4.91\sigma\epsilon_p c \quad (4)$$

at the crack tip.

Under cyclic loading stress and strain must be replaced by stress range and strain range. The replica work showed that the microcracks remained open throughout most of the compression-tension loading cycle; therefore in calculating ΔJ the whole of the strain range was used.

Crack depth was estimated from the surface crack lengths observed on the replicas, assuming a c/a ratio of 0.82. Crack growth rates were calculated from a piecewise quadratic curve fit.

The results are given as a function of ΔJ at the crack tip in Figs. 5a and 5b for the ferritic and pearlitic irons respectively. Also plotted on these figures are the results of crack growth tests on compact tension specimens at R -ratios of 0.1, 0.33, and 0.7. The observed crack growth rates are very similar for the two matrix structures.

From these plots crack growth rates can be approximated by

$$\frac{dc}{dN} = 2 \times 10^{-8} \Delta J^{2.0} \quad (5)$$

for the ferritic irons, and

$$\frac{dc}{dN} = 1.3 \times 10^{-8} \Delta J^{1.69} \quad (6)$$

for the pearlitic irons.

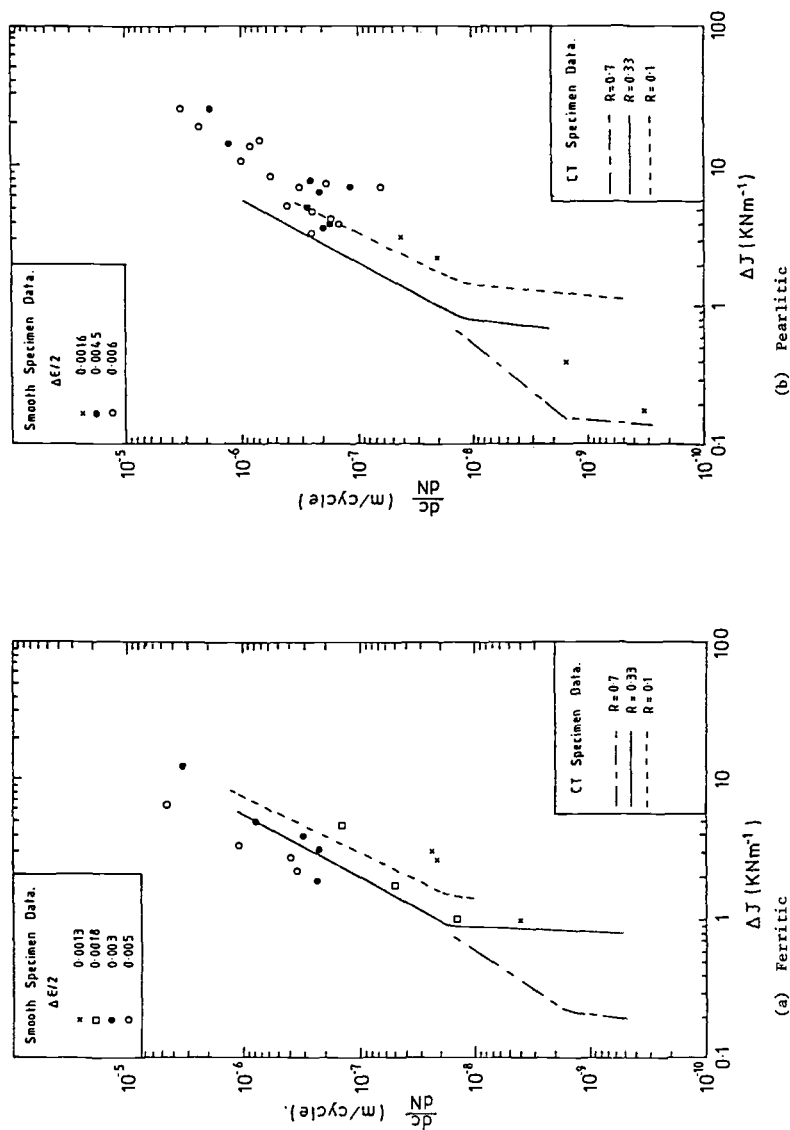


FIG. 5—Crack growth as a function of ΔJ .

These equations were integrated in incremental steps from the starting pore geometry to a crack 1 to 2 mm in depth. After each step the crack shape was modified. This integration was carried out for the observed initiating pore shapes in each specimen tested.

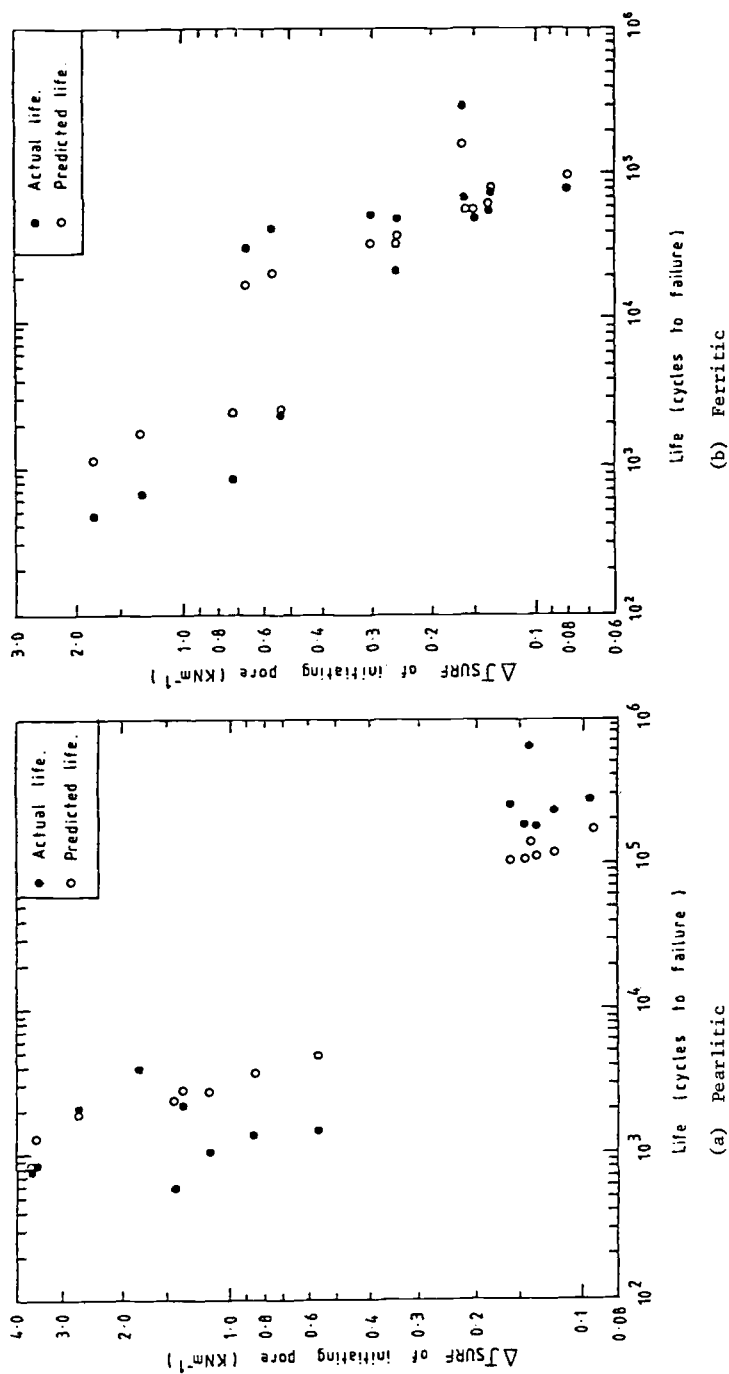
Results of Life Prediction

In Figs. 6a and 6b the predicted lives have been plotted as a function of the initial value of ΔJ at the surface of the pore, together with the actual lives obtained. At short lives (less than 10^4 cycles) the predicted lives are somewhat longer than the observed lives. At long lives (greater than 10^4 cycles) the predicted lives of the ferritic specimens are reasonably accurate, whilst the lives predicted for the pearlitic specimens are shorter than those observed. All predicted lives are within a factor of four of the actual lives.

As they grew, the modelled cracks eventually adopted a constant c/a ratio of 0.87 for the ferritic irons and 0.88 for the pearlitic irons, which is in good agreement with the observed shapes. For a typical pore, J at the specimen surface was higher than J at the pore tip. Consequently crack growth rates were initially much higher at the surface than at the tip. A large proportion of life was spent growing the crack before it adopted a constant c/a ratio. This is illustrated in Fig. 7, which shows the calculated crack depth and half the predicted surface length as a function of life for an initiating pore of typical geometry. Although the crack geometry did not stabilize until 70 percent of life, the crack was then only 240 μm deep, that is, 1.5 times its starting depth.

In addition to predicting the fatigue life of specimens with known pore geometry, the integration technique can be used to explore the reasons for the dominance of pores over nodules. By considering a nodule as a crack-like defect, the effect on life of the differences in geometry and size of the two crack initiators can be examined, assuming crack initiation to be instantaneous. Similarly, by comparing the integrated lives obtained from the smallest and largest pores measured by metallographic techniques, the extent of possible scatter in fatigue life can be calculated.

A typical nodule has a diameter of 40 μm and a large nodule a diameter of 80 μm . The smallest pore observed to initiate failure was 20 by 60 μm and the largest pore found was 300 by 120 μm . The lives predicted for crack-like starting defects of these sizes, for the applied strain amplitudes used in the tests, are given in Table 3. This shows that from size considerations alone an average nodule would give similar lives to a very small elongated pore, whilst a large nodule would reduce this life by half. This observation is independent of strain amplitude. A difference in life of a factor of four is predicted between a small and a large pore in a pearlitic specimen and six in a ferritic specimen.

FIG. 6—Predicted specimen life and actual life as a function of ΔJ_{SURF} of the pore-initiating failure.

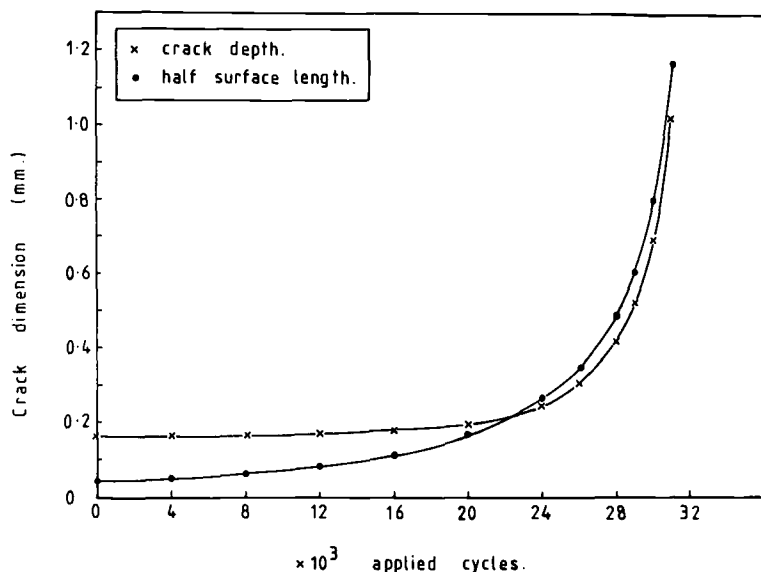


FIG. 7—Predicted change in shape of a typical fatigue crack (ferritic specimen tested at a strain amplitude of 0.0018).

Discussion

Agreement of predicted lives with actual lives is fair, all being within a factor of 4 and most within a factor of 3. There are many possible reasons for the discrepancies, which perhaps serve to illustrate the complexity and difficulty in making accurate fatigue life predictions in even this relatively simple case. Some of these are as follows:

1. The model disregards crack initiation cycles.
2. The starting defect is treated as a crack rather than a notch.

TABLE 3—Predicted lives (cycles) of specimens containing extremes of defect sizes.

Defect	Pearlitic		Ferritic	
	$\frac{\Delta\epsilon}{2} = 0.0018$	$\frac{\Delta\epsilon}{2} = 0.005$	$\frac{\Delta\epsilon}{2} = 0.0018$	$\frac{\Delta\epsilon}{2} = 0.005$
Typical nodule, 40 μm diameter	207 000	5500	116 000	4500
Large nodule, 80 μm diameter	125 000	3350	58 000	2200
Small pore, 60 by 20 μm	201 000	5400	114 000	4400
Large pore, 300 by 120 μm	58 000	1500	19 000	720

3. No account has been taken of short crack effects.
4. Crack closure behavior may vary with strain amplitude.
5. The linking of multi-ply initiated cracks has been ignored.

It is likely that the first three factors all have negligible effects, as it is known that initiation generally occurred within 15 percent of fatigue life at sharp pores 50 to 200 μm deep. Hence soon after initiation the pore and crack can be considered together as a longer crack of a size greater than the 100 μm limit [7] for short crack behavior.

The other two factors could cause the major errors in the predictions. At short lives cycles-to-failure are over-estimated for both irons, whilst at long lives the lives of the pearlitic specimen are under-estimated and those of the ferritic specimens are predicted with reasonable accuracy. At these long lives, the pearlitic specimens were fully elastic, whilst the ferritic specimens contained some plasticity. The differences in life prediction at these low strains may perhaps be attributed to differences in crack closure behavior as the proportion of plastic to elastic strain is varied. In specimens tested at high strains, replica observations showed the crack to be open throughout the load cycle. Closure behavior has not, however, been closely investigated at low strains, and it may be that crack closure during the compressive half of the cycle could reduce the effective ΔJ and prolong life, when strains are elastic.

At high strains the predictions over-estimate fatigue life. At these strains, multiple crack initiation was observed and some of the crack growth occurred by crack coalescence rather than by crack-tip advance through the specimen. Hence a single crack model will tend to over-estimate life.

There are two major points of difference between the nodules and the pores. Firstly, Fig. 2 shows that there is a substantial difference in the size distribution of the two although there is some overlap; secondly, the pores have much sharper radii of curvature and so are more effective stress concentrators. If a small pore and a similar sized nodule are treated as crack-like defects, the integrations predict that similar lives can be expected.

A more valid analysis would treat the nodules and pores as notches. Stress intensity solutions of a crack growing from a circular hole (nodule) and an elliptical hole (pore) of similar diameters or lengths are given in Ref 22. This shows that once the crack has initiated and grown a distance equal to the hole diameter or length, there will be little difference in crack growth behavior between the cracks growing from nodules, and those growing from pores of the same length. There is a much greater difference in stress intensity (or J -value) between cracks emanating from pores of different sizes than between pores and nodules of the same size. Thus, in the absence of crack initiation effects, starting defect size is the major influence in life.

However, small pores have been observed to cause failure in preference to nodules. The lower stress concentration of the nodules will affect crack initiation as well as crack growth, and it is thought that crack initiation from the

nodules may be quite slow. To investigate this, the recorded replicas were studied further to observe the behavior of cracks initiating at nodules. At high strains, a large number of such cracks were found. Most of these cracks did not, however, show measurable growth until about 50 percent of life. At low strains very few cracks were found. Those associated with nodules were very small, even at failure lives.

At low strains approaching the fatigue limit, the work of Murakami and Endo [23] suggests that nodules and pores less than a certain size will develop nonpropagating cracks. Murakami and Endo showed that artificial holes less than 100 μm in diameter had no effect on the fatigue limit of mild steel, since the cracks initiating from them became nonpropagating. The pores and nodules in these cast irons are of similar size. Further replica work is in progress to see if such cracks can be observed.

The integration predicts that a ferritic specimen containing a very small 60- μm pore will last six times as long as a specimen with a very large 300- μm pore, whatever the applied strain amplitude. In the course of work on these irons, a hundred strain life tests have been performed on specimens cut from commercial axle casings and a scatterband of lives obtained. At low strain amplitudes this variation in fatigue life is actually observed, but at high strains the observed scatterband is much narrower than predicted. The reasons for this discrepancy are not clear. At high strains, multiple crack initiation and crack linkage were common, and these may reduce the dependence of fatigue life on the extremes of defect sizes.

Traditionally nodule size is one of the parameters used to judge the quality of SG iron castings. The present work, however, shows that nodules do not affect fatigue life. For maximum fatigue resistance the size and distribution of microshrinkage pores must be controlled, since these are the defects initiating fatigue failure.

Conclusions

1. Failure cracks in smooth specimens of SG irons have been observed to initiate invariably at pores rather than nodules. Initiation generally occurred within a few percent of the total fatigue life, the remainder of life being occupied by microcrack growth.
2. The growth rates of these small cracks, less than 4 mm in surface length, have successfully been correlated, in the presence of large plastic strains, with the parameter ΔJ .
3. Using a crack growth law derived from the ΔJ correlation, fatigue lives of smooth specimens containing a variety of pore and nodule sizes have been calculated by assuming the pores and nodules to be crack-life defects. The predicted life tends to over-estimate observed lives at high strains. All estimates are within a factor of four of the observed value.
4. In general, pores are much larger than nodules, and calculated lives in-

dicating that from size considerations alone the pores will produce a substantially shorter life.

5. Small pores have additionally been observed to initiate failure cracks in preference to nodules larger than themselves. This suggests that cracks initiate more readily from the pores.

6. This deduction has been supported by replica observations. Nodules do not initiate cracks until late in life and at failure these cracks are still very small.

7. For maximum fatigue resistance the size and number of microshrinkage pores must be kept to a minimum. The size of the graphite nodules is unimportant.

Acknowledgments

The authors would like to thank Dr. T. L. Johnston, Director of GKN Technology Limited for permission to publish this paper. Professor T. H. Topper provided many helpful discussions and Professor A. Plumtree assisted in the determination of the stable crack shape. V. Kumar helped with experimental work. The finite-element analysis was carried out by Mrs. J. Hill.

References

- [1] Coffin, L. F., *Proceedings of the Institute of Mechanical Engineers*, Vol. 188, 1974, p. 109.
- [2] Grosskreutz, J. C. in *Metal Fatigue Damage—Mechanism, Detection, Avoidance, and Repair*, ASTM STP 495, American Society for Testing and Materials, 1971, pp. 5–60.
- [3] de Lange, R. G., *Transactions of the Metallurgical Society of AIME*, Vol. 230, June 1964, p. 644.
- [4] Mayr, P. and Macherauch, E., "Principles of the Fatigue Behaviour of Plain Carbon Steels," in *Proceedings*, International Symposium on Low Cycle Fatigue Strength and Elasto-plastic Behaviour of Materials, Stuttgart, Pub. DVM, 1979, p. 129.
- [5] El Haddad, M. H., Smith, K. N., and Topper, T. H., *Journal of Engineering Materials and Technology*, Vol. 101, Jan. 1979, p. 42.
- [6] Hill, S. J. and Boutle, N. F., "Practical Aspects of Fatigue Crack Growth in Rail and Structural Steels," in *Fracture 1977*, Vol. 2, ICF 4, Waterloo, Canada, 19–24 June 1977.
- [7] Elsander, A., Hopkins, P., and Batte, A. D., *Metals Technology*, June 1980, p. 256.
- [8] Ikawa, H. and Ohira, G., *AFS Cast Metal Research Journal*, March 1967, p. 11.
- [9] Gilbert, G. N. J., *BCIRA Journal*, March 1964, p. 170.
- [10] Mitchell, M. R., *FCP Report No. 23*, College of Engineering, University of Illinois, Urbana, 1976.
- [11] de Leiris, H. and Meneorelli, E., *Revue de Metallurgie*, Jan. 1968, p. 59.
- [12] Ohasi, M., Kurosawa, M., et al, *Journal of Japanese Foundrymen Society*, Aug. 1970, p. 32.
- [13] Palmer, K. B., *BCIRA Journal*, March 1978, p. 124.
- [14] Ostensson, B., *Journal of the Iron and Steel Institute*, Sept. 1973, p. 628.
- [15] Testin, R. A., "Characterisation of the Cyclic Deformation and Fracture Behaviour of Nodular Cast Iron," M.S. thesis, University of Illinois, Urbana, 1973.
- [16] Starkey, M. S. and Irving, P. E., "Influence of Microstructure on Fatigue Crack Initiation in Spheroidal Graphite Cast Irons," in *Proceedings*, International Symposium on Low Cycle Fatigue Strength and Elasto-Plastic Behaviour of Materials, Stuttgart, Pub. DVM, 1979.

- [17] Dowling, N. E. in *Cyclic Stress-Strain and Plastic Deformation Aspects of Fatigue Crack Growth*, ASTM STP 637, American Society for Testing and Materials, 1977, pp. 97-121.
- [18] Underwood, E. E., *Quantitative Stereology*, Addison-Wesley, Reading, Mass., 1970.
- [19] MARC-CDC, "*Non-linear Finite Element Analysis Program, User Information Manual*," Vols. 1-111, Publication Nos. 17309500, 17311600, 17311700, Control Data Co., Minneapolis.
- [20] Parks, D. M., *International Journal of Fracture*, Vol. 10, No. 4, Dec. 1974, p. 487.
- [21] Shih, C. F. and Hutchinson, J. W., "Fully Plastic Solutions and Large Scale Yielding Estimates for Plane Stress Crack Problems," Division of Engineering and Applied Physics, Report No. S-14, Harvard University, Cambridge, Mass., 1975.
- [22] Tada, H., Paris, P., and Irwin, G., *The Stress Analysis of Cracks Handbook*, Del Research Corporation, 1973.
- [23] Murakami, Y. and Endo, T., *International Journal of Fatigue*, Jan. 1980, p. 23.

Growth of Physically Short Corner Cracks at Circular Notches

REFERENCE: Leis, B. N. and Galliher, R. D., "Growth of Physically Short Corner Cracks at Circular Notches," *Low-Cycle Fatigue and Life Prediction, ASTM STP 770*, C. Amzallag, B. N. Leis, and P. Rabbe, Eds., American Society for Testing and Materials, 1982, pp. 399-421.

ABSTRACT: This paper presents and discusses experimental results concerning the initiation and continued growth of cracks in thin circularly notched sheets. Data are reported for specimens and test conditions selected to examine the influence of (1) free surface and (2) inelastic action on the behavior of cracks at notch roots. Results of the study suggest that proximity to a free surface causes first a decrease and then an increase in the growth rate of physically short cracks at notches. This is postulated as being due to blunting of very short cracks and growth in a plane stress field, respectively. Inelastic action at notch roots, by contrast, is associated with increased growth rate within the notch plastic field. Its influence, therefore, is felt over distances equal to the plastic zone size so that its effect need not be restricted to physically short cracks. It is shown that current models which attempt to account for the influence of inelastic action and free surface on crack growth rate through empirical modifications to linear elastic fracture mechanics analysis are, in general, both inappropriate and inadequate.

KEY WORDS: physically short cracks, fatigue, fatigue crack growth rate, inelastic action, notches, corner cracks, free surface

Research in fatigue life prediction schemes during the last several years has culminated in recent attempts to couple previously independent developments in crack initiation and crack propagation analysis (for example, [1]).² Studies in crack initiation had focused on nonlinear models of a damage process which predicts the formation of a small crack using reference data developed from small diameter smooth specimens (for example, [2]). In contrast, studies in crack propagation analysis have utilized linear elastic fracture mechanics (LEFM) to predict the crack growth rate using reference data developed from specimens containing macrocracks (for example, [3]). Clearly, the fatigue process being modeled in this context does not undergo a distinct transition from that modeled by the smooth specimen to that modeled by the

¹Senior Research Scientist and Research Scientist, respectively, Battelle Columbus Laboratories, Columbus, Ohio 43201.

²The italic numbers in brackets refer to the list of references appended to this paper.

macrocrack geometry. As such, difficulties have been encountered in achieving similitude in the damage processes being compared [4,5]. These difficulties have in turn resulted in a number of studies which discuss the analytical marriage of initiation and propagation models (for example, [4–10]) and the phenomenology of the damage process (for example, [11–17]). With regard to initiation, these studies have examined factors which control growth first as a microcrack, then as a macrocrack. In the context of growth, similar studies have been performed to establish factors which cause the observed nonunique correlation of stress intensity factor, K , and crack growth rate, da/dN (for example, [11–15]).

The purpose of this paper is to present and discuss experimental results on the nucleation and continued growth of corner cracks at circular notches in thin aluminum sheet specimens. The object of this study is to develop a better understanding of the nucleation and early growth of fatigue cracks. Specifically, specimens and test conditions have been chosen to examine two aspects considered significant with regard to microcrack growth and the observed nonunique correlation of K and da/dN . The first pertains to a study of the postulate that observed differences in physically long and short cracks are due in part to displacement controlled growth of cracks at inelastically strained notch roots. The second pertains to a study of free surface effects on crack development. These aspects are examined at length following sections which address experimental details and results, and data analysis. Finally, the paper closes with a general discussion of how these results impact on present models of the so-called short crack behavior.

Experimental Aspects

Material and Specimens

The data to be presented have been developed from thin sheet specimens tested under conditions chosen to create either a small notch root plastic zone or a moderate but still contained plastic zone. Thin sheets have been used to develop corner cracking to emphasize the role of a free surface. Notch profile was, however, fixed as circular because the desire was also to examine a situation commonly found in practical problems.

The geometry chosen was a plate 7.62 cm (3 in.) wide by 15.25 cm (6 in.) long containing a central circular hole 1.25 cm (0.5 in.) in diameter. For the sheet thickness of 0.23 cm (0.090 in.), three-dimensional elasticity solutions [18] and elastic-plastic finite element analysis [19] indicated essentially a plane stress state exists at the notch root. Also, finite element analysis indicated the theoretical elastic stress concentration factor, K_t , was 2.5 at the point of maximum stress on the notch boundary. Experiments [20] indicated K_t was 2.56.

The material investigated was part of a pedigreed heat of 2024 series aluminum alloy extensively explored by NASA and their contractors since the

1950s. Using current nomenclature, the materials designation would be 2024 T351. Specimens were aligned with their long axis parallel to the rolling direction. Machining practices used were selected so as to reduce residual stresses. Notches were honed after boring. Further details regarding the material, including cyclic deformation and fatigue resistance, and specimens can be found in Refs 19 and 20.

Crack Measurement Technique

Optical methods involving essentially continuous observation at $\times 40$ via a traveling microscope with a least count of $10\text{ }\mu\text{m}$ were used to detect and monitor the growth of small cracks. Included were initial crack lengths as small as $25\text{ }\mu\text{m}$. Before considering results of such measurements, it is appropriate to discuss the accuracy of the measured crack length in the short crack domain. As elaborated in Ref 16, there are at least three possible sources of error: locating the crack tip, determining the absolute length of the crack, and determining the relative advance of the crack. To reduce the influence of these errors, surfaces of the specimens near the notch root have been metallographically prepared using standard techniques down to $1\text{-}\mu\text{m}$ diamond paste. Even so, these errors are important and so are further elaborated.

The first significant point relates to the repeatability in locating a tight crack tip that lies in a region of significant cyclic plasticity. Uncertainties of 10 percent are not unreasonable in this context. A second significant source of error enters through the resolution of the microscope vernier. In this and other comparable studies, the resolution is about $10\text{ }\mu\text{m}$, approximately one half of the length of the crack being measured. Clearly then, an uncertainty of 50 percent is possible in a worst-case sense. Finally, there is at least one further source of uncertainty which arises in the context of crack extension. Say, for example, that the short crack domain is on the order of $125\text{ }\mu\text{m}$ (0.005 in.). If one chooses to make five readings in this domain, then one would seek to measure increments of $25\text{ }\mu\text{m}$, just twice the resolution of the vernier. Again, on a worst-case basis, the uncertainty is on the order of 50 percent. Thus, in a worst-case sense, the most probable error is $(0.1^2 + 0.5^2)^{1/2} \approx 50$ percent for either the absolute length or the increment in crack growth. Therefore caution must be used in interpreting the data that will be presented both here and in papers using comparable techniques. Such care should be taken even if the uncertainty is less than that for this crude worst-case analysis.

Experimental Procedure and Program

Experiments have been performed in axial load control. Data have been developed from constant-amplitude fully reversed cycling and zero to tension cycling. Antibuckling guides have been used to avoid instability for the fully reversed loading condition. Details of these guides and other related in-

formation can be found in Refs 19 and 20. Fully reversed cycling at ± 144.7 MPa (21 ksi) was used to generate very limited notch root plasticity, whereas zero to tension cycling at a maximum stress of 255 MPa (37 ksi) was used to generate a much larger but still confined plastic zone. Finite element analysis of this test geometry [19] indicates these stresses develop plastic zones with lengths of $12.5\text{ }\mu\text{m}$ (0.0005 in.) and 0.33 cm (0.13 in.), respectively, along the transverse net section. Data were developed from a total of 27 microcracks which initiated and grew in 3 specimens, one tested at $R = -1$ and two at $R = 0.01$.

Experimental Results

Raw Data

Data generated in fatigue crack growth studies are characterized by two variables: crack length and cycles. Raw data developed in this study are pre-

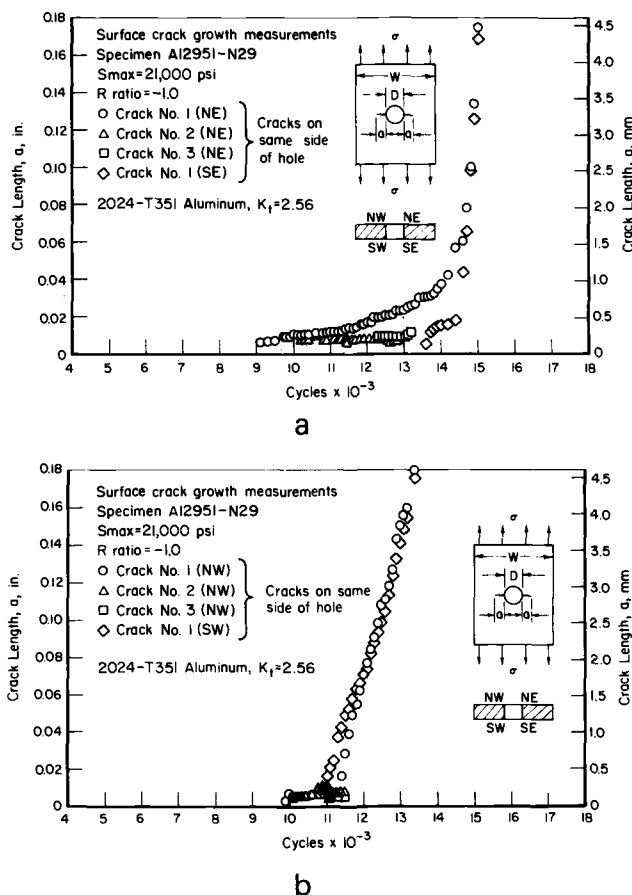
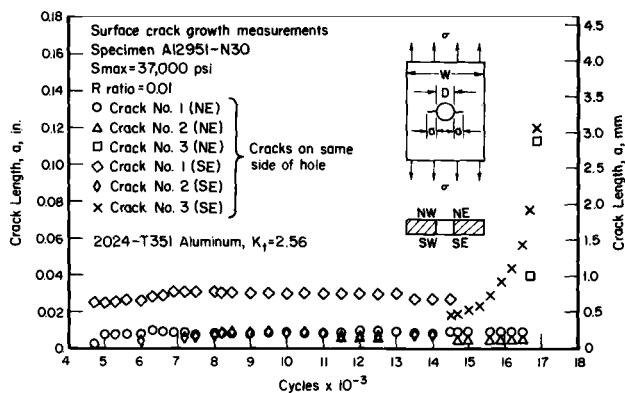
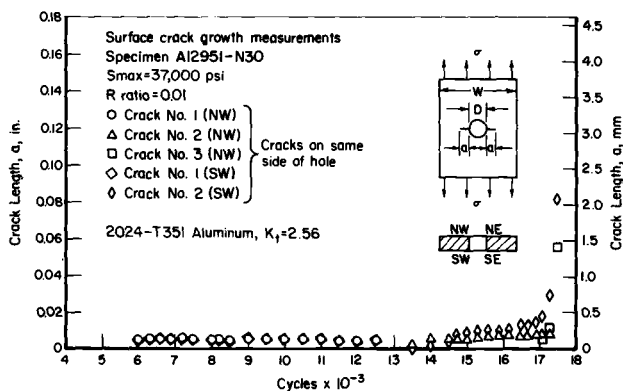


FIG. 1—Crack length as a function of cycles; Specimen N29. (a) NE/SE side. (b) NW/SW side.



a

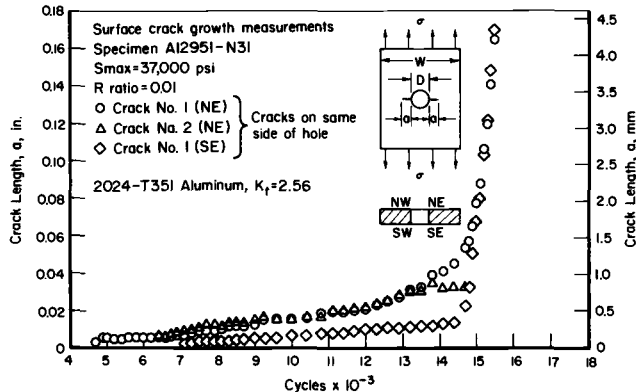


b

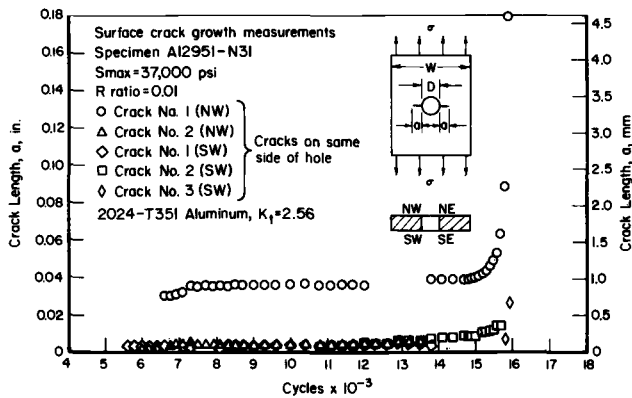
FIG. 2—Crack length as a function of cycles; Specimen N30. (a) NE/SE side. (b) NW/SW side.

sented in parts *a* and *b* of Figs. 1, 2, and 3, on linear coordinates of crack length versus applied cycles. Note that while only $3 \times 2 = 6$ notch roots, data are presented for a total of 27 cracks. This is because numerous cracks nucleate and exist for many cycles before a dominant crack develops or corner cracks link up. Note too that the length plotted is taken with respect to the edge of the notch, not the center of the hole.

It is appropriate to comment here on the term crack length. Unless non-destructive techniques which measure crack area are used, one is obliged to make surface measurements of crack position. In this study, such measurements have been made on the face of the specimen. Crack lengths reported in Figs. 1 to 3 are therefore surface measurements. They do not reflect the two-, possibly three-dimensional nature of the crack. The second dimension of growth has been obtained for purposes of analysis via detailed low-power



a



b

FIG. 3—Crack length as a function of cycles; Specimen N31. (a) NE/SE side. (b) NW/SW side.

stereo-optical microscopy ($\times 10$ to $\times 40$) and higher power scanning electron microscopy (SEM; $\times 50$ to $\times 5000$). Details of this study, with the exception of the brief discussion that follows, are beyond the scope of this paper, but are reported elsewhere [21].

Fractography indicated that most cracks initiated as corner cracks. Initiated corner cracks had aspect ratios (that is, surface length from notch root divided by depth through thickness or a/c) of about 1.0 and, for the most part, grew in a self-similar fashion until their rather quick transition to a planar front. Fractography also indicated multiple through-thickness initiation sites in a few cases, but this is not surprising in that the driving force for growth based on notch stress is greatest at the notch root. Generally,

both corner and midthickness initiation/microcracking occurred on macroplanes perpendicular to the maximum principal stress, as shown in Fig. 4. Figure 5, by contrast, shows that the growth process of a dominant crack certainly does not occur on a single macroplane and involves much branching. Scanning microscopy indicated that, in the vicinity of initiation, the fracture surface is feature free, almost brittle-like, as shown in Figs. 6 and 7. Once away from the initiation site, the fracture surfaces showed patches of striations with locally different orientations until far enough away that a dominant crack front developed. The brittle-like appearance, perhaps associated with crystallographic Stage I growth, is compatible with the burst of growth recorded using a very sensitive eddy-current detection scheme in a prior study on identical specimens [19].

Observe in Fig. 1*a*, which plots data for $R = -1$ cycling at an amplitude of 144.7 MPa, that three corner cracks develop on the side designated NE. One initiates and goes dormant, a second initiates, grows somewhat and then goes dormant, whereas a third initiates and becomes dominant. After the dominant crack is about halfway through the thickness, a crack develops on the other face and very quickly grows to match its counterpart. At the other notch root, designated NW, results for which are plotted in Fig. 1*b*, three cracks again initiate. One crack quickly dominates and grows rather quickly. Likewise, a crack develops on the other face and also grows rather quickly. There is certainly little unusual about this behavior, with perhaps the exception of the multiple initiation and growth of the secondary cracks long after

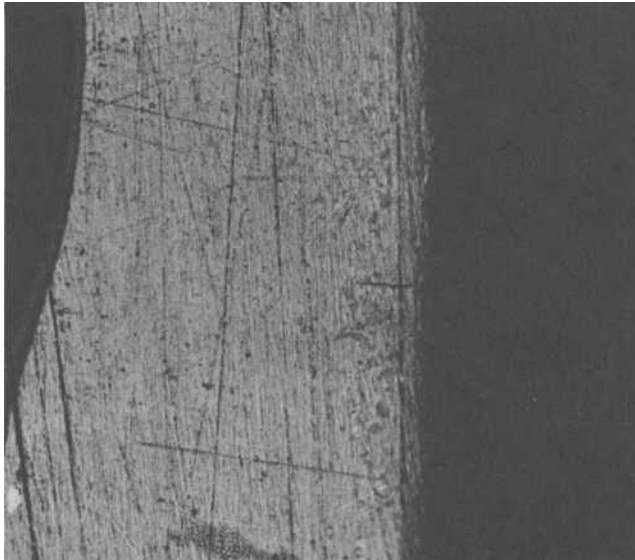


FIG. 4—Fatigue microcrack; Specimen N31; optical at $\times 250$.

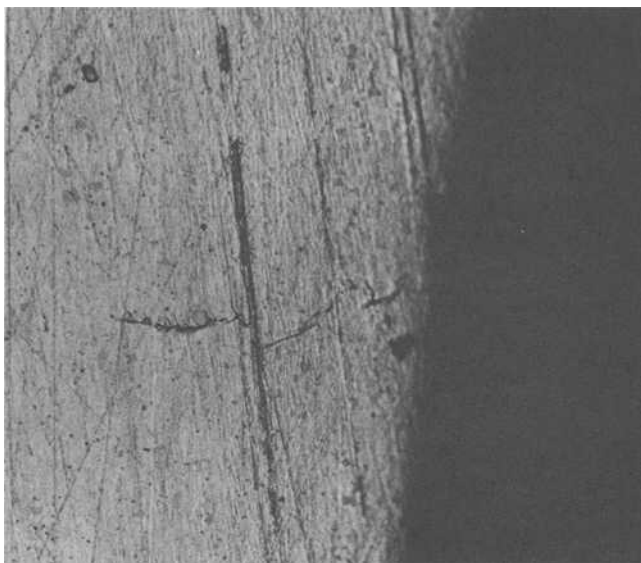


FIG. 5—Fatigue microcrack; Specimen N31; optical at $\times 250$.

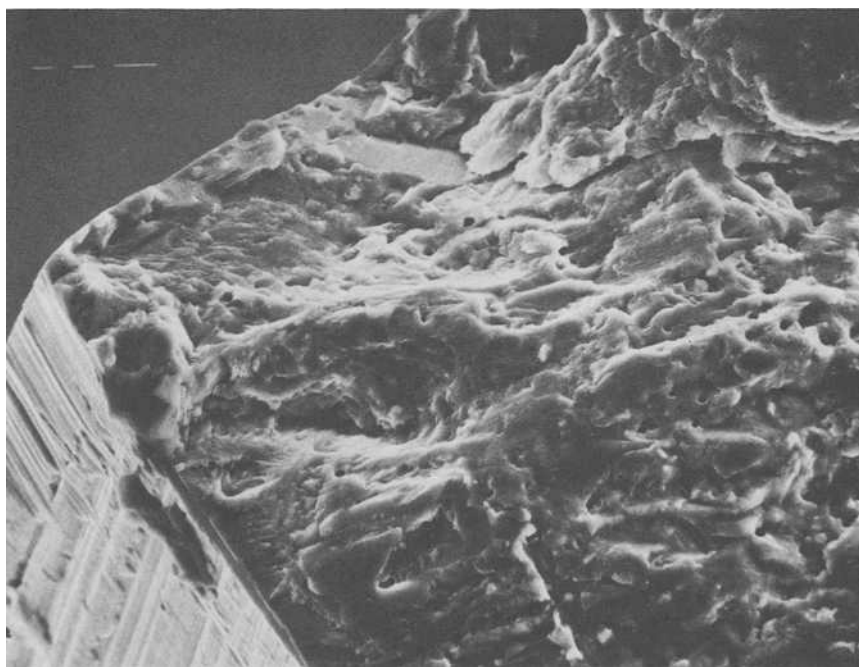


FIG. 6—View of fracture surface; Specimen N29; SEM at $\times 500$.

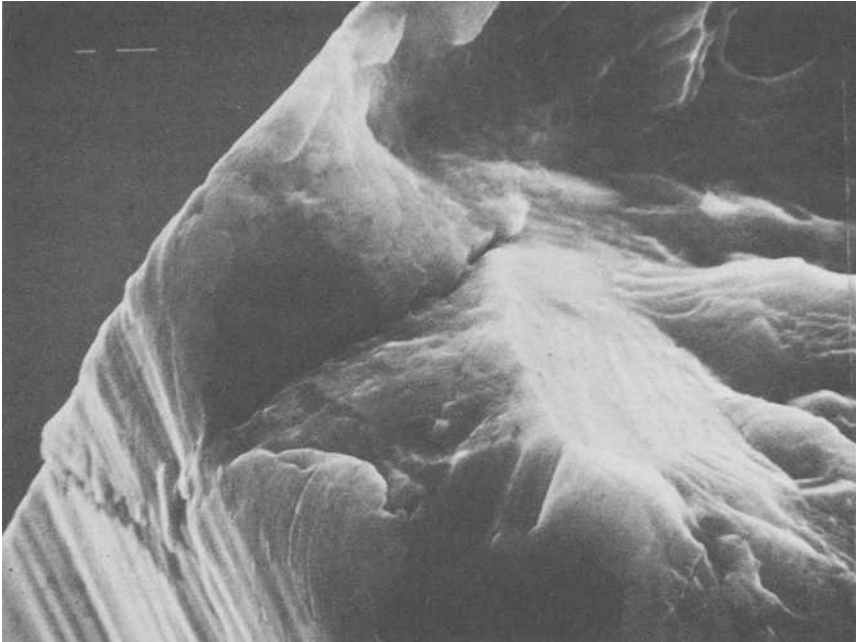


FIG. 7—View of fracture surface at corner; from Fig. 6; SEM at $\times 5000$.

a dominant crack develops. Such multiple initiation is common even at sharper notches.

Figures 2 and 3 present data for $R = 0.01$ cycling at a maximum stress of 255 MPa. Note that six cracks initiate in Fig. 2a. Of these, one appears on each of the opposite faces of the plate less than 100 cycles after the most recent inspection for cracks. The initiation and early growth, therefore, occur very quickly. But measurements and fractography indicate that the early growth is not continuous. In one of the two cases, crack 1 on the SE side, a very large crack developed. If its growth had been continuous, the rate would be on the order of 5.08×10^{-4} cm/cycle (2×10^{-4} in./cycle)! It is believed that, based on the feature-free appearance of the fracture at initiation, much of this advance occurs in a very few cycles, perhaps as brittle crystallographic advances near and on the free surface. A total of four other cracks initiate and grow before two become dominant.

It is significant to note that the first cracks to initiate in the foregoing cases do not become the dominant cracks. Equally interesting is the apparently dormant nature of the cracks once initiated. Such behavior, however, has been observed before (for example, [22]). It would appear on the basis of these results that the "initiation" of a small crack, say, $125 \mu\text{m}$ (0.005 in.) long, is a process which occurs rather quickly, and that the initiated crack

may then lie dormant for some time. Depending on the frequency of observation, one could say then that "initiation" occurred over a broad range of cycle numbers. That is, ascertaining when the initiation event occurs is somewhat uncertain.

Given the results in Fig. 2*b* which in essence parallel those of Fig. 2*a*, one could say that the aforementioned observations are not unique and therefore they are not a statistically rare occurrence. Again, initiation occurs very soon after the most recent inspection, and then the first-to-initiate cracks lie dormant for some time. Likewise, the first-to-initiate cracks do not necessarily develop into the dominant cracks leading to separation. As with the companion notch root, all cracks begin as corner cracks. All dominant cracks are plane fronted near the transition from relatively slow growth to more rapid growth.

Results presented in Fig. 3 have been developed under test conditions identical to those for the data in Fig. 2. As with the results in Fig. 2, these data exhibit patterns seen in the other data as well as some unusual trends. In keeping with the other data, cracks are observed very soon after the most recent detailed visual check. Several initiate and again a dormant behavior is evident, with the exception of cracks 1 and 2 on the NE corner (Fig. 3*a*). In this case, the growth of two different cracks occurs in an apparently continuous fashion. Strangely, both cracks grew some 0.76 mm (0.03 in.) before one became dominant. Note in Fig. 3*b* that the multiple initiation and dormant period followed by the initiation of yet another crack which becomes dominant, reminiscent of the data of Fig. 2, is also evident. Also evident are results for two cracks which developed at the NW corner. Of these two, one initiated at the notch root, the other some distance from it in the bulk material. After initiation, both lie dormant before that which initiates in the bulk became dominant.

Generally speaking, the trends evident in Figs. 2 and 3 are not that different from Fig. 1, with the possible exception of the dormant behavior and the fact that the first-to-initiate crack did not grow to become dominant. In all cases, "initiation" occurred very soon after the most recent detailed visual inspection, with the first observed crack being quite large, namely 25 to 125 μm (0.001 to 0.005 in.). Concern for the existence of a threshold of detection at that level grew as a consequence of this trend. However, companion studies in which the sample is removed and examined at $\times 250$ in a metallurgical microscope at periodic visual inspections indicated that the apparent burst of growth which appears to constitute the initiation event is not an artifact, at least for this material. Finally, it might be noted that fractographic examination suggests that the trend of increasing growth rates following the dormant period is associated with the transition from corner to near planar cracking. This transition appears to occur through corner crack link-up with cracks which initiate after the corner cracks at or near midthickness.

Growth Rate as a Function of Crack Length

Before crack growth rates can be pursued as a function of crack length, scheme(s) to compute growth rates from discrete data must be selected. A simple slope (point-to-point) scheme could be used. Alternatively, a three-point divided difference scheme or an incremental polynomial that is fit to some larger number of data points could also be used. But, if indeed there are significant changes in the growth rate as the crack extends, grouping a large number of points in the analysis may mask such a trend. In this study, only the three-point scheme has been considered.

Crack growth rate data determined as noted above are plotted as a function of the surface crack length in Figs. 8, 9, and 10. Data presented in Fig. 8 correspond to those of Fig. 1, whereas data in Figs. 9 and 10 correspond to those of Figs. 2 and 3, respectively. In contrast to Figs. 1 to 3, these figures plot fewer curves. This is a consequence of the fact that, with the exception of four corner cracks per notch, once initiated all other cracks went dormant. No useful da/dN data is generated by these basically dormant cracks. In view of this, each of Figs. 8 to 10 include at most four data trends.

With respect to Fig. 8, note that data plotted, which reflect all three growing cracks, follow the same trend. At short crack lengths, beyond the plastic

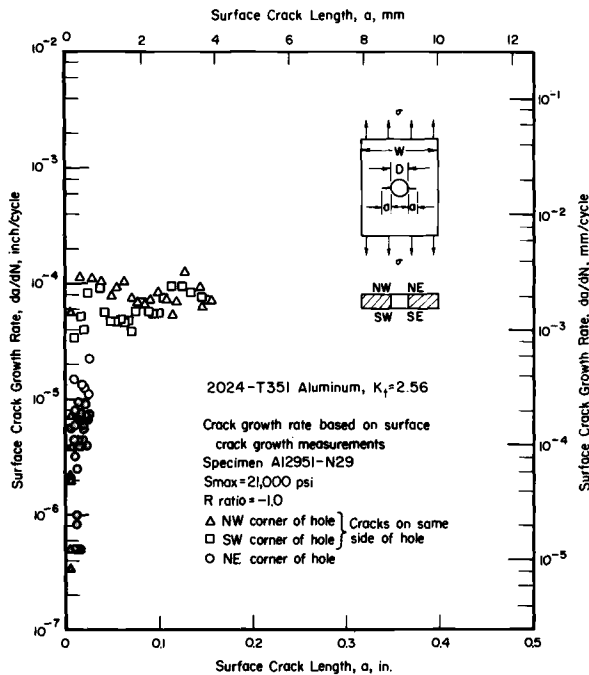


FIG. 8—Crack growth rate as a function of crack length; Specimen N29.

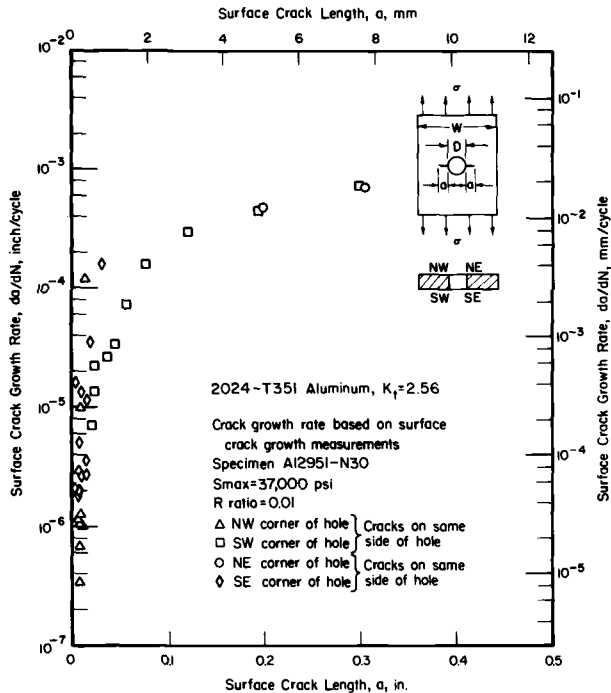


FIG. 9—Crack growth rate as a function of crack length; Specimen N30.

zone but shorter than the apparent transition to planar cracks, the growth rate appears to increase in a log-linear fashion with crack length. This apparent trend, however, is not borne out by tabulated data which consistently show that, amidst the scatter, there is an increase in rate, followed by a decrease, followed again by an increase as the crack transitions to through crack. Beyond that, the rate of increase in growth rate decreases abruptly but retains a positive slope. This change in the rate of change of growth rate with crack length occurs well beyond the notch plastic field. Indeed, all data shown are beyond the notch field, so that interaction with the notch plastic zone must be ruled out in examining this trend. It remains then to explore the influence of free surface on this behavior.

As shown in Fig. 8, the change in growth rate behavior is associated with at least the transition from surface to planar cracking. This is evident in the figure by comparing shaded points which denote corner cracks as opposed to open points which denote essentially planar or planar fronted cracks. In this context, one can argue that the free surface influence on growth rate is significant, although as noted later it is not entirely responsible for this trend. Similar trends occur for the results presented in Figs. 9 and 10.

Data plotted in Figs. 9 and 10 have been obtained under circumstances for

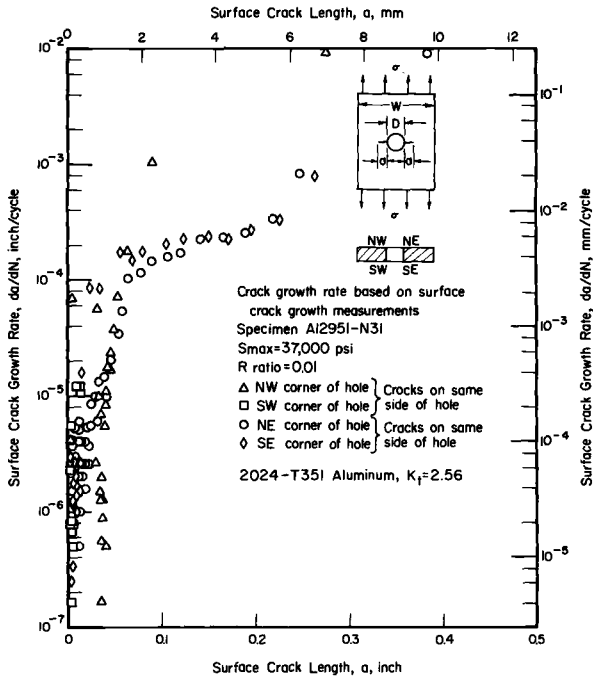


FIG. 10—Crack growth rate as a function of crack length; Specimen N31.

which the notch plastic zone encompasses the crack until it is about 0.33 cm (0.13 in.) long. As shown by the trends for each of the four cracks for each notch, the initial behavior parallels that of the lower stress data presented in Fig. 8. Indeed, a check shows that the transition in growth rate behavior does match the transition from corner to planar cracking as shown in the figures. Beyond the apparent plateau in growth rates evident in Figs. 8 to 10, Figs. 9 and 10 show a trend for growth rate to again increase, whereas Fig. 8 does not. This may be due to yet another possibly significant factor which contributes to the behavior shown in Figs. 8 to 10, as elaborated next.

Cracks in Fig. 8 grow in a load-controlled elastic domain perturbed only by the crack-tip plastic zone. In contrast, up to a length of about 0.33 cm (0.13 in.), those in Figs. 9 and 10 grow in the inelastic field of the notch. Beyond that, they grow in a domain such as that for the data of Fig. 8. Both Figs. 9 and 10 show that there is an abrupt change in the rate of crack growth once the cracks grow beyond this notch plastic field. The question to be answered in this regard is: Does the essentially displacement-controlled domain of the notch plastic field alter the growth rate behavior? To answer this requires that the data of Figs. 8 to 10 be plotted on a common basis. The linear elastic fracture mechanics (LEFM) stress intensity factor, K_I , is such a basis.

Stress Intensity Factor Analysis

In simple functional form, K is defined for Mode I loading as

$$K = \beta(a)S\sqrt{\pi a} \quad (1)$$

where S is the far field stress, a is the semicrack length, and $\beta(a)$ is a function of the geometry and crack length. It has been postulated [23,24] that the fatigue crack growth rate is a unique function of K and other constant parameters that pertain to the loading, specifically the ratio of the minimum to maximum stress, R :

$$\frac{da}{dN} = g(\Delta K, R) \quad (2)$$

In this equation, ΔK is defined from the cyclic range of stress, ΔS , inserted into Eq 1. It should be emphasized that in LEFM the confined crack-tip plastic zone size, r_p , is a unique function of K :

$$r_p \propto K^2 \quad (3)$$

Consequently, care must be exercised in interpreting data from histories where r_p is history-dependent and not uniquely related to the current value of ΔK (or K_{\max}). Likewise, a significant limitation to the utility of LEFM in the present context is that it is valid only so long as the plastic zone is small compared with the crack length. Although it is recognized that this limitation can cause difficulties in using Eq 1 [25], the LEFM ΔK will be used because (1) crack tip and notch plasticity are reasonably confined, and (2) there is no rigorously developed alternative as yet.

The use of Eqs 1 and 2 requires definition of $\beta(a)$ for the geometry of interest. Values for $\beta(a)$ can be obtained for the geometry at hand via detailed numerical analysis or by compounding available solutions. Both approaches have been pursued in the present, the results of which are shown in Fig. 11. Note that several avenues to compute $\beta(a)$ are included. With respect to Fig. 11a, which presents results for through-thickness cracks, note that finite element results developed using the work energy method [26] for the geometry of interest differ significantly from both the Bowie solution [27] and another numerical result [28], both of which are for an infinite sheet. This difference is particularly significant at the shorter crack lengths, obviously because of the notch field. In view of this, there is a need for K -solutions for the specific geometry of concern if sense is to be made of the growth of physically short cracks. As such, in dealing with through cracks in this study, the solution for the geometry of interest was used to estimate $\beta(a)$. That curve is denoted "this study".

Figure 11b presents results for part-through (corner) cracks with an aspect ratio, $a/2c$, of 0.5. Results are presented for a variety of geometries, all of which are reasonable approximations to that of interest in this paper. Notice

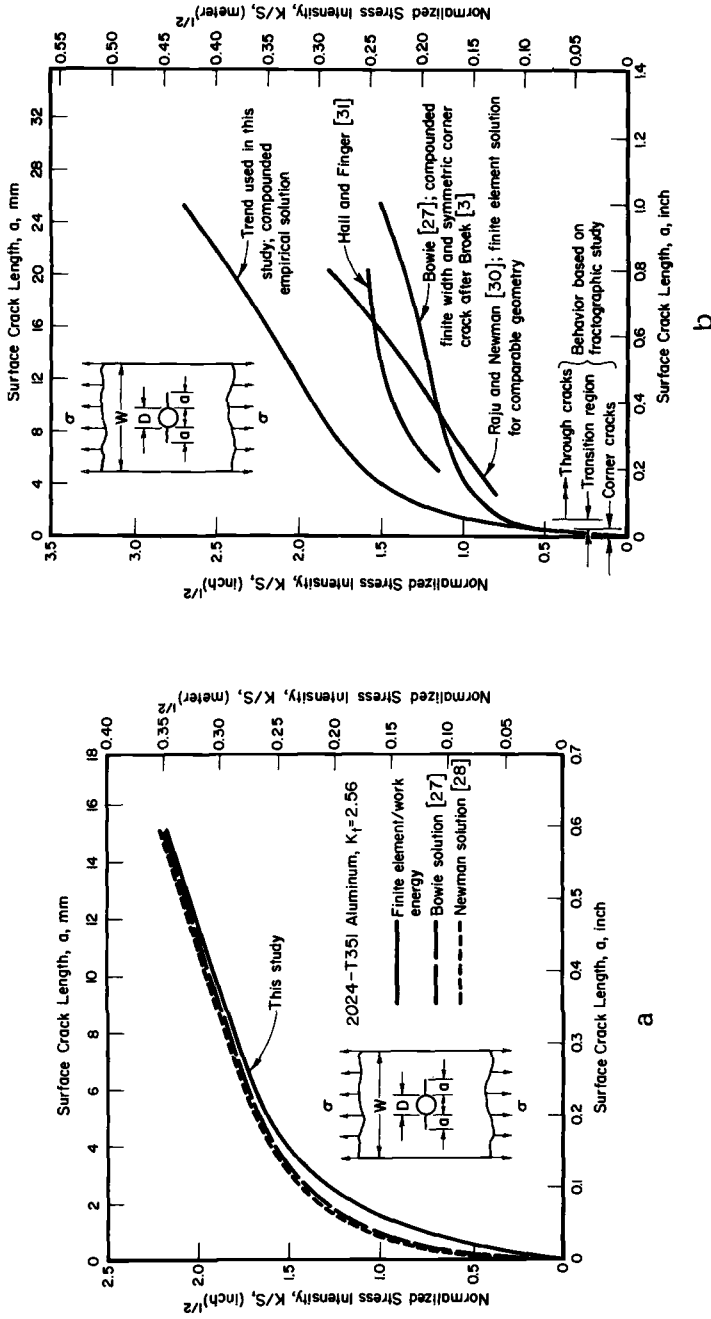


FIG. 11—Normalized stress intensity factor as a function of crack length. (a) Through-thickness crack. (b) Corner crack.

that a very large variation exists in K at a given crack length, depending on which solution is chosen. A similar observation has been made by Crews et al [29], who studied longer corner cracks in a geometry comparable to that considered here. Note too that, for a given crack length, the stress intensity is much less than that for a through crack of the same length. Finally, note that all corner cracks observed in this study transitioned to planar cracks at lengths less than 0.76 mm (0.003 in.). In this regime, there is little apparent difference in the solutions, although stress intensity is still a very strong function of crack length.

For purposes of this study, a curve compounded from corner and through crack solutions has been developed to estimate $\beta(a)$. Corner crack trends are used up to crack lengths 0.76 mm (0.03 in.) long. Thereafter, a trend which increases more rapidly than the Newman [30] transition to through cracks, shown in Fig. 11*b*, is used to smoothly shift to the through crack curve denoted as "this study" in Fig. 11*a*. This compounded empirical K -solution has been used for all corner cracks. It differs very little from the through crack solution for two reasons. Firstly, at small crack lengths, there is little difference between solutions for through and corner cracks. Secondly, the transition from corner to through cracks occurs at quite small sizes, which leaves only a very small interval over which there can be a difference. While empirical, it is believed that the K versus a curve adopted is reasonable. It should be emphasized, however, that there is a need for parametric numerical studies to reduce the uncertainty in this regard.

Crack Growth Rate as a Function of Stress Intensity

Figures 12, 13, and 14 present the crack growth rate as a function of the maximum stress intensity factor, K_{mx} . In keeping with this paper's emphasis on physically short cracks, these figures show data only during the initial growth stage, representing crack lengths from 25 μm to 1.02 cm (0.001 to 0.40 in.) long, the emphasis being at the shorter lengths.

With respect to the data presented in Fig. 12 that represent results developed beyond the inelastic notch field, note that a trend of first decreasing then increasing growth rate exists at both notch roots. This trend reflects this consistent pattern in the tabulated data as a function of crack length. That is, even in the absence of inelastic action at a notch root, crack growth rate is not a unique function of stress intensity factor. With regard to these results, note that corner crack and through-thickness crack data compare well in the domain they overlap, suggesting the empirical K versus crack length behavior adopted is reasonable. Note too that the transition in growth rate from decreasing to increasing occurs at a crack size on the order of that for which corner cracks transition to through-thickness cracks. Transition crack lengths of 0.31 and 0.51 mm (0.012 and 0.02 in.) are indicated by the figure, whereas fractographic data indicated lengths of 0.25 and 0.51 mm (0.01 and

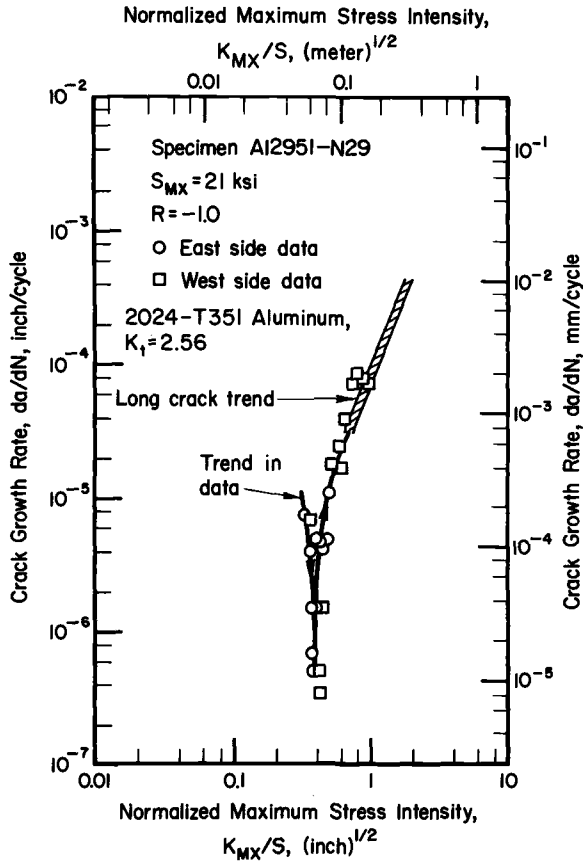


FIG. 12—Crack growth rate as a function of stress intensity factor; Specimen N29.

0.02 in.), respectively. Aside from the initial decreasing rate, the results of Fig. 12 are not unusual in that the trend for the longer cracks matches that for other published data for this material [32].

Consider next the data presented in Figs. 13 and 14. Recall that, in contrast to the test condition reflected by the data of Fig. 12, these data represent cracks which grew in the displacement controlled inelastic field of the notch for about the first 0.33 cm (0.13 in.) of growth. Thereafter they grew in a load controlled domain (compare the results of Fig. 12). At lower stress intensities, the first decreasing then increasing growth rate pattern of Fig. 12 is also evident in these data. Transition values from decreasing to increasing rates occur at crack lengths of 0.51, 0.38, 0.51, and 0.31 mm (0.02, 0.015, 0.02, and 0.012 in.). These compare well with values of 0.38, 0.25, 0.25, and 0.31 mm (0.015, 0.01, 0.01 to 0.03, and 0.01 in.), respectively, determined in the fractographic study. Beyond this transition, growth rates increased in a

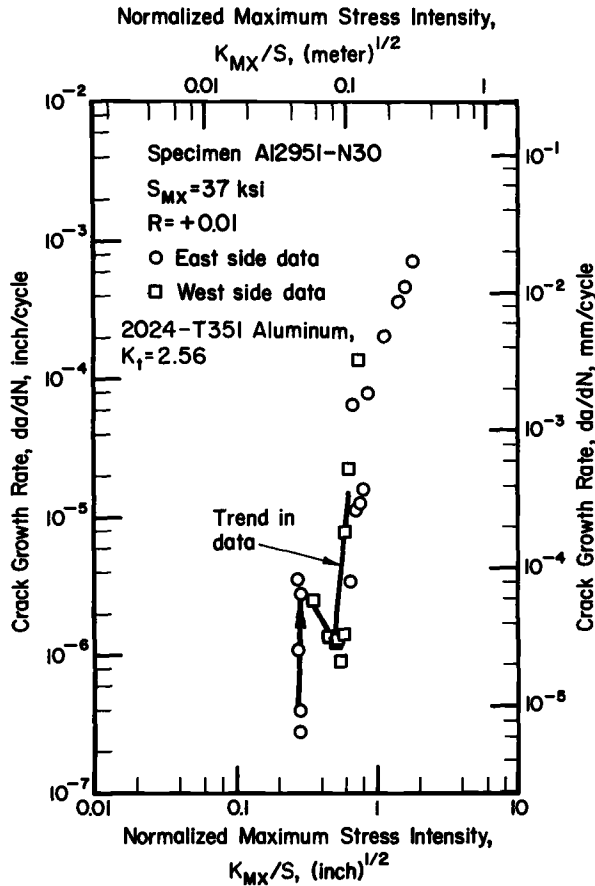


FIG. 13—Crack growth rate as a function of stress intensity factor; Specimen N30.

regular pattern. However, in all cases for which data are available (3 of 4 notch roots), once the crack becomes about 0.38 cm (0.15 in.) long, this pattern is broken. As evident in the figures, the rate of change in growth rate as a function of maximum stress intensity increases as compared to the apparent trend. This transition in the rate of change in growth rate as compared to the prior trend ends at crack lengths of 0.48, 0.43, and 0.30 cm (0.19, 0.17, and 0.12 in.). Thereafter, the growth rate trend blends into the trend published for this material [32]. It is significant that this transition in behavior corresponds closely to the notch plastic zone size of 0.33 cm (0.13 in.), an observation the significance of which will be pursued in the following section.

Discussion

In examining the growth of corner cracks at notches, a number of interesting observations have been made. Each is considered in turn in the following paragraphs.

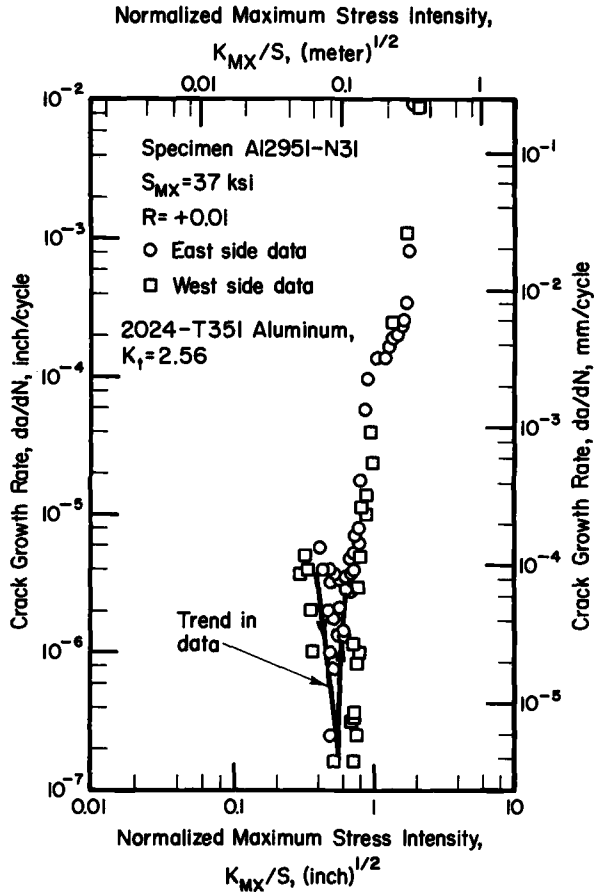


FIG. 14—Crack growth rate as a function of stress intensity factor; Specimen N31.

The initiation event occurs primarily as a consequence of corner crack initiation based on fractographic analysis. In most cases, fractography suggests this event is associated with a burst of growth which in this material, appears brittle-like, but perhaps is crystallographic Stage I growth. This observation implies the existence of a critical volume, a concept popularized in the context of size effect theories for notches. But, given the variability in the size at a given notch root, it is likely that its dimensions relate more to microstructural features like grain size, orientation, etc., as compared, for example, to some measure based on mechanics. Associated with this burst of growth are periods of rapid crack growth. The process is not continuous, however, so that these bursts are mixed into otherwise dormant periods. As many as four cracks have been observed to exhibit this behavior at one corner of a given notch root. In several cases, the first crack to initiate did not grow into the dominant crack. Indeed in several cases, many cracks initiate at comparable cycle numbers and then lie dormant until much later

when yet another crack initiates and grows stably to failure. Such periods of dormancy might be associated with blunting of the microcrack tip due to the large growth burst. This hypothesis is supported, in part, by the observation that cracks which grew continuously after initiation are not associated with large early bursts of growth.

With regard to da/dN versus a , a consistent pattern is exhibited by all cracks. At very short lengths, bursts of growth lead to locally quite high growth rates. After the growth burst, the growth rate decreases until the corner crack transitions into a through crack, a trend supported by fractographic observations. Beyond the transition to a through crack, there may be another transient in the growth rate behavior. This seems to occur when the crack grows out of the inelastic displacement controlled notch field into the load controlled "long-crack" field.

Given the aforementioned trends, the growth of these cracks from notches is controlled by free surface and inelastic action, as suggested schematically in Fig. 15. These same trends are, as expected, also manifest when these growth rate data are plotted in terms of stress intensity factor, as shown schematically in Fig. 16. Note that as the stress intensity increases, the rate decreases then increases, then goes through a transition from that increasing trend to blend into the usual "long crack" data for the material. In all cases, the trend shift decreasing to increasing rate correlated with the corner to through crack transition. Likewise, the transition to the long crack trend correlated with the shift from displacement to load controlled growth (that is, notch plastic zone size).

Summary

In view of the above, both free surface and the size of the inelastic notch field significantly influence growth rate. Now, the former depends heavily on microstructure and local constraints and the latter on notch acuity and nominal stress. Therefore it is very unlikely that the extent to which these factors cause growth rate to be a nonunique function of stress intensity can be accounted for by a simple empirical correction. As such, the success of the scheme of El Haddad et al [15], which hypothesizes that a pseudo crack length (suggested to be a material's constant) when added to the physical crack length will correlate nonunique growth rates, is open to question in more general applications. This is particularly so for large-scale plasticity [16,33]. In this context, it should be emphasized that current attempts to account for notch effects on the growth rate include an elastic correction to $\beta(a)$ in Eq 1. While inelastic stress (strain) fields could be used in place of their elastic counterpart, Eq 1 would still fail to reflect the difference in local (crack tip) control conditions; that is, the crack would still grow as a load controlled crack even though the results of this study suggest otherwise. It may be, however, that this difference in growth rate which depends on control condition could be implemented through Eq 2. In any event, it is clear

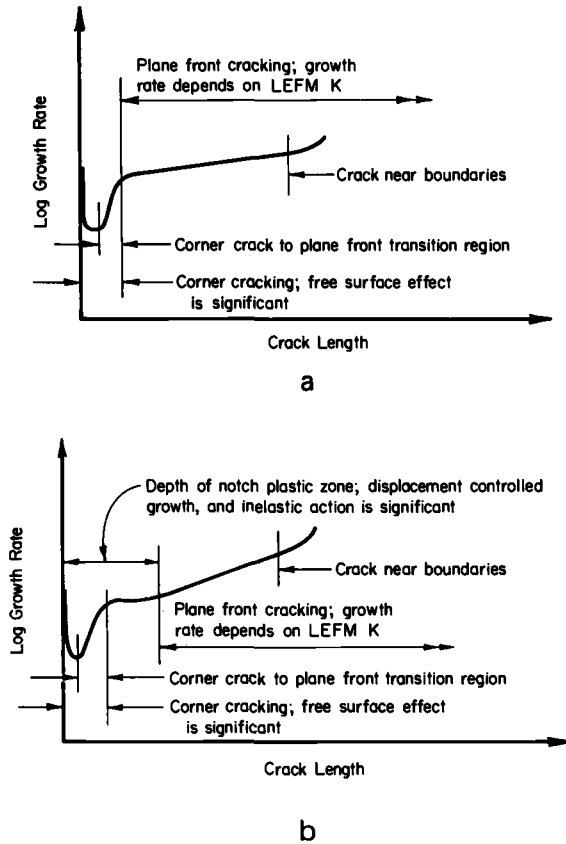


FIG. 15—Schematic of factors controlling growth rate; da/dN versus a . (a) Elastic behavior at notch root. (b) Inelastic behavior at notch root.

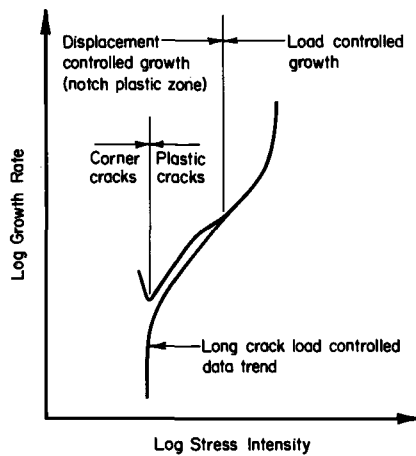


FIG. 16—Schematic of factors controlling growth rate; da/dN versus K_{MX} .

that as currently employed Eqs 1 and 2 do not reflect the growth rate process in the notch plastic field.

Finally, this paper has focused on a particular segment of the general problem of tracking initiation and propagation damage in structures. Its suggestion that free surface and inelastic action are significant in this context should not be taken to infer that they are the only important factors. The key in tracking damage seems to be careful attention to detail, ensuring that all significant factors are accounted for and that the damage processes being compared are similar.

Conclusions

A number of significant conclusions follow from this study. Included are:

1. Free surface and inelastic action at notch roots are major factors in explaining observed differences in the growth rates of cracks when correlated in terms of stress intensity. Free surface influences physically short cracks, whereas inelastic action influences the growth rate within the notch field—that is, its influence is not limited to physically short cracks.
2. Inelastic analysis that accurately portrays the driving force for crack growth in the plastic field of the notch, including the local control condition, is needed before useful predictions of growth rate and life can be made.

Acknowledgments

The experiments discussed have been performed by Mr. Norm Frey. His patience and efforts are gratefully acknowledged as is Battelle Columbus Laboratories' financial support in the area of modeling the fatigue damage process. The work energy finite element analysis reported in Fig. 11a has been done by Mr. S. H. Smith.

References

- [1] Broek, D. and Leis, B. N., "Fatigue Crack Initiation and Growth Analysis for Structures," SAE Paper No. 790511, 1979, in *Fatigued Resistance Testing and Forecasting*, SAE.SP-448, Sept. 1979, pp. 1-12.
- [2] Leis, B. N., "Predicting Crack Initiation Fatigue Life in Structural Components," in *Methods of Predicting Fatigue Life*, ASME, 1979, pp. 57-76.
- [3] Broek, D., *Elementary Engineering Fracture Mechanics*, Noordhoff, The Netherlands, 1974.
- [4] Leis, B. N. and Broek, D., *Shock and Vibration Digest*, Vol. 13, No. 8, Aug. 1981, pp. 15-28.
- [5] Broek, D. and Leis, B. N., "Similitude and Anomalies in Fatigue Crack Growth Rates," in *Materials, Experimentation, and Design in Fatigue*, Westbury House, IPC Science Press, U.K., March 1981, pp. 129-146.
- [6] Leis, B. N., "An Approach for Fatigue Crack Initiation Life Prediction with Applications to Complex Components," in *Fatigue Life of Structures under Operational Loads*, Proceedings of the 9th International Committee on Aeronautical Fatigue Meeting, ICAF Doc. 960, Laboratorium für Betriebsfestigkeit, May 1977, pp. 3.4/1-47.
- [7] Leis, B. N., "Fatigue Analysis to Assess Crack Initiation Life for Notched Coupons and

- Complex Components," Ph.D. thesis, University of Waterloo, Waterloo, Ontario, Canada, Sept. 1976.
- [8] Dowling, N. E. in *Fracture Mechanics, ASTM STP 677*, American Society for Testing and Materials, 1979, pp. 247-273.
 - [9] Smith, R. A., and Miller, K. J., *International Journal of Mechanical Sciences*, Vol. 19, 1977, pp. 11-22.
 - [10] Hammouda, M. M., and Miller, K. J. in *Elastic Plastic Fracture, ASTM STP 668*, American Society for Testing and Materials, 1979, pp. 703-719.
 - [11] Broek, D., "The Propagation of Fatigue Cracks Emanating From Holes," NLR TR 72134 U, Nov. 1972.
 - [12] Gowda, C. V. B., Leis, B. N., Charlton, R. G. and Manherz, D. W., "Effect of Gross Plasticity on Fatigue Crack Propagation in Elliptically Notched Plates," in *Proceedings*, 3rd International Conference on Fracture, Munich, April 1973.
 - [13] Dowling, N. E., "Crack Growth During Low Cycle Fatigue of Smooth Axial Specimens," Westinghouse Research Laboratories, Paper 76-1E7-PALFA-P2, 16 June 1976.
 - [14] Pearson, S., *Engineering Fracture Mechanics*, Vol. 7, 1975, pp. 235-247.
 - [15] El Haddad, M. H., Smith, K. N., and Topper, T. H. in *Fracture Mechanics, ASTM STP 677*, American Society for Testing and Materials, 1979, pp. 274-289.
 - [16] Leis, B. N. and Forte, T. P. in *Fracture Mechanics, ASTM STP 743*, American Society for Testing and Materials, 1981, pp. 100-124.
 - [17] Fine, M. E., *Metallurgical Transactions*, Vol. 11A, March 1980, pp. 365-379.
 - [18] Sternberg, E., and Sadowsky, M. A., *Journal of Applied Mechanics, Transactions of ASME*, March 1949, pp. 27-38 (Paper No. 48, APM-21).
 - [19] Leis, B. N. and Sampath, S. G., "Development of an Improved Method of Consolidating Fatigue Life Data," NASA CR 145312, Aug. 1977.
 - [20] Leis, B. N. and Frey, N. D., "Cyclic Inelastic Deformation and Fatigue Resistance Behavior of Notched Aluminum Plates," *Experimental Mechanics*, SESA, in press.
 - [21] Leis, B. N., "A Study of Corner Crack Initiation and Microcrack Growth via Optical and Scanning Microscopy," submitted to *Metallurgical Transactions*.
 - [22] Hunter, M. S., and Fricke, W. G. in *Proceedings*, ASTM, Vol. 54, 1954, pp. 717-736; see also Vol. 55, pp. 942-954, and Vol. 56, pp. 1038-1050.
 - [23] Paris, P. C., "The Mechanics of Fracture Propagation and Solutions to Fracture Arrestor Problems," Document No. D2-2195, Boeing Company, 1957; see also Paris, G. C., Gomez, M. P., and Anderson, W. D., "A Rational Analytic Theory of Fatigue," *The Trend in Engineering*, University of Washington, Vol. 13(1), 1961, pp. 9-14.
 - [24] Schijve, T., Broek, D., and deRijk, P., "The Effect of the Frequency of an Alternating Load on the Crack Rate in a Light Alloy Sheet," N.L.R. Report M 2092, 1961.
 - [25] Gowda, C. V. B., Leis, B. N., and Topper, T. H. in *Proceedings*, International Conference on Mechanical Behavior of Materials, Kyoto, Japan, Vol. II, 1972, pp. 187-198.
 - [26] Rybicki, E. F. and Kanninen, M. F., *Engineering Fracture Mechanics*, Vol. 9, 1977, pp. 931-938.
 - [27] Bowie, O. L., "Analysis of an Infinite Plate Containing Radial Cracks Originating from the Boundary of an Internal Circular Hole," *Journal of Mathematics and Physics*, Vol. 35, 1956.
 - [28] Newman, J. C., "An Improved Method of Boundary Collocation for the Stress Analysis of Cracked Plates with Various Shaped Boundaries," NASA TN D-6376, Aug. 1971.
 - [29] Sova, J. A., Crews, J. H., and Exton, R. J., "Fatigue-Crack Initiation and Growth in Notched 2024-T3 Specimens Monitored by a Video Tape System," NASA TN D-8224, Aug. 1976.
 - [30] Raju, I. S. and Newman, J. C. in *Fracture Mechanics, ASTM STP 677*, American Society for Testing and Materials, 1979, pp. 411-430.
 - [31] Hall, L. R. and Finger, R. W., "Fracture and Fatigue Growth of Partially Embedded Flaws," AFFDL-TR-70-144, USAF, Dec. 1970.
 - [32] Leis, B. N., "Displacement Controlled Fatigue Crack Growth in Elastic-Plastic Notch Fields and the Short Crack Effect," for publication in *Engineering Fracture Mechanics*.

Fatigue Crack Initiation of Cr-Mo-V Steel in High-Temperature Environment

REFERENCE: Wada, Kaoru, Iino, Yutaka, and Suzuki, Masahiko, "Fatigue Crack Initiation of Cr-Mo-V Steel in High-Temperature Environment," *Low-Cycle Fatigue and Life Prediction, ASTM STP 770*, C. Amzallag, B. N. Leis, and P. Rabbe, Eds., American Society for Testing and Materials, 1982, pp. 422-435.

ABSTRACT: The fatigue crack initiation behavior of chromium-molybdenum-vanadium steel in high-temperature air and steam was studied in respect with the cyclic frequency and oxygen concentration in the surrounding atmosphere. Fatigue tests were conducted at 565°C in air and steam at frequencies of 10, 1, and 0.1 cpm. The number of cycles to crack initiation was determined by the potential drop technique. It was found that the fatigue life to crack initiation is significantly reduced by decreasing frequency. At a low cycling frequency, the oxygen concentration determines the reduction of cycles to crack initiation. In the case of crack initiation related to inclusions, the reduction of number of cycles to crack initiation is remarkable.

KEY WORDS: fatigue crack initiation, high-temperature environment, super heated steam, oxygen concentration, cyclic frequency, chromium-molybdenum-vanadium steel, inclusion, manganese sulfide

Recent metallurgical investigation and fracture mechanics analysis have been concerned with the development of large cracks early in the service life of some steam turbine rotors. The prediction of the number of cycles to fatigue crack initiation is obviously important for the integrity assessment of such components. Fatigue cracking in turbo-machinery can arise from repeated thermally induced strains, which occur while the temperature is changing. Under high-temperature environment, however, the fatigue behavior is influenced by mechanical factors (stress level, stress ratio, cyclic frequency, etc.) and environmental conditions. Significant influences of environment on fatigue crack growth rate have been found in many metal/

¹ Graduate Student, Tohoku University, Sendai, Japan; presently on assignment to Mitsubishi Heavy Industries Ltd., Sagami-hara Machinery Works, Sagami-hara, Japan.

² Assistant Professor, Tohoku University, Sendai, Japan; presently Associate Professor, Toyota Technological Institute, Nagoya, Japan.

³ General Manager, Toyota Motor Company, Ltd., Toyota, Japan; presently Professor, Toyota Technological Institute, Nagoya, Japan.

environment systems. It has been revealed, for example, that the crack growth rate in nuclear pressure vessel steel in high-temperature water is strongly influenced by oxygen content in water and that the crack growth is enhanced as cycling frequency decreases [1].⁴ It has been shown, furthermore, that the fatigue crack growth rate in alloy steel under steam and high-temperature air depends strongly upon the cyclic shape [2]. The aforementioned fatigue behavior relates the contribution of time-dependent phenomena, such as corrosion or oxidation damage, to crack advance. With respect to environmental effects on fatigue crack initiation, it has been found that a small amount of water reduces the time to initiation of a fatigue crack in a cast steel [3]. Taking into account the environmental influences upon the fatigue crack behavior described above, one may investigate the influence of cyclic frequency and environmental conditions on fatigue crack initiation.

The experiments described in this paper attempt to examine the fatigue crack initiation of a steam turbine rotor steel under high-temperature air and steam. The tests were conducted isothermally at the maximum temperature of interest with linear elastic fracture mechanics analysis. Although the crack initiation is influenced remarkably by stress ratio and the degree of stress concentration, the crack initiation was examined mainly with respect to the environmental conditions and cycling frequency. From the evidence that some cracks were observed to be related to inclusions, the metallurgical states of the material were also taken into account in connection with crack initiation.

Material and Experimental Conditions

The material tested was 1Cr-1Mo-0.25V steel used in a steam turbine rotor. Chemical composition and mechanical properties are given in Tables 1 and 2, respectively. 1T compact tension specimens (CTS) (Fig. 1) were taken from a steam turbine rotor as shown in Fig. 2. The slit of the compact tension specimen (CTS) was made by a circular grinder cutter of 0.3 mm thick. The slit

TABLE 1—*Chemical composition of 1Cr-1Mo-0.25V steel.*

Element	Weight %
Carbon	0.27
Silicon	0.26
Manganese	0.67
Phosphorus	0.010
Sulfur	0.008
Nickel	0.34
Chromium	1.11
Molybdenum	1.23
Vanadium	0.25

⁴ The italic numbers in brackets refer to the list of references appended to this paper.

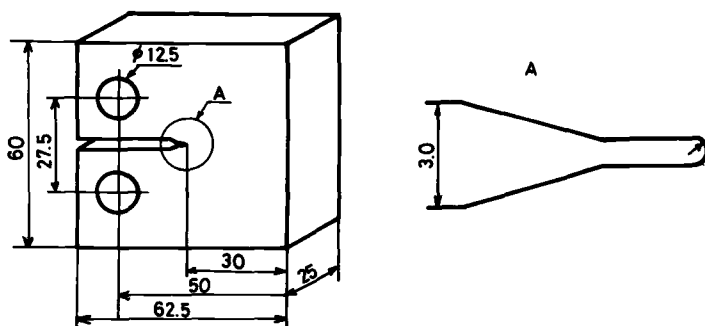
TABLE 2—*Mechanical properties of 1Cr-1Mo-0.25V steel.*

	Tensile Strength, MPa	0.2% Yield Strength, MPa	Reduction of Area, %
20°C	820	670	62
566°C	540	400	89

plane orientation was C-R as given in ASTM Test for Plane-Strain Fracture Toughness of Metallic Materials (E 399). The slit tip configuration is shown in Fig. 3. The radius of the slit tip bottom is about 0.32 mm.

Taking into account the environment in which the actual steam turbine rotor is exposed, we performed tests mainly in steam and air at 565°C. While the steam pressure in an actual steam turbine is high, the tests in this study were conducted under the steam pressure of 190 kN/m², since a compilation of data obtained by Manning and Metcalfe [4] showed that surface oxide growth is independent of steam pressure in the range of 0.1 to 16 MN/m² [5]. As a reference, the tests were performed in air at room temperature and under argon gas at 565°C. In order to examine the influence of environmental conditions upon the crack initiation, the partial pressure of oxygen in surrounding atmosphere was used as a parameter that might control the crack initiation behavior. The oxygen concentration was determined by gas chromatographic techniques.

The fatigue tests were performed in an apparatus comprised of a reserve tank, boiler, super heater, condenser, and test section (Fig. 4). The electrical conductivity of the water in reserve tank was presented at 0.5 μ mho/cm by means of the ion exchange prepared in a bypass loop parallel to the boiler-condenser loop. Dissolved oxygen in the water in reserve tank was held below 0.3 ppm by means of argon gas bubbling into the water. By using the water thus prepared, the super-heated steam was produced by boiler and super heater. Super-heated steam thus produced (pressure of 190 kN/m² and temperature at 300°C) was allowed to enter the test section, which was com-

FIG. 1—*Specimen geometry.*

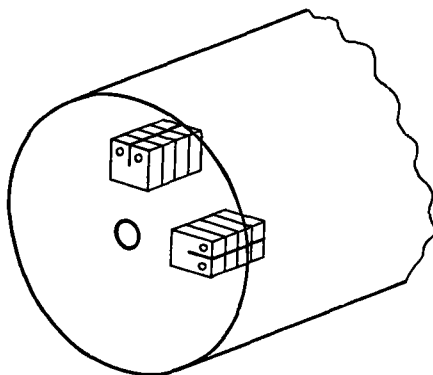


FIG. 2—*Specimen preparation.*

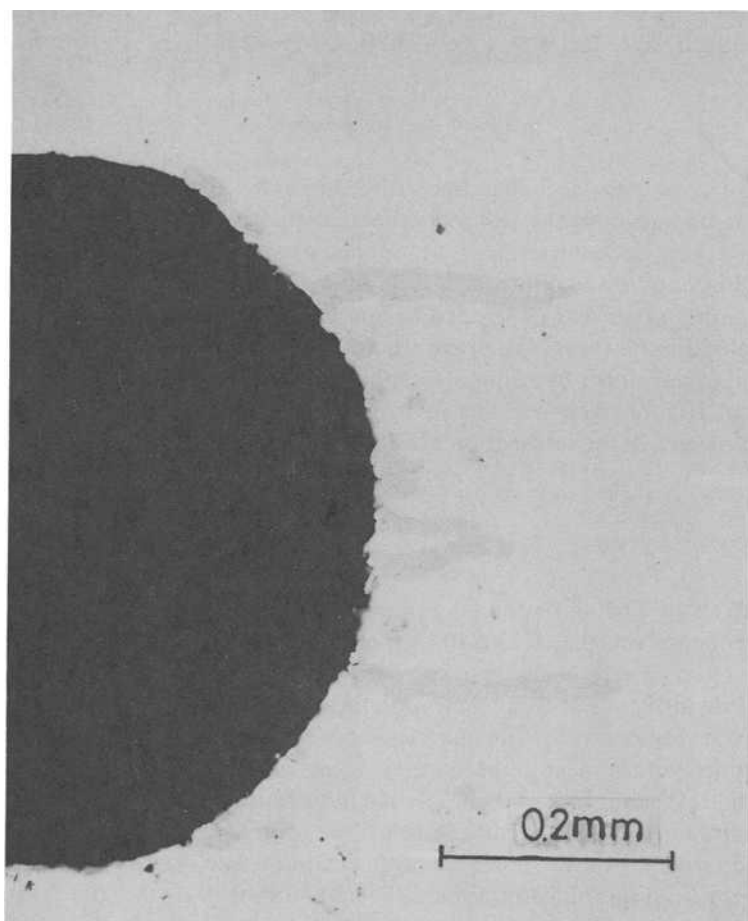


FIG. 3—*Slit tip configuration.*

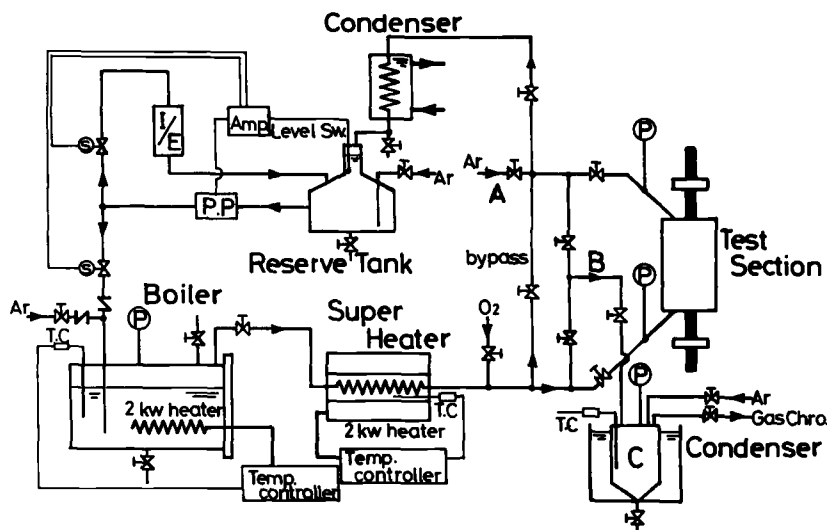


FIG. 4—Testing apparatus.

posed of a stainless steel chamber with a surrounding electrical heater. The steam temperature in the test section was maintained at $566 \pm 6^\circ\text{C}$. In the case of argon gas environment, argon gas was flowed into the test section through A and flowed out from B (Fig. 4). The temperature in high-temperature argon and air was controlled to $566 \pm 1^\circ\text{C}$.

Employing the foregoing apparatus, we conducted fatigue tests under a triangular waveform by using a servohydraulic machine with a loading capacity of 10 tons under various environmental conditions. The partial pressure of oxygen in the test section under various environments is given below:

Super-heated steam:	1.8×10^{-2} torr	at flow rate of 50 L/min
Argon gas:	9×10^{-3} torr	at flow rate of 10 L/min
Argon gas:	1.0 torr	at flow rate of 1 L/min
Air:	150 torr	

The effects of cycling frequency upon crack initiation were also examined. The frequency was 0.1, 1, and 10 cpm. The tests in air at room temperature, conducted as a reference, were carried out under a frequency of 600 cpm, since little influence of frequency upon fatigue crack behavior is observed in air at room temperature. The number of cycles to fatigue crack initiation was determined with respect to the apparent stress intensity factor range, because the radius of the slit root of the CTS used in this study is finite. The stress ratio was maintained to be 0.05 during test. Crack initiation from the notch root was monitored by the d-c potential drop technique, and was also subsequently checked metallographically. Figures 5a and 5b show the potential drop with respect to the number of loading cycles obtained in tests under high-temperature argon and steam, respectively. The potential decreases initially by in-

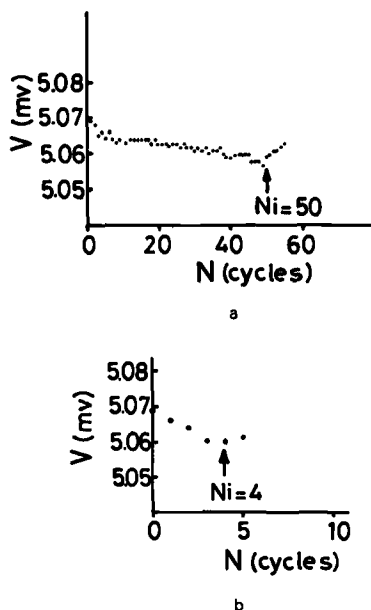


FIG. 5—Direct-current potential drop during fatigue test. (a) Argon, 0.1 cpm, $\Delta K = 46 \text{ MN m}^{-3/2}$. (b) Steam, 0.1 cpm, $\Delta K = 46 \text{ MN m}^{-3/2}$.

creasing the number of cycles, but increases at a certain number of cycles. Metallographic observations performed after these potential changes occurred, revealed that micro-cracks were initiated at the bottom of the notch root (Figs. 6a and 6b). This shows that the crack initiation can be determined by the potential drop change. The number of cycles to crack initiation therefore was determined by the d-c potential drop technique, although initiation of cracking is a difficult event to define quantitatively.

Results

The relation between the number of cycles to fatigue crack initiation (N_i) under various environmental conditions and the apparent stress intensity factor range (ΔK) are shown in Fig. 7 together with the results obtained in air at room temperature. In the table in Fig. 7, Ar(Hp) and Ar indicate the environmental conditions in which the flow rate of argon gas is 10 and 1 L/min, respectively. It can be seen distinctly that values of N_i in the elevated temperature environment are remarkably small compared with those obtained in air at room temperature. The relation between N_i and ΔK under a constant frequency can be given by the following equation, except for those cases of N_i in high-temperature air at a cycling frequency of 0.1 cpm:

$$N_i \propto (\Delta K)^{-4}$$

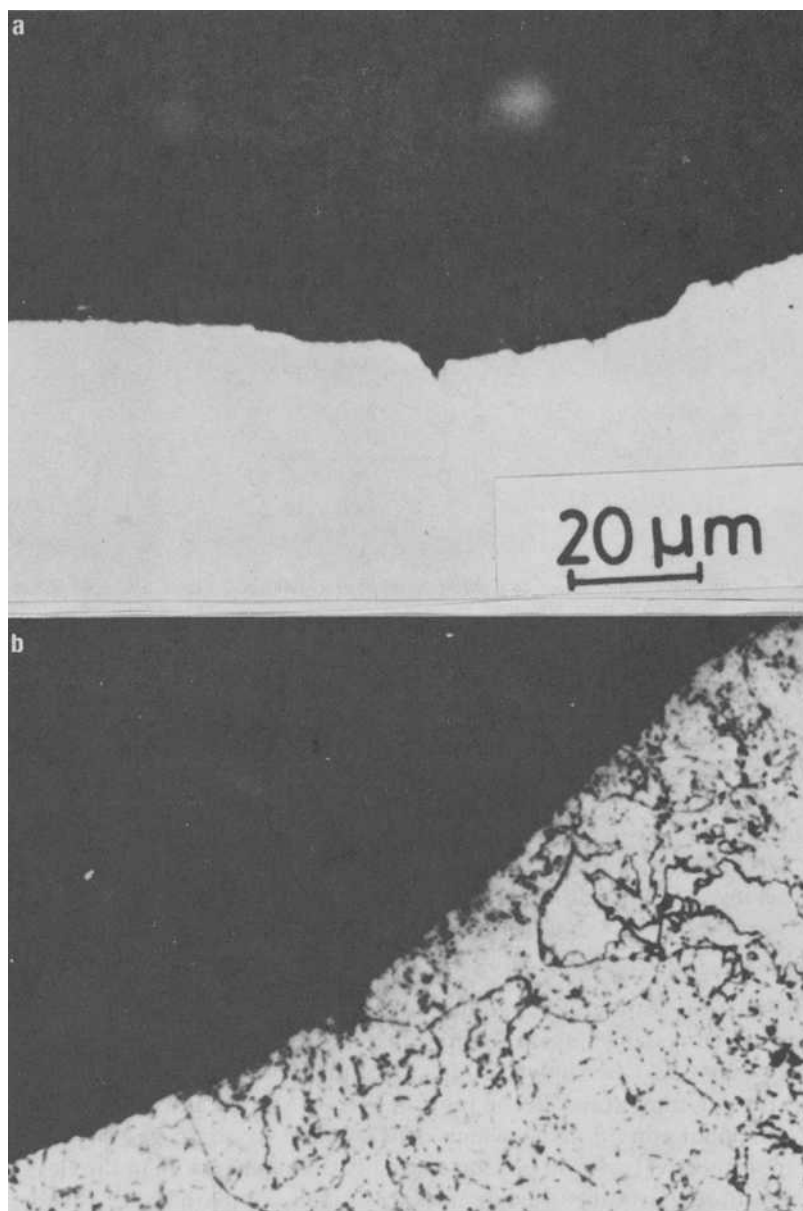


FIG. 6—Micro-crack initiation. (a) Argon, 0.1 cpm, $\Delta K = 46 \text{ MN m}^{-3/2}$. (b) Steam, 0.1 cpm, $\Delta K = 46 \text{ MN m}^{-3/2}$.

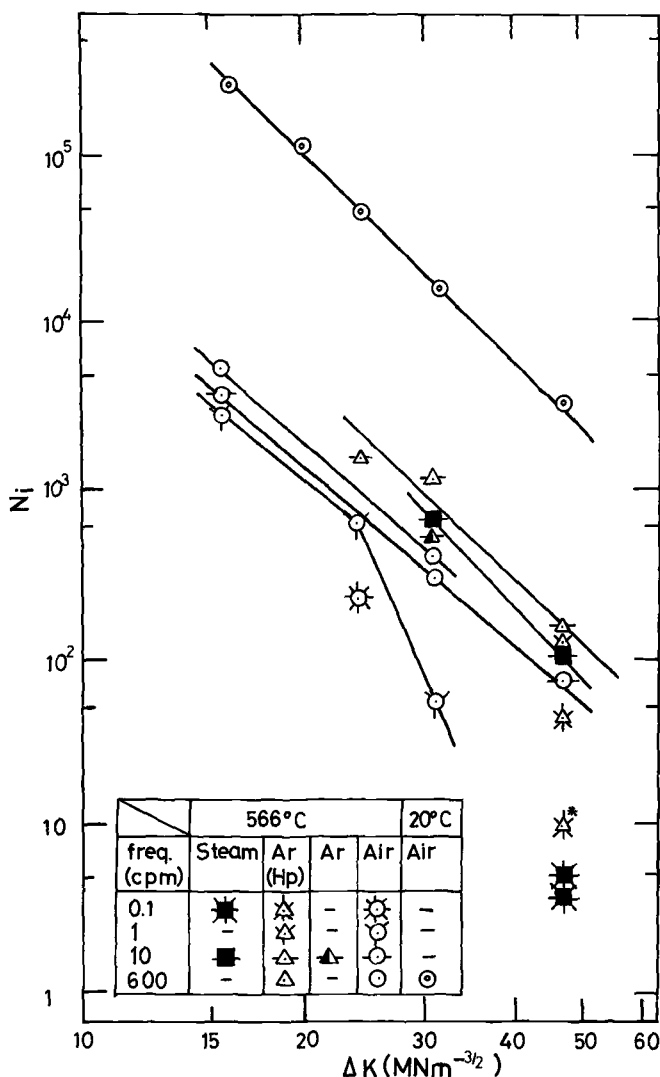


FIG. 7—Relation between number of cycles to fatigue crack initiation and stress intensity factor range.

Results shown in Fig. 7 reveal that N_i is strongly influenced by environmental condition and particularly by frequency. Under the same environmental condition, such as air at high temperature, it can be seen that N_i decreases with decreasing frequency. Although the environmental data of N_i in steam are few, the same dependency of N_i upon frequency may be observed under steam environment, since the fatigue behavior associated with oxidation at high temperature is a time-dependent phenomenon. While the dependence of

N_i upon ΔK is given by $N_i \propto (\Delta K)^{-4}$ at a frequency above 10 cpm, the relation between N_i and ΔK at 1 cpm is different. At a slow frequency of 1 cpm, N_i decreases promptly with increasing ΔK in the range of $\Delta K > 31 \text{ MN m}^{-3/2}$. The above results show that remarkable influences upon crack initiation occur when the frequency is lower than 10 cpm. In order to know which surrounding atmosphere is the most severe, the results obtained in various environments are compared by using data obtained under the same frequency, since the dependence of N_i upon ΔK varies with frequency. In the range of $\Delta K = 31 \sim 46 \text{ MN m}^{-3/2}$, it is seen that N_i in steam is midway between air and argon having the partial oxygen pressure of 9×10^{-3} torr. The most severe environment for crack initiation investigated in this work is air at 565°C . Under this environment condition, N_i decreases with decreasing the frequency and with increasing ΔK . Particular reduction N_i is observed under low frequency, such as 0.1 cpm.

Besides the environmental condition and frequency, the metallurgical state of the material relates to crack initiation behavior. * in Fig. 7 is the result obtained when a crack initiation is related to the manganese sulfide that existed at the bottom of the notch root (Fig. 8). In such circumstances, the fatigue crack initiation is facilitated several times faster than where no such inclusion exists at the bottom of the notch.

In order to understand the dependence of N_i upon the environmental conditions and frequency, the data shown in Fig. 7 were replotted with the ratio of number of cycles to crack initiation in high-temperature environment ($N_{i\text{ENV}}$) to those in air at room temperature ($N_{i\text{RT}}$). Figure 9 shows $N_{i\text{ENV}}/N_{i\text{RT}}$

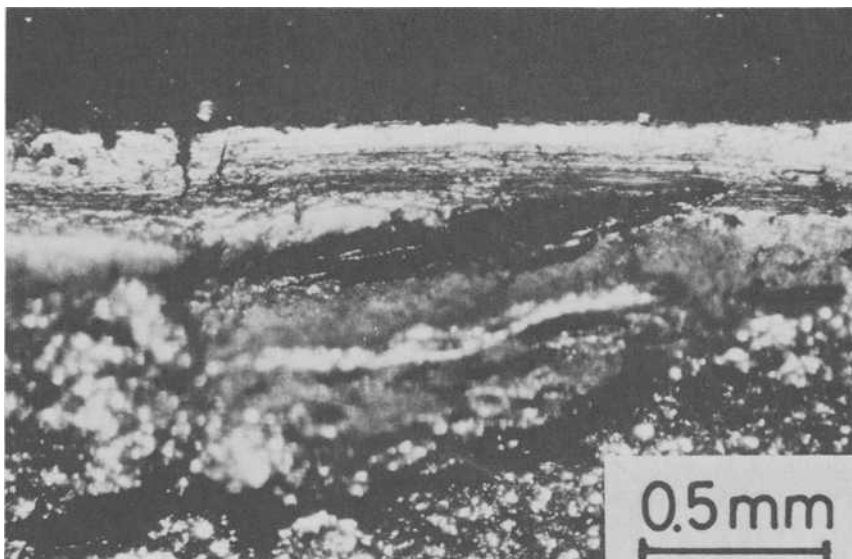
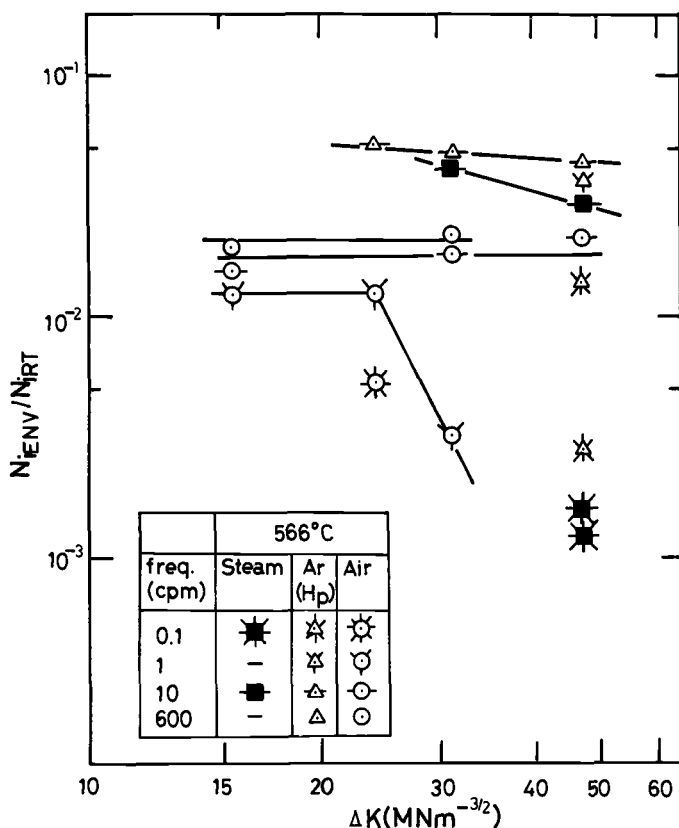


FIG. 8—Crack initiation associated with manganese sulfide.

FIG. 9—Dependence of N_{iENV}/N_{iRT} upon stress intensity factor range.

as a function of ΔK . The ratio N_{iENV}/N_{iRT} gives the reduction behavior of the number of cycles to crack initiation caused by environmental influence. It can be seen that the number of cycles to crack initiation at elevated temperature N_{iENV} is reduced to nearly 1/50 to 1/1000 of the N_{iRT} , depending on the environmental condition. At a frequency above 10 cpm, the ratio N_{iENV}/N_{iRT} obtained in argon and air does not depend upon ΔK in the range of 15 to 46 $\text{MN m}^{-3/2}$. At a low frequency such as 1 cpm, on the other hand, the ratio decreases at a certain value of ΔK with increasing ΔK . Although no experimental data were obtained in super-heated steam at a frequency lower than 10 cpm except the cases of $\Delta K = 46 \text{ MN m}^{-3/2}$ and $31 \text{ MN m}^{-3/2}$, the aforementioned tendency of reduction of the ratio may occur with increasing ΔK and with decreasing cyclic frequency.

To investigate the influence of cyclic frequency and the environment upon crack initiation separately, the dependence of N_{iENV}/N_{iRT} upon frequency was examined by using the results shown in Fig. 9. The result is shown in

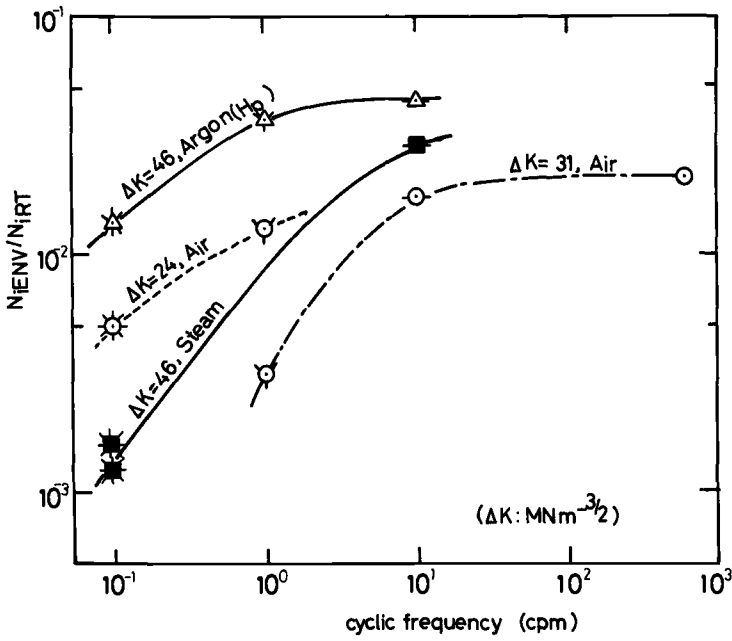


FIG. 10—Dependence of N_{Env}/N_{IRT} upon frequency.

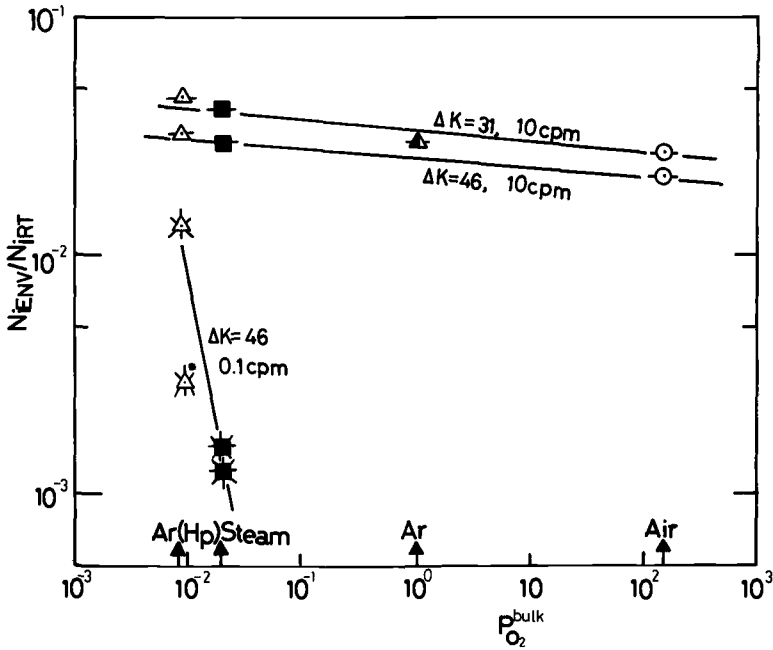


FIG. 11—Dependence of N_{Env}/N_{IRT} upon oxygen concentration.

Fig. 10. This reveals that N_{iENV}/N_{iRT} does not depend upon a frequency higher than 10 cpm, and N_{iENV}/N_{iRT} begins to decrease at 10 cpm. Furthermore, it can be seen that the dependence of N_{iENV}/N_{iRT} is influenced by the magnitude of ΔK and the environmental condition.

It seems probable that the number of cycles to crack initiation is reduced by oxidation of the material. Therefore N_{iENV}/N_{iRT} was re-examined with respect to the oxygen concentration in the surrounding atmosphere. Figure 11 shows the dependence of N_{iENV}/N_{iRT} on oxygen concentration. Oxygen concentration is given by partial pressure of oxygen. These results show that the influence of oxygen is remarkably great when the frequency is 0.1 cpm. At a high frequency such as 10 cpm, on the other hand, N_{iENV}/N_{iRT} does not depend on the oxygen concentration even at high ΔK such as $46 \text{ MN m}^{-3/2}$. It was found in addition that N_{iENV} is reduced remarkably when a crack initiates at the location where inclusion exists even under low oxygen concentration.

Discussion

In this work the number of cycles to fatigue crack initiation from a slit in a compact tension specimen was determined from tests conducted thermally at the maximum temperature of interest in steam and argon gas environment. The influence of the high-temperature environment upon the number of cycles to crack initiation was examined and compared with the results obtained in tests in air at room temperature. Although the tests conducted thermally at the maximum temperature of interest are the most damaging [5] compared with other cycles experienced in practice, it is clear that the number of cycles to fatigue crack initiation depends strongly on the frequency and the partial pressure of oxygen in the surrounding environment.

Reduction of the ratio N_{iENV}/N_{iRT} with reference to the partial pressure of oxygen shown in Fig. 11 illustrates the influence of high-temperature environment upon the fatigue crack initiation. It can be seen that environmental conditions have a great influence on crack initiation with increasing ΔK and decreasing frequency. It is particularly noted that the contribution of oxygen concentration to the reduction of the number of cycles of fatigue crack initiation appears remarkably at a low frequency such as 0.1 cpm. Despite the lack of experimentation in air at 566°C under higher ΔK than $31 \text{ MN m}^{-3/2}$, it can be estimated that the reduction of N_i in high-temperature air under high ΔK and low frequency becomes large compared with that in steam under the same ΔK and frequency.

The results obtained in this work reveal that the effect of cyclic frequency is notable at high stress intensity factors (Fig. 10). This fact does not coincide with that in corrosion fatigue, where mechanical damage is more dominant than environmental damage at higher stress amplitudes. Nonetheless, it has been shown that the fatigue crack growth rate of 1Cr-1Mo-0.25V at 550°C is large at high stress intensity factors at low cyclic frequencies such as 0.6 and

0.06 cpm [6]. Thus it appears that the creep effects at the crack tip appear to be significant only at a combination of high stress levels and very low frequencies. With regard to fatigue crack initiation from a slit bottom, the same creep effects can be considered as a cause of reduction of N_i . With regard to the influence of oxidation upon fatigue behavior in high temperature, it was found that the crack growth rate in Cr-Mo-V steel is strongly affected by oxide formation [2], which differs in various environments such as vacuum, air, and steam. It has been revealed in this work that the same influence of oxidation upon fatigue crack initiation is observed; namely, oxide formation at the notch root depends upon the partial pressure of oxygen in environment. In high-purity argon gas, in which oxygen concentration is 9×10^{-3} torr, there is no oxide formation in the macroscopic sense. In low-purity argon gas (oxygen concentration of 1 torr) and steam (oxygen concentration of 1.8×10^{-2} torr), on the other hand, the oxide Fe_3O_4 is formed at the notch root. In the air environment at 566°C the oxide formed at the notch root is Fe_2O_3 . These events indicate why the crack initiates easier in air than in steam: the interval of oxide detachment and metal loss in air contributes directly to crack initiation, while the oxide formed in steam is very adherent.

As discussed previously, the number of cycles to fatigue crack initiation is strongly influenced by oxide formation, which is a time-dependent phenomenon and therefore influenced by the magnitude of the stress intensity factor range and cyclic frequency. When examining and predicting the crack initiation in steam turbine rotors, therefore, one must pay particular attention to both the oxygen concentration in the environment and to the frequency.

It can be additionally noted that the existence of inclusions, such as manganese sulfide, in this alloy has remarkable influence upon crack initiation. When such inclusion exists at the region where strain concentrates, the crack initiates promptly (Fig. 7). The reduction of $N_{i\text{ENV}}$ caused by crack initiation related to inclusion may occur in the steam environment. The lowest value of $N_{i\text{ENV}}/N_{i\text{RT}}$ in this work is about $1/1000$, which was obtained in steam under the conditions of $\Delta K = 46 \text{ MN m}^{-3/2}$ and at a frequency of 0.1 cpm. If one takes into account the existence of the inclusion, however, this value may be reduced. Furthermore, particular attention should be paid to the crack initiation at the center bore in the rotor, because the environmental condition at the center bore is high-temperature air, and the inclusion density at the center bore surface is higher than that at the outer surface of the rotor.

Conclusions

1. Low frequency heavily influences the fatigue crack initiation in a high-temperature environment.
2. At low frequency, the oxygen concentration in the surrounding atmosphere has a large effect upon the reduction of the number of cycles to crack initiation.

3. While the environmental influence upon fatigue crack initiation is remarkable at low frequency, little reduction of N_i occurs at high frequency in the most severe environmental condition (for example, air at 566°C).

4. In the case of crack initiation associated with inclusion, such as manganese sulfide, the reduction of N_i is remarkably expedited.

Acknowledgments

This work was carried out at the Department of Engineering Science, Tohoku University, Sendai, Japan. We wish to thank Professor Hideaki Takahashi and Dr. Yo Sasabuchi, Tohoku University, for valuable discussions. We also wish to thank Mr. Takeshi Iwanami for his cooperation in performing the experiments.

References

- [1] Kondo, T., Kikuyama, T., Nakajima, M., Shindo, M., and Nagasaki, R., *Corrosion Fatigue*, National Association of Corrosion Engineers, 1972, pp. 539-556
- [2] Skelton, R. P., *Materials Science and Engineering*, Vol. 35, 1978, pp. 297-298.
- [3] Holder, R., *The Influence of Environment on Fatigue*, Institute of Mechanical Engineers Conference Publication 1977-4, London, pp. 37-41.
- [4] Manning, M. I. and Metcalfe, E. in *Proceedings*, Conference on Ferritic Steels for Reactor Steam Generators, British Nuclear Energy Society, London, 1977, Paper 63.
- [5] Skelton, R. P. and Bucklow, J. I., *Metal Science*, Vol. 12, 1978, p. 64.
- [6] Haigh, J. R., *Engineering Fracture Mechanics*, Vol. 7, 1975, pp. 271-284.

Fatigue Behavior of Carbon Steel Components in High-Temperature Water Environments

REFERENCE: Ranganath, S., Kass, J. N., and Heald, J. D., "Fatigue Behavior of Carbon Steel Components in High-Temperature Water Environments," *Low-Cycle Fatigue and Life Prediction, ASTM STP 770*, C. Amzallag, B. N. Leis, and P. Rabbe, Eds., American Society for Testing and Materials, 1982, pp. 436-459.

ABSTRACT: This paper describes the results of a combined experimental/analytical program on the fatigue initiation behavior of carbon steel components. Based on this study, several improvements in the fatigue analysis procedures are suggested: (1) a notch factor for local strains, (2) a mean stress factor, (3) improved fatigue strength reduction factor for butt welds, and (4) an environmental correction factor. It is shown that with the suggested fatigue analysis procedures, the fatigue design margins of the ASME Code will be maintained even with unusually severe local strain and mean stress.

KEY WORDS: carbon steel, fatigue analysis, ASME Code, environmental effects, local strain, mean stress effect, piping design

Pressure-retaining components are designed to meet the requirements of Section III of the ASME Boiler and Pressure Vessel Code (hereafter cited as "ASME Code" or "Code") [1].² In addition to prescribing stress limits for various applied loads (for example, pressure, dead weight, thermal, and seismic), the Code also requires a fatigue evaluation for the transient stresses that occur during normal operation. Specifically, the Code provides procedures for fatigue usage calculation and requires that the cumulative fatigue usage based on a conservative fatigue design curve should be less than 1.0. The ASME Code fatigue design curve was obtained based on strain-controlled fatigue data for small specimens of austenitic and ferritic steels and by applying a factor of 2 on stress or 20 on cyclic life to the mean data curve. This factor was intended to account for data scatter, temperature, surface roughness, environment, and size effects. In this paper, the fatigue behavior of carbon

¹ Manager, Stress and Fracture Analysis Unit; Manager, Plant Materials and Experimental Mechanics Unit; and Principal Engineer and Technical Leader, respectively, General Electric Company, Nuclear Energy Engineering Division, San Jose, Calif. 95125.

² The italic numbers in brackets refer to the list of references appended to this paper.

steel components is described and compared with the ASME Code fatigue curve. Some modifications are suggested for local strain, mean stress, and environmental effects, and it is shown that Code margins are further improved.

This paper describes the results of a combined experimental/analytical program on the fatigue initiation behavior of carbon steel components. The results show that the conventional Code evaluation procedures do not always account adequately for localized surface effects. However, when the effects of local notch strain, mean stress, and environment are evaluated as shown here, it is found that all the data can be accounted for by using the ASME Code approach. Based on this study, several improvements in the fatigue analysis procedures are suggested: (1) a notch factor for local strains, (2) a mean stress factor, (3) improved fatigue strength reduction factor for butt welds, and (4) an environmental correction factor. It is shown that with the suggested fatigue analysis procedures, the fatigue design margins of the Code will be maintained even with unusually severe local strain and mean stress.

Experimental Program on Fatigue Initiation Behavior of Carbon Steel

The purpose of carbon steel crack initiation testing was to evaluate the effect of high-purity water environments on the resistance to fatigue crack initiation. Parameters that may affect fatigue crack initiation of carbon steel are operating temperature, water environment, and cyclic stress levels. The experimental program was designed to measure the effects of each of these parameters and to compare them with the ASME Code approach for fatigue life prediction.

Fatigue tests in this program were conducted under (1) fully reversed strain control on smooth specimens, the method used to generate the data serving as the basis of the ASME Code fatigue design curve; (2) zero-tension load control on smooth and notched specimens; and (3) zero displacement to maximum displacement with small mean stress on notched samples, representing the type of loading typically found in service.

Baseline Air Tests

A total of 16 uniaxial specimens [0.0064 m ($\frac{1}{4}$ in.) diameter³] were tested to establish baseline air data at both room temperature and 288°C (550°F). The specimens were machined from 12-in. Schedule 160 SA333-Gr6 carbon steel pipe and were oriented in the longitudinal direction in the pipe. All tests were conducted in fully reversed, strain-controlled loading mode. Chemical and mechanical properties for this heat are shown in Table 1. These tests were designed to compare the behavior of SA333-Gr6 with the set of data

³The original measurements were made in U.S. Customary units (in parentheses).

TABLE 1—*Chemical and mechanical properties of carbon steel.*

Chemical Composition							
Alloy	Heat No.	C	M _n	P	S	Si	Fe
SA333-Gr 6	64032	0.12	1.05	0.010	0.030	0.23	balance
SA333-Gr 6	234099	0.26	0.94	0.011	0.017	0.24	balance
SA106-Gr B	HD7123	0.18	0.92	0.013	0.011	0.09	balance
Mechanical Properties							
Alloy	Heat No.	Room Temperature		288°C (550°F)			
		σ_{YS} , ksi ^a	σ_{UTS} , ksi	σ_{YS} , ksi	σ_{UTS} , ksi		
SA333-Gr 6	64032	44.8	62.0	31.0	66.5		
SA333-Gr 6	234099	48.7	74.0	22.7	68.7		
SA106-Gr B	HD7123	49.2	72.2	37.7	81.0		

^a 1 ksi = 6.895 MPa.

used to establish the ASME Code fatigue design curve, and were also used to evaluate the effect of test temperature.

A group of two notched specimens was tested to evaluate the effects of mean stress in air at room temperature. The test section was machined from SA333-Gr6 piping material. Chemical and mechanical properties for this heat are shown in Table 1. End adapters were welded to the test section to provide a connection to the 45 400 kg (100 kip) test machine, and final machining of the specimens was done after welding. Transverse notches ($K_t = 1.7$) were machined at the center of each face of the specimen test section. These tests were conducted in the load control mode fully reversed or zero tension; the waveshape was sinusoidal, and the frequency was 2.0 Hz.

Seven notched tubular specimens were tested to assess notch effects at 288°C. The material used was SA106B in the form of 0.019-m (3/4-in.) Schedule 160 pipe. Properties of this heat are also shown in Table 1. Adapters were welded to the test section to provide connection to the test machine. The tests were conducted at 0.13 to 0.20 Hz with sinusoidal zero-tension loading.

Air test data from the open literature were also utilized. Results of several test series conducted by Krempl and by Hale on SA106B notched bars at room temperature and 288°C provided a substantial enlargement of the existing test data base [2–6].

Small Specimen Environmental Tests

Several sets of tests were conducted in high-temperature, high-purity oxygenated water at 288°C. The high pressure/temperature water environment used for these tests was provided by a high-flow [0.77 Ls/s (12 gal/min)] recirculating test loop. Dissolved oxygen level, pH, and water conductivity were

TABLE 2—*Environments.*

	0.2 ppm O ₂	8 ppm O ₂
Pressure	1120 ± 50 psig ^a	1120 ± 50 psig
Temperature	282 ± 7°C	282 ± 7°C
Dissolved oxygen	0.2 ± 0.1 ppm	6 ± 2 ppm
Conductivity	0.5 ± 0.2 mho/cm at 24°C	0.5 ± 0.2 mho/cm at 24°C
pH	6.5 ± 0.5 at 24°C	6.0 ± 0.5 at 24°C
Additives	none	none

^a 1.0 psig = 0.006895 MPa.

monitored continuously. Most of the testing was conducted in nominally 0.2 ppm oxygenated water, with some work at 8 ppm oxygen. The water chemistry specification data are shown in Table 2.

The first set of tests was conducted in an operating plant. Reference 7 provides a detailed description of this work. The environment was consistent with the 0.2 ppm oxygenated water conditions of Table 2. The material used in this study is described in Table 1. Cantilever beam specimens were tested under fully reversed conditions. No notched specimens were included in the study.

The notched tubular specimen was used to conduct 0.2 ppm oxygenated water environment tests, as well as the air tests described previously. The same material was studied as in the air tests. In the water environment tests, 0.003-m ($\frac{1}{8}$ -in.)-diameter pressure sensor tube was welded to the end of each specimen to provide a means to signal through-wall leaking. The specimens were connected in series and tested concurrently. Zero-tension loading with a sawtooth waveshape and 0.003 Hz frequency was employed. A few tests were conducted at slower frequencies or with mean stress.

An additional set of 0.2 ppm oxygenated water environment tests was conducted using notched specimens. The tests were conducted from zero to maximum displacement, which resulted in displacement control tests having a small mean stress. The tests were conducted with a sawtooth waveshape and 0.003 Hz frequency. These tests simulated the type of loading expected for pipes in service.

Pipe Tests

The final set of water environment tests is unique. Instead of utilizing small laboratory specimens, the test involved 0.10-m (4-in.) Schedule 80 welded pipe. The test section is about 1.22 m (4 ft) long and contains 11 butt welds spaced about one diameter apart. The welding parameters are typical of those used in the field, and the welds are postweld ground to reproduce field conditions on the inside diameter. The pipes contain 8.3 MPa (1200 psig) water on the inside and are subjected to an externally applied axial stress. In addition to the external load, the pipe welds also experience the weld residual

stress. The pipe tests were conducted in 288°C air and in 0.2 and 8 ppm oxygenated water, under zero-tension load control with trapezoidal wave shapes at 183 μ Hz. A few of the test pipes had specially machined sharp notches in addition to the butt welds. Reference 8 provides a more detailed description of the pipe test method.

Evaluation of Results

All test data are listed in Table 3. It should be emphasized that, for most of the tests, stress ranges and loading modes used in the program were outside the allowable values permitted by the ASME Code. In addition, some of the tests were conducted in 8 ppm oxygenated water, which is a known [9,10,11] accelerant for crack initiation. Evidence that the 8 ppm oxygenated water is accelerated over that of the service environment is provided by three sources. The first is provided in Ref 9, which compares stainless steel pipe test data in 8 ppm oxygenated water to the normal service 0.2 ppm water. Reference 10 contains similar data for carbon steel. Reference 11 contains results of corrosion potential measurements made during many stages of operation at reactor sites. It is clear that the 8 ppm oxygenated water data are accelerated when compared with service operations. This environment is not found under normal operating conditions. Hence these tests are not representative of service conditions and, as such, comparison with ASME Fatigue Design procedures requires corrections to account for local strains, mean stress, and environmental effects. To illustrate this, data are evaluated using conventional Code procedures and compared with the Code curves in Fig. 1. The appropriate corrections and the re-evaluation of the data are discussed later.

Comparison of the uncorrected data with the ASME Code Curve leads to the following observations: (1) the smooth specimen strain control test data in air at 288°C lie below the room temperature air data by a factor of about 2 on cycles; (2) comparison of the small specimen environmental data with the air data shows a clear environmental effect; and (3) the welded pipe tests, which were conducted under load control stresses exceeding the net section yield stress and in 8 ppm oxygenated water (all except one pipe in 0.2 ppm oxygenated water), further illustrate the effects of environment, mean stresses, and notches.

Throughout the test program, it was noted that the fracture locations most often occurred at discontinuities such as section thickness changes and at the weld fusion line. Figure 2 is an example of this for the pipe tests. The fracture surface is transgranular. It is difficult to discern any more detailed features of the fracture surface because of the thick oxide on the surface. The fact that cracks occurred at discontinuities suggests that notch effects may be important.

In the remainder of this section, analytic procedures are developed for further analysis of the notched specimen and pipe test data.

TABLE 3—Carbon steel test data.

Room Temperature Air, Load Control, Zero to Tension							
Specimen No.	Material	Frequency, cpm ^a	Wave Shape	K _t	Net Section Stress Range, ksi ^b	N _t	Reference
1	SA106B	10	sine	3.0	33.0	64 000	6
2	SA106B	10	sine	3.0	36.0	38 000	6
3	SA106B	10	sine	3.0	39.00	26 000	6
4	SA106B	10	sine	3.0	43.0	17 000	6
5	SA106B	10	sine	3.0	46.0	12 000	6
6	SA106B	10	sine	3.0	49.0	10 100	6
7	SA106B	10	sine	3.0	51.0	3 800	6
8	SA106B	10	sine	3.0	54.0	1 600	6
9	SA3336	120	sine	1.7	45.3	140 000	this study
10	SA3336	120	sine	1.7	42.7	300 000	this study
288°C (550°F) Air, Load Control, Zero to Tension							
20	SA106B	6.0	sine	3.0	48.0	4 800	2
21	SA106B	6.0	sine	3.0	42.0	13 000	2
22	SA106B	6.0	sine	3.0	36.0	33 000	2
23	SA106B	6.0	sine	3.0	33.0	70 000	2
24	SA106B	12.0	sine	5.0	48.6	5 000	this study
25	SA106B	8.0	sine	3.8	32.4	86 800	this study
26	SA106B	8.0	sine	3.8	43.8	12 700	this study
27	SA106B	8.0	sine	3.8	50.3	7 200	this study
28	SA106-B	8.0	sine	3.8	57.6	4 800	this study
29	SA106-B	8.0	sine	3.8	64.1	3 100	this study
30	SA106-B	8.0	sine	3.8	72.8	1 900	this study
79	SA106-B	0.011	sawtooth	1.8	46.7	4 400	{ this study pipe test
	SA333-6			2.16			
288°C (550°F) 0.2 ppm O ₂ Water, Load Control, Zero to Tension							
34	SA106-B	0.18	sawtooth	1.0	55.2	7 810	this study
35	SA106-B	0.18	sawtooth	1.0	51.0	45 500	this study
36	SA106-B	0.18	sawtooth	1.0	48.4	20 000	this study
37	SA106-B	0.18	sawtooth	1.0	43.7	45 500	this study
38	SA106-B	0.18	sawtooth	1.0	39.8	45 500	this study
39	SA106-B	0.18	sawtooth	5.2	49.1	300	this study
40	SA106-B	0.18	sawtooth	2.9	35.7	4 000	this study
41	SA106-B	0.18	sawtooth	2.8	31.6	11 000	this study
42	SA106-B	0.18	sawtooth	2.7	26.9	45 500	this study
43	SA106-B	0.18	sawtooth	5.8	29.0	35 900	this study
44	SA106-B	0.18	sawtooth	2.9	22.9	38 000	this study
45	SA106-B	5.0	sawtooth	5.2	49.1	1 350	this study
46	SA106-B	5.0	sawtooth	2.9	35.7	9 000	this study
47	SA106-B	0.18	sawtooth	1.7	54.3	5 700	this study
48	SA106-B	0.037	sawtooth	1.7	54.3	1 300	this study
70	SA106-B	0.011	sawtooth	1.8	45.1	2 600	{ this study pipe test
	SA333-6			2.16			

TABLE 3—(Continued).

Specimen No.	Material	Frequency, cpm ^a	Wave Shape	K_t	Net Section Stress Range, ksi ^b	N_t	Reference	
288°C (550°F) 0.2 ppm O ₂ Water, Load Control, Tension to Tension, $R = 0.6$								
49	SA106-B	0.12	sawtooth	5.2	17.5	454	this study	
50	SA106-B	0.12	sawtooth	2.9	13.1	2 100	this study	
51	SA106-B	0.012	sawtooth	5.2	17.5	1 500	this study	
52	SA106-B	0.012	sawtooth	2.9	13.1	1 500	this study	
288°C (550°F) 8.0 ppm O ₂ Water, Load Control, Zero to Tension, Pipe Tests								
71	SA106-B SA333-6	0.011	sawtooth	1.8 Code 2.16 Rule	46.7	127	this study	
72	SA106-B SA333-6	0.011	sawtooth	1.8 Code 2.16 Rule	46.7	514	this study	
73	SA106-B SA333-6	0.011	sawtooth	1.8 Code 2.16 Rule	46.7	583	this study	
74	SA106-B SA333-6	0.011	sawtooth	1.8 Code 2.16 Rule	43.2	920	this study	
75	SA106-B SA333-6	0.011	sawtooth	5.7	46.7	24	this study	
76	SA106-B SA333-6	0.011	sawtooth	8.1	34.6	30	this study	
77	SA106-B SA333-6	0.011	sawtooth	1.8 Code 2.16 Rule	31.1	5 850	this study	
78	SA106-B SA333-6	0.011	sawtooth	1.8 Code 2.16 Rule	38.1	3 900	this study	
288°C (550°F) 0.2 ppm O ₂ Water, Deflection Control, Zero to Maximum Deflection								
31	SA333-6	0.18	sine	1.7	54.3	7 500	this study	
32	SA333-6	0.18	sine	1.7	90.0	340	this study	
33	SA333-6	0.037	sine	1.7	54.3	2 460	this study	
288°C (550°F) 0.2 ppm O ₂ Water, Strain Controlled, Fully Reversed, Beading								
Specimen No.	Material	Frequency	Wave Shape	K_t	Strain Range, %	ϵE	N_t	Reference
137	SA516	0.06	trapezoidal	1.0	0.67	174	1 050	3
138	SA516	0.06	trapezoidal	1.0	0.67	174	1 150	3
139	SA516	0.06	trapezoidal	1.0	0.67	174	1 200	3
140	SA516	0.06	trapezoidal	1.0	0.67	174	1 400	3
141	SA516	0.06	trapezoidal	1.0	0.50	130	2 900	3
142	SA516	0.06	trapezoidal	1.0	0.33	85.9	4 000	3
143	SA516	0.06	trapezoidal	1.0	0.33	85.9	5 200	3
144	SA516	0.06	trapezoidal	1.0	0.33	85.9	7 000	3
145	SA516	0.06	trapezoidal	1.0	0.33	85.9	9 000	3

TABLE 3—(Continued).

Specimen No.	Material	Frequency	Wave Shape	K_t	Strain Range, %	ϵE	N_f	Reference
Room Temperature Air, Strain Controlled, Fully Reversed, Axial								
103	A333Gr6	16	sawtooth	1.0	0.75	231	10600	this study
104	A333Gr6	16	sawtooth	1.0	0.75	212	12489	this study
101	A333Gr6	12.5	sawtooth	1.0	1.0	306	4386	this study
102	A333Gr6	12.5	sawtooth	1.0	1.0	289	6164	this study
106	A333Gr6	24	sawtooth	1.0	0.5	147	41229	this study
105	A333Gr6	24	sawtooth	1.0	0.5	148	36647	this study
107	A333Gr6	35	sawtooth	1.0	0.35	108	120476	this study
288°C (550°F) Air, Strain Controlled, Fully Reversed, Axial								
125	A333Gr6	12.5	sawtooth	1.0	1.0	268	3614	this study
126	A333Gr6	12.5	sawtooth	1.0	1.0	273	3440	this study
128	A333Gr6	16.0	sawtooth	1.0	0.75	209	9768	this study
127	A333Gr6	16.0	sawtooth	1.0	0.75	201	5546	this study
130	A333Gr6	24.0	sawtooth	1.0	0.5	139	26174	this study
129	A333Gr6	24.0	sawtooth	1.0	0.5	136	15627	this study
131	A333Gr6	45	sawtooth	1.0	0.35	93.8	33187	this study

^a 1.0 cpm = 0.0167 Hz.^b 1.0 ksi = 6.895 MPa.

Local Strain Analysis of Notches

The principal focus in the evaluation of notched specimen data is on the development of the local strain analysis at notches using Neuber's Rule. In order to compare low-cycle fatigue data from notched specimens with the fatigue curve based on smooth specimen tests, it is necessary to determine the local strain range at the notch. The use of the cyclic stress-strain curve to determine the local strain range at the notch has been established [12]. Once the stress and strain ranges at the notch are determined, fatigue life predictions can be made based on strain-controlled smooth specimen data. Implied in this approach is the assumption that both the smooth and notched specimens will have the same fatigue initiation life, provided that the stress-strain history at the crack initiation site are the same.

Detailed elastic-plastic analysis using the cyclic stress-strain curve can be used to predict the local strain. However, Neuber's Rule provides a more convenient means of determining the local strain at the notch. Neuber's relationship is

$$k_p q_p = K_t^2 \quad (1)$$

where K_t is the elastic stress concentration factor, and k_p and q_p are the plastic stress and strain concentration factors defined by the expressions

$$k_p = \sigma_a / S_a$$

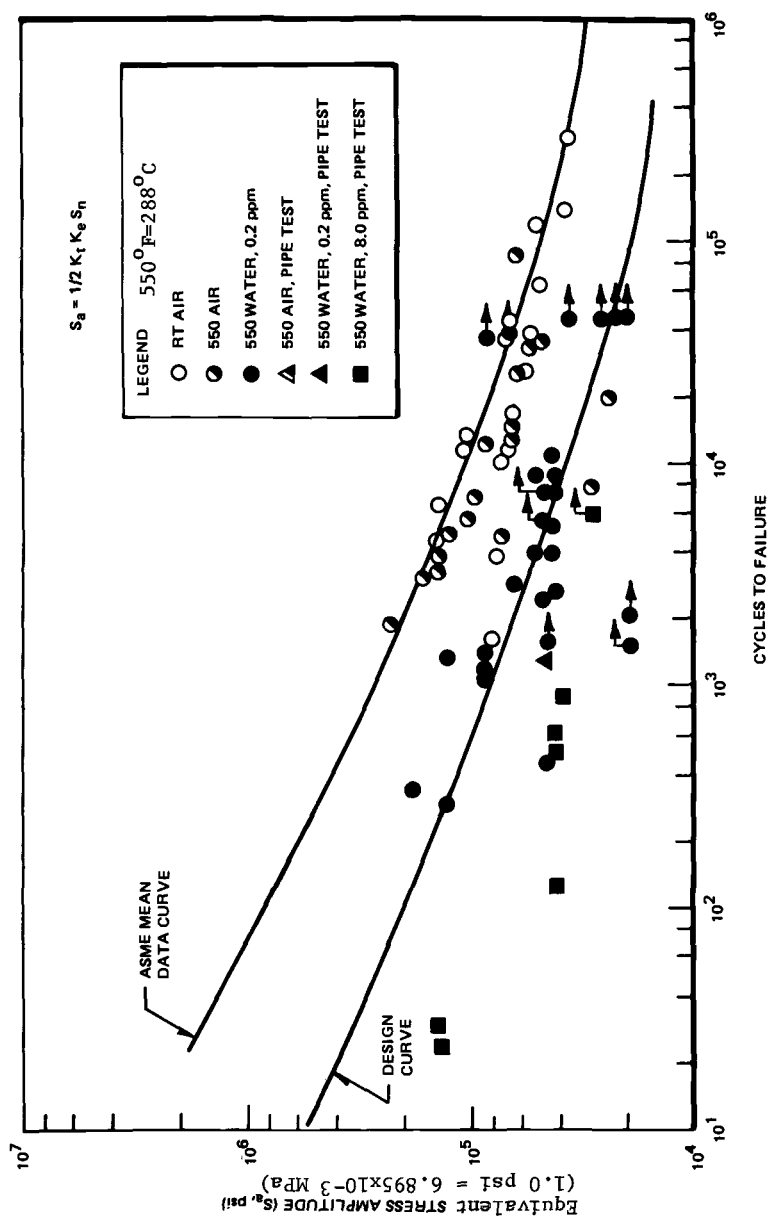


FIG. 1—Uncorrected fatigue results plotted on ASME Code basis.

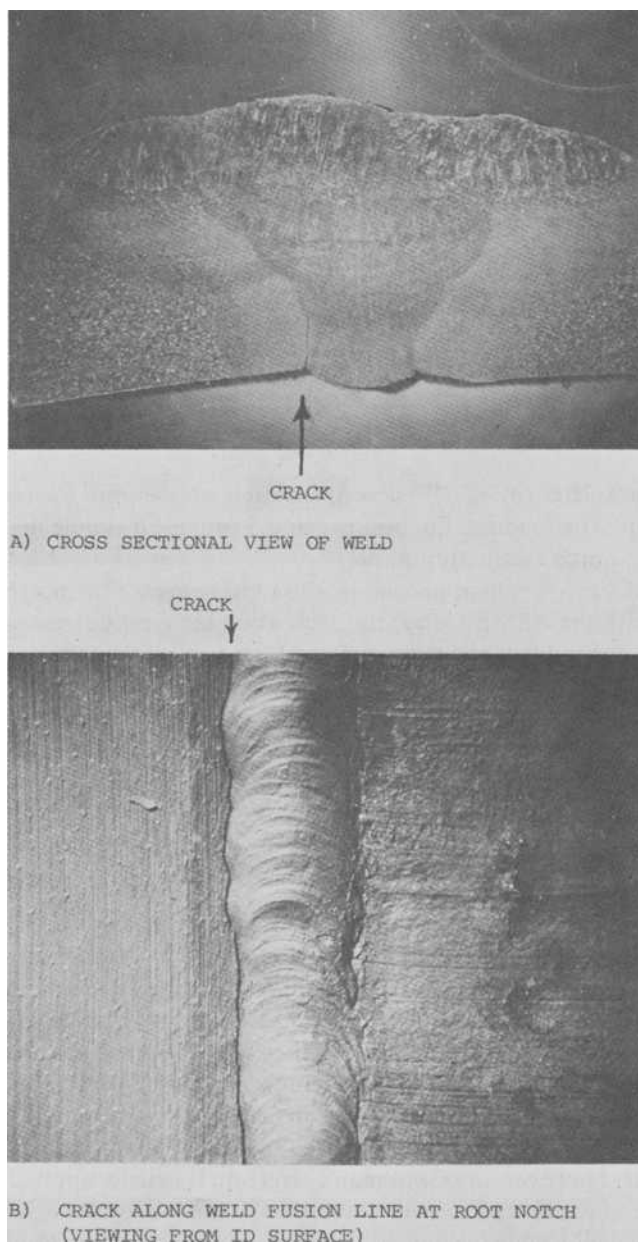


FIG. 2—Cracks associated with weld root notch on the new weld prep design.

and

$$q_p = \epsilon_a / e_a$$

and σ_a and ϵ_a are the local stress and strain *amplitudes* respectively at the notch, and S_a and e_a are the nominal stress and strain amplitudes respectively. This can be rewritten as

$$(\sigma_a \cdot \epsilon_a \cdot E)^{1/2} = K_t (S_a \cdot e_a \cdot E)^{1/2} \quad (2)$$

when the net section is still elastic, $e_a \cdot E = S_a$, and Eq 2 reduces to

$$(\sigma_a \cdot \epsilon_a \cdot E)^{1/2} = K_t S_a \quad (3)$$

It is seen that Eq 2 applies to all values of nominal stress, whereas Eq 3 applies to nominal stresses in the elastic regime only. When the cyclic stress range is sufficiently small to assure elastic behavior even at the notch location, then $\sigma_a = E\epsilon_a$, and Eq 3 reduces to the familiar form

$$\sigma_a = K_t S_a$$

Thus the parameter $(\sigma_a \epsilon_a E)^{1/2}$ describes notch stress-strain for both elastic and elastic-plastic loading. Equations 2 and 3 provide a simple means of estimating the notch strain amplitude.

This local stress-strain approach was used to compare the notched specimen data with the ASME Code approach using the elastic stress concentration factor. Table 4 lists the specimens and the strain calculations. Since the available data showed significant differences between different heats of material, the local strains were calculated for the two extreme curves. It is seen that the local strain approach predicts higher strains and stresses at the notch compared with the method based on the elastic stress concentration factor.

Mean Stress Effects

In the evaluation for notched specimens, no correction was applied for mean stresses even though the tests were controlled by load. Since the specimens were severely notched, reverse yielding occurs at the notches, and the local mean stress approaches zero. In such cases the mean stress correction is small. In the evaluation of the pipe test, however, the mean stress effects become more significant and should be included to properly interpret the data.

There are several mean stress correction factors discussed in the literature, but the one most popular is the modified Goodman correction used in the ASME Code. However, the Goodman correction is usually applied for high-cycle data and could lead to over-correction in the low-cycle regime. A correction factor applicable for low-cycle fatigue and based on the Neuber notch analysis approach has been suggested by Smith et al [13]. In the Neuber analysis for alternate tension-compression cycling, the factor $(\sigma_a \epsilon_a E)^{1/2}$ is the appropriate fatigue parameter. For zero-tension loading, instead of plotting the parameter $(\sigma_a \epsilon_a E)^{1/2}$, Smith et al recommend the use of the function

TABLE 4—Notched specimen fatigue data evaluation.

Specimen No.	K_t	Elastic Stress ($K_t S_a$), ksi ^a	Local Strain (ϵ_a) ^b , %		Stress ($E \epsilon_a$) ^c , ksi		Cycles to Failure
			A	B	A	B	
1	2.9	51.8	0.210	0.280	55.4	73.9	4 022
2	2.8	44.2	0.190	0.225	50.2	59.4	11 007
3	2.7	36.3	0.145	0.160	38.3	42.2	22 571 ^d
9	5.2	127.7	0.900	1.200	237.0	316.8	301
10	5.8	84.1	0.440	0.630	116.0	166.3	12 942 ^d
11	6.0	68.7	0.320	0.460	85.0	121.4	1 051.8 ^d

^a 1.0 ksi = 6.895 MPa.^b Stress strain curve A = Krempf 228°C (550°F); stress strain curve B = Jaske 204°C (400°F) (Ref 10).^c $E = 26\,400$ ksi.^d No failure, test continuing.

$(\sigma_{\max} \epsilon_a E)^{1/2}$ where σ_{\max} is the maximum local tensile stress at the notch. For reversed loading, $\sigma_{\max} = \sigma_a$ and the two parameters reduce to the same value. σ_{\max} can be estimated from the cyclic stress-strain curve by determining the stress corresponding to the strain $\epsilon_{\max} = 2\epsilon_a$. In applying the mean stress correction to the conventional S - N curve, the ratio $(\sigma_{\max} \epsilon_a E)^{1/2} / (\sigma_a \epsilon_a E)^{1/2} = (\sigma_{\max} / \sigma_a)^{1/2}$ can be used. Note that mean stress effects are not used in the Code curve, since they are developed from reversed loaded specimens. The ratio $(\sigma_{\max} / \sigma_a)^{1/2}$ is therefore a reasonable measure of the mean stress correction.

ASME Fatigue Evaluation Procedures for Piping Compared with Test Data

The fatigue evaluation procedure recommended in the ASME Code for piping components uses the stress index approach. Table NB-3683.2-1, Section III, ASME Code provides the appropriate stress indices to be used in piping analysis.

Rodabaugh and Moore [14] have summarized available fatigue data on piping components and compared them with the cyclic life predicted by the ASME Code fatigue design curves. In comparing the experimental fatigue data to the Code, the ratio of the actual number of cycles to failure and the Code predictions, N_t/N_c , is determined.

The Code "design curve" was obtained from the "failure" S - N curves by applying a factor of 2 on stress or a factor of 20 on life, whichever was more conservative at each point. Accordingly a ratio of $N_t/N_c = \sim 20$ in the test data indicates adequate conservatism of the Code indices method.

Girth Butt Welds

The ASME Code fatigue strength reduction factors are based on the extensive data developed by Markl [15]. The ratio of the actual number of cycles to failure in Markl's tests and the cyclic life limit as taken from use of the ASME Code design curve ranged from 13 to 18 (Table 5). This is somewhat

lower than the "factor of 20" intended by the ASME Code. Newman's data [16] for 0.01-m ($\frac{3}{8}$ -in.)-thick piping suggest that the margin of actual number of cycles to failure over the Code Design Curve Limit might be even lower than that found by Markl. This margin is further eroded if the piping weld has fabrication defects (for example, porosity, lack of penetration, etc.). The lack of adequate margin in girth butt welds is supported further by the results of Kiss et al [17] shown in Table 5. The evaluation of the data (mostly at room temperature and without environment) indicates that the margin on cyclic life for piping butt welds is well below the factor of 20 implied in the Code design curve.

Elbows

The fatigue strength reduction factors in the Code for elbows are much higher than those for butt welds. Also, the maximum stresses in the elbow occur in the body of the elbow and not in the weld where imperfections are likely to exist. This further increases the conservatism of the Code. The results of tests by Markl and by Kiss et al confirm the Code conservatism. Table 5 shows that the Code margins on cyclic life are high, in some cases approaching 2600. Thus the Code design procedures have a large built-in safety margin for elbows.

Tees and Other Fittings

Like elbows, the fatigue strength reduction factors for tees and other fittings are high and in many cases require the use of the simplified elastic-plastic analysis. As in elbows, the high stresses occur in the body of the fitting where the likelihood of defects is smaller than in the welds. As seen from the fatigue data for tees in Table 5, the highest margin was up to 500. Clearly, for tees, the Code stress index method produces conservatism that is well in excess of the factor of 20 implied in the Code.

The differences in the way the Code handles butt welds, elbows, and tees is best illustrated by selecting three tests from Table 5 (shown by an asterisk), representing the three piping components. The three tests were selected so that the nominal "pipe" bending stress, M/Z , is approximately the same in all three cases. From the calculation of the C_2 , K_2 , and K_e factors, it is seen that even though the nominal stress in the pipe itself is about the same, the calculated secondary and peak stresses are quite different. Because of the higher secondary stress S_n , the elbow and tee stresses are multiplied by the strain correction factor K_e , which can be very significant. Table 6 shows the comparison of the three cases. It is seen that for the same nominal pipe stress, the Code Design Curve cyclic life limit is 2500 cycles for the butt weld, 38 for the tee, and less than 10 for the elbow. The use of higher stress indices for fittings introduces significant conservatisms for fittings compared with butt welds.

The comparison of the carbon steel piping fatigue data and the Code pre-

TABLE 5—Evaluation of fatigue tests on piping components.

Type of Component	$\frac{M}{Z}$, psi ^a	S_n , psi	$\frac{S_n}{3S_m}$	S_p , psi	K_a	$\frac{K_a S_p}{2}$, psi	ASME Code (N_c)	Test (N_t)	$\frac{N_t}{N_c}$
Girth butt weld, 4 in., std. wt.	90 000	90 000	1.50	162 000	2.00	162 000	190	2500 to 3500	13 to 18
Girth butt weld,* 6 in., std. wt.	58 200	58 200	1.08	105 000	1.16	60 800	2500	35 740	14.3
Short-radius elbow, 6 in., std. wt.	43 500	280 000	5.20	280 000	5.00	700 000	<10	760	>76
Short-radius elbow, 6 in., std. wt.	43 100	278 000	5.15	278 000	5.00	695 000	<10	26 100	>2600
Short-radius elbow,* 4 in., std. wt.	56 000	310 000	5.17	310 000	5.00	775 000	<10	1200 to 3000	>120
Short-radius elbow, 0.072 in. wall	20 000	250 000	4.17	250 000	5.00	625 000	~10	2800	~280
Short-radius elbow, 4 in., std. wt.	56 000	310 000	5.17	310 000	5.00	775 000	<10	2800	>280
Forged welding tee, 4 in., std. wt.	100 000	290 000	4.85	290 000	5.00	725 000	<10	900	>90
Forged welding tee, 4 in., std. wt.	86 000	250 000	4.17	250 000	5.00	625 000	~10	1500 to 5000	150 to 500
Forged welding tee, 4 in., std. wt.	104 000	300 000	5.00	300 000	5.00	750 000	<10	1500	>150
Forged welding tee, 4 in., std. wt.	86 000	250 000	4.17	250 000	5.00	625 000	<10	700 to 4000	>70
Forged welding tee,* 12 in. Sch. 80	54 500	155 000	2.57	155 000	4.14	321 000	38	2070	55

^a 1 psi = 0.006895 MPa.

* These tests are compared in detail in Table 6.

TABLE 6—Comparison of code cyclic life predictions for components with approximately the same nominal (M/Z) pipe stresses.

Type of Component	C_2, K_2	M/Z , ksi ^a	$S_n =$ $C_2 M/Z$, ksi	$S_n/3 S_m$	$S_p =$ $K_2 C_2 M/Z$, ksi	K_e	$\frac{S_a = K_e S_p}{2}$, ksi	Code Predicted Cyclic Life (N_c)
Pipe butt weld, 6 in., std. wt.	$C_2 = 1.0$ $K_2 = 1.8$	58.2	58.2	1.08	105.0	1.16	60.8	2500
Short radius elbow, 4 in., std. wt.	$C_2 = 5.54$ $K_2 = 1.0$	56.0	310	5.17	310	5.00	775	<10
Forged welding tee, 12 in., Schedule 80	$C_2 = 2.84$ $K_2 = 1.0$	54.5	155	2.57	155	4.14	321	38

^a 1.0 ksi = 6.895 MPa.

diction leads to the following conclusions: (1) piping components (for example, elbows, tees) except girth butt welds under moment loading showed cyclic margins well in excess of the "factor of 20"; (2) girth butt welds under cyclic moment loading show a lower margin on cyclic life even without considering environment, temperature effects, and weld imperfections; and (3) because of the differences in the cyclic margins for butt welds as opposed to other components, higher fatigue strength reduction factors for butt welds may be appropriate to provide greater fatigue margin.

Proposed Design Rules

The evaluation of the notched specimen and pipe test data as well as the extensive test data on piping components suggest four areas where improvements to the present Code procedures are appropriate: (1) new fatigue strength reduction factors for butt welds, (2) notch factor to account for the effects of local yielding when $K_t S_a$ exceeds the elastic range, (3) mean stress correction factor, and (4) environmental correction factor.

With the inclusion of the four factors for piping analysis the peak stress amplitude S_p would be given by

$$S_p = \frac{1}{2} K_f K_n K_m K_e K_{en} S_n \quad (4)$$

where

S_n = range of alternating primary and secondary stresses calculated using conventional Code procedures,

K_f = fatigue strength reduction factors for which existing Code expressions apply, except for butt welds for which new factors will be developed in the next section,

K_n = correction factor for local notch yielding developed based on Neuber analysis,

K_m = mean stress correction factor,

K_e = plastic strain correction factor (based on simplified elastic-plastic analysis) specified in NB-3653.6, and

K_{en} = water environment factor.

The new factors proposed are the notch factor K_n , the mean stress correction factor K_m , and the water environment factor K_{en} . The K_t -factor is different only for pipe butt welds.

Analytical Procedure for Determining Fatigue Strength Reduction Factors for Butt Welds in Piping

Although an experimental fatigue testing program is necessary to determine fatigue strength reduction factors for piping welds, an analytical procedure based on Peterson's equation [18] for notch factor can be used to determine limiting values for fatigue strength reduction factors. The procedure, originally proposed by Lawrence et al [19], assumes that a weld inherently produces highly strained regions at notches (for example, fabrication defects, suckback, and weld toes). Since practically any value of notch radius can exist at these locations, it is necessary to use a bounding value which gives the highest fatigue strength reduction factor at these welds. Assuming an inverse square root dependence on notch radius for the stress concentration factor and maximizing the fatigue strength reduction factor K_t , the following expression can be obtained:

$$(K_t)_{\max} = 1 + 2\sqrt{t} \quad (5)$$

where t is the pipe thickness.

Figure 3 shows the analytically predicted fatigue strength reduction factor as a function of pipe wall thickness.

Equation 5 predicts K_t -values higher than the 1.8 value suggested by the Code for moment loading. Also, the proposed approach implies a size effect (increasing K_t with thickness), whereas the Code values are constant. Although extensive data are not available for pipe butt welds of different thicknesses, the limited comparison between the results of Markl and Newman supports the thickness dependence. Lawrence's test data on flat butt welds also support the proposed approach.

Fatigue strength reduction factors were also developed for notches using the approach suggested by Neuber [20]. This approach considers the effect of yielding at very sharp notches so that K_t does not become unbounded for notch radii approaching zero. The expression used was

$$K'_t = 1 + (K_t - 1)/(1 + \sqrt{0.000048/\text{root radius (metres)}})$$

Analytical Procedure for the Notch Factor (K_n)

When the local notch stress is in the elastic range, the local strain ϵ_a is given by $K_{te}\epsilon_a$, where ϵ_a is the nominal strain. When there is local yielding at

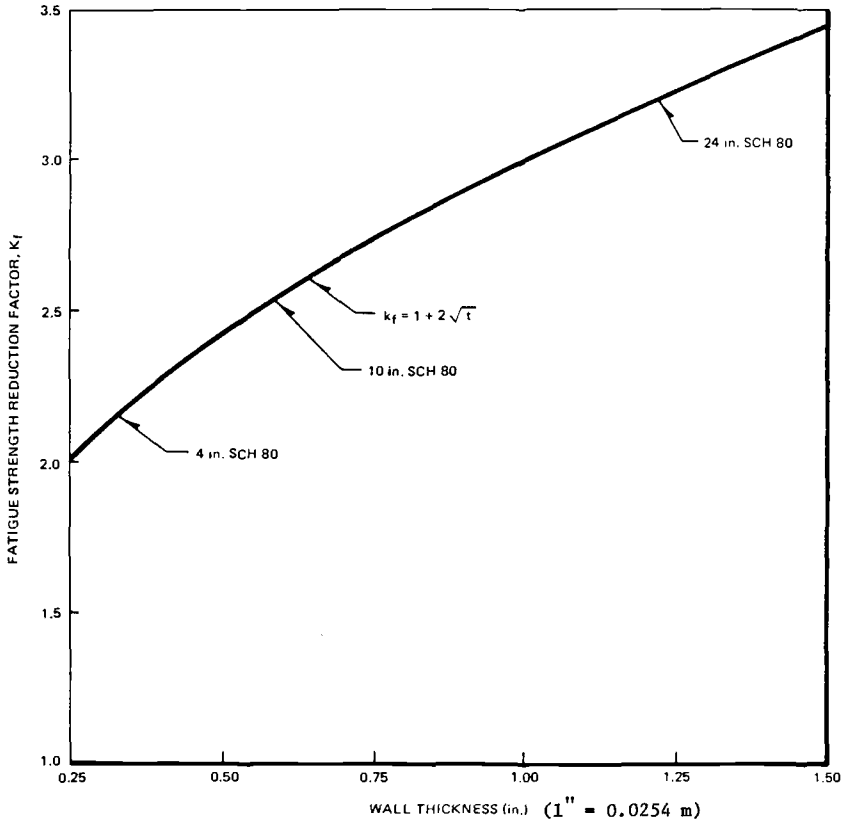


FIG. 3—Proposed fatigue strength reduction factors for pipe butt welds.

the notch tip, the local notch strain is given by

$$\epsilon_a = K_t K_n e_a$$

Applying Neuber's Rule for the notch, we obtain

$$(\sigma_a \epsilon_a E)^{1/2} = K_t (S_a e_a E)^{1/2}$$

The procedure described earlier can be used to calculate ϵ_a for a given value of e_a . This is complicated, however. For use in a piping analysis, a simple procedure based on the Ramberg-Osgood [21] assumption can be used. A stress-strain relationship of the type $\sigma = A \epsilon^n$ can be used as a fit to the cyclic stress-strain curve. When both the local stress and the nominal stress exceed the yield point, both stress states can be represented by the relationship $\sigma = A \epsilon^n$. Substituting this expression and assuming $n = 0.2$ for carbon steel, the notch factor K_n is given by

$$K_n = K_t^{0.67} \quad (6)$$

The notch factor K_n is 1.0 when the local stress $K_f S_n \leq 3S_m$ (or $S_n/3S_m \leq 1/K_f$), where S_m is the Design Stress Intensity defined in Section III of the Code. It is given by $K_f^{0.67}$ when the nominal stress S_n exceeds $3S_m$ (or $S_n/3S_m \geq 1$) and the net section experiences yielding. For values of $1/K_f \leq S_n/3S_m \leq 1$ linear interpolation is assumed. Figure 4 shows the actual notch factor calculated using two bounding cyclic stress-strain curves and by the simple relationship described above. It is seen that the simplified rules are conservative and describe the notch effect well.

Mean Stress Correction Factor (K_m)

It is generally understood that the Code fatigue curves already contain a built-in correction for mean stress and that no additional factor is necessary. This is strictly valid under the assumptions of the Code elastic-perfectly plastic behavior, yielding occurring at the Code minimum yield strength and under purely strain-controlled cycling. These assumptions are not realistic

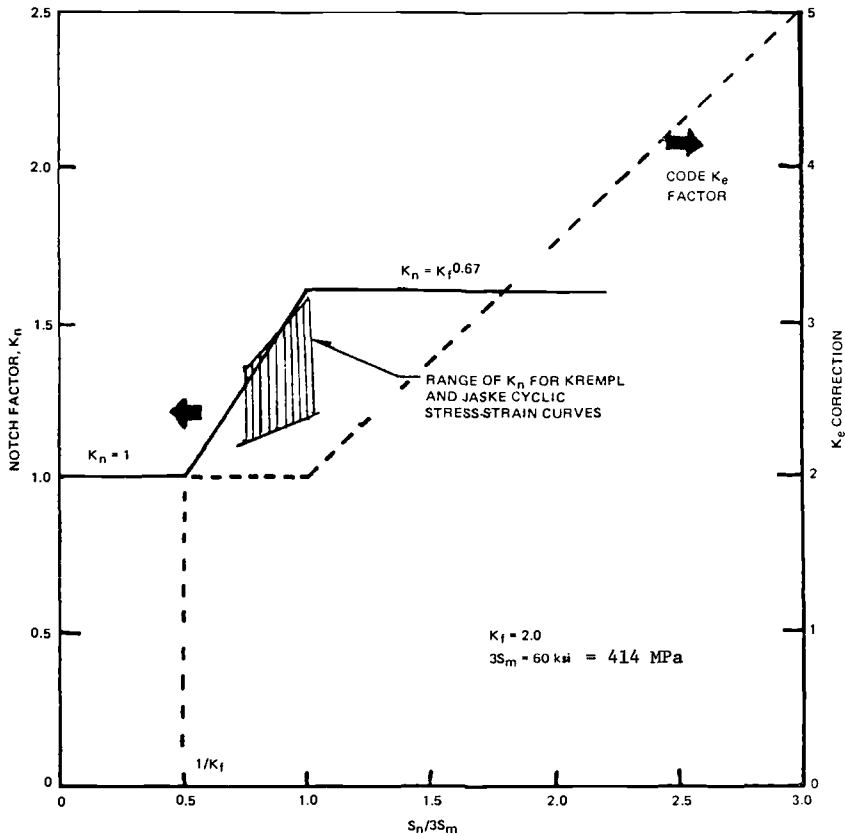


FIG. 4—Comparison of notch factors determined from actual cyclic stress-strain curve and from assumed Ramberg-Osgood curve of the type $\sigma = A\epsilon^n$ ($n = 0.2$).

under service conditions in piping. For example, the assumption that gross yielding occurs for stress ranges exceeding $3S_m$ (374 MPa at 288°C) is not strictly true, since carbon steel shows cyclic-hardening behavior. In fact, the cyclic stress-strain curve for carbon steel shows virtually elastic behavior for stress ranges exceeding 690 MPa (100 ksi). This shows that mean stress effects exist for stress ranges well in excess of $3S_m$. The fact that Code minimum yield strength values are used is another reason why the Code mean stress correction factors are not always adequate. In addition to higher than Code minimum yield strength for the piping material, the yield strength near welds is likely to be still higher because of the cold work.

As discussed earlier, the ratio $(\sigma_{\max}/\sigma_a)^{1/2}$ can be used as a mean stress correction factor. Again using the Ramberg-Osgood relationship [21] and assuming $\epsilon_{\max}/\epsilon_a = 2$ (zero-tension strain cycling) and $n = 0.2$ for carbon steel, the mean stress correction factor for fully plastic conditions is $(\sigma_{\max}/\sigma_a)^{1/2} = 2^{0.1} = 1.07$ (to be rounded off to 1.1). This shows that for large values of S_n the mean stress correction factor is small. Since the experimental data indicate that fully plastic conditions exist for $S_n/3S_m$ values approaching 2.0, it will be assumed that the mean stress correction factor is 1.1 when $S_n/3S_m = 2.0$. Linear interpolation is used for $1/K_f \leq S_n/3S_m \leq 2.0$.

Environmental Correction Factor (K_{en})

The environmental factor developed empirically is based on the 288°C (550°F) oxygenated water data. The zero to tension load control fatigue results were selected as the data base, since almost all the oxygenated water test data have been generated in this manner.

Figure 5 shows the 288°C (550°F) air and water data plotted as a function of $S_n/3S_m(1 - R)$, where R is minimum stress/maximum stress. This stress ratio was used to correlate the environmental effect, since it measures the maximum net section stress during a fatigue cycle.

As can be seen from Fig. 5, there is a well-defined upper bound for the air data and lower bound for the water data. The figure shows the difference between the air and water data, and shows that the environmental effect increases as the maximum net section stress increases. The proposed environmental factor is the ratio of the bounding lines in Fig. 5 for air and water. Since the bounding lines intersect at a stress ratio of 0.35, no environmental correction below this value is needed. The analytical forms for the environmental factor are (S_m -values taken from ASME Boiler and Pressure Vessel Code, Section III, Appendix A)

$$\text{For } S_n/3S_m(1 - R) \leq 0.35: \quad K_{en} = 1.0 \quad (7)$$

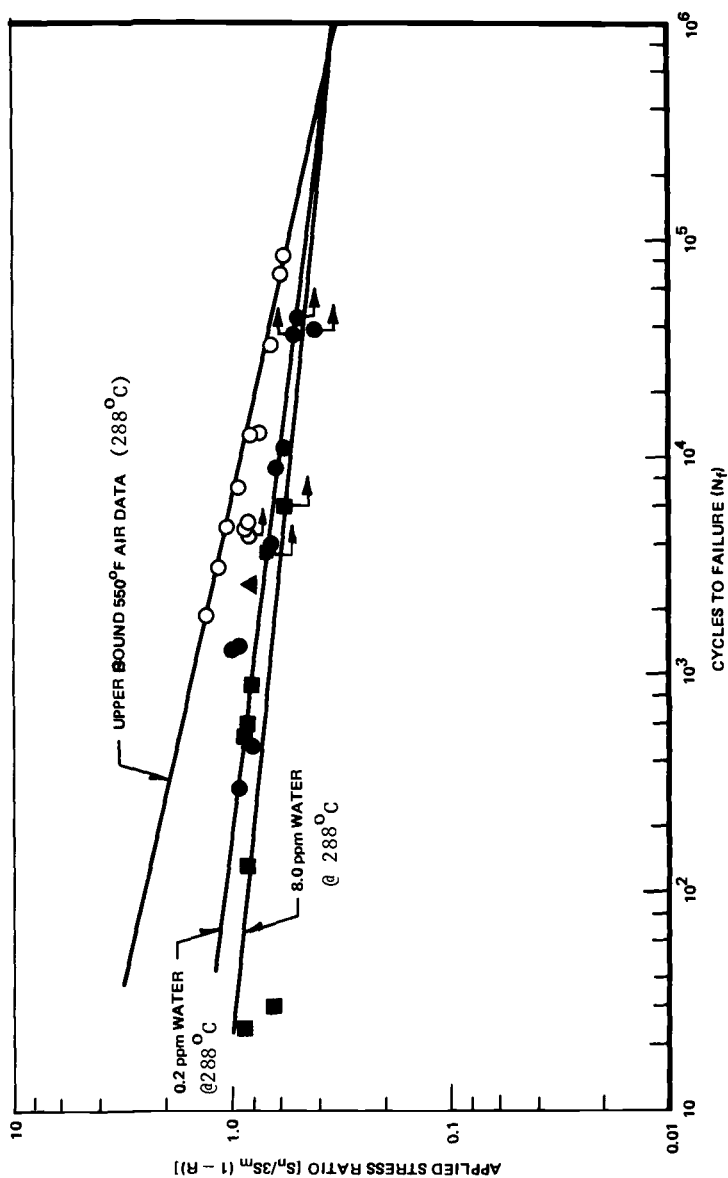


FIG. 5—Effect of water environment on fatigue life.

For $0.35 < S_n/3S_m(1 - R) < 1.0$:

$$K_{en} = 1.0 + H (S_n/3S_m(1 - R) - 0.35)$$

For $S_n/3S_m(1 - R) > 1.0$: $K_{en} = 1 + 0.65 H$ (proposed truncation)

where H is a material constant that depends on environmental conditions. The constant H will vary, depending on the given set of environmental conditions, specifically oxygen concentration, temperature, wave shape, and frequency. Based on present data at 288°C, $H = 2.0$ for 0.1 to 0.3 ppm oxygenated water, and $H = 3.5$ for 4.0 to 8.0 ppm water. The environmental factor K_{en} is shown in Fig. 6 as a function of $S_n/3S_m(1 - R)$. The environmental factors may be much lower at temperatures below 200°C.

Evaluation of Data Using the Proposed Design Rules

The fatigue test data were re-evaluated using the tentative design rules developed in this paper. The results are shown in Fig. 7 and compared with the ASME Code curve. It is seen that the data fall above the design curve, even for stress levels higher than permitted by the ASME Code.

The analytical approach described in this report is focused on improved procedures for determining local strain, mean stress, and environmental effect. The approach is to determine correction factors to be used with the current ASME approach.

It is possible that in some cases the different factors may overlap and lead to overly conservative results. Consequently, the effect of these rules on piping design must be assessed by application to specific examples. It should be emphasized that the proposed rules are tentative and are in a continuing process of development. Further changes may be proposed based on experience in piping evaluation and continued evaluation of the test data. One of the most promising areas for further development lies in more detailed assessment of effects of water temperature and cycle frequency. Initial results suggest that use of the K_{en} -factor is not needed when the water temperature is below about 200°C. Furthermore, at rapid cycle frequencies there is insufficient time for the environment to play a role in the cracking process. Initial studies have been completed to assess the effect of cycle frequencies ranging from about 10^{-1} to 10^{-4} Hz. It is clear that the more rapid frequencies result in no environmental effects; thus rapid loading events such as thermal or stress transients of durations less than a few minutes need not be considered for evaluation with the K_{en} -factor.

Acknowledgments

Funding for this study was provided by the Electric Power Research Institute (EPRI) and technical support was provided by R. Jones and M. Fox, both of EPRI. This support is gratefully acknowledged. The authors express

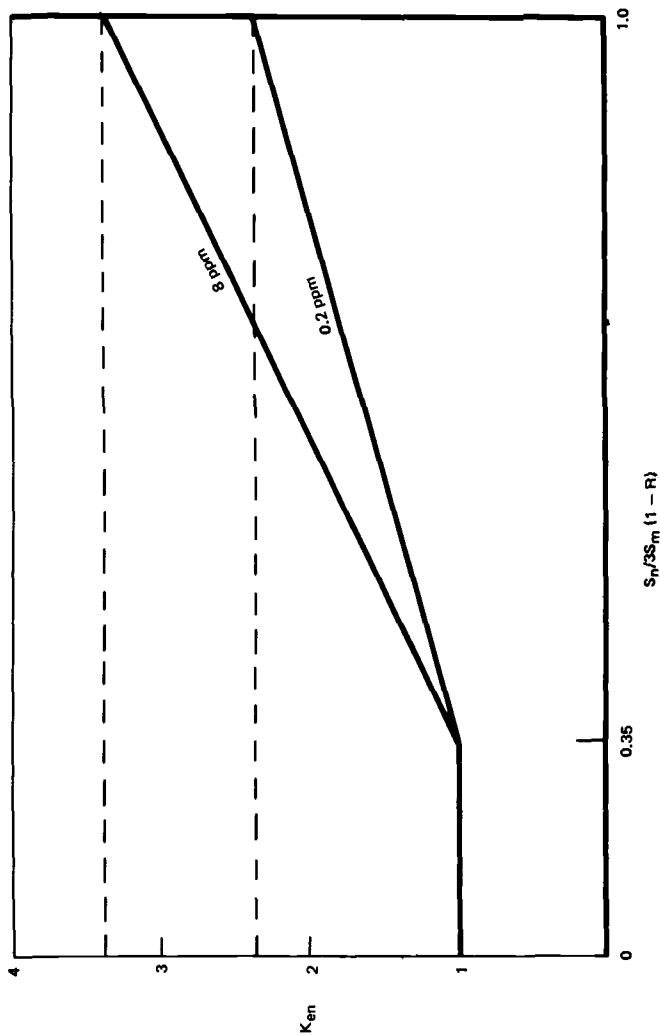


FIG. 6—Environmental correction factor.

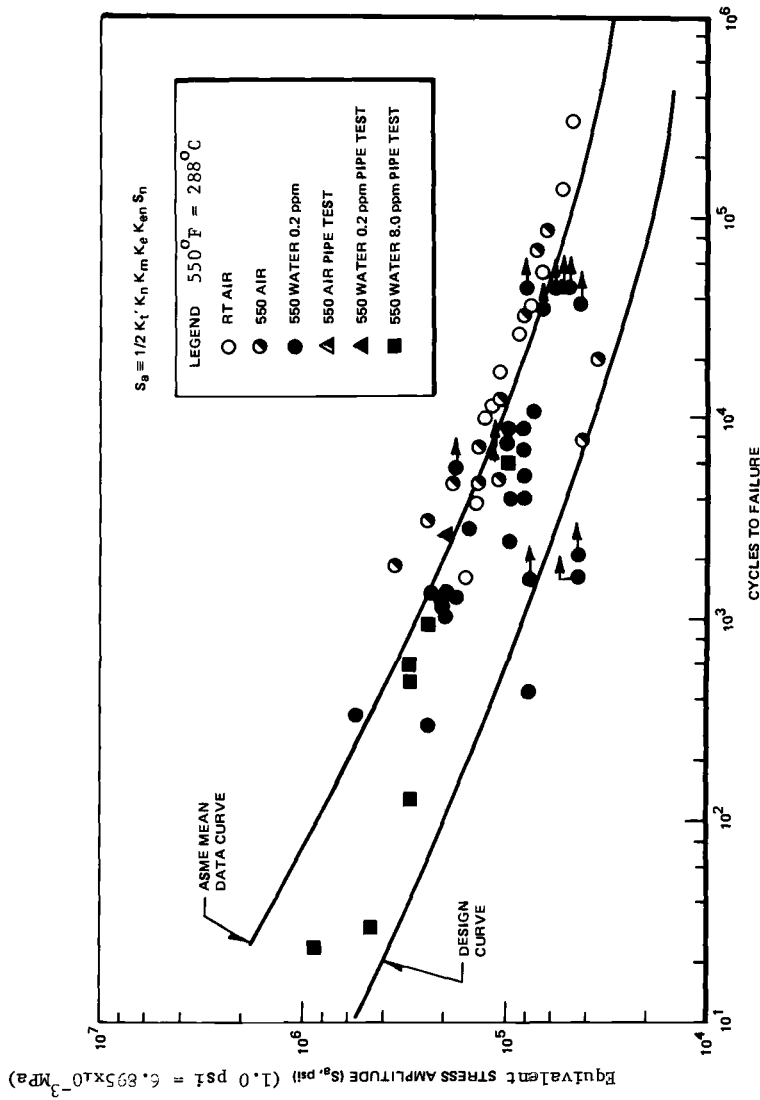


FIG. 7—Test results evaluated by proposed rules.

their appreciation to D. Weinstein, W. F. English, Drs. G. M. Gordon, T. L. Gerber, L. F. Coffin, S. Yukawa, and E. Kiss for their guidance and useful discussions.

References

- [1] American Society of Mechanical Engineers, "Nuclear Power Plant Components," *ASME Boiler and Pressure Vessel Code*, Section III.
- [2] Kreml, E. E., GEAP-10090, General Electric Atomic Power Equipment Department, Aug. 1969.
- [3] Hale, D. A., GEAP-20244, General Electric Atomic Power Equipment Department, Sept. 1977.
- [4] Kreml, E. E., GEAP-5147, General Electric Atomic Power Equipment Department, March 1966.
- [5] Kreml, E. E., GEAP-5714, General Electric Atomic Power Equipment Department, Jan. 1969.
- [6] Kreml, E. E., GEAP-5410, General Electric Atomic Power Equipment Department, Jan. 1967.
- [7] Hale, D. A., "Low Cycle Fatigue Behavior of Commercial Piping Steels in BWR Environment," *Journal of Engineering Materials and Technology, Transactions of ASME*, in press.
- [8] Kass, J., *Corrosion*, June 1980, p. 299.
- [9] Diaz, T. P., "Parametric Studies for Stress Corrosion in Type 304 Stainless Steel Pipe," NEDC-24187-6, Sixth Semi-Annual Report, General Electric Company, San Jose, Calif., May 1981.
- [10] Weinstein, D. L., "BWR Environmental Cracking Margins," NEDC-25322, Fourth Semi-Annual Report, General Electric Company, San Jose, Calif., July 1980.
- [11] Hughes, N., "Evaluation of Near Term BWR Piping Remedies," NEDC-21463, General Electric Company, San Jose, Calif.
- [12] *Fatigue under Complex Loading—Analyses and Experiments*, R. M. Wetzel, Ed., Society of Automotive Engineers, 1977.
- [13] Smith, K. N., Watson, P., and Topper, T. H., *Journal of Materials*, Vol. 5, No. 4, Dec. 1970, pp. 767-778.
- [14] Rodabaugh, E. C. and Moore, S. E., "Comparisons of Test Data with Code Methods for Fatigue Evaluation," Phase Report No. 115-10, ORNL-TM-3520, Oakridge National Laboratory, Nov. 1971.
- [15] Rodabaugh, E. C., Maxey, W. A., and Eiber, R. J., "Review and Assessment of Research Relevant to Design Aspects of Nuclear Power Plant Piping Systems," NUREG-0307, Nuclear Regulatory Commission, July 1977.
- [16] Newman, R. P., *Transactions of the Institute of Marine Engineers*, Vol. 68, 1956, pp. 153-172.
- [17] Kiss, E., Heald, J. D., and Hale, D. A., "Low Cycle Fatigue of Prototype Piping," GEAP 10135, General Electric Company, Jan. 1970.
- [18] Peterson, R. E. in *Metal Fatigue*, Series and Waisman, Ed., McGraw-Hill, New York, 1959, pp. 293-306.
- [19] Lawrence, F. V., Mattos, R. J., Higashida, Y., and Burk, J. D. in *Fatigue Testing of Weldments*, ASTM STP 648, American Society for Testing and Materials, 1978, pp. 134-158.
- [20] Neuber, H., "Theory of Notch Stress," English translation, University Microfilms, 1979.
- [21] Ramberg, W., "Description of Stress Strain Curves by Three Parameters," NACA Technical Note #902, July 1943.

Effect of Light-Water Reactor Environments on Fatigue Crack Growth Rate in Reactor Pressure Vessel Steels

REFERENCE: Törrönen, Kari and Cullen, W. H., Jr., "Effect of Light-Water Reactor Environments on Fatigue Crack Growth Rate in Reactor Pressure Vessel Steels," *Low-Cycle Fatigue and Life Prediction, ASTM STP 770*, C. Amzallag, B. N. Leis, and P. Rabbe, Eds., American Society for Testing and Materials, 1982, pp. 460–481.

ABSTRACT: This paper presents an overview of the effect of light-water reactor environments on the fatigue crack growth rate in reactor pressure vessel steels. The effect of different variables known to influence the environmental assistance—stress intensity range, load ratio, frequency, temperature, water chemistry, and irradiation—is described. The fractographic phenomena and mechanisms of fatigue crack propagation associated with environmental influence is emphasized. An analytical approach for predicting the crack growth rates based on the hydrogen embrittlement model is described. Finally, a discussion of the effect of different transients occurring in the nuclear reactors on the crack growth rate predictions is presented.

KEY WORDS: fatigue (materials), corrosion fatigue, crack propagation, hydrogen embrittlement, pressure vessel steels

An integral part of the safety assessment of nuclear pressure vessels is the quantitative estimation of defect growth during service. This estimation is essential for determining whether the defect, detected during inspection, should be repaired, or whether the size of the defect, even after its expected growth, is small enough to leave the integrity of the vessel unaffected.

Numerous sources generate fatigue cycling in reactor pressure vessels. During the lifetime of a typical vessel, startup/shutdown procedures account for about 250 cycles, power loading/unloadings for about 50 000 cycles, step increases/decreases in output for about 10 000 cycles, minor trips of reactor or turbine for about 1000 cycles, and deliberate hydroleak tests for about 20 cycles. This cyclic loading may introduce defect growth, which is further enhanced once reactor water comes into contact with the growing crack.

¹ Technical Research Centre of Finland, Metals Laboratory, Espoo, Finland.

² Materials Engineering Associates, Inc., Lanham, Md. 20706.

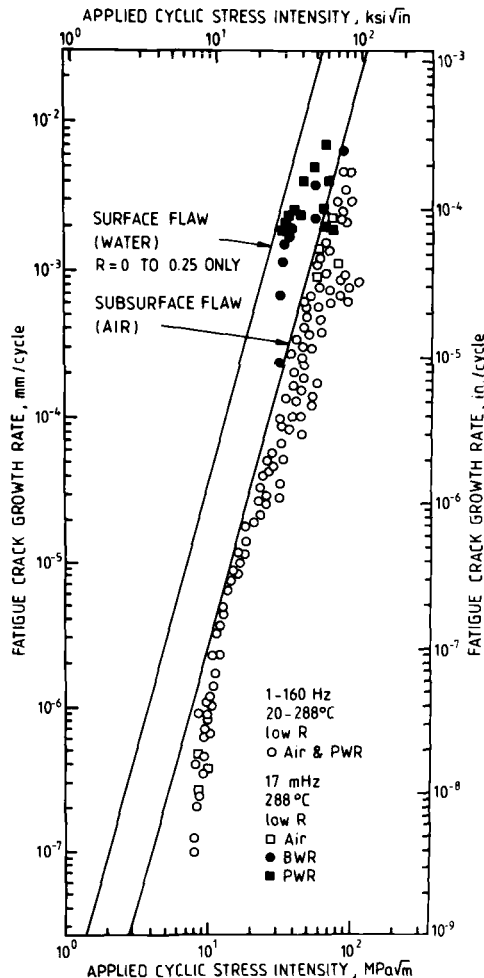


FIG. 1—Current (1980) ASME Code Section XI reference curves, with supporting data [1-5].

Appendix A of Section XI of the ASME Code [1], Rules for In-Service Inspection of Nuclear Power Plant Components, presents suggested upper limits for fatigue crack growth in air and water environments.³ These limits were derived on the basis of some early research that evaluated fatigue crack growth rates in A533B and A508-2 pressure vessel steels in air environments over a wide range of temperatures [2,3] and in high-temperature, pressurized reactor-grade water environments [4,5]. The current version of these curves (1980), with the data upon which they were based, is shown in Fig. 1.

³ The italic numbers in brackets refer to the list of references appended to this paper.

Since the original formulation of the ASME reference curves, additional research has defined some conditions, involving aqueous environments and high mean stresses, for which crack growth rates can exceed the default lines of the Section XI. Hence, in recent years there has been a concentrated effort in several laboratories to obtain additional fatigue crack growth rate data in the high-temperature, pressurized reactor-grade water environment typical of the light-water reactors [6].

The purpose of this paper is to summarize how different variables such as stress intensity range, load ratio, frequency, temperature, water chemistry, and irradiation affect the cyclic crack growth in reactor-grade water. The mechanism underlying the environmental influence and an analytical approach for predicting crack growth rates based on this mechanistic model are described. Finally, a discussion of the effect of different transients occurring in the nuclear reactors on the crack growth rate predictions is presented.

Summary of Observations of Fatigue Crack Growth in Light-Water Reactor Environments

Crack growth rates observed for ferritic pressure vessel steels in light-water reactor environments have been found to be dependent on several variables that have little or no effect on crack growth in dry air. These variables may be divided into three groups, which are material-, stress-, and environment-related. In addition to these, a temperature dependence has been observed. A review of the effects of these variables based on the published data up to the end of 1979 has been given elsewhere [6]; the findings may be summarized as follows.

1. The effect of materials and environmental variables is minor compared with the stress-related effects. The pressure vessels in current light-water reactors are of ferritic medium-strength low-alloy steels of A508 Class 2 and A533B Class 1 or equivalent grades. The behavior of these steels is identical. Data are also available to demonstrate that other medium-strength carbon and low-alloy steels show very similar behavior in water environments [7]. The behavior of weld material and heat-affected zones (HAZ) follows the same pattern as the base metals; however, the observed crack growth rates of the weld and HAZ materials fall close to the upper bound of the scatter band. Retardations also occur in the data fairly regularly. These retardations are more pronounced at higher load ratios and may be related to the material inhomogeneity in weld and HAZ materials.

Recent results [8,9] have introduced a new factor, which can strongly influence the susceptibility of the reactor pressure vessel steels to a given water environments, namely material chemistry. It appears that the sulfur content of the steel has a strong impact on its environmental sensitivity, with the higher content resulting in more susceptibility.

2. The environmental variables of concern in light-water reactors are basically those connected to the pressurized or boiling water reactor water chemistries. The basic difference is in the dissolved oxygen content: under PWR conditions deoxygenated water with only an insignificant amount of oxygen (<1 ppb) is used, whereas a constant concentration of oxygen (about 200 ppb) is maintained under BWR conditions. In addition to this, a certain amount of boric acid and lithium hydroxide is added to the PWR water whereas no additions are used in the BWR water. Although the basic difference in dissolved oxygen content is thought to introduce some differences in the environmentally influenced crack growth mechanism, the observed crack growth rates in both environments show fairly good agreement under comparable loading conditions.

3. The loading history related variables have the most pronounced effect on the observed crack growth behavior. These variables include the cyclic stress intensity range ΔK , load ratio R , and frequency or rise time of the cycle and waveform. Temperature and water chemistry add some complications to the general trends. It should be kept in mind that in reality the loads, and the rates and waveforms associated with the application of these loads, in an operating power reactor form a variable amplitude/variable frequency load sequence, while all the data generated so far are from constant-amplitude load or constant stress intensity range types of tests with simple waveforms.

The general trends of the data can be divided into three distinct groups (Fig. 2). The trends shown are typical for steels containing fairly high amounts of the sulfur and represent the bulk of test materials used up to the beginning of 1980.

The first group of data resides along the ASME Code Section XI air default line. This data band, termed low, comprises all the air data and the data generated in simulated reactor-grade water using frequencies and/or waveforms that do not allow any environmental effects. To produce an accelerated crack growth rate (above the air results), a sufficiently long rising part of the load cycle is needed; that is, the ramp time must be on the order of 1 s or slower or the frequency be on the order of 1 Hz or lower. The data generated to date showing environmental acceleration can be divided further into two groups based on the applied load ratio R . This grouping may be artificial, however, as tests with intermediate R -values have not been performed. Lower load ratio value tests ($R \leq 0.2$) produce data with less acceleration than tests with higher values ($R = 0.63, \dots, 0.75$), as shown in Fig. 2. No data are available at load ratios higher than 0.75. Limited data obtained in seawater at $R = 0.85$ [10] indicate that the load ratio effect does not continue to increase for load ratio values exceeding 0.75 in room-temperature seawater. Without any experimental evidence in reactor-grade water, however, no generalization can be made.

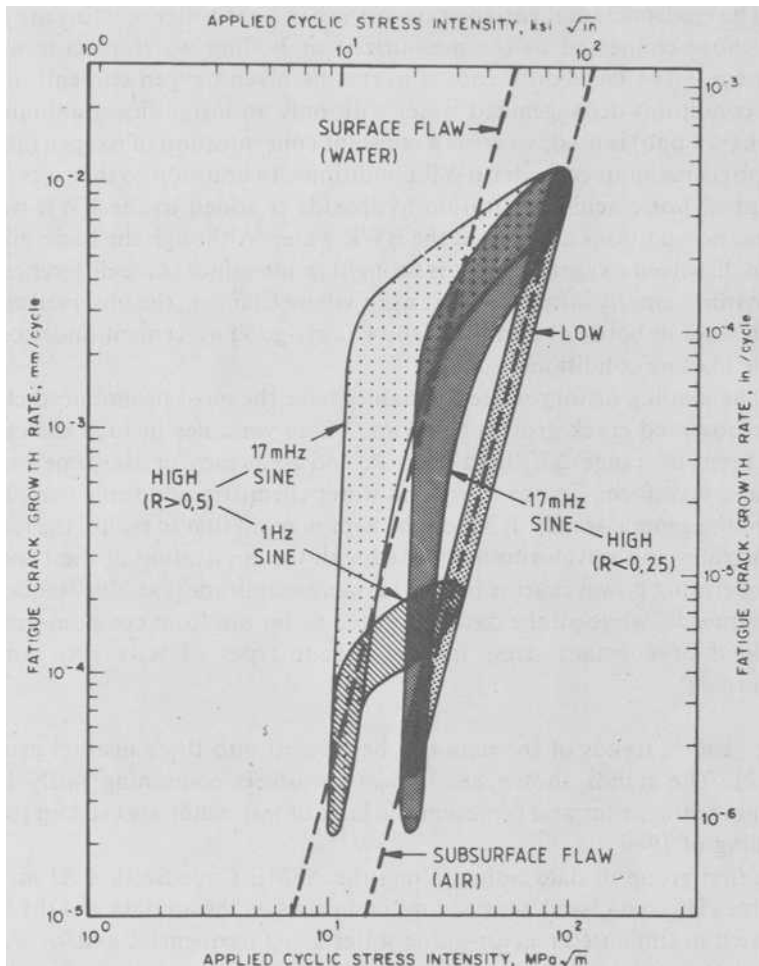


FIG. 2—General trends of the cyclic crack growth rate in high-temperature high-pressure reactor-grade water. Three distinct groups can be observed. See text for further details.

Once the environmental acceleration starts only a small increase of applied ΔK is needed for a large increase in crack growth rate. When a certain crack growth rate/frequency combination is attained, a bend-over occurs; that is, the environmental influence diminishes and the data band returns to the air default line. The highest bend-over—the maximum environmental acceleration—seems to occur with 17 mHz (1 cpm) sinewave loading, at least in PWR conditions. With higher frequencies the bend-over occurs earlier (Fig. 2). Lower frequencies have not been tested with high load ratio values, but with lower load ratios a difference between PWR and BWR conditions is seen. Frequencies lower than 17 mHz (1 cpm) in PWR conditions produce

less environmental acceleration; most of the data bands reside actually in the low category along the air default line. In BWR conditions, however, a saturation is seen and the data remain in the high regime shown in Fig. 2.

Other waveforms than sinewave have produced data in a somewhat confusing way. In many cases the environmental influence is shown to be dependent on the rise time of the loading. However, rise times on the order of 20 to 60 s, which is comparable to 17 mHz sinewave, have produced data both in the low and the high category. This discrepancy still remains to be resolved. The hold time in trapezoidal waveforms has been proven to have no influence on the observed crack growth rates.

The effect of temperature modifies somewhat the aforementioned behavior, which is relevant to the operating temperature of the nuclear reactors (roughly 290°C); for lower temperatures (data are available only below 100°C) accelerated crack growth is always observed with frequencies higher or on the order of 1 Hz. The general trends are shown in Fig. 3.

As indicated in Fig. 2, no data are available at or close to the threshold region for operating temperatures. The data bands suggest that no environmental influence is seen below a certain ΔK -value that is dependent on the load ratio. Whether this is a true behavior or simply connected to the startup phenomena of tests remains to be solved.

Post-irradiation fatigue crack growth rate tests, in a simulated PWR environment, have demonstrated that irradiation does not further increase the growth rates beyond those increases that are due to the environment itself [11,12]. These data are, however, limited to the low load ratio regime and base materials only.

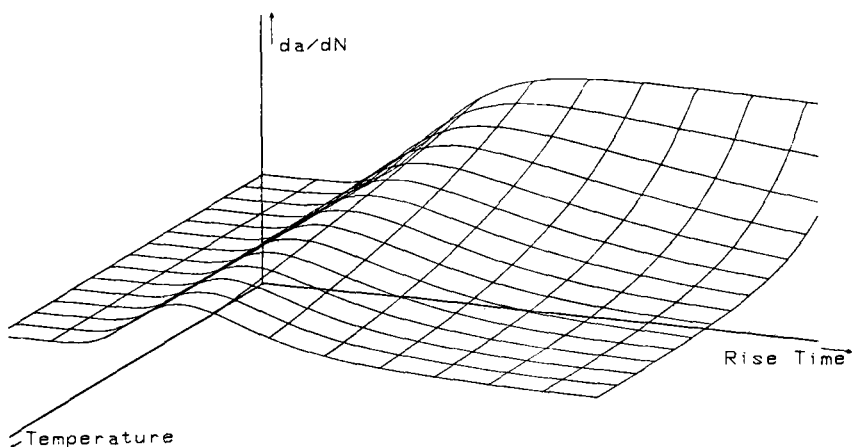


FIG. 3—A conceptualized three-dimensional surface of crack growth rates, for a fixed value of ΔK , as a function of ramp time and temperature. The edge closest to the viewer depicts the growth rate behavior at higher test temperature ($\sim 290^\circ\text{C}$), beginning with low growth rates for fast ramps, then high growth rates for 17 mHz sinewave equivalent ramps, and reverting to low growth rates for long ramp times.

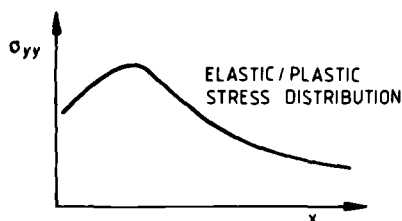
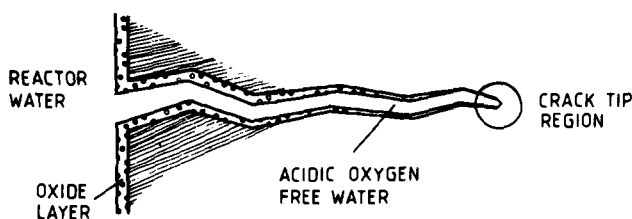
This overview of the observed crack growth behavior suggests that further research is urgently needed. Specific areas requiring attention are tests with higher load ratios (>0.7), intermediate load ratios ($0.3 \text{ -- } 0.5$), intermediate temperatures, complex load spectra, and applied ΔK -values approaching threshold, as well as tests aiming to clarify the influence of material chemistry, especially sulfur content.

Mechanism of Environmentally Accelerated Crack Growth

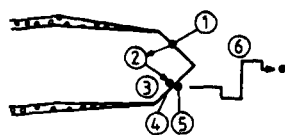
Two basic mechanisms, dissolution assistance and hydrogen assistance, have generally been proposed to explain environmentally enhanced crack growth in simulated PWR and BWR environments [13–18]. In the former process the advancement of the crack is assisted by removal (dissolution) of the metal at the crack tip, whereas in the latter process the mechanical separation at the crack tip is facilitated by hydrogen embrittlement. The authors favor the latter mechanism, and our opinion is based primarily on the copious fractographic evidence [17–24], which certainly rules out the dissolution assistance mechanism. Thus, although further evidence may be lacking, the hydrogen-assisted mechanism, when adapted to the general trends of the environmental enhancement in cyclic crack growth rate, does not fail to predict the observed behavior.

In aqueous environments, the electrochemical conditions at the crack tip during both sustained and low-frequency cyclic loading have been shown to be different from the bulk electrochemistry. Under a free corrosion potential, the pH is found to be in the acidic regime, regardless of the bulk dissolved oxygen content [25–28]. Under these circumstances an anodic reaction involving metal-surface dissolution occurs at the crack tip. This must be balanced by a corresponding cathodic reaction, and this reaction takes place either at the crack-tip region or on the external surface. In the absence of dissolved oxygen, the cathodic reaction involves the reduction of hydrogen ions to atomic hydrogen, which can then enter the metal. When dissolved oxygen is present in the bulk water, another cathodic reaction can occur on the external surface, namely the reduction of dissolved oxygen to hydroxyl ions. This reaction cannot occur, or occurs to a lesser degree, near the crack tip, where the solution is nearly or totally deoxygenated.

Hydrogen evolution occurs only during rise time of the fatigue cycles as the fresh metal surface at the advancing crack tip is exposed to the environment. This is evident as introduction of any length of hold time at peak load does not increase the environmental acceleration of crack growth rate. On the contrary, a retardation is sometimes seen. Evolved hydrogen can subsequently enter the metal provided certain requirements, concerning adequate surface reaction time, competing repassivation, and possibly adequate fresh surface area, are met. Once the hydrogen has entered the metal, it diffuses along the stress gradient towards the region of high triaxial stress just ahead



CRACK TIP REGION



1. LOCAL ANODIC REACTION
 $\text{Fe} \rightarrow \text{Fe}^{2+} + 2\text{e}^-$
2. HYDROLYSIS AND GENERATION OF H^+
 $\text{Fe}^{2+} + \text{H}_2\text{O} \rightarrow \text{FeOH}^+ + \text{H}^+$
3. LIQUID PHASE TRANSPORT
4. LOCAL CATHODIC REACTION
 $\text{H}^+ + \text{e}^- \rightarrow \text{H}$
5. HYDROGEN ADSORPTION
6. HYDROGEN TRANSPORT IN LATTICE

FIG. 4—Schematic illustration of hydrogen assistance during cyclic crack growth of reactor pressure vessel steels in high-temperature high-pressure reactor-grade water.

of the crack tip. The bulk diffusion rate at the elevated temperatures in question is high enough to allow, within seconds, an excess concentration of hydrogen in the plastic enclave [29]. The presence of hydrogen in the plastic enclave introduces a macroscopic embrittling effect and a subsequent increase in cyclic crack growth rate. At least nine different mechanisms have been proposed for hydrogen-assisted cracking at the atomistic or lattice level [30]. At the present time no preference for a particular model can be expressed. As stated in a recent review [30], it is possible that several of the proposed mechanisms may contribute to the overall cracking process. The presented model is outlined in Fig. 4.

The fractography and metallography performed strongly support the hydrogen-embrittlement model [17–24]. Typical features of specimens showing no environmental influence in water or air are a transgranular fracture path, coupled with ductile striations and dense microcracking or branching (Fig. 5a). When accelerated crack growth rates are observed, the fracture mode changes at lower temperatures (around 100°C) to cleavage-like planes with no striations (Fig. 5b). At the operating temperature of the reactor (288°C) several fracture modes are observed with increasing applied cyclic stress intensity range. In the lowest ΔK -range the fracture propagation remains ductile. Whether this is a true phenomenon or simply connected to the startup of the test before the specific water chemistry conditions within the crack have been established remains to be solved. When the environmentally assisted crack growth acceleration is seen, the striations become brittle as defined by Forsyth [31].

As the amount of microcracking decreases, fracture propagates along roughly cleavage-like planes, and fan-shaped patterns typical of hydrogen-assisted cracking can be seen (Fig. 5c). A rather abrupt change in the fracture mode appears with still higher ΔK -values. Essentially no striations or microcracks can be seen. Crack propagation along cleavage-like planes and features typical of hydrogen embrittlement are evident (Fig. 5d). In the final region, in which the growth rates are characterized by the bend-over towards the ASME Section XI air default line, brittle striations and microcracks, some fairly large and connected to inclusions, can be seen (Fig. 5e). A comparison of the environmentally assisted fatigue crack features with the low-temperature fast fracture area obtained after test termination is given in Fig. 5f. This shows the close similarity between the environmentally assisted crack growth area and the quasi-cleavage type fast fracture. The four fractographically different crack growth areas are superposed on a typical da/dN - ΔK curve in Fig. 6.

Reportedly, the fractographic features also depend on the material being tested. Contrary to the features reviewed above, the mechanism of fatigue crack growth in the weld specimens is void coalescence, both in the presence and the absence of the environmental influence [17]. The large number of coarse carbides in the weld specimens is suggested to be sufficient to influence the void nucleation process and explain the occurrence of this mechanism of crack propagation. As discussed by Thompson [32], hydrogen may enhance the rate of microvoid formation and growth, and thus introduce the crack growth rate acceleration.

Application of Hydrogen-Assisted Cyclic Crack Growth Model for Explaining Experimental Data

The aforementioned hydrogen-assisted cyclic crack growth model can now be applied to explain the observed crack growth behavior. The overall trends of the observed behavior presented in Fig. 2 show several regimes to

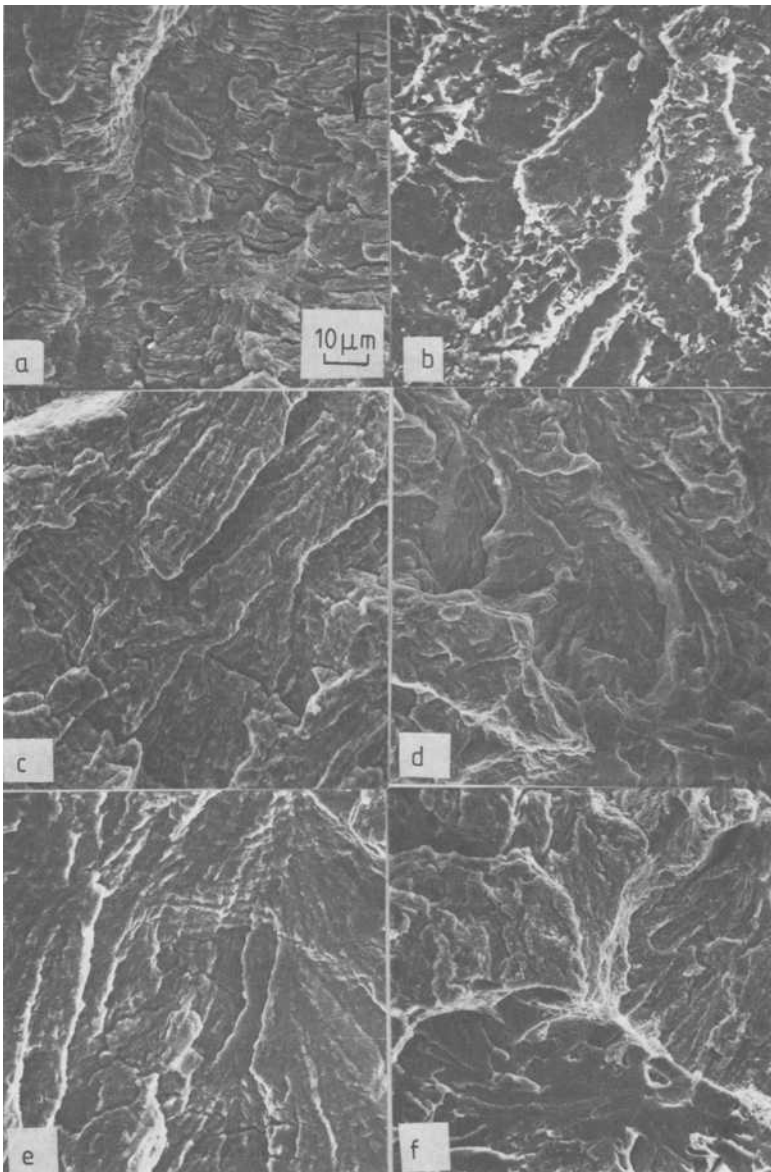


FIG. 5—Typical fracture surface areas from different cyclic crack growth tests. (a) 1 Hz test at 288°C showing no environmental influence; $\Delta K = 41 \text{ MPa} \sqrt{\text{m}}$. (b) 1 min ramp, no-hold test at 93°C showing environmental influence; $\Delta K = 41 \text{ MPa} \sqrt{\text{m}}$. (c) 17 mHz test at 288°C showing environmental influence; $\Delta K = 36 \text{ MPa} \sqrt{\text{m}}$. (d) Same; $\Delta K = 41 \text{ MPa} \sqrt{\text{m}}$. (e) Same; $\Delta K = 50 \text{ MPa} \sqrt{\text{m}}$. (f) Same; fast fracture area obtained after test termination is also seen; $\Delta K = 60 \text{ MPa} \sqrt{\text{m}}$.

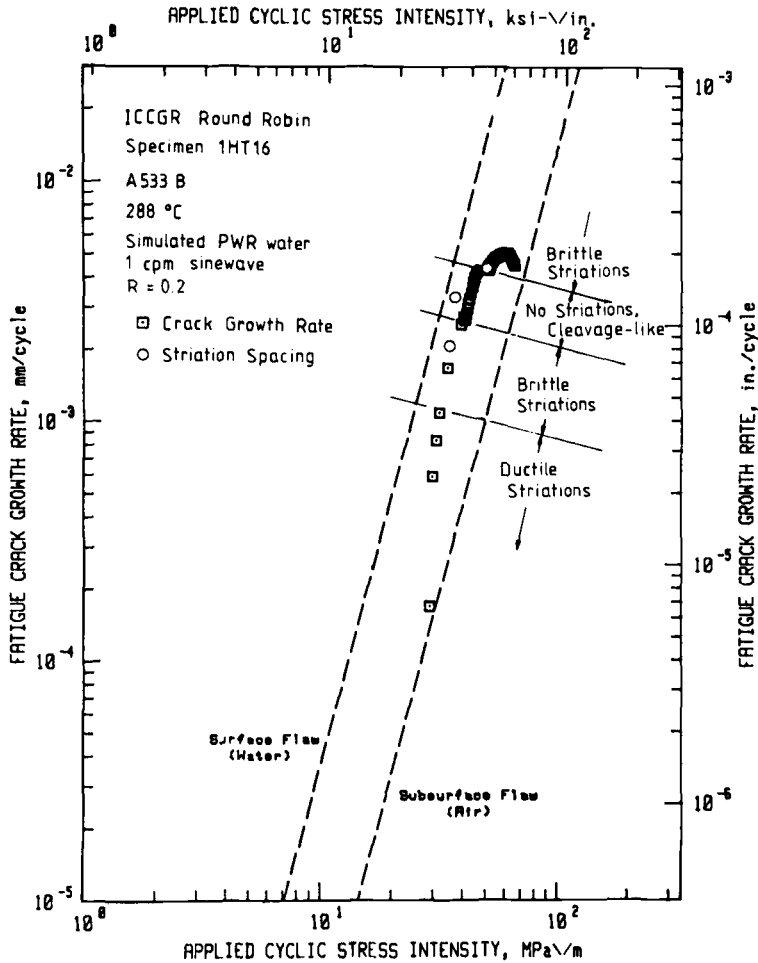


FIG. 6—Location of the four fractographically different crack growth areas in environmentally assisted cyclic crack growth compared with a typical $da/dN-\Delta K$ curve.

be considered. These regimes may be divided into five categories (see also Fig. 8): (1) threshold region, (2) intermediate crack growth region with no environmental assistance, (3) rapidly increasing crack growth rate region, (4) diminishing environmental assistance region (bend-over region), and (5) final crack growth region.

Threshold Region

No high-temperature data in this region are currently available. Room-temperature tests performed with only low load ratio values [3] give ΔK_{th} of roughly $8 \text{ MPa} \sqrt{\text{m}}$. Higher load ratio values are known to produce lower

ΔK_{th} -values in air [3]. Whether this is also the case in water environments remains to be seen.

Intermediate Growth Region

Again no valid data are available. Experiments conducted in room-temperature hydrogen [33,34] and seawater [18] indicate, however, that an intermediate region exists between the threshold and the onset of hydrogen-assisted acceleration. Based on this observation, Ritchie [34] has developed a model using a critical stress criterion for crack growth. According to this model, the influence of a hydrogen-containing environment on the onset of the environmentally assisted acceleration is related to the stress-assisted accumulation of hydrogen that occurs in the maximum triaxial stress state near the crack tip. Thus for a given yield strength, temperature, and environment the amount of hydrogen accumulated depends only on K_{max} . This predicts that the onset of the environmentally assisted crack growth acceleration is dependent on the load ratio. The observed trend bands shown in Fig. 2 support this prediction, as do data generated in seawater [18]. Critical K_{max} -values for SA542-3 steel tested in hydrogen were found to be 19 to 24 MPa \sqrt{m} [33], and for BS4 360 Grade 50D steel tested in seawater 22 MPa \sqrt{m} [18], independent of load ratio or frequency. The review of the published data on high-temperature water suggests a K_{max} -value of roughly 24 MPa \sqrt{m} for the reactor pressure vessel steels, which is in close agreement with Ritchie's result in hydrogen and seawater. This further indicates that the model developed for hydrogen environment is also applicable to the high-temperature water environment.

The foregoing discussion suggests, although without any actual data, that an intermediate crack growth rate regime exists for cyclic crack growth in high-temperature reactor water. The ASME Code Section XI air default line is obviously representative for this regime so long as growth rates remain independent of frequency or loading rate and the load ratio.

Environmentally Accelerated Crack Growth

Once the apparent critical K_{max} is obtained, the cyclic crack growth rate increases with the applied cyclic stress intensity much faster in the high-temperature water than in air (Fig. 2). This environmental acceleration is due to the accumulation of hydrogen in the crack-tip region and subsequent embrittlement, as discussed previously. The environmental influence does not continue indefinitely, but once a certain frequency-dependent crack growth rate is exceeded, a deceleration starts.

Whether the environmental acceleration does or does not occur depends on the frequency or loading rate, as discussed earlier. At high frequencies the interaction of the exposed metal with the environment is of no consequence, because the rate at which the metal fails by ductile fracture exceeds the rate

at which the environment can affect fracture via hydrogen embrittlement. At lower frequencies the formation of passivating film can inhibit the entry of hydrogen at the crack tip. This film can be formed provided the rates of the anodic and cathodic reactions are sufficiently slow, as would be the case in completely deoxygenated water (PWR conditions), and provided that the crack-tip straining rate is rather monotonic, as in trapezoidal load waveform testing. On the other hand, in the sinewave load testing, the continuous changes in the crack-tip straining rate may prevent the passive film formation and hence facilitate the hydrogen entry and subsequent crack growth enhancement. If the frequency is lowered sufficiently, however, the film formation may occur, thus preventing the hydrogen entry. In the presence of dissolved oxygen (BWR conditions) the reaction rates may again be higher. This may facilitate pronounced hydrogen evolution even with longer ramp times, which in turn will result in the accelerated crack growth rates seen in BWR results at these frequencies. At lower temperatures, where crack growth enhancement is observed even at very low frequencies, the oxide, which prevails, is of hematite type as opposed to the more adherent magnetite, which forms at higher temperatures [35]. Thus it is possible that the oxide layer at lower temperatures, if formed, is porous enough to allow hydrogen admission.

It has been shown that in a water environment the crack growth rate is limited by the oxidation rate of freshly exposed surface at the crack tip [36]. Thus the resultant cyclic crack growth rate must be directly related to the area of the fresh surface generated during the crack advancement within one cycle. Furthermore, crack advancement is directly related to crack-tip opening displacement (CTOD) [37], which for plain strain conditions is of the form

$$\text{CTOD} \cong 0.5 \frac{1}{\sigma_y E} (K_{\max}^2 - K_{\min}^2) \quad (1)$$

Inserting ΔK and load ratio R , we obtain

$$\text{CTOD} \cong 0.5 \frac{(\Delta K)^2}{\sigma_y E} \frac{1 - R^2}{(1 - R)^2} \quad (2)$$

where σ_y is the yield strength and E is Young's modulus of elasticity.

Equation 2 can be used to calculate ΔK for a certain cyclic crack growth rate and R -ratio. Thus the modified Paris equation for the accelerating part of the environmentally assisted cyclic crack growth is

$$\frac{da}{dN} = C (\Delta K)^m \left(\frac{\sqrt{1 - R^2}}{1 - R} \right)^m \quad (3)$$

The expressions fits well with the observed data. However, for load ratios higher than 0.7, where no data are available, it has been postulated, as stated

earlier, that no further enhancement of crack growth rates will occur with increasing load ratio. This is contrary to the trend given by Eq 3, but no explanation for this possible discrepancy can be given.

Bend-Over Region

A decrease in the environmental influence starts when a certain frequency-dependent or loading rate dependent cyclic crack growth rate is exceeded. The higher the test frequency, the lower the value of the crack growth rate at which the data bends over, which indicates a crack velocity dependence. As the growth rate accelerates due to hydrogen embrittlement, it eventually reaches a velocity where the rate-limiting surface reaction does not allow a sufficient amount of hydrogen to be generated at the triaxial stress state region. The crack growth rate then slows down to a rate determined by the rate of hydrogen accumulation, becoming only weakly dependent on ΔK [17]. Testing at a slower frequency allows more hydrogen to accumulate per cycle, and thus a faster crack growth rate. A recent evaluation of some experimental results in seawater and reactor-grade water, based on comparisons between crack velocity in water environment and air, indicates that the bend-over occurs around 5×10^{-3} mm/min crack velocity [38]. This is in a good agreement with the trends shown in Fig. 2, where the bend-over for the 17-mHz test occurs roughly around 5×10^{-3} mm/min and for the 1-Hz test around 1×10^{-2} mm/min.

The data obtained to date in the bend-over region are very scattered. This is obviously connected to the appearance of crack branching, which is strongly materials dependent [17]. As macrobranches are often connected to slag inclusions [21,24], their size and distribution can certainly affect the crack growth behavior.

In the bend-over region of the two groups describing the results of 17-mHz tests ($R < 0.25$; $R > 0.50$) the general trend of the data is directed at a focal point at about $\Delta K_{t,0} = 90 \text{ MPa } \sqrt{\text{m}}$, $da/dN = 10^{-2}$ mm/cycle, where $\Delta K_{t,0}$ denotes the onsets of the final region of crack growth, as seen in Fig. 2. Thus, if the Paris equation is re-written as

$$\frac{da}{dN} = C \left(\frac{\Delta K}{\Delta K_{t,0}} \right)^m \quad (4)$$

then C becomes equal to the crack growth rates at the point of intersection, and m becomes the slope of the trend line that best represents the data in the bend-over region. In this fashion, the growth rate preference line for the bend-over region may be constructed.

Final Crack Growth Region

No data are available in this region due to the relatively small size of the test specimens, which limits the maximum ΔK obtainable. As no environ-

mental influence is to be expected in this region, the ASME Code Section XI air default line is thought to be applicable up to the point when limiting K_{Ic} is obtained.

Reference Curves

A comparison of Figs. 1 and 2 shows clearly that the current ASME reference curves need modification. Although a restriction for using the water default line only with load ratio values equal to or less than 0.2 has been added recently, some of the obtained data bands reach to the unconservative side of the line. Several ways to modify the curves have been suggested [39–41], and the ASME subcommittee responsible for the reference curves has accepted new curves as shown in Fig. 7 [7]. A basic change of philosophy has occurred. The curves are no longer upper-bound curves; instead, they have been developed based on 95 percent global confidence limits of all available data. As such, the reference curves are approximately a factor of two higher than the mean of the data.

The revised curves result in slightly higher calculated crack growth rates for high load ratio transients than the old curves. If the combination of high and low load ratio transients typical of design transient specifications is considered, the calculated crack growth is slightly less severe than with the current reference curve.

Initially, before general agreement on the mechanism of the environmental influence had been achieved, it was obvious that the reference curves incorporated into any code must be based only on the mean or upper bound of the experimental data. However, once the mechanism is understood and sufficiently proven, new reference curves should be based on that understanding. An attempt in that direction, based on the aforementioned hydrogen-embrittlement model, is shown in Fig. 8. As discussed earlier, a lack of data is evident in the threshold and near-threshold regions; otherwise the presented curves agree fairly well with the experimental data.

Above the threshold, the curves consist of a series of lines for which Paris-type equations can be determined. In the environmentally accelerated crack growth region the effect of load ratio can be accounted for by using Eq 3. The decelerating environmental influence region is shown as based on 17-mHz data trends representing the upper-bound curve. No numerical expressions have been determined for the proposed reference curves, but two basic values of importance are the critical K_{max} for the onset of environmental influence, which is about $24 \text{ MPa } \sqrt{\text{m}}$, and the critical cyclic crack growth rate for the onset of bend-over, which is roughly $2.5 \times 10^{-3} \text{ mm/cycle}$.

The proposed ASME Code Section XI reference curves and the reference curves based on the hydrogen-embrittlement model are compared with each other and with the experimental data bands from Fig. 2 in Fig. 9. The latter curves seem to fit the data bands much better; the lack of agreement between the proposed ASME reference curves and experimental data is considerable

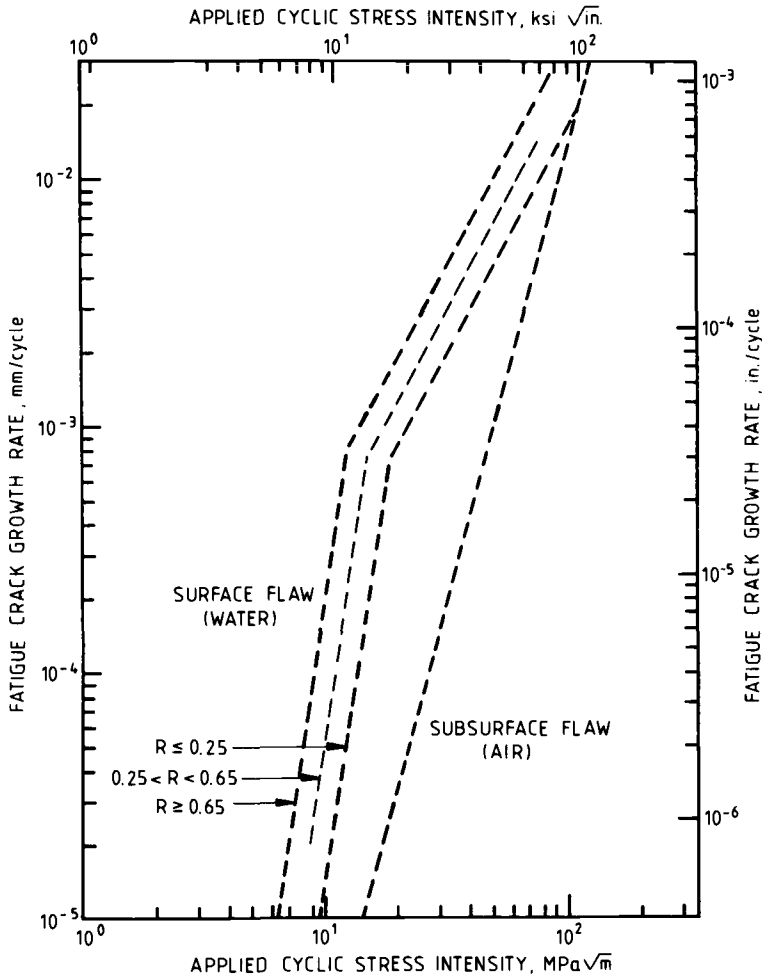


FIG. 7—Proposed ASME Code Section XI reference fatigue crack growth curves for carbon and low-alloy ferritic steels [7]. Linear interpolation is recommended to account for load ratio dependence of water environment curves for $0.25 \leq R \leq 0.65$.

with crack growth rates below 10^{-4} mm/cycle. The ASME reference curves are very conservative in this region compared with the hydrogen-embrittlement model based curves. On the other hand, the ASME reference curves are less conservative in the bend-over region.

Application of Reference Curves

The ASME Code Section XI procedure for predicting the cyclic crack growth is based on the linear damage summation; that is, the crack growth increment is calculated one by one for each transient. The inaccuracy of this

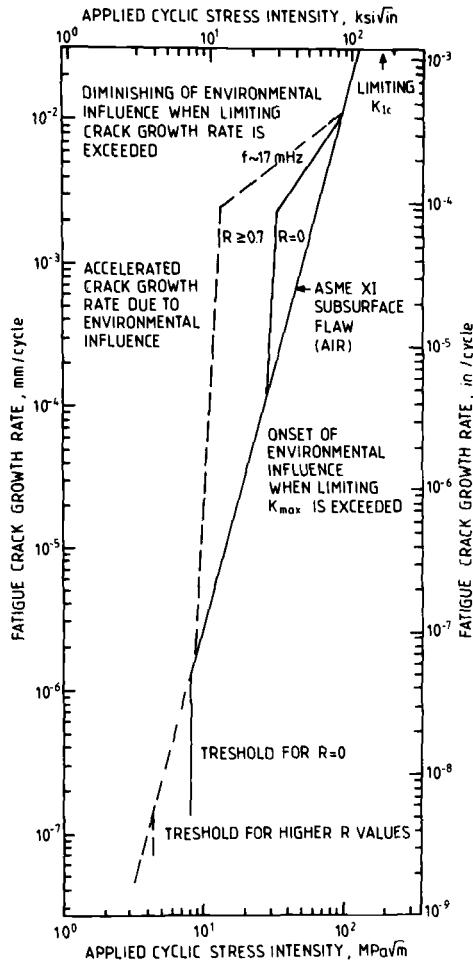


FIG. 8—Proposed reference fatigue crack growth curves based on the hydrogen embrittlement model. The effect of load ratio between $R = 0$ and 0.7 is taken into account by using Eq 3.

type of calculation is well known [40,42], even when there is no concern of environmental effects. Significantly, overloading has been shown to introduce subsequent cyclic crack growth retardation [43,44], which is not taken into account when using linear damage summation. On the other hand, experimentally measured crack growth rates, which are an order of magnitude higher than those calculated, have been measured for variable-amplitude loading conditions [40]. To overcome this problem it is essential to generate data using variable-amplitude loading waveforms that are representative of, and therefore applicable to, power reactors.

The reversals and accelerations in the cyclic crack growth data are often connected to test interruptions, overload-type transients, or changes in test

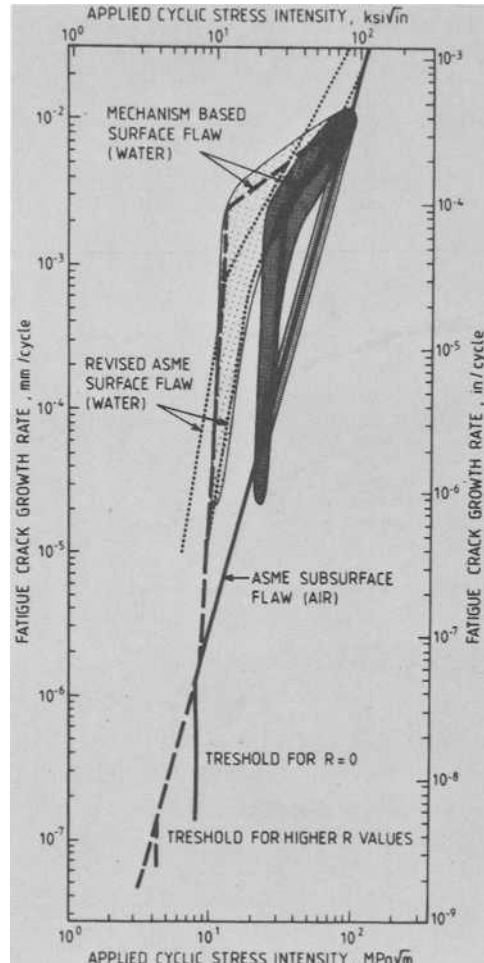


FIG. 9—Comparison between the proposed ASME Code Section XI reference curves, the hydrogen embrittlement model based reference curves, and actual experimental data.

parameters such as frequency etc. [17,45]. It is obvious, based on the presented hydrogen-embrittlement model, that if test parameters are used which do *not* allow hydrogen evolution, the fracture mode changes to ductile type and microbranching occurs. This microbranching can then develop into macrobranching and hence introduce reversal in the cyclic crack growth rate, as is experimentally observed during beachmarking [17]. However, a recent test [46], in which three specimens were tested in the same autoclave in a daisy chain under exactly the same conditions, shows that material-to-material differences among the specimens introduce more reversals and accelerations in cyclic crack growth than external factors like test interruptions (Fig. 10).

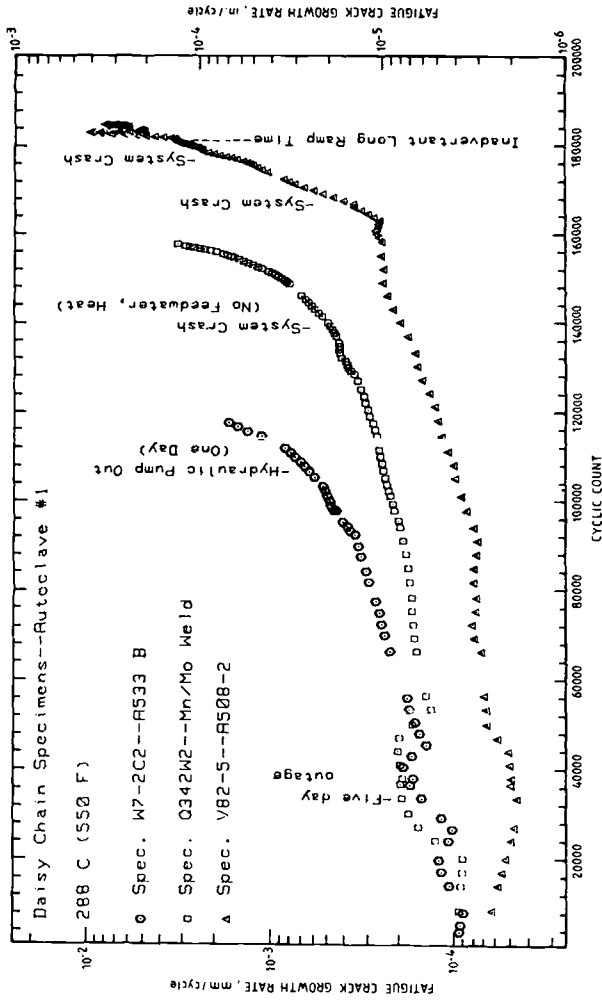


FIG. 10—Cyclic crack growth rates versus total cyclic count for three specimens tested simultaneously in a multispecimen autoclave. This plot shows the lack of influence of test practice on ensuing crack growth rates. The absolute difference in fatigue crack growth rate are due to the three different initial values of ΔK appropriate to each specimen.

Summary and Conclusions

It is well established that light-water reactor environments accelerate fatigue crack growth rates above those obtained in air. The loading history related variables have the most pronounced effect on the observed crack growth behavior. For higher load ratios most of the experimental data lie above the current ASME Code Section XI water default line; furthermore, as a category, the 17-mHz (1-cpm) sinewave loading produces the most accelerated crack growth compared with other frequencies and other waveforms, for both low and high load ratios. The materials-related variables may be more important than previously thought, although only a limited amount of analyzed data is available. Recently, a considerable influence of the sulfur content of the steel on the environmental enhancement has been found. Environment-related variables, including irradiation, have little influence on observed crack growth rates.

The environmental influence is due to hydrogen embrittlement, which is shown by extensive fractographic work. Reference curves for crack growth predictions can be constructed based on the hydrogen-assisted cracking model. These curves are shown to fit the experimental data better than the proposed revision of the ASME Code Section XI reference curves.

There are some important areas for future research. Cyclic crack growth rate for the threshold region, as a function of load ratio, needs to be determined. Along with this, the effects of startup and thermal cycling transients need to be established, and testing with combined waveforms (that is, variable amplitude, variable frequency tests) is definitely required to generate data under more realistic conditions.

Acknowledgments

This research was sponsored partly by the Ministry of Trade and Industry in Finland (K.T.) and the Reactor Safety Research Division of the U.S. Nuclear Regulatory Commission (W.H.C.). The continuing support of these agencies is appreciated. Additional support was provided by the Walter Ahlstrom Foundation and Suomen Kulttuurirahasto (K.T.).

References

- [1] *ASME Boiler and Pressure Vessel Code*, "Rules for In-Service Inspection of Nuclear Power Plant Components," Section XI, American Society of Mechanical Engineers, 1977.
- [2] Clark, W. G., Jr., *Journal of Materials*, Vol. 16, 1971, pp. 134-149.
- [3] Paris, P. C., Bucci, R. J., Wessel, E. T., Clark, W. G., and Mager, T. R. in *Stress Analysis and Growth of Cracks, ASTM STP 513*, American Society for Testing and Materials, 1972, pp. 141-176.
- [4] Mager, T. R. and McLoughlin, V. J., "The Effect of Environment of High Temperature Primary Grade Nuclear Reactor Water on the Fatigue Crack Growth Characteristics of A533, Grade-B, Class 1 Plate and Weldment Material," Heavy Section Steel Technology (HSST) Technical Report 16, WCAP-7776, Oct. 1971.

- [5] Legge, S. A. and Mager, T. R. in *Heavy Section Steel Technology Program Progress Report for Period Ending August 31, 1972*, J. Witt, Ed., ORNL-4855, April 1973, pp. 12-16.
- [6] Cullen, W. H. and Törrönen, K., "A Review of Fatigue Crack Growth of Pressure Vessel and Piping Steels in High-Temperature, Pressurized Reactor Grade Water," NUREG/CR-1576, NRL Memorandum Report 4298, Naval Research Laboratory, Washington, D.C., March 1980.
- [7] Bamford, W. H., *Journal of Pressure Vessel Technology, Transactions of ASME*, Vol. 102, No. 4, 1980, pp. 433-442.
- [8] Cullen, W. H., Loss, F. J., Watson, H. E., Bamford, W. H., and Ceschini, L. J. in *8th Water Reactor Safety Research Information Meeting*, Gaithersburg, Md., National Bureau of Standards, 30 Oct. 1980.
- [9] Amzallag, C. and Bernard, J. L. in *IAEA Specialists' Meeting on Subcritical Crack Growth*, Fraunhofer-Institut für Werkstoffmechanik, Freiburg, FRG, 13-15 May 1981, pp. 412-427.
- [10] Scott, P. M. and Silvester, D. R. V., "The Influence of Mean Tensile Stress on Corrosion Fatigue Crack Growth in Structural Steel Immersed in Sea Water," Technical Report UKOSRP 3/02, UKAEA, Harwell Corrosion Service, May 1979.
- [11] Cullen, W. H., Watson, H. E., Taylor, R. E., and Törrönen, K. in *Effects of Radiation on Materials, ASTM STP 725*, American Society for Testing and Materials, 1981, pp. 102-114.
- [12] Cullen, W. H., Watson, H. E., Taylor, R. E., and Loss, F. J., *Journal of Nuclear Materials*, Vol. 96, 1981, pp. 261-268.
- [13] Atkinson, J. D. and Lindley, T. C. in *The Influence of Environment on Fatigue*, Institution of Mechanical Engineers, London, 1977, pp. 65-74.
- [14] Atkinson, J. D. and Lindley, T. C., *Metal Science*, Vol. 13, No. 7, 1979, pp. 444-448.
- [15] Tomkins, B., *Metal Science*, Vol. 13, No. 7, 1979, pp. 387-395.
- [16] Cullen, W. H., Provenzano, V., Törrönen, K. J., Watson, H. E., and Loss, F. J., "Fatigue Crack Growth of A508 Steel in High-Temperature, Pressurized Reactor Grade Water," NUREG/CR-0969, NRL Memorandum Report 4063, Naval Research Laboratory, Washington, D.C., Sept. 1979.
- [17] Bamford, W. H. and Moon, D. M., *Corrosion*, Vol. 36, No. 6, 1980, pp. 289-298.
- [18] Johnson, R., McMinin, A., and Tomkins, B. in *ICM3*, K. J. Miller and R. F. Smith, Eds., Vol. 2, Pergamon Press, Elmsford, N.Y., 1979, pp. 371-382.
- [19] Mager, T. R., Landes, J. D., Moon, D. M., and McLoughlin, V. J., "The Effect of Low Frequencies on the Fatigue Crack Growth Characteristics of A533B Class 1 Plate in an Environment of High Temperature Primary Grade Nuclear Reactor Water," HSST Program Technical Report No. 35, HSST-TM-35, Dec. 1973.
- [20] Mager, T. R., Moon, D. M., Landes, J. D., and McLoughlin, V. J. in *HSST Semiannual Progress Report ORNL-4971*, Aug. 1973, pp. 25-29.
- [21] Cullen, W. H., Watson, H. E., Törrönen, K. J., Provenzano, V., Loss, F. J., and Gabetta, G. in *Structural Integrity of Water Reactor Pressure Boundary Components*, F. J. Loss, Ed., NUREG/CR-0943, NRL Memorandum Report 4064, Sept. 1979, pp. 43-54.
- [22] Cullen, W. H., Watson, H. E., and Provenzano, V. in *Structural Integrity of Water Reactor Pressure Boundary Components*, F. J. Loss, Ed., NUREG/CR 1128, NRL Memorandum Report 4122, Dec. 1979, pp. 43-81.
- [23] Cullen, W. H., Watson, H. E., Törrönen, K., and Provenzano, V. in *Structural Integrity of Water Reactor Pressure Boundary Components*, F. J. Loss, Ed., NUREG/CR 1268, NRL Memorandum Report 4174, Jan. 1980, pp. 27-36.
- [24] Provenzano, V., Törrönen, K., Cullen, W. H., and Gabetta, G. in *Analytical and Experimental Fracture Mechanics*, G. C. Sih and M. Mirabile, Eds., Sijthoff and Noordhoff, The Netherlands, 1981, pp. 211-222.
- [25] Brown, B. F., Fujii, C. T., and Dahlberg, E. P., *Journal of the Electrochemical Society*, Vol. 116, 1969, pp. 218-219.
- [26] Brown, B. F., *Corrosion*, Vol. 26, 1970, pp. 249-250.
- [27] Smith, J. A., Peterson, M. H., and Brown, B. F., *Corrosion*, Vol. 26, 1970, pp. 539-542.
- [28] Barsom, J. M., *International Journal of Fracture Mechanics*, Vol. 7, 1971, pp. 163-182.
- [29] Louthan, M. R., Derrick, R. G., Donovan, J. A., and Caskey, G. R. in *Effect of Hydrogen on Behavior of Materials*, A. W. Thompson and I. M. Bernstein, Eds., Metallurgical Society of American Institute of Mechanical Engineers, 1976, pp. 337-347.
- [30] Hirth, J. P., *Metallurgical Transactions*, Vol. 11A, No. 6, 1980, pp. 861-890.

- [31] Forsyth, P. J. E. in *Proceedings, Crack Propagation Symposium*, The College of Aeronautics, Cranfield, Miss., Vol. 1, 1961, pp. 76-94.
- [32] Thompson, A. W. in *Environmental Degradation of Engineering Materials*, M. R. Louthan and R. P. McNitt, Eds., Virginia Technical College, Blacksburg, Va., 1977, pp. 13-17.
- [33] Ritchie, R. O. in *Analytical and Experimental Fracture Mechanics*, G. C. Sih and M. Mirabile, Eds., Sijthoff and Noordhoff, The Netherlands, 1981, pp. 81-108.
- [34] Ritchie, R. O., *Journal of Engineering Materials and Technology, Transactions of ASME, Series H*, Vol. 99, No. 3, 1977, pp. 195-204.
- [35] Videm, K. in *Proceedings, 7th Scandinavian Corrosion Congress*, Trondheim, Norway, 1975, pp. 444-456.
- [36] Simmons, G. W., Pao, P. S., and Wei, R. P., *Metallurgical Transactions*, Vol. 9A, 1978, pp. 1147-1158.
- [37] McClintock, F. A. in *Fatigue Crack Propagation, ASTM STP 415*, American Society for Testing and Materials, 1967, pp. 170-174.
- [38] Takahashi, H., Shoji, T., Suzuki, M., and Kondo, T., submitted to *Journal of Engineering Materials and Technology, Transactions of ASME, Series H*, 1980.
- [39] Scott, P. M., *Metal Science*, Vol. 13, No. 7, 1979, pp. 396-401.
- [40] Scott, P. M. in *Tolerance of Flaws for Pressurized Components*, Institute of Mechanical Engineers, Conference Publications, London, 1978-10, pp. 77-86.
- [41] Bamford, W. H., *Journal of Engineering Materials and Technology, Transactions of ASME, Series H*, Vol. 101, No. 2, 1979, pp. 182-190.
- [42] Freudenthal, A. M., *Engineering Fracture Mechanics*, Vol. 5, 1973, pp. 403-414.
- [43] Bernard, P. J., Lindley, T. C., and Richards, C. E. in *Fatigue Crack Growth under Spectrum Loads, ASTM STP 595*, American Society for Testing and Materials, 1976, pp. 78-97.
- [44] Rolfe, S. T. and Barsom, J. M., *Fracture and Fatigue Control in Structures, Application of Fracture Mechanics*, Prentice-Hall, Englewood Cliffs, N.J., 1977, pp. 268-291.
- [45] Hale, D. A., Yuen, J., and Gerber, T., "Fatigue Crack Growth in Piping and RPV Steels in Simulated BWR Water Environment," GEAP-24098, General Electric Company, San Jose, Calif., Jan. 1978.
- [46] Cullen, W. H., Taylor, R. E., Watson, H. E., and Rohrs, W. in *Structural Integrity of Water Reactor Pressure Boundary Components*, F. J. Loss, Ed., NUREG/CR-1472, NRL Memorandum Report 4254, Aug. 1980, pp. 16-36.

Two Decades of Progress in the Assessment of Multiaxial Low-Cycle Fatigue Life

REFERENCE: Brown, M. W. and Miller, K. J., "Two Decades of Progress in the Assessment of Multiaxial Low-Cycle Fatigue Life," *Low-Cycle Fatigue and Life Prediction, ASTM STP 770*, C. Amzallag, B. N. Leis, and P. Rabbe, Eds., American Society for Testing and Materials, 1982, pp. 482-499.

ABSTRACT: A number of studies of the influence of multiaxial stresses and strains on low-cycle fatigue life have been published during the past 20 years. Development of correlations is reviewed and comparisons are made with high-cycle fatigue theories. It is recommended that the more advanced criteria should be incorporated in design procedures to replace the octahedral equivalent strain approach currently used.

KEY WORDS: biaxial stresses, fatigue life, fatigue (materials), fatigue strength at N cycles, hydrostatic stress, torsion tests, triaxial stresses, yield strength

Nomenclature

a, C, g, h, j, k	Constants
b	Bending fatigue strength
N_f	Fatigue life
S_b	Bending stress
S_t	Torsional stress
TF	Triaxiality factor ($\sqrt{2}\sigma_{\text{oct}}/\tau_{\text{oct}}$)
t	Torsional fatigue strength
α, β	Constants
γ	Engineering shear strain
γ	Torsional strain
Δ	Strain range
ϵ	Normal strain
ϵ	Axial strain

¹ Mechanical Engineering Department, University of Sheffield, Sheffield, U.K.

λ	σ_2/σ_1
λ'	$\Delta\gamma/\Delta\epsilon$
ν	Poisson's ratio
ξ	ϵ_2/ϵ_1
σ	Normal stress
τ	Shear stress
ω	Angular frequency

Subscripts

A,B	Cases A and B
alt	Alternating
c	Critical
e	Elastic
eq	Equivalent
max	Maximum shear
mean	Mean value
n	Normal strain on shear plane
oct	Octahedral
p	Plastic
t	Total
T	'Total strain'
z	Axial
θ	Failure plane
1,2,3	Principal planes

The study of the influence of different multiaxial states of strain in low-cycle fatigue (LCF) testing has been limited to the past 20 years, although high-cycle fatigue (HCF) and, in particular, strength at the fatigue limit have attracted considerable attention since the beginning of the century. Since design for finite endurance has become a widely used, if not common, procedure, the necessity of evaluating predictive techniques and simplified design methods for the high strain fatigue analysis of components and structures that are subject to complex loading systems would seem to be of great importance. But this has not been borne out by the number of research projects to be found in the open literature, since this shows a lack of emphasis on the multiaxial problem compared with other areas of fatigue research. The reasons for this are legion, some of the more significant ones being (1) the complexity of biaxial fatigue machines and extensometry, (2) the large number of test results required to develop or disprove empirical criteria, (3) intricate specimen design and strain analysis, and (4) the expense.

In view of the importance of multiaxial LCF research and the comparative scarcity of data, we have included in this overview most if not all the work on this topic known to the authors, at the risk of giving insufficient consideration to some of the results. An initial introduction to aspects of multiaxiality in HCF reveals common areas of correlation with LCF. No attempt has been made, however, to give an exhaustive treatment of HCF theories or results, since many other reviews have appeared recently, concerning LCF [1], HCF [2], and both regimes [3].² Carden [4] has produced a bibliography of the subject, and Evans [5] has discussed at length different methods of multiaxial testing, stress-strain analysis, and some particular problems of specimen geometry. This paper will consider the various criteria for multiaxial fatigue life correlation and their ability to predict endurance satisfactorily.

Yield and Strength Theories

Of the many criteria for initial yield of isotropic materials, two have been shown to have wide validity, namely the Tresca criterion for a critical maximum shear stress,

$$\begin{aligned}\tau_{\max} &= \text{constant} \\ &= (\sigma_1 - \sigma_3)/2\end{aligned}\quad (1)$$

and the Von Mises criterion of critical distortional strain energy, which is equivalent to octahedral shear stress,

$$\begin{aligned}\tau_{\text{oct}} &= \text{constant} \\ &= \sqrt{[(\sigma_1 - \sigma_2)^2 + (\sigma_2 - \sigma_3)^2 + (\sigma_3 - \sigma_1)^2]}/3\end{aligned}\quad (2)$$

where σ_1 , σ_2 and σ_3 are the principal stresses, and $\sigma_1 \geq \sigma_2 \geq \sigma_3$. Both of these equations have been used to correlate fatigue strength in the HCF regime with a degree of success, particularly at the fatigue limit in ductile metals that do not form nonpropagating cracks. In this case, one might anticipate the suitability of yield criteria for crack initiation, since the nucleation of cracks has been associated with the onset of plasticity, albeit at a microscopic level, corresponding to the formation of persistent slip bands.

However, for low ductility materials yield theories proved unsatisfactory, and attention was turned to other theories of strength; for example, Rankine's theory of a critical tensile stress,

$$\sigma_1 = \text{constant} \quad (3)$$

where σ_1 is the maximum principal stress. Equation 3 was found to be more suitable for cast metals which exhibited some porosity from where cracks

²The italic numbers in brackets refer to the list of references appended to this paper.

were initiated. Other strength theories applied to fatigue conditions have been listed previously [3].

High-Cycle Fatigue Criteria

Although it was natural to consider previously used theories of strength as possible fatigue correlations, discrepancies between theory and experimental data originated a search for new criteria specifically designed for cyclic loading. A wide variety of results on various steels and cast irons led Gough et al [6,7] to propose two equations for describing the results of combined bending and torsion tests, namely the ellipse quadrant for ductile materials,

$$(S_t/t)^2 + (S_b/b)^2 = 1 \quad (4)$$

and the ellipse arc for brittle materials,

$$(S_t/t)^2 + (S_b/b)^2(b/t - 1) + (S_b/b)(2 - b/t) = 1 \quad (5)$$

where S_t and S_b are the torsional and bending stresses, and t and b the torsional and bending fatigue strengths respectively. Here t and b must be found experimentally, with any required mean stress conditions incorporated in those tests. With two material constants, as opposed to one in Eqs 1 to 3, more accurate correlation is possible over a wide range of materials. The ellipse quadrant is equivalent to Eq 1 for $t/b = 0.5$, and Eq 2 for $t/b = 0.577$. Similarly the ellipse arc is the same as Eq 1 for $t/b = 0.5$, and Eq 3 for $t/b = 1.0$. Equation 5 was based on the suggestion of Stanfield [8] that for brittle materials a more suitable correlation might be obtained from Guest's Law [9],

$$(\sigma_1 - \sigma_3) + k(\sigma_1 + \sigma_3) = C \quad (6)$$

which is in fact equivalent to Eq 5, the constants k and C being related to t and b . Notched specimens of either brittle or ductile material may also be analyzed with this equation [10].

A further important theory was developed by Sines [11], which may be written as

$$(\tau_{oct})_{alt} = C - k(\sigma_{oct})_{mean} \quad (7)$$

to relate the amplitude and mean values of octahedral shear and normal stresses respectively, where $\sigma_{oct} = (\sigma_1 + \sigma_2 + \sigma_3)/3$. Although this reduces to Eq 2 for fully reversed cyclic loads, Sines's theory requires much less experimental data in order to predict mean stress effects. Another theory incorporating mean stress, based on the concept of fatigue failure occurring on a critical plane, was proposed by Findley et al [12]:

$$\tau_{c\theta} = C - k\sigma_\theta \quad (8)$$

where $\tau_{c\theta}$ and σ_{θ} are the critical shear and normal stresses on the failure plane, respectively.

A common feature of all these criteria developed specifically for HCF is that they contain two constants. Since the majority of biaxial fatigue tests have involved axial and torsional loading systems, it is probable that the need for two constants arises partly from variations in the ratio t/b . It has been established that in torsion life depends on specimen geometry, since it is a function not only of the ratio of internal to external diameters [13] but also of size [14]. The size effect may be correlated in terms of the ratio of grain size to specimen diameter [15], assuming that the endurance is related to average strain across grains at the surface where cracks initiate. A similar size effect appears in bending tests, but not in push-pull. Therefore it is inevitable that the ratio t/b will vary between one test situation and another, b being the *uniaxial* fatigue strength, although such variations should be less pronounced when b is determined by reversed bending. This effect has been observed for both HCF [16] and LCF [17], and is compounded by the fact that t/b changes not only with material and specimen geometry but also with the endurance at which strength is determined [18].

Early Work (the 1960s)

In low-cycle fatigue, an early assessment of multiaxial strain effects was made by Kennedy [19] for the elevated temperature behavior of Inconel in the creep range. Endurance was correlated with a creep rupture criterion using octahedral shear stress (Eq 2), together with a frequency modified life. However, comparisons of torsional and uniaxial failures by a fatigue mechanism at lower temperatures led to the first LCF criteria. Halford and Morrow [20] related life to the hysteresis energy accumulated, but this approach was not always successful when comparing the energies in uniaxial and torsional tests [21–23]. Yield theories, as used for HCF, may be extended to the high strain regime by using effective strains from plastic flow rules. The octahedral shear strain

$$\gamma_{oct} = 2\sqrt{[(\epsilon_1 - \epsilon_2)^2 + (\epsilon_2 - \epsilon_3)^2 + (\epsilon_3 - \epsilon_1)^2]}/3 \quad (9)$$

where ϵ_1 , ϵ_2 and ϵ_3 are the principal strains, has been widely used as a correlating parameter when comparing tension and torsion data, successfully in some cases [17,21], but in others both overestimating [17,21,23] and underestimating [17,22] torsional life. Similarly reversed bending tests [24] for wide cantilevers and round plates of pressure vessel steels were in agreement with Eq 9, whereas earlier work [25] on a similar steel and aluminum alloys comparing push-pull with bending tests found no such correlation.

In view of this variation in reported results, machines were built to examine fatigue under controlled multiaxial strain conditions. A combined tension and torsion machine was developed by Taira et al [26–28], who exam-

ined a carbon steel at 450°C and ambient temperature. For in-phase cyclic strains, the Von Mises and Tresca equivalent strains were compared as failure parameters (Eq 9 and maximum shear strain respectively), using both the Mises-Hencky and the Tresca flow rules for strain analysis. At 450°C, the former flow equations combined with the Mises equivalent strain [26]; that is,

$$\epsilon_{eq} = \sqrt{[\epsilon^2 + \gamma^2/3]} \quad (10)$$

where ϵ and γ are the axial and torsional strain amplitudes, fitted the data, although at 20°C the Tresca-Tresca equivalent strain gave a slightly better correlation [28]. For out-of-phase loading, however, a more complex correlation was needed to account for rotation of the principal strain axes, giving an effective mean strain range of

$$\Delta\epsilon_{eq} = 2 \frac{\omega}{\pi} \int_0^{\pi/\omega} (\epsilon^2 + \gamma^2/3)^{1/2\alpha} dt \quad (11)$$

where α is the Coffin-Manson equation exponent and ω is the angular frequency.

Zamrik et al [29,30] also found that the octahedral shear strain could be used for 7075-T651 aluminum under anticlastic bending for shear, cantilever bending for uniaxial and reversed bending of round plates for equibiaxial strains. However, rather than assuming that Poisson's ratio could be equated to 0.5 for the LCF regime (as in the case of Eq 10 above), they derived an effective Poisson's ratio for determining the principal strains. This was inserted into Eq 9 together with an anisotropy correction factor to get an effective total octahedral shear strain which related biaxial fatigue life to the uniaxial strain versus endurance curve. Further data to support this approach were provided by Mattavi [31] using centrifugal stresses in notched rotors to obtain positive biaxial strain ratios, ϵ_2/ϵ_1 .

In deriving effective strain correlations as above, experimental results are usually presented on a graph of equivalent strain versus life, N_f , such as shown in Fig. 1. Selection of the most suitable criterion is made by the somewhat subjective comparison of the best data fit to a single line when plotted in terms of various effective strains. While there are advantages in the simplicity of the effective strain approach, genuine trends of the results may be disguised by being related to "experimental scatter" in these figures, particularly when logarithmic axes are used.

Not all the results generated in the 1960s, however, supported the octahedral shear strain theory. Crosby et al [32] tested a low-ductility Al-4Cu alloy, and found that even for low life a linear elastic fracture mechanics analysis could be used. This points to Eq 3 as a suitable failure criterion for this material. Libertiny [33,34] argued that superposed hydrostatic pressure influences endurance, contrary to the implied prediction of the yield theories, which are insensitive to variations of the hydrostatic stress. He modified the Coffin-

Manson equation

$$\Delta \epsilon_1 N_f^\alpha = C \quad (12)$$

by making both constants, α and C , depend on stress state through the parameter $L = (\sigma_1 + \sigma_2 + \sigma_3)/\sigma_1$. Further evidence for the influence of pressure was later provided in uniaxial tests [35,36], increased pressure extending the life. Although pressure does not influence the flow properties of a ductile metal—that is, the cyclic stress-strain curve—it does increase fracture ductility [36,37], which one would expect to cause a corresponding increase in LCF endurance. However, oil entering fatigue cracks under pressure may reduce life by the “hydrowedge effect”, so that overall changes of crack growth rate may be more complex than this simple prediction technique [36]. The hydrowedge effect is particularly pronounced in tests of thick-walled cylinders under repeated internal pressure [38], which have been reviewed by Crossland [39].

Two new types of fatigue testing machine were developed in the 1960s to embrace the full range of biaxial stress states using a single specimen geometry [40,41]. Pascoe and de Villiers [40] used a cruciform specimen, and developed a modification of Eq 12 where α and C depended on the octahedral shear and normal strains as well as the maximum principal strain. Havard and Topper [41] subjected thin-walled steel tubes to internal/external pressure and axial load, deriving an empirical stress-based equation

$$\tau_{\max} + \frac{1}{4} \sigma_{\text{oct}} = f(N_f) \quad (13)$$

Both of these correlations were able to allow for some influence of hydrostatic pressure on life. While providing greater expense and complexity in biaxial fatigue research, these two studies were precursors of the new LCF criteria to be developed in the 1970s, replacing the traditional strength theories.

In view of the many different correlations for relating endurance under multiaxial strains, Pascoe [40,42] suggested that a graphical presentation of design data would be appropriate. Contours of fatigue strength for a given life were plotted in terms of the principal surface strains, as in Fig. 2. This method is an improvement on the effective strain approach in that it overcomes the aforementioned criticism of disguising genuine data trends, although very many more data are needed to draw the curves of Fig. 2 for any one material, temperature, and strain rate.

Fatigue Failure Criteria (the 1970s)

Extensive studies of both endurance [43] and modes of crack growth [44] in QT35 and AISI 304 steels have been described by Parsons and Pascoe, with results presented graphically as in Fig. 2. LCF life was related, rather significantly, to a crack propagation rule [45], to give the correlation

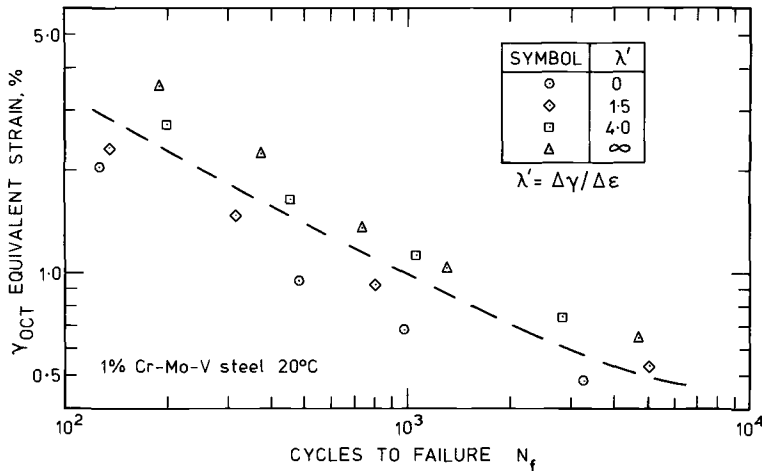


FIG. 1—Correlation of biaxial data by octahedral shear equivalent strain; 1Cr-Mo-V steel at 20°C [49].

$$\begin{aligned} \Delta\sigma_1 \sqrt{[1 - 0.5\lambda + \lambda^2]} &= C & \text{for } \lambda > 0 \\ \Delta\sigma_1 &= C & \text{for } \lambda < 0 \end{aligned} \quad (14)$$

where $\lambda = \sigma_2/\sigma_1$, the ratio of the applied stresses on a cruciform specimen. However, in HCF they recommend the Von Mises equation, where life is probably dominated by crack initiation.

Another approach to the biaxial problem was developed by Brown and Miller [3], who considered the directions of crack growth. They proposed that the maximum shear strain, $\gamma_{\max} = (\epsilon_1 - \epsilon_3)$, governed plastic deformation and consequently fatigue crack development. However, growth may also be influenced by the normal strain on maximum shear planes, $\epsilon_n = \frac{1}{2}(\epsilon_1 + \epsilon_3)$, since this will assist propagation through the variation of fracture ductility. Thus for a given endurance

$$(\epsilon_1 - \epsilon_3)/2 = f[(\epsilon_1 + \epsilon_3)/2] \quad (15)$$

where $\epsilon_1 \geq \epsilon_2 \geq \epsilon_3$. Constant endurance contours were drawn on graphs called Γ -Planes relating these critical strains to life [46], as in Fig. 3. Analysis of a wide range of experimental data revealed two distinct cracking systems, sketched in Fig. 4. In tests such as combined tension and torsion, the strains ϵ_1 and ϵ_3 are parallel to the surface plane, giving shallow Stage I and Stage II cracks [47], which are labelled Case A. But for tests with positive biaxial stresses ($\lambda > 0$), the strain ϵ_3 is normal to the free surface. Different slip planes are activated, giving deep cracks growing away from the surface, classified as Case B. Because of the change of crack plane with respect to the surface, one finds different fatigue lives in Case A and B systems, as shown in Fig. 3.

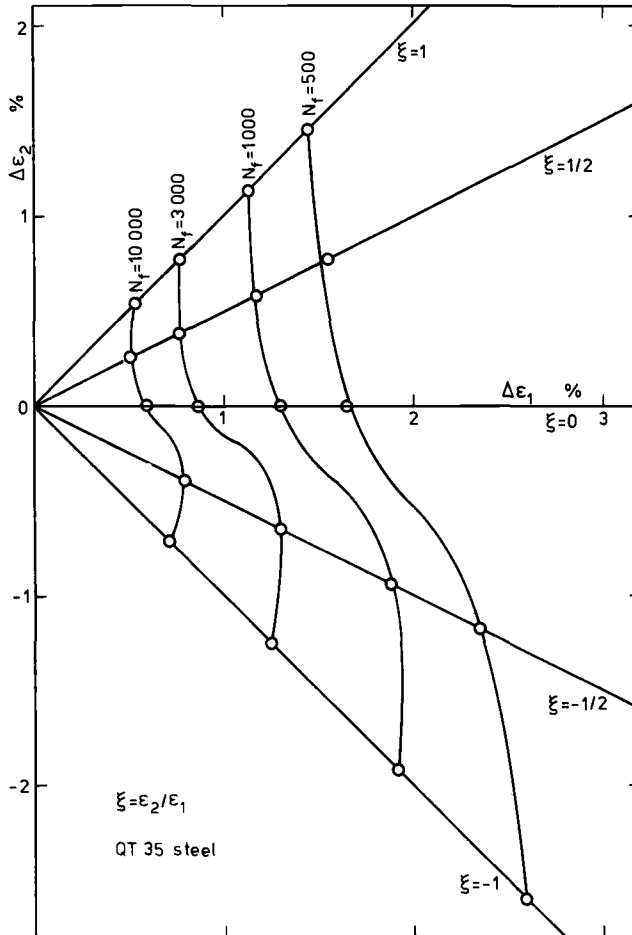


FIG. 2—Fatigue endurance contours for QT35 ferritic steel at 20°C [43] on plane of principal surface strains.

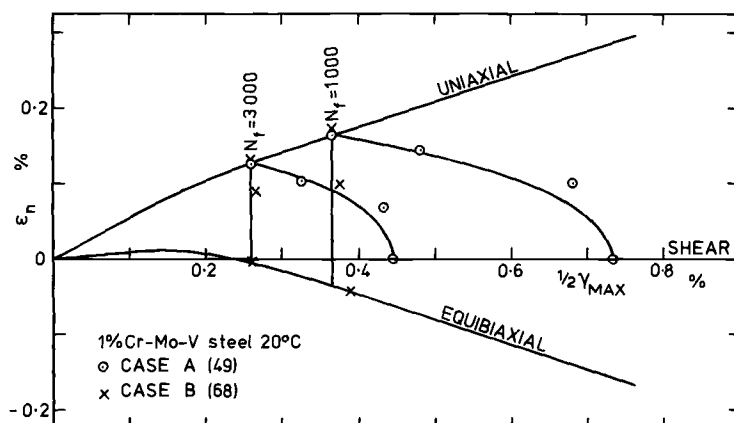
Specific forms for Eq 15 were later developed by Brown and Miller [48,49]. For Case A:

$$(\gamma_{\max}/2g)^j + (\epsilon_n/h)^j = 1 \quad (16)$$

g , h , and j being empirical life-dependent functions, although useful approximations for j are 2 for ductile and 1 for brittle materials. For Case B a Tresca correlation was proposed [48]:

$$\gamma_{\max}/2 = C \quad (17)$$

Examples are shown in Fig. 3 for a ductile steel and in Fig. 5 for RR58 aluminum alloy as a brittle material, having a relatively low fracture ductility.

FIG. 3— Γ -Plane for 1Cr-Mo-V steel at 20°C.

Another experimental study on tubular specimens under internal/external pressure and axial load was published by Ellison and Andrews [50], who used Eq 9 with a formula for an effective Poisson's ratio to determine the third principal strain. Their results in Fig. 5, however, show that an improved representation may be given by Eqs 16 and 17. Lohr and Ellison [51] have recently proposed a modification to Eq 15 in which the strain ϵ_3 is replaced by the strain normal to the surface. Therefore for Case A the terms of Eq 15 are effectively replaced by the second principal shear strain, $\gamma^* = (\epsilon_1 - \epsilon_2)/2$, and its corresponding normal strain, $\epsilon_n^* = (\epsilon_1 + \epsilon_2)/2$. They propose a linear relationship

$$\gamma^* + k\epsilon_n^* = C \quad (18)$$

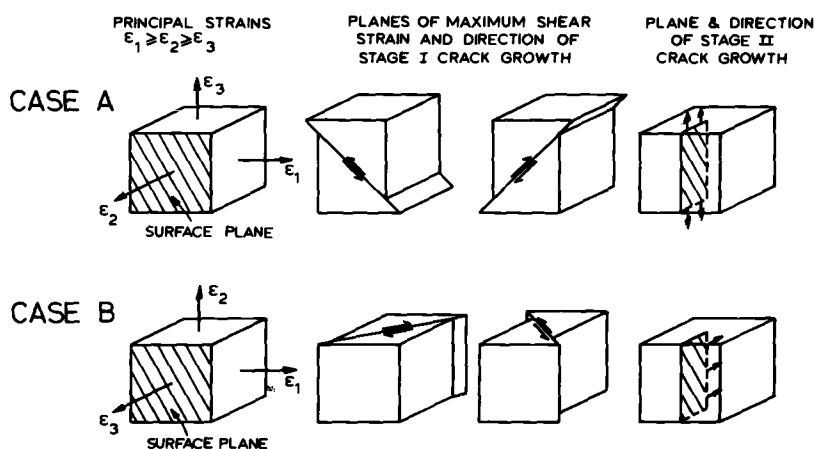
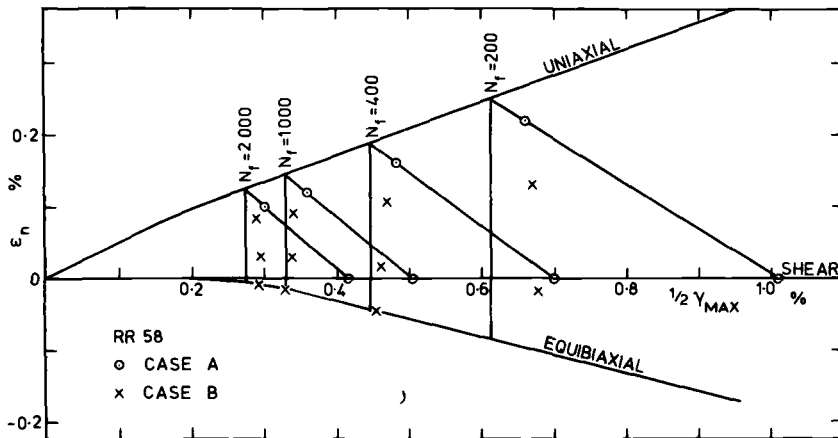


FIG. 4—Stage I and Stage II crack growth systems under general multiaxial cyclic strains [3].

FIG. 5— Γ -Plane for RR58 aluminum alloy at 20°C [50].

Note that for Case B, γ^* and ϵ_n^* are as defined in Eq 15. This presupposes, however, that $\epsilon_3 (= -\epsilon_1)$ in pure torsion has no effect on crack growth rate or crack shape.

Konter et al [52] have developed a quadratic expression for an equivalent strain range using plastic strain components

$$\Delta\epsilon_{eq}^2 = (16 - 9\beta) \Delta\epsilon_n^2 + \beta(\Delta\gamma_{max}/2)^2 \quad (19)$$

applicable to Case A, which may be extended to Case B by using a different β -value. They suggest that the life contour on the graph of principal surface strains (Fig. 2) should be smooth on passing from Case A to B. The respective β -values are then interdependent such that

$$\beta_B = 8/3 - \beta_A \quad (20)$$

Equation 19 is plotted in Fig. 6 for QT35 steel, being fitted to the Case A data. Equation 20 gives here a safe prediction of the Case B regime, which may be plotted on the Γ -Plane as a hyperbola when $\beta_B > 16/9$.

Zamrik initially supported the octahedral theory [29,30,53]. However, on turning to out-of-phase loads [54], a total strain was defined as

$$\epsilon_T = \sqrt{(\epsilon_1^2 + \epsilon_2^2 + \epsilon_3^2)} \quad (21)$$

which was evaluated at each instant throughout a loading cycle. The maximum range of ϵ_T was determined and related to endurance. For a Poisson's ratio of 0.5 with in-phase loads, ϵ_T is equivalent to the octahedral shear strain. Later work by Blass and Zamrik [55] showed that for AISI 304 at elevated temperatures the octahedral approach of the ASME Boiler and Pressure Vessel Code, Case N-47-12, 1977 [56] was unsatisfactory. They fitted a set of 84 results to a bilinear correlation

$$\Delta\epsilon_Z = a_3 N_f^{a_1} + a_4 N_f^{a_2} \quad (22)$$

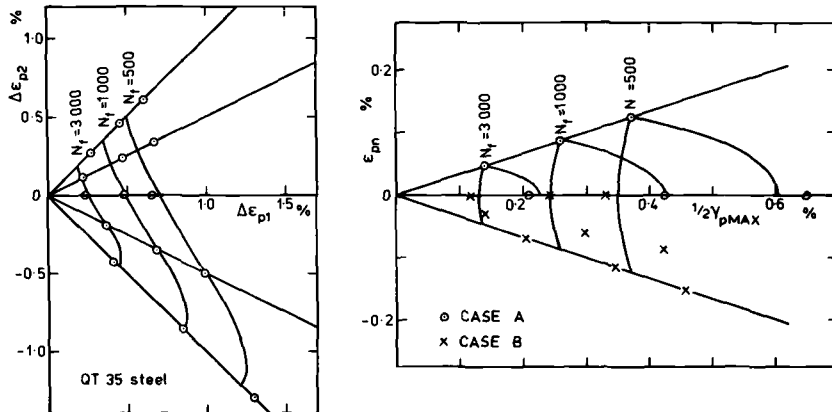


FIG. 6—Equation 19 fitted to plastic strain/endurance data for QT35 steel [43] on plane of principal surface strains and the Γ -Plane for $\beta_A = 0.67$ and $\beta_B = 2.00$.

where a_1 and a_2 depend on temperature, a_3 and a_4 on temperature and strain state. However, they also predicted that a straight-line correlation on the Γ -Plane would be suitable, although later [57] they consider a quadratic equation (such as Eq 19) to be preferable.

A different approach to the out-of-phase problem by Kanazawa et al [58] related life to the Γ -Plane method. They demonstrated that Stage I cracks grew on the planes experiencing the greatest range of shear strain as anticipated. Endurance was determined by γ_{\max} and ϵ_n , high values of the latter term giving significant reductions in life. Further work on the graphical presentations of both Pascoe (Fig. 2) and Brown and Miller (Fig. 3) for elevated temperature data showed the versatility of such methods in representing multiaxial fatigue effects [59].

Havard and Topper [60,61] reanalyzed their results for mild steel and conducted a survey of other data for this material. They defined a total strain range

$$\Delta\epsilon_t = \Delta\epsilon_e + \Delta\epsilon_p(1 + \alpha\lambda) \quad (23)$$

where $\Delta\epsilon_e$ and $\Delta\epsilon_p$ are the elastic and plastic components of the octahedral shear strain, respectively, and α is an empirical constant, found to be 0.1 for the best fit of endurance data for mild steel.

Manson and Halford [62] also followed the octahedral approach in the strain range partitioning method. However, they modified their analysis at a later date [63] by introducing a triaxiality factor, $TF = \sqrt{2}\sigma_{\text{oct}}/\tau_{\text{oct}}$, to correct the octahedral equivalent strain

$$\epsilon_{\text{eq}} = \gamma_{\text{oct}}/(2 - TF) \quad (24)$$

There does not appear to be a great deal of experimental data presented in support of this equation, which predicts a fixed ratio of torsional to uniaxial fatigue strengths.

An important contribution has been made by Ohji et al [64,65] using anticlastic bending of anisotropic steel plates. Although the laminated structure in the ferritic/pearlitic steel affected crack growth rates in different directions, cracks still grew on the maximum shear plane. They concluded that "the maximum shear stress plays the most important role in the crack initiation and probably in an initial phase of crack growth, although the normal stress component on the crack surface seems essential in crack propagation". Thus even in strongly anisotropic metals Eq 15 is able to relate the relevant strains to fatigue life for both the initiation and propagation phases.

The energy concepts of Halford and Morrow [20] have been extended by Garud [66], who related fatigue life to plastic work per cycle. Incremental plasticity theory is used to relate the plastic work to the constitutive equations. However, the addition of an extra empirical factor to match both uniaxial and torsional results enabled a far better fit to the out-of-phase results of Kanazawa et al [58].

Further work on 1Cr-Mo-V steel has been published by Adams and Stanley [67] for Case B, Brown and Miller [49] for Case A, and Lohr and Ellison [68] for both regimes, all working on the same batch of material. Figure 3 is a composite figure derived from these data, showing good correlation to Eqs 16 and 17. The Case B data have been normalized with respect to the uniaxial test in order to compensate for the effects of mean strain, oil environment, and different specimen geometry in the tests on pressurized tubes.

Discussion

It is apparent from this chronological review that the evolution of fatigue failure criteria in LCF has followed a progression similar to the earlier development of rules in the HCF regime. Initial attempts at correlation used yield theories for ductile metals and fracture criteria for brittle or notched material. Because of the unsatisfactory results obtained, new theories were suggested for fatigue failure, which gave improved correlation by (1) incorporating two or more material constants, and (2) considering directly those quantities believed to govern the mechanism of failure. Until the size effect is specifically included in failure correlations, it is inevitable that two sets of data from differing strain states will be required in any general criterion.

Further similarity may be found between HCF and LCF work by rephrasing stress based equations in terms of applied strains. For example, the Gough ellipse quadrant (Eq 4) may be rewritten in terms of the strains on the maximum shear plane, γ_{\max} and ϵ_n , to obtain a special case of Eq 15,

$$\left(\frac{\gamma_{\max}}{\gamma_t}\right)^2 + 4\left(\frac{1+\nu}{1-\nu}\right)^2\left(\frac{1}{\gamma_b^2} - \frac{1}{\gamma_t^2}\right)\epsilon_n^2 = 1 \quad (25)$$

where γ_t and γ_b are the shear strain amplitudes for fatigue strengths in torsion and bending respectively. This is the quadratic form used by Konter et

al [52], Blass and Zamrik [57], and Brown and Miller [49] in Eq 16 for $j = 2$. For suitable values of the ratio γ_t/γ_b , it can also represent Eq 9 or 10, that is, the octahedral equivalent strain. A similar rearrangement of Gough's ellipse arc or Guest's rule shows that these are equivalent to Eq 16 also, but with $j = 1$. Therefore Eq 16 is seen to be particularly versatile, covering both ductile and brittle materials, HCF and LCF regimes, for Case A loads. It should also be able to predict results for those metals falling between the ductile and brittle categories with intermediate values of j .

The quadratic form of correlation has obviously proved to be a useful expression, as has been suggested independently by various people. It has also been a controversial one for many years [9,63], so it is to be hoped that it will receive more attention in the 1980s in order to clarify its validity for ductile metals. Results on brittle or flawed materials are sparse, thus highlighting another area where more effort could be concentrated in assessing the use of a linear rule for Case A loading, such as Eqs 5, 6, 13, 18, and 16 for $j = 1$.

In the Case B area of positive stress ratios, the complexities of testing methods and specimen geometry have led to considerably less LCF data being produced than for Case A. The results available appear to support Eq 17, except in situations where the hydrowedge effect is important. The theories of Konter et al [52] and Lohr and Ellison [51] give differing predictions for this regime, although both are related to the assumption of continuity between the Case A and B systems. While there are no experimental data to verify this concept of a smooth transition from A to B, there are also insufficient data to disprove it. However, the present authors' opinion is that, of the results covered in this review, only a few are compatible with Eqs 18, 19, and 20.

Miller [69] studied the Case B regime using uniaxial and equibiaxial specimens for a range of materials and concluded that octahedral equivalent strain was a suitable parameter for correlation, although a few plane strain tests were conducted on one material only. However, the use of these two particular strain states alone fails to differentiate between octahedral and maximum shear strain criteria (Eqs 9 and 17) and Konter's theory applied to Case B, Eq 19. In demonstrating the applicability of any one multiaxial fatigue failure correlation to a given material, it is suggested that a minimum of three strain states must be examined in each of the two loading regimes, Cases A and B, in order to reveal the relative merits of different strength criteria.

Another area in which progress might be made is cumulative damage. Although there are a few studies of changes in strain amplitude in the list of references [31,53,55], the problem of changing the state of strain during the course of life has not been satisfactorily addressed to date. Tests run by the authors to examine this problem have shown that for Case A the Palmgren-Miner rule is inapplicable, and that the importance of changes in crack growth direction needs to be accounted for in life determination [70]. In this context, fracture modes should be examined in multiaxial fatigue tests and

crack growth directions should be reported in publications to aid the reader in his own analysis and assessment of endurance data. It is also important to include full tension test results, including reduction in area as the measure of ductility on which the choice of j in Eq 16 should depend.

Work on crack growth under biaxial stresses can also lead to LCF correlations, as shown in a recent review [70] where similar behavior was observed both in smooth specimens and in crack propagation tests. It is to be hoped that multiaxial failure criteria will have some impact on design practice, since current design procedures are based on the octahedral shear theory [56,71] in spite of the weight of evidence now available against such an approach. It is of some significance that a number of those who initially advocated the octahedral shear strain criterion, as discussed above, later abandoned it in favor of more sophisticated theories. Because of the wide range of applicability found for the more recent criteria, it is recommended that the use of octahedral equivalent strain in design codes should be replaced by the maximum shear strain criterion (Eq 17) for Case B, being a good approximation to the other criteria used in this loading regime, and that either the quadratic form or the linear rule be used for Case A. This will mean that some torsional fatigue tests must be run in addition to the uniaxial data currently collected to provide a design curve, so that the t/b ratio may be determined.

Anisotropic materials appear to be amenable to representation by current failure theories [41,64], although the empirical constants to be determined will clearly depend on crack orientation with respect to the axes of anisotropy. The influence of stress concentrating features has not been studied in LCF, but the concepts of Gough et al [10,72] for HCF, who advocated the ellipse arc for notched components, may be extrapolated to higher strains by using Eq 16 with $j = 1$ for Case A loading.

In this review, little attention has been paid to the choice between total or plastic strain based criteria. Both components of strain have been used widely, individually and in combination [61]. Although no systematic comparisons have been made of correlations in terms of both total and plastic effective strains, Brown [48] showed that simpler expressions could be found by using total applied strain in the form of Eq 16.

Conclusions

This review of the evolution of criteria for multiaxial low-cycle fatigue failure shows that the simpler theories of yield and fracture are in many cases unsatisfactory. Expressions specifically developed to represent fatigue strength have a far wider range of applicability and are suitable for both ductile and brittle materials. The use of these improved correlations is recommended for design procedures in both high and low cycle regimes. Studies of crack growth planes have shown that two distinct regimes of biaxial loading exist, which should be considered separately in assessments of fatigue endurance.

References

- [1] Krempl, E., *The Influence of State of Stress on Low-Cycle Fatigue of Structural Materials*, ASTM STP 549, American Society for Testing and Materials, 1974.
- [2] McDiarmid, D. L., "Failure Criteria and Cumulative Damage in Fatigue under Multiaxial Stress Conditions", Ph.D. thesis, City University, London, 1972.
- [3] Brown, M. W. and Miller, K. J. in *Proceedings*, Institution of Mechanical Engineers, Vol. 187, 1973, pp. 745-755.
- [4] Carden, A. E., "Bibliography of the Literature on Multiaxial Stress Fatigue," Report No. MH-67-AEC-2, University of Alabama, University, Ala., 1967.
- [5] Evans, W. J., "Deformation and Failure under Multiaxial Stresses—A Survey of Laboratory Techniques and Experimental Data," Note No. NT833, National Gas Turbine Establishment, Farnborough, U.K., 1972.
- [6] Gough, H. J. and Pollard, H. V. in *Proceedings*, Institution of Mechanical Engineers, Vol. 131, 1935, pp. 3-103.
- [7] Gough, H. J. and Pollard, H. V. in *Proceedings*, Institution of Automobile Engineers, Vol. 31, 1937, p. 821-893.
- [8] Stanfield, G. in *Proceedings*, Institution of Mechanical Engineers, Vol. 131, 1935, p. 93.
- [9] Guest, J. J. in *Proceedings*, Institution of Automobile Engineers, Vol. 35, 1940-41, pp. 33-72.
- [10] Gough, H. J., Pollard, H. V., and Clenshaw, W. J., "Some Experiments on the Resistance of Metals to Fatigue under Combined Stresses," Report R and M 2522, Aeronautical Research Council, HMSO, London, 1951.
- [11] Sines, G., "Failure of Materials under Combined Repeated Stresses with Superimposed Static Stresses," NACA Technical Note TN 3495, National Advisory Committee for Aeronautics, Washington, D.C., 1955.
- [12] Findley, W. N., Coleman, J. J., and Hanley, B. C. in *Proceedings*, International Conference on Fatigue of Metals, American Society of Mechanical Engineers, Institution of Mechanical Engineers, London, 1956, pp. 150-157.
- [13] Miller, K. J. and Chandler, D. C. in *Proceedings*, Institution of Mechanical Engineers, Vol. 184, 1969-70, pp. 433-448.
- [14] Kelly, D. A. and Morrison, J. L. M. in *Proceedings*, Institution of Mechanical Engineers, Vol. 185, 1970-71, pp. 655-664.
- [15] Findley, W. N., *Journal of Mechanical Engineering Science*, Vol. 14, 1972, pp. 424-425.
- [16] Forrest, P. G., *Fatigue of Metals*, Pergamon Press, Elmsford, N.Y., 1962, pp. 108-113.
- [17] Kikukawa, M., Ohji, K., Kotani, S., and Yokoi, T., *Bulletin*, Japan Society of Mechanical Engineers, Vol. 15, 1972, pp. 889-898.
- [18] Grover, H. J., Gordon, S. A., and Jackson, L. R., *Fatigue of Metals and Structures*, Thames and Hudson, London, 1956.
- [19] Kennedy, C. R. in *Symposium of Fatigue Tests of Aircraft Structures: Low-Cycle, Full-Scale, and Helicopters*, ASTM STP 338, American Society for Testing and Materials, 1962, pp. 92-104.
- [20] Halford, G. R. and Morrow, J. in *Proceedings*, American Society for Testing and Materials, Vol. 62, 1962, pp. 695-709.
- [21] Benham, P. P., *Journal of the Institute of Metals*, Vol. 91, 1962-63, pp. 404-407.
- [22] Mackenzie, C. T., Burns, D. J., and Benham, P. P. in *Proceedings*, Institution of Mechanical Engineers, Vol. 180 (3 I), 1965-66, pp. 414-423.
- [23] Yokobori, T., Yamanouchi, H., and Yamamoto, S., *International Journal of Fracture Mechanics*, Vol. 1, 1965, pp. 3-13.
- [24] Ives, K. D., Kooistra, L. F., and Tucker, J. T., *Transactions of ASME*, Vol. 88(D), 1966, pp. 745-754.
- [25] Sachs, G., Gerberich, W. W., Weiss, V. and Latorre, J. V. in *Proceedings*, American Society for Testing and Materials, Vol. 60, 1960, pp. 512-529.
- [26] Taira, S., Inoue, T., and Takahashi, M., "Low Cycle Fatigue under Multiaxial Stresses (in the Case of Combined Cyclic Tension-Compression and Cyclic Torsion in the Same Phase at Elevated Temperature)," in *Proceedings*, Tenth Japan Congress on Testing Materials, 1967, pp. 18-23.
- [27] Taira, S., Inoue, T., and Yoshida, T., "Low Cycle Fatigue under Multiaxial Stresses (in the Case of Combined Cyclic Tension-Compression and Cyclic Torsion Out-of-Phase at Ele-

- vated Temperature)," in *Proceedings*, Eleventh Japan Congress on Materials Research, 1968, pp. 60-65.
- [28] Taira, S., Inoue, T., and Yoshida, T., "Low Cycle Fatigue under Multiaxial Stresses (in the Case of Combined Cyclic Tension-Compression and Cyclic Torsion at Room Temperature)," in *Proceedings*, Twelfth Japan Congress on Materials Research, 1969, pp. 50-55.
 - [29] Zamrik, S. Y. and Goto, T., "The Use of Octahedral Shear Strain Theory in Biaxial Low Cycle Fatigue," in *Proceedings*, First Inter-American Conference on Materials Technology, American Society of Mechanical Engineers, 1968, pp. 551-562.
 - [30] Shewchuk, J., Zamrik, S. Y., and Marin, J., *Experimental Mechanics*, Vol. 8, 1968, pp. 504-512.
 - [31] Mattavi, J. L., *Transactions of ASME*, Vol. 91(D), 1969, pp. 23-31.
 - [32] Crosby, J. R., Burns, D. J., and Benham, P. P., *Experimental Mechanics*, Vol. 9, 1969, pp. 305-312.
 - [33] Libertiny, G. Z., *Journal of Strain Analysis*, Vol. 2, 1967, pp. 91-95.
 - [34] Libertiny, G. Z. in *Proceedings*, Institution of Mechanical Engineers, Vol. 182 (3C), 1967-68, pp. 58-64.
 - [35] Lunsford, G., Pense, A. W., Venkatesan, P. S., and McIntosh, M. J., *Transactions of ASME*, Vol. 95(H), 1973, pp. 157-160.
 - [36] Ohji, K., Ogura, K., Sugimoto, K. and Yaji, K., "Some Experiments on Push-Pull Low-Cycle Fatigue Strength of Metals under Very High Pressures," in *Proceedings*, Sixteenth Japan Congress on Materials Research, 1973, pp. 104-110.
 - [37] Crossland, B. in *Proceedings*, Institution of Mechanical Engineers, Vol. 168, 1954, pp. 935-944.
 - [38] Austin, B. A. and Crossland, B. in *Proceedings*, Institution of Mechanical Engineers, Vol. 180 (3A), 1965-66, pp. 134-145.
 - [39] Crossland, B. in *Mechanical Behaviour of Materials under Pressure*, H. L. D. Pugh, Ed., Elsevier, London, 1970, Chapter 7, pp. 299-354.
 - [40] Pascoe, K. J. and de Villiers, J. W. R., *Journal of Strain Analysis*, Vol. 2, 1967, pp. 117-126.
 - [41] Havard, D. G. and Topper, T. H. *Ontario Hydro Research Quarterly*, Vol. 21, No. 2, 1969, pp. 1-12.
 - [42] Pascoe, K. J., "Low Cycle Fatigue in Relation to Design," in *Proceedings*, Second International Conference on Fracture, Chapman and Hall, London, 1969, pp. 677-687.
 - [43] Parsons, M. W. and Pascoe, K. J. in *Proceedings*, Institution of Mechanical Engineers, Vol. 188, 1974, pp. 657-671.
 - [44] Parsons, M. W. and Pascoe, K. J., *Materials Science and Engineering*, Vol. 22, 1976, pp. 31-50.
 - [45] Joshi, S. R. and Skewchuk, J., *Experimental Mechanics*, Vol. 10, 1970, pp. 529-533.
 - [46] Liddle, M. and Miller, K. J., "Multiaxial High Strain Fatigue," in *Proceedings*, Third International Conference on Fracture, Munich, 1973.
 - [47] Brown, M. W. and Miller, K. J., *Fatigue of Engineering Materials and Structures*, Vol. 1, 1979, pp. 231-246.
 - [48] Brown, M. W., "High Temperature Multiaxial Fatigue," Ph.D. thesis, Cambridge University, 1975.
 - [49] Brown, M. W. and Miller, K. J., *Fatigue of Engineering Materials and Structures*, Vol. 1, 1979, pp. 217-229.
 - [50] Ellison, E. G. and Andrews, J. M. H., *Journal of Strain Analysis*, Vol. 8, 1973, pp. 209-219.
 - [51] Lohr, R. D. and Ellison, E. G., *Fatigue of Engineering Materials and Structures*, Vol. 3, 1980, pp. 1-17.
 - [52] Konter, A. W. A., Janssen, G. T. M., and Husslage, W., "Effect of Biaxial Loading and Geometry on Prediction of Low-Cycle Fatigue Life," in *Proceedings*, International Conference on Structural Mechanics in Reactor Technology, Berlin, 1979, Division L, paper 13/1.
 - [53] Zamrik, S. Y. and Tang, P. Y., "Aspect of Cumulative Damage Fatigue under Multiaxial Strain Cycling," in *Proceedings*, First International Conference on the Mechanical Behaviour of Materials, Kyoto, 1971, Vol. 2, pp. 381-390.
 - [54] Zamrik, S. Y. and Frishmuth, R. E., *Experimental Mechanics*, Vol. 13, 1973, pp. 204-208.
 - [55] Blass, J. J. and Zamrik, S. Y., "Multiaxial Low Cycle Fatigue of Type 304 Stainless Steel," in *1976 ASME-MPC Symposium on Creep-Fatigue Interactions*, American Society of Mechanical Engineers, 1976, pp. 129-159.

- [56] Fuchs, H. O., *Fatigue of Engineering Materials and Structures*, Vol. 2, 1979, pp. 207-215.
- [57] Blass, J. J. and Zamrik, S. Y., *Transactions of ASME*, Vol. 99(H), 1977, pp. 285-286.
- [58] Kanazawa, K., Miller, K. J., and Brown, M. W., *Transactions of ASME*, Vol. 99(H), 1977, pp. 222-228.
- [59] Miller, K. J. and Pascoe, K. P., "Some Recent High Temperature Biaxial Low Cycle Fatigue Results," Conference on the Mechanics and Physics of Fracture, Institute of Physics, 1975.
- [60] Havard, D. G. and Topper, T. H., "A Criterion for Biaxial Fatigue of Mild Steel at Low Endurance," in *Proceedings*, First International Conference on Structural Mechanics in Reactor Technology, Berlin, 1972, Vol. 6, Division L, pp. 413-432.
- [61] Havard, D. G., Williams, D. P. and Topper, T. H., "Biaxial Fatigue of Mild Steel: Data Compilation and Analysis," in *Proceedings*, Third International Conference on Structural Mechanics in Reactor Technology, London, 1975.
- [62] Manson, S. S. and Halford, G. R., "Treatment of Multiaxial Creep-Fatigue by Strain Range Partitioning," in *1976 ASME-MPC Symposium on Creep-Fatigue Interactions*, American Society for Mechanical Engineers, 1976, pp. 299-322.
- [63] Manson, S. S. and Halford, G. R., *Transactions of ASME*, Vol. 99(H), 1977, pp. 283-285.
- [64] Ohji, K., Ogura, K., Harada, S., and Senga, H., *Bulletin*, Japan Society of Mechanical Engineers, Vol. 17, 1974, pp. 32-40.
- [65] Ohji, K., Ogura, K., and Harada, S., *Bulletin*, Japan Society of Mechanical Engineers, Vol. 18, 1975, pp. 17-24.
- [66] Garud, Y. S., "A New Approach to the Evaluation of Fatigue Under Multiaxial Loadings," in *Proceedings*, Symposium on Methods for Predicting Material Life in Fatigue, American Society of Mechanical Engineers, 1979, pp. 247-264.
- [67] Adams, W. and Stanley, P., "Uniaxial and Biaxial Low Cycle Fatigue of 1% Cr-Mo-V Steel in Bending under Isothermal and Variable Temperature Conditions," Mechanical Engineering Department Research Report, University of Nottingham, 1971.
- [68] Lohr, R. D. and Ellison, E. G., *Fatigue of Engineering Materials and Structures*, Vol. 3, 1980, pp. 19-37.
- [69] Miller, J., *Journal of Materials*, Vol. 7, 1972, pp. 307-314.
- [70] Brown, M. W. and Miller, K. J., "Defect Orientation in Fatigue Fracture Under Multiaxial Stress-Strain Conditions," presented at the International Symposium on Defects and Fracture, Tuczno, Poland, October 1980.
- [71] Gonyea, D. C. in *Fatigue at Elevated Temperatures*, ASTM STP 520, American Society for Testing and Materials, 1973, pp. 678-687.
- [72] Thurston, R. C. A. and Field, J. E., in *Proceedings*, Institution of Mechanical Engineers, Vol. 168, 1954, pp. 785-796.

Multiaxial Nonproportional Cyclic Deformation

REFERENCE: McDowell, D. L., Socie, D. F., and Lamba, H. S., "Multiaxial Nonproportional Cyclic Deformation," *Low-Cycle Fatigue and Life Prediction, ASTM STP 770*, C. Amzallag, B. N. Leis, and P. Rabbe, Eds., American Society for Testing and Materials, 1982, pp. 500-518.

ABSTRACT: A model employing a modified Mroz kinematic hardening rule with a Tresca yield surface is derived for a state of plane stress, combining together successful attributes of previous nonproportional incremental plasticity theories. Results from several nonproportional tests on oxygen-free high-conductivity copper are compared with computer predictions. Solution sensitivity to the particular cyclic stress-strain curve used, its piecewise linearization for the Mroz-type hardening rule, and the magnitude of the effective strain increment in the analysis is studied. A trade-off between the number of surfaces used in the Mroz-type rule and the effective strain increment size is observed for optimum solution with respect to convergence and speed.

KEY WORDS: multiaxial, biaxial, nonproportional, cyclic hardening, cyclic plasticity, cyclic stress-strain curve, deformation

Nomenclature

σ_{eff}	Effective stress
ϵ_{eff}	Effective total strain
σ_1	Largest principal stress
σ_3	Smallest principal stress
ϵ_{eff}^p	Effective plastic strain
ϵ_1	Largest principal plastic strain
ϵ_3	Smallest principal plastic strain
f_i	i th Tresca hardening surface

¹ Graduate Research Assistant and Assistant Professor, respectively, Department of Mechanical and Industrial Engineering, University of Illinois, Urbana, Ill. 61801.

² Scientist, International Harvester Company, Hinsdale, Ill. 60521.

N	Number of Tresca surfaces in hardening rule
S_1^i	Largest in-plane principal stress with respect to center of i th surface
S_3^i	Smallest in-plane principal stress with respect to center of i th surface
R_i	Effective stress value at end of i th linear segment of piecewise linear cycle stress-strain curve
$\underline{\alpha}_i$	Vector with components α_x^i , α_y^i , and α_{xy}^i denoting center of i th Tresca surface in plane stress space
$\underline{\sigma}$	Stress vector with components σ_x , σ_y , and τ_{xy} in plane stress space
$\epsilon_m^e, \epsilon_m^p$	Elastic and plastic components of total engineering strain ϵ_m with components ϵ_x , ϵ_y , and γ_{xy} for $m = 1, 2, 3$, respectively
$d\lambda$	Positive scalar in flow rule
H_i	Plastic hardening modulus of i th Tresca surface
C_i	Slope of linear segment between R_i and R_{i+1}
E	Young's modulus
G	Elastic shear modulus
\underline{n}	Unit normal to yield surface at $\underline{\sigma}$ with components n_x , n_y , and n_{xy}
M	Scalar parameter in hardening rule
\underline{D}	Translation vector in hardening rule
K	Scalar parameter in hardening rule
f_N	Tresca limit surface
$\Delta\epsilon_{\text{INT}}$	Constant strain interval for piecewise linear cyclic stress-strain curve
$\Delta\sigma_{\text{INT}}$	Constant stress interval for piecewise linear cyclic stress-strain curve
ν	Poisson's ratio
ϕ	Normalized plastic work

Most mechanical components that fail under cyclic loading are subjected to multiaxial nonproportional loading in the plastic range. Fatigue is the primary mode of failure in these cases, yet predictive fatigue theories remain relatively undeveloped for nonproportional multiaxial straining. Some analysts involved with life prediction view nonproportional fatigue life only as a function of cyclic effective stress magnitudes on critical planes. Others consider the plastic work per load cycle as a viable predictive tool.

Indeed, the development of a useful, accurate fatigue criterion for nonproportional loading is formidable. Regardless of the criterion chosen, it is essential to develop practical constitutive equations to describe material response under complex loading. Delay in the formulation of adequate constitutive plasticity relations is due in part to a lack of nonproportional experimental data. The use of advanced testing apparatus with electronic data acquisition has recently permitted the assessment of a number of proposed plasticity theories.

The object of the present paper is to develop a model combining the more successful characteristics of these plasticity theories for cyclically stable material response. Furthermore, the predictions of this model will be compared with several experimentally obtained biaxial stress histories. The details of an optimal solution will be investigated for these histories.

Overview of Plasticity Theory

A mathematical description of plastic flow during nonproportional loading requires an incremental plasticity theory. The three basic components of an incremental plasticity theory are: (1) an initial yield surface, within which the stress-strain response is linear elastic; (2) a flow rule that relates plastic strain increments to stress increments; and (3) a hardening rule that specifies the movement of the initial yield surface and subsequent surfaces in stress space. A yield surface in stress space is the locus of points for which yielding is said to occur. The von Mises and Tresca yield conditions define two commonly used yield surfaces in stress space.

For analysis of multiaxial states of stress, it is conventional to use effective stresses and strains normalized to the axial case. Assuming that the material remains isotropic, the Tresca effective stress, σ_{eff} , may be expressed as

$$\sigma_{\text{eff}} = \sigma_1 - \sigma_3 \quad (1)$$

The Tresca effective plastic strain, ϵ_{eff}^p , is defined as

$$\epsilon_{\text{eff}}^p = (2/3)(\epsilon_1 - \epsilon_3) \quad (2)$$

The most commonly used flow rule requires the plastic strain increment to be in the direction of the exterior normal to the yield surface at the stress point.

Many types of hardening rules have been proposed. Among them, kinematic and isotropic hardening are the most commonly used. Kinematic hardening allows the yield surface to translate without changing shape. Isotropic hardening permits the yield surface to expand or contract without translation. In some cases, the two have been combined [1,2].³

Of particular interest to this study is a Mroz-type hardening model in kinematic form [3]. Lamba [4], in studies of nonproportional deformation of oxygen-free high-conductivity (OFHC) copper, found a combination of a Mroz-type hardening rule with the Tresca yield condition to be more reliable than other prominent kinematic rules for a simple two-surface model. The Mroz-type model is used to simulate stable cyclic deformation by approximating a stable cyclic stress-strain curve by a series of line segments whose endpoints define an integral number of hardening surfaces in stress space, including the initial yield surface. These hardening surfaces describe the non-

³The italic numbers in brackets refer to the list of references appended to this paper.

linear material hardening characteristics, since the change in effective stress with an increment of effective plastic strain is computed from the slope of each linear segment when the effective stress lies in that region.

Transient deformation behavior is neglected in this study. Only path-dependent stable deformation behavior is considered. Instead of approximating the original monotonic stress-strain curve by linear segments and predicting its transient hardening to the cyclically stable state, the actual steady-state cyclic stress-strain curve is used in this analysis to predict stable behavior. The stable cyclic stress-strain curve is found experimentally just after stable cycles of interest. This is a convenient method to circumvent the difficult problem of transient cyclic hardening.

Any stable cyclic stress-strain curve in terms of effective stresses and strains will be referred to as a stable effective cyclic stress-strain curve. It may be determined from an incremental step test or by applying Masing's relation [3] to a stable hysteresis loop. An example of a stable effective cyclic stress-strain curve approximated by linear segments, as in the Mroz model, and the resulting Tresca hardening surfaces is shown in Fig. 1. The surfaces in Fig. 1 are defined for a previously undeformed, isotropic material in plane stress space with $\tau_{xy} = 0$, a degenerate three-dimensional case.

Each of the N Tresca hardening surfaces is defined by the expression

$$f_i(\underline{\sigma} - \underline{\alpha}_i, R_i) = (\sigma_1 - \sigma_3)_i - R_i = 0 \quad \text{for } i = 1, 2, \dots, N \quad (3)$$

where $(\sigma_1 - \sigma_3)_i$ denotes the difference of the largest and smallest principal stresses, respectively, of the stress point $\underline{\sigma}$ with respect to $\underline{\alpha}_i$.

The components of $\underline{\sigma}$ and $\underline{\alpha}_i$ in (three-dimensional) plane stress space are $\sigma_x, \sigma_y, \tau_{xy}$, and $\alpha_x^i, \alpha_y^i, \alpha_{xy}^i$, respectively. For an initially undeformed state, as in Fig. 1, $\underline{\alpha}_i = \underline{0}$ for each surface.

In plane stress space, the Tresca yield criterion consists of three cases that represent discrete sections of the i th hardening surface. If S_1^i and S_3^i represent the largest and smallest in-plane principal stresses, respectively, of $\underline{\sigma}$ with respect to $\underline{\alpha}_i$, these three cases are

1. If $S_1^i > S_3^i > 0$,

$$(\sigma_1 - \sigma_3)_i = \frac{\sigma_x - \alpha_x^i + \sigma_y - \alpha_y^i}{2} + \left[\frac{(\sigma_x - \alpha_x^i - \sigma_y + \alpha_y^i)^2}{4} + (\tau_{xy} - \alpha_{xy}^i)^2 \right]^{1/2} \quad (4)$$

2. If $S_3^i < S_1^i < 0$,

$$(\sigma_1 - \sigma_3)_i = -\left(\frac{\sigma_x - \alpha_x^i + \sigma_y - \alpha_y^i}{2} \right) + \left[\frac{(\sigma_x - \alpha_x^i - \sigma_y + \alpha_y^i)^2}{4} + (\tau_{xy} - \alpha_{xy}^i)^2 \right]^{1/2} \quad (5)$$

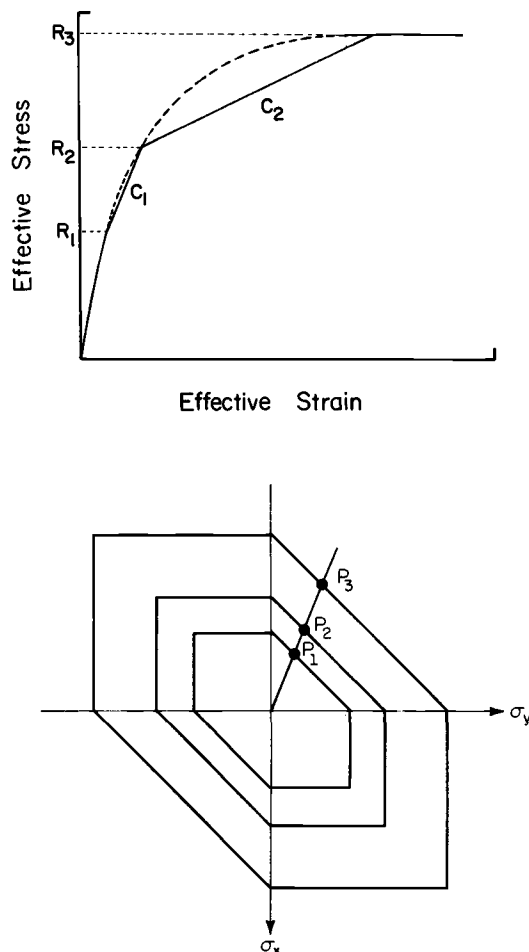


FIG. 1—Example of an approximated effective cyclic stress-strain curve and the resulting Tresca hardening surfaces in plane stress space with $\tau_{xy} = 0$.

3. If $S_1^i > 0 > S_3^i$,

$$(\sigma_1 - \sigma_3)_i = 2 \left[\frac{(\sigma_x - \alpha_x^i - \sigma_y + \alpha_y^i)^2}{4} + (\tau_{xy} - \alpha_{xy}^i)^2 \right]^{1/2} \quad (6)$$

An example of a Tresca hardening surface in three-dimensional plane stress space is shown in Fig. 2.

The specific form of the kinematic hardening rule presented by Mroz was modified by Garud [5] to include hardening along nonproportional stress paths for finite stress increments and hardening surfaces which do not possess a unique exterior normal at each point. The Mroz rule is valid strictly

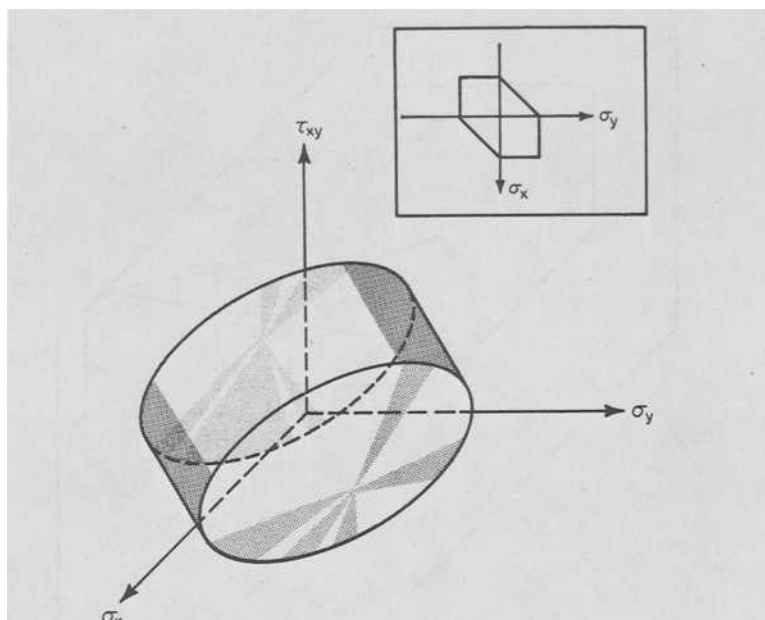


FIG. 2—A Tresca hardening surface in three-dimensional plane stress space.

only for infinitesimal stress increments which would be quite limiting for computer applications. Garud's Mroz-type hardening rule is illustrated in Fig. 3 for Tresca hexagonals in the $\tau_{xy} = 0$ plane. Define the similar points for the hardening surfaces as the intersection of any line emanating from the origin with each surface in the initially undeformed state. P_1 , P_2 , and P_3 are similar points in Fig. 1. By Garud's rule, for a stress increment PP'' during plastic flow, the instantaneous motion of a surface f_i , reached by the stress point P , is directed toward the position for which f_i would be tangent to the next surface f_{i+1} at the stress point P'' such that f_i and f_{i+1} have a common exterior normal at P'' and the similar points are coincident at P'' . For stress increments less than PP'' , such as PP' , the amount of translation of the surface f_i is then calculated by the constraint that the stress point lie on the shifted surface.

Development of Model

This model assumes small strain analysis, material isotropy, cyclic stability, rate insensitivity, and time independence. It is derived in three-dimensional plane stress space for generality so that thin plates as well as thin-walled tubes can be modeled. This is less restrictive than deriving the model in two-dimensional stress space with regard to a cylindrical coordinate system which would accommodate only thin-walled tube analysis.

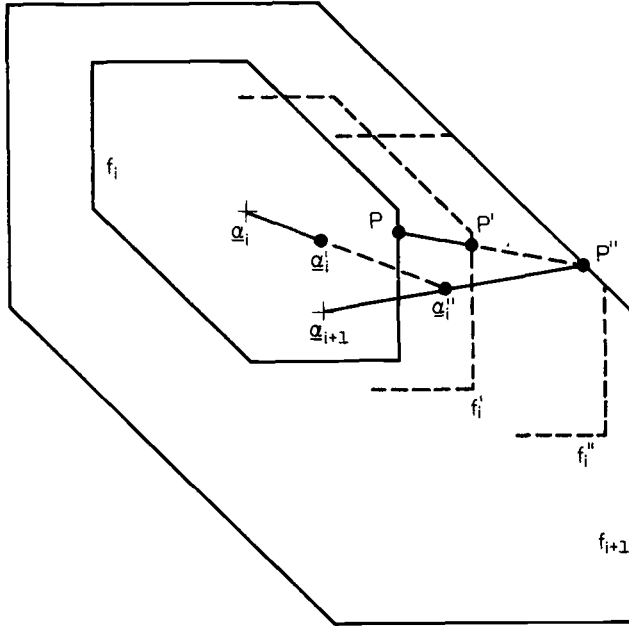


FIG. 3—Garud's hardening rule for stress increments in the $\tau_{xy} = 0$ plane.

Plastic Flow Rule

The flow rule, based on Drucker's postulate [6], for regular points of the yield surface is

$$d\epsilon_m^p = d\lambda \frac{\partial f_1}{\partial \sigma_m}$$

where $\sigma_m = \sigma_x, \sigma_y, \tau_{xy}$, for $m = 1, 2, 3$, respectively.

The argument of $f_1(\underline{\sigma} - \underline{\alpha}_1, R_1)$ has been omitted for brevity.

If $H_i d\epsilon_m^p$ is the projection of $d\sigma_m$ on the exterior normal to the yield surface at σ_m , then the resulting equation is

$$d\epsilon_k^p = [1/H_i][\partial f_1/\partial \sigma_k]\{[(\partial f_1/\partial \sigma_m) d\sigma_m]/[(\partial f_1/\partial \sigma_j)(\partial f_1/\partial \sigma_j)]\} \quad (7)$$

where $k = 1, 2, 3$, $H_i = d\sigma_{\text{eff}}/d\epsilon_{\text{eff}}^p$, and the repeated subscripts m and j are summed from 1 to 3. H_i is the plastic hardening modulus for the surface f_i reached by the stress point. H_i is determined from the piecewise linear approximation of the stable effective cyclic stress-strain curve. If C_i , for $i = 1, 2, \dots, N-1$, is the slope of the linear segment between points represented by R_i and R_{i+1} in Fig. 1, then $H_i = [(1/C_i) - (1/E)]^{-1}$ where E denotes Young's modulus. The partial derivatives in Eq 7 can be determined from the Tresca condition for the initial yield surface in Eq 3. The derivatives must be computed with respect to the Tresca case in Eqs 4, 5, and 6 which corre-

sponds to the current stress point $\underline{\sigma}$. In Eq 7, the surface f_1 could equivalently be replaced by f_i since the hardening rule stipulates that the surfaces f_1, f_2, \dots, f_i contact at points with a common exterior normal.

The elastic relations for plane stress are

$$\begin{aligned} d\epsilon_x^e &= \frac{1}{E} (d\sigma_x - \nu d\sigma_y) \\ d\epsilon_y^e &= \frac{1}{E} (d\sigma_y - \nu d\sigma_x) \\ d\gamma_{xy}^e &= \frac{d\tau_{xy}}{G} \end{aligned} \quad (8)$$

Since the total strain is the sum of the elastic and plastic strains, Eqs 7 and 8 may be combined to form a set of elastoplastic equations which are easily set in matrix form [7]. These equations may be inverted for strain control.

For stresses within the initial yield surface, only the relations in Eqs 8 are used. Once the stress point reaches the plastic region, plastic strains will result for a stress increment if and only if

$$\underline{n} \cdot \Delta \underline{\sigma} > 0 \quad \text{and} \quad f_1(\underline{\sigma} - \underline{\alpha}_1, R_1) = 0 \quad (9)$$

The components of \underline{n} in plane stress space are

$$\begin{aligned} n_x &= (\partial f_1 / \partial \sigma_x) / \{[(\partial f_1 / \partial \sigma_j)(\partial f_1 / \partial \sigma_j)]^{1/2}\} \\ n_y &= (\partial f_1 / \partial \sigma_y) / \{[(\partial f_1 / \partial \sigma_j)(\partial f_1 / \partial \sigma_j)]^{1/2}\} \\ n_{xy} &= (\partial f_1 / \partial \tau_{xy}) / \{[(\partial f_1 / \partial \sigma_j)(\partial f_1 / \partial \sigma_j)]^{1/2}\} \end{aligned}$$

If neither of the conditions in Eqs 9 holds, elastic unloading occurs. For determination of elastic unloading from the limit surface during strain control, $\Delta \underline{\sigma}$ in Eq 9 is calculated from the elastic relations in Eqs 8 applied to the total strain components $\Delta \epsilon_m^e + \Delta \epsilon_m^p$, for $m = 1, 2, 3$.

Hardening Rule

Garud's kinematic hardening rule can be applied to surfaces described in Eq 3 along nonproportional stress paths. This rule can be applied to finite effective stress increments in contrast to the infinitesimal increments in the Mroz rule. Assume that N hardening surfaces exist from a piecewise linearization as in Fig. 1. To model limit plasticity, the stage at which the effective stress increases negligibly with additional plastic strain, the outermost surface, f_N , is assumed to be stationary and centered at the origin in stress space. Thus, $f_N(\underline{\sigma} - \underline{0}, R_N) = (\sigma_1 - \sigma_3)_N - R_N = 0$ defines the limit surface. Here, $(\sigma_1 - \sigma_3)_N = (\sigma_1 - \sigma_3)$ since $\underline{\alpha}_N = \underline{0}$.

If $i < N$ and the stress point is on f_i , but not on f_{i+1} , the following shifts are made for f_1, f_2, \dots, f_i after an increment of plastic strain:

$$\Delta \underline{\alpha}_i = M \underline{D}$$

where $\underline{D} = (1 - R_i/R_{i+1})(\underline{\sigma} - \underline{\alpha}_{i+1} + K \Delta \underline{\sigma}) + (\underline{\alpha}_{i+1} - \underline{\alpha}_i)$, and K = the positive scalar parameter determined by solving

$$f_{i+1}(\underline{\sigma} + K \Delta \underline{\sigma} - \underline{\alpha}_{i+1}, R_{i+1}) = 0$$

where f_{i+1} is defined according to the Tresca case corresponding to the relative position of the stress point $\underline{\sigma} + K \Delta \underline{\sigma}$ and its center, $\underline{\alpha}_{i+1}$, and M = the positive root of

$$f_i(\underline{\sigma} + \Delta \underline{\sigma} - \underline{\alpha}_i - M \underline{D}, R_i) = 0$$

where f_i is defined according to the Tresca case corresponding to the relative position of the stress point $\underline{\sigma} + \Delta \underline{\sigma}$ and its center, $\underline{\alpha}_i + M \underline{D}$. K and M may be determined numerically by an incremental search technique followed by interval-halving.

Following the shifting of the surface f_i , the surfaces f_1, f_2, \dots, f_{i-1} are shifted so that they are all coincident at similar points with the same exterior normal at $\underline{\sigma} + \Delta \underline{\sigma}$. Thus

$$\Delta \underline{\alpha}_k = \underline{\sigma} + \Delta \underline{\sigma} - (R_k/R_i)(\underline{\sigma} + \Delta \underline{\sigma} - \underline{\alpha}_i - \Delta \underline{\alpha}_i) - \underline{\alpha}_k$$

where $k = 1, 2, 3, \dots, i-1$. The surfaces f_{i+1}, \dots, f_N are not shifted. If $K < 1$, the stress point is advanced to the surface f_{i+1} , the shifting procedure enacted, and the new increment, $(\Delta \underline{\sigma})_{\text{new}} = (1 - K) \Delta \underline{\sigma}$, is applied.

Limit Surface

Since the effective stresses cannot exceed the outermost surface, the limit surface defined by Eq 3 as $f_N(\underline{\sigma} - \underline{0}, R_N) = (\sigma_1 - \sigma_3) - R_N = 0$, the incremental stress vector, $\Delta \underline{\sigma}$, must be tangential to the limit surface during plastic flow at the limit state. The limit surface is a mathematical means of limiting the magnitude of the total stress vector, $\underline{\sigma}$. This limit surface is stationary and fixed in size in this model for simplicity; in general it may be allowed to translate and expand.

The flow rule for plane stress can be expressed as

$$\begin{aligned} d\epsilon_x &= \frac{1}{E} (d\sigma_x - \nu d\sigma_y) + d\lambda \frac{\partial f_N}{\partial \sigma_x} \\ d\epsilon_y &= \frac{1}{E} (d\sigma_y - \nu d\sigma_x) + d\lambda \frac{\partial f_N}{\partial \sigma_y} \\ d\gamma_{xy} &= \frac{d\tau_{xy}}{G} + d\lambda \frac{\partial f_N}{\partial \tau_{xy}} \end{aligned} \quad (10)$$

In addition, the vanishing of the total differential of f_N yields the condition

$$(\partial f_N / \partial \sigma_x) d\sigma_x + (\partial f_N / \partial \sigma_y) d\sigma_y + (\partial f_N / \partial \tau_{xy}) d\tau_{xy} = 0 \quad (11)$$

Equation 11 can be used to eliminate $d\lambda$ from Eqs 10 (see Ref 7).

Flow at Edges and Vertices

When the current state of stress is on an edge of the Tresca hardening surface in Fig. 2, the flow rule may be generalized by assuming that the plastic flow on an edge is a linear combination of the flows on either side of the edge. Thus, for stress states within the limit surface,

$$\begin{aligned} d\epsilon_x^p &= d\lambda_A \left[\frac{\partial f_1}{\partial \sigma_x} \right]_A + d\lambda_B \left[\frac{\partial f_1}{\partial \sigma_x} \right]_B \\ d\epsilon_y^p &= d\lambda_A \left[\frac{\partial f_1}{\partial \sigma_y} \right]_A + d\lambda_B \left[\frac{\partial f_1}{\partial \sigma_y} \right]_B \\ d\gamma_{xy}^p &= d\lambda_A \left[\frac{\partial f_1}{\partial \tau_{xy}} \right]_A + d\lambda_B \left[\frac{\partial f_1}{\partial \tau_{xy}} \right]_B \end{aligned}$$

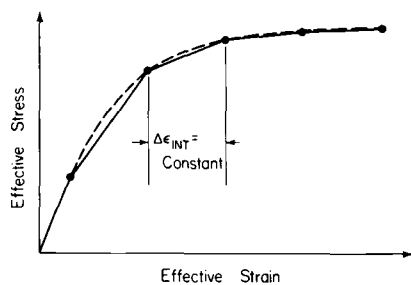
where the subscripts A and B pertain to the Tresca cases on either side of the edge. This leads to an expression similar in form to Eq 7. Plastic flow at the two vertices is treated in a similar manner. Plastic flow at edges and vertices on the limit surface is discussed in Ref 7.

Computer Results

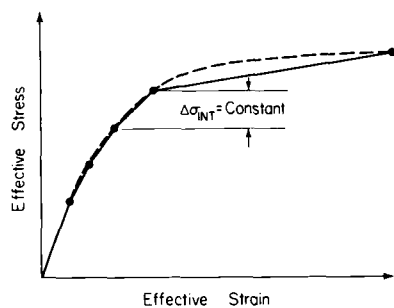
A computer program was developed which employs the present model. Studies were made to determine the solution sensitivity to: (1) varying the number of surfaces, (2) different types of approximations of the stable effective cyclic stress-strain curve, and (3) varying the increment size of the control variable.

Cyclic Stress-Strain Curve

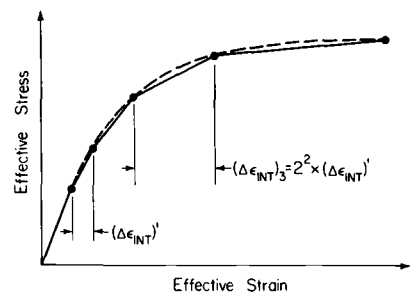
Three different methods were used to approximate the stable effective cyclic stress-strain curve as piecewise linear. The curve was divided into equal strain intervals $\Delta\epsilon_{INT}$, equal stress intervals $\Delta\sigma_{INT}$, and geometrically increasing strain intervals (Fig. 4). These are defined as constant strain, constant stress, and geometric piecewise linearizations, respectively. For the geometric piecewise linearization, the strain increments used in the analysis were also increased geometrically. The differences in computer application of these three piecewise linearizations are discussed later.



(a)



(b)



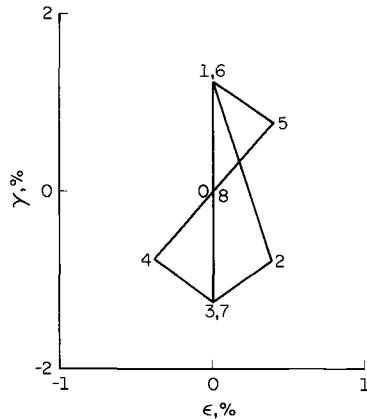
(c)

FIG. 4—Types of piecewise linearizations. (a) Constant strain. (b) Constant stress. (c) Geometric.

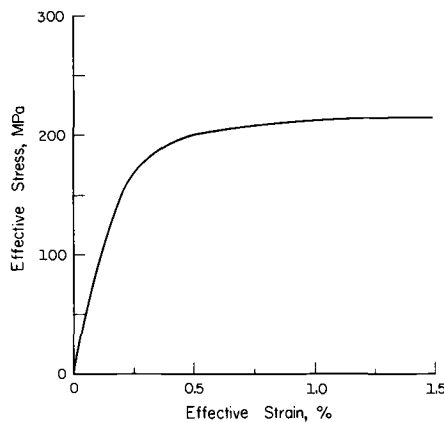
History 1: Random Nonproportional Path

Lamba [4] subjected a thin-walled tubular specimen of OFHC copper to 90-deg out-of-phase sinusoidal strains ϵ_y and γ_{xy} ($\sigma_x = 0$). When the stress response stabilized, the nonproportional strain path in Fig. 5a was imposed. The stable effective cyclic stress-strain curve is shown in Fig. 5b. The actual stress response appears in Fig. 6.

Assuming that plane stress adequately approximates the actual gage sec-



(a)



(b)

FIG. 5—History 1. (a) Imposed strain path. (b) Stable effective cyclic stress-strain curve used in analysis.

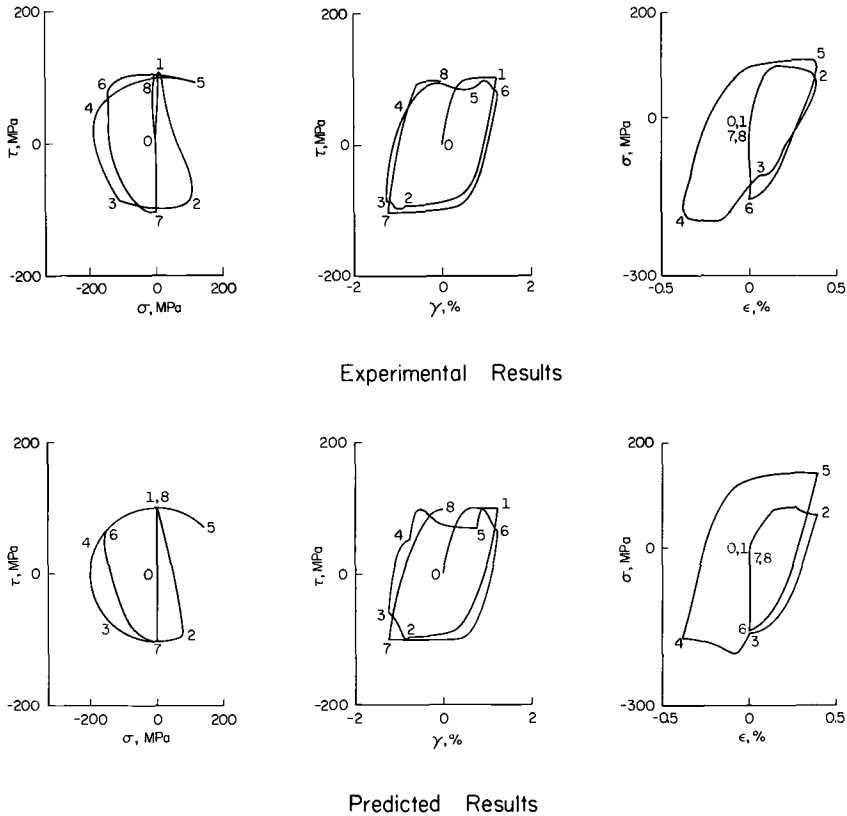


FIG. 6—Stress-strain response to strain history 1.

tion behavior, we introduced the same strain history into the computer program. For analysis, 13 surfaces were used with effective strain increments, $\Delta\epsilon_{\text{eff}}$, ranging from 0.01 to 0.45 percent. The stable cyclic stress-strain curve received a constant strain piecewise linearization. $E = 115 \text{ GPa}$ and $\nu = 0.33$ in the analysis. The predicted stress history for $\Delta\epsilon_{\text{eff}} = 0.03$ percent is shown in Fig. 6 for comparison with experimentally obtained results.

In Fig. 6, paths 4-5 and 5-6 in stress space coincide in theory but not in experiment. This is due to the constraint of the stationary limit surface in the theory. Paths 4-5 and 5-6 are along the outermost limit surface in the computer solution. If the limit surface had been allowed to isotropically expand during continued accumulation of plastic strain, the increase in effective stress along path 5-6 could have been predicted. Along path 4-5, the predicted axial stress is higher than the experimentally determined axial stress; again, the stationary limit surface determines the stress excursion and plastic flow.

The measure of accuracy selected to compare predicted and measured re-

sults is the normalized plastic work per cycle, Φ .

$$\Phi = (\text{predicted plastic work per cycle}/\text{actual plastic work per cycle})$$

For nonproportional loading, it is extremely difficult to use single scalar parameters other than Φ for quantitative comparison of predicted and actual results. Stress and strain discrepancies for each point in the cycle would have to be considered in some statistical manner, for example.

The normalized effective strain increment is defined as

$$(\Delta\epsilon_{\text{eff}})/(\Delta\epsilon_{\text{INT}}) = \frac{\text{effective strain increment}}{\text{strain interval in piecewise linearization of cyclic stress-strain curve}}$$

Figure 7 indicates that the predicted plastic work per cycle converges to the actual value within one percent for small strain increments and 13 surfaces. The actual value of plastic work per cycle is 9.05 MJ/m^3 .

Small effective strain increments in conjunction with many surfaces (fine mesh) are wasteful of computer time. An optimum solution can be arbitrarily defined as one which converges to within one percent of the plastic work per cycle from the fine mesh solution but minimizes execution time. A trade-off between the number of surfaces and the normalized effective strain increment for an optimum solution was observed as shown in Fig. 8. The number of surfaces and the effective strain increment for the fine mesh solution in this case were 13 and 0.01 percent, respectively. For this fine mesh solution, $\Phi \approx 1.01$; thus the curve in Fig. 8 is the locus of points for which Φ is within one percent of 1.01. Exceeding the optimum strain increment may lead to calculated plastic work 10 to 20 percent higher than for the fine mesh solution. The plastic hardening modulus is overestimated when entire linear sections of the approximated cyclic stress-strain curve are skipped.

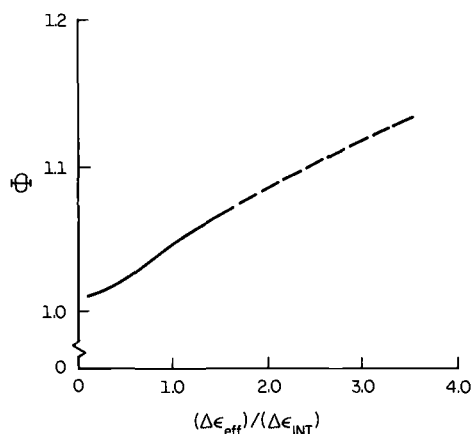


FIG. 7—Solution sensitivity to normalized effective strain increment.

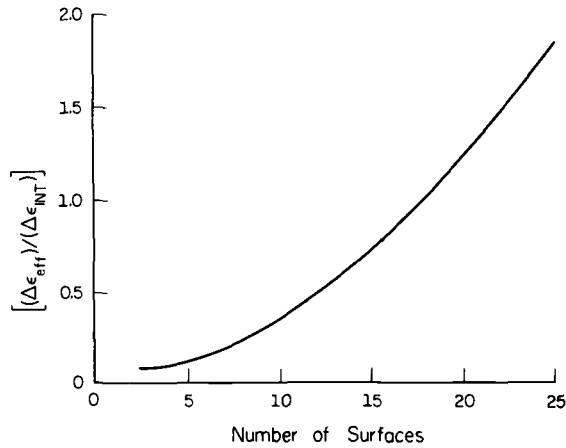


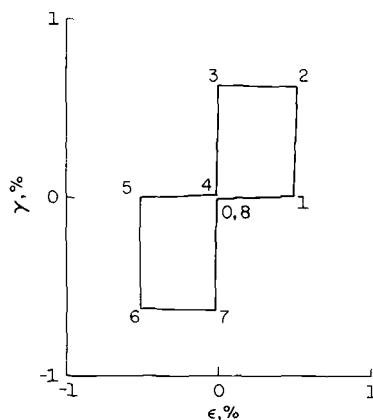
FIG. 8—Trade-off between normalized effective strain increment and number of surfaces for optimum solution.

By comparing the predicted and actual stress paths in Fig. 6, it is apparent that some transient isotropic hardening occurred within the loading cycle. The model is not capable of predicting this effect. The stresses and strains at each endpoint of the loading cycle are exhibited in Table 1 for History 1; note that this model predicts the biaxial response as accurately as Lamba's earlier model [4]. Lamba's earlier model used two Tresca surfaces and the Mroz infinitesimal kinematic hardening rule. The average error in predicted axial and shear stresses at the designated points 0-8 of the loading cycle is only 10 percent for both this study and that of Lamba and Sibebottom. However, the increment size for strain in the current model is at least ten times larger than for Lamba's previous model, since the finite increment

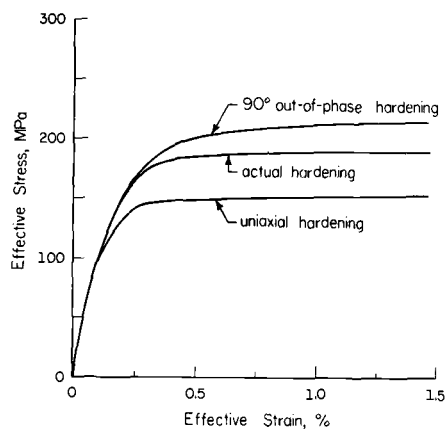
TABLE 1—History 1.^a

Point	Strain Path		Predicted					
			This Study		Lamba Study [4]		Experiment	
	ε	γ	σ	τ	σ	τ	σ	τ
0	0.0	0.0	0	0	0	0	0	0
1	0.0	1.2	0	99	0	95	0	102
2	0.38	-0.8	65	-95	66	-93	81	-91
3	0.0	-1.2	-163	-58	-160	-65	-127	-85
4	-0.38	-0.75	-172	51	-193	39	-187	47
5	0.38	0.75	143	70	145	73	110	83
6	0.0	1.2	-157	60	-128	74	-153	78
7	0.0	-1.2	0	-100	0	-93	0	-103
8	0.0	0.0	0	99	0	88	0	95

^aUnits: strain, %; stress, MPa.



(a)



(b)

FIG. 9—History 2. (a) *Imposed strain path.* (b) *Stable effective cyclic stress-strain curves used in analysis.*

hardening rule is used. Thus the present model is considerably more efficient for computer applications and is justified.

History 2: Square Path

Lamba subjected another tubular OFHC copper specimen to the strain path shown in Fig. 9a until cyclically stable. The effective cyclic stress-strain curve was obtained by converting a subsequent pure torsion hysteresis loop to effective stresses and strains via Eqs 1 and 2 and Masing's relation.

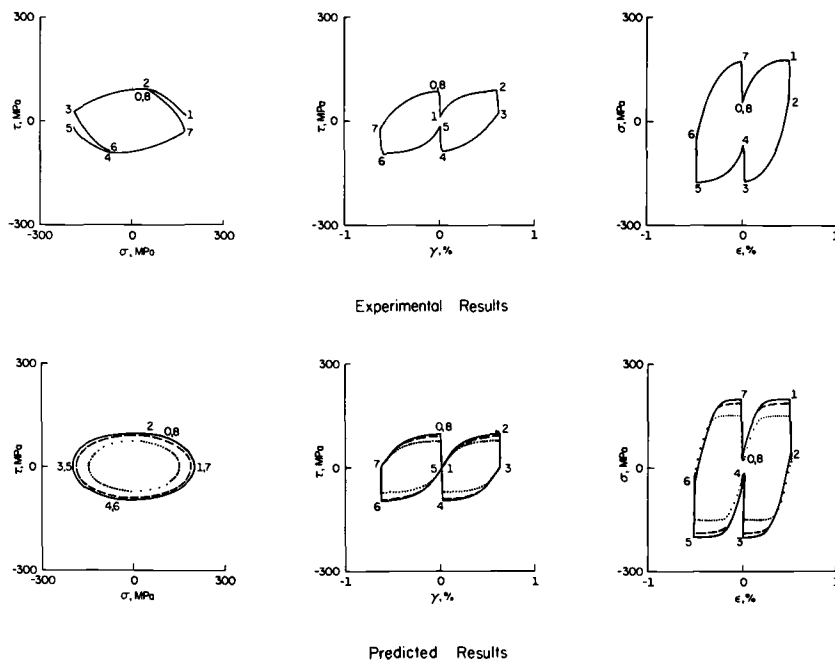


FIG. 10—Stress-strain response to strain history 2: dashed, solid, and dotted curves represent solutions using the actual, 90-deg out-of-phase, and uniaxial stable effective cyclic stress-strain curves, respectively.

A material cyclically hardens to a greater extent during nonproportional loading. The case of 90-deg out-of-phase loading represents the largest upward shift in the stable effective cyclic stress-strain curve. The degree of hardening seems to be associated with the variation in direction of the principal stress [8]. For the strain path in Fig. 9a, hardening is less than that of the 90-deg out-of-phase case, but more than for the uniaxial case. The stable effective cyclic stress-strain curve for each case is shown in Fig. 9b.

In the analysis, each of the three effective cyclic stress-strain curves was divided into nine surfaces with a constant strain piecewise linearization. An effective strain increment of 0.03 percent was applied. The actual and predicted stress-strain responses appear in Fig. 10 for comparison. The actual value of plastic work per cycle is 3.72 MJ/m^3 .

In the stress space of Fig. 10, the predicted path is a closed ellipse, but the experimental path is partially open. Again, the stress path follows the limit surface in theory, contributing to more predicted relaxation of shear stress on path 2-3 than experimentally observed. Note also that the slope of the predicted axial stress-strain curve along path 6-7 decreases more quickly than that of its corresponding experimental path. This suggests that the limit surface used in the model may not entirely represent reality. Translation of the limit surface in this case may have resulted in a more accurate prediction.

For the actual, 90-deg out-of-phase and uniaxial stable cyclic stress-strain curves shown in Fig. 9b, the corresponding Φ -values for the response in Fig. 10 are 1.28, 1.34, and 1.08, respectively. Again, these high values reflect the excursion of the stress point along the limit surface only. The plastic work per cycle obtained by using the uniaxial cyclic stress-strain curve generally provides the lowest estimate of the damage to this material if damage is viewed in terms of plastic work per cycle. Hence, for design purposes, it is advisable to use the 90-deg out-of-phase curve in this case if the actual cyclic stress-strain curve is not available.

The magnitude of stresses and strains at each endpoint of the loading cycle for History 2 is shown in Table 2. As expected, the actual effective stable cyclic stress-strain curve best correlated prediction with experiment; the average error of both predicted axial and shear stresses at points of maximum absolute value in the loading cycle is less than 7.5 percent.

Further Results

Other nonproportional loading paths obtained by Lamba, Kanazawa, Miller, and Brown [8] were analyzed to determine the effectiveness of the model. An account of this analysis may be found in Ref 7. The constant stress and constant strain piecewise linearizations described in Fig. 4 yield nearly identical results and Fig. 8 is applicable for each. The geometric piecewise linearization, however, resulted in solution instability and inaccuracy in spite of fast execution time.

Conclusions

1. The developed constitutive equations are able to accurately model a bi-axial plane stress state along nonproportional stress-strain paths.

TABLE 2—History 2.^a

Point	Strain Path		Predicted ^b						Experiment	
			σ			τ				
	ϵ	γ	A	B	C	A	B	C	σ	τ
	0	0.0	-0.01	20	30	30	75	89	97	51
1	0.47	0.0	149	187	200	0	0	0	177	13
2	0.47	0.60	24	30	30	75	89	97	85	89
3	0.0	0.62	-149	-187	-200	0	0	0	-175	26
4	0.0	0.02	-20	-30	-30	-75	-89	-97	-70	-85
5	-0.47	0.0	-149	-187	-200	0	0	0	-180	-14
6	-0.47	-0.60	-25	-30	-30	-75	-89	-97	-75	-92
7	0.0	-0.62	149	187	200	0	0	0	173	-25
8	0.0	-0.01	20	30	30	75	89	97	51	85

^a Units: strain, %; stress, MPa.

^b A, uniaxial curve; B, actual curve; C, 90-deg out-of-phase curve.

2. A Mroz-type hardening rule is quantitatively accurate. The optimum number of surfaces is 10 to 15, but as few as four or five may be used with a slight compromise in accuracy for finite-element applications.

3. There is a trade-off between the number of surfaces in a Mroz-type hardening rule and the effective strain increment for optimum solution with respect to accuracy and speed. The manner in which the cyclic stress-strain curve is linearized is not as crucial as effective strain increment size.

4. Use of the 90-deg out-of-phase stable effective cyclic stress-strain curve in analysis may be conservative for strain-controlled nonproportional load histories applied to cyclically hardening materials if damage is viewed in terms of plastic work per cycle. If damage is viewed in terms of plastic strain range, the uniaxial curve may yield conservative results.

5. The introduction of a translating limit surface would aid quantitative accuracy for the stable, kinematic response.

Acknowledgments

The support of this work by the National Science Foundation (NSF ENG 78-23549) is gratefully acknowledged.

References

- [1] Eisenberg, M. A., *Journal of Engineering Materials and Technology, Transactions of ASME*, July 1976, pp. 221-228.
- [2] Tanaka, M. and Miyagawa, Y., *Ingenier-Archiv*, Vol. 44, No. 4, 1975, pp. 255-268.
- [3] Mroz, Z., *Mathematical Models of Inelastic Material Behaviour*, Solid Mechanics Division, University of Waterloo, Ontario, 1973, pp. 130-141.
- [4] Lamba, H. S. and Sidebottom, O. M., *Journal of Engineering Materials and Technology, Transactions of ASME*, Jan. 1978, pp. 96-111 (see also Lamba, H. S., TAM Report No. 413, University of Illinois, Urbana, 1976).
- [5] Garud, Y. S. in *Proceedings*, Symposium on Methods for Predicting Material Life in Fatigue, American Society of Mechanical Engineers, Dec. 1979, pp. 247-263.
- [6] Drucker, D. C., "Paper for First Symposium on Naval Structural Mechanics Plasticity," Technical Report No. 41, Division of Applied Mathematics, Brown University, Providence, R.I., 1958.
- [7] McDowell, D. L., "Multiaxial Nonproportional Cyclic Deformation," M.S. thesis, Department of Mechanical and Industrial Engineering, University of Illinois, Urbana, 1980.
- [8] Kanazawa, K., Miller, K. J., and Brown, M. W., *Fatigue of Engineering Materials and Structures*, Vol. 2, 1979, pp. 217-228.

Low-Cycle Fatigue under Biaxial Strain

REFERENCE: Moguerou, A., Vassal, R., Vessiere, G., and Bahuaud, J., "Low-Cycle Fatigue under Biaxial Strain," *Low-Cycle Fatigue and Life Prediction*, ASTM STP 770, C. Amzallag, B. N. Leis, and P. Rabbe, Eds., American Society for Testing and Materials, 1982, pp. 519-546.

ABSTRACT: The present work aims to obtain some information about the crack initiation criterion under biaxial low-cycle fatigue strain in phase or 180 deg out of phase. The investigation was carried out on A 316 stainless steel.

A servohydraulic experimental rig was developed for application of biaxial high-strain reversed cycles. The strains were controlled and the axes of principal strain were fixed during these tests. The test specimens are thin-walled tube on which we apply axial tension-compression and internal-external pressure difference by using two hydraulic servosystems. The results obtained for three different strain ratios are plotted as a function of half of the equivalent Tresca strain.

The Tresca criterion has been shown to be nonconservative for cases where the axes of principal strain rotate continuously, but in our tests we observe that torsion is less damaging than plane strain, which is less severe than tension. In other words the Tresca criterion is conservative, which is in agreement with the ASME code.

Finally, the fatigue crack growth is studied by a scanning electron microscope, and a propagation law is proposed.

KEY WORDS: low-cycle fatigue, biaxial strain, equivalent strain, crack propagation

The components of pressure installations, like nuclear vessels, are subjected to cyclic biaxial loads. While fatigue tests allow the forecasting of plastic strains and other tests have shown the possibility of calculating the number of cycles at rupture for uniaxial strains or stresses, there are far less results for predicting the number of cycles at rupture in the case of biaxial strains.

For high-endurance fatigue, several useful testing programs have been carried out to investigate the influence of multiaxial fatigue stresses or strain. Cruciform and thin-walled tube specimens have been used. The most commonly used specimen in multiaxial works has been the thin-walled tube on which the tests are performed by tension compression and by internal and external pressure and torsion.

¹Institut National des Sciences Appliquées de Lyon, Laboratoire de Mécanique des Solides, 69621 Villeurbanne Cedex, France.

Among the variety of tests we can note those of Halford and Morrow [1], who used pure torsion on aluminum alloy, as did Taira [2].² Zamrik [3] by means of an hydraulic actuator applied tension and compression as well as torsion loads in phase and out of phase. Crosby [4] used internal pressure and axial load on aluminum or copper tubes. Havard and Topper [5] produced five distinct biaxial-stress states by simultaneous direct pressurization and axial loading of thin-walled cylindrical specimens; four variations of stress state are obtained by the use of two sizes of specimen and by reversal of the pressurizing connections and the fifth state is obtained by direct pressurization without axial load.

Andrews and Ellison [6,7] tested RR 58 aluminum alloy under low-cycle fatigue by applying cyclic internal pressure, external pressure, and axial load to thin-walled tubular specimens, both at room temperature and at 140°C.

In this investigation, we developed a biaxial rig in order to realize a low-cycle fatigue test under imposed longitudinal and transversal strains on a thin-walled tube. It consists of an hydraulic actuator which applies axial tension/compression and another hydraulic system which applies a difference of pressure between the internal and external part of the thin tube wall.

It is then possible to apply biaxial high cyclic strains in phase and 180 deg out of phase on a small element of the tube. We note ϵ_L (the total longitudinal strain) and ϵ_T (the total transversal strain) (Fig. 1). The real-time measurement of ϵ_L and ϵ_T by strain transducers allows us to drive the test by means of biaxial imposed total strains. The imposed signals have the form

$$\begin{aligned}\epsilon_L &= \epsilon_{Lm} + \epsilon_{La} \sin \omega t \\ \epsilon_T &= \epsilon_{Tm} + \epsilon_{Ta} \sin (\omega t + \Phi)\end{aligned}$$

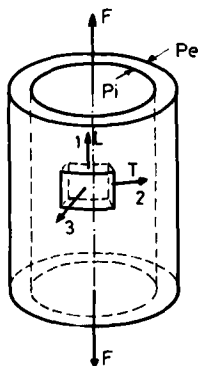


FIG. 1—The small element of the tube.

²The italic numbers in brackets refer to the list of references appended to this paper.

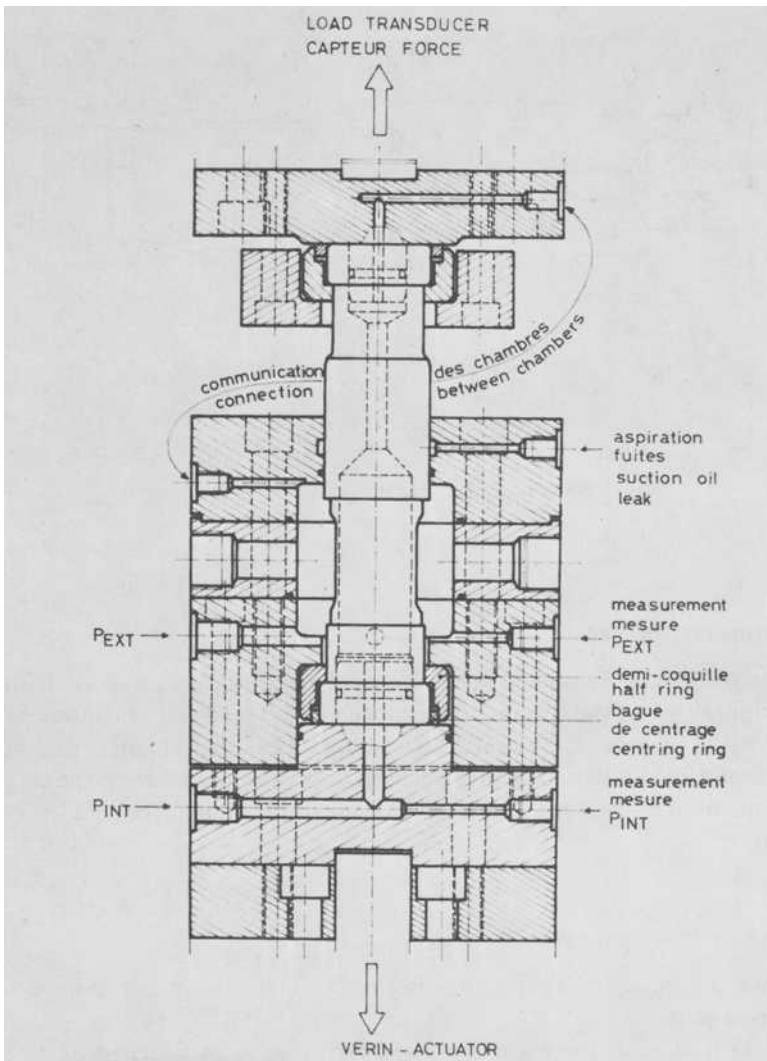


FIG. 2—Loading system.

where ϵ_{Lm} and ϵ_{Tm} are the mean components of the imposed strain. ϵ_{La} and ϵ_{Ta} are the alternative components, and Φ controls the phase difference. We consider, however, that the loading cases for $\theta = 180$ deg are not really out of phase. The two signals would be out of phase if they did not reach their respective peaks simultaneously.

Strain and load measurements were used in conjunction with two *XY*-recorders to obtain hysteresis loops throughout the cyclic tests.

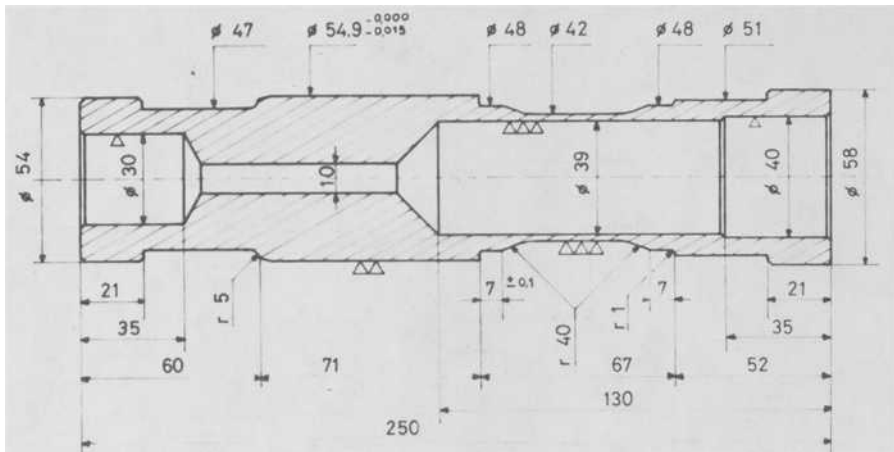


FIG. 3—Dimensions of the thin-walled tubular specimen.

Experimental Procedure

Figure 2 shows the tubular specimen mounted inside the pressure chamber. The upper part of the specimen is attached to the load cell; the lower part is attached to the actuator. Axial load is obtained by means of an hydraulic actuator of ± 200 kN capacity, and the pressure difference between the external and the internal part of the thin-walled tube is generated from a 28-MPa oil pump.

Specimen Development

The final shape of the specimen is given in Fig. 3. A specimen has several different parts:

1. At both ends there are two shoulders, one to be fastened to the load transducer, the other to the actuator.
2. An adjustable massive part assures the tightness of the oil chamber.
3. At both ends of the gage length there are two radii of 40 mm. This dimension was chosen after some experimental tests in order to initiate cracks at the center of the gage length, and this certainly resulted in a nonuniform strain distribution. Because the strain gradient is along the gage length the strains are determined by a strain gage at the midsection. If a crack appears out of the midsection, the test is excluded. The thickness and the gage length of the wall have been determined in order to obtain a compromise between a sufficient plastic strain and the buckling tendency.

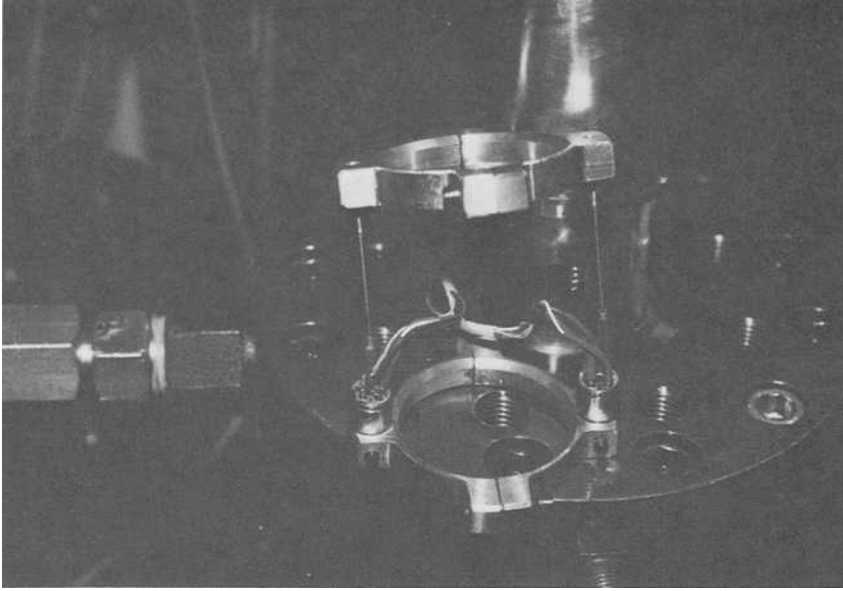


FIG. 4—Longitudinal strain transducers.

Longitudinal Transducers

The longitudinal measuring device consists of two frames mounted at each end of the gage length (Fig. 4). The displacements are measured by two inductive transducers mounted diametrically opposite each other with an amplitude up to ± 1 mm.

Transverse Transducers

These are mounted diametrically opposite each other on either side of the midsection of the specimen (Fig. 5). The transducers are fixed inside the pressure chamber. The inductive movable parts are extended by a feeler consisting of pins in contact with the specimen and giving an amplitude up to ± 1 mm.

Strain Measurement

The transversal transducers measure the radial change in the cylinder, giving directly $\epsilon_r = \Delta R_{\text{measured}} / R_{\text{initial}}$. In order to calculate the real values of the longitudinal strains from the measured ones, we must cement strain gages on the midpart of the gage length.

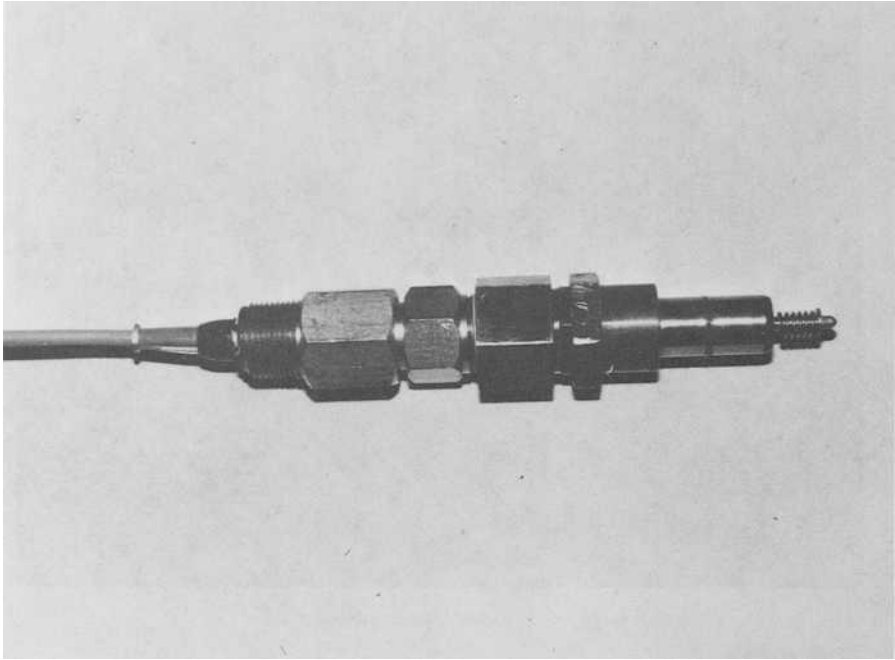


FIG. 5—*Transversal strain transducers.*

Servohydraulic Control

The overall system used in the biaxial fatigue test is illustrated in Fig. 6. We have effectively two control loops with two servovalves, one controlling the axial strains (as axial loads) and one controlling the transversal strains (as the pressure difference). The schematic layout of the electronic system is given in Fig. 7. Those two control loops are not independent, but are connected by the test specimen and its four functions:

1. The F1-function relates the longitudinal strain ϵ_L to the force F developed by the actuator.
2. The F2-function relates the transversal strain ϵ_T to F .
3. The F3-function relates ϵ_T to the pressure difference Δp .
4. The F4-function relates ϵ_L to Δp .

Thus the material characteristics are those which allow us to drive the test. The two servovalves deliver loads by means of the actuator on one side and the compression chamber on the other side, therefore subjecting the specimen to a state of stresses and consequently to a state of strains. We can measure the longitudinal and transverse displacements and then compare them with the imposed values given by a minicomputer.

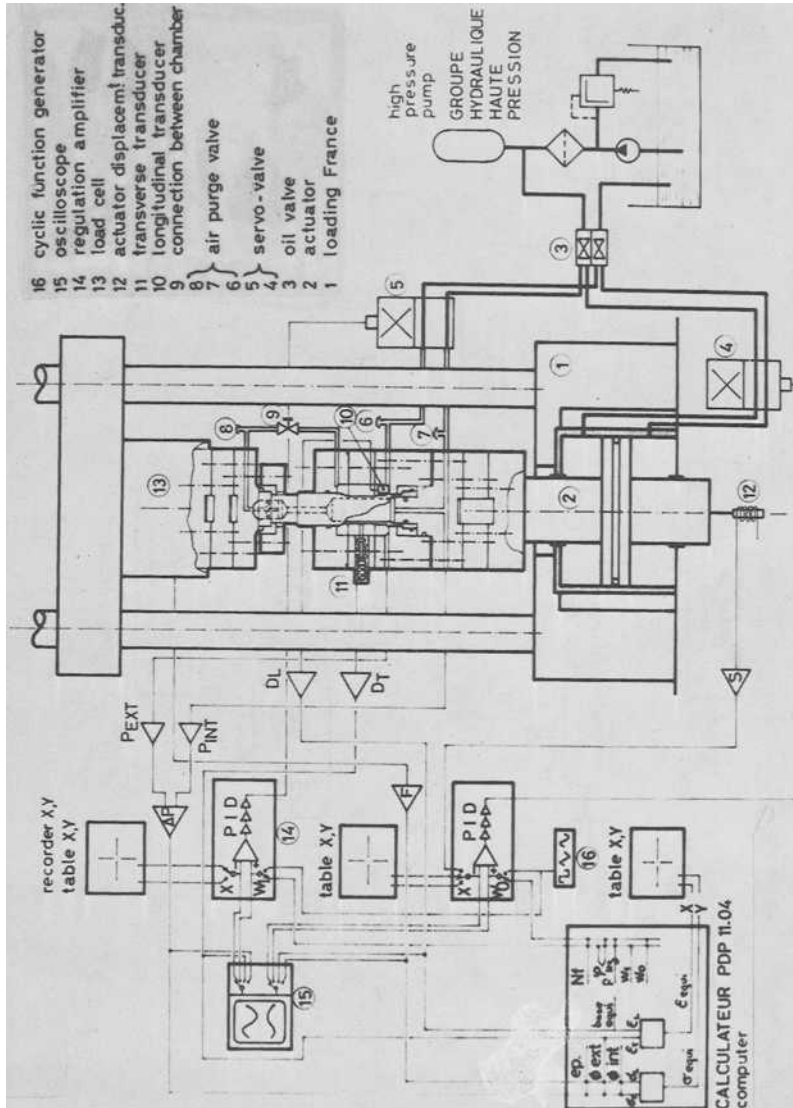


FIG. 6—Hydraulic and electrical system for biaxial testing.

TABLE 1—*Chemical composition of test steel.*

C	Mn	Si	S	P	Mi	Cr	Mo	N	Cu	Co
0.029	1.8	0.5	0.012	0.032	12.6	17.54	2.38	0.077	0.26	0.18

Material Data

This work was carried out at room temperature on austenitic stainless steel Z3 CND 17-12 (steel grade ICL 167 F) quenched in water at 1070°C. The chemical composition is given in Table 1. Table 2 shows the mechanical properties. Figure 8 gives the cyclic and monotonic tension curves. Figure 9 shows the uniaxial fatigue curves for this material on solid specimens.

Biaxial Cyclic-Strain Data

The different kinds of biaxial tests depend on the ratio between the longitudinal and transversal strains. The range of the biaxial strain we imposed to have a crack at a given number of cycles is calculated by using the uniaxial low-cycle fatigue curve, and the Tresca equivalent strain (ASME Code [8] for nuclear vessels). The Tresca equivalent strain is defined as

$$\epsilon_{eq, Tresca} = \frac{4}{3} R$$

where R is half the maximum engineering shear strain. The mean equivalent Tresca strain rate was fixed at $4 \cdot 10^{-3}$ /s. Our different tests have been performed with $\epsilon_{Lm} = \epsilon_{Tm} = 0$.

Pure Plastic Tension Test:

$$\epsilon_{La} = \frac{\Delta \epsilon_{eq, Tresca}}{2}; \epsilon_{Ta} = 0.5 \epsilon_{La}; \Phi = 180 \text{ deg}$$

Torsion Test:

$$\epsilon_{La} = \frac{3}{4} \frac{\Delta \epsilon_{eq, Tresca}}{2}; \epsilon_{La} = \epsilon_{Ta}; \Phi = 180 \text{ deg}$$

TABLE 2—*Mechanical properties of test steel.*

0.2% Yield Strength, MPa	Tensile Strength, MPa	Elongation, %	Reduction of Area, %	Young's Modulus, MPa
270	588	61	77	200 100

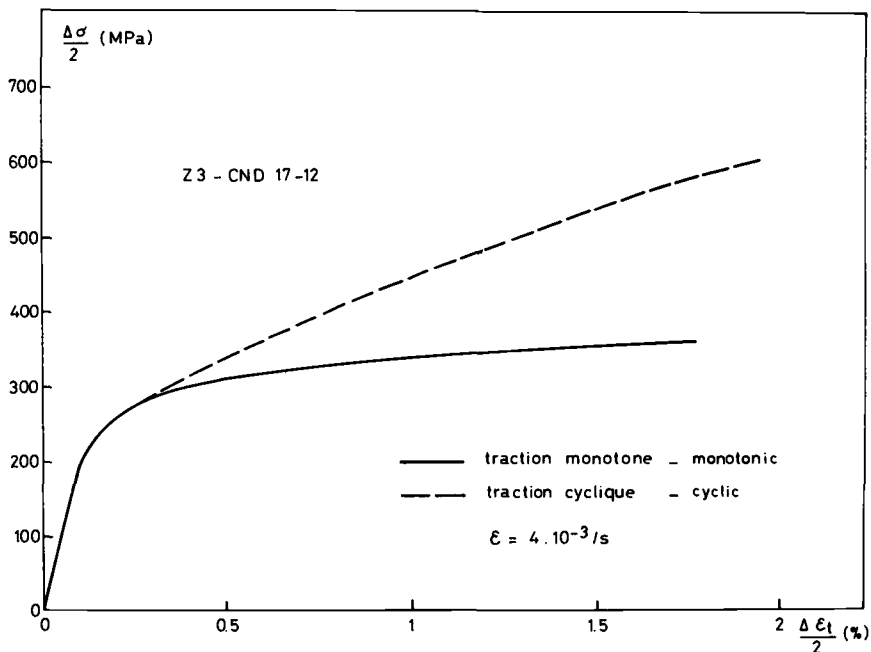


FIG. 8—Cyclic and monotonic traction curve.

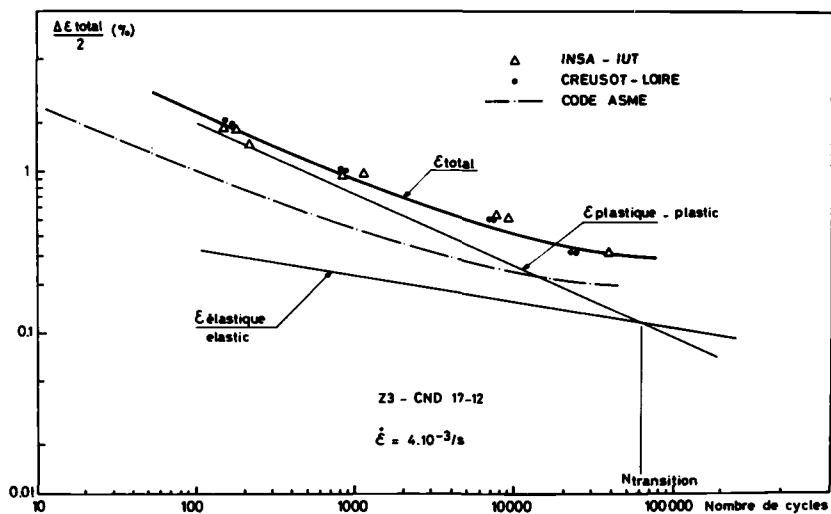


FIG. 9—Uniaxial fatigue curves.

Plane Strain Test:

$$\epsilon_{La} = \frac{3}{4} \frac{\Delta \epsilon_{eq, Tresca}}{2}; \epsilon_{Ta} = 0; \Phi = 0 \text{ deg}$$

During the test we recorded longitudinal and transversal strains and also load and pressure on two *XY*-recorders. Thus we obtained hysteresis loops (Figs. 10, 11, and 12):

$$F = f(\text{longitudinal strain}) = f(\epsilon_L)$$

$$P = P_E - P_I = g(\text{transversal strain}) = g(\epsilon_T)$$

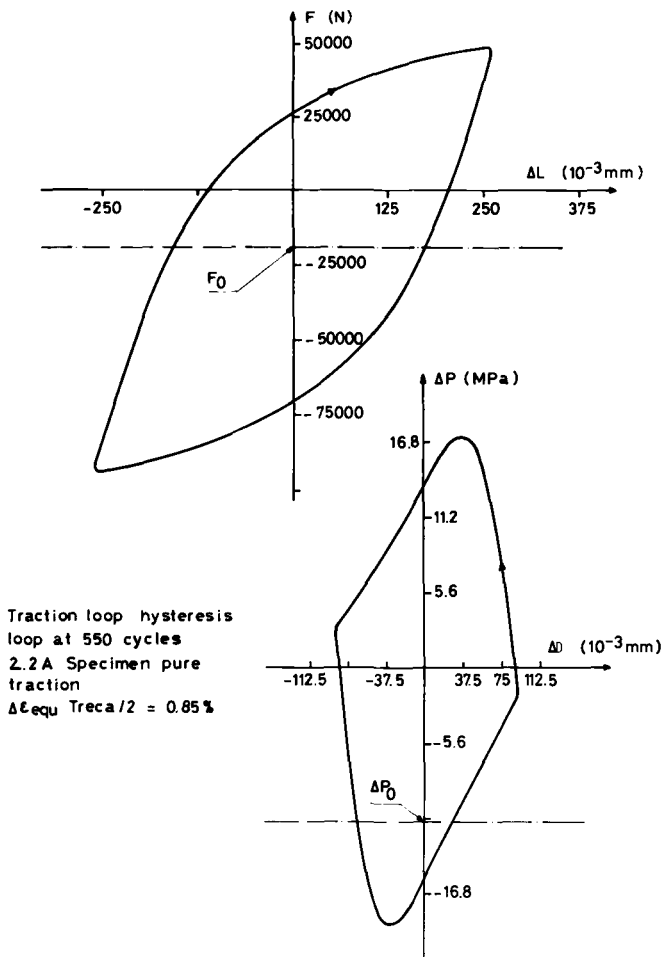


FIG. 10—Traction hysteresis loops.

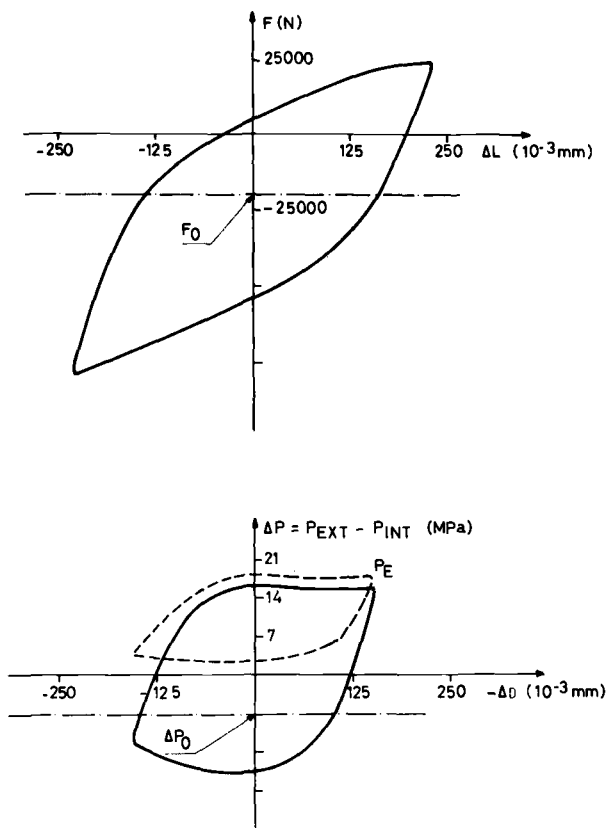


FIG. 11—Torsion hysteresis loops.

The fatigue test concludes when the hysteresis loops show a distortion. We can see this distortion when the internal and external oil chambers are connected by a small crack. We also use a more sensitive method to see a small crack appearing. When the two oil chambers are connected there is an oil flow between them, and the servovalve current increases rapidly. Recording this current we can have the number of cycles for the emerging crack (Fig. 13).

Test Results

Fatigue Life Results

Figure 14 shows the curves giving the Tresca equivalent strain amplitude plotted against the number of cycles to failure (emerging crack) for the three different types of tests. We can see that torsion is less damaging than plane strain, which is less severe than tension. In other words, the Tresca criterion is conservative, in agreement with the ASME code.

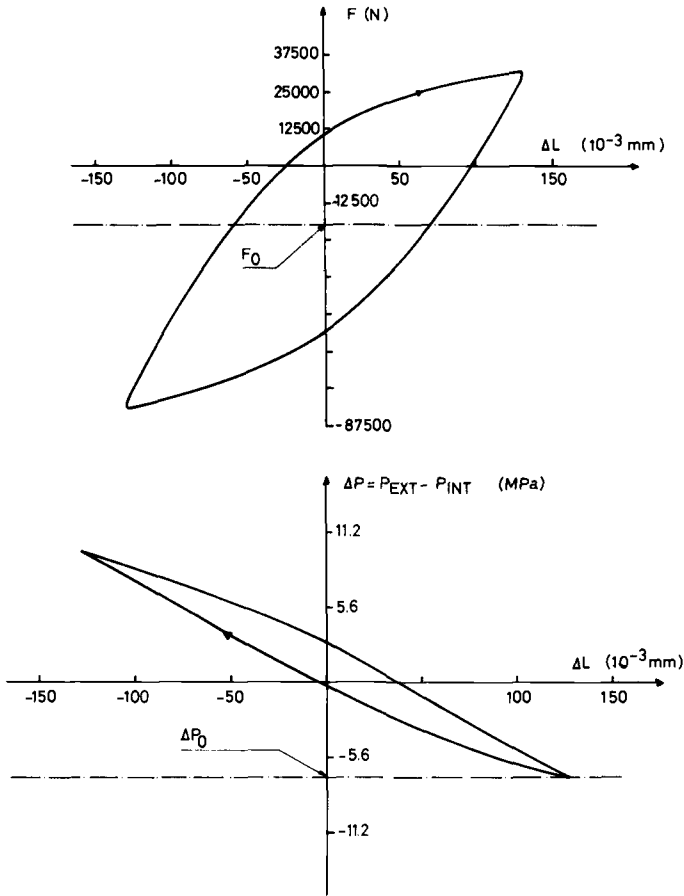


FIG. 12—Plane strain hysteresis loops.

In the ϵ_L and ϵ_T plane the constant life contours have the same shape (Fig. 15).

In order to check the biaxiality effects we plot our points in the Miller [9] Γ -plane; this gives the maximum shear strain amplitude as a function of tensile strain amplitude normal to the plane of maximum shear (Fig. 16). For tests where the normal strain to the maximum shear plane is null (torsion tests and plane strain tests), we can see a large difference for the allowed maximum shear for a same number of cycles obtained for an emerging crack. The direction of the maximum shear plane in respect to the specimen surface has an influence on the material life. Numerous multiaxial fatigue criteria have been proposed. Assuming that we have a biaxial state of strain and that Poisson's ratio $\nu = 0.5$, we can plot these failure criteria on the Γ -plane (Fig. 17).

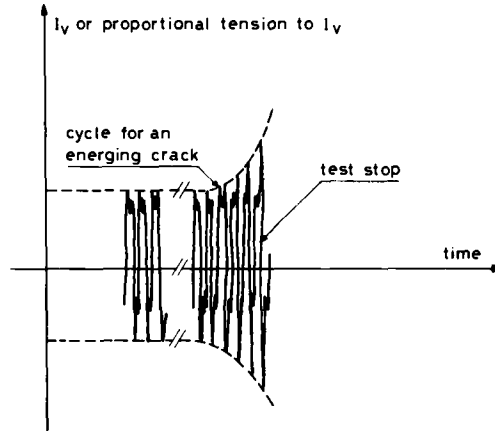


FIG. 13—Servovalve current.

The Tresca, St Venant, and Von Mises's criteria do not show the influence of the maximum shear plane direction in respect to the specimen surface. For the null normal strain there is only one value of the allowed maximum shear, independent of the strain ratio. However, the Rankine and the generalized Von Mises criteria (see Appendix) show two distinct curves between traction and torsion, and traction and plane strain, respectively, as has been shown in

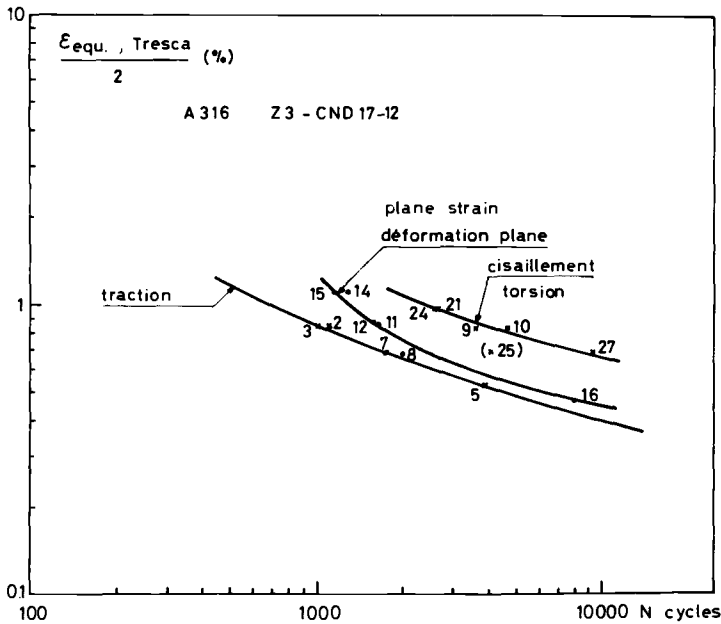


FIG. 14—Correlation of biaxial data by Tresca equivalent strain.

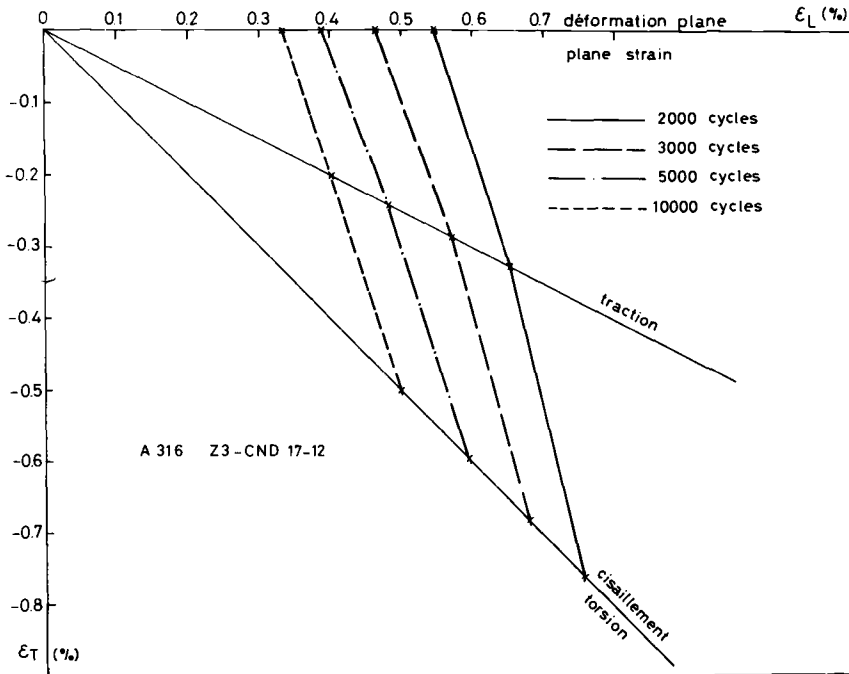


FIG. 15—Constant life curves.

this experimental work. With the Rankine criterion all the experimental points are not on the conservative side. The most promising method appears to be based on the generalized Von Mises criterion, and the correlation with our data is better (Fig. 17).

Fractographic Aspect of the Fracture Surface

The cracks are initiated at the internal side of the thin tube. They propagate along the thickness or parallel to the surface, and keep their initial direction as they emerge at the external side of the tube (Figs. 18a, 18b, and 18c). The crack initiated in the maximum shear plane propagates in the plane perpendicular to the direction of the maximum stress. The propagation mode is transgranular in the case of a polycrystalline material, as we can see in Figs. 19a, 19b, 19c, and 19d. The fracture surfaces were observed by means of scanning electron microscopy.

It has been recognized that each well-defined striation of the fracture surface corresponds approximately to each strain cycle shown by McMillan and Pelloux [10]. Therefore the crack propagation rate per cycle can be obtained from the striation spacings. The crack propagation rate, dl/dN , has been calculated in the case of pure traction and plane strain along the thickness of the tube. In this case of the torsion the fatigue striations do not appear

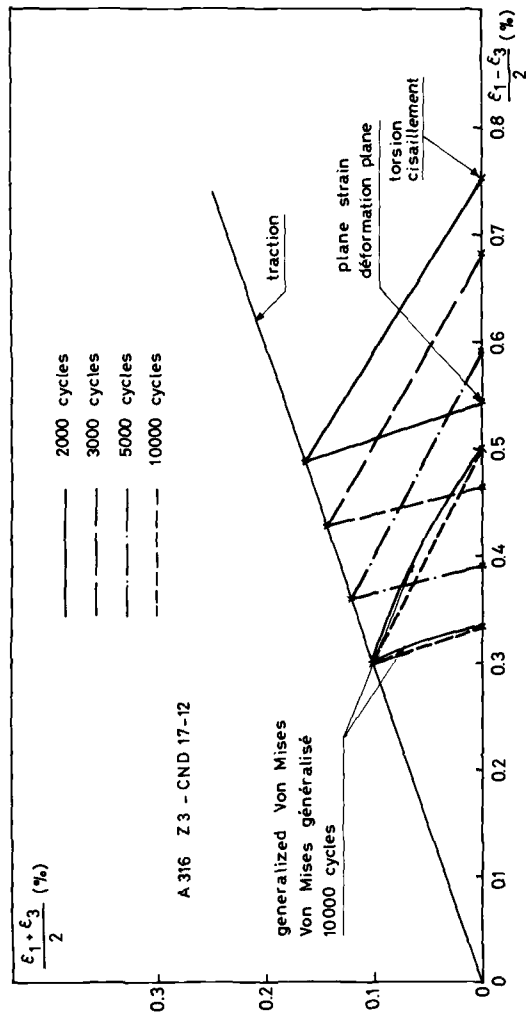


FIG. 16— Γ -plane.

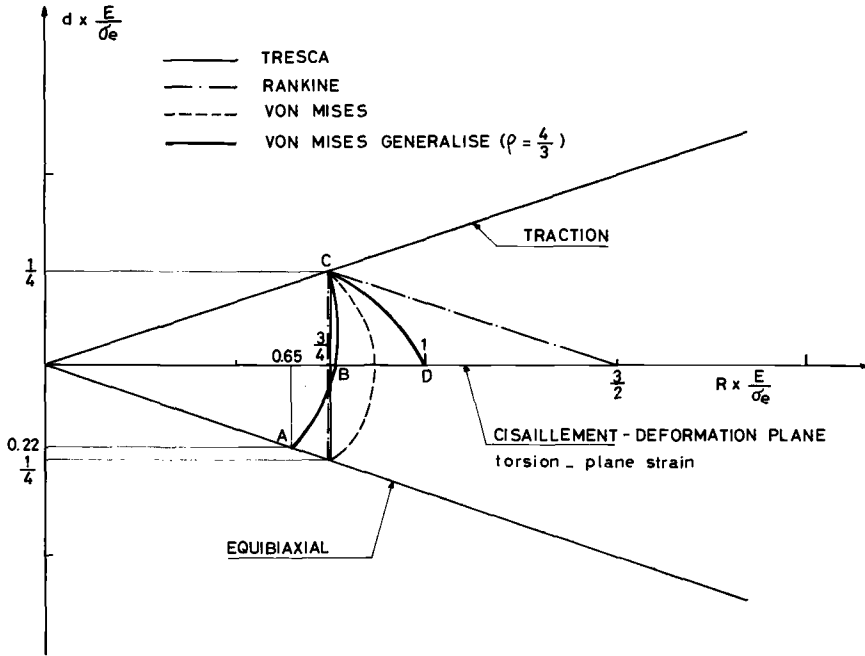


FIG. 17—Failure criteria.

clearly. We have only secondary striations. If we assume a propagation law of the form

$$\frac{dl}{dN} = A \left(\frac{\Delta \epsilon_{\text{Tresca}}}{2} \right)^m l^n$$

we obtain in the plane strain case with four fractographic specimens

$$\frac{dl}{dN}_{(\text{mm/cycle})} = 11.8 \cdot 10^{-3} \left(\frac{\Delta \epsilon_{\text{Tresca}}}{2} \right)_{\%}^{2.47} l^{1.33}_{(\text{mm})}$$

In the case of pure traction, n has been found equal to 1.2. This value compares very well with other values [11–15]. The authors obtain for uniaxial low-fatigue tests an exponent as $1 < n < 1.4$.

Fatigue Life at the Initiation of a Crack of a Given Length

We define the initiation as the nucleation and growth of a fatigue crack at Stage I. This initiation corresponds to microcracks of 50 to 100 μm . (It is nearly the grain size.) It is then possible to calculate the number of cycles at the initiation, N_i , which is the difference between the fatigue life N_f (emerging crack) and N_{II} (number of the cycles corresponding to Stage II crack growth).

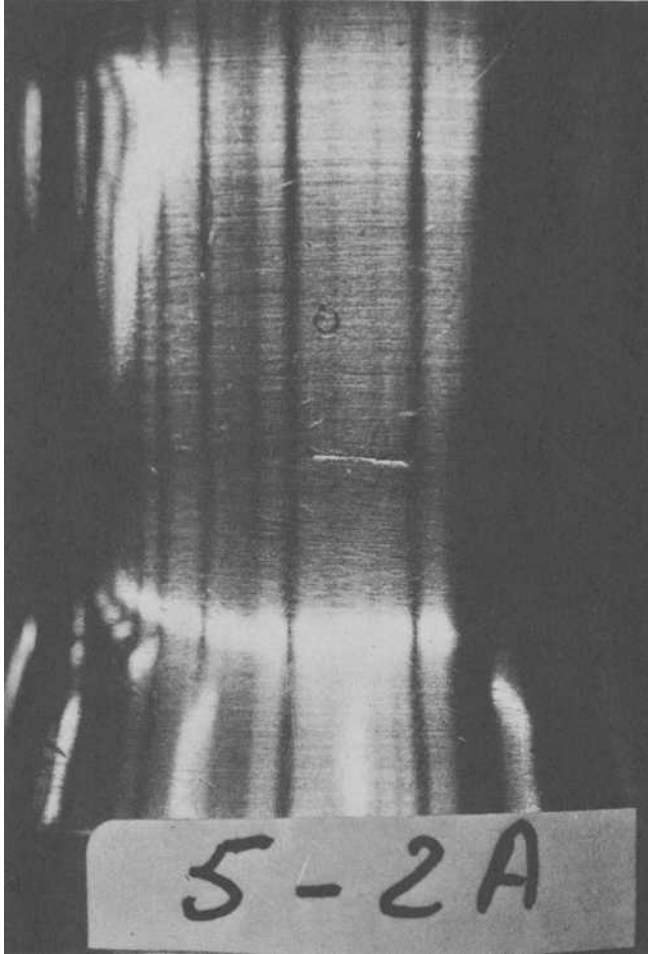


FIG. 18a—Traction cracks.

By integrating the proposed crack propagation law, from $l = 0.1$ mm to the thickness l_f of the specimen wall, we obtain the value of N_{II} . These results are then plotted in the plane N_i/N_R percent against N_R (Fig. 20). We can see that the initiation part is about 60 to 75 percent of the fatigue life. These values are also obtained by Manson [16] and Maya [17].

Conclusion

The purpose of this experimental work was to obtain same information on the effect of biaxiality on the low-cycle fatigue of 316 stainless steel at room temperature. An original material testing rig has been developed. High-strain fatigue data have been obtained under biaxial conditions for three dif-

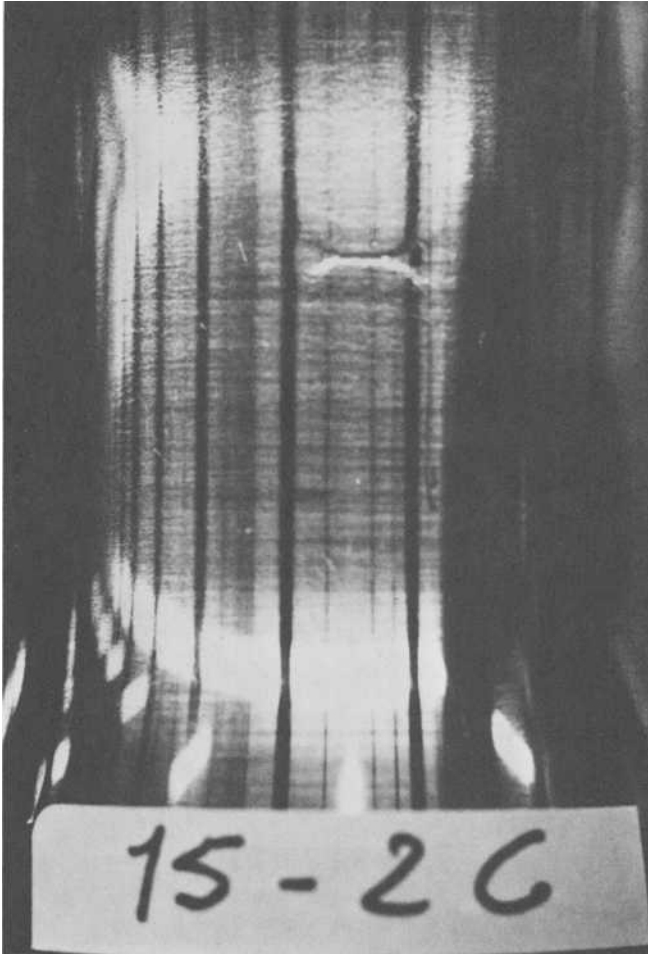


FIG. 18b—Plane strain cracks.

ferent strain ratios in phase and at 180 deg out of phase. These data show that the Tresca criterion is conservative. We propose a generalized Von Mises criterion which seems more realistic. Finally the fatigue crack growth has been studied and a rate propagation law is given for the pure traction and plane strain.

We shall next investigate out-of-phase biaxial low-cycle fatigue.

Acknowledgments

The authors acknowledge the financing support of this investigation by DGRST (Délégation Générale à la Recherche Scientifique et Technique).

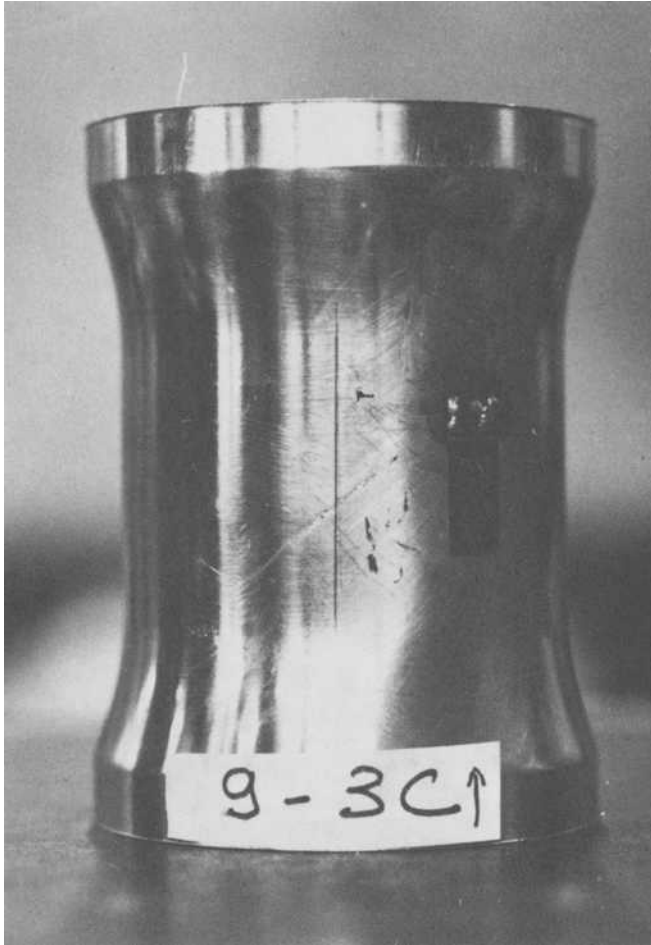


FIG. 18c—*Torsion cracks.*

The authors wish to thank A. Pellissier-Tanon and J. L. Bernard from Framatome for their valuable suggestions and assistance.

APPENDIX

Generalized Von Mises Criterion

Abandoning the assumption of incompressible plastic flow and expressing the fact that yielding in a compressible medium depends on the first invariant of the stress tensor, Von Mises gave a generalized yield condition in 1925 [18]. It has the form

$$J_2 - \phi(I_1) = 0 \quad (1)$$

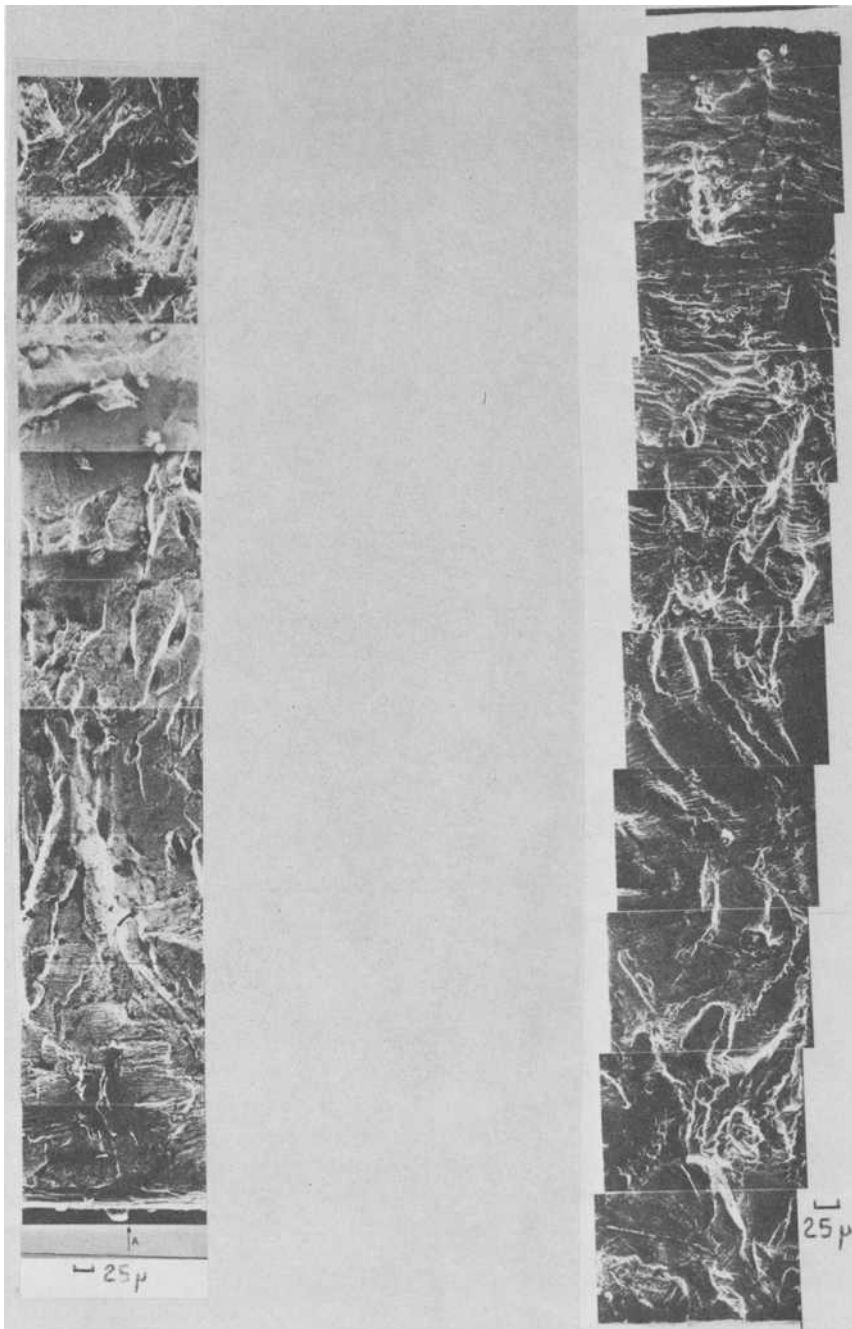


FIG. 19a—Propagation mode; plane strain; Specimen 16-14.

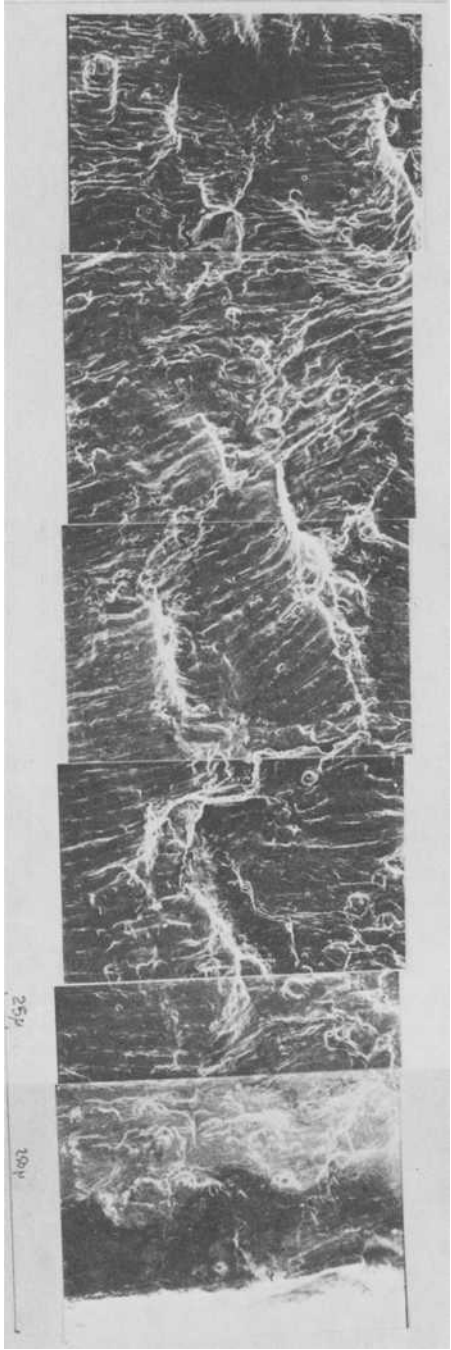


FIG. 19b—Propagation mode; traction test 2 2A.

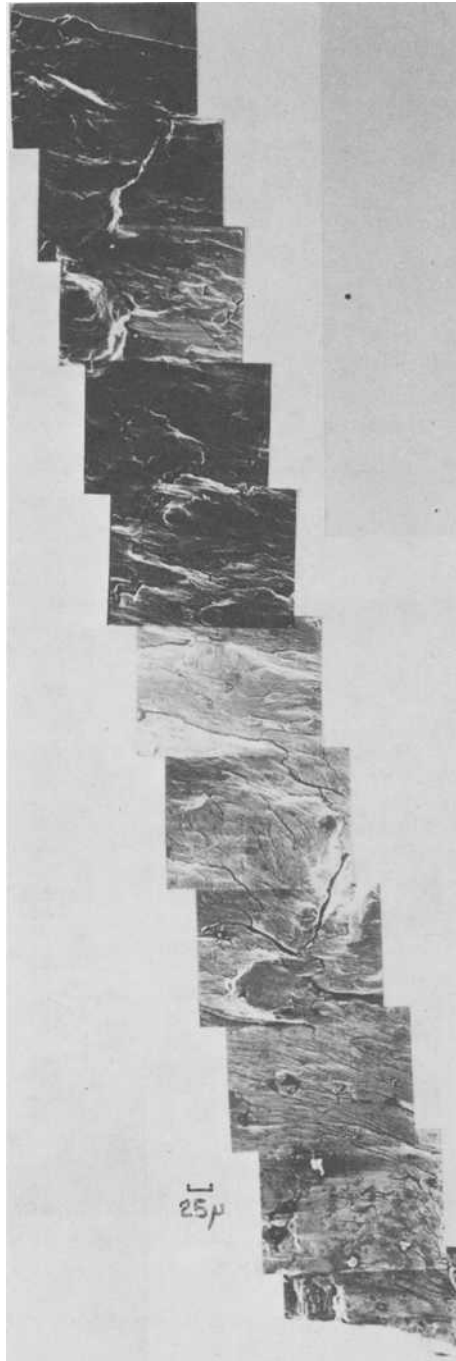


FIG. 19c—*Propagation mode; torsion; Specimen 27.*

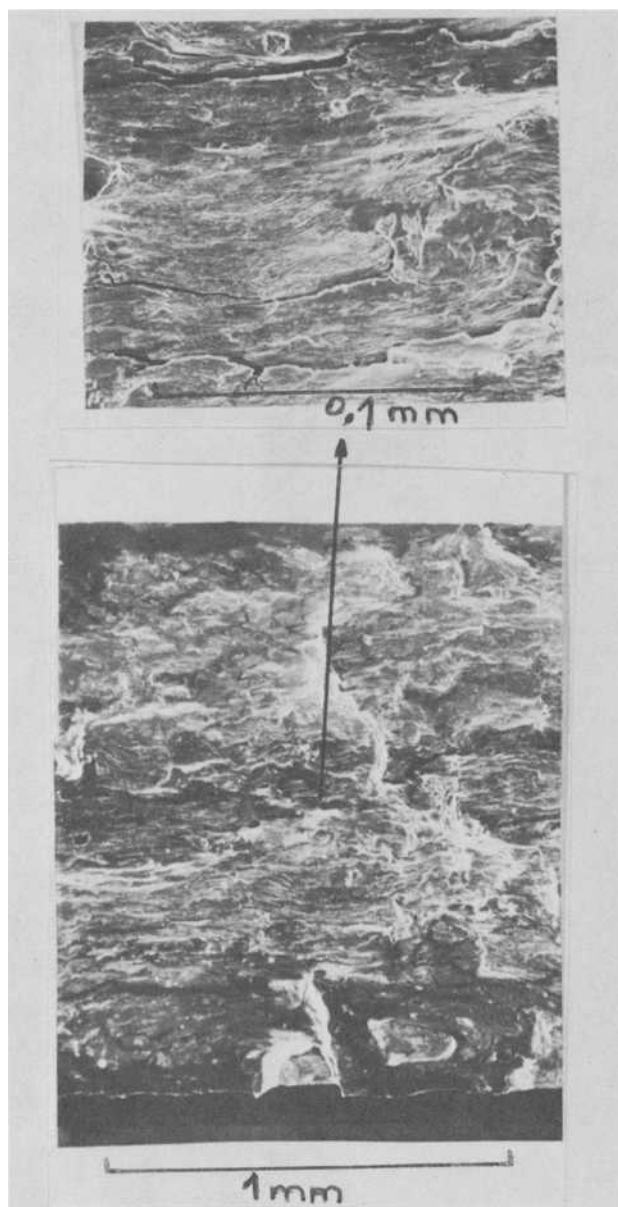
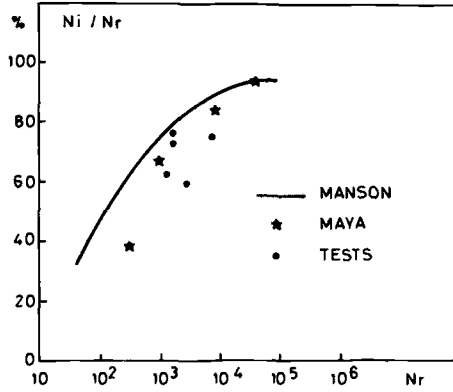


FIG. 19d—Propagation mode; torsion; Specimen 21.

FIG. 20—Variation in N_i/N_r ratio to N_r .

where

$$I_1 = \sigma_1 + \sigma_2 + \sigma_3 \quad (2)$$

$$J_2 = \frac{1}{6} [(\sigma_1 - \sigma_2)^2 + (\sigma_2 - \sigma_3)^2 + (\sigma_3 - \sigma_1)^2]$$

and various assumptions can be made with the respect to the function $\phi(J_1)$ either to fit experimental results or for reasons of mathematical expediency.

Considerations of the first kind suggested to Torre [19] a function of the form

$$\phi = \frac{1}{3} \sigma e [\rho \sigma e - (\rho - 1) I_1] \quad (3)$$

where σe is the yield stress in tension and $\rho \approx 3(\tau e / \sigma e)^2$, τe being the yield stress in shear.

Equation 1 combines with Eq 3 to take the form

$$3 J_2 + \sigma e (\rho - 1) I_1 - \rho \sigma e^2 \approx 0 \quad (4)$$

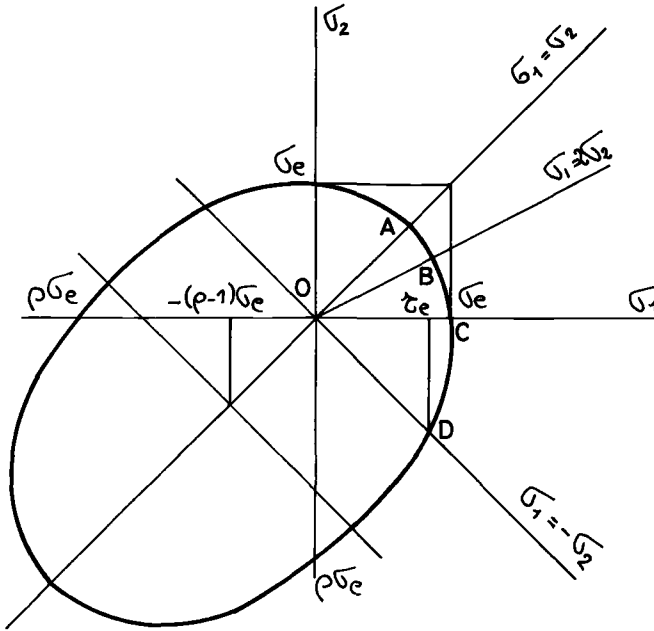
Experimental results obtained by D'Alia [20] confirm Eq 4 at the fracture. On the other hand, experimental evidence about the plastic compressibility [21] and the consideration of mathematical expediency [22] justify following a Bahaud and Boivin function of the form

$$\phi = \frac{\sigma e}{2(1 + \bar{\nu}_{\text{act}}^p)} \left(\rho \sigma e - (\rho - 1) I_1 - (1 - 2\bar{\nu}_{\text{act}}^p) \frac{I_1^2}{3\sigma e} \right) \quad (5)$$

leading to the yield condition

$$2(1 + \bar{\nu}_{\text{act}}^p) J_2 + (1 - 2\bar{\nu}_{\text{act}}^p) \frac{I_1^2}{3} + \sigma e (\rho - 1) I_1 - \rho \sigma e^2 = 0 \quad (6)$$

where $\bar{\nu}_{\text{act}}^p$ is the actual plastic Poisson's ratio. Generally it is slightly below 0.5 and remains constant during the work hardening.

FIG. 21—Generalized Von Mises criterion in σ_1, σ_2 plane.

Using Eq 6 in conjunction with the method of the characteristic lines, various aspects of plastic behavior have been explained [23]. For our purpose we obtain a good approximation putting $\bar{\nu}_{act}^p = 0.5$ into the yield condition (6). Then the yield condition (4) appears as a simplified form of the yield condition (6).

For plane stress $\sigma_3 = 0$, the condition equation is written as

$$\sigma_1^2 + \sigma_2^2 - \sigma_1\sigma_2 + \sigma e(\rho - 1)(\sigma_1 + \sigma_2) - \rho\sigma e^2 = 0 \quad (7)$$

In the (σ_1, σ_2) plane this is the equation of an ellipse, a plot of which is shown in Fig. 21. By means of Hooke's law the yield condition (Eq 7) can be written as a function of the principal strains ϵ_1, ϵ_2 , or, as suggested by Brown and Miller [9], as a function of half the maximum engineering shear strain R and of the tensile strain on the plane of maximum shear d .

We have been carrying out four kind of tests: equibiaxial tests ($\sigma_1 = \sigma_2$ or $\epsilon_1 = \epsilon_2$), plane strain tests ($\sigma_1 = 2\sigma_2$ or $\epsilon_2 = 0$), pure tension tests ($\sigma_2 = 0$ or $\epsilon_1 = -2\epsilon_2$), and pure shear or torsion tests ($\sigma_1 = -\sigma_2$ or $\epsilon_1 = -\epsilon_2$). The corresponding points A, B, C, D, respectively, are in the first and fourth quadrant on the (σ_1, σ_2) plane (Fig. 17).

For the first quadrant we have after computations the relations

$$\begin{cases} \sigma_1 = \frac{2}{1 + \nu} ER \\ \sigma_2 = \frac{E}{(1 + \nu)} [-(1 + \nu)d + (1 - \nu)R] \end{cases} \quad (8)$$

and for the fourth quadrant

$$\left\{ \begin{array}{l} \sigma_1 = \frac{(1 - \nu)ER + (1 + \nu)Ed}{1 - \nu^2} \\ \sigma_2 = \frac{-(1 - \nu)ER + (1 + \nu)Ed}{1 - \nu^2} \end{array} \right. \quad (9)$$

where E and ν are Young's modulus and the elastic conventional Poisson's ratio, respectively.

Substitute Eqs 8 and 9 for principal stresses in terms of the shear strain R and the tensile strain d . The yield condition becomes for the first quadrant

$$\frac{1}{\nu^2} \left\{ d^2 + \frac{2(2\nu - 1)}{1 - \nu} Rd + \frac{7\nu^2 - 4\nu + 1}{(1 + \nu)^2} R^2 \right\} + \sigma e(\rho - 1) \frac{1}{1 + \nu} \left\{ 2R + \frac{1}{\nu} [-(1 + \nu)d + (1 - \nu)R] \right\} = \frac{2\rho\sigma e^2}{E} \quad (10)$$

and for the fourth quadrant

$$\left[\frac{d^2}{(1 - \nu)^2} + \frac{3}{(1 + \nu)^2} R^2 \right] + \frac{2\sigma e}{E} (\rho - 1) \frac{(1 + \nu)}{1 - \nu^2} d = 2\rho \left(\frac{\sigma e}{E} \right)^2 \quad (11)$$

If one plots R and d as rectangular coordinates (Γ -plane [9]), then the expressions above give two curves (Fig. 17) (the curves are drawn assuming $\nu = 0.5$ and $\rho = 4/3$).

Finally, using the fact that to predict the fatigue limit at zero mean stress the used criteria are usually the accepted criteria for predicting the onset of plastic deformation under static combined stress loading [24], we propose to predict the strength associated with a given life from the criteria (Eqs 10 and 11), taking $\nu = 0.5$.

Thus from the experimental results from torsion and tension tests it is possible to find the experimental results in plane strain with a very good approximation (Fig. 16).

References

- [1] Halford, G. R. and Morrow, J. D., "Low Cycle Fatigue in Torsion," in *Proceedings, American Society for Testing and Materials*, Vol. 62, 1962.
- [2] Taira, S., Inoue T. and Yoshida S., "Low Cycle Fatigue Under Multiaxial Stresses," in *Proceedings, 12th Japan Congress on Testing Materials*, 1969.
- [3] Zamrik, S. Y., "An Investigation of Strain Cycling Behavior of 7075-T6 Aluminium under Combined State of Strain," Technical Report, NASA, 1972.
- [4] Crosby, J. R., Burns, D. J., and Benham, P. P., "Effect of Stress Biaxiality on the High Strain Fatigue Behavior of an Aluminium Copper Alloy," *Experimental Mechanics*, Vol. 2, 1969.
- [5] Havard, D. G. and Topper, T. H., "New Equipment for Cyclic Biaxial Testing," *Experimental Mechanics*, Vol. 9, 1969.
- [6] Andrews, J. M. H. and Ellison, E. G., "A Testing Rig for Cycling at High Biaxial Strain," *Journal of Strain Analysis*, Vol. 8, No. 3, 1973.
- [7] Ellison, E. G. and Andrews, J. M. H., "Biaxial Cyclic High-Strain Fatigue of Aluminium Alloy RR58," *Journal of Strain Analysis*, Vol. 8, No. 3, 1973.
- [8] *ASME Boiler and Pressure Vessel Code*, Section III, and Div. 2 Sec. VIII, 1977.
- [9] Brown, M. W. and Miller, K. J., "A Theory for Fatigue Failure under Multiaxial Stress-strain Conditions," Cambridge University, 1976.

- [10] McMillan, J. and Pelloux, R. M., "Fatigue Crack Propagation under Programmed and Random Loads," *Boeing Research Laboratories*, 1966.
- [11] Boettner, R. C., Laird, C., McEvilly, A. J., Jr., "Crack Nucleation and Growth in High-Strain Low Cycle Fatigue," *Transactions of the Metal Society*, 1965.
- [12] Tomkins, B., "Fatigue Crack Propagation, an Analysis," *Philosophical Magazine*, Vol. 18, No. 155, 1968.
- [13] Solomon, H. D., "Low Cycle Fatigue Crack Propagation in 1018 Steel," *Journal of Materials*, Vol. 7, 1972.
- [14] Taupin, "Etude de l'endommagement en fatigue oligocyclique sur un acier inoxydable austénitique Z3.CND. 17-12," Thèse de docteur-ingénieur, Université de Compiègne, 1978.
- [15] Yamaguchi, K., Kanazawa, K., and Yoshidas, S., "Crack Propagation in Low Cycle Fatigue of Type 316 Stainless Steel at Temperatures Below 600°C Observed by Scanning Electron Microscopy," *Materials Science and Engineering*, 1978.
- [16] Manson, S. S., "Fatigue: A Complex Subject—Some Simple Approximations," NASA Report, 1965.
- [17] Maya, P. S., "Considerations of Crack Initiation and Crack Propagation in Low-Cycle Fatigue," *Scripta Metallurgica*, Vol. 9, 1975.
- [18] Von Mises, R., *Zeitschrift fuer Angewandte Mathematik und Mechanik*, Vol. 5, 1925, p. 147.
- [19] Torre, C., *Ost Ing.*, Vol. 1, 1946, p. 36; Vol. 4, 1950, p. 174.
- [20] D'Allia, Stassi, "Flow and Fracture of Materials According to a new Limiting Condition of Yielding," *Meccanica*, Sept. 1967.
- [21] Bahuaud, J. and Boivin, M., "Etude du coefficient de Poisson pour des déformations élastiques, élastico-plastiques petites ou finies," *Journal de Mécanique*, Vol. 7, No. 1, March 1968.
- [22] Boivin, M., "Contribution à l'étude des déformations finies dans les matériaux écrouissables," Thèse de Docteur es-sciences physiques, No. 711, Lyon, 1970.
- [23] Gaudel, G., Boivin, M., and Bahuaud, J., "Yield Criteria and Characteristics Methods," *Annales de l'I.T.B.T.P.*, supplement to No. 330, July-Aug. 1975.
- [24] Vassal, R., Boivin, M., and Bahuaud, J., "Utilisation des résultats des essais de fatigue par le mécanicien," 15e colloque de Métallurgie, C.E.A., Saclay, 21-22 June 1972.

Applications

The Concept of Uniform Scatter Bands for Analyzing S-N Curves of Unnotched and Notched Specimens in Structural Steel

REFERENCE: Haibach, E. and Matschke, C., "The Concept of Uniform Scatter Bands for Analyzing S-N Curves of Unnotched and Notched Specimens in Structural Steel," *Low-Cycle Fatigue and Life Prediction, ASTM STP 770*, C. Amzallag, B. N. Leis, and P. Rabbe, Eds., American Society for Testing and Materials, 1982, pp. 549-571.

ABSTRACT: From an extensive test program, 53 S-N curves, established for alternating, zero-tension, or fluctuating tension constant amplitude loading conditions, are obtained for unnotched and three types of centrally notched flat specimens of structural steel Ck 45 (SAE 1045) and 42 CrMo 4 (SAE 4140). These S-N curves are intended to improve existing fatigue design data for application of the two steels tested in cases of finite life design.

The comparative evaluation of the test series reveals the possibility of describing the test results in log S-logN diagrams in terms of uniform scatter bands when distinguishing between the unnotched specimens, the notched specimens in the annealed condition, and the notched specimens in the quenched and tempered condition. These experimental findings are compared with an analytical analysis based on the local stress-strain approach using Neuber's rule. This analysis explains that the derived concept of uniform scatter bands is in accordance with our present understanding of the fatigue behavior of notched elements. Moreover, it allows the agreement of the analytical model and the actual material behavior to be critically examined. In conclusion the paper outlines the link between the nominal stress concept and the local stress-strain approach for deriving engineering fatigue design data.

KEY WORDS: S-N curve, steel Ck 45 (SAE 1045), steel 42 CrMo 4 (SAE 4140), stress ratio, stress concentration factor, uniform scatter bands, slope, cut-off point, local stress-strain approach, Neuber's rule, design data

In order to improve the available design data for components in heavy machinery an extensive test program was carried out to investigate the fatigue properties of steel Ck 45 (SAE 1045) and steel 42 CrMo 4 (SAE 4140) (Table 1). The particular interest in these two types of steel arose from a study of service failures in components of machinery in steel works, which showed these steels to be widely used for components subject to fatigue load-

¹ Fraunhofer-Institut für Betriebsfestigkeit, Darmstadt, Fed. Rep. of Germany.

TABLE 1—Chemical composition of the steels tested.

Steel	Product	C	Si	Mn	P	S	Cr	Mo	Ni	V
Ck45 (SAE 1045)	plate	0.52	0.24	0.61	0.010	0.029	0.01	0.02	0.04	0.02
	spindle	0.46	0.27	0.62	0.023	0.018	0.066	...	0.053	...
	rod	0.45	0.17	0.80	0.018	0.024
42 CrMo 4 (SAE 4140)	plate	0.43	0.31	0.75	0.021	0.034	1.15	0.22
	rod	0.43	0.23	0.68	0.010	0.020	1.10	0.23

ing $[I]$,² and that existing design data were lacking when considering finite life design techniques.

Unnotched and notched specimens, as shown in Fig. 1 and having stress concentration factors $K_t = 1.0, 2.5, 3.6$, and 5.2 , were taken from plate material, round bars, or a heavy spindle (500 to 800 mm diameter), and were tested under axial loading. The various heat treatments and the resulting mechanical properties are given in Table 2. The table also provides a survey of the test program and of the fatigue strength values derived from the statistically established $S-N$ curves under alternating, zero-tension, and (in some cases) fluctuating tension loading.

Of particular interest was steel Ck 45 in the annealed condition ($S_u = 650$ N/mm²) and steel 42 CrMo 4 in the quenched and tempered condition ($S_u = 910$ N/mm²). The corresponding $S-N$ curves were established by 4 to 6 tests on each of three or four pre-selected stress levels and by 12 staircase tests at $2 \cdot 10^6$ cycles. The complementary test series were restricted to unnotched and notched specimens of $K_t = 3.6$ with the staircase tests omitted. The test results have been reported elsewhere in detail [2,3].

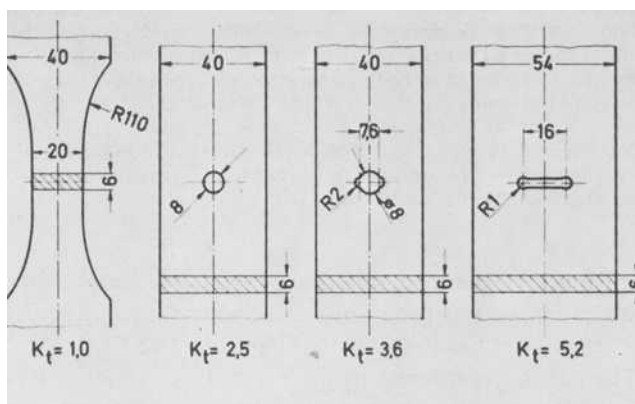


FIG. 1—Specimens tested under axial loading.

² The italic numbers in brackets refer to the list of references appended to this paper.

TABLE 2—*Test program, material properties, and fatigue strength values derived.*

Product ^a	Steel Ck 45 (SAE 1045)				Steel 42 CrMo 4 (SAE 4140)			
	Plate		Spindle		Plate		Bar	
	long. annealed ^b	long. q & t	long. q & t	axial annealed	long. annealed ^b	long. q & t	long. q & t	axial q & t
Position of specimen								
Heat treatment								
S_u (N/mm ²)	730	750	600	695	595	1095	1095	915
S_y (N/mm ²)	440	540	335	440	460	840/820	1030	745
SCF								
K_t								
stress ratio S_{min}/S_{max}								
1.0	-1 0 (>0)	255 215	320 250	250 200	255 215	430/430 300/300	510 375	
2.5	-1 0 (>0)		135/- 115(110)/-			215/- 180/-	* *	
3.6	-1 0 (>0)	110 95	105/100 90(85)/85	105 90	115 90	165/165* 135/135*	190* 160*	140
5.2	-1 0 (>0)		80/- 67(57)/-			125/- 105/-	* *	

^aPlate, $t = 6$ mm; spindle, $D = 500$ to 800 mm; bar, $D = 130$ mm.^bAs-received.

The present paper is aimed at presenting a summary evaluation of the available S - N data in terms of uniform scatter bands, a concept that already has been successfully applied in analyzing the S - N curves of welded joints in structural steel and in aluminum alloys [4-7]. The procedure of graphically and statistically defining the shape and parameters of the uniform scatter bands is described, their use in analyzing S - N data and in deriving the fatigue strength values given in Table 2 is explained, and limitations of their applicability are outlined. Thereafter it is intended to give further support to the concept of uniform scatter bands by an analytical analysis based on the local stress-strain approach with reference to the strain-life diagram and Neuber's rule. Finally, the agreement between the analytical model and the actual material behavior is critically examined.

Summary Evaluation of Test Results

Graphical Definition of Uniform Scatter Bands

The first step in the analyzing procedure was a graphical evaluation of the available test data in terms of $\log S$ - $\log N$ diagrams. By inspection of these diagrams it became obvious that the series for unnotched and notched specimens had to be treated separately. Later a further distinction between the series for notched specimens in the annealed and those in the quenched and tempered condition was found necessary. Hence three groups of test series resulted.

Referring to one of those groups and having the test results from the corresponding test series plotted separately on transparent paper it was found possible by superposing and vertically shifting these plots to fit all data points into a narrow scatter band (Figs. 2 to 4). To this scatter band an averaging sloped line was fitted and two parallel lines qualitatively indicating the width of the scatter band. In the case of unnotched specimens the lines have an (inverse) slope of $k = 15$ down to a cut-off point at $N_A = 1 \cdot 10^6$ cycles. For the notched specimen the (inverse) slope is a value of $k = 5$ in combination with a cut-off point at $N_A = 1 \cdot 10^6$ or $N_A = 3 \cdot 10^5$ cycles for the annealed and the quenched and tempered specimens, respectively. For either condition the same type of scatter band applies to specimens from both steel Ck 45 and steel 42 CrMo 4.

Because of the logarithmic scale the vertical shift of the diagrams may be understood as a conversion of the nominal stress amplitudes S_a plotted on the ordinates to a relative scale, for which the particular reference value is the stress amplitude S_A at the cut-off point of the averaging line. The derived values of S_A are listed in Table 2. Analytically the S - N relationship represented by the averaging line may be written

$$N = N_A \cdot (S_a/S_A)^{-k} \quad \text{for } S_a \geq S_A \quad (1)$$

$$S_a = S_A \cdot (N/N_A)^{-k} \quad \text{for } N \leq N_A \quad (1a)$$

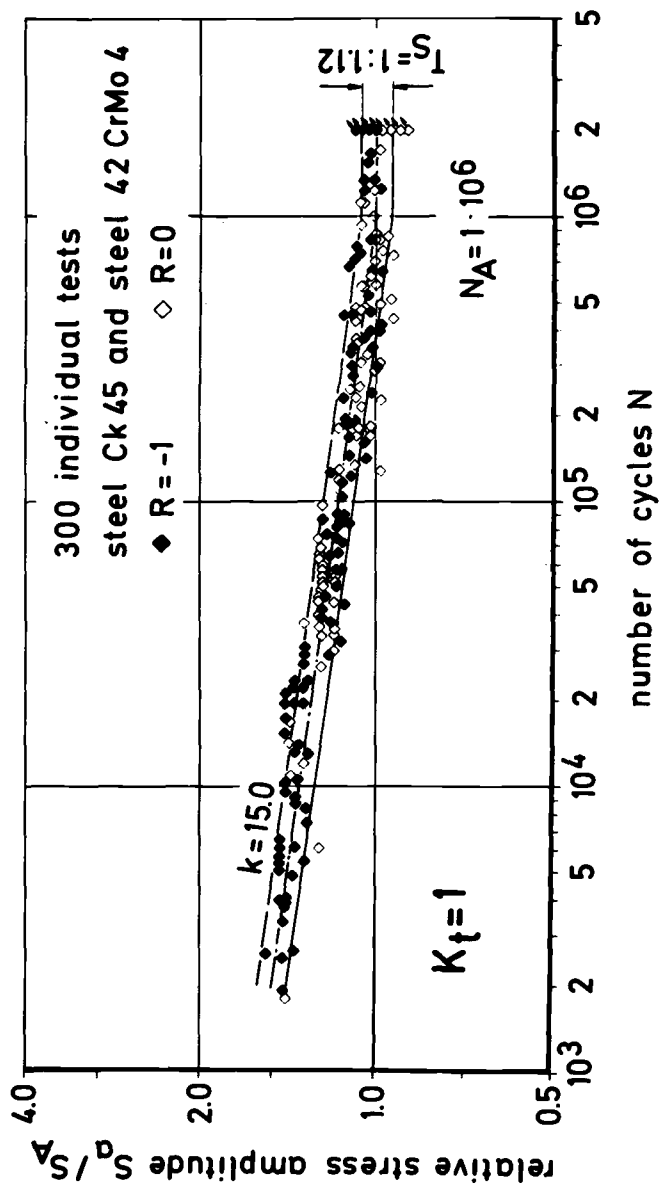


FIG. 2.—Test results from unnotched specimens plotted on a relative scale and fitted by a uniform scatter band.

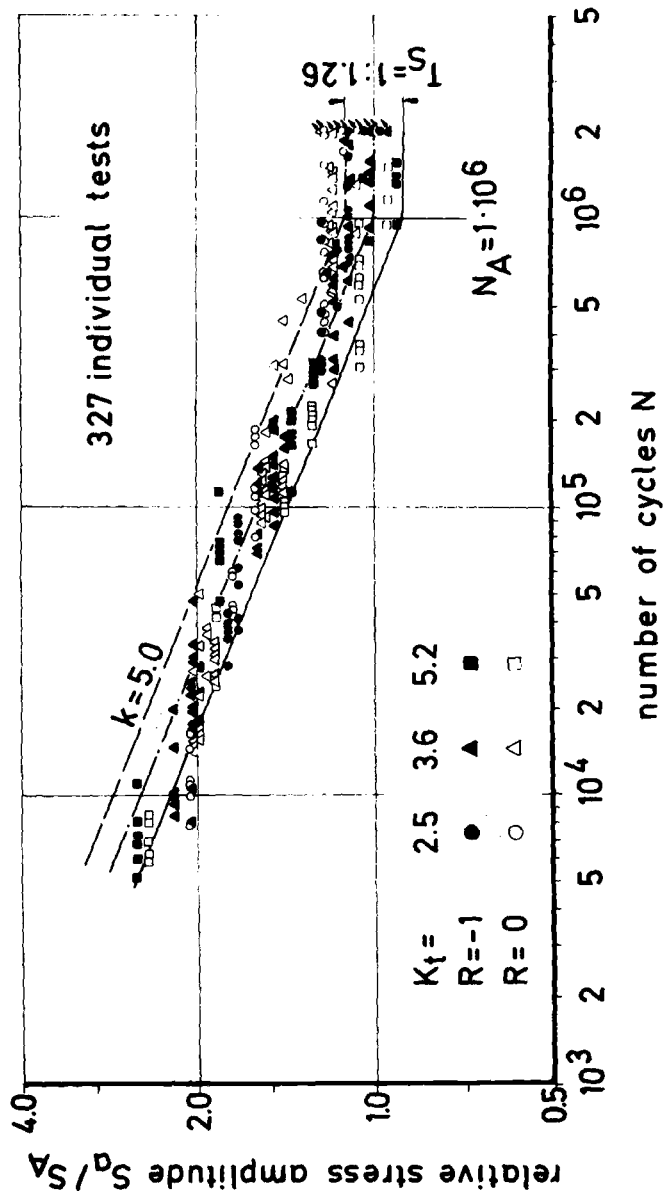


FIG. 3—Test results from notched specimens in the annealed condition plotted on a relative scale and fitted by a uniform scatter band.

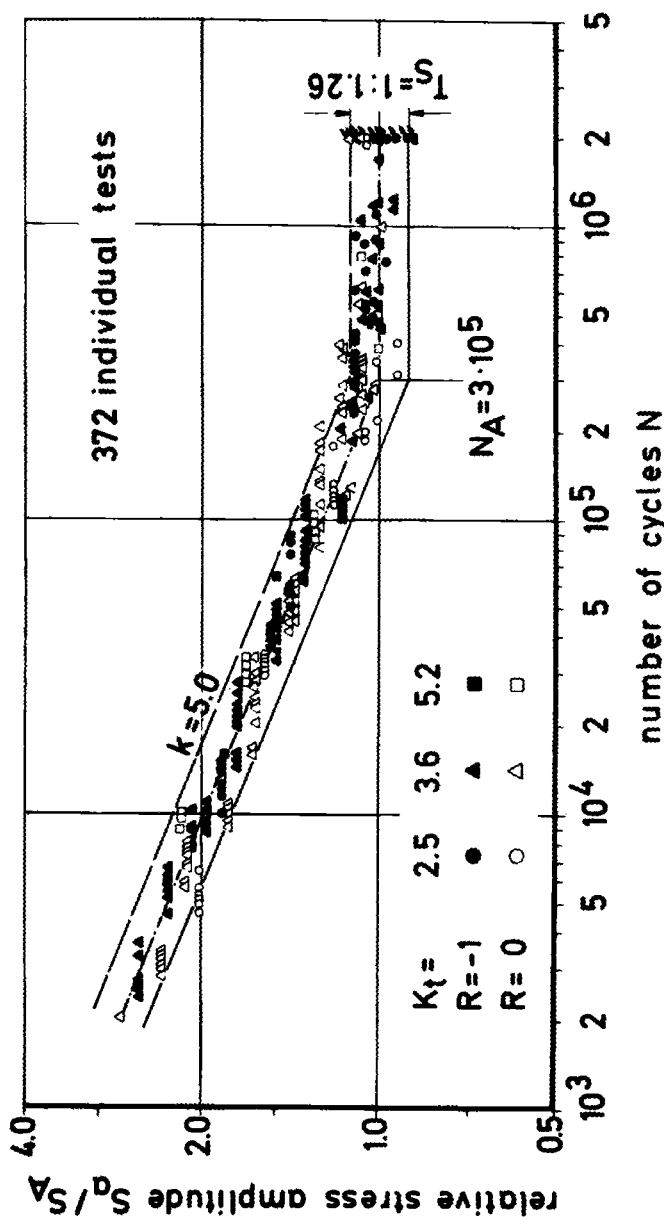


FIG. 4—Test results from notched specimens in the quenched and tempered condition plotted on a relative scale and fitted by a uniform scatter band.

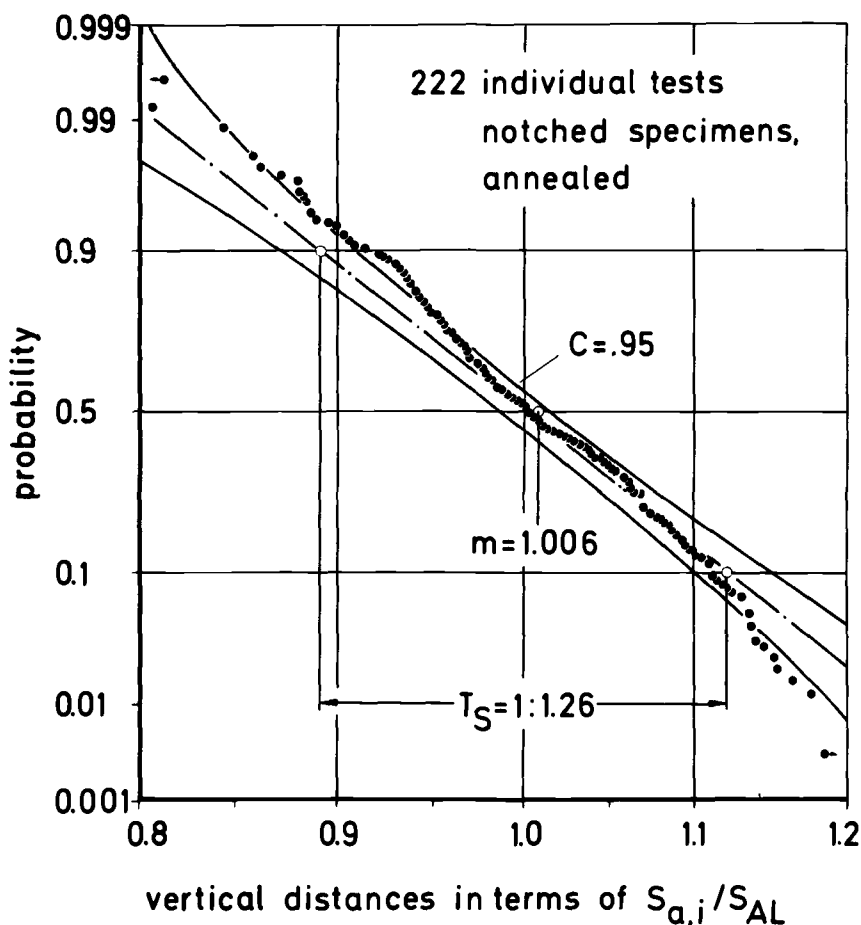


FIG. 5—Probability plot of the vertical distances the data points in Fig. 3 observe from the averaging line of the scatter band.

Statistical Substantiation of Uniform Scatter Bands

The slopes, the cut-off points, and the widths of the so-derived scatter bands may be statistically verified through a maximum likelihood analysis. For the data and scatter band in Fig. 4 this kind of analysis has been reported elsewhere [8]. A simplified way of performing the statistical analysis (by neglecting the run-outs at $2 \cdot 10^6$ cycles) is illustrated in Fig. 5. Plotted in this probabilistic diagram are the vertical distances the individual data points ($S_{a,i}$; N_i) observe from the averaging line of the scatter band ($S_{AL} = S_a$ as defined by Eq 1a); on the logarithmic scale in Fig. 5 these distances are represented by a ratio expression

$$S_{a,i}/S_{AL} = [S_{a,i}/[S_A (N_i/N_A)^{-1/k}]] \quad (2)$$

Provided the averaging line be drawn in the exact position a probability $P = 0.5$ is to be expected for a ratio $S_{a,i}/S_{AL} = 1$; the actual value 1.006 is only slightly different. Further, a measure $T_S = 1:1.26$ of the scatter within the range $P = 0.9$ and $P = 0.1$ may be derived from Fig. 5, and has been used to adjust the outside lines of the scatter band in Fig. 3. Owing to the log-normal distribution provided, the so-defined range of scatter compares to ± 1.28 standard deviations of $\log S_a (= \pm 1.28 \times 0.039)$. For the notched specimens in the quenched and tempered condition the analysis would indicate a somewhat smaller range of scatter ($T_S = 1:1.19$) (Fig. 4); nevertheless, $T_S = 1:1.26$ was adopted, as the smaller values were felt to need justification from additional tests. If we keep in mind both values, the most likely common value of T_S for notched specimens irrespective of their heat treatment may be a value between 1:1.19 and 1:1.26. For the unnotched specimens a value of $T_S = 1:1.12$ was found.

Applicability of Uniform Scatter Bands

Figure 6 illustrates the use of the uniform scatter bands in evaluating individual test series. The proper vertical position of the appropriate type of scatter band may be easily found by inspection and, thereafter, it may simply be checked by a statistical analysis of the vertical distances. As a result the fatigue strength value S_A may be read from the diagram at the cut-off level; in Fig. 6, $S_A = 115 \text{ N/mm}^2$. In combination with Eq 1 and with the parameters $k = 5$, $N_A = 1 \cdot 10^6$, and $T_S = 1:1.26$ of the present type of scatter band the value of S_A provides a comprehensive description of the test series under consideration.

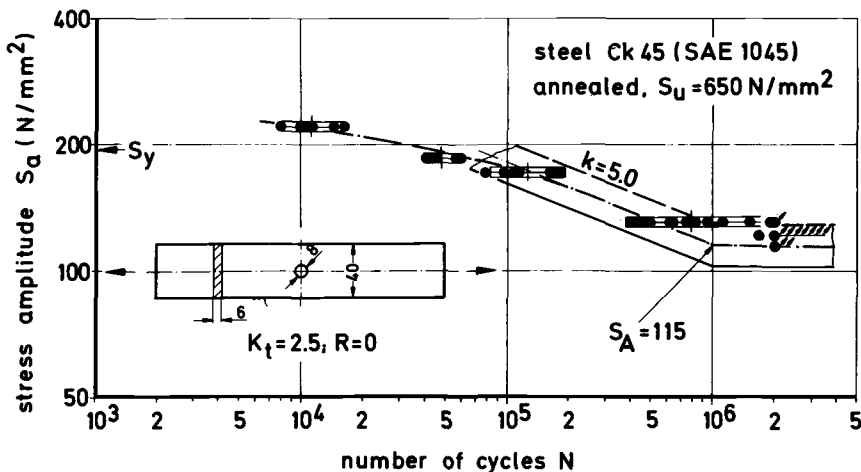


FIG. 6—Illustration of the use of uniform scatter bands in evaluating individual test series and the limits of their applicability.

Moreover, Fig. 6 points out an upper limit to be observed in extrapolating the uniform scatter bands. At stress levels close to the yield stress S_y of the material the data points fall below the extrapolated scatter band, thus indicating a bend of the actual S - N curve to the left. Therefore the applicability of uniform scatter bands is strictly limited to stress levels well below the yield stress:

$$S_{\max} = \left(\frac{2}{1-R} \right) \cdot S_a < S_y \quad (3)$$

In the summary evaluation (Figs. 2 to 4) stress levels close to S_y were omitted.

Regarding the situation around the cut-off point a continuous transition from the sloped to the horizontal part of the S - N curve would appear to be in better agreement with the data points than the sharp edge chosen. However, for reasons of simplicity both in evaluating test results [8] and in design application, a sharp edge of the uniform scatter band was felt an acceptable approximation on the safe side. In this context it also has to be mentioned that from fracture mechanics considerations the position of the cut-off point may change due to size effects, an increased surface roughness at the notch, cold-working the notch, or corrosive effects, and in design applications it may become necessary to allow for these influences.

Finally, the applicability of the uniform scatter bands is restricted to test series established for a constant stress ratio rather than a constant mean stress $S_m \neq 0$, because under the latter test condition considerably different slopes may be obtained.

Separating Crack Initiation and Crack Propagation

Figures 2 to 4 give the fatigue life in terms of the number of cycles to failure. For notched specimens in the quenched and tempered condition the number of cycles for initiating a first (semi-elliptical) crack of about 1 mm^2 at the notch is shown in Fig. 7 (top). Figure 7 (bottom) gives the complementary number of cycles to failure—that is, the number of cycles in crack propagation. The reference stresses S_A are from Table 2. At first glance the major portion of the fatigue life appears to be governed by crack initiation as defined by the above criterion. In a more detailed analysis the partition between crack initiation life and crack propagation life is found to depend on the stress level, the stress ratio, and the stress concentration factor, as known from the literature.

Conflicting Arguments

The authors are aware that the presented analysis in terms of uniform scatter bands conflicts with the specialists' opinion documented in the literature, according to which the slope of S - N curves should be considered a func-

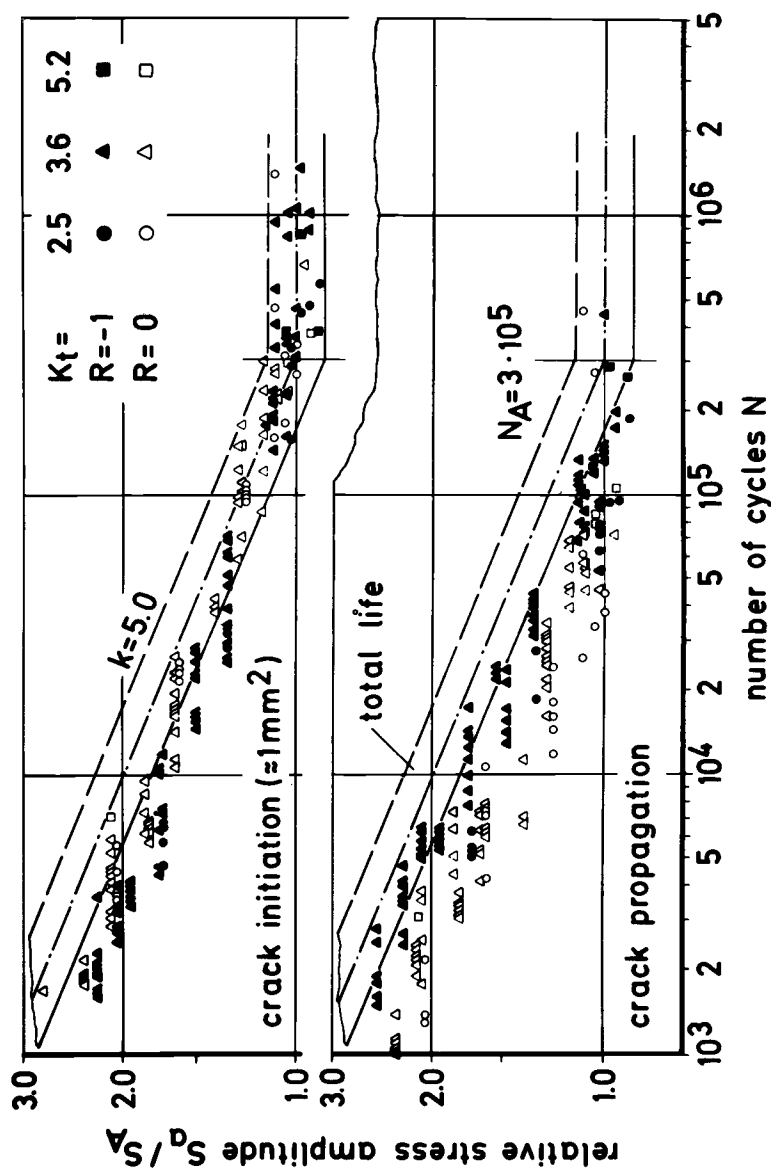


FIG. 7.—Uniform scatter band according to Fig. 4 and test results plotted (top) in terms of the number of cycles to initiation of a first crack ($\approx 1 \text{ mm}^2$) and (bottom) in terms of the complementary number of cycles for crack propagation.

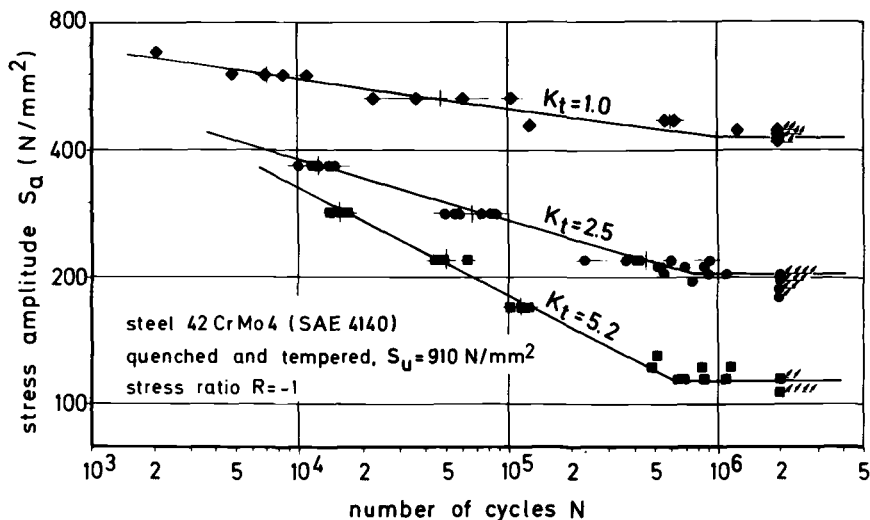


FIG. 8—Present test results described by S - N curves the slopes of which depend on the stress concentration factor (hitherto adopted concept).

tion of the stress concentration factor. The present test results also allow that kind of evaluation (Fig. 8). It appears a convincing way of analysis as there may be stated a continuous transition from the shallow slope of the S - N curve of unnotched specimens to the steeper slopes typical of the S - N curves of notched specimens.

In contrast, the evaluation in terms of uniform scatter bands assumes a uniform slope of $k = 5$ applying to S - N curves of notched specimens up to some maximum stress well below the yield stress (Eq 3), but a different, more shallow slope of $k = 15$ fitting to the S - N curve of unnotched specimens (Fig. 9). Hence the authors' proposal provokes the question: For what value of the stress concentration factor $1 < K_t < 2.5$ should one expect the slope of the S - N curve to change from $k = 15$ to $k = 5$? The following considerations are aimed at clarifying the conflicting situation.

Analytical Analysis

Basic Relations

The following analysis is based on low-cycle fatigue data in terms of the strain-life diagram, as they are conveniently used to present the strain cycling resistance of materials by describing the endurance as a function of both an elastic and plastic strain amplitude. The analysis is performed under the assumption of a material behaving cyclically stable and observing Masing's hypothesis. Thus there is a unique relation between the shape of the cyclic stress-strain curve and the form and size of the hysteresis loop under cyclic load applications. These cyclic loads may be assumed here to be alternating and of constant amplitude.

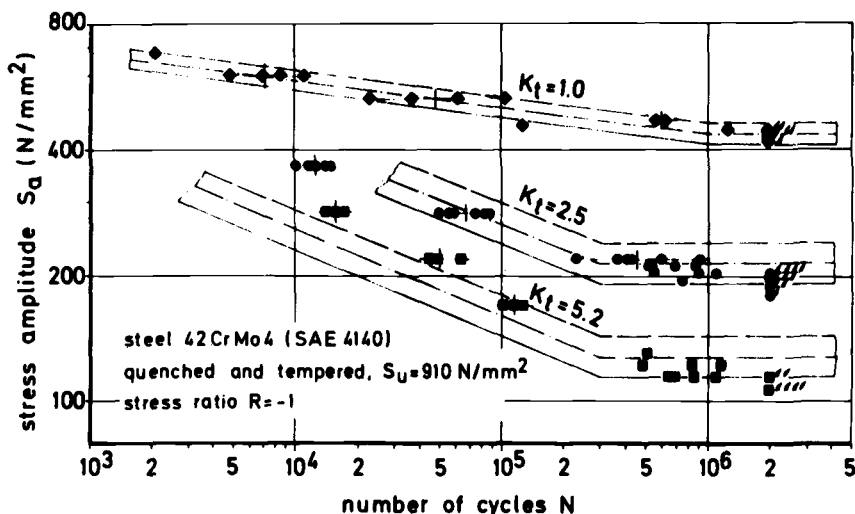


FIG. 9—Test results as in Fig. 8, described by means of uniform scatter bands.

For an unnotched specimen the applied nominal stress amplitude S_a is equal to the local stress amplitude σ_a at the point of crack initiation:

$$S_a = \sigma_a \quad \text{for } K_t = 1 \quad (4)$$

The cyclic stress-strain curve (Fig. 10) defines the corresponding (total) strain amplitude ϵ_a , which is the sum of the elastic and the plastic strain amplitude:

$$\epsilon_a = \epsilon_{a,el} + \epsilon_{a,pl} \quad (5)$$

Following the local stress-strain approach the size of the hysteresis loop is further correlated with the number of cycles obtained in a constant amplitude test. Hence the number of constant amplitude cycles N that one obtains as a function of σ_a and ϵ_a may be indicated along the cyclic stress-strain curve:

$$N = f(\sigma_a, \epsilon_a) \quad (6)$$

With that addition, Fig. 10 contains exactly the same information as usually presented in terms of the strain-life diagram (Fig. 11):

$$\epsilon_a = (\sigma'_t/E) \cdot (2N)^b + \epsilon'_t \cdot (2N)^c \quad (7)$$

A marked point in Fig. 11 is the so-called transition life N^* for which the plastic strain amplitude is equal to the elastic strain amplitude:

$$\epsilon_{a,el} = \sigma_a/E = \epsilon_{a,pl} = \epsilon^* = \sigma^*/E \quad \text{for } N = N^* \quad (8)$$

ϵ^* and N^* may serve as reference values that describe the existing relations between stress, strain, and life in a simple and universal manner (see Appendix). One of these relations is that the strain-life diagram (Fig. 11 and Eq 7)

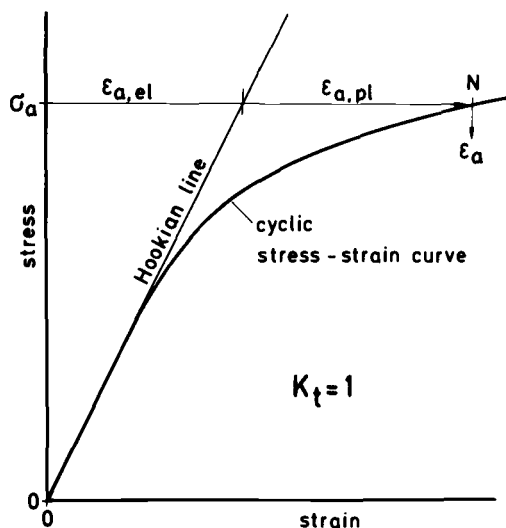


FIG. 10—Cyclic stress-strain curve indicating the elastic and plastic strain amplitude, $\epsilon_{a,el}$ and $\epsilon_{a,pl}$, respectively, and the number of cycles, N , obtained under alternating application of a stress amplitude $S_a = \sigma_a$ to an unnotched specimen.

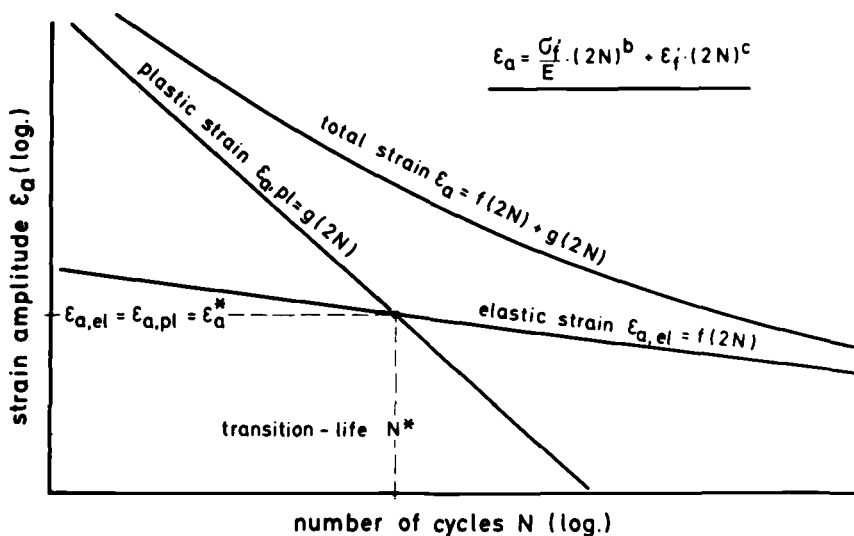


FIG. 11—Strain-life diagram and definition of the transition life N^* .

implies a cyclic stress-strain curve of the type

$$\epsilon_a = (\sigma_a/E) + 0.002 \cdot (\sigma_a/\sigma'_y)^{1/n'} \quad (9)$$

where σ'_y is the cyclic yield stress defined by a plastic strain amplitude of 0.2 percent, and where the cyclic strain hardening exponent n' is

$$n' = b/c \quad (10)$$

S-N Curve of Unnotched Specimens

For unnotched specimens the slope of the elastic line in Fig. 11 should agree with that of the *S-N* curve presented in Fig. 2. Referring to the elastic term of Eq 7 one obtains

$$S_a = \sigma_a = E \cdot \epsilon_{a,el} = \sigma'_f \cdot (2N)^b \quad (11)$$

and from comparison with Eq 1a it follows that

$$b = -1/k \quad \text{for } K_t = 1 \quad (12)$$

$$\sigma'_f = \sigma_A \cdot (2 \cdot N_A)^{1/k} \quad \text{for } K_t = 1 \quad (13)$$

Taking $k = 15$ (Fig. 2), a value of $b = -0.067$ results; this seems quite reasonable when compared with values of $b = -0.075$ to -0.080 for SAE 1045 and SAE 4142 steel according to data compiled by Landgraf et al [9]. Numerically a less good agreement, however, exists with the "universal slope" of $b = -0.12$ of the elastic line as derived in a summary analysis of 29 materials by Manson [10]. Further with reference to Manson we may expect a universal slope of the plastic line of $c = -0.5$ or $c = -0.6$, if N is defined as the life to crack initiation or to final failure of the specimen, respectively. According to Eq 10 the slope $b = -0.12$ would result in rather high values of the strain-hardening exponent of $n' = 0.24$ to 0.20 . For the two types of steel in question Landgraf et al quoted values of $c = -0.6$ to -0.76 in combination with values of $n' = 0.12$ to 0.17 , but the particular values of b , c , and n' are not always consistent with Eq 10.

An investigation of the reasons behind these numerical discrepancies would be beyond the scope of the present paper. It may be concluded, however, that the uniform scatter band in Fig. 2 is in substantial agreement with Manson's concept of universal slopes, and that it is further supported by the small variance among the values of b reported by Landgraf et al.

S-N Curves of Notched Specimens

For notched specimens the local stress-strain concept implies the endurance to be controlled by the local stress and strain at the notch. As nominal stresses are plotted in Figs. 3 and 4, the analysis of those curves requires a conversion between the nominal stress applied and the local stress and strain occurring at the notch.

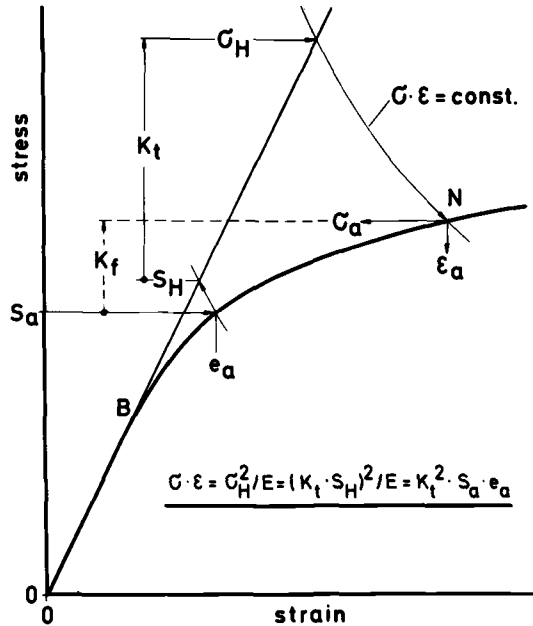


FIG. 12—Illustration of Neuber's rule and notations used.

Adopting Neuber's rule [11] the conversion is illustrated in Fig. 12 for the more general situation, where the nominal stress S_a is applied at such a high level as to cause a considerable overall plasticity of the notched section in question (nominal strain amplitude $e_a > S_a/E$). Allowing for that effect leads to an increased, fictitious value of the nominal stress S_H on the Hookian line. The multiplication of S_H with the stress concentration factor K_t results in the Hookian stress σ_H . The local stress and strain and the corresponding endurance N is obtained by following the hyperbola $\sigma \cdot \epsilon = \text{const}$ from the point σ_H on the Hookian line downward to the point where it intersects the cyclic stress-strain curve. For a stress concentration factor approaching $K_t = 1$ not only will S_a and σ_a become equal (Fig. 10), but also the fictitious nominal stress S_H and the Hookian stress σ_H will coincide. This simply explains that the locus defining S_H is a hyperbola, too. Further, it becomes clear that the Hookian stress of an unnotched specimen is different from the nominal stress applied, and that the well-known difference between the stress concentration factor K_t and the fatigue strength factor K_f as dependent on the endurance N is implied in Neuber's rule as well. Analytically the general form of Neuber's rule reads

$$\sigma_a \cdot \epsilon_a \cdot E = \sigma_H^2 = (K_t \cdot S_H)^2 = K_t^2 \cdot S_a \cdot e_a \cdot E \quad (14)$$

From the following it will be recognized, however, that the simpler situation is practically more important, where lower levels of nominal stress are

applied (levels below point B in Fig. 12 at which the curve branches from the Hookian line). As a consequence the nominal strain of the notch section is elastic, the applied and the fictitious nominal stress are equal, and the Hookian stress becomes proportional to the nominal stress applied:

$$\sigma_a \cdot \epsilon_a \cdot E = \sigma_H^2 = (K_t \cdot S_a)^2 \quad \text{if } e_a \text{ is elastic} \quad (14a)$$

A family of computed S - N curves is shown in Fig. 13. The S - N curve for $K_t = 1$ simply followed from the elastic line of the strain-life diagram (Eq 7). The S - N curves for notched specimens of $K_t = 2.5$ and 5.2 resulted from the strain-life diagram by using Neuber's rule (Eq 14) in addition. Further, the transition life N^* and the corresponding stress level σ^* , which may be taken as having some equivalence to the yield stress, were indicated.

Compared with the S - N curve for $K_t = 1$ the curves for $K_t = 2.5$ and 5.2 come out markedly steeper at stress levels below σ^* , while they become shallow and asymptotic to the curve for $K_t = 1$ at stress levels above σ^* . The dashed curves are those obtained under the provision of the Hookian stress being proportional to the nominal stress throughout (Eq 14a), that is, neglecting any overall notch section plasticity. The dashed curves are of equal shape and parallel, just shifted vertically in proportion to the stress concentration factor K_t . At nominal stress levels well below σ^* the dashed curves are identical with the original curves according to the "simpler situation" mentioned above. For stress levels approaching σ^* the original curves branch to the left in equivalence to the branching criterion discussed with Fig. 12, and this phenomenon agrees to the upper limit of stress specified with reference to Fig. 6 by Eq 3.

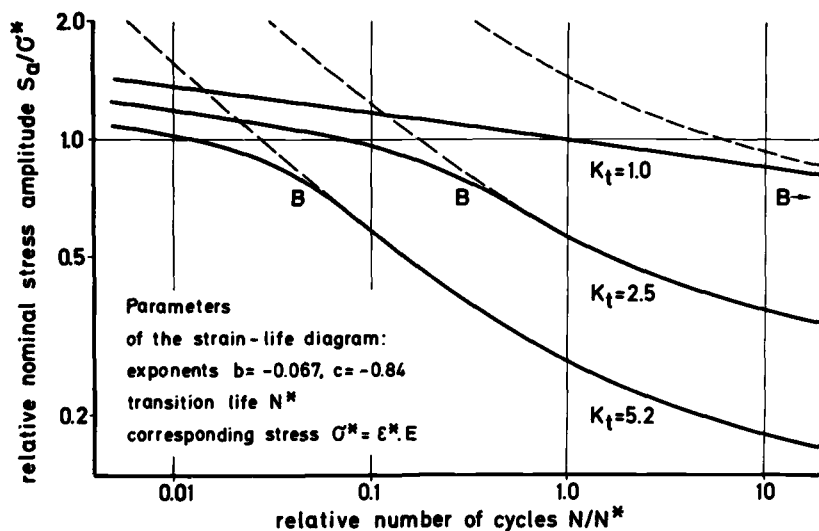


FIG. 13—Family of S - N curves for unnotched and notched specimens as computed from the strain-life diagram by use of Neuber's rule (qualitatively correct only).

Discussion of Computed S-N Curves

Because a primary object in the designing and dimensioning of most structural components is the avoidance of plastic deformation under maximum load, the allowable maximum stress has to observe an appropriate safety factor against the yield stress (or the stress σ^*) (Eq 3). In practical terms that means a nominal maximum stress S_{\max} not exceeding the level of the branching points B in Fig. 12. (If, in special situations, higher levels of stress shall be applied, the nominal stress concept is no longer appropriate, since the resulting plastic strain has to be taken into account as well.) Hence in the stress regime of particular interest the "simpler situation" does apply, and the *S-N* curves of differently notched members can be assumed to be of the same shape and just being shifted vertically according to the stress concentration factor in question (extremely sharp notches and notches having a very small notch root radius may be disregarded here for reasons of clarity). In other words, the analytical analysis conclusively justifies the concept of uniform scatter bands as presented in Figs. 3 and 4.

Figure 12 also provides the explanation of how the slope of the *S-N* curves comes to change from $k = 5$ for notched specimens to $k = 15$ for unnotched specimens. Above the branching points B any *S-N* curve changes slope asymptotically to $k = 15$. The position of the branching point, however, moves to the higher endurance, the lower the stress concentration factor. In consequence the steep part of the *S-N* curve will degenerate. For unnotched specimens the branching point may even be beyond the cut-off point; hence all the sloped part of the *S-N* curve is above the branching point and observes a slope of $k = 15$. In other words, and provided Eq 3 to be a basic condition in dimensioning components, the transition from the uniform scatter band of slope $k = 5$ as derived for notched specimens to the uniform scatter band for unnotched specimens having a slope of $k = 15$ is not a transition in terms of continuously changing slope (Fig. 8), but a transition in terms of the position of the branching point in function of the stress concentration factor (Fig. 13).

Comparison with Experimental Results

In order to emphasize the characteristics of interest a somewhat unrealistic value of $c = -0.84$ was chosen in computing the *S-N* curves in Fig. 13; thus these curves are only qualitatively correct. The curves in Figs. 14 and 15 were computed with the more realistic values of $b = -0.067$ and $c = -0.50$ for comparison with the experimental results. The position of the curves as defined by N^* and σ^* , however, resulted from a fitting procedure. Having in mind that strain-life data refer to the crack initiation life and considering the respective evaluation in Fig. 7 (top), a positioning of the computed curves that would provide an average curve to the data points for $K_t = 2.5$ was felt the most reasonable solution.

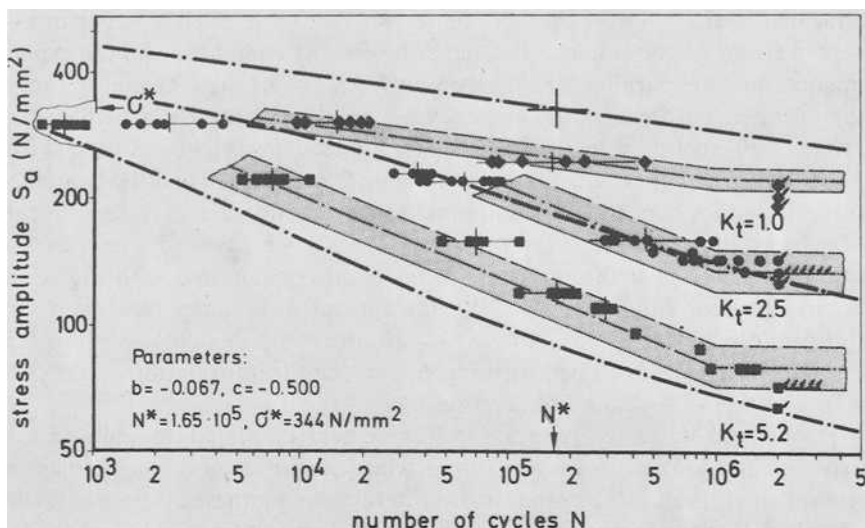


FIG. 14—Computed S-N curves fitted to test results for steel Ck 45 in the annealed condition.

At first glance the agreement of the curves and the experimental results is not very convincing, but a closer look reveals that there is at least an excellent fit to the data points for $K_t = 2.5$, except at the uppermost level for steel Ck 45. Further, for quenched and tempered steel 42 CrMo 4 (Fig. 15), the curve for $K_t = 1.0$ provides an average line to the particular data points. For

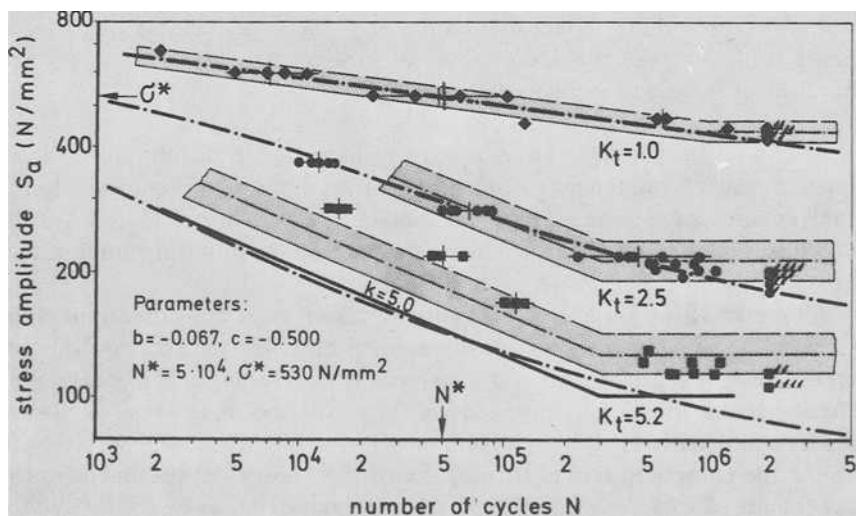


FIG. 15—Computed S-N curves fitted to test results for steel 42 CrMo 4 in the quenched and tempered condition.

annealed steel Ck 45 the data points for $K_t = 1.0$ are much lower than expected from the computed curve; nevertheless, the computed and the experimental lines are parallel. The data points for $K_t = 5.2$ are reasonably above the curve in both diagrams, and they are found exceptionally high in the range of 10^4 to 10^5 cycles, when compared with the results for $K_t = 2.5$ (or $K_t = 3.6$) or to the results for $K_t = 5.2$ and $R = 0$ [2,3]. Most likely a fracture mechanics concept for small cracks at sharp notches may explain the nonconforming test results obtained from the $K_t = 5.2$ type of specimens. If the slope $k = 5.0$ of the uniform scatter band is compared with the computed curve for endurance $N < 10^5$ the agreement is rather satisfactory in this point as well (Fig. 15). Above $N = 10^5$ the computed curves follow the trend of the results discussed with Fig. 6, but lack the information on the cut-off point from the strain-life diagram.

Hence, qualitatively, quite a good agreement of the computed and the experimental S - N curves may be stated, while quantitatively the agreement is less satisfactory in some instances. In order to explain these discrepancies an actual material behavior different than that of the simple analytical model may be anticipated because of the following reasons:

1. The pronounced cyclic softening of both steels and in particular of the annealed steel Ck 45.
2. The considerable portion of the fatigue life spent in crack propagation of the sharply notched specimens of $K_t = 5.2$.
3. A likely difference of the grain structure in the perpendicular planes of crack origin at the unnotched specimens (plate surface, ground) and at the notched specimens (plane in thickness direction along the notch root).
4. A statistical size effect due to the large or small volume of material being subject to the considered level of local stress and strain at the unnotched or notched specimen, respectively.

Obviously the softening effect is most pronounced in the unnotched specimens because of all the material being strained at the same high level. In the sharply notched specimens, however, only a small volume of material at the notch is highly strained and is passed through by the initiating crack rather quickly.

A practical aspect that becomes apparent from these considerations is the problem of making use of "small specimen data" in the dimensioning of large structural components if the material is undergoing a considerable cyclic softening. In large components a large volume of material is always highly strained even at notches. Hence a solution on the safe side would be to adjust the computed curves to the data of the unnotched specimens in the case of steel Ck 45, for example. On the other hand, it may be considered interesting to make use of the actual material behavior for structural optimization of small components in a series production by means of experimentally

evaluating how much the actual material behavior is superior to the behavior predicted from a simplified material model in the early design stage.

Summary and Conclusions

Experimental fatigue data for steel Ck 45 and steel 42 CrMo 4 have been presented in terms of uniform scatter bands of S - N curves. The concept of uniform scatter bands has been shown to be in accordance with our present understanding of the fatigue behavior of notched and unnotched structural elements, and the limits of its applicability have been outlined. The analytical considerations presented to support the concept of uniform scatter bands provide a link between the nominal stress concept and the local stress-strain approach in assessing the structural fatigue behavior.

The shape of the uniform scatter bands has been simply specified by a sloped straight line becoming horizontal at some cut-off point; any differences the actual S - N curves may observe from the simplified shape have been accounted for in determining the width of the scatter band. The uniform scatter bands derived from the present test data have been found to fit test data for other types of steel as well.

Uniform scatter bands have been demonstrated to be particularly useful in analyzing S - N test results with the aim of deriving statistically well-defined fatigue strength values suitable for design application and for input to a data bank. In combination with the appropriate type of scatter band the derived fatigue strength value provides a comprehensive description of the S - N curve in question—that is, in the stress range of practical interest up to a nominal maximum stress close to the yield stress of the material. Even from small samples, being limited to a few results at the sloped part of the S - N curve, the analysis by means of uniform scatter bands allows an estimate of the complete S - N curve to be obtained and a fatigue strength value to be derived. Confidence limits of the derived fatigue strength values may be specified and appropriate safety factors may be deduced by considering the width of the uniform scatter band to define the population variance. The derived fatigue strength values may serve to perform a summary evaluation of comparable data obtained from different investigations, as well as to assess the fatigue properties of different types of material in a systematical manner [5–7].

The simplified shape of the uniform scatter bands proves to be particularly convenient in performing a cumulative damage calculation by Miner's rule as modified by fracture mechanics considerations [12]. Some aspects related to fatigue life predictions based on S - N data in terms of uniform scatter bands have been published elsewhere in greater detail [13, 14]. When making use of "small specimen data" in design it is important to make conservative allowance for possible differences of the actual material behavior compared with predictions obtained from a simplified material model.

Acknowledgments

Acknowledgements are made to the Verein Deutscher Eisenhüttenleute (VDEh), the Arbeitsgemeinschaft Industrieller Forschungsvereinigungen (AIF), and the Commission of the European Communities (CEC) for granting the financial means to perform the investigation at the Fraunhofer-Institut für Betriebsfestigkeit (LBF). The authors thank Mr. W. Noack, Mrs. H. Wüstendörfer, Mrs. M. Kömmling, and Mrs. S. Przygoda for their assistance during various stages of the investigation and in preparing the reports and this manuscript.

APPENDIX

Stress-Strain and Strain-Life Relations Related to Transition Life N^* and Corresponding Strain ϵ^* or Stress σ^*

The strain-life relation (Eq 7) is

$$\epsilon_a = (\sigma'_t/E) \cdot (2N)^b + \epsilon'_t \cdot (2N)^c$$

where (Eq 5)

$$\epsilon_a = \epsilon_{a,el} + \epsilon_{a,pl}$$

The transition life N^* is defined by a plastic strain amplitude $\epsilon_{a,pl}$ equal to the elastic strain amplitude $\epsilon_{a,el}$ (Eq 8):

$$\epsilon_{a,el} = \sigma_a/E = \epsilon_{a,pl} = \epsilon^* = \sigma^*/E \quad \text{for } N = N^*$$

Hence it follows from Eqs 5 and 8 that

$$\epsilon^* = (\sigma'_t/E) \cdot (2N^*)^b \quad (15)$$

$$\epsilon^* = \epsilon'_t \cdot (2N^*)^c \quad (16)$$

Dividing Eq 7 by ϵ^* and using Eqs 15 and 16 yields the related form of the strain-life relation

$$\left(\frac{\epsilon_a}{\epsilon^*} \right) = \left(\frac{N}{N^*} \right)^b + \left(\frac{N}{N^*} \right)^c \quad (17)$$

In equivalence to Eqs 5 and 8 there is

$$\left(\frac{\epsilon_{a,el}}{\epsilon^*} \right) = \left(\frac{N}{N^*} \right)^b = \left(\frac{\sigma_a}{\sigma^*} \right) \quad (18)$$

By inserting σ_a/σ^* in Eq 17 we obtain the corresponding cyclic stress-strain relation

$$\left(\frac{\epsilon_a}{\epsilon^*} \right) = \left(\frac{\sigma_a}{\sigma^*} \right) + \left(\frac{\sigma_a}{\sigma^*} \right)^{c/b} \quad (19)$$

From Eq 9

$$\epsilon_a = (\sigma_a/E) + 0.002 \cdot (\sigma_a/\sigma'_y)^{1/\kappa'}$$

it follows that

$$\left(\frac{\epsilon_a}{\epsilon^*}\right) = \left(\frac{\sigma_a}{\sigma^*}\right) + \frac{0.002E}{\sigma^*} \cdot \left(\frac{\sigma^*}{\sigma'_y}\right)^{1/n'} \cdot \left(\frac{\sigma_a}{\sigma^*}\right)^{1/n'} \quad (20)$$

where

$$n' = b/c \quad (21)$$

and

$$\sigma'_y = \sigma^* \cdot \left(\frac{0.002E}{\sigma^*}\right)^{n'} \quad (22)$$

Accordingly the related form of Neuber's rule (Eq 14) reads

$$\left(\frac{\sigma_a}{\sigma^*}\right) \cdot \left(\frac{\epsilon_a}{\epsilon^*}\right) = \left(\frac{\sigma_H^2}{\sigma^*}\right) = K_t^2 \cdot \left(\frac{S_a}{\sigma^*}\right) \cdot \left(\frac{e_a}{\epsilon^*}\right) \quad (23)$$

References

- [1] Ungerer, W., "Ermüdungsschwerpunkte im Schwermaschinenbau: Schadensschwerpunkte in Hüttenwerken," Betriebsforschungsinstitut (BFI), Düsseldorf, BFI-Bericht Nr. 553, 1975.
- [2] Haibach, E. and Matschke, C., "Schwingfestigkeit von Stahl Ck 45 bei verschiedenen Formzahlen und Spannungsverhältnissen," Fraunhofer-Institut für Betriebsfestigkeit (LBF), Darmstadt, LBF-Bericht Nr. FB-129, 1980.
- [3] Haibach, E. and Matschke, C., "Schwingfestigkeit von Stahl 42 CrMo 4 bei verschiedenen Formzahlen und Spannungsverhältnissen," Fraunhofer-Institut für Betriebsfestigkeit (LBF), Darmstadt, LBF-Bericht Nr. FB-153, 1980.
- [4] Haibach, E., "Die Schwingfestigkeit von Schweißverbindungen aus der Sicht einer örtlichen Beanspruchungsmessung," Fraunhofer-Institut für Betriebsfestigkeit (LBF), Darmstadt, LBF-Bericht Nr. FB-77, 1968.
- [5] Haibach, E. and Atzori, B., *Aluminium*, Vol. 51, No. 4, 1975, pp. 267-272.
- [6] Nowak, B., Saal, H., and Seeger, T., *Der Stahlbau*, Vol. 44, No. 9, 1975, pp. 257-268 and No. 10, pp. 306-313.
- [7] Olivier, R. and Ritter, W., "Wöhlerlinienkatalog für Schweißverbindungen aus Baustählen," Deutscher Verlag für Schweißtechnik (DVS), Düsseldorf, DVS-Bericht Nr. 56/1 bis V.
- [8] Spindel, J. E. and Haibach, E. in *Statistical Analysis of Fatigue Data, ASTM STP 744*, R. E. Little and J. C. Ekvall, Eds., American Society for Testing and Materials, 1981, pp. 89-113.
- [9] Landgraf, R. W., Mitchell, M. R., and La Pointe, N. R., "Monotonic and Cyclic Properties of Engineering Materials," Ford Motor Company, Metallurgy Department, Dearborn, Mich., 1972.
- [10] Manson, S. S., *Experimental Mechanics*, Vol. 5, No. 7, 1965, pp. 193-226.
- [11] Neuber, H., *Journal of Applied Mechanics*, Vol. 28, 1961, pp. 544-550.
- [12] Haibach, E., contribution to discussion in *Proceedings*, Conference on Fatigue of Welded Structures, Brighton, England, The Welding Institute, 1970, pp. xx-xxii.
- [13] Haibach, E., "Fatigue Data for Design Applications," in *Materials, Experimentation and Design in Fatigue, Proceedings of Fatigue '81*, F. Sherratt and J. B. Sturgeon, Eds., Westbury House, IPC Science and Technology Press Ltd., 1981, pp. 365-389.
- [14] Haibach, E., *International Journal of Fatigue*, Vol. 1, No. 1, 1979, pp. 7-16.

Fatigue Life Evaluation of the A-7E Arresting Gear Hook Shank

REFERENCE: White, D. J., Ellis, J. R., Dumesnil, C. E., and Gray, T. D., "Fatigue Life Evaluation of the A-7E Arresting Gear Hook Shank," *Low-Cycle Fatigue and Life Prediction, ASTM STP 770*, C. Amzallag, B. N. Leis, and P. Rabbe, Eds., American Society for Testing and Materials, 1982, pp. 572-584.

ABSTRACT: This paper describes a program conducted to develop criteria, based on test results, to safely extend the service life of the A-7E arresting gear hook shank. Fracture mechanics techniques provided a method for assessing the significance of proof testing and correlating proof loads with remaining life under operating loads. Additional tests were performed to validate the proof-test criteria.

The proof load developed in this program defined the maximum possible flaw size that could exist in the structure and provided data for establishing remaining life under operating loads. In addition, local yielding resulted in residual stresses that maximized crack growth retardation. As a result, an increase in fatigue life was produced by periodically inserting the proof load into the operating load spectrum. The primary impact of this program was to demonstrate that the proof test interval for the hook shank could be extended from 100 to 550 arrested landing cycles, and that the total service life could be extended from 500 to an indeterminate number of arrestments.

KEY WORDS: fatigue, fracture mechanics, proof test, stress spectra, retardation

This paper describes the results of a test and evaluation program conducted for the Naval Air Systems Command.² The object was to develop criteria through testing that would safely extend the proof-test interval and overall service life of the A-7E arresting gear hook shank and return retired hook shanks to service. The original Navy overhaul/retirement criteria for the A-7E arresting gear required the hook shank to be removed from the aircraft for inspection and proof test after every 100 carrier arrestments. The hook shank was retired from service after 500 arrestments. The test program consisted of fatigue and damage tolerance testing of 30 retired A-7 hook shanks. The test data evaluation included considerations of scatter and salt water environment. Fracture mechanics techniques provided a method for

¹ Manager, Engineering Specialist, and Technical Managers, respectively, Structural Life Management, Vought Corporation, Dallas, Tex. 75265.

² Ellis, J. R., "Fatigue and Fracture Evaluation of A-7E Arresting Gear Hook Shank," Vought Report No. 2-30400/9R-52133, May 1979.

assessing the significance of proof tests and correlating proof loads with remaining operating life.

The results of this program showed that a proof load of 0.778 MN (175 kips) ensured structural integrity for a minimum remaining life of 550 arrestments at the maximum operating load of 0.503 MN (113 kips). In addition, retired shanks could be returned to service and remain in service so long as they continued to successfully pass the proof test. These are significant improvements over the original 100-arrestment proof test intervals and 500-arrestment total life.

Technical Approach

The conventional proof-test technique for qualifying a structural component takes on added significance when fracture mechanics theory is applied. To assess the condition of a component in terms of existing flaws, nondestructive inspection (NDI) procedures are generally relied upon. The proof test, however, can be considered one of the most positive inspection procedures available. A successful proof test actually defines the maximum possible flaw size that exists in the structure. This results from the functional relationship between applied stress and flaw size as defined by the crack-tip stress intensity factor, K ,

$$K = f(\sigma\sqrt{a})$$

where σ is the stress level and a represents the crack size. Fracture occurs when the stress and crack size are such that $K = K_{Ic}$, which is the critical stress intensity factor or the material fracture toughness. Therefore fracture data generated from test can relate stress or load at failure to flaw size. This is presented schematically in Fig. 1. If a proof load, which is α times greater than the operating load, is successfully applied the maximum existing flaw size is a_i . If the critical flaw size for the operating condition is a_{cr} , there exists a minimum flaw growth potential from a_i to a_{cr} . To associate remaining life with the flaw growth potential, it is necessary to determine how long it takes a crack to grow from a_i to a_{cr} under operating conditions. The method for predicting fatigue crack growth is based upon fatigue testing and the stress intensity concept.

It has been shown by Tiffany and Masters³ that the number of cycles to failure at a given stress level depends on the initial stress intensity, K_i , compared with the critical stress intensity, K_{Ic} . Therefore

$$N = f\left(\frac{K_i}{K_{Ic}}\right)$$

³ Tiffany, C. F. and Masters, J. N. in *Fracture Toughness Testing and Its Applications*, ASTM STP 381, American Society for Testing and Materials, 1965, p. 249-278.

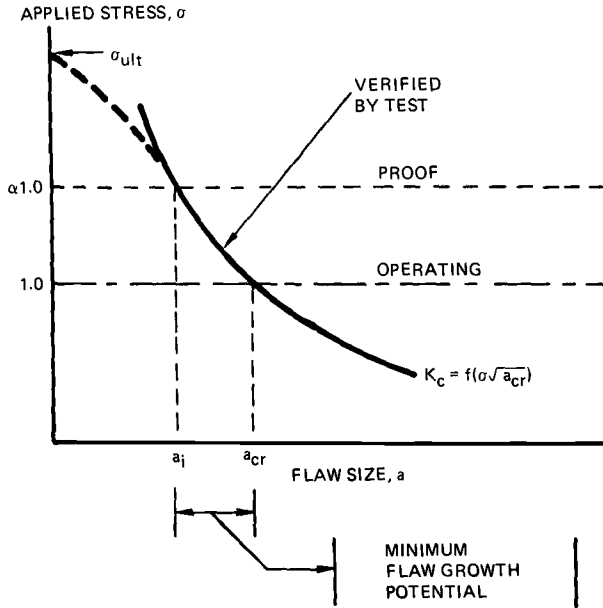


FIG. 1—Stress versus flaw size relationship.

where N is the number of cycles to failure. The stress intensity ratio is related to the ratio of initial flaw size to critical flaw size as

$$\left(\frac{K_i}{K_{Ic}} \right) = \left(\frac{a_i}{a_{cr}} \right)^{1/2}$$

Thus test data can be used to develop the relationship between the flaw size ratio and the number of cycles to failure. These data are presented graphically in Fig. 2. With this type of data, the cycles required for any given flaw to grow to critical size can be predicted. Conversely, for a given life requirement, the maximum allowable initial flaw size can be determined. Knowing the maximum allowable initial flaw size for a required remaining life, data represented by Fig. 1 can be used to establish the necessary proof load.

Component Description

The A-7E arresting gear hook shank, hook point, and drag link are shown in Fig. 3. The hook shank is a 4340 machined steel forging heat-treated to an ultimate strength of 1240 MPa (180 ksi). The shank has a tubular section, the forward end is pinned to a drag link through a set of lugs, and the aft end contains an integral boss which attaches to the hook point. The hook point is secured to the shank by a 1.905-cm ($3/4$ -in.)-diameter steel tension bolt that passes through the hook point and the center of the cylindrical boss.

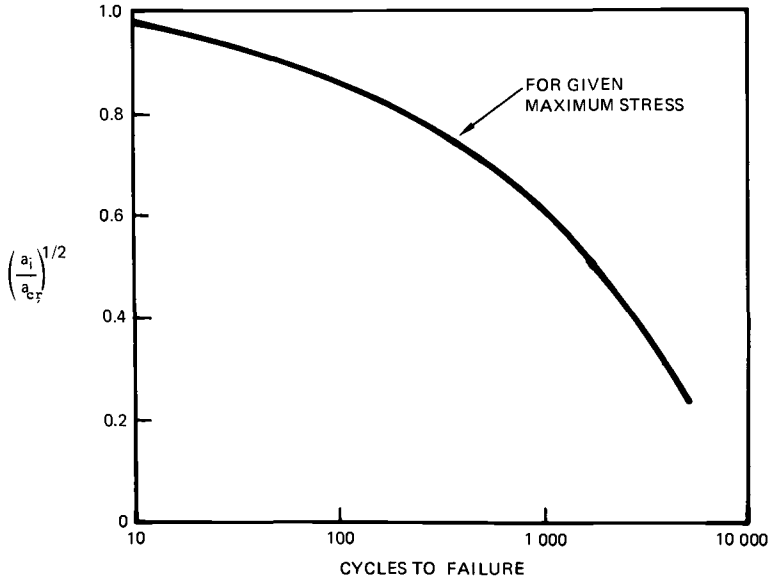


FIG. 2—Flaw size ratio versus cycles to failure.

On carrier arrestment, the carrier deck cable is engaged by the hook point. During run-out of the cable, arresting loads are transmitted through the shank and drag link to the fuselage arresting gear keel structure.

The static ultimate design load for the hook shank is a 0.794 MN (178.5 kips) axial load applied at the hook. Off-angle and off-center arrestments result in side loads which are reacted at the drag link, but because the hook

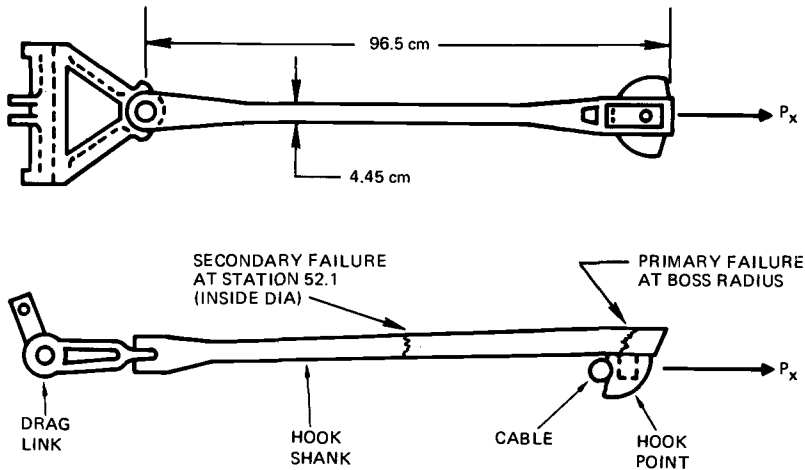


FIG. 3—Hook shank assembly and failure locations.

shank is pivoted from the drag link, only axial loading was used in this program. Bending is induced into the shank since the hook load is eccentrically applied at the boss approximately 4.32 cm (1.70 in.) below the neutral axis of the shank section.

The operating (fatigue) loads were derived from data contained in AR-58 "U.S. Navy Catapulting and Arresting Gear Forcing Functions for Aircraft Structural Design," using a 0.122 MN (27 500 lb) gross landing weight and 133.5-knot engagement speed. The shank was originally designed for the Mk 7 Mod 1 arresting gear loads. However, the A-7E now operates from carriers having Mod 2 or Mod 3 arresting gear systems, which produce substantially lower load spectra, as shown below:

Mk 7, Mod 1 Gear (Design)	90% of loads at $P_x = 0.574$ MN (129 kips) 10% of loads at $P_x = 0.632$ MN (142 kips)
Mk 7, Mod 2 & 3 Gear (Operational)	90% of loads at $P_x = 0.445$ MN (100 kips) 10% of loads at $P_x = 0.503$ MN (113 kips)

Experimental Procedure

The test assembly included not only the hook shank, but also the drag link and hook point (Fig. 3). The hook shank assembly was tested in a vertical test frame where loads were applied at the hook point and reacted at the base of the drag link fitting. The hook point load was applied by using a steel plate which contained a cutout that was machined with a radius equivalent to the arresting cable. The test assembly was free to pivot from the base of the drag link to insure a realistic deflected shape. All cyclic fatigue loading was performed by a single hydraulic load actuator using a load ratio $R = 0.10$ ($P_{\min}/P_{\max} = 0.10$).

There were a total of 30 hook shank specimens tested. The first 22 specimens were tested to obtain basic fatigue and fracture data and to determine a meaningful proof load and proof-test interval. These 22 tests are summarized in Table 1. The last eight tests were verification tests using the related proof load and proof-test interval and are summarized in Table 2.

Fatigue failures occurred at two locations in the shank: the radius at the base of the integral boss (the expected failure location), and the section change in the tube inside diameter at station 52.1 (Fig. 3). It is also noted that two of the tests (shakedown and residual strength) produced failures in the attachment lugs of the shank and three validation test specimens were retired with no failures. The attachment lug failures occurred during residual strength tests at loads above design ultimate.

Analysis of Test Data

The test program focused on the primary failure location at the hook point attachment boss. The tube cracks were considered secondary failure locations

TABLE 1—Tests for basic data.^a

Test	Cyclic $P_{max} \sim$ MN	Environment	Type of Data	Total Cyclic Life	Failure Information
1	0.445 to 0.623	laboratory air	shakedown	6 500	upper lugs at 1.010 MN
2	0.445	laboratory air	a_{cr} and N_f	11 000	tube failure
3	0.534	laboratory air	a_{cr} and N_f	7 774	boss failure
4	0.578	laboratory air	a_{cr} and N_f	8 409	boss failure
5	0.503	laboratory air	a_{cr} and N_f	8 228	boss failure
6	0.578	laboratory air	a_{cr} and N_f	6 018	boss failure
7	0.445	laboratory air	da/dN	11 404	tube failure
8	0.534	laboratory air	da/dN	9 370	boss failure
9	0.623	laboratory air	da/dN	1 087	boss failure
10	0.534	laboratory air	da/dN	4 371	boss failure
11	0.623	laboratory air	da/dN	1 989	boss failure
12	0.503	salt water	da/dN	8 018	boss failure
13	0.534	salt water	da/dN	6 476	boss failure
14	0.534	salt water	da/dN	5 322	boss failure
15	0.623	salt water	da/dN	2 321	boss failure
16	0.503	salt water	da/dN	7 874	boss failure
17	0.503	salt water	da/dN	8 650	boss failure
18	0.503	laboratory air	residual strength	13 000	boss at 0.765 MN
19	0.534	laboratory air	residual strength	8 500	no failure at 0.832 MN
20	0.534	laboratory air	residual strength	8 580	upper lugs at 0.832 MN
21	0.578	laboratory air	residual strength	6 445	boss at 0.832 MN
22	0.503	laboratory air	residual strength	8 228	tube failure during cycle

^a a_{cr} = critical crack size; N_f = cycles to failure; da/dN = crack growth rate; all tests cycled at $R = +0.1$.

TABLE 2—Verification tests for proof loads = 0.778 MN at 550-arrestment intervals.^a

Test	Pre-crack Cycles	Environment ^b	No. of Proof Load Intervals ^c	Total Cyclic Life	Failure ^d
23	0	laboratory air	42	23 142	no failure
24	0	salt water	28	15 423	no failure
25	0	salt water	28	15 434	at boss
26	5000	salt water	10	10 513	in tube
27	7000	salt water	13	14 164	in tube
28	5000	salt water	6	8 307	in tube
29	0	salt water	24	15 429	no failure
30	3000	salt water	6	6 307	in tube

^aEach 550-arrestment block contains 495 cycles at 0.445 MN and 55 cycles at 0.503 MN.

^b3.0 percent salt solution inside tube and externally applied to boss area.

^cProof load held for 3 min after each block.

^dAll failures occurred at the 0.778-MN proof load.

with a criticality that did not exceed that of the primary failure location during the expected useful life of the shank.

The effect of cyclic load level on the basic fatigue life of the shank can be seen in Fig. 4, where the applied load, P_{\max} , was plotted versus cycles to failure. The test points showed the effect of reducing the maximum operating loads. In general, as the maximum cycling load was reduced from 0.623 to 0.503 MN (140 to 113 kips), the average fatigue life increased from approximately 1000 cycles to 9000 cycles.

The 0.503 MN (113 kips) tests were important because they represented the maximum operating loads for the MK 7 Mod 2 and Mod 3 gear systems, which were the basis for projected future usage. The minimum fatigue life of a shank cycled at 0.503 MN (113 kips) was 7874 cycles. This was Test 16, which was tested in salt water and failed at the boss radius. The minimum life of the three specimens that failed in the tube section was 8228 cycles.

The fatigue crack at the radius of the boss is shown in detail in Fig. 5. The visible crack length was designated as $2c$ and the crack depth was designated as a . The inspection data taken during tests involved recording the $2c$ dimension of the crack at periodic intervals. The shape of the flaw, described by the parameter $a/2c$, was assessed by fractographic examination of the crack surface after failure. The cracks were found to be relatively shallow, $a/2c = 0.25$, in the early stages of growth. The aspect ratio tended to increase to $a/2c = 0.40$ or 0.50 as the crack became larger.

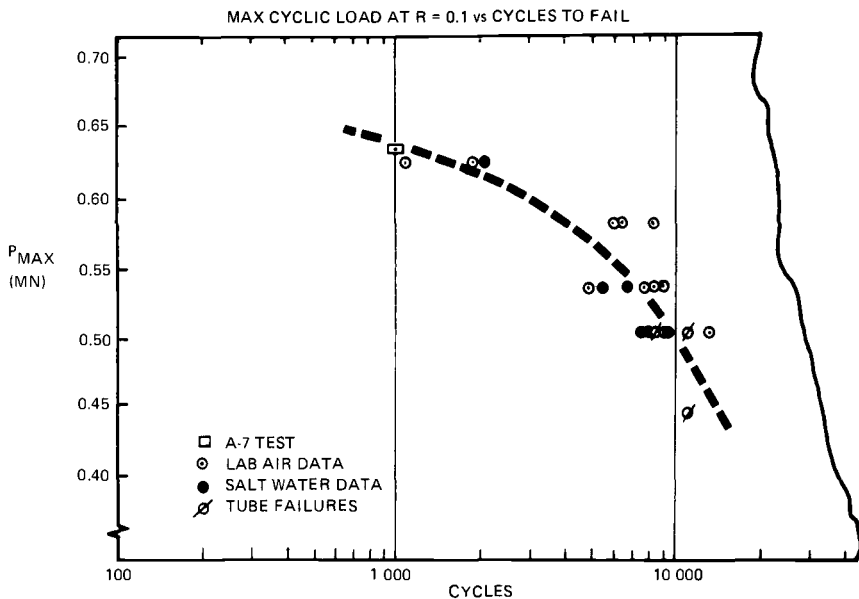


FIG. 4—Fatigue data from shanks cycled to failure at various load levels.

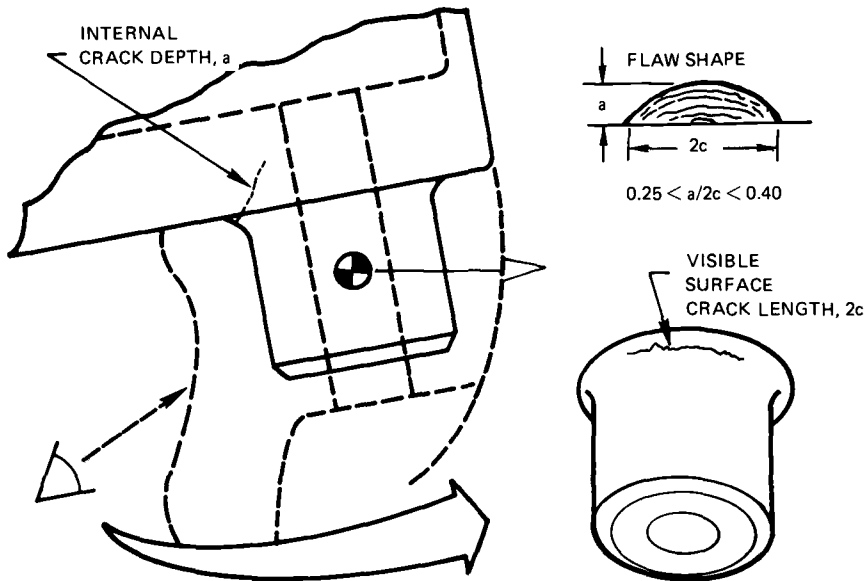


FIG. 5—Local crack geometry at base of boss.

The crack growth behavior was presented as crack length, $2c$, versus remaining life in cycles. Figure 6 shows data from specimens tested at 0.503 MN (113 kips), 0.534 MN (120 kips) and 0.623 MN (140 kips). The curves representing mean lives were generated using regression methods. There was little difference between the 0.503 MN (113 kips) and 0.534 MN (120 kips) data, but there was a dramatic reduction in life for the 0.623 MN (140 kips) data, which represented the original operating loads. Data for $P_{\max} = 0.445$ MN (100 kips) was not plotted since it virtually coincided with the 0.503 MN (113 kips) data.

Figure 7 presents data from tests at 0.503 MN (113 kips) conducted in both lab air and 3 percent salt solution. The data scatter was large enough to warrant the use of a scatter factor on the mean life curve to ensure that the worst case was covered. A factor of 2.0 was therefore applied to the mean salt water data, and this curve became the basis for relating initial crack size to remaining life for the shank operating under the reduced loads.

In order to establish the significance of the proof test, data were generated that described residual static strength as a function of crack size. The residual strength versus flaw size data is shown in Fig. 8. The critical surface crack length for the operating load of 0.503 MN (113 kips) was about 4.11 cm (1.62 in.). As the crack size decreased, the residual strength increased until at $2c \leq 2.54$ cm (1.0 in.) at $P = 0.832$ MN (187 kips) the hook shank began to undergo yielding. Based on these data, the maximum potential proof load was chosen to be 0.778 MN (175 kips). A higher proof load could result in

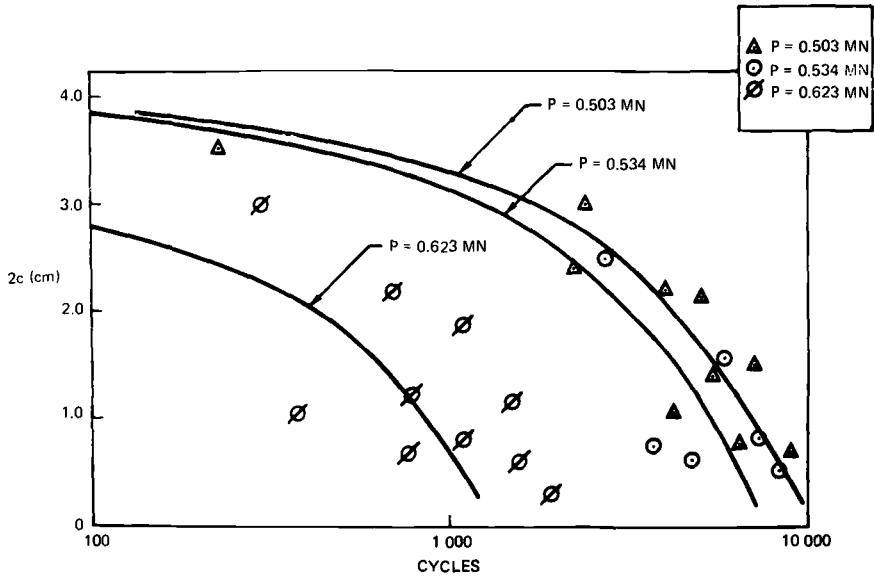


FIG. 6—Initial flaw size versus remaining life for three load levels.

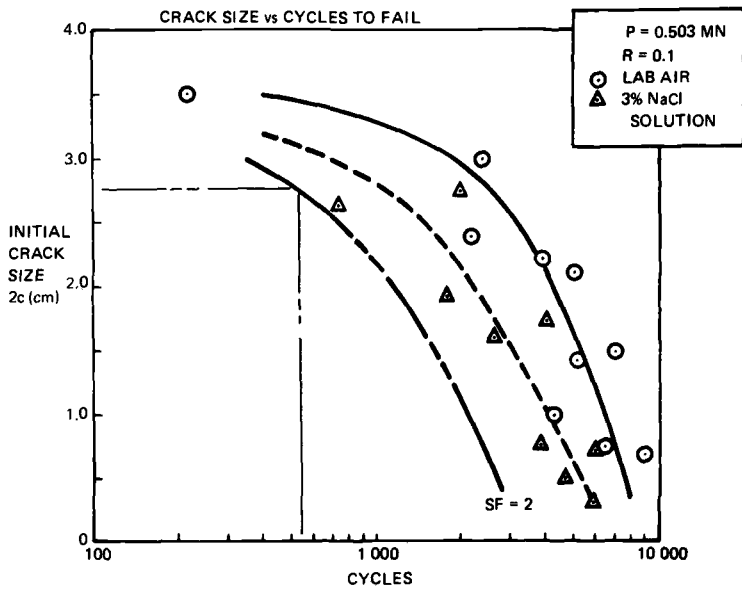


FIG. 7—Data for 0.503-MN load level in laboratory air and 3 percent salt solution.

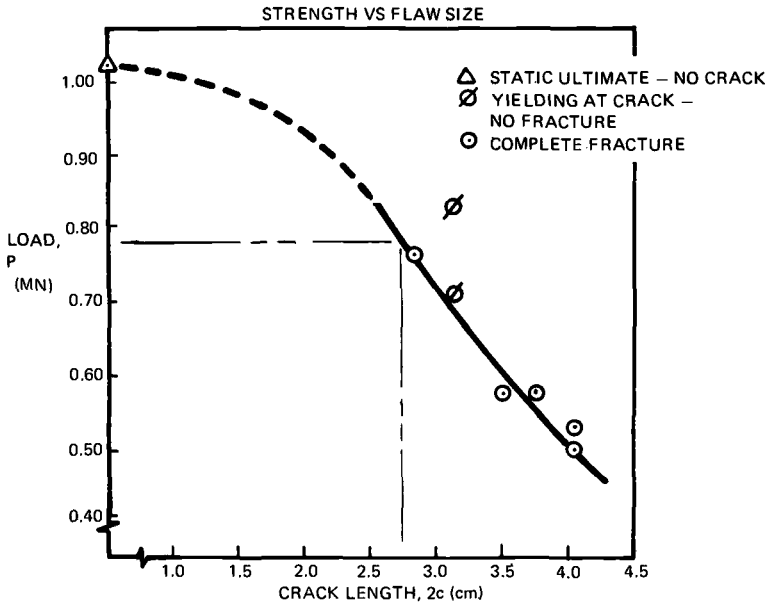


FIG. 8—Residual strength as a function of flaw size.

local yielding either at the hook point boss area or at the forward attachment lugs. If a shank successfully sustained this proof load, the maximum size of an undetected crack was $2c = 2.79$ cm (1.10 in.).

Figure 7 shows that a 2.79-cm (1.10-in.) crack will not grow to failure in less than 550-arrestment cycles for an operating load of 0.503 MN (113 kips). This life was based on the data which included a scatter factor of 2.0. Therefore the verification tests were conducted using a proof load of 0.778 MN (175 kips) applied with a proof-load interval of 550-arrestment load cycles.

The tube failures resulted from fatigue cracks which initiated inside the tube at station 52.1 where the inside diameter begins to change from 2.54 to 1.905 cm (1.00 to 0.75 in.). These cracks progressed as part-through-cracks on the tension side of the tube, and became critical before they progressed through the thickness of the tube wall. The inside radius of the tube is 1.27 cm (0.50 in.) and the outside radius is 2.223 cm (0.875 in.); therefore under normal bending the outer fiber stress would be 1.75 times higher than at the inside surface. Combining the axial and bending stresses at $P = 0.503$ MN (113 kips), the outer fiber stress is only 1.33 times higher than at the inside diameter. The change in section on the inside surface produced a stress concentration, K_t , high enough to make the inside surface more fatigue critical than the smooth outer surface.

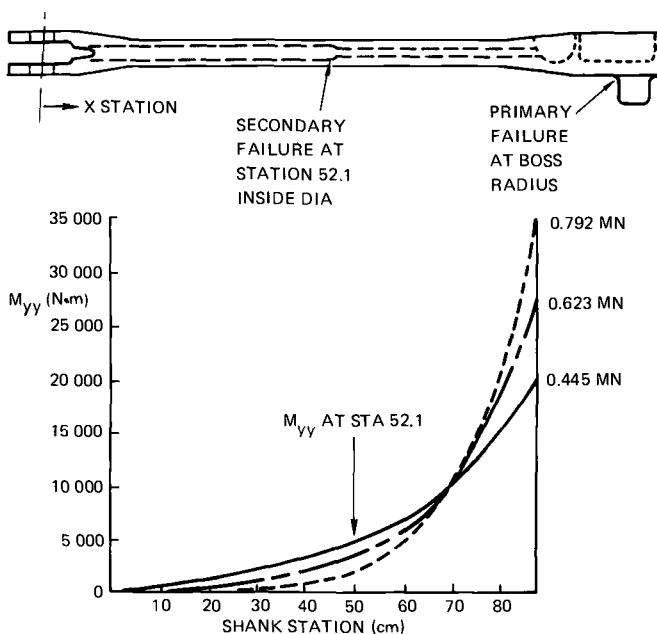


FIG. 9—Bending moment along shank.

The bending moment along the shank was significantly affected by the deflected shape. Figure 9 shows the moment distribution for three applied loads. As the applied load was reduced, the deflected shape relaxed, changing the resulting bending distribution and actually increasing the moment at station 52.1. The peak moment at this section was 3730 N·m (33 000 in·lb) at $P = 0.445$ MN (100 kips) and 1470 N·m (13 000 in·lb) at $P = 0.792$ MN (178 kips). Although reducing the axial cyclic load significantly improved the local stress at the hook point boss, there was essentially no net reduction in the stress at station 52.1. This resulted in increased cyclic life due to reduced stresses at the boss, but cracks tended to form in the tube and become critical. The test results supported this general observation, since tube failures occurred only when the maximum cyclic load was 0.503 MN (113 kips) or lower and the total life of the specimens was above 8000 cycles.

Verification Testing

The last eight hook shank tests were designed to verify the proof-test interval. For a given proof load and proof-test interval, acceptable results were based on two conditions: (1) fatigue failures did not occur between proof tests, and (2) the magnitude of the proof load was not detrimental to the subsequent service life interval for surviving components.

The use of this proof test criteria in service does not imply that hook shanks with detectable cracks would be allowed to remain in service. The

proof test was designed as a safety measure to accompany standard inspection techniques which may overlook existing cracks. Any shank found to be cracked would, of course, be removed and replaced.

The verification tests were conducted to determine the end result assuming that the cracks went undetected. A summary of results for the eight verification tests is presented in Table 2.

Each specimen was tested to block spectrum loading where each block contained 495 cycles at 0.445 MN (100 kips) and 55 cycles at 0.503 MN (113 kips), with $R = 0.10$ in all cases. Each 550-cycle block of loads were followed by a static proof test to 0.778 MN (175 kips) where the proof load was held for 3 min.

The first three verification specimens showed an exceptionally long life. This was apparently due to the retardation effect on crack growth brought about by the proof load. In order to produce failures in a reasonable amount of time, four of the five remaining specimens were cycled at $P = 0.503$ MN (113 kips) for varying numbers of cycles (from 3000 to 7000) to generate cracks prior to the block loading and proof test sequence.

The results showed that all failures occurred during the proof test, which indicated that the 550-cycle interval was compatible with the 0.778 MN (175 kips) proof load. Therefore a shank that passed the proof test could be expected to last for 550 more arrestment cycles. The data indicated that even though failure may be expected in the tube as well as at the boss, the proof load is sufficient to isolate tube cracks that might become critical during the subsequent 550 arrestments.

Strain gage data indicated that local yielding occurred at both critical locations during proof loading to 0.778 MN (175 kips). The local yielding did not have a detrimental effect on the shank, since verification tests included as many as 42 successful proof-load applications on a single shank. The local overload, in fact, had a beneficial effect by retarding the subsequent growth of cracks that might exist at the base of the boss and in the tube. Work by Gray and Gallagher⁴ indicated that overload factors of 1.5 in 4340 steel can cause a significant number of delay cycles before normal crack growth rates return. The local yielding of the material in the tube caused residual stresses that maximized retardation effects.

The test data, summarized in Tables 1 and 2, were analyzed using sequence accountable crack initiation and crack propagation analysis models to estimate the increase in fatigue life produced by the proof loads. The results of this analysis gave the life without the proof loads to be 13 200 arrestments and the life with proof loads to be 18 150 arrestments. This represents a 37.5% increase in fatigue life due to the effects of the overload proof tests.

⁴ Gray, T. D. and Gallagher, J. P. in *Mechanics of Crack Growth*, ASTM STP 590, American Society for Testing and Materials, 1976, p. 331-334.

Conclusions

The primary location for crack initiation in the hook shank is at the radius of the hook point boss. The inside of the tube at station 52.1 becomes a likely spot for crack initiation under extended service life at reduced operating loads.

The 0.778 MN (175 kip) proof load used in the verification testing is sufficient to qualify the hook shank for 550 subsequent arrestments under MK 7 Mod 2 and 3 operating loads. Based on the verification tests, the proof load effectively tests for tube cracks as well as cracks at the boss radius. All failures occurred during proof testing.

The results of this program indicate the potential for significant cost savings in spare parts and especially in logistics costs associated with component tracking and proof testing during the fleet life of the aircraft system.

Acknowledgments

This investigation was conducted at Vought Corporation, Dallas, Texas, by the Structural Life Management Group of the Structures Technologies Section for the Naval Air Systems Command, Washington, D.C., under CMES TASK LTV 78-5.

Use of Low-Cycle Fatigue Data for Pressure Vessel Design

REFERENCE: Lawton, C. W., "Use of Low-Cycle Fatigue Data for Pressure Vessel Design," *Low-Cycle Fatigue and Life Prediction, ASTM STP 770*, C. Amzallag, B. N. Leis, and P. Rabbe, Eds., American Society for Testing and Materials, 1982, pp. 585-599.

ABSTRACT: Pressure vessels are usually designed for only a few thousand stress cycles and seldom for more than 10^5 cycles. For fatigue analysis to be practical for most of the ASME Code applications, a concept has been developed different from the practice used in machine design for high-cycle fatigue in rotating machinery. The concept uses fatigue design curves developed for the different materials. The curves account for most of the factors that reduce fatigue life as shown by a comparison with fatigue data generated with laboratory specimens. Because most pressure vessels are of welded fabrication, the fatigue design curves have full corrections for tensile mean stress in the applicable region to account for tensile residual stresses. For corrosive conditions, the fatigue design curves may require further corrections. A modified concept of strain range partitioning has been developed for the analysis of the creep and fatigue interaction for high-temperature design. The concept uses the strain difference range to calculate creep and fatigue damage, which is similar to the shear stress failure used in lower temperature design.

The use of the fatigue design curves is demonstrated with the evaluation for fatigue life of two fossil-fuel boiler components. One of these components illustrates the difference in use of the fatigue design curves when creep is a further consideration.

KEY WORDS: fatigue, low cycle fatigue, elevated temperature fatigue, strain range partitioning, pressure vessel design, ASME Boiler and Pressure Vessel Code

In the United States the electric utility companies are using fossil-fueled steam generators to supply the variable electrical demand. The nuclear steam supply systems are based loaded, a requirement of United States government regulations. Thus many of the fossil steam generator units must be two-shifted; that is, the unit is operated for 14 to 16 h and shut down for the remainder of the 24-h period. In order to use fuel more efficiently, some of the units are built with sliding pressure capability. Under this type of operation, the ability to withstand fatigue damage is a major consideration. The concepts used in developing fatigue design curves for pressure vessels from fatigue data will be illustrated with steam boiler components.

¹Staff Engineer, Engineering Development Fossil Power Systems, Combustion Engineering, Inc., Windsor, Conn. 06095.

Power boilers in the United States are fabricated to the requirements of Section I of the ASME Power Boiler and Pressure Vessel Code [1],² which is a fabrication code that establishes the minimum requirements to satisfy public safety. Only those factors concerning materials, general design, fabrication, and inspection that can be controlled during fabrication are a part of the Code. Specific designs are not considered by the Code committee, but are approved by insurance companies, various state boiler inspectors, or both. Under the ASME Code rules, the manufacturer is held responsible for meeting Code requirements and furnishing additional engineering design analysis to meet additional requirements as may be required. The Code as written is not a "handbook" and requires an experienced designer to use it. The subject of fatigue is not addressed in Section I of the ASME Code, and the fatigue analysis is left to the designer.

Although fatigue is a basic type of failure and influences the safety of the vessel, any cracks that do form take a considerable length of time to progress to a critical length or to a point at which leakage occurs. Although a fatigue crack could lead to leakage in a high-temperature vessel during operation, the most dangerous period exists during a routine hydrostatic test after maintenance work when there is a chance of brittle fracture. Fatigue damage is closely associated with operational procedures and corrosion. In part, the probability of fatigue damage in service may be reduced during fabrication by focusing attention on cyclic operating conditions, establishing suitable stress levels, limiting some objectionable design details, and establishing certain fabrication rules and inspection requirements. In steam boiler components, the high-temperature water may be fairly corrosive; therefore control of boiler water chemistry is an important aspect in limiting fatigue damage.

Fatigue Analysis

When the temperature of the component is below the creep range for the material, the fatigue design procedures of the ASME Boiler and Pressure Vessel Code Section VIII Division 2 are used [2]. The number of stress cycles usually encountered in pressure vessel design are only a few thousand and seldom exceeds 10^5 cycles. In the two-shifting operation a design life of 7000 cycles will cover most cases. To make the fatigue analysis practical for most of the ASME Code applications, a different concept of fatigue design has been developed from that used in most machine design practice for high-cycle fatigue. In the low-cycle fatigue region, the strains to cause failure are in excess of yield strains. Fatigue damage in the plastic region has been found to be a function of plastic strains, and therefore the fatigue curves for this region are based on tests made under strain control. For convenience in use, the strains have been multiplied by the elastic modulus to obtain ficti-

²The italic numbers in brackets refer to the list of references appended to this paper.

tious stresses which may be compared to the stresses obtained by the assumption of elastic behavior.

In order to make the fatigue analysis valid using elastic analysis, it is necessary to use all the stress limits in ASME Code Section VIII Division 2 [2]. The use of the two times yield strength limit in itself is not sufficient to assure shakedown to elastic action. If nonlinear plastic analysis methods are used, the strains may be multiplied by the elastic modulus to obtain fictitious stresses, or the more common practice is to construct a new set of curves based on strain range. The maximum shear stress criterion for failure is used for pressure vessel design, and the stress intensities are obtained from the differences of the principal stresses, which are the values used to compare with allowable design values. In use, a particular plane is selected and the stress intensities determined for each variation in stress history. In the case of rotating directions for the principal stresses more than one plane may need to be investigated. The advantage of the use of principal stress differences is that an algebraic sign is obtained to determine strain ranges if a consistent set of axis are used. Since most of the pressure vessels are of welded construction, a tensile mean stress correction is built into the fatigue design curves to account for tensile residual stresses.

The data from strain-controlled fatigue tests of small, smooth specimens are used to construct a fatigue failure curve as shown in Fig. 1 [3]. Because there was little difference in the fatigue curves for carbon steel (top) and low-alloy steels (bottom) all were combined into a single curve. The fatigue failure curve is used to construct a fatigue design curve by applying a reducing factor of 20 on cycles or 2 on stress, whichever is the larger correction. These factors cover such effects as environment, size effect, surface finish, and data scatter. In general, though corrosion has a major influence on fatigue life, it is not built into the design curve, and thus the designer must evaluate this effect on fatigue life. Figure 2 shows a number of pressure vessel tests which have been made to verify the fatigue design curve [4]. Test number 25 was a welded longitudinal long seam which had an unidentified defect in the weld that caused early failure for this vessel. Thus a pressure vessel is not expected to last 20 times the design life, and these factors should not be considered as safety factors but factors which correct fatigue data from small specimens to actual components.

When the temperature of the component will be in the creep range of the material for some of the operating time the concepts of strain range partitioning are used to evaluate the creep and fatigue damage [5]. Since there is little difference whether the failure theory of maximum shear stress or the Mises-Hencky relationship is used to evaluate strain ranges, it has been our practice to use the maximum shear stress theory for complex loadings where it is necessary to consider algebraic signs. Manson and Halford have developed a set of rules for dominant and secondary direction to determine appropriate algebraic sign for use with the Mises-Hencky relationships, but it is

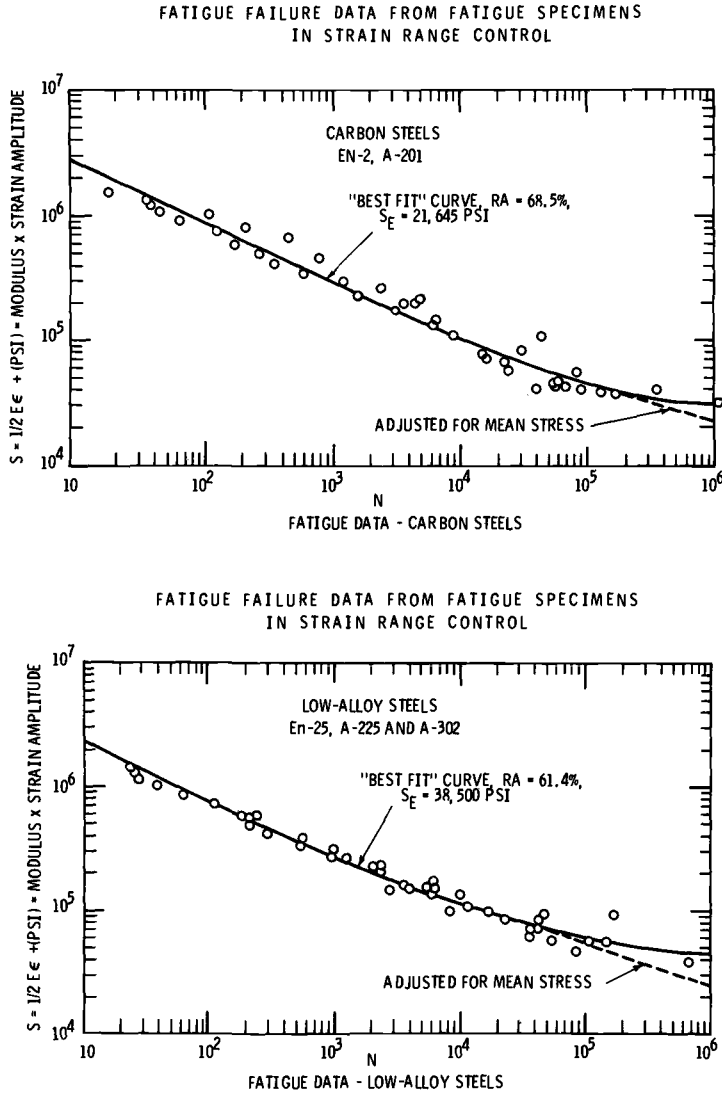


FIG. 1—Fatigue failure data from fatigue specimens in a strain range control [3].

difficult to apply to computer processing in complex loading conditions [6]. The use of the maximum shear stress theory for high temperatures is a continuation of the procedures used for lower temperatures, except that the curves have been developed in terms of strain range. As background, the ASME Code procedure below the creep range is now given. Assume

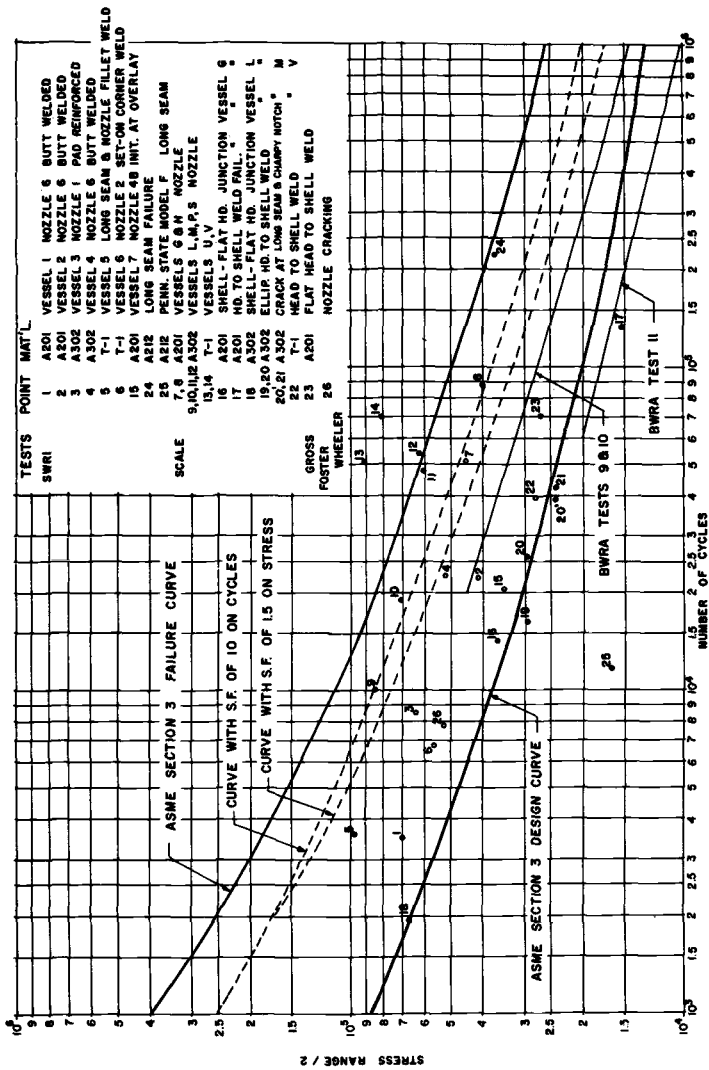


FIG. 2—Comparison of ASME fatigue design curves and fatigue fractures in test pressure vessels [4].

$$\sigma_1 < \sigma_2 < \sigma_3 \quad (1)$$

$$\sigma_1 - \sigma_3 = E\epsilon_{\text{axial test}} \quad (2)$$

$$\text{maximum stress intensity} = \sigma_1 - \sigma_3 = \frac{E}{1 + \mu} (\epsilon_1 - \epsilon_3) \quad (3)$$

$$\text{fatigue curve } \epsilon_{\text{axial}} = \frac{\epsilon_1 - \epsilon_3}{1 + \mu} \quad (4)$$

In the case of boiler components which are two shifted, the load history for analysis is readily developed since it is repeated each day. Thus there is the startup, load variations, and the shutdown. In the stress analysis a hysteresis loop is established which is broken down into the various parts for strain range partitioning [6]. In most cases the hysteresis loop is unbalanced and some permanent creep strain is accumulated. For most materials the strains calculated on the first loading cycle are quite different from subsequent cycles; thus it is usually necessary to carry the calculations through several load cycles to reach a stabilized behavior.

In order to evaluate the various types of strains, a strain range versus life relationship must be developed as shown in Fig. 3. To construct these relationships requires four different types of tests with different variations on either load or strain control to provide results as shown in Fig 4. Linear exhaustion of ductility is used to evaluate the plastic and creep ratchetting strains in an unbalanced cycle. Ductility values may be obtained from tension tests at appropriate temperatures and from creep rupture tests. Since boiler components are expected to last for many years, it will be necessary to use extrapolation procedures to develop suitable ductility values.

The damage from the interaction of creep and fatigue is determined for each cycle and is expressed by [5]

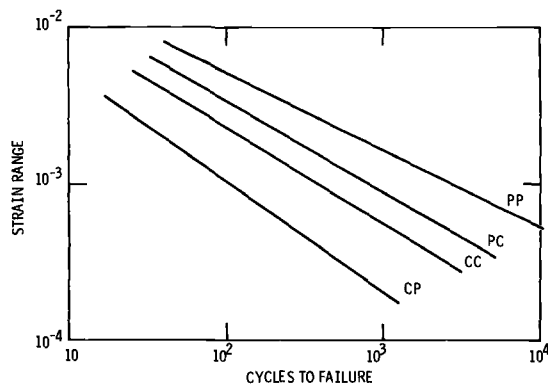


FIG. 3—Typical partitioning strain range—life relationships used to characterize material behavior [5].

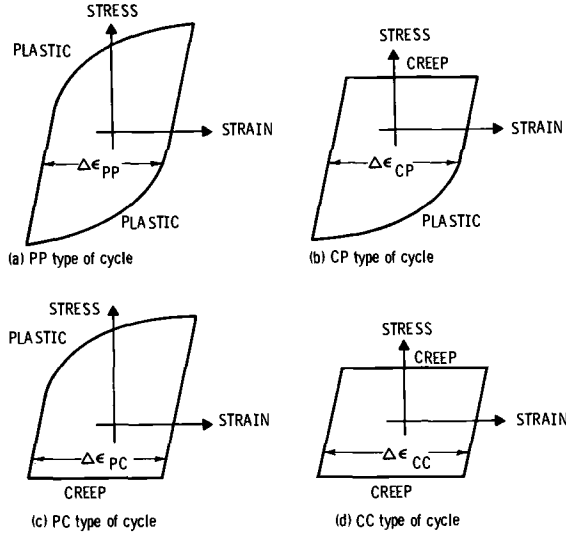


FIG. 4—Idealized hysteresis loop used to define and generate individual partitioning strain range—life relationships [5].

$$\text{damage cycle} = \frac{F_{pp}}{N_{pp}} + \frac{F_{cc}}{N_{cc}} + \frac{F_{cp}}{N_{cp}} + \frac{F_{pc}}{N_{pc}} + \frac{\delta_p}{D_p} + \frac{\delta_c}{D_c} = \frac{1}{N_f} \quad (5)$$

where

F = strain range fraction,

$$F_{pp} = \Delta\epsilon_{pp}/\Delta\epsilon_{in},$$

$$F_{cc} = \Delta\epsilon_{cc}/\Delta\epsilon_{in},$$

$$F_{cp} = \Delta\epsilon_{cp}/\Delta\epsilon_{in},$$

$$F_{pc} = \Delta\epsilon_{pc}/\Delta\epsilon_{in},$$

$$\Delta\epsilon_{in} = \text{total inelastic strain range} = \Delta\epsilon_{pp} + \Delta\epsilon_{cc} + \Delta\epsilon_{cp} \text{ or } \Delta\epsilon_{pc},$$

$$\delta_p = \text{plastic ratchet strain per cycle},$$

$$\delta_c = \text{creep ratchet strain per cycle},$$

$$D_p = \text{plastic ductility} = \ln [1 - (RA)_p],$$

$$(RA)_p = \text{reduction in area in tension test},$$

$$D_c = \text{creep ductility} = \ln [1 - (RA)_c],$$

$$(RA)_c = \text{reduction in area in creep rupture test},$$

$$N_{pp} = \text{PP life obtained from Fig. 3 for inelastic strain range},$$

$$N_{cc} = \text{CC life obtained from Fig. 3 for inelastic strain range},$$

$$N_{cp} = \text{CP life obtained from Fig. 3 for inelastic strain range},$$

$$N_{pc} = \text{PC life obtained from Fig. 3 for inelastic strain range, and}$$

$$N_f = \text{expected cycle life if cycle repeated to failure}.$$

Since the size of the hysteresis loop changes with the first few cycles, it is necessary to repeat the damage calculations for each cycle until the deforma-

tion behavior stabilizes. Total damage is the sum of the damages of each individual cycle.

The only ASME design procedure for fatigue at high temperatures is Nuclear Code Case N47 [7], which sets minimum thickness for components and limits the mechanical load stresses for average cross-sectional stresses and bending stresses. In the Code Case there are numerous checks to make to determine if inelastic analysis is necessary. The procedure for damage evaluation is a linear summation of creep and fatigue damage which is nonmandatory; however, the procedure may be used without further justification. Only a single damage diagram is given for each material, and the published diagrams are based on behavior with very little creep strain. To date, no one has developed a procedure to use several damage diagrams which are temperature dependent. Thus our high-temperature design procedures are based on the concept of strain range partitioning, and we have developed special test machines to generate the basic fatigue data and to study typical hysteresis loops encountered in boiler components.

Fatigue Evaluation of Boiler Components

Steam Separator

A boiler component which operates below the creep range for the material and has high thermal transients is the steam-water separator in a sliding pressure steam boiler. This component is a dynamic steam-water separator which works on the cyclone principle. On startup the unit has an entering

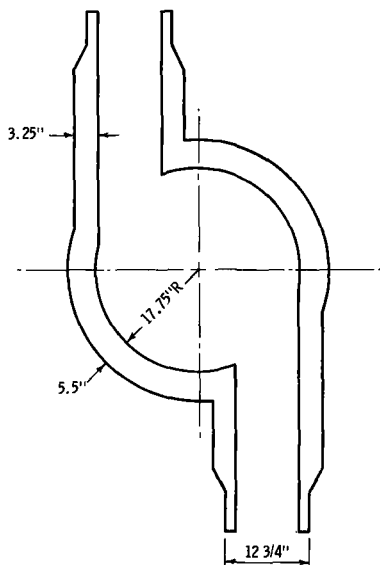


FIG. 5—A steam separator cross section at critical region.

TABLE 1—*Principal stresses.*

	σ_1	σ_2	σ_3
A	-20 300	-15 200	-2250
B	38 500	8 550	-3800
C	44 300	39 200	-3400
D	34 400	7 650	-3400
E	28 200	23 100	-4000
F	40 400	9 000	-4000
G	37 500	32 400	-4200
H	42 400	9 400	-4200
I	45 100	40 000	-3000
J	30 400	6 750	-3000
K	44 200	39 100	-1800
L	0	0	0

fluid which goes from water to a water-steam mixture and finally to dry steam; meanwhile, the pressure is increasing from subcritical pressure level to a final pressure of 28 958 kPa (4200 psi) for the unit at full load. As the load on the boiler is decreased, the pressure is allowed to slide or decrease to meet the thermodynamic requirement of the unit and to keep the superheater outlet temperature at a constant value over a large proportion of the load range.

One of the critical regions for fatigue is the intersection of the tangent inlet nozzle with the shell of the separator. The shell and nozzle have the basic dimensions shown in Fig. 5. The separator is made from a C-1/2Mo material [ASME Specification SA204C, which has negligible creep deformation up to 427°C (800°F)]. An elastic stress analysis of this region shows that during a typical operating cycle the principal stresses vary as shown in Table 1.

The stress intensities are calculated by obtaining the stress differences of the principal stress as shown in Table 2.

TABLE 2—*Principal stress differences.*

	$S_{1-2} = \sigma_1 - \sigma_2$	$S_{2-3} = \sigma_2 - \sigma_3$	$S_{3-1} = \sigma_3 - \sigma_1$
A	-5 100	-13 000	18 100
B	30 000	12 400	-42 300
C	5 100	42 600	-47 700
D	26 800	11 100	-37 800
E	5 100	27 100	-32 200
F	31 400	13 000	-44 400
G	5 100	36 600	-41 700
H	33 000	13 600	-46 600
I	5 100	43 000	-48 100
J	23 700	9 750	-33 400
K	5 100	40 900	-46 000
L	0	0	0

The stress intensity amplitudes are one half the stress intensity range. In this example each condition is repeated 7000 times except for item D which is repeated 21 000 times in the required life of the unit. The stress intensity range is the difference between the minimum and maximum stress intensity values. As an example, for S_{1-2} , the largest range is $[33\,000 \text{ psi} - (-5100 \text{ psi})] = 38\,100 \text{ psi}$.³ Items A and H each occur 7000 times and thus there will be 7000 cycles. The next largest stress intensity range is between items F and L and is $31\,400 \text{ psi} - 0 = 31\,400 \text{ psi}$. This calculation procedure is repeated for each of the stress intensities, S_{1-2} , S_{2-3} , and S_{3-1} , and results are presented in Tables 3 and 4. The allowable design cycles for each of these stress intensity amplitudes is determined from the ASME fatigue design curve [2].

Since the design temperature for this component is 427°C (800°F), the use of this curve is justified because at 427°C there is negligible creep in this C- $\frac{1}{2}$ Mo material. A fatigue analysis is made at the discretion of the boiler designer for Section I of the ASME Code and thus does not influence the code stamping of the unit. The 371°C (700°F) limit for the fatigue analysis in the ASME Code is based on the behavior of carbon steel. If there were a mandatory Code requirement, relief could be obtained by a Code Case or by presenting data to change the Code. An examination of the calculated stress intensity amplitudes shows that only two of the values are sufficient to show appreciable fatigue damage. Table 5 shows the determination of fatigue damage.

The ASME Code uses a linear cumulative damage procedure with a summation equation equal to or less than one:

$$\Sigma N_R/N_A = 0.64 + 0.26 = 0.9 < 1$$

TABLE 3—Range of principal stress differences.

S_{1-2} Ranges		S_{2-3} Ranges		S_{3-1} Ranges	
psi ^a	Cycles	psi	Cycles	psi	Cycles
38 100	7 000	56 000	7 000	66 200	7 000
31 400	7 000	42 600	7 000	47 700	7 000
24 900	7 000	31 200	7 000	14 400	7 000
21 700	21 000	25 500	7 000	12 600	7 000
18 600	7 000	16 600	7 000	6 600	7 000
		2 500	7 000	4 500	7 000
		600	7 000	3 900	7 000

^a 1 psi = 6.9 kPa.

³ 1 psi = 6.9 kPa.

TABLE 4—*Stress intensity amplitudes.*

S_{1-2} Ranges		S_{2-3} Ranges		S_{3-1} Ranges	
psi ^a	Cycles	psi	Cycles	psi	Cycles
19 100	7 000	28 000	7 000	33 100	7 000
15 700	7 000	21 300	7 000	23 900	7 000
12 500	7 000	15 600	7 000	7 200	7 000
15 900	21 000	12 800	7 000	6 300	7 000
9 300	7 000	8 300	7 000	3 300	7 000
		1 250	7 000	2 250	7 000
		300	7 000	1 950	7 000

^a 1 psi = 6.9 kPa.

Superheater Outlet Header

A boiler component in the high-temperature region for the material where there is an interaction between fatigue and creep damage is the superheater outlet header. The material for this header is 2¼Cr-1Mo, which has good creep properties at 583°C (1000°F). In this unit the outlet steam temperature is held constant over most of the load range while the outlet pressure varies. The large thermal stresses occur at heatup and cooldown and occur once each day. To meet ASME Code requirements the thickness is determined by Code formulas in Section I of the ASME Code [1]. A small amount of extra thickness may be added for nozzle and nipple reinforcement for a better balance in stiffness between nozzle and shell. Strain range partitioning life curves at the present time require plastic and creep inelastic strains; this requires an inelastic analysis.

At a critical region in the header the plastic strains in Table 6 were determined at heatup, cooldown, and shutdown. Since the stresses and strains vary with time, it is necessary to plot the variation of the strain differences with time to determine the maximum strain difference ranges at critical times.

The strains at shutdown show that after the first cycle there are residual strains which will enter into the calculations on the next cycle; thus it is nec-

TABLE 5—*Fatigue damage.*

S_{3-1} , psi ^a	Temperature Modulus Correction(S_{3-1}), psi	Allowable Design Cycles (N_A)	Required Design Cycles (N_R)	Damage (NR/NA)
33 100	38 600	11 000	7 000	0.64
23 900	27 900	28 000	7 000	0.26

^a 1 psi = 6.9 kPa.

TABLE 6—Principal strains.

Plastic Strains $\times 10^{-7}$ in./in.			
	ϵ_1	ϵ_2	ϵ_3
Heatup-A	-357	-135	+492
Cool-down-B	+178	+ 54	-232
Shutdown-C	+ 95	+ 31	-126

Creep Strains $\times 10^{-7}$ in./in.			
	ϵ_1	ϵ_2	ϵ_3
Heatup-A	-195	- 67	+262
Cool-down-B	+405	+143	-548
Shutdown-C	+284	+ 60	-344

essary to analyze more than one cycle. A table of the strain differences may be determined from the strains in Tables 7 and 8.

There is no direct relationship between the plastic strain differences and the stress differences, since the plastic strains do not enter into the calculation of stresses. In the elastic region it can be shown that the relationship between the axial strain in a fatigue test and the strain difference is, for the maximum shear theory of failure,

$$\epsilon_{\text{axial}} = \frac{\epsilon_1 - \epsilon_2}{1 + \mu} \quad (6)$$

By analogy the concept is assumed to apply to plastic strain differences. However, the cyclic strain range partitioning life curves are failure curves for small laboratory specimens. The concept of strain range partitioning is relatively new to pressure vessel design, and a set of design curves have not been developed which contain factors to relate the fatigue test to actual full-size components. The mechanisms controlling the damage in the interaction between creep and fatigue are not the same as the damage in lower temperature

TABLE 7—Strain difference.

Plastic Strain Difference $\times 10^{-7}$ in./in.			
	$\epsilon_1 - \epsilon_2$	$\epsilon_2 - \epsilon_3$	$\epsilon_3 - \epsilon_1$
Heatup-A	-222	-627	+849
Cool-down-B	+124	+286	-410
Shutdown-C	+ 64	+157	-221

Creep Strain Difference $\times 10^{-7}$ in./in.			
	$\epsilon_1 - \epsilon_2$	$\epsilon_2 - \epsilon_3$	$\epsilon_3 - \epsilon_1$
Heatup-A	-128	-329	+457
Cool-down-B	+262	+691	-953
Shutdown-C	+224	+404	-626

TABLE 8—Strain difference range.

Plastic Strain Difference Range $\times 10^{-7}$ in./in.			
	$\epsilon_1 - \epsilon_2$	$\epsilon_2 - \epsilon_3$	$\epsilon_3 - \epsilon_1$
A - B	346	913	1259
B - C	60	129	189
Creep Strain Difference Range $\times 10^{-7}$ in./in.			
	$\epsilon_1 - \epsilon_2$	$\epsilon_2 - \epsilon_3$	$\epsilon_3 - \epsilon_1$
A - B	390	1020	1410
B - C	38	287	327

fatigue, and thus a different approach has been developed. In the high-temperature area the influence of temperature is a major consideration, and it is probable that the degradation from temperature is a larger factor for the small test specimens than for full-size components because of surface area differences. As a conservative approach, the plastic strain difference range has been used in design evaluations. Thus it is assumed that

$$\epsilon_{\text{axial}} = \epsilon_1 - \epsilon_2 \quad (7)$$

and the largest set of strain range differences are used.

From the results in Table 8, the following values may be developed.

$$\epsilon_{pp} = 189 \times 10^{-7} \text{ in./in.}$$

$$\epsilon_{cc} = 327 \times 10^{-7} \text{ in./in.}$$

$$\epsilon_{pc} = 1070 \times 10^{-7} \text{ in./in.}$$

$$\delta_c = 13 \times 10^{-7} \text{ in./in.}$$

$$\Delta\epsilon_{in} = 1586 \times 10^{-7} \text{ in./in.}$$

$$F_{pp} = \frac{\Delta\epsilon_{pp}}{\Delta\epsilon_{in}} = \frac{189 \times 10^{-7}}{1586 \times 10^{-7}} = 0.12$$

$$F_{cc} = \frac{\Delta\epsilon_{cc}}{\Delta\epsilon_{in}} = \frac{327 \times 10^{-7}}{1586 \times 10^{-7}} = 0.21$$

$$F_{pc} = \frac{\Delta\epsilon_{pc}}{\Delta\epsilon_{in}} = \frac{1070 \times 10^{-7}}{1586 \times 10^{-7}} = 0.67$$

From cyclic curves for strain-range [8,9] partitioning for $\Delta\epsilon_{in} = 1586 \times 10^{-7}$ in./in., we obtain

$$N_{pp} = 101\,000 \text{ cycles}$$

$$N_{cc} = 70\,000 \text{ cycles}$$

$$N_{pc} = 25\,000 \text{ cycles}$$

For 2½Cr-1Mo the same curve is used for N_{pc} and N_{cp} .

The damage per cycle is

$$\frac{F_{pp}}{N_{pp}} + \frac{F_{cc}}{N_{cc}} + \frac{F_{pc}}{N_{pc}} + \frac{\delta}{D_c} = \text{damage/cycle}$$

$$\frac{0.12}{101\,000} + \frac{0.21}{70\,000} + \frac{0.67}{25\,000} + \frac{13 \times 10^{-7}}{0.2} = 373 \times 10^{-7}$$

If this cycle were repeated, the design life would be

$$N_D = \frac{1}{\text{damage/cycle}}$$

$$N_D = \frac{1}{373 \times 10^{-7}} = 26\,800 \text{ cycles}$$

Since only 7000 cycles are required for the design condition, an increase in heatup and cooldown rates would be possible for this header unless some other component is limiting the thermal rates. In most cases the first cycle contains the most damage as the component tends to shake down, although there may be creep ratchet strain for each cycle.

Comparison Between Effective Strain and Strain Differences

From the results in Tables 7 and 8 the effective strains may be calculated from the equation

$$\epsilon_e = \frac{2}{3} \sqrt{(\epsilon_1 - \epsilon_2)^2 + (\epsilon_2 - \epsilon_3)^2 + (\epsilon_3 - \epsilon_1)^2}$$

For comparative values to use for strain differences, the following equation is used with Poisson's ratio of 0.5 for plastic strains:

$$\epsilon_A = \text{greater of} \left(\frac{\epsilon_1 - \epsilon_2}{1 + \mu}, \frac{\epsilon_2 - \epsilon_3}{1 + \mu}, \frac{\epsilon_3 - \epsilon_1}{1 + \mu} \right)$$

A comparison of the results from these concepts yields Table 9.

TABLE 9—*Plastic strain range.*

Strain Differences	Effective Strain
$\Delta\epsilon_{pp} = 126 \times 10^{-7} \text{ in./in.}$	$\Delta\epsilon_{pp} = 111 \times 10^{-7} \text{ in./in.}$
$\Delta\epsilon_{cc} = 218 \times 10^{-7} \text{ in./in.}$	$\Delta\epsilon_{cc} = 206 \times 10^{-7} \text{ in./in.}$
$\Delta\epsilon_{pc} = 715 \times 10^{-7} \text{ in./in.}$	$\Delta\epsilon_{pc} = 640 \times 10^{-7} \text{ in./in.}$
$\delta_c = 9 \times 10^{-7} \text{ in./in.}$	$\delta_c = 5 \times 10^{-7} \text{ in./in.}$
$\Delta\epsilon_{in} = 1059 \times 10^{-7} \text{ in./in.}$	$\Delta\epsilon_{in} = 957 \times 10^{-7} \text{ in./in.}$
$N_{pp} = 185\,000 \text{ cycles}$	$N_{pp} = 210\,000 \text{ cycles}$
$N_{cc} = 120\,000 \text{ cycles}$	$N_{cc} = 140\,000 \text{ cycles}$
$N_{cp} = 60\,000 \text{ cycles}$	$N_{pc} = 70\,000 \text{ cycles}$
$N_t = 74\,100 \text{ cycles}$	$N_t = 83\,400 \text{ cycles}$

The more conservative approach of using the concepts of maximum shear theory for design results in an approximately 10 percent life difference. The big advantage of this approach is that an algebraic sign is available for determining ranges where complex loadings must be analyzed.

Summary

The fatigue data generated on small specimens require certain design factors to adopt the fatigue curves to the design of pressure vessels. At high temperatures there is an interaction between creep and fatigue. A modified concept of strain range partitioning may be used to design high-temperature pressure vessels for complex loading. The use of strain difference range results in algebraic signs which aid in determining strain ranges.

References

- [1] American Society of Mechanical Engineers, "Power Boiler," *ASME Boiler and Pressure Vessel Code*, Section I, 1980.
- [2] American Society of Mechanical Engineers, "Pressure Vessels," *ASME Boiler and Pressure Vessel Code*, Section VIII, Division 2, 1980.
- [3] American Society of Mechanical Engineers, *ASME Boiler and Pressure Vessel Code*, Sections III and VIII, Division 2, 1965.
- [4] Lawton C. W., "High Temperature—Low Cycle Fatigue: A Summary of Industry and Code Work," Society for Experimental Stress Analysis, spring meeting, Westport, Conn., May 1967.
- [5] Manson, S. S., Halford, G. R., and Hirschberg, M. H., "Creep Fatigue Analysis by Strain Range Partitioning," in *First Symposium on Design for Elevated Temperature Environment*, American Society of Mechanical Engineers, New York, 1971.
- [6] Manson, S. S. and Halford, C. R., "Treatment of Multi-Axial Creep-Fatigue by Strain Range Partitioning," in *1976 ASME-MPC Symposium on Creep-Fatigue Interaction-MPC-3*, R. M. Curran, Ed., American Society of Mechanical Engineers, New York, 1976.
- [7] American Society of Mechanical Engineers, *ASME Boiler and Pressure Vessel Code*, Nuclear Code Case N47, 1980.
- [8] Halford, G. H. and Saltzman, V. F., "Strain Range Partitioning Life Predictions of Long Time MPC Creep-Fatigue," *Methods for Predicting Material Life in Fatigue*, J. R. Whitehead, Ed., American Society of Mechanical Engineers, 1979.
- [9] Unpublished combustion engineering data (restricted data).

Materials-Data Needs for Fatigue Design of Pressure Vessel Systems

REFERENCE: Jaske, C. E., "Materials-Data Needs for Fatigue Design of Pressure Vessel Systems," *Low-Cycle Fatigue and Life Prediction, ASTM STP 770*, C. Amzallag, B. N. Leis, and P. Rabbe, Eds., American Society for Testing and Materials, 1982, pp. 600-611.

ABSTRACT: Materials data are essential to the proper formulation of fatigue-design guidelines for pressure-vessel systems. These data are needed for two main reasons: (1) to develop and evaluate prediction methods used in fatigue-damage analysis and (2) to quantify the fatigue behavior of various alloys from which pressure vessels are fabricated. The former reason involves verification of models of the fatigue-damage process and must include both deformation and life prediction as well as demonstrating that the reference damage basis and damage rules are relevant to actual hardware. The latter reason relates to the establishment of an adequate data base and must incorporate material variability, environmental effects, and temperature effects.

In the above context, this paper addresses the data needs within the framework of the American Society of Mechanical Engineers (ASME) Boiler and Pressure Vessel Code. Low-temperature (negligible creep) and high-temperature (significant creep) regimes and crack-initiation and crack-propagation damage criteria are addressed. The background for existing fatigue-design guidelines of the ASME Code is briefly reviewed. Areas where fatigue-damage criteria need to be improved are creep/fatigue/environmental interaction at low strain ranges and long times, thermal-mechanical fatigue, multiaxial fatigue, and long-life fatigue. Existing guidelines for crack initiation are based mainly on strain cycling of uniaxially loaded specimens. There are some crack-initiation data on notch effects at low temperature, but more information is needed for high temperatures and welded components. Additionally, crack-initiation data are needed for multiaxial conditions, especially nonproportional loading, for thermal-mechanical cycling, and for high-cycle fatigue. To apply fatigue crack growth methodology, data on the size, shape, and distribution of initial flaws, methods of dealing with small cracks, and techniques for treating cracks in inelastic strain fields are required. With these requirements in mind, guidelines for the development of fatigue data are discussed, and recommended guidelines for data development are outlined.

KEY WORDS: materials, fatigue data, fatigue design, tests, pressure vessels, piping

Materials data play a key and essential role in the formulation of fatigue-design rules for pressure vessels and piping systems. There are two main reasons why such data are needed: (1) to use in developing and evaluating the

¹ Research Scientist, Physical Metallurgy Section, Materials Department, Battelle Columbus Laboratories, Columbus, Ohio 43201.

life-prediction methods that are employed in fatigue-damage analysis, and (2) to fully quantify the fatigue behavior of alloys that are used in the construction of pressure vessels and piping systems.

The first item includes development of information on the material's fatigue resistance by means of a set of well-defined experiments to establish a reference damage basis for fatigue-life prediction. For example, a strain range (or stress range) versus cyclic life curve for fully reversed, constant-amplitude, uniaxial loading of smooth specimens is commonly used to define this reference state of fatigue damage. In addition, cyclic-deformation response should be well characterized so that constitutive equations employed in mechanics analyses can be properly formulated. Cyclic stress-strain curves are an example of this type of datum. Finally, information on fatigue behavior under variable-amplitude loading histories needs to be developed so that damage rules, such as Miner's Rule, can be developed and evaluated.

In the second item, one is concerned with the intrinsic variability in material behavior, such as heat-to-heat differences, product form differences, and microstructural variations. The characterization of the influence of environment on fatigue behavior is another important aspect of the second item. Aggressive gaseous and liquid environments often have extremely deleterious effects on fatigue behavior. Proper quantification of these effects is essential to assuring adequate service performance of materials under cyclic-loading conditions. Also, temperature can significantly alter the fatigue resistance of materials. Embrittlement at cryogenic temperatures and creep/fatigue interaction and thermal-mechanical fatigue at elevated temperatures are examples of temperature-related phenomena that can markedly degrade fatigue resistance.

For purposes of this discussion, the scope of this paper is limited to addressing fatigue data needs within the framework of the American Society of Mechanical Engineers (ASME) Boiler and Pressure Vessel Code. Low temperatures where creep effects are negligible and high temperatures where creep effects are important are covered. Also, initiation of fatigue cracking and fatigue crack propagation concepts are relevant.

Background

As background information to the ensuing sections of this paper, it is useful to briefly review the existing fatigue-design approach of the ASME Code. The present approach is based upon the use of design fatigue curves, which are log-log plots of allowable stress amplitude, S_a , versus the allowable number of cycles, N . Such curves are presently included in Section III and Section VIII, Division 2 of the ASME Code for carbon, low-alloy, and high-tensile steels and high-strength steel bolting at temperatures not exceeding 371°C (700°F), and for austenitic steels, Ni-Cr-Fe alloy, Ni-Fe-Cr alloy, Ni-Cu alloy, and 70 Cu-30Ni alloy at temperatures not exceeding 427°C

(800°F). ASME Code Case N-47 provides design-fatigue curves for Types 304 and 316 stainless steel and for Ni-Fe-Cr Alloy 800H at temperatures above 427°C (800°F). These high-temperature curves are expressed in terms of total design-fatigue strain range, ϵ_t , rather than S_a . All these curves are limited to the cyclic range of $N = 10$ to 10^6 cycles.

Figure 1 shows a typical example of one of these design-fatigue curves that is presently used for austenitic stainless steels at temperatures not exceeding 427°C (800°F) [1].² The plotted symbols represent results of strain-controlled low-cycle fatigue tests of axially loaded smooth specimens of wrought material. Cyclic-loading amplitude was constant and fully reversed during each test, and fatigue life was the number of cycles to fracture for a small specimen (about 6 to 7 mm in diameter). Only specimens taken from wrought material were used. Thus none of these data were for cast or welded material. The stress amplitude was actually a pseudo stress amplitude, S ,

$$S = \frac{1}{2} E \Delta \epsilon_t \quad (1)$$

where E is the elastic modulus and $\Delta \epsilon_t$ is the total strain range. The value of S differs from the value of S_a in that S does not include a reduction factor. Using the Langer equation [2], a best-fit curve to the actual mean trend of the data was obtained [1,3]. The best-fit curve was then adjusted to account for the "worst-case" effects of tensile mean stress [1]. The design curve was developed from this adjusted curve by applying a reduction factor of 20 on cyclic life or 2 on S , whichever gave the lowest value [1].

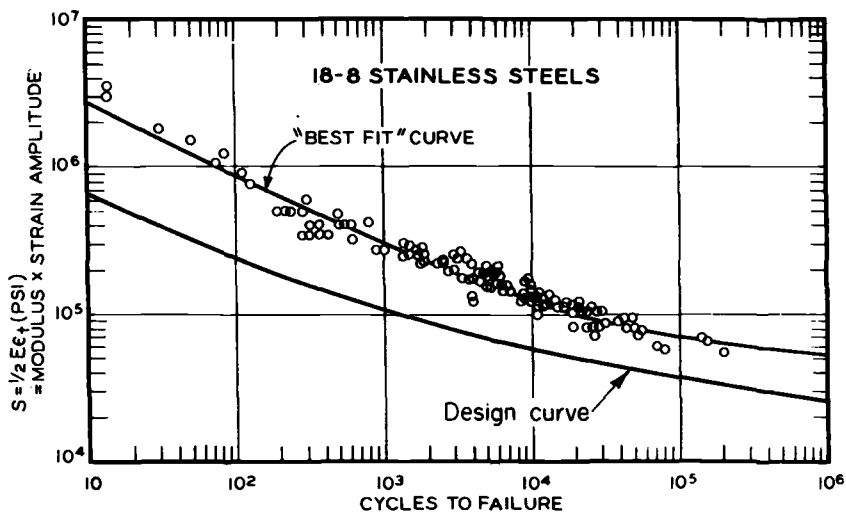


FIG. 1—Fatigue data and design fatigue curve for austenitic stainless steels currently used in ASME Code [1].

² The italic numbers in brackets refer to the list of references appended to this paper.

These reduction factors are intended to account for data scatter, size effects, effects of mildly aggressive environments, and errors in assessment of loading histories [1]. For variable-amplitude loading, usage factors are computed as the ratio of applied to allowable cycles for each distinct stress amplitude. In other words, this is a Miner's Rule type of computation based on values of S_a and allowable cyclic life. For acceptable design, the usage factor must not exceed 1.0. The validity of this type of approach has been partially verified by means of low-cycle fatigue tests of prototypical welded pressure vessels [1,4]. Figure 2 shows the results of such fatigue tests reported by Lawton [4]. The upper heavy solid line shows the fatigue curve based on actual failure of laboratory test specimens, such as the upper curve in Fig. 1. The lower heavy solid line is the current ASME design fatigue curve applicable to carbon and low-alloy steels. The plotted points show the results of tests on pressure vessels. As expected, these data points typically fall somewhere between the mean-life, best-fit curve for smooth, polished specimens and the design fatigue curve. These results indicate that the ASME Code curves are conservative, but they do not assess important factors, such as elevated temperature, variable-amplitude loading, and aggressive environments. It is the designer's responsibility to account for these factors in his analysis.

Current Status

Many years of satisfactory service experience indicate that the ASME Code's fatigue-design approach is a sound, viable one. There is, however, room for improvement in several aspects of the Code. The ensuing discussion emphasizes these areas where improvement is desirable. These are not areas of marked deficiency, but rather areas where an already sound approach to fatigue design can be improved further. There are four major problem areas associated with the current ASME fatigue design approach. Firstly, there is a limited knowledge of the types of load histories to which pressure and piping systems are typically subjected during their operational lifetimes. Secondly, there has been only limited experimental verification of the cumulative-damage procedures used in ASME Code fatigue-design analysis. Thirdly, there has been no explicit incorporation of environmental effects into the fatigue-design procedures. Fourth, although Section XI of the ASME Code requires consideration of fatigue crack propagation for in-service inspection, there are no design rules for explicitly including fatigue crack propagation methodology in the ASME Code. Of these four items, load histories and environmental effects are especially important. Lack of knowledge in these two areas has been identified as a critical issue in nuclear applications [5].

Information from field experience and component testing is needed to help develop needed methodology in these four areas. Information from service failures and failure analyses can help in assessing the validity of

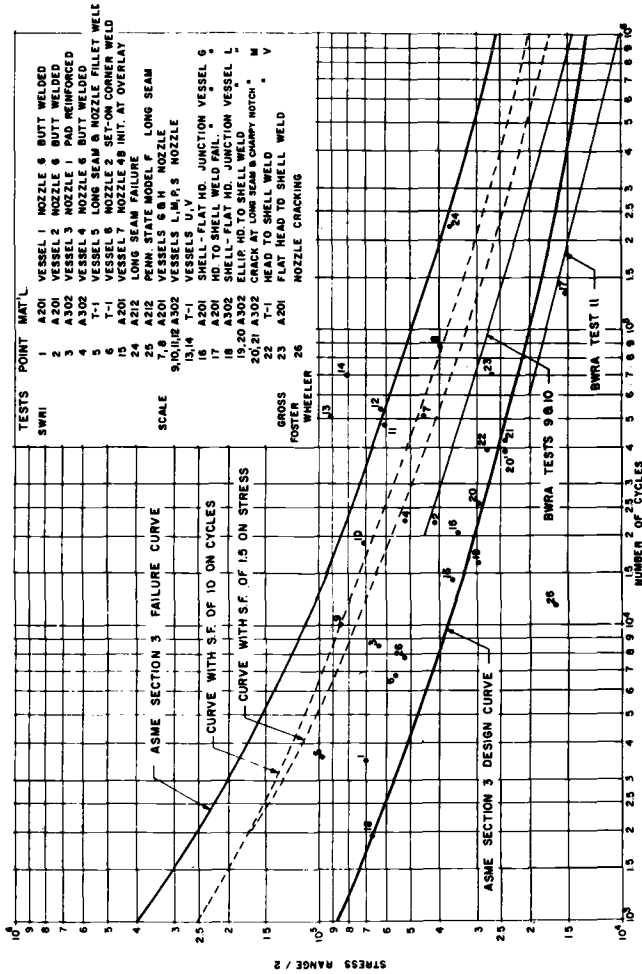


FIG. 2—Comparison of fatigue design curves with data from fatigue tests of pressure vessels [4].

available methods of fatigue-life prediction. Field data on load histories, environmental conditions, and operating temperatures need to be obtained and cataloged on a systematic basis to provide a data base of reference information for design of future structural components and equipment. Also, field experience can provide detailed documentation of actual configuration and fabrication variables in real hardware. Although the importance of field experience and component testing is widely recognized, there has been little progress in factoring them into the development of fatigue-life prediction methods. Instead, most of the work on predicting fatigue life in pressure vessel and piping system application has concentrated on using data from simple laboratory tests on smooth specimens. For example, at a recent ASME symposium on prediction of fatigue life [6], only one of the 17 papers presented attempted fatigue life predictions of structural components. All the other papers dealt with only simple smooth and/or notched laboratory test specimens.

To quantify the fatigue behavior of materials, information is needed on both crack initiation and crack propagation behavior. The current status of each of these two items will be reviewed separately in the following paragraphs.

Most of the data used to develop fatigue-design concepts for the ASME Code are from tests of smooth specimens subjected to uniaxial loading. Notch effects on fatigue have been examined extensively for room-temperature conditions using the local stress-strain approach. Both Leis [7] and Dowling et al [8] have reviewed the work in this area. Little has been done, however, to extend these concepts for dealing with notched members to elevated-temperature applications where creep is significant [9]. Also, more fatigue-crack initiation data are needed for welded components. Recognizing this need, the Subgroup on Fatigue Strength of the ASME Boiler and Pressure Vessel Committee recently formed a task group on fatigue properties of weldments.

Dealing with multiaxial stress/strain states is essential in the fatigue design of complex structural components by means of mechanics analysis. Most of the currently advanced procedures for dealing with multiaxial fatigue damage (for example, Refs 10 to 12) are limited to dealing with proportional loading conditions. As pointed up by Leis and Laflen [13], these concepts cannot adequately treat nonproportional cycling, which includes most thermal fatigue and creep/fatigue problems. Additional research in the area of fatigue damage accumulation under nonproportional cycling is desperately needed.

The design fatigue curves in the ASME Code are for isothermal, low-cycle ($<10^6$ cycles to failure) fatigue conditions. Realistically, however, both thermal-mechanical and high-cycle fatigue ($>10^6$ cycles to failure) problems are important. Consider, for example, Jaske's [14] data on thermal-mechanical fatigue of AISI 1010 steel shown in Fig. 3. Using the ASME Code's reference damage basis of total strain range shows that thermal-mechanical strain cy-

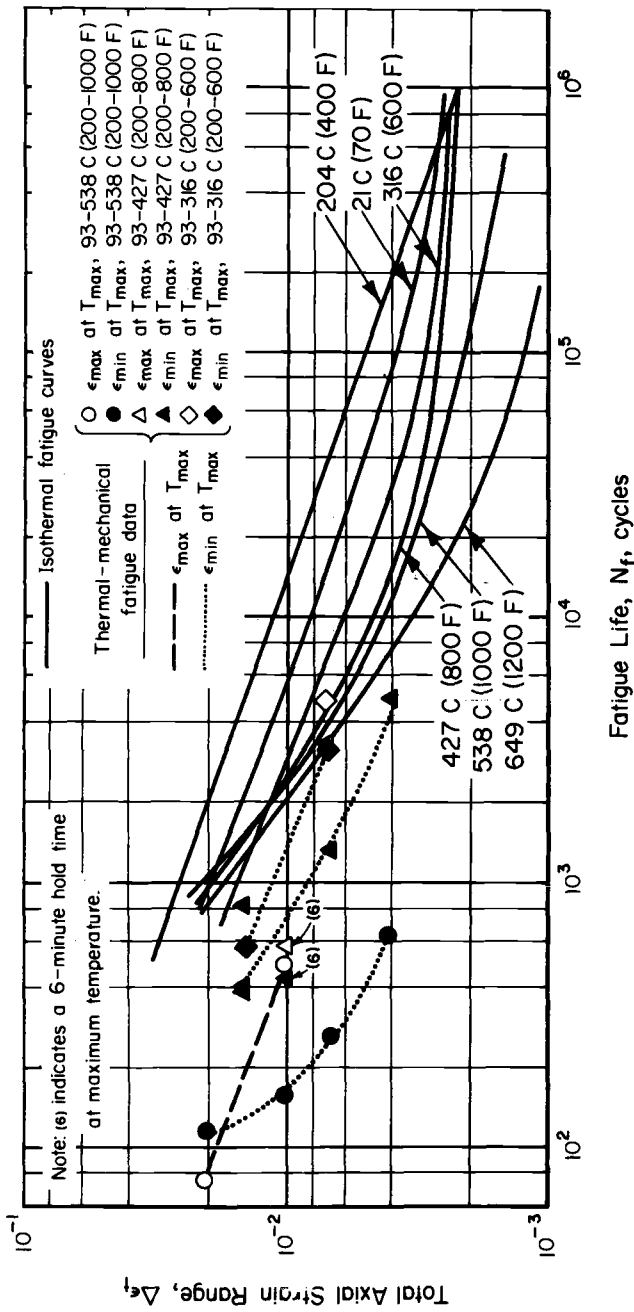


FIG. 3—Comparison of thermal-mechanical and isothermal fatigue resistance of AISI 1010 steel [14].

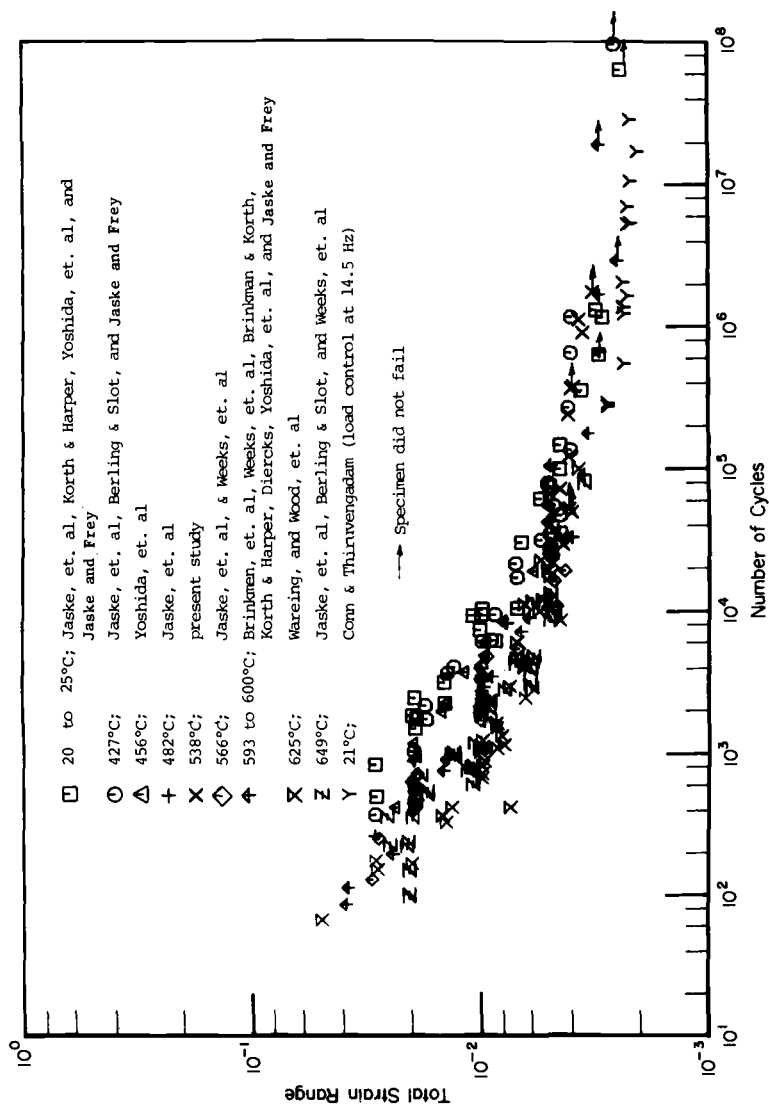


FIG. 4—Fatigue data for strain-controlled cycling of Type 316 stainless steel [15].

cling is much more deleterious to fatigue resistance than isothermal strain cycling. Similar information should be developed for other materials commonly used in pressure vessels and piping in order to see if isothermal fatigue curves are appropriate for dealing with thermal-mechanical fatigue problems. There has been concern also with extending the existing design fatigue curves to the high-cycle regime [3]. However, as shown by the example for Type 316 stainless steel in Fig. 4, for the strain-controlled cycling conditions of interest to the ASME Code there are little long-life fatigue data currently available [15]. Thus more experimental work on strain-controlled, high-cycle fatigue is desirable.

Application of fatigue crack propagation methods to design of pressure vessels and piping systems is an important area where development is needed. A task group on fatigue crack propagation has been working on this problem as part of the activities of the Subgroup on Fatigue Strength of the ASME Boiler and Pressure Vessel Committee, but design rules for Code use have not yet been developed. In order to apply the crack growth concepts of fracture mechanics, the size, shape, and distribution of initial cracks and flaws needs to be known. It is usually necessary to assume a certain crack size, shape, and location. Information from field studies, examinations, and inspections is needed to assure that these assumptions are realistic. Fracture mechanics typically deal with a single large dominant crack. For fatigue applications, it is also necessary to develop methods of dealing with small, short cracks [16–18]. Finally, where significant cyclic plasticity can occur and low-cycle fatigue crack propagation is of concern, methods for dealing with cracks in inelastic strain fields need to be developed [19,20].

Guidelines for Data Development

Two documents [21,22] describe the currently recommended guidelines for developing fatigue data for ASME Code use. Both are concerned with uniaxial fatigue testing of smooth specimens to develop crack initiation fatigue life data. No document is available for fatigue crack propagation data development for the ASME Code.

For low-temperature applications—that is, those temperatures where for a given metal or alloy creep effects are considered to be insignificant—the guidelines are given in Ref 21. The chemical composition, microstructure, hardness, and heat treatment should be characterized, documented, and shown to satisfy the applicable specification(s). Tensile properties should be measured at room temperature (20 to 25°C) and at temperatures up to (or down to) the maximum (or the minimum) use temperature. Duplicate tension tests should be performed at each test temperature, and the intervals between test temperatures should not exceed 56°C (100°F). Strain-controlled fatigue tests of smooth, polished, uniaxially loaded specimens about 6.35 mm (0.25 in.) in diameter should be performed under fully-reversed constant-amplitude cycling. Uniform-gage specimens are preferred, but hourglass-

shaped specimens may be used if anisotropy is not a significant factor. Fatigue tests should be conducted at room temperature and at the maximum (or minimum) use temperature. Strain ranges should be selected so that at least three data points are developed for each \log_{10} cycle of cyclic fatigue life. Finally, all the above work should be carried out on at least three heats or lots of the material.

The guidelines for high-temperature applications, those where creep is considered to be a significant factor, are presented in Ref 22. The material should again be well characterized. Tensile properties and fatigue behavior under continuous strain cycling at a strain rate of 10^{-3} s^{-1} should be determined. Moreover, data on creep/fatigue interaction effects should be obtained. Here the type of testing to be carried out depends on the type of creep/fatigue damage approach that is to be used. Strain-controlled cycling with hold periods of constant peak strain (stress relaxation) have been employed in much of the experimental work used to develop information currently included in ASME Code Case N-47 [23]. However, load hold periods, varying loading rates, and/or types of combined creep/fatigue loading can be used. Tensile, compressive, and combined tensile and compressive loadings should be evaluated to determine which type is most deleterious. Experiments should be conducted at the maximum use temperature and at other temperatures in the creep range below this level selected so that adjacent temperatures differ by no more than 111°C (200°F). A total of at least 12 data points on creep/fatigue interaction behavior should be developed at each temperature of interest.

In summary, guidelines for developing low-cycle strain range versus fatigue life curves are well defined. Similar guidelines need to be developed for high-cycle fatigue data development. The guidelines for developing creep/fatigue data are tentative and somewhat vague because there is no general agreement as to what type of data and associated creep/fatigue damage analysis method are most appropriate. For fatigue-crack growth data, no guidelines are available at present.

Future Needs

In concluding this paper, it is appropriate to outline the important areas in which materials data for fatigue design of pressure vessels and piping systems are needed in future experimental studies. The six most important areas are listed below:

- low strain ranges and long hold times
- multiaxial stresses and strains—components
- variable-amplitude loading
- crack growth as well as initiation
- thermal-mechanical loading
- environmental effects

Most work on creep/fatigue interaction has been at relatively high strain ranges (≥ 0.5 percent) and short hold times (≤ 2 h). In actual applications, strain ranges below 0.5 percent and hold times of 100's or 1000's of hours are most relevant. Fatigue analysis of complex components requires understanding multiaxial stress/strain effects. It is especially important that methodology for dealing with fatigue damage accumulation under nonproportional cycling be developed. Effects of variable-amplitude loading spectra that are representative of typical pressure vessel and piping service need to be evaluated. Experience in the aircraft and automotive industry should be factored into this evaluation. Methods and background experimental data for incorporating fatigue-crack growth methodology into design procedures should be developed, with emphasis on inelastic effects. Thermal-mechanical fatigue is often important in pressure vessels and piping, but most data are for isothermal conditions. Since thermal-mechanical cycling may be more deleterious than cycling under isothermal conditions, it should be evaluated more extensively. Most fatigue experiments are carried out in air. Since components are often exposed to aggressive environments, the influence of such environments on fatigue crack initiation and growth should be assessed.

The major problem encountered in carrying out much of this needed experimental work is the time and money constraint placed on such projects. The experiments are complicated, costly ones. Long-term studies of time-dependent creep and environmental effects require a great deal of resources, patience, and long-term planning. These studies cannot be conducted on a piece-meal approach. A cooperative government/industrial program needs to be developed to achieve the desired goals. This program must have a long-term (at least 10 years) plan and commitment of resources.

References

- [1] "Criteria of the ASME Boiler and Pressure Vessel Code for Design by Analysis," in Sections III and VII, Division 2 of the *ASME Boiler and Pressure Vessel Code*, American Society of Mechanical Engineers, 1969.
- [2] Langer, B. F., *Journal of Basic Engineering*, Vol. 84, No. 3, 1962, pp. 389-402.
- [3] Jaske, C. E. and O'Donnell, *Journal of Pressure Vessel Technology*, Vol. 99, No. 4, 1977, pp. 584-592.
- [4] Lawton, C. W., *Experimental Mechanics*, Vol. 8, No. 6, 1968, pp. 257-266.
- [5] Shao, L., discussion of "Issue II—Safety Factors in Fatigue Design: Arbitrary or Rational?," ASME Symposium on Critical Materials and Fabrication Issues for Pressure Vessels, Piping, Pumps, and Valves, San Francisco, 14-15 Aug. 1980.
- [6] *Methods for Predicting Material Life in Fatigue*, W. J. Ostergren and J. R. Whitehead, Eds., American Society of Mechanical Engineers, 1979.
- [7] Leis, B. N. in *Proceedings*, 9th ICAF Symposium on Fatigue Life of Structures under Operational Loads, ICAF Doc. 960, Laboratorium für Betriebstestigkeit, May 1977, pp. 3.4/1-47.
- [8] Dowling, N. E., Brose, W. R., and Wilson, W. K. in *Fatigue under Complex Loading: Analyses and Experiments*, SAE6, Society of Automotive Engineers, 1977, pp. 55-84.
- [9] Raske, D. T. and Mayia, P. S. in *Ductility and Toughness Considerations in Elevated Temperature Service*, MPC-8, American Society of Mechanical Engineers, 1978, pp. 199-210.

- [10] Brown, M. W. and Miller, K. J., *Proceedings of the Institution of Mechanical Engineers*, Vol. 187 65/73, 1973, pp. 745-755.
- [11] Krempl, E., *The Influence of State of Stress on Low-Cycle Fatigue of Structural Materials: A Literature Survey and Interpretive Report*, ASTM STP 549, American Society for Testing and Materials, 1974.
- [12] Blass, J. J. and Zamrik, S. Y., "Multiaxial Low-Cycle Fatigue of Type 304 Stainless Steel," ORNL/TM-5609, Oak Ridge National Laboratory, Oak Ridge, Tenn., Oct. 1976.
- [13] Leis, B. N. and Laflen, J. H., *Journal of Engineering Materials and Technology*, Vol. 102, No. 1, 1980, pp. 127-134.
- [14] Jaske, C. E. in *Thermal Fatigue of Materials and Components*, ASTM STP 612, American Society for Testing and Materials, 1976, pp. 170-198.
- [15] Jaske, C. E. and Frey, N. D., "Long-Life Fatigue of Type 316 Stainless Steel at Temperatures Up to 593 C," Paper 81-MAT-2, 1981 ASME Pressure Vessels and Piping Conference, Denver, 21-26 June 1981.
- [16] El Haddad, M. H., Smith, K. N., and Topper, T. H., *Journal of Engineering Materials and Technology*, Vol. 101, No. 1, 1979, pp. 42-46.
- [17] Leis, B. N. and Forte, T. P., "Fatigue Growth of Initially Physically Short Cracks in Notched Aluminum and Steel Plates," paper presented at 13th National Symposium on Fracture Mechanics, June 1980.
- [18] Dowling, N. E. in *Fracture Mechanics*, ASTM STP 677, American Society for Testing and Materials, 1979, pp. 247-273.
- [19] Dowling, N. E. and Begley, J. A. in *Mechanics of Crack Growth*, ASTM STP 590, American Society for Testing and Materials, 1976, pp. 82-103.
- [20] Jaske, C. E. and Begley, J. A. in *Ductility and Toughness Considerations in Elevated Temperature Service*, MPC-8, American Society of Mechanical Engineers, 1978, pp. 391-409.
- [21] "Recommended Test Procedure for Low-Cycle Fatigue Testing of Metallic Materials Below the Creep Range," Subgroup on Fatigue Strength, American Society of Mechanical Engineers, June 1973.
- [22] Halford, G. R., "Fatigue in the Creep Range-Material Testing, Documentation and Interpretation," position paper for Task Force on Creep-Fatigue, American Society of Mechanical Engineers, Jan. 1973.
- [23] "Criteria for Design of Elevated Temperature Class 1 Components," in Section III, Division 1 of the *ASME Boiler and Pressure Vessel Code*, American Society of Mechanical Engineers, 1976.

Influence of Local Strain Distribution on Low-Cycle Fatigue Behavior of Thick-Walled Structures

REFERENCE: Grubisic, Vatroslav and Sonsino, C. M., "Influence of Local Strain Distribution on Low-Cycle Fatigue Behavior of Thick-Walled Structures," *Low-Cycle Fatigue and Life Prediction*, ASTM STP 770, C. Amzallag, B. N. Leis, and P. Rabbe, Eds., American Society for Testing and Materials, 1982, pp. 612-629.

ABSTRACT: An optimum design of thick-walled components such as high-pressure vessels and reactor vessels requires knowledge of the local strain distribution, the strain/stress state, and the material's behavior under elastic-plastic deformations. The multiaxial strain-state is transformed into a uniaxial strain-state according to Von Mises's yield criterion. Fatigue experiments on planar and cylindrical specimens with high strain concentrations and biaxial strain-states prove that low-cycle material properties as determined from unnotched specimens can be applied for design based on a defined initial crack length. A design including the stage of crack-propagation can be practiced only in special cases; in general it can not be recommended because of very high strain intensities and the resulting small critical crack depths, as service experience shows. For the functional reliability of the component it is also important that the local structural yield point, which can be a multiple of the material's yield point, is not exceeded by maximum loading. When designing such structures prestrains resulting from manufacturing or overloading must also be considered. Tests carried out with prestrained specimens show that fatigue life is decreased with increased pre-strain due to cyclic softening.

KEY WORDS: low-cycle fatigue, thick-walled structures, stress-strain curves, fracture mechanical data, fatigue-life curves, geometry and strain distribution, multiaxial strain/stress state, structural yield point, structural size, probability of failure, manufacturing influence, life prediction

Nomenclature

Strains

ϵ_{tot} , ϵ_{el} , ϵ_{pl}	Total, elastic, and plastic strains
ϵ_l , ϵ_t , ϵ_r	Principal strains in longitudinal, tangential, and radial direction
ϵ_{eq}	Equivalent strain

¹ Head of Department of Stress Analysis and Strength Evaluation, and Research Engineer, respectively, Fraunhofer-Institut für Betriebsfestigkeit (LBF), Darmstadt, Federal Republic of Germany.

ϵ_m	Mean strain
ϵ_R	True strain at fracture
ϵ_a	Strain amplitude

Stresses

$\sigma_{0.2}$	0.2 percent yield strength, monotonic or cyclic
σ_B	Ultimate tensile strength
σ_R	True tensile strength
σ_{eq}	Equivalent stress

Fracture Mechanics

K	Stress intensity
K_{Ic}	Fracture toughness
da/dN	Crack propagation rate
a, a_c	Crack depth, critical crack depth

Fatigue Life

N_{cr}	Life to crack initiation
N_{prop}	Crack propagation life
N_t	Total life

Other Symbols

ψ	Area reduction
δ	Elongation
a_k	Impact strength
T, t, S, s	Constants of the strain-life relationship
μ, μ_{el}	Poisson's ratio, elastic Poisson's ratio
E, E_s	Young's and secant modulus
$R_\epsilon, R_\sigma, R_F$	Strain, stress, or load ratio, $\epsilon_{min}/\epsilon_{max}$ etc.
F	Load
A_n	Nominal cross section
$F_F, \epsilon_{eq,F}$	Load and strain for material yield point
$F_{0.2}, \epsilon_{eq,0.2}$	Load and strain for structural yield point
n_F, n_ϵ	Load and strain-support factors
l	Strain-gage length
r	Radius

K_t	Stress concentration factor
P_s	Probability of survival
T_N	Scatter
φ	Prestrain
f	Frequency
Δ	Range

During the service life of various structural thick-walled components, such as high-pressure vessels for isostatic pressure technology, reactor vessels, containers, and piping as used in the chemical industry (Fig. 1), a relatively low number of load cycles will occur. In these cases an optimum design, including an economic use of material, can be achieved if cyclic straining ex-

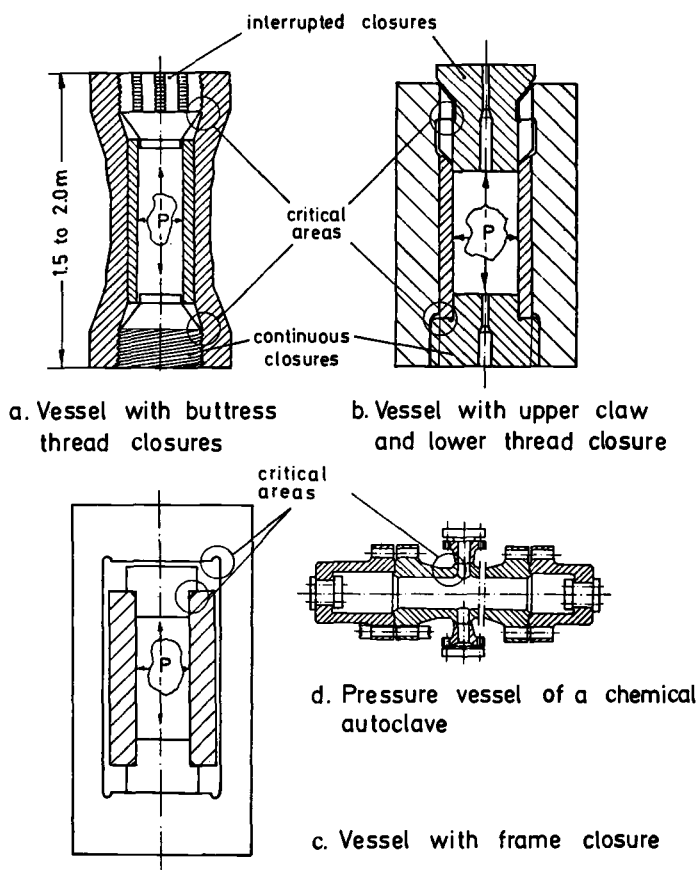


FIG. 1—Different types of high-pressure vessels.

ceeding the respective material's 0.2 percent yield point in highly strained areas can be allowed. Therefore for the determination of the fatigue life, it is necessary to know the local strain distribution, the stress-strain state, and the material's behavior under elastic-plastic deformation. The most important feature of thick-walled structures is the strain-controlled behavior of highly strained areas. Present techniques of strain analysis and simulation in the laboratory enable one to determine the fatigue behavior and to derive design criteria, respectively.

Referring to recent work on the fatigue behavior of high-pressure vessels and to experience as obtained from thick-walled structures [1], we will discuss the criteria for designing against fatigue in the low-cycle range and describe the procedures which allow them to be taken into account.²

Material Behavior

The low-cycle fatigue behavior under high strain concentration is determined by the elastic-plastic deformation, which can be described with the strain-life relation [2]

$$\Delta\epsilon_{\text{tot}}/2 = \Delta\epsilon_{\text{pl}}/2 + \Delta\epsilon_{\text{el}}/2 = T \cdot N_{\text{cr}}^{-t} + S \cdot N_{\text{cr}}^{-s} \quad (1)$$

The constants T , t , S , and s can be derived for each material from strain-controlled tests. If test results are not available, the fatigue-life curve can be estimated by using $s = 0.12$, $t = 0.6$, $S = 1.75 \sigma_B/E$, and $T = 0.5 \{\ln [1/(1 - \psi)]\}^{0.6}$, which are mean values found in fatigue tests for several structural steels [2]. The knowledge of conventional properties like the monotonic 0.2 percent yield point $\sigma_{0.2}$, ultimate tensile strength σ_B , true tensile strength σ_R , and reduction ψ , elongation δ , impact strength α_k , allow only a qualitative evaluation of the material. In connection with the constants T , t , S , and s , these allow only an approximate estimate of the relation between the deformation $\Delta\epsilon$ and the number of cycles to crack initiation N_{cr} . For a reliable quantitative determination of the fatigue behavior, strain-controlled fatigue life curves, so-called fatigue-dependent cyclic stress-strain curves,³ and fracture mechanical data of the material (Fig. 2) under service conditions must be known. For example, low frequencies and increasing hold-times intensify the corrosive influence of the environment. They lead, like irradiation effects, to a shorter fatigue life of crack initiation as well as to an acceleration of crack growth.

Generally preference should be given to a material that allows greater total strain amplitudes $\Delta\epsilon_{\text{tot}}/2$, has a superior ratio of plastic to elastic deformation $\Delta\epsilon_{\text{pl}}/\Delta\epsilon_{\text{el}}$, shows a lower crack-propagation rate da/dN , and has a better fracture toughness K_{Ic} . This is, for instance, the case for low-annealed

² The italic numbers in brackets refer to the list of references appended to this paper.

³ The fatigue-dependent cyclic stress-strain curve is derived from strain-controlled fatigue tests for the hysteresis loops at $n = N_{\text{cr}}/2$ cycles.

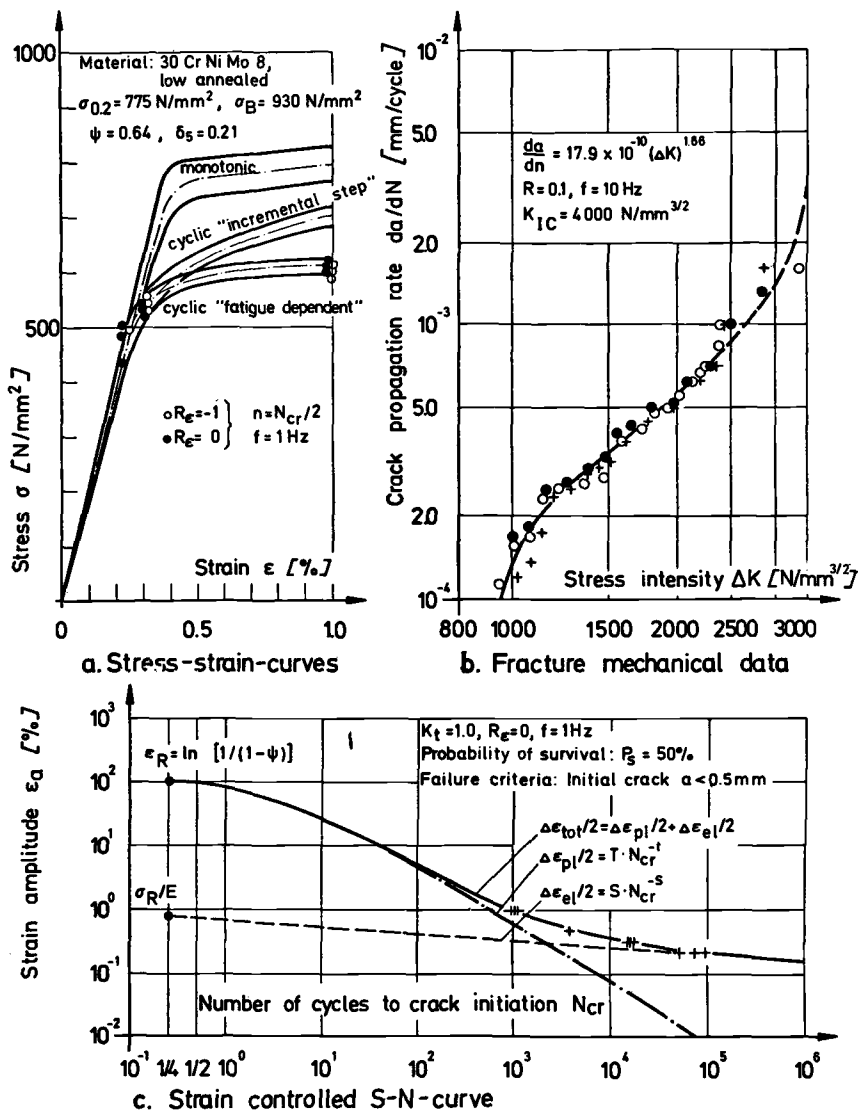


FIG. 2—Material properties.

structural steel 30Cr-Ni-Mo8 compared with its high-annealed form. Although low-annealed 30Cr-Ni-Mo8 has inferior values of ultimate tensile strength, monotonic 0.2 percent yield point, and endurance limit, it has better low-cycle fatigue properties in the range up to 10 000 cycles and better fracture mechanical data than high-annealed 30Cr-Ni-Mo8 [1]; the lower crack propagation rate and the superior fracture toughness are advantageous for not developing a crack or better detecting a crack within a given period of time.

Multiaxial Strain Evaluation

Due to complex loading or structural discontinuities local strains are mainly of the multiaxial nature. For the strain evaluation this multiaxial strain-state has to be converted into an equivalent uniaxial strain-state using a valid failure criterion. The equivalent strain ϵ_{eq} can be compared with allowable strains as found on uniaxially stressed unnotched specimens [1,3-5].

For the frequently occurring case of an in-phase strain-state at a free surface with constant principal strain directions and determined principal strains ϵ_1 , ϵ_t and $\epsilon_r = -\mu(\epsilon_1 + \epsilon_t)/(1 - \mu)$ the equivalent strain is [1]

$$\epsilon_{eq} = \frac{\epsilon_1}{1 - \mu^2} \left\{ (1 - \mu + \mu^2) \left[1 + \left(\frac{\epsilon_t}{\epsilon_1} \right)^2 \right] - \frac{\epsilon_t}{\epsilon_1} (1 - 4\mu + \mu^2) \right\}^{1/2} \quad (2)$$

Poisson's ratio μ has to be obtained in the elastic-plastic range from the fatigue-dependent cyclic stress-strain curve by using the elastic Poisson's ratio μ_{el} , Young's modulus E , and secant modulus E_s [4]:

$$\mu = 0.5 - (0.5 - \mu_{el}) \frac{E_s}{E} \quad (3)$$

The equivalent stress σ_{eq} is determined by relating the equivalent strain to the fatigue-dependent cyclic stress-strain curve.

Influence of Structural Geometry

The geometry of a structural component (cross-section discontinuities, notches, etc.) causes local strains that exceed the material's 0.2 percent yield point in the low-cycle fatigue range. Due to the inhomogeneous multiaxial strain distribution along the surface and through the thickness an uncontrolled flowing of the material is restricted by the support of the less strained areas. By unloading the structure the less—that is, elastically—strained areas constrain the highly strained, plastically deformed areas. The amount of constraint depends on the load, strain distribution, strain concentration, and the local structural yield point. The relation between these design data will be discussed next on planar and cylindrical specimens having dimensions of small autoclaves (Fig. 3).

Figure 4 shows the longitudinal and tangential strain distribution along the inside and outside surfaces of cylindrical specimens, illustrating the effect of notch geometry. For the same load, the longitudinal strain at the notch root with the radius of 2 mm is higher and the strain gradient along the surface is steeper compared with the specimen with the 5-mm radius. Steeper gradients result in smaller volumes of highly strained material [6] and higher constraint. The influence of the size of highly strained volume on fatigue life will be considered and evaluated in the next section.

The relation between load and maximum longitudinal strain is shown in Fig. 5. Although the material's 0.2 percent yield point is exceeded on the first

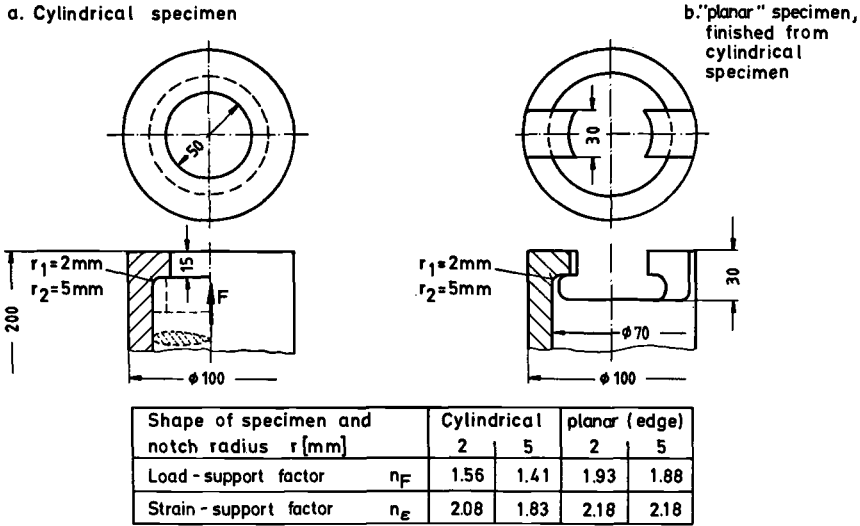


FIG. 3—Shape of the component-like specimens.

loading, an uncontrolled yielding of the material does not occur. The following unloading and subsequent reloadings and unloadings obey a linear load-strain behavior due to the high constraint provided, if the maximum load and the structural yield point are not exceeded.

To determine the local stress-strain behavior the biaxial strain-state must first be transformed into a uniaxial strain-state characterized by the equivalent strain and stress from Eq 2. By using the derived equivalent strains and relating them to the material's fatigue-dependent cyclic stress-strain curve, we obtain the local stress-strain history. The mean value and the amplitude of the equivalent strain determine the fatigue life.

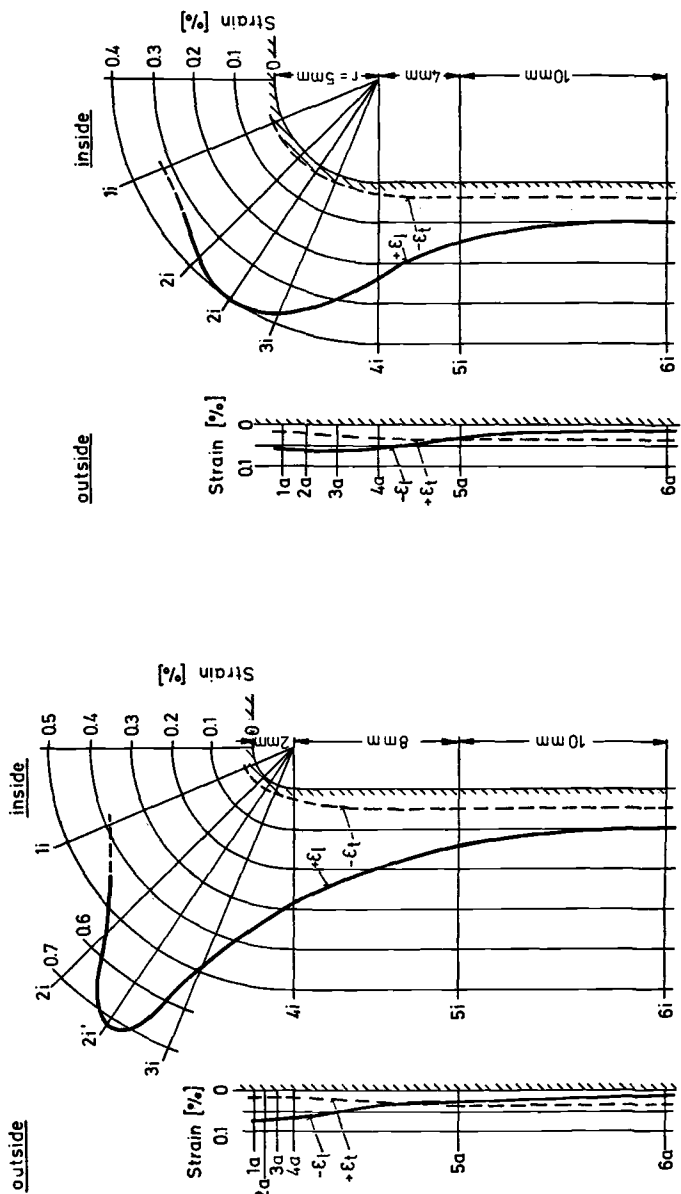
Like Fig. 5, Fig. 6 also shows that depending on the degree of constraint, the local strain can be significantly higher than the material's 0.2 percent yield point. The position of the structural 0.2 percent yield point is described by the factors of load- and strain-support

$$n_F = \frac{F_{0.2}}{F_F} \quad (4)$$

$$n_\epsilon = \frac{\epsilon_{eq,0.2}}{\epsilon_{eq,F}} \quad (5)$$

where $\epsilon_{eq,F}$ characterizes the material yield point reached at the load F_F , and $\epsilon_{eq,0.2}$ characterizes the structural yield point reached at the load $F_{0.2}$ (Fig. 6). Both strains are local equivalent strains calculated by Eq 2.

These factors n_F and n_ϵ can be derived by load- and strain-measurements or by calculation. The structural yield point is a limit that should not be ex-



$\epsilon_{\text{nominal}} = F/E \cdot A_n = 0.056 [\%]$; $F = 450\text{ kN}$
Gage length: $l = 0.6\text{ mm}$

FIG. 4—Strain distribution on cylindrical specimens with $r = 2$ and 5 mm notch radius.

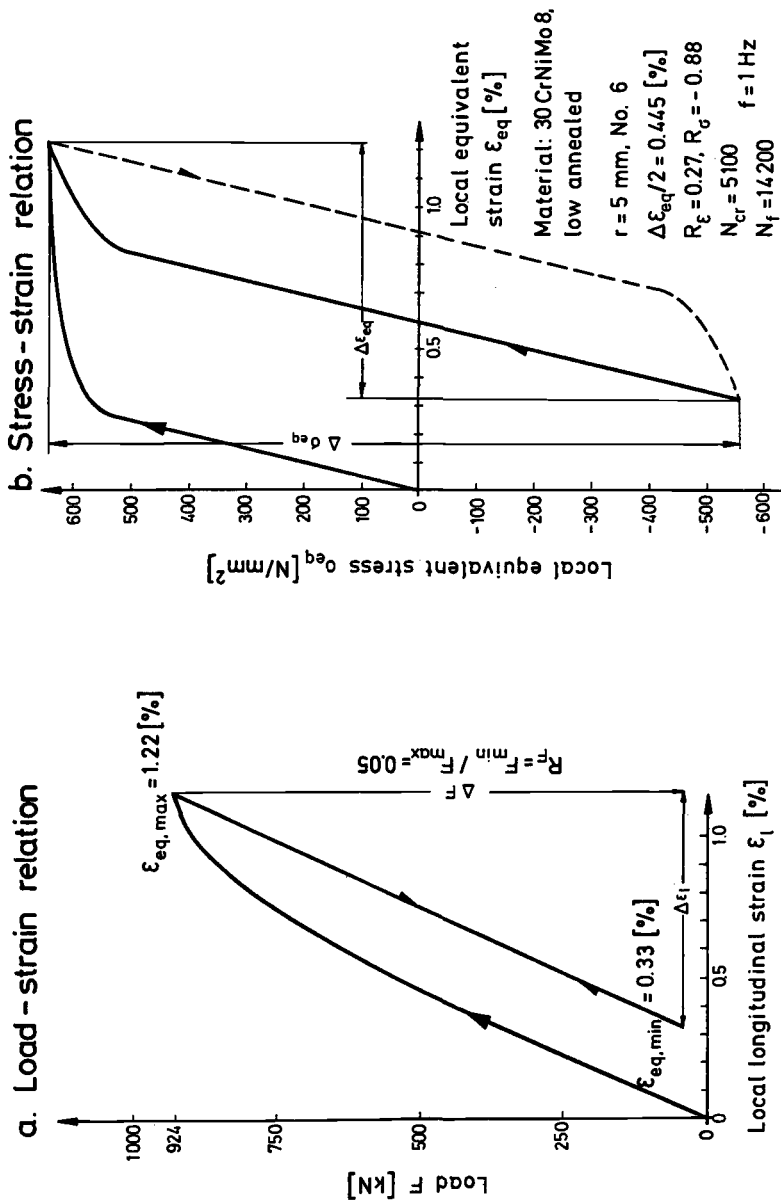
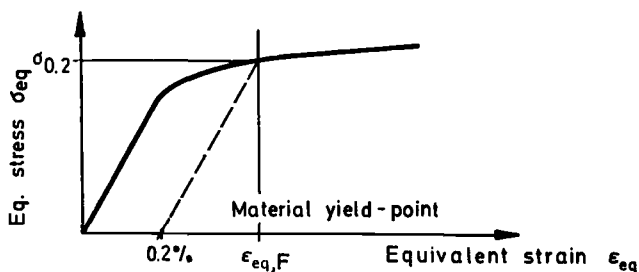
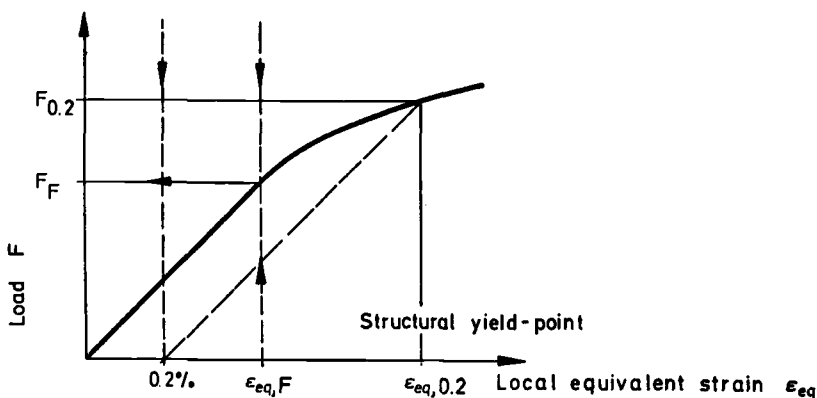


FIG. 5—Load-controlled biaxial stresses in notch root of a cylindrical specimen.

a. Monotonic stress-strain-curve ($K_t=1$)b. Monotonic load-strain-curve ($K_t > 1$)

Load-support factor :

Strain-support factor :

$$\eta_F = \frac{F_{0.2}}{F_F} > 1 \quad \eta_E = \frac{\varepsilon_{eq,0.2}}{\varepsilon_{eq,F}} > 1$$

$$\eta_F = \eta_E - \frac{0.002}{\varepsilon_{eq,F}}$$

FIG. 6—Support factors in relation material and structural yield point.

ceeded, because the structural function and the material's fatigue behavior can be affected so that its service performance and life can not be guaranteed. For many structures a stress concentration factor K_t can not be defined. By performing finite-element calculations or local strain-measurements for critical areas it can be determined if the structural yield point is exceeded or not. The approximation explained in Fig. 7 may also be used. The first step (1) is to obtain the local elastic behavior of the component by loading to the point where the equivalent strain is at the elastic limit of the cyclic stress-strain curve. The second step (2) is the linear extrapolation to the required proof

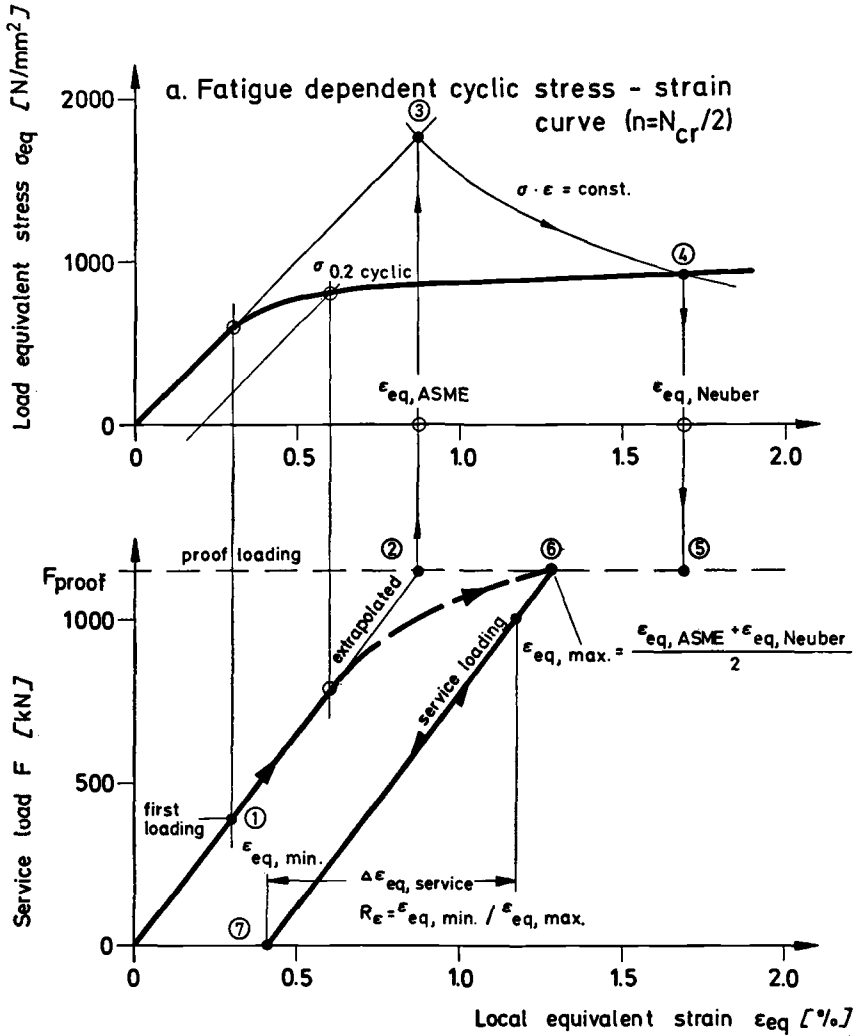


FIG. 7—Estimation of the load-local strain-curve.

load or service load, resulting in the equivalent strain $\epsilon_{eq, ASME}$ obtained from the ASME Code. This corresponds to the linear extrapolation of the cyclic stress-strain curve to the same equivalent strain, shown by step 3. By using the stress and strain values of point 3 and the Neuber rule [7],

$$\sigma \cdot \epsilon = \sigma_{point 3} \cdot \epsilon_{point 3} = \text{constant} \quad (6)$$

the equivalent strain $\epsilon_{eq, Neuber}$ is obtained, see steps 4 and 5. Experiments on several notched structures having high strain concentrations and on the component-like specimen (Fig. 3) show an underestimation of the local strain using the linear rule obtained from the ASME Code and an overestimation using the Neuber rule. A satisfactory approximation for the strain is obtained by the mean value of the two estimates, as at step 6.

$$\epsilon_{eq, max} = \frac{\epsilon_{max, ASME} + \epsilon_{eq, Neuber}}{2} \quad (7)$$

Between this value and the strain corresponding to the material's cyclic yield point $\sigma_{0.2, cyclic}$ a curve can be drawn and the structural yield point estimated. It can be then decided whether the initially required proof or service load can be accepted or should be reduced. After that, the first loading cycle can be completed and the local load-strain curve measured.

Fatigue Life to Crack Initiation and Crack Propagation

The results of the fatigue tests carried out with unnotched specimens and notched planar as well as cylindrical specimens are shown in Fig. 8. A comparison of the S - N curves for the unnotched and component-like notched specimens (Fig. 3) shows that by using the equivalent strain amplitude the fatigue life can be estimated with fatigue data from unnotched specimens. The larger scatter in the fatigue data of the notched specimens compared with the unnotched specimens, quantified by

$$T_N = 1 : (N_{cr, P_s=10\text{ percent}} : N_{cr, P_s=90\text{ percent}}) \quad (8)$$

(the ratio of fatigue lives N_{cr} for 10 and 90 percent probability of survival P_s) can be explained by the fact that different heats of material were used for the planar and cylindrical specimens. For the component-like specimens the fatigue life with the probability of survival $P_s = 50$ percent is higher than for the unnotched specimens, because of the smaller volume of highly strained material. For structures with a large highly strained material volume, the fatigue life will be shorter, because the statistical probability of material inhomogeneities (weak points) responsible for failure initiation is greater. This statistical size effect can be considered for large structures by relating their median life to the fatigue curve obtained with small unnotched specimens having a high probability of survival ($P_s > 90$ percent). The ratio between the life according to the design curve and the curve with $P_s = 50$ percent is a function of the scatter, which is cycle-dependent [1]. Considering these, we can derive statistical data fatigue design curves. It is assumed that the materials for specimen and component have identical technological properties and the same chemical composition, heat treatment, manufacturing, and finishing.

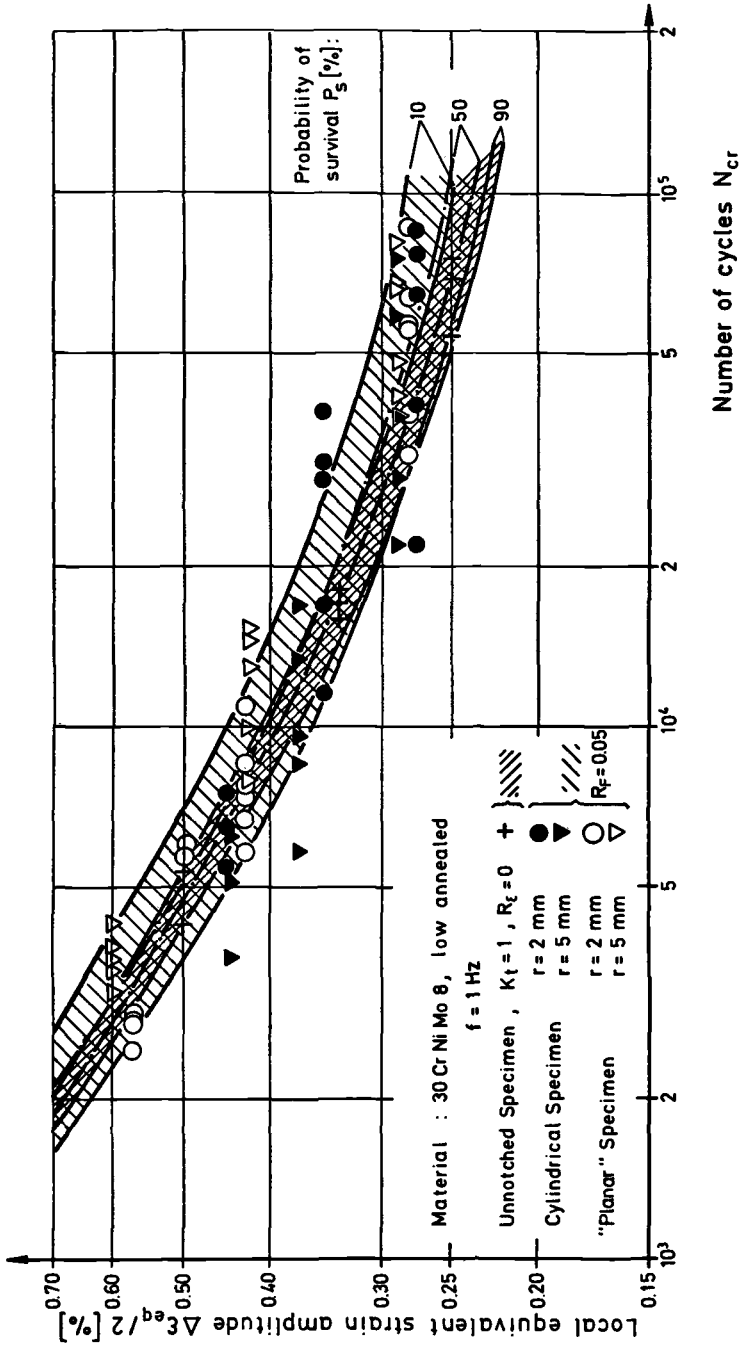


FIG. 8—S-N test results on unnotched and component-like specimens.

Having the same equivalent strains on specimen and structure, the fatigue life to crack initiation N_{er} will be the same, but the crack propagation life N_{prop} will be different. This part of the total life N_t is determined by the loading, the structural geometry, and the strain distribution along the crack propagation direction. By knowledge of fracture mechanical data and geometrical correction functions, derived from consideration of the geometrical size effect, the crack propagation life can be estimated. The decision of whether a crack propagation can be allowed depends on the functional reliability and security requirements.

From the fatigue tests (Fig. 8) it was observed that the unnotched specimens had a crack propagation life of about 20 percent of the total life to failure N_t , and the component-like specimen about 30 to 80 percent, depending on the notch radius and loading. Figure 9 shows that similar fatigue lives to crack initiation are expected for cylindrical specimens with $r = 2$ and 5 mm if the local equivalent strain is the same. However, for equal local strains, a higher load is applied to the $r = 5$ mm specimen than to the $r = 2$ mm specimen; the crack propagates faster for the specimen under higher loading because of the higher strain intensity at the crack tip. These results show that in some structures significant crack propagation lives can be expected. Service experience with thick-walled components shows that catastrophic failure occurs because of very small fatigue cracks, which are normally very difficult to detect and especially to evaluate [1]. For such cases only a fatigue life to crack initiation can be allowed.

Manufacturing Influences

In forming thick material sheets to vessel bodies or frames, cold-working up to $\epsilon_{pl} = 10$ percent may be induced. Such amounts of plastic deformations can also occur because of a proof load or an overload. If the subsequent cyclic strainings in service remain elastic, a higher fatigue life than for unprestrained material can be expected, because of the advantageous influence of the strength increase as well as the residual stress-strain state. If large cyclic plastic strain occurs, as is the case in the low-cycle fatigue range, the residual stress-strain states lose their importance. The fatigue life can also be affected by the value of prestrain. Tests carried out in the low-cycle fatigue range ($500 < N_{er} < 20\,000$) show that a mean strain equal to the strain amplitude has no effect or a negligible detrimental effect; the brittler the material the greater is this influence [1,5]. The maximum amount of these mean strains resulting from prestrains was $\epsilon_m \approx 1$ percent for the structural steels 30Cr-Ni-Mo8, 28Ni-Cr-Mo74, and FeE47. In further investigations on the fine-grained structural steel FeE47 [9] it was found that prestrains of $\epsilon_{pl} = 1$ and 5 percent had a marked influence on the fatigue life in the low-cycle range (Fig. 10). The load-controlled tests were carried out on notched specimens, prestrained prior to notching, with a frequency of $f = 1$ Hz. The increasing

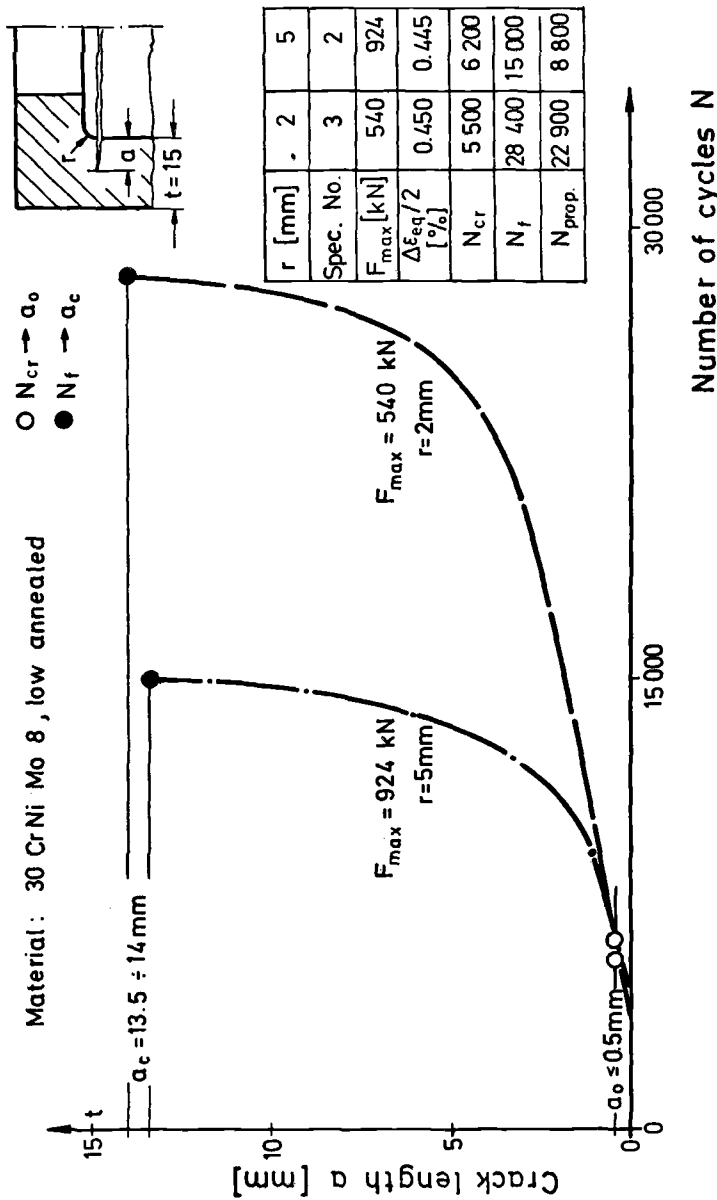


FIG. 9—Crack propagation curves for cylindrical specimen with $r = 2$ and 5 mm notch radius.

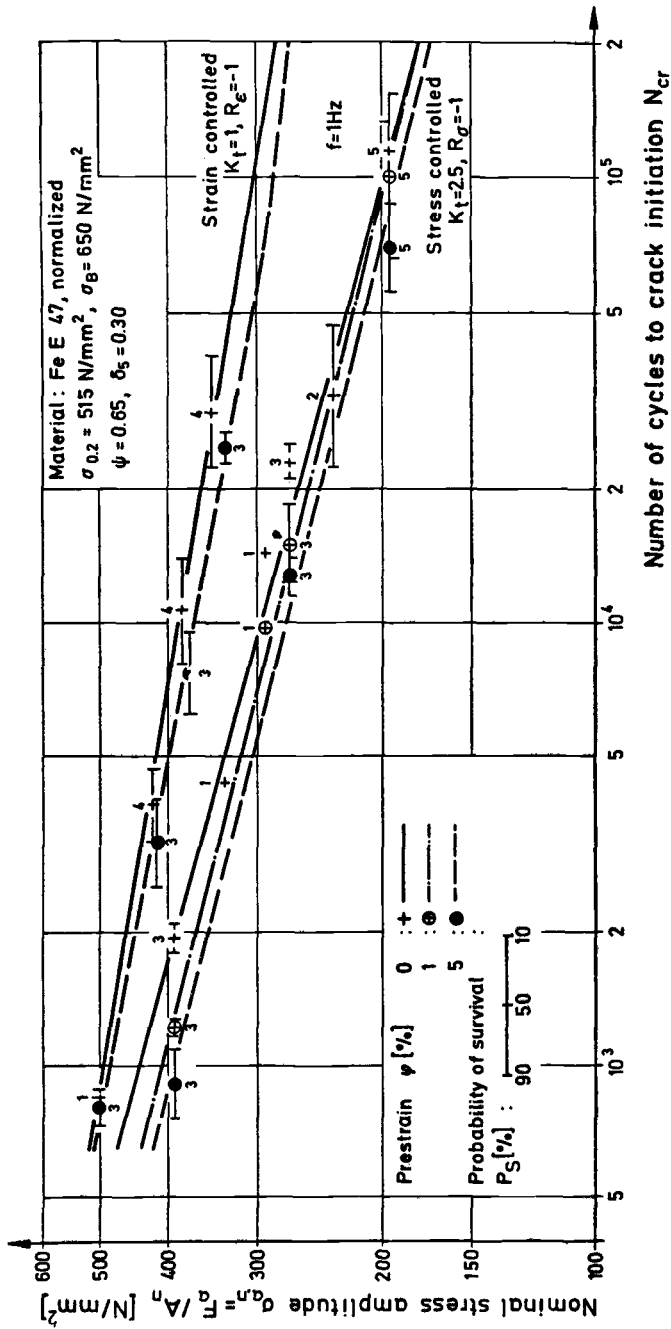


FIG. 10—Influence of prestrains on fatigue life.

reduction of fatigue life to crack initiation with increasing prestrain is owing to the cyclic softening (Bauschinger effect), which is favored by the low cyclic frequency and the strain distribution in the notch root. The cyclic softening observed by continuously increasing notch-ovality decreases the structural yield point. The fatigue life reduction for 5 percent prestrain was about two. It can be expected that for lower loading frequencies, which is the case for many pressure vessels, the fatigue-life reduction will be greater. These observations show the importance of cold-working induced by manufacturing or overloading on fatigue life and structural yield point. An optimum design must consider these effects.

Summary

An optimum design of thick-walled structures for a relatively low number of cycles requires knowledge of the local strain-state, its relation to the loading, and the knowledge of material properties—in particular, fatigue-life curves, fatigue-dependent cyclic stress-strain curves, and fracture mechanical data—all under service conditions. Using a valid failure criteria, the multi-axial strain-state can be transformed into a uniaxial strain-state by calculating an equivalent strain. From the relation between the load and the local equivalent strain, the component's yield point may be derived; depending on the strain concentration and the constraint it can be significantly higher than the material's yield point. In service the maximum operational load should not exceed the component's yield point in order to preserve its functional reliability. The fatigue life to a crack initiation (first detectable crack with defined length) can be estimated by comparing the equivalent strain with fatigue data from uniaxially stressed unnotched specimens. The size of the highly stressed material volume is considered by relating a high probability of survival to the fatigue-life curve obtained with strain-controlled tests on a small specimen having the same technological features as the structure. A crack propagation life can only be allowed in very special cases because of the necessity for security precautions. Experience proves that in thick-walled structures the critical crack length can be very small in comparison to structural dimensions, because of very high strain intensities on the crack tip. Investigations with prestrained specimens show that a plastic deformation between 1 and 5 percent can lead to a significant fatigue-life reduction due to softening effects which decrease the structural yield point. Such prestrains can result from manufacturing or loading beyond the structural yield point. The consideration of these details can enable one to derive fatigue curves that allow reliable fatigue-life predictions.

References

- [1] Grubisic, V. and Sonsino, C. M., "Fatigue Behaviour of High-Pressure Vessels," Rep. No. FB-148, Fraunhofer-Institut für Betriebsfestigkeit (LBF), Darmstadt, 1979, in German.
- [2] Manson, S. S., *Experimental Mechanics*, Vol. 5, No. 7, July 1965, pp. 193-226.

- [3] Grubisic, V. and Simbürger, A., "Fatigue under Combined Out-of-Phase Multiaxial Stresses," in *Fatigue Testing and Design*, Vol. 2, pp. 27.1-27.28, International Conference of Society of Environmental Engineers, 5-9 April 1976, City University, London.
- [4] Gonyea, D. C. in *Fatigue at Elevated Temperatures*, ASTM STP 520, American Society for Testing and Materials, 1973, pp. 678-687.
- [5] Grubisic, V. and Sonsino, C. M., "Strength Evaluation of Steel Structures for Low-Cycle Fatigue," Rep. No. FB-134, Fraunhofer-Institut für Betriebsfestigkeit (LBF), Darmstadt, 1977, in German.
- [6] Raske, D. T., *Journal of Testing and Evaluation*, Vol. 1, No. 5, Sept. 1973, pp. 394-404.
- [7] Neuber, H., "Research on the Distribution of Tension in Notched Construction Parts," WADD TR 60-906, Jan. 1961.
- [8] "ASME Boiler and Pressure Vessel Code," Section III, Division 1, Rules for Construction of Nuclear Power Plant Components, 1974.
- [9] Sonsino, C. M. and Hagedorn, K. E., *Archiv Eisenhüttenwesen*, Vol. 51, No. 8, 1980, pp. 341-345.

Summary

Summary

The purpose of the conference organized by the Centre de Recherches Unieux of Creusot-Loire, in collaboration with ASTM, at Firminy, France, on 23–25 September 1980, was to discuss the state of the art of low-cycle fatigue problems and to provide a forum for an exchange of views between people working both in research and in design areas of low-cycle fatigue and life prediction.

The main industries directly concerned are those of mechanical engineering and particularly aeronautics and nuclear energy, with an increasing interest in the latter industry for obvious safety reasons. A substantial part of the conference was devoted to energy production problems.

Six themes were treated:

1. High-temperature fatigue—Thermal fatigue—Environment
2. Application of plastic fatigue to crack initiation
3. Constitutive laws of fatigue plasticity—Damage prediction
4. Related problems
5. Complex loadings (multiaxial and variable amplitude testing)
6. Use of low-cycle fatigue data in the design of components

Some of these themes were introduced by review papers, which presented the main findings of the literature and proposed areas where further research is necessary. Most of the papers presented are discussed below.

A review of creep-fatigue interaction problems by *Chaboche* described the possibilities of phenomenological lifetime relations based on strain variables, and also presented alternative approaches based on continuous damage mechanics. This review emphasized the need to relate the continuous damage approach to microscopic theories in order to improve the modeling of physical processes, and also to avoid the simplifying hypothesis of creep and fatigue damage additivity.

Concerning the first aspect—that is, phenomenological creep-fatigue models—*Bernstein* evaluated the ability of four current creep-fatigue models to predict the high-temperature low-cycle fatigue behavior of nickel-base super alloys: (1) strainrange-partitioning model, (2) frequency-separation model, (3) frequency-modified damage function, and (4) damage-rate model. The author presented an empirical lifetime expression that appears

to correlate better with his results. *Mottot et al* also applied different methods for extrapolating results on a 316L stainless steel to the very long hold times encountered in fast breeder reactor components (~ 1000 h). These methods were based on a time-temperature equivalence comparable to those used for extrapolating creep-rupture data. A correlation between the reduction of fatigue life with the amount of stress relaxation during hold times was also found.

Concerning the second aspect—that is, microscopic theories—*Levaillant and Pineau* showed that quantitative measurements of intergranular damage made on creep-fatigue specimens could be used to model creep-fatigue interaction in two austenitic stainless steels. The results of this and previously published studies were used to extrapolate short-term data.

Plastic fatigue has been applied to crack initiation using both the physical mechanisms and mechanics approaches. *Magnin and Driver* investigated the mechanisms of low-cycle fatigue damage of very high purity ferritic alloys, using both single and polycrystalline specimens. The cyclic stress-strain behavior and the fatigue crack initiation mechanisms in polycrystals are sensitive to the applied strain rate and the crystal orientation; crack initiation in these steels tends to be transgranular at low and medium strain rates and intergranular at high strain rates.

A mechanical approach to crack initiation was presented by *Truchon*, which correlated classical low-cycle fatigue test results to notched specimen behavior in high-strength steels by using Neuber's rule. An elasto-plastic fatigue strength reduction factor was used to account for local plasticity effects in fatigue crack initiation.

The particularly interesting field of short crack growth during high strain fatigue and thermal cycling was reviewed by *Skelton*. Growth rates in high strain fatigue can be related to those in stress intensity controlled tests by using either a strain-based intensity parameter or a J -integral, in order to predict component failure. Experimental and theoretical high strain fatigue growth rates were shown to be consistent with smooth specimen endurances. The effects of temperature, environment, tension dwells, and microstructural damage in several alloys were also discussed. The accelerating effect of creep during dwell appears to require the greatest corrections to the experimental and theoretical growth relations.

The initiation and growth of short cracks at circular notches in a 2024 aluminum alloy was experimentally examined by *Leis and Galliher*. The free surface was shown to influence short crack behavior, whereas inelastic action influences the growth rate within the entire notch field. The authors conclude that an inelastic analysis which allows for the driving force for crack growth in the plastic notch field is required.

A study of thermal fatigue by *Reuchet et al* examined the accumulation of low-cycle fatigue damage in a Mar M 509 superalloy under sequential testing

at two temperature levels. A large deviation from the linear cumulative damage rule was observed. This behavior was qualitatively explained on the basis of the temperature-dependent initiation mechanisms and the microcracking processes. It would be useful if further experimental and analytical studies were conducted in the field of thermal fatigue.

High-temperature environmental effects are described in detail on different materials: a carbon pressure vessel steel (*Ranganath et al*), a Cr-Mo-V steel (*Wada et al*), and a titanium-based alloy (*Hoffmann et al*).

Air environment plays an important role in determining the fatigue lifetime and fatigue crack initiation process during high-temperature low-cycle fatigue of titanium alloys: (1) in air, crack initiation occurs at the specimen surface predominantly along α - β interfaces as a result of preferential oxidation; and (2) in vacuum, crack initiation occurs beneath the surface, and the role of surface cracking in vacuum is minimal.

The aforementioned study of Wada et al of a Cr-Mo-V steel in high-temperature air and steam confirmed the detrimental effect of decreasing frequencies and increasing levels of oxygen content.

Cyclic plasticity and its relation to low-temperature creep and fatigue damage was examined by several authors.

Two studies examined the cyclic stress-strain response of a 316 stainless steel (*Pellissier-Tanon et al* and *Nomine et al*) under strain and load control. In both studies progressive deformation occurred, by creep, at room temperature under repeated loading at maximum stresses greater than a critical value. Pellissier-Tanon et al showed that progressive deformation is possible between 20 and 300°C for stress amplitudes greater than some critical range. These results show that the ASME Code rule which limits the range of primary plus secondary stress intensity gives an effective guarantee against progressive deformation for operating conditions in the range of 20 to 300°C. The study of Nomine et al also examined room-temperature creep behavior for constant loads after cycling.

An experimental study of fatigue damage accumulation during low-cycle fatigue of notched aluminum alloy specimens by *Bathias et al* demonstrated that an energy modified Miner's law could be used to predict lifetimes under sequential loadings.

The room-temperature low-cycle fatigue of cast iron and structural steels for different applications is treated in several papers. In particular, *Starkey and Irving* demonstrate the possibility of combining microstructural and fracture mechanics approaches to predict fatigue lifetimes in smooth specimens of SG irons. ΔJ -values and integrated crack growth rates were calculated as a function of pore size, and the predicted fatigue life-times were compared with the experimental values. Fatigue lifetimes were found to be sensitive to pore size rather than to nodule size, in agreement with the predictions.

D'Haeyer and Simon describe a statistical analysis of the low-cycle fatigue behavior of several high-strength steel plates, candidate materials for pressure vessels. The fatigue properties of such steels are relatively insensitive to variations of mechanical properties or chemical composition, and their use could be considered for the fabrication of pressure vessels.

Lieurade and Maillard-Salin have carried out low-cycle fatigue tests on different types of welded joints in structural steels. In the case of butt joints, the results show differences in behavior, depending on the welding process; submerged arc welding gave better results than manual arc welding. These differences are explained by the bead profile and the microgeometry at the bead toe.

The evolution, during the past twenty years, of criteria for multiaxial low-cycle fatigue failure is reviewed by *Brown and Miller*. It appears that the octahedral equivalent strain approach currently used for yield and fracture is unsatisfactory. Improved correlations containing two strain parameters are proposed to cover both ductile and brittle materials in the high and low cycle fatigue regimes. The form of these correlations may be related to the mechanisms of crack nucleation and growth, so that certain criteria may be selected which are linked to the strain conditions found on the observed planes of crack growth.

An experimental study of biaxial low-cycle fatigue of 316 stainless steel is reported by *Moguerou et al.* The cyclic behavior of thin-walled tubes in axial tension-compression and internal-external pressure was determined using both in-phase and 180-deg out-of-phase cycles. The Tresca criterion was found to be conservative and a generalized von Mises criteria was proposed.

Finally, several papers are concerned with the use of low-cycle fatigue data for the design of structures.

Jaske indicates that materials data are essential to the proper formulation of fatigue design guidelines for pressure vessel systems: (1) to substantiate and verify prediction methods used in fatigue damage analysis, and (2) to quantify the fatigue behavior of various alloys from which pressure vessels are fabricated. In this context, *Jaske* addresses the data needs within the framework of the ASME Boiler and Pressure Vessel Code. Both low-temperature (negligible creep) and high-temperature (significant creep) regimes together with crack-initiation and crack-propagation damage criteria are addressed. Areas where fatigue damage criteria need to be improved are creep-fatigue environmental interaction at low strain ranges and long times, thermal-mechanical fatigue, multiaxial fatigue, and long-life fatigue.

Lawton illustrates the use of fatigue design curves by demonstrating the evaluation of fatigue life for two fossil fuel boiler components.

The aforementioned paper by *Ranganath et al* describes the results of a combined experimental-analytical program on the fatigue initiation behav-

ior of carbon steel components in high-temperature environments. The analytical approach is focused on improved procedures for determining local strain, mean stress, and environmental effects. The approach is to determine correction factors to be used with current ASME Code practice.

C. Amzallag

Creusot-Loire, Firminy, France; symposium
co-chairman and co-editor

B. N. Leis

Battelle Columbus Laboratories, Columbus,
Ohio; co-editor

P. Rabbe

Creusot-Loire, Firminy, France; symposium
co-chairman and co-editor

Index

A

A-c potential drop technique, 259
 Aeronautical structures, use of aluminum in, 23, 25, 29, 39
 Aging effects, 184, 370
 Dynamic, 197
 Alloys (*see also* specific classes; Superalloys)
 Fatigue behavior of, 601
 Turbine disk, 146
 Aluminum, 400
 Chemical composition of, 24
 Damage accumulation in, 23–44
 High-strength, 270, 285
 Tensile properties, 25
 Argon gas environment, 424, 426–431, 434
 ASME Codes
 Boiler and Pressure Vessel Code, 69, 135, 492, 588, 608, 622, 623
 Section I, 586, 594, 595
 Section III, 79, 436–438, 440, 444, 446–448, 454, 601
 Section VIII, 79, 586, 587, 601
 Section XI, 603
 Subcommittee on Fatigue Strength, 605, 608
 Nuclear Code Case N47, 592, 602, 609
 Nuclear vessels for, 527, 530
 Rules for In-Service Inspection of Nuclear Power Plant Compo-

nents, Section XI, 461–463, 468, 471, 474, 475, 477, 479
 ASME design curves, 305, 306, 589
 ASME fatigue design, 440, 594, 603
 ASME N47 TI420-2, 165, 166, 168
 ASME Specification SA204C, 593
 ASTM Test for Plane-Strain Fracture Toughness of Metallic Materials (E 399), 424

B

Body-centered-cubic materials, low-cycle fatigue damage in, 212–225
 Buckling, 522

C

Carbides, 195, 201, 208
 Oxidation of, 206, 207, 209
 Size of, 207
 Cavities (*see also* Cracks; Flaws)
 Damage, 128
 Grain boundary, 82
 Growth, 125, 128, 130, 190
 Size, 125, 127
 Chemical plants, 81
 Cold-working, 625, 628
 Corrosion, 143, 147, 148, 423 (*see also* Environmental-corrosion sensitive materials; Environmental effects)

- Effects, 558, 586, 587
- Potential measurements, 440
- Crack
 - Advance (*see* Growth)
 - Closure, 148, 293, 395
 - Critical size, 127
 - Density, 210
 - Depth, 390, 392
 - Detection, 242, 243
 - Engineering, 285
 - Growth, 140, 391
 - Accelerated, 12, 42, 142, 170, 247, 468, 615
 - At circular notches, 399–420
 - Cycles for, 176, 189, 190
 - Damage accumulation at, 42, 135
 - Dependence on microstructure, 6
 - Environmentally accelerated, 464, 465, 471–473
 - Equation, 130
 - Hydrogen-assisted, 468–474, 479
 - Measurement techniques, 401
 - Mechanisms of, 466–468
 - Model, 138–141
 - Path, 198
 - Process, 125
 - Reduction of, 182, 184
 - Resistance to, 6, 20, 21
 - Retardation, 476
 - Growth law, modification, 375–378, 396
 - Growth rate, 138, 140, 148, 174, 181, 191, 234, 384, 387, 390, 392, 412, 423, 464, 465, 478, 492
 - As function of crack length, 409–411
 - As function of stress intensity, 414–416, 417
 - Factors controlling, 418, 419
 - Frequency-dependent, 471
 - HSF, 340–349, 365–367, 374, 376
 - Light-water reactor effect on, 460–479
 - Predicting, 402
 - Growth region
 - Final, 473, 474
 - Intermediate, 471
 - Initiation
 - Actual versus predicted, 271, 282–284, 294
 - Analysis of, 36, 37
 - At notches, 254–267, 289–295
 - At notch roots, 29–35, 39–42
 - Criterion, 31, 207
 - Cycles to, 204, 209, 243, 246, 250, 251, 260, 320, 321
 - Detection of, 231, 257–259, 265, 275
 - Deterioration, following, 86
 - Environment, high-temperature, 422–435
 - Experimental behavior, 289–291
 - Fatigue life, 12, 23, 231, 623–625
 - In unnotched specimens, 289–295
 - Life behavior, 281, 566
 - Location, 8, 12, 14–17, 19, 113, 198, 208, 320, 322–326, 395
 - Macroscopic, 81, 82, 83, 84
 - Mechanisms of, 195, 221–223, 271, 272
 - Microstructure, dependence on, 6
 - Period, definition of, 206–211
 - Predictions, 254, 265, 279–281, 285–289
 - Premature, 6, 228
 - Process, 12, 13, 21
 - Resistance to, 6
 - Separating, 558
 - Temperature, 200, 201, 212
 - Transgranular, 203
 - Initiation life curves, 277, 278
 - Intergranular, 177, 178, 181, 182, 188, 221, 225

- Length, 139, 141, 174, 175, 177, 231, 242, 341, 360, 412, 418
 - As function of cycles, 402-404
 - Effect of, 31
 - Growth rate, 409-411
 - Measurement of, 233
 - Variations in, 204, 205
 - Versus cycles, 234
- Nucleation of, 138, 225
- Propagation (*see also* Growth)
 - Analysis, 399
 - Fatigue life to, 623-625
 - Law, 535-537
 - Low-cycle fatigue, 608
 - Mode, 539-542
 - Periods, 195, 206, 209
 - Reduction of, 207, 209
 - Separating crack initiation, 558
 - Stage I, 174, 181, 200, 204, 206, 270, 271, 342, 489, 491, 493, 535
 - Stage II, 201, 204, 206, 342, 348, 489, 491, 535
- Retardation, 289, 293, 583
- Short
 - Corner, 399-420
 - Effects, 395
 - Growth of, 337-378
- Size, 265, 289
- Small, 289
 - Analysis of behavior, 291-293
 - Initiation of, 294
- Subsurface, 19-21
- Thermal fatigue, 373
- Crack tip
 - Advance, 395, 466, 467
 - Opening displacement (CTOD), 341, 349, 361, 369, 370, 372, 472
 - Radius, 139
 - Strain concentration, 347
 - Stress-strain near, 138
- Cracking, stages of, 289, 290, 294, 295
- Creep, 5, 46, 49, 61, 113
 - Behavior, 76, 77, 107
 - Compressive, 83
 - Crack initiation under, 81
 - Cyclic, 46
 - Cyclic tension deformed material, 56
 - Cumulative, 194
 - Damage, 83, 84, 90, 91, 132, 143, 148, 165-167, 170, 181, 183, 194, 195, 354, 377, 587, 595
 - Deformation, 108, 109, 131, 136, 154, 165
 - Deformed material, 56, 68
 - Ductility, 591
 - Effect, 141, 147, 148
 - Elongation, 54-56, 60-63, 76
 - Endurance, 91
 - Failure, 92
 - Mechanical, 183
 - Prediction of, 92
 - Primary, 156, 161, 162
 - Process, 98
 - Properties, 154, 156, 171, 595
 - Pure, 98, 100
 - Rate, 49, 119
 - Remaining-life studies under, 89
 - Resistance, 106, 152-168, 183
 - Rupture, 49, 91, 98, 99, 154, 156, 165, 590, 591
 - Secondary, 156, 161
 - Strain, 63, 82, 84, 161, 590
 - Stress, 63, 68
 - Tests, 47-49, 52, 56, 76, 78, 88, 108, 117, 154, 188
- Creep-fatigue, 177, 178
 - Austenitic steels, 153
 - Cycle, 182
 - Damage, 99, 100, 359
 - Initiation behavior, 338
 - Interactions, 81, 86, 89, 96-99, 101, 109, 135, 138, 139, 162, 167, 181, 189, 211, 363, 609, 610
 - Loading, 190, 191

Mechanisms, 170
 Models, 105–133
 Properties, 169, 184
 Resistance, 180
 Tests, 157–159, 165, 171
 Crystallographic Stage I growth, 405, 417
 Cycles to failure, 10, 83, 85, 93, 114, 115, 117, 119, 143, 156, 189, 198, 199, 429, 433, 447, 530, 574, 575, 578
 Function of strain amplitude, 260
 Versus total strain range, 13

D

Damage

Accumulation, 42, 135, 202, 610
 Effects of, 25
 In HTLCF, 135–150
 In smooth specimens, 35–38
 Linear, 25, 162, 163
 Low-cycle fatigue, 23–44
 Bulk, 171, 178–180, 182, 183
 Creep, 90, 91, 141, 339
 Creep and fatigue interaction, 590, 592, 599
 Cumulative, 81–101
 Definition of, 85–89, 277
 Equations, 89, 90, 93
 Evaluation concepts, 289
 Haibach/Lehrke, 277, 280, 281, 284
 New, 283–289, 294
 Rainflow counting, 277
 Smith et al, 278, 279, 281, 284, 285, 294
 Fatigue, 84, 91–95, 101, 162, 194, 586, 594, 595
 From continuous cycling, 127
 Function, 182, 191, 192 (*see also* Frequency-modified damage function)

Function of, 35, 37
 Grain boundary, assessment, 178–180
 Intergranular, 169–191
 Load sequence effects, influence of, 281–285, 289, 293
 Low-cycle fatigue, 73, 123, 125
 In body-centered-cubic materials, 212–225
 Measure of, 85–87
 Mechanics, continuous, 82, 84, 101
 Mechanisms, 159
 Low-cycle fatigue, 212–225
 Nonlinear, 270
 Process, 271, 400, 420
 Analysis of, 281–289
 Rubbing, 177
 Rule
 Interaction, 116
 Linear, 165, 166, 208–210, 283
 Stress-dependent, 93
 Time-dependent, 113, 119, 123, 131
 Damage-rate model (DRM), 106, 120, 125–132
 D-c potential drop technique, 339, 426, 427
 Defects, 6, 395, 396 (*see also* Cracks; Flaws)
 Effects of, 31
 Micro, 82
 Sizes of, 387, 394, 396
 Deformations, 61, 62, 68
 Behavior, 56
 Due to creep, 56, 68, 593
 Cyclic, 212, 220, 221, 401
 Plastic, 219, 224
 Elastic-plastic, 275, 615
 From cyclic tension, 63
 High-temperature fatigue, 339
 Multiaxial nonproportional cyclic, 501–518
 Plastic, 48, 56, 78, 190, 220, 225, 278, 489, 625, 628
 Prediction of, 45

Progressive, 46
 Resistance to, 69–80
 Time-dependent, 76
 Zone, 340, 361, 377
 Design
 Application, 569
 “Fail safe”, 6
 Assessment, 339
 Of heavy machinery, 549, 550
 Pressure vessel, 585–599, 600–610
 Requirements, 81
 Rules, 450–456
 Deterioration process, time-controlled, 90
 Discontinuities
 Effect of, 227–252
 Environment interaction, 237, 242, 252
 Dislocation
 Density, 62, 63, 224
 Pile-up, 82
 Substructures, 62, 63
 Ductility, 6, 13, 28, 91, 106, 265, 590
 Creep-rupture, 116, 117
 Dwell, effect of, 353–355, 357–359, 362, 363, 366

E

Elastic field, 140
 Elastoplastic fatigue strength reduction factor, 260, 265
 Elastoplastic incompatibilities, 223
 Elastoplastic structure analysis, 78
 Elongation, 47, 49, 56
 Creep, 49, 54–56, 60–63
 During cyclic tension, 57–61
 Of crystals, 218
 Embrittlement effect, 466–468, 472–477, 479
 Cryogenic temperatures, 601
 Endurance, 340–349
 Crack growth, 348, 349
 Fatigue, 174

Integrated, 359–362
 Phases of, 23
 Reduction in, 364
 Energy, 29, 82, 139, 141–143, 148, 150
 Engineering applications, 45
 Engines, jet, 81
 Environmental attack
 By oxidation, 119 (*see also* Oxidation)
 Cause of damage, 113, 123, 131, 132
 Interaction with creep, 106, 109
 Environmental correction factor, 454–457
 Environmental-corrosion sensitive materials, 142
 Environmental effects, 357, 367–369, 603, 605, 609, 610
 Accelerated crack growth, 464, 465, 471–473
 Aggressive, 603, 610
 Corrosive, 615
 On crack initiation and propagation, 242
 Discontinuities interaction, 237, 242, 252
 Fatigue, 13, 101, 109, 132, 236
 High-temperature, 422–435
 High-temperature water, 436–457
 Interaction with creep, 109
 Interaction with creep and fatigue, 109, 132
 Light-water reactor, 460–479

F

Failure, 6, 20, 90, 290
 Criterion, 321, 322, 535
 Life, 143, 148
 Location, primary, 576, 578
 Mechanism of, 494
 Mode, for disks, 105
 Pore initiated, 392, 393
 Shear theory, 596

Fatigue

Analysis, 594

Behavior, 5, 110–113, 131

Isothermal, 198–201

Of carbon steel components,
436–457

Of forging steels, 227–252

Temperature-dependent, 195,
198

Criteria, 488–494

High-cycle, 485, 486

Damage, 84, 91–95, 101, 194, 594,
595

High-endurance, testing for, 519

High-strain (HSF), and growth of
short cracks, 337–378

High-temperature, 139

High-temperature low-cycle
(HTLCF), 6, 8, 10, 12, 20, 21,
105, 106, 108, 109

Assessment of, 169–191

Damage accumulation, 135–150,
194–211

Fracture life in, 135–150

Isothermal, 605, 606, 608

Life, 12, 21, 113, 132, 145, 157,
160, 161, 165–168

At crack initiation, 535–536

Continuous cycling, 173

Decrease in, 13

From biaxial strain, 530–533

Hydrogen, effects on, 229

Multiaxial low-cycle, assessment
of, 483–496Prediction of, 110, 116, 117, 165–
167, 183, 188–191, 383–397,
437, 443

Range, 323–332

Reductions in, 159, 165–168,
181–184

Relationships, 315

Low-cycle (LCF), 6, 23, 27–29, 35,
260–265

Plastic, 23

Process, 29, 106

Properties, 157

Pure, 100, 181, 188, 191

Resistance, 5–21, 28, 29, 42, 148,
157–159, 163, 210, 211, 213,
223, 601

Strength, 12, 20, 551, 569

Thermal-mechanical, 605, 606,
608, 610

Time-independent, 123

Fatigue notch factor, 34, 36, 250–252,
323–325

Fatigue performance, low-cycle

Effect of chemical composition on,
309Effect of tensile properties on, 308,
309Influence of yield stress/tensile
strength ratio on, 309

Fatigue-relaxation, 152–168

Fatigue strength reduction factor,
264, 437, 447, 448, 450–452Fatigue stress concentration factors,
250Fatigue testing (*see also* Testing
methods, fatigue)

High-cycle (HCF), 483

Low-cycle (LCF), 483, 520

Flaw size, 573, 575, 579, 580 (*see also*
Cavities; Defects)

Critical, 247, 574

Residual strength, 581

Fracture

Appearance of, 159

Elongation, 308, 309

Fatigue, 21

Formation, 125

Intergranular, 167, 178, 180

Life, 135–150

Mechanics

Analysis of, 422, 487

Considerations, 568, 569

Elastic-plastic, 293

In predicting fatigue life of SG

- iron, 383–397
 - Linear elastic (LEFM), 338, 339, 341, 349–353, 354–359, 362–365, 367, 369, 371–373, 375, 377, 399, 411, 412, 423
 - Techniques, 572, 573
 - Utilization of, 34, 82
 - Morphology, 12
 - Surface, 12, 19, 159, 175, 177, 178, 200, 201, 244–246, 406, 407
 - Fractographic aspect of, 533–535
 - Toughness, 5, 6, 615, 616
 - Transgranular, 173
 - Frequency
 - Compression-going, 141
 - Cycle, 10, 12, 13, 121, 123, 423, 426, 429–435
 - Effect of, 353, 354, 358, 378
 - Influence of, 148
 - Tension-going, 119, 121, 141
 - Test, 56
 - Frequency-modified damage function (FMDF), 106, 120, 123–125, 130–132
 - Frequency-modified life relation, 82, 84
 - Frequency-separation (FS) Model, 106, 119–122, 130–132
- G**
- Generator
 - Fossil-fueled steam, 585
 - Rotor forgings, 228–252, 337
 - Guests' law, 485, 494, 495
- H**
- Hardening, 6, 27, 29, 100
 - Curves, 198
 - Cyclic, 98, 99, 158, 161, 163, 219, 220, 223, 224
 - Influences of, 96
 - Isotropic, 514
 - Monotonic strain, 79
 - Of crystals, 215–217
 - Plastic, 513
 - Rapid, 214
 - Rule, 507, 508
 - Garud's, 505–507
 - Mroz-type, 502–505, 507, 514, 518
 - Tresca, 503–505, 508, 509
 - Healing, crack, 140 (*see also* Crack, closure)
 - Heat-affected zone (HAZ), 313–315, 322, 327, 335, 371, 462
 - Heat-treatment, 5, 7, 25, 313, 322, 334, 550, 608
 - Hold time, effects of, 157–161
 - Hook shank, A-7E arresting gear, fatigue life evaluation, 572–584
 - HTLCF (*see* Fatigue, high-temperature low-cycle)
 - Hydrogen
 - Accumulation, 473
 - Assisted cracking, 467–474, 479
 - Effects of on fatigue life, 229, 231, 233, 234, 236, 237, 247
 - Embrittlement, 466, 468, 472–477, 479
 - Hysteresis loop, 108, 113, 119, 138, 139, 141, 143, 147, 148, 218, 219, 277, 278, 298, 302, 338, 340, 341, 350, 503, 515, 521, 529–531, 560, 561, 591, 592
- I**
- IN 100, 136
 - IN 939, 140
 - Inconel 718, 138, 140, 145, 146
 - Intensity factor, strain-based, 352, 353 (*see also* Stress intensity factor)
 - Iron, prediction of fatigue life in, 383–397
 - Iron-based alloy, 212–225

J

Joints, welded, low-cycle fatigue behavior in, 311–326

L

Landgraf's law, 38, 39, 42
 Life duration, 27, 29, 30, 35
 Life reductions, component, 153
 Lifetime, predictions, 116–118, 120–124, 128, 129, 131, 132, 138, 164
 According to Miner's rule, 204
 Application of crack initiation period to, 206–211
 High-temperature conditions, 81–101
 Techniques, 141
 Load sequence effects, analysis of, 281–285, 289, 293, 294

M

Macrocracks, formation of, 125, 127, 291, 293, 299, 400
 Manson-Coffin curve, 255, 266
 Manson-Coffin law, 116, 119, 121, 123, 131, 132, 195, 487, 488
 Manufacturing influence on structural steels, 625–628
 Microcrack, 82, 468
 Density, 206
 Fatigue, 405, 406
 Formation of, 206, 208
 Forming macrocracks, 125, 127
 Growth, 139, 275, 400
 Initiation, 427, 428
 Mechanisms, 204
 Origin of, 201, 204
 Process, 198, 210
 Propagation, 89, 91, 101, 125
 Microstructure
 Effects of, 369–372
 Influence on titanium alloy fatigue

resistance, 5–21

Microvoid formation, 468
 Miner's damage, 204, 205
 Miner's law (rule), 35, 38, 39, 42, 44, 203, 204, 206, 208–210, 569, 601, 603
 Linear, 84, 85

N

Neuber control method, 270
 Neuber control tests, 275, 285–288
 Neuber equation, 275
 Neuber relation, 376
 Neuber rule, 35, 247, 255, 257, 260, 262, 263, 266, 267, 331, 332, 443, 452, 552, 564, 565, 571, 622, 623
 Neuber simulation, 262, 265, 267
 Nickel-base alloys, 89, 95–97, 100, 143, 144
 Notch analysis
 Computerized, 275–278
 Evaluation program, 271–281
 Numerical prediction capability of, 270–294
 Of damage accumulation process, 281–289
 Prediction versus actual behavior, 278–281
 Notch
 Circular, crack growth at, 399–420
 Compact tension specimen, 234, 238–241
 Effect, 332, 333
 Factor, analytical procedure for, 451–453
 Field, 414, 415
 Influence on cracking, 291, 293, 410, 411
 Root, 23, 404, 405, 426, 427
 Crack initiation at, 29–35, 38–42, 287
 Plasticity, 402

Stress-strain behavior, 276
 Stress-strain history of, 260, 285, 289
 Weld, cracks in, 445
 Severity, influence of, 260, 261
 Nuclear plants, 81
 Applications, 100, 154, 603
 Vessels, 519
 ASME Code for, 527

O

Oxidation, 119, 377, 423
 At elevated temperature, 12, 106, 195
 Carbides, 201, 206–208, 210, 211
 Cause of crack initiation, 20, 349, 367, 434
 Damage, 194, 195
 Effects of on fatigue behavior, 7, 181, 191
 Environments, 368, 369
 Increased, 13
 Of titanium, 6
 Oxygen
 Concentration, 432–434, 456
 Diffusion of, 12, 13, 21, 367
 Dissolved, 424, 438, 463
 Bulk, 466
 Penetration, 13, 367
 Water environment, 438–440, 454
 Oxygen-free high-conductivity (OFHC) copper, 502, 511, 515

P

Plastic accommodation, 46, 70, 71, 75–80
 Plastic flow, 69, 70, 99, 508, 509
 Compressive, 83
 Criteria, 79
 Rule, 506–507
 Tensile, 83

Plasticity, cyclic, 213, 401, 608
 Theories, 501–505
 Plastic shakedown, 70, 78–80
 Potential drop techniques (*see* A-c potential drop technique; D-c potential drop technique)
 Pressure, 519, 520
 Differences, 524
 Levels, 593
 Pressure vessels
 Construction of, 45, 69, 303
 Design, 585–599
 Materials data, need for, 600–610
 Fatigue of high-strength steel plates in, 297–311
 Ferritic, 462
 Nuclear, 423
 Prestrain, influence of, 625, 627, 628

R

Rankine criteria, 532, 533, 535, 537
 Reactors
 Environments, 460–479
 Liquid-metal fast breeder (LMFBR), 153
 Use of stainless steel in, 154
 Nuclear, 337
 Pressure vessel steels, 460–479
 Pressurized water, 70, 464–466, 472
 Sodium-cooled fast, 169
 Reduction of area, 309, 310
 Regulations, U.S. government, 585
 René 95, 138, 145, 146, 148, 149
 Rupture, 23, 29
 Cycles to, 35, 168
 Ductile, 190
 Due to secondary creep, 49
 Intergranular, 159, 177, 178, 181, 191
 Life, 177
 Time to, 117
 Transgranular, 159

S

Scatter bands, uniform and analyzing

S-N curves, 549–571

Applicability of, 557, 558

Service life

Of engine turbine disks, 105

Of structural steels, 614, 621

Shear decohesion model, 340, 341

Sines's theory, 485

Slip, 218–221, 223–225

S-N curves, analyzing, 549–571

Softening

Cyclic, 628

Effects, 568

Of crystals, 214–217, 224

Steel

Annealed, 47, 63, 171

Cyclic tension tests on, 49–56, 63

Austenitic, 45, 63, 101, 153, 365, 369, 527, 602

HTLCF assessment of, 169–191

Carbon, fatigue behavior of, 436–457, 587, 695

Fatigue crack initiation in, 422–435

Ferritic, 366–369, 375

Forging, low-cycle fatigue behavior of, 227–252

High-strength, 256, 265

Fatigue behavior of welded joints in, 311–336

Low-cycle fatigue behavior in, 297–310

Structural, 549–571, 615, 616

Structures, thick-walled

Effect of local strain distribution on, 614–628

Influence of structural geometry, 617–623

Type 304, 46, 56, 135, 169, 186, 187, 338, 348, 349, 352, 361, 370, 602

Type 316, 89, 137, 138, 169–171, 173, 174, 176–180, 183–189,

338, 341, 348, 349, 352, 353, 356, 361, 367–372, 602, 607, 608

And creep and cyclic tension, 45–68

Deformation, resistance to, 69–80

In fatigue relaxation, 152–168

Strain, 23, 27

Amplitude, 38, 197, 213–221, 223–225, 334, 335, 384, 385, 562, 563

Amplitude life curve, 330–332

Analysis of notches, 443–446

Biaxial, low-cycle fatigue under, 519–545

Concentration factor, 31, 35, 325

Controlled, 28, 29, 71, 100, 219–221, 314

Creep, 82, 84, 596–598

Cycle, 77, 78, 84, 218

Distribution, influence of, 614–628

Effective versus differences, 598

Elastic, 27, 136, 137, 161, 272, 317–320, 507

Energy, 23, 29, 38, 139

Evolution, maximum plastic, 87

Hardening effect, 332

Histories, 281, 287, 511–517

Increment, 513, 514

Inelastic, 84, 125, 127, 131, 136–138

Measurement, 523

Multiaxial, evaluation of, 617

Path, nonproportional, 511–515

Plastic, 27, 29, 35, 69, 82, 84, 112, 173, 214, 215, 217, 221, 224, 308, 309, 492, 493, 496, 507, 508, 596–598

Range, 10, 83, 108, 109, 156, 163, 166–168, 175, 184, 189, 201, 345, 588

Elastic, 81, 323–325, 352

Inelastic, 81, 100, 113, 115–117, 119, 123

- Partitioning (SRP), 83, 84, 106, 116–119, 120, 130–132, 135, 136, 170, 195, 590–592, 595–597
- Plastic, 10, 13, 21, 174, 188, 198, 199, 202, 325–332, 342, 343, 348, 349, 358, 368, 372, 373, 595
- Total, 111, 114, 115, 150, 602
- Versus stress range, 11
- Rate, 108, 109, 144, 156, 213, 217, 219–221, 223–225
- Recovery, 119
- Strain-age-hardening influence, 108
- Strain correction factor, 448, 451
- Strain-hardening, cyclic, 140–142, 145, 162
- Strain-life, 566, 568, 570, 571
- Strength
 - Fatigue, 28
 - Loss of, 86
 - Tensile, 106
 - Theories, 484, 485
- Stress, 23, 30, 46, 70, 76, 79, 99, 100, 109, 224, 247, 274, 276, 291, 587
- Amplitude, 70, 75, 76, 78, 262, 385, 560, 561, 602, 603
- Life curves, 335
- Variations in, 320–326
- Applied, 49, 56, 63, 87
- Bending, 576, 581, 582
- Bore, 247
- Compressive, 110, 117, 121, 125, 127, 130, 148, 215, 216
- Concentration, 23, 87, 276, 446
- Concentration factor, 35, 230, 252, 298, 323, 325, 331, 443, 550, 558, 560, 564–566, 621
- Correction factor, mean, 447, 450, 451, 453, 454
- Corrosion effect, 140, 143, 148
- Cyclic, 56, 68, 78, 165, 214, 215, 219
- Effective, cause of damage, 86–89
- Hookian, 564, 565
- In tension, ultimate, 24
- Intensity, 355–357, 362–364, 373, 375, 383, 463
- Amplitude, 594, 595
- And crack growth rate, 414–417
- Factor, 31, 34, 148, 400, 411–414, 418, 426, 427, 429, 573
- Maximum, 48, 49, 61, 63, 68, 108
- Mean, 25, 42, 44, 75, 76, 78, 94, 111, 117, 132, 147, 150, 262, 265, 437, 439, 440, 446, 447, 454, 455, 558
- Mechanical load, 592
- Nominal, 28, 231, 260, 317, 320
- Predicted, 514, 516, 517
- Prediction of, 162, 512
- Principal, 593, 594
- Range, 10, 11, 35, 91, 177
- Relaxation, 119, 161–163, 165–167, 184–186, 188–191
- Shear, 587, 588
- Tensile, 107, 108, 110, 123, 125, 127, 130, 143, 159, 183, 189, 215, 216, 587
- Yield, 46, 69, 70, 140, 231, 275, 440, 543, 558, 565, 566, 569
- Tensile strength rates, 309
- Stress-strain behavior, 89, 113, 119, 138
- At notch root, 276
- Cyclic, 110, 198, 224
- Of René 95, 107–109
- Stress-strain curves, 49, 53, 313, 314
- Cyclic, 25–27, 70, 71, 77, 78, 132, 157, 188, 189, 217, 219, 255, 260, 313, 314, 443, 447, 503, 504, 506, 509–518, 560–564, 621, 622
- Fatigue-dependent, 615, 617, 618
- Stress-strain field, 294, 339
- Stress-strain history, 254, 260, 265, 443
- Stress-strain hysteresis loop, 197, 262

- Stress-strain law, 69, 266
- Stress-strain relation, cyclic, 74, 570
- Stress-strain response, 23, 512, 516
 - Cyclic, 213–221
 - Simulation of, 275
- Striation spacing measurements, 176, 177
- Superalloys
 - Cobalt-base, 195, 352, 365
 - Creep-fatigue models for, 105–133
 - Nickel-base, 352
- T**
- Temperature effects (*see also* Deformation; Fatigue)
 - Cryogenic, 601
 - Degradation from, 597
 - High, 81–101, 609
 - Low, 608
 - On fatigue life, 13, 101, 187, 364–367
 - On fatigue resistance, 601, 603, 605
- Tensile properties, effect on fatigue performance, 307–309
- Tensile strength/yield stress ratio, 309
- Tension
 - Behavior, cyclic, 45–68
 - Compression, 519, 520
 - Repeated, 61, 70
- Tension-going frequency model (TGFM), 121
- Testing environments (*see also* Environmental effects; Oxygen)
 - Air, 10–15, 20, 237–241
 - Hydrogen (*see also* Hydrogen), 233, 234, 236, 237, 239, 241, 242
 - Vacuum, 10–13, 16, 17, 19–21
- Testing methods (*see also* Fatigue testing)
 - Baseline air, 437, 438
 - Bending, 485, 486
 - Carbon steel data, 441–443
 - Continuous cycling, 106, 108, 110, 112, 143, 144
 - Creep, 47–49, 52, 56, 76, 78, 99, 154, 188
 - Creep-creep (CC), 142
 - Creep-plasticity (CP), 142, 144–145
 - Cyclic, 98, 100
 - Loading, 47
 - Plastic deformation, 213
 - Stress-strain, 108
 - Tension, 48–56, 70
 - Dual-rate, 113, 119
 - Elastic-plastic, 350
 - Fast-fast, 142–145, 147, 148, 150
 - Fast-slow, 112, 128, 143, 146–147, 150
 - Fatigue, 23, 95, 110, 112, 123, 233, 234, 255–257, 265, 604
 - High-load, 236, 237
 - High-temperature low-cycle fatigue, 7, 12, 20
 - HSF dwell, 364
 - Low-cycle fatigue (LCF), 110, 154, 156, 157, 171, 172, 190, 230, 254–267, 297
 - Low-frequency, 79
 - Low-load, 235–236
 - Nondestructive techniques, 228, 271, 573
 - Pipe, 439, 440
 - Plane-strain, 529, 531
 - Plasticity-creep (PC), 142
 - Plasticity-plasticity (PP), 142
 - Pure plastic tension, 527, 544, 545
 - Push-pull, 361
 - Sequential fatigue, 202–207
 - Slow-fast, 112, 121, 125, 130, 143–145, 147
 - Slow-slow, 143, 148
 - Small specimen environmental, 438, 439
 - Staircase, 550
 - Strain-controlled, 98, 278, 281,

285, 303, 310, 608, 615
 Strain-hold, tensile, 110, 113, 116,
 121, 123, 125, 128, 130
 Stress-controlled fatigue, 86, 96,
 310
 Tension, 108, 544
 Thermal shock, 340, 352
 Thermomechanical, 339, 352
 Torsion, 527, 531, 544, 545
 Two-temperature, 194–211
 Ultrasonic, 228
 Verification, 110, 119–121, 123,
 128, 130, 138, 577, 581–583
 Thermal cycling and growth of short
 cracks, 337–378
 Thermal fatigue damage (*see also*
 Fatigue, high-temperature),
 194
 Thermal ratchet criteria, 79
 Thermomechanical processing (TMP)
 treatment, 106
 Time-dependent influence, 13
 Time-temperature equivalence, 164–
 167, 170
 Titanium alloy, 5–21
 Tresca equivalent strain, 527, 530,
 532, 537
 Turbines
 Disks, 105, 106

Alloy, 136, 137
 Gas, 81, 195, 337
 Steam, 422, 424

V

Viscoplastic behavior, 81, 93
 Void formation (*see also* Microvoid
 formation), 135, 139
 Von Mises criterion, 502, 532, 533,
 535, 537–545

W

Wöhler method, 28

Y

Yield
 Conditions
 Surface, 506, 507
 Tresca, 502, 503
 Von Mises, 502
 Point, 615, 617, 618, 621, 623, 628
 Strength, 13, 336, 587
 Stress (*see* Stress, yield)
 Theories, 484, 485, 487
 Zone, 344

